

**Basic Investigations on PVK-based
Photorefractive Polymers
Focussing on their Applicability as
Mass Data Storage Media**

Inaugural - Dissertation

zur

Erlangung des Doktorgrades

der Mathematisch-Naturwissenschaftlichen Fakultät

der Universität zu Köln

vorgelegt von

Reinhard Bittner

aus München

December 2003

Berichtersteller:

Prof. Dr. Klaus Meerholz
Institut für Physikalische Chemie, Lehrstuhl II
Universität zu Köln

PD Dr. Theo Woike
Institut für Mineralogie
Universität zu Köln

Tag der mündlichen Prüfung:
12. Dezember 2003

Kurzzusammenfassung

Photorefraktive (PR) Polymere gelten als vielversprechende reversible optisch-holographische Speichermedien, die eine mit den besten derzeit bekannten anorganischen Materialien vergleichbare PR Performanz aufweisen, ja diese sogar in einigen Belangen übertreffen. Zusätzlich bieten PR Polymere gegenüber anorganischen oder auch organischen PR Kristallen eine Reihe wichtiger Vorteile. Bei gleichzeitig geringen Kosten zeichnen sich PR Polymere durch hohe optische Qualität und gute Reproduzierbarkeit aus, sind strukturell flexibel, einfach herzustellen und leicht zu verarbeiten.

Im Rahmen dieser Dissertation wurden auf dem photoleitenden Polymer Poly(N-vinylcarbazol) aufbauende PR Polymere untersucht, wobei den speziellen Eigenschaften besonderes Augenmerk zuteil wurde, die eine mögliche Anwendung dieser vergleichsweise neuen Materialien als holographische Massenspeichermedien erfordern. Zu diesem Zweck wurde die Zusammensetzung des untersuchten Materialtyps systematisch variiert, ohne die Grundzusammensetzung nennenswert zu verändern, und die Materialien wurden verschiedenen experimentellen Bedingungen ausgesetzt. Dabei war das vorrangige Ziel dieser Arbeit, einen möglichst umfassenden Eindruck vom dynamischen Verhalten des untersuchten Materialtyps bezüglich Hologrammaufbau, Löschen der Hologramme, sowie Zerfall der Hologramme im Dunklen zu erhalten. Weiterhin sollten wichtige Details offen gelegt und die dahinter stehenden physikalischen Ursachen ermittelt, oder auf der Basis bekannter theoretischer Ansätze konkretisiert werden. In diesem Zusammenhang wurden auch Fragen des stationären Verhaltens der untersuchten Materialien behandelt, da sich daraus wertvolle Erkenntnisse über allgemeine Eigenschaften des PR Raumladungsfeldes bei den unterschiedlichen Materialzusammensetzungen und unter den unterschiedlichen experimentellen Bedingungen ableiten lassen, die hier untersucht bzw. verwendet wurden. Zum Abschluß wurden die allgemeinen Multiplexingfähigkeiten des untersuchten Typs PR Polymere experimentell getestet.

Mit Hilfe einer stark vereinfachten Modellrechnung wurden die allgemeinen Beugungseigenschaften eines dicken holographischen Gitters bei gleichzeitigem Auftreten starker Zweiwellenkopplung untersucht. Dabei wurde die typische geometrische Konfiguration für Beugungsexperimente an PR Polymeren zugrunde gelegt. Es konnte gezeigt werden, daß starke Zweiwellenkopplung, die eine Verbiegung der Gitterebenen des Bragg-Gitters zur Folge hat, die Beugungseigenschaften des Gitters bei entarteter Vierwellenmischung im experimentell zugänglichen Bereich nicht nennenswert beeinflußt.

Die Ausprägung der stationären und der dynamischen PR Eigenschaften der im Rahmen dieser Dissertation behandelten Materialien wurde in Abhängigkeit von der Glasktemperatur und in Abhängigkeit vom Gehalt an nichtlinear optischem Farbstoff erforscht. Dabei wurde festgestellt, daß der reduzierten Temperatur eine entscheidende Bedeutung zukommt. Die reduzierte Temperatur ist die Glasktemperatur bezogen auf die Umgebungstemperatur als Nullpunkt. Es wurde beobachtet, daß die stationäre PR Performanz der Materialien mit hohem Farbstoffgehalt in Abhängigkeit von der reduzierten Temperatur ein absolutes Maximum durchläuft. Dies konnte auf den Einfluß zweier gegenläufiger Effekte zurückgeführt werden. Einerseits wird in Richtung abnehmender reduzierter Temperatur die Orientierungsbeweglichkeit der Farbstoffmoleküle in der Polymermatrix größer und deren Ausrichtung entlang des Summenvektors der elektrischen Felder in einem PR Polymer erleichtert. Somit sind kleinere externe elektrische Felder erforderlich, um ein gegebenes Maß an elektrischer Polung des Materials zu erreichen. Andererseits nimmt das PR Raumladungsfeld in Richtung abnehmender reduzierter Temperatur ab, sobald die reduzierte Temperatur negativ

wird. Dies ist eine Folge langsamer langreichweitiger Konformationsänderungen der Polymermatrix, die dazu führen, daß sich die energetischen Positionen der einzelnen molekularen Einheiten, die sich für den Ladungsträgertransport verantwortlich zeichnen, ständig verändern. Da diese molekularen Einheiten zugleich auch potentielle Ladungsträgerfallen repräsentieren, werden darin gefangene Ladungsträger wieder freigelassen, wenn die obengenannte Änderung der energetischen Position zu einer Verringerung der energetischen Tiefe der betroffenen Falle führt. Im Mittel wird dadurch die effektive Anzahldichte an PR Ladungsträgerfallen und damit das PR Raumladungsfeld reduziert. Um diesen Effekt zu kompensieren, muß das externe Feld erhöht werden um eine gegebene PR Brechungsindexmodulation zu erreichen. Es läßt sich ableiten, daß dieses Wechselspiel der zwei vorgenannten gegenläufigen Effekte prinzipiell nicht vom Farbstoffgehalt abhängt, jedoch für verschiedene Farbstoffgehalte unterschiedlich gewichtet ist, so daß ein Optimum der PR Performanz für alle untersuchten Farbstoffkonzentrationen zu erwarten ist, auch wenn es bei den Materialien mit geringem Farbstoffgehalt im experimentell untersuchten Bereich nicht mehr nachgewiesen werden konnte.

In Bezug auf das dynamische Verhalten der untersuchten Materialien ergab sich, daß die Geschwindigkeit des Hologrammaufbaus bei positiver reduzierter Temperatur durch die Orientierungsbeweglichkeit der Farbstoffmoleküle innerhalb der Polymermatrix begrenzt wird und demzufolge mit steigender reduzierter Temperatur abnimmt. In diesem Bereich hängt die Geschwindigkeit des Hologrammaufbaus außerdem stark vom Farbstoffgehalt ab: sie sinkt mit steigender Konzentration an Farbstoffmolekülen. Dieser Effekt läßt sich durch eine gegenseitige Behinderung der Farbstoffmoleküle während der Orientierung im anliegenden elektrischen Summenfeld erklären, die mit steigender Farbstoffkonzentration an Bedeutung gewinnt ("Backstein"-Effekt). Im Bereich negativer reduzierter Temperaturen wird die Dynamik der Materialien von der Dynamik des PR Raumladungsfeldes bestimmt. Dementsprechend läßt sich dann auch keine Abhängigkeit vom Farbstoffgehalt beobachten.

Außerdem wurden Experimente zum Einfluß der Sensibilisatorkonzentration auf das stationäre und das dynamische photorefraktive Verhalten des untersuchten Materialtyps durchgeführt. Diese lieferten insbesondere wertvolle Informationen zu den Ladungsträgerfallen, die zum PR Effekt beitragen. Es ergaben sich eindeutige Hinweise, daß in PR Polymeren zwei grundsätzlich verschiedene Typen von Ladungsträgerfallen auftreten, nämlich konformative Fallen, die im unbesetzten Zustand elektrisch neutral sind, und Coulomb-Fallen, die im unbesetzten Zustand entgegengesetzt zur beweglichen Ladungsträgersorte geladen sind. Erstere sind von Anfang an vorhanden, und ihre Anzahldichte hängt nicht von der Konzentration an Sensibilisatormolekülen ab. Die Anzahldichte der Coulomb-Fallen dagegen hängt systematisch von der Sensibilisatorkonzentration ab, was eine Zuordnung dieser Fallen zu ionisierten Sensibilisatormolekülen erlaubt. Diese Fallen werden erst erzeugt, während das Hologramm geschrieben wird, ihre Anzahldichte ist also zusätzlich zeitabhängig. Die Gesamtzahl aktiver Ladungsträgerfallen für den PR Prozeß ergibt sich aus der Summe beider Fallentypen und nimmt daher für gegebene Betriebsbedingungen mit steigender Sensibilisatorkonzentration zu. Dies führt ab einer gewissen Mindestkonzentration an Sensibilisatormolekülen einerseits zu einer verbesserten stationären PR Performanz, jedoch andererseits zugleich zu einem komplizierteren Ansprechverhalten der Materialien. Schließlich wurden deutliche Anzeichen dafür gefunden, daß die Aufbaudynamik des PR Raumladungsfeldes in den untersuchten Materialien von der Beweglichkeit der freien Ladungsträger bestimmt wird und nicht von deren Erzeugungsrate. Diese Aussage ist gültig für typische Sensibilisatorkonzentrationen in PR Polymeren, wogegen davon auszugehen ist, daß es eine untere Konzentrationsschwelle gibt, ab der die Erzeugungsrate den Ausschlag gibt.

Unter Berücksichtigung verschiedener Glasktemperaturen wurde ferner das Löschverhalten von photorefraktiven Brechungsindexgittern in Materialien des untersuchten Typs eingehend untersucht. Als geschwindigkeitsbestimmende Schritte für den Löschvorgang der Hologramme ergaben sich bei positiven reduzierter Temperaturen (d.h. die Glasktemperatur ist größer als die Umgebungstemperatur) erneut die dipolare Relaxation der Materialien und bei negativen reduzierter Temperaturen wiederum die Dynamik (d.h. hier der Abbau) des PR Raumladungsfeldes. Bei allen untersuchten Materialien wurde eine ausgeprägte Korrelation zwischen der Löschdynamik und der Schreibdauer der Hologramme gefunden, wobei der Löschvorgang bei länger geschriebenen Hologrammen langsamer verlief. Im Falle positiver reduzierter Temperaturen läßt sich dieses Verhalten damit erklären, daß die Polymermatrix unter dem Einfluß der bei der Reorientierung der Farbstoffmoleküle auftretenden inneren Spannung viskos zu fließen beginnt. Das Ausmaß der dadurch beim Schreiben der Hologramme auftretenden Änderung der inneren mechanischen Struktur nimmt mit der Schreibzeit zu und muß beim Löschen weitestgehend revidiert werden, was zu einer schreibzeitabhängigen Löschdynamik führt. Im Falle negativer reduzierter Temperaturen konnte bewiesen werden, daß die optische Aktivierung von tiefen Fallenzuständen für die beobachtete Verlangsamung des Löschprozeß in Abhängigkeit zunehmender Schreibdauer der Hologramme verantwortlich zu machen ist. Es konnten zwei grundsätzlich verschiedene Typen von optisch aktivierten Ladungsträgerfallen identifiziert werden, nämlich erneut Coulomb-Fallen und elektrisch neutrale Fallenzustände. Von diesen bestimmen erstere die Löschgeschwindigkeit der Hologramme zu Anfang des Löschvorganges, während sich letztere für die langsame Komponente des Löschvorganges verantwortlich zeichnen.

Während das Auftreten von optisch aktivierten Coulomb-Fallen bereits zuvor gezeigt wurde und somit zu erwarten war, überraschte der Befund optisch aktivierter neutraler Fallenzustände und wurde daher eingehender betrachtet. Die ermittelten Eigenschaften dieser Fallenzustände legen die Annahme nahe, daß es sich um Carbazol Dimere handeln könnte, deren optische Aktivierung indirekt erfolgt, d.h sie bilden sich erst in Anwesenheit eines optisch erzeugten freien Ladungsträgers und liegen im gefüllten Zustand als Radikalkationen vor. Wird eine solche Falle geleert, löst sich der Fallenzustand vollständig auf. Entscheidende Indikatoren für diese Annahmen sind die experimentellen Befunde einer vollständigen Reversibilität der optischen Aktivierung und eine ausgeprägte Abhängigkeit des Prozesses der optischen Aktivierung von der reduzierten Temperatur. Mit Hilfe der bereits besprochenen langreichweitigen Konformationsänderungen der Polymermatrix bei negativen reduzierten Temperaturen würden solche Fallenzustände mechanisch zerstört.

Zuletzt konnte gezeigt werden, daß von der Existenz einer optimalen reduzierten Temperatur für die Anwendung der untersuchten Materialien für holographisches Multiplexen auszugehen ist.

Auf Basis der Erkenntnisse der vorangehenden Untersuchungen wurden die untersuchten Materialien mit extrinsischen tiefen Ladungsträgerfallen für Löcher dotiert, um eine Stabilisierung der Löschdynamik zu erreichen. Jedoch zeigten die so modifizierten, neuartigen Materialien ein noch komplizierteres Löschverhalten. Es wurde festgestellt, daß die photorefraktive Brechungsindexmodulation (d.h. die Stärke des Hologrammes) bei Anwendung von kurzen Schreibzeiten und geringer Lichtenergie in der Anfangsphase des Löschprozesses weiter zunimmt. Diese Ergebnisse konnten phänomenologisch gedeutet werden, wobei die besonderen Ladungstransporteigenschaften fallendotierter ungeordneter organischer Festkörper und die spezifische räumliche Verteilung der elektrischen Felder in einem PR Gitter in Betracht gezogen wurden. Mit Hilfe dieses phänomenologischen Modells konnten auch alle weiteren experimentellen Beobachtungen qualitativ erklärt werden, die in Bezug auf die fallendotierten Materialien gemacht wurden.

Ferner wurde der Dunkelzerfall von Hologrammen in den untersuchten Materialien eingehend untersucht. Dabei wurden sowohl unterschiedliche reduzierte Temperaturen berücksichtigt als auch Materialien mit und ohne Dotierung mit extrinsischen tiefen Ladungsträgerfallen. Im Rahmen des untersuchten Bereiches sowohl negativer als auch positiver reduzierter Temperaturen wurde als geschwindigkeitsbestimmender Schritt im Dunkelzerfall der Hologramme in allen Fällen der Zerfall des PR Raumladungsfeldes identifiziert. Ferner konnte gezeigt werden, daß die Phasenverschiebung zwischen dem hologrammerzeugenden Interferenzmuster und dem PR Gitter für die Geschwindigkeit des Dunkelzerfall der Hologramme von herausragender Bedeutung ist. Die Dunkelzerfallsgeschwindigkeit der Hologramme wird mit zunehmender Phasenverschiebung deutlich verlangsamt. Dieses Ergebnis ist von besonderer Bedeutung, da es für bildinformationstragende Hologramme einen inhomogenen Dunkelzerfall impliziert.

Schließlich wurde experimentell untersucht, ob holographisches Multiplexen mit Materialien des untersuchten Typs generell möglich ist. Dazu wurde ein erweiterter numerischer Formalismus für einen Belichtungsplan für holographisches Multiplexen entwickelt, der den Besonderheiten des dynamischen Verhaltens der untersuchten holographischen Speichermedien Rechnung trägt. Anhand von peristrophischen Multiplex-Experimenten konnte gezeigt werden, daß die untersuchten Materialien holographisches Multiplexen zwar grundsätzlich zulassen, jedoch mit schwerwiegenden Mängeln bezüglich eines möglichen Einsatzes als Speichermedium in holographischen Massenspeichern behaftet sind.

Zusammenfassend läßt sich feststellen, daß die Materialien des untersuchten Typs als Speichermedien in holographischen Massenspeichern nicht anwendbar sind. Dies ist hauptsächlich auf ihr kompliziertes und für Massenspeicher unvorteilhaftes dynamisches Verhalten zurückzuführen, das eine inhärente Eigenschaft des untersuchten Materialtyps oder gar der gesamten Materialklasse zu sein scheint und eine sinnvolle Anwendung holographischer Multiplex-Techniken vereitelt. Darüberhinaus sind sowohl die vergleichsweise kurze Dunkelspeicherzeit als auch das inhomogene Dunkelzerfallsverhalten informationstragender Hologramme für einen holographischen Massenspeicher ungeeignet. Stattdessen könnte diese Klasse von optischen Speichermaterialien als Medium für flüchtige holographische Speicher Anwendung finden (Echtzeit-Anwendungen). Beispiele hierfür wären Anwendungen als assoziative Speicher, als holographische Pufferspeicher, oder als Speichermedium für zeitgetaktete holographische Bilderzeugung (TGHI, time gated holographic imaging).

Abstract

Photorefractive (PR) polymers are considered as highly promising reversible optical holographic storage media, which compete and in some aspects even surpass the performance of the best currently known PR inorganic materials. In contrast to inorganic or organic PR crystals, PR polymers offer significant advantages like good optical quality, high structural flexibility, good reproducibility, easy processing and low cost.

In the frame of this work poly(N-vinylcarbazole)-based PR polymer composites were investigated focussing on the particular features required for a potential application of this relatively new class of materials as optical holographic storage media in mass data storage devices. Therefore, the composition of the investigated type of material was systematically altered, and various experimental conditions were applied. The main objective of this work was to get a more detailed insight into and a better understanding of the dynamic recording, erasure and dark decay behavior of holograms in this type of PR polymer. Steady-state performance issues were also addressed as they yield important information on the general properties of the PR space-charge field for the varying material compositions and experimental conditions applied. Finally, the general holographic multiplexing capabilities of the investigated type of material were examined.

By means of a simplified model calculation the general diffraction properties of a hologram in PR polymers in the presence of strong beam coupling were examined. It could be proven that hologram bending due to strong beam coupling does not notably affect the diffraction properties of a holographic grating in organic PR devices within the range of the externally applied field experimentally possible.

The dependence of the steady-state and the dynamic PR performance of the considered materials on the glass-transition temperature as well as on the doping level of electro-optic chromophores was investigated. The reduced temperature, which is the glass-transition temperature relative to the ambient temperature, was identified as a factor of outstanding importance. A steady-state performance optimum in the highly-doped materials as a function of the reduced temperature was observed, which is a result of two counteracting effects: On the one hand, the orientational mobility of the chromophores increases with decreasing reduced temperature, leading to a reduction of the external field required to achieve a certain degree of electrical poling. On the other hand, for negative and further decreasing reduced temperatures the PR space-charge field is more and more reduced as a result of a decrease of the effective PR trap density due to slow collective motion of the photoconducting polymer matrix. The hologram build up speed was found to be limited by the orientational mobility of the electro-optic chromophores for positive reduced temperatures. In this regime, the grating build-up time also depends strongly on the chromophore density due to sterical effects. For negative reduced temperature the formation of the space-charge field was identified as the rate-limiting step in the onset dynamics of the refractive index modulation. In this regime the chromophore doping level turned out to be insignificant for the hologram build-up dynamics.

Considering the influence of the sensitizer concentration on the steady-state and the dynamic PR behavior of the investigated type of materials, strong indication was found that the active PR trap manifold consists of conformational traps on the one hand and of coulombic traps formed by charged sensitizers on the other. The first exist ab initio and their number density does not depend on the sensitizer content. The latter are formed during the grating recording process (i.e., their number density is a function of time) and add to the conformational traps. This leads to improved steady-state PR performance on the one hand but to a more complicated build-up dynamics of the hologram on the other. Both effects are not observed until a certain threshold concentration of sensitizer moieties is provided. Furthermore, strong indication was

found that the hologram build-up dynamics in the investigated type of PR polymers is limited by the charge carrier mobility as long as the sensitizer concentration is not too low.

The general erasure behavior of PR gratings in the considered type of materials was investigated in detail taking into account different glass-temperatures. In general the PR grating erasure was found to be determined by the relaxation dynamics of the orientational order of the chromophores for the case of positive reduced temperatures (i.e., for glass-transition temperatures above the ambient temperature), whereas the decay of the PR space-charge field governed the hologram erasure dynamics in the case of negative reduced temperatures. For all materials investigated, a strong correlation between the erasure dynamics of a hologram and its corresponding recording time was observed. In all cases, the grating erasure process was found to slow down as a function of increasing recording time. For positive reduced temperatures this can be attributed to a viscous flow of the polymer matrix, whereas optical activation of trapping sites was identified to cause this effect, if the reduced temperature is negative. Two fundamentally different types of optically activated traps could be identified, which are coulombic traps ruling the initial grating erasure and deep traps of non-coulombic nature ruling the erasure behavior on longer time scale. The latter trap species might be carbazole dimer radical cations. It could be shown that an optimum reduced temperature must be anticipated for a potential application of the investigated materials in holographic multiplexing.

Doping the investigated materials with large amounts of extrinsic deep traps in an attempt to stabilize the erasure dynamics led to an even more complicated erasure behavior. Applying short recording times and low recording as well as low erasure intensity, a further increase of the hologram strength was observed during the initial erasure process. A phenomenological mechanistic picture of the recording and the erasure process of a hologram in a material showing trap controlled charge transport was developed taking into account the spatial distribution of electrical fields within the PR grating. This model can qualitatively explain the experimental observations made for this novel type of material.

The dark decay of holograms in the considered materials was investigated in detail taking into account different glass-transition temperatures as well as extrinsic trap doping. Within the range of reduced temperatures investigated (i.e., even for positive reduced temperatures) the dark decay was found to be governed by the decay of the PR space-charge field. Furthermore, the phase shift of the PR grating turned out to be a crucial parameter yielding fast dark decay for small PR phase shifts, whereas the dark decay was increasingly retarded as the phase shift became larger.

Eventually the general feasibility of holographic multiplexing in the investigated type of materials was investigated. An expanded numerical formalism for a multiplexing exposure schedule was devised, which accounts for the complicated dynamic behavior of the type of holographic storage media investigated. By means of peristrophic multiplexing experiments the general feasibility of holographic multiplexing in the investigated materials could be demonstrated as well as the shortcomings of this new class of materials for potential application as storage medium in mass data storage devices.

In conclusion, the investigated type of holographic storage medium was found to be inapplicable in holographic mass data storage devices. This is mainly due to the complicated and unfavorable dynamic behavior, which appears to be an inherent feature of the investigated type of material, or possibly even the entire class of materials, and which prevents a reasonable application of holographic multiplexing techniques as well as long time storage. However, this class of holographic storage materials may find application in any kind of volatile holographic storage like, among others, associative memories, buffer holograms, or time gated holographic imaging.

CONTENTS

<u>1.) Introduction</u>	1
<u>2.) Theory</u>	4
2.1.) Theoretical aspects of elementary optics	4
2.1.1.) The electro-magnetic theory of light	4
2.1.2.) Superposition of electro-magnetic waves	8
2.1.2.1.) Polarization	8
2.1.2.2.) Interference	10
2.1.2.3.) Coherence	12
2.1.2.4.) Phase- and group-velocity	13
2.1.2.5.) Diffraction	14
2.1.2.5.1.) The Huygens-Fresnel principle	15
2.1.2.5.2.) Fraunhofer and Fresnel diffraction	15
2.1.3.) Light in linear media	16
2.1.3.1.) Material equations	16
2.1.3.2.) The oscillator model (Lorentz-model)	17
2.1.3.3.) Loss-free and lossy media	19
2.1.3.3.1.) Energetic considerations	19
2.1.3.3.2.) Loss-free media	20
2.1.3.3.3.) Lossy media	21
2.1.4.) Reflection and refraction	22
2.1.4.1.) Phenomenological treatment of reflection and refraction	23
2.1.4.1.1.) Fermat's least-time principle	23
2.1.4.1.2.) Reflection law and Snellius' refraction law	24
2.1.4.2.) The electro-magnetic approach to reflection and refraction	25
2.1.4.2.1.) Fresnel's equations	25
2.1.4.2.2.) Interpretation of Fresnel's equations	27
2.1.4.3.) Uniaxial birefringence	29
2.1.4.3.1.) Optical axis	29
2.1.4.3.2.) Phenomenology of uniaxial birefringence	30
2.1.4.3.3.) Wave and beam velocity	30
2.1.4.3.4.) Beam refractive index	32
2.1.4.3.5.) Wave refractive index	33
2.1.4.3.6.) Wave propagation in anisotropic media - the index ellipsoid	35
2.1.4.4.) Bragg diffraction	38
2.2.) Basic aspects of non-linear optics	40
2.2.1.) Nonlinear interaction between light and matter	40
2.2.1.1.) Nonlinear polarization	42
2.2.1.2.) Kleinman's symmetry rule	43
2.2.2.) Electro-optic effects	44
2.2.2.1.) Pockels effect	45
2.2.2.2.) Kerr effect	46
2.2.3.) Degenerate four wave mixing and NLO phase matching	47
2.2.4.) Photorefraction	49
2.3.) Holography	50

2.3.1.)	<i>The holographic process</i>	50
2.3.1.1.)	Holographic recording and retrieval	51
2.3.1.2.)	Types of holograms	52
2.3.2.)	<i>Coupled wave theory for thick hologram gratings</i>	53
2.3.2.1.)	The coupled-wave equations	53
2.3.2.1.1.)	<i>s-Polarization</i>	53
2.3.2.1.2.)	<i>p-Polarization</i>	56
2.3.2.2.)	Solution of the coupled wave equations	57
2.3.2.3.)	Transmission holograms	58
2.3.2.3.1.)	<i>Loss-free phase grating</i>	59
2.3.2.3.2.)	<i>Lossy phase grating</i>	59
2.3.3.)	<i>Holographic data storage</i>	60
2.3.3.1.)	The principle of holographic data storage	60
2.3.3.2.)	Holographic multiplexing	61
2.3.3.2.1.)	<i>The principle of holographic multiplexing</i>	61
2.3.3.2.2.)	<i>Holographic multiplexing methods</i>	63
2.3.3.3.)	System metrics for holographic multiplexing in erasable media	65
2.3.3.3.1.)	<i>The exposure schedule</i>	66
2.3.3.3.2.)	<i>The M-number (M/#)</i>	68
2.4.)	Physical aspects of organic polymers	70
2.4.1.)	<i>Relaxation and thermodynamics in polymers</i>	70
2.4.1.1.)	Phenomenology of viscoelastic transitions	71
2.4.1.2.)	Static and dynamic glass-transition temperatures	73
2.4.1.3.)	Theoretical approaches to the glass-transition	74
2.4.1.3.1.)	<i>Free-volume theory</i>	74
2.4.1.3.2.)	<i>Thermodynamic approaches</i>	78
2.4.1.3.3.)	<i>General trends in influencing the glass-transition temperature</i>	79
2.4.1.4.)	Viscoelastic response in a creep-relaxation experiment	81
2.4.1.5.)	Physical aging	82
2.4.2.)	<i>Electrical poling of organic polymers - the oriented gas model</i>	83
2.4.2.1.)	Steady-state solutions of the oriented gas model	85
2.4.2.1.1.)	<i>Steady-state distribution function</i>	85
2.4.2.1.2.)	<i>Linear optical properties of poled polymers</i>	87
2.4.2.1.3.)	<i>Nonlinear optical properties of poled polymers</i>	89
2.4.2.1.4.)	<i>Local field correction</i>	91
2.4.2.2.)	Transient solutions of the oriented gas model	92
2.4.2.2.1.)	<i>Turning on the poling field</i>	94
2.4.2.2.2.)	<i>Turning off the poling field</i>	95
2.4.3.)	<i>Electrical conduction in organic polymers</i>	95
2.4.3.1.)	Space-charge-limited currents	96
2.4.3.2.)	Basic charge transport models for organic polymers	99
2.4.3.2.1.)	<i>Empirical description of the electrical conduction in disordered organic solids</i>	100
2.4.3.2.2.)	<i>The polaron model</i>	102
2.4.3.2.3.)	<i>The Baessler formalism (disorder model)</i>	104
2.4.3.2.4.)	<i>Concentration and matrix dependence</i>	105
2.4.3.2.4.1.)	<i>Homogenous lattice gas concept</i>	105
2.4.3.2.4.2.)	<i>The percolation model</i>	106
2.4.3.3.)	Dispersive charge transport	108

2.4.3.3.1.) <i>The Einstein relationship</i>	108
2.4.4.)<i>Charge generation and recombination in organic polymers</i>	109
2.4.4.1.) <i>Onsager formalism</i>	110
2.4.4.2.) <i>The situation in organic polymers</i>	112
2.4.4.2.1.) <i>Important Onsager based models</i>	113
2.4.4.3.) <i>Langevin theory of geminate recombination</i>	115
2.5.)<i>The photorefractive effect</i>	118
2.5.1.)<i>Phenomenology of the photorefractive effect</i>	118
2.5.2.)<i>The photorefractive effect in inorganic crystals</i>	119
2.5.2.1.) <i>The band-transport model of the photorefractive effect (Kukhtarev-model)</i>	119
2.5.2.1.1.) <i>Steady-state solution for the space-charge field</i>	120
2.5.2.1.2.) <i>Dynamics of the space-charge field</i>	121
2.5.2.1.2.1.) <i>Build-up dynamics</i>	121
2.5.2.1.2.2.) <i>Erasure dynamics</i>	122
2.5.3.)<i>Photorefractivity in amorphous organic polymers</i>	122
2.5.3.1.) <i>Limitations of Kukhtarev's model</i>	123
2.5.3.2.) <i>Schildkraut's model</i>	124
2.5.3.2.1.) <i>Steady state solutions for the space-charge field in polymers</i>	125
2.5.3.2.2.) <i>Build-up dynamics for the space-charge field in polymers</i>	126
2.5.3.2.3.) <i>Erasure dynamics of the space-charge field in polymers</i>	127
2.5.3.2.3.1.) <i>Erasure dynamics in Schildkraut's model</i>	127
2.5.3.2.3.2.) <i>Cui's approach to the erasure dynamics</i>	128
2.5.3.3.) <i>Orientalional enhancement effect</i>	131
2.5.3.3.1.) <i>First order grating</i>	135
2.5.3.3.2.) <i>Second order grating</i>	136
2.5.3.3.3.) <i>The enhancement - a comparison</i>	136
2.5.3.4.) <i>PR refractive index modulation in low-Tg PR polymers</i>	138
2.5.4.)<i>Photorefractive two-wave mixing</i>	138
2.5.4.1.) <i>Phenomenology of two-beam coupling</i>	139
2.5.4.2.) <i>Theoretical formulation of two-beam coupling</i>	141
2.5.5.)<i>Photorefractive characterization parameters and figures of merit</i>	145
2.5.5.1.) <i>Figures of merit for purely electro-optic PR materials</i>	145
2.5.5.2.) <i>A figure of merit for orientationally enhanced PR materials</i>	147
2.5.5.3.) <i>Photorefractive sensitivity</i>	148
<u>3.) Photorefractive polymers</u>	150
3.1.)<i>General requirements</i>	151
3.1.1.)<i>Performance issues</i>	151
3.1.1.1.) <i>Dynamic range</i>	151
3.1.1.2.) <i>Photorefractive response time</i>	152
3.1.1.3.) <i>The PR sensitivity</i>	154
3.1.1.4.) <i>The PR phase shift and the PR gain</i>	154
3.2.)<i>Material concepts and approaches - a brief survey</i>	155
3.2.1.)<i>Gels</i>	155
3.2.2.)<i>Liquid crystalline systems</i>	156
3.2.3.)<i>Low molecular mass glasses</i>	157

3.2.4.) Monolithic polymers	160
3.2.5.) Polymer composites	164
3.2.5.1.) Milestones	165
3.2.5.2.) General problems	166
3.2.5.2.1.) Miscibility	167
3.2.5.2.2.) Absorption and the problem of isomerization gratings	167
3.2.5.2.3.) Relation of the energy levels of the components	167
3.2.5.3.) The polymer matrix	168
3.2.5.4.) The plasticizer	169
3.2.5.5.) The chromophore	170
3.2.5.5.1.) Bond-length alternation (BLA) model and related approaches	171
3.2.5.5.2.) Characteristic examples	173
3.2.5.6.) The sensitizer	176
<u>4.) Experimental techniques and general evaluation</u>	178
4.1.) Preparation of materials and sample structure	179
4.2.) Wave mixing experiments	181
4.2.1.) General wave mixing setup configuration and parameters	181
4.2.1.1.) Experimental wave mixing setup and equipment	181
4.2.1.1.1.) 2BC setup	183
4.2.1.1.2.) DFWM setup	184
4.2.1.1.3.) Wave mixing measurement circuitry	185
4.2.1.2.) Two-beam-coupling (2BC)	186
4.2.1.2.1.) 2BC measurement procedures	186
4.2.1.2.2.) Evaluation of the 2BC experiments	188
4.2.1.2.2.1.) Basic equations for evaluation of the 2BC experiments	188
4.2.1.2.2.2.) Consideration of systematic errors in the 2BC experiments	190
4.2.1.2.2.3.) 2BC evaluation procedure	192
4.2.1.3.) Degenerate four-wave-mixing (DFWM)	193
4.2.1.3.1.) DFWM measurement procedures	193
4.2.1.3.2.) Evaluation of the DFWM experiments	195
4.2.1.3.2.1.) Basic equations for evaluation of the DFWM experiments	195
4.2.1.3.2.2.) Simplification of Kogelnik's equation and error discussion	196
4.2.1.3.2.3.) DFWM evaluation procedure	197
4.2.1.4.) Polarization anisotropy for PR wave mixing experiments	199
4.2.1.5.) Holographic multiplexing experiments	201
4.2.1.5.1.) Experimental holographic multiplexing setup, sample holder and measurement procedure	201
4.2.1.5.2.) Evaluation of the peristrophic multiplexing experiments	203
4.2.1.6.) Intensity determination	204
4.2.1.7.) Isomerization gratings	205
4.3.) Transmission ellipsometric experiments	207
4.3.1.) Experimental transmission ellipsometry setup and procedure	207
4.3.1.1.) Evaluation of the transmission ellipsometric experiments	208

5.) Results	211
5.1.) Influence of hologram bending on the diffraction efficiency in PR thin film devices: A simple model calculation	214
5.1.1.) <i>The simulation model</i>	214
5.1.2.) <i>Simulation parameters</i>	218
5.1.3.) <i>Results and discussion of the diffraction efficiency simulations</i>	220
5.1.4.) <i>Quintessence of the diffraction efficiency simulations</i>	225
5.2.) The PR performance of PVK based polymer composites at varying glass-transition temperatures	226
5.2.1.) <i>Experimental aspects</i>	226
5.2.2.) <i>The relation between the glass-transition temperature and the steady-state performance in PVK based PR polymers</i>	228
5.2.2.1.) Experimental results on the T _g dependence of the steady-state PR performance	229
5.2.2.2.) Discussion of the T _g dependence of the steady-state PR performance	233
5.2.2.3.) Quintessence of the investigations on the steady-state performance at varying glass-transition temperatures	242
5.2.3.) <i>The relation between the glass-transition temperature and the dynamic performance in PVK based PR polymers</i>	243
5.2.3.1.) Theoretical consideration of the relaxation dynamics in poled polymers	244
5.2.3.2.) Experimental results on the T _g dependence of the build-up dynamics of PR gratings in polymers	249
5.2.3.3.) Discussion of the T _g dependence of the dynamic PR performance	252
5.2.3.4.) Summary of the investigations on the build-up dynamics of PR gratings at varying glass-transition temperatures	255
5.3.) The influence of the sensitizer concentration on the PR performance of PVK based polymer composites	257
5.3.1.) <i>Experimental aspects</i>	257
5.3.2.) <i>Experimental results on the sensitizer concentration dependence of the PR performance</i>	259
5.3.3.) <i>Discussion of the influence of the sensitizer concentration on the PR performance in polymers</i>	262
5.3.4.) <i>Conclusions from the influence of the sensitizer concentration on the PR performance</i>	270
5.4.) The erasure behavior of PR gratings in PVK based polymer composites	271
5.4.1.) <i>PR grating erasure in systems without extrinsic deep traps</i>	272
5.4.1.1.) Experimental aspects	273
5.4.1.2.) Results of the PR grating erasure experiments in systems without extrinsic deep traps	274
5.4.1.3.) Discussion of the erasure behavior of PR polymers without extrinsic deep traps	281
5.4.1.3.1.) <i>Discussion of the ellipsometric experiments</i>	281

5.4.1.3.2.)	<i>Discussion of the DFWM experiments</i>	283
5.4.1.3.3.)	<i>Experimental verification of optical trap activation</i>	285
5.4.1.3.4.)	<i>A theoretical approach to PR space-charge field erasure</i>	289
5.4.1.3.5.)	<i>Discussion of the relation between the PR trap situation and PR grating erasure</i>	291
5.4.1.3.6.)	<i>Conclusions on the nature of the PR traps</i>	296
5.4.1.3.7.)	<i>The impact on holographic multiplexing in PR polymers</i>	297
5.4.1.4.)	<i>Quintessence of the investigations on the PR grating erasure in systems without extrinsic deep traps</i>	299
5.4.2.)	<i>PR grating erasure in systems doped with extrinsic traps</i>	300
5.4.2.1.)	<i>Experimental aspects</i>	301
5.4.2.2.)	<i>Experimental results on PR grating erasure in trap-doped systems</i>	302
5.4.2.3.)	<i>Discussion of the PR grating erasure in the trap-doped polymer composites</i>	309
5.4.2.3.1.)	<i>The PR recording process in the trap-doped systems</i>	311
5.4.2.3.2.)	<i>The PR erasure process in the trap-doped systems</i>	312
5.4.2.3.3.)	<i>The dependence on the erasure intensity</i>	314
5.4.2.3.4.)	<i>The dependence on the applied electrical field</i>	314
5.4.2.4.)	<i>Summary of the investigations on the PR erasure behavior of trap-doped polymers</i>	315
5.5.)	<i>Dark decay of PR gratings in PVK-based polymer composites</i>	317
5.5.1.)	<i>Experimental aspects</i>	317
5.5.2.)	<i>Results of the dark decay experiments</i>	319
5.5.3.)	<i>Discussion of the dark decay behavior</i>	322
5.5.4.)	<i>Quintessence of the investigations on the PR dark decay behavior</i>	327
5.6.)	<i>Holographic multiplexing in PVK based PR polymers</i>	329
5.6.1.)	<i>Experimental aspects</i>	329
5.6.2.)	<i>Theoretical considerations - derivation of a suitable multiplexing schedule</i>	330
5.6.3.)	<i>Results and discussion of the holographic multiplexing experiments</i>	332
5.6.4.)	<i>Conclusions from the holographic multiplexing experiments in PR polymers</i>	337
<u>6.)</u>	<u>Summary and Conclusion</u>	338
<u>References</u>		343
<u>Appendix A:</u>	<u>Overview of selected PR holographic storage materials</u>	A1
<u>Appendix B:</u>	<u>Source code for the numerical simulations in 5.1.)</u>	B1-B2
<u>Appendix C:</u>	<u>Frequently used abbreviations</u>	C1-C2
<u>Appendix D:</u>	<u>Chemical structures</u>	D1-D8
<u>Appendix E:</u>	<u>The Baessler formalism (disorder model)</u>	E1-E8
<u>Appendix F:</u>	<u>Dispersive charge transport in disordered organic solids</u>	F1-F7
<u>Appendix G:</u>	<u>Theoretical treatment of the photorefractive effect in crystals</u>	G1-G10
<u>Appendix H:</u>	<u>Theoretical treatment of the photorefractive effect in polymers</u>	H1-H12
<u>List of publications</u>		
<u>Acknowledgements</u>		

1.)Introduction

The human society of the 20. century was formed by the achieved enormous technical and scientific progress. In particular, traffic engineering, which dramatically facilitated the covering of long distances, has been a key technology enabling the development of an industrialized human society. A traffic infrastructure has been built, which is still the basis of welfare and success in the industrialized countries. Therefore, the twentieth century is often referred to as the “age of transportation”. However, within the past decade information technology has emerged as the new key technology, which is going to form the human society of the 21. century. A new infrastructure, known as the “Internet”, has emerged, which enables the transportation, processing and storage of information. Thus, today’s human society and the current era are already referred to as the “modern information society” and the “age of information”, respectively.

The amount of digital data to be transported, processed and stored worldwide has recently been estimated to be in order of magnitude of 10^{20} Bits (12 Exabytes) and is expected to increase exponentially in the future [1]. Therefore, great research and engineering efforts have been made in order to provide sufficiently powerful technologies, which can be expected to be able to handle such an enormous amount of data.

These efforts already led to the introduction of optical technologies in digital communication. Today’s optical fibre digital communication technologies enable transmission bandwidths of several tens of Gigabits per second and have been the technological basis for the rapid development of the Internet during the last decade. Today it is a matter of course that (almost) everybody can easily connect to the Internet and down- or upload Megabytes of data within minutes. Only ten years ago this was mere fiction.

In data storage technologies the Compact Disc (CD) and the Digital Versatile Disc (DVD) are state of the art for removable read only digital data storage media. On both media data is stored optically in two dimensions (on DVD’s additionally on multiple layers). The storage densities of these media is physically limited by the optical diffraction limit for a single recording spot. Up to 2×10^9 Bits/cm² may theoretically be achieved utilizing blue laser light of 480nm. Today’s optical disk drives, however, still work with red laser light of about 650nm wavelength, which quarters the maximum achievable storage density. Despite there are ‘rewritable’ CD’s and DVD’s available, both types of storage media actually cannot be considered as ‘real’ rewritable storage media, since the possible number of read/write cycles is strongly limited to several hundreds. For real rewritable mass data storage media, magnetic media like hard disc drives (HDD) and tape drives are still state of the art. These media store data by means of micro-domains of defined magnetic orientation on the surface of the medium, i.e. also in two dimensions. Their maximum storage density is physically limited by the super-paramagnetic limit, which describes the minimum size of a magnetized area being stable against thermal demagnetization. Today’s HDD’s achieve storage densities of up to 15×10^9 Bits/cm². However, the physical limits of digital mass data storage on magnetic storage media already loom at the horizon of further development.

Finally, data processing is still done purely electronically and there is no alternative technology in sight, which may count out the traditional data processing devices based on semiconductors. The general feasibility of purely optical logical devices has been proven in the laboratory, however, this technology is still in its very childhood [2].

A very promising technology for a new class of high density mass data storage devices is optical holographic data storage [B8, B13, B16]. In holographic data storage, whole pages of digital data are imprinted into a laser light beam by means of a spatial light modulator and are

stored as an interference pattern in a suitable storage medium. Therewith data are stored in three instead of two dimensions. The theoretical storage density limit for holographic data storage was estimated to $1/\lambda^3$ [19] corresponding to about 10^{12} Bits/cm³ for wavelengths of visible light. The stored data are retrieved by diffracting an undisturbed reference laser beam at the stored hologram. Therewith the original object beam carrying the digital information of the stored hologram is reconstructed. Since the thus retrieved digital information is a whole data page, retrieval of holographically stored data is intrinsically of parallel nature, which allows for fast data rates.

The special nature of the holographic data retrieval process furthermore allows for associative comparison of data inside the holographic storage medium. Therefore a reference beam is used for read out of a stored hologram, which is not undisturbed but already carries some information. In this case, the reconstructed object beam will only contain data, which are correlated to the information “imprinted” in the reference beam (optical correlation, associative memories [B8, B13, B16]). Thus, holographic storage media may also actively participate in data processing.

Besides the above discussed applications in information technology, there are numerous applications of holographic techniques, which utilize the special nature of the holographic recording and retrieval process [B8, B13, B16]: Among others, phase-conjugation of light waves can be performed and laser beams can be cleaned and reshaped. Holographical interferometry techniques allow for non-destructive material testing including contact-free vibrational analysis and deformation testing. Recording a hologram at a certain wavelength and retrieving it using a shorter wavelength may be used for purely optical coherent image magnification. Finally, holographic techniques may improve optical coherence tomography (OCT) [3]. OCT enables in-depth optical imaging in strongly scattering media like biological tissues and, thus, is an important non-invasive method for medical diagnosis. In contrast to conventional OCT scanning a medium pointwise, the introduction of holographic techniques would allow for fast imaging of complete layers of the medium, which would be a significant progress. Recently, the technique of time gated holographic imaging (TGHI) has been developed, which promises significant progress in this field [4 to 7].

Besides the special case of read-only holographic mass data storage devices, for all the aforementioned applications of holography, reversible holographic storage media are highly preferable or even indispensable. The currently most promising reversible holographic storage media are photorefractive (PR) materials. In these materials, the hologram to be stored is reversibly translated into a spatially non-uniform electrical field, the so called PR space charge field, which modulates the refractive index of the medium via electro-optic effects. The PR effect is known since 1969, when it was discovered in inorganic crystals [8, 9]. Great research efforts in the field of PR inorganic crystals have recently led to first attempts to realize commercial holographic mass data storage systems promising highly persistent high density data storage.

In 1990, the PR effect was also discovered in organic crystals [10, 11] and soon thereafter in amorphous organic polymers [12]. Finally, the development of the first high performance PR polymer in 1994 [13], which competes and in some aspects even surpasses the performance levels of the best currently known inorganic materials initiated considerable research efforts in this field. In contrast to PR inorganic or organic crystals, PR polymers offer significant advantages like good optical quality, high structural flexibility, good reproducibility, easy processing and low cost.

In this work, PVK-based amorphous organic PR polymers derived from the aforementioned first high performance PR polymer [13] were investigated. Their steady-state

and dynamic PR performance was considered. The details of the dynamic behavior was mainly focussed upon in order to investigate the potential applicability of the considered type of PR polymers as holographic mass data storage media.

As a first objective of this work, the chemical composition of the investigated materials was systematically altered in order to optimize their holographic performance. The glass-transition temperature (T_g) was altered by varying the ratio of polymer and plasticizer. Additionally, different concentrations of NLO chromophores were taken into account. The influence of T_g and of the concentration of chromophores on the steady-state and the dynamic PR performance was investigated.

The second goal of this work was to get a deeper insight into the physical processes determining the steady-state and dynamic performance of the investigated type of PR polymers. Therefore, the role of the sensitizer in the PR process was considered by means of holographic experiments on materials containing different concentrations of sensitizer molecules. The erasure behavior as well as the dark decay behavior of the holographic gratings were investigated in detail using different material compositions, including materials extrinsically doped with deep trapping sites, and applying various experimental conditions. The formation of charge carrier traps turned out to be highly important and was, therefore, elaborated upon in detail. Established experimental techniques were refined and novel experimental methods were devised in order to obtain new information on the stability of the recorded holograms in the dark and their behavior during recording and erasure. The obtained results may serve as a theoretical basis for future development of materials meeting the requirements of holographic mass data storage media.

Finally, the general mass data storage capabilities of the investigated class of materials were experimentally tested by means of peristrophic holographic multiplexing experiments. These experiments clearly demonstrated the shortcomings of PVK based PR polymers for this potential application.

2.)Theory

2.1.)Theoretical aspects of elementary optics

Optics is one of the oldest natural sciences. The laws of geometrical optics date back for over 2000 years. The wave concept of Christian Huygens (1690) has been a milestone in the development of optical sciences, which finally led to the assignment of optics to electrodynamics, which in turn was initiated by the electro-magnetic theory developed by James Clark Maxwell between 1855 and 1862. Heinrich Hertz was finally successful in proving the electro-magnetic nature of light experimentally in 1887.

However, the electro-magnetic theory neither takes the fact into account, that light has to be described as a stream of particles in certain experiments, nor is the basic understanding and the quantitative description of the impact of the propagation medium on the propagation of electro-magnetic waves included. The latter is introduced in Maxwell's theory only phenomenologically as "refractive index" and "permittivity". These parameters are explained in a satisfactory way by quantum mechanics and quantum electrodynamics, which were developed, among others, by Heisenberg, Schrödinger and Dirac in the 1920's.

The following chapter concerns some basic aspects of elementary optics as far as they are directly relevant to the framework of this theses.

2.1.1.) The electro-magnetic theory of light

The electromagnetic theory of light is based on Maxwell's equations, which cannot be derived, but are postulated as the basic equations of electrodynamics. Maxwell's equations consist of two field equations and two constraints, which may be expressed both in integral or in differential form. Hereafter, the physically more ostensive integral form will be used for the basic discussion. Both forms can be transferred into one another by applying the integral laws of vector analysis (Gauss and Stokes integral laws).

The first field equation is based on Faraday's induction law and connects a time dependent varying magnetic induction (flux density) \vec{B} through an open surface A , limited by a closed contour C , with an electrical rotational field \vec{E} in C :

$$\oint_C \vec{E} \cdot d\vec{s} = -\iint_A \frac{\partial \vec{B}}{\partial t} \cdot d\vec{n} \quad \text{eq. (2.1 - 1)}$$

where \vec{s} is the line vector of C and \vec{n} is the surface vector to A . It states, that a temporally varying magnetic field changing as a function of time always generates an electrical rotational field encircling the magnetic field lines. The differential form of eq. (2.1 - 1) may be written as:

$$\text{rot} \vec{E} = \nabla \times \vec{E} = -\frac{\partial \vec{B}}{\partial t} \quad \text{eq. (2.1 - 2)}$$

The second field equation is Ampere's law, which was extended by Maxwell. This new formulation of Ampere's law correlates a current density \vec{j} through an open surface A limited by a closed contour C including the total current (old form of Ampere's law) as well as a time dependent dielectric displacement \vec{D} through A (Maxwell's extension) with a magnetic rotational field \vec{H} within C , according to:

$$\oint_C \vec{H} \cdot d\vec{s} = - \iint_A \left(\vec{j} + \frac{\partial \vec{D}}{\partial t} \right) \cdot d\vec{n} \quad \text{eq. (2.1 - 3)}$$

where \vec{s} is the line vector of C and \vec{n} is the surface vector to A . This relation states in particular that (besides a flowing current) an electrical field changing as a function of time always generates a magnetic rotational field encircling the electrical field lines. The differential form of this law may be written as:

$$\text{rot} \vec{H} = \nabla \times \vec{H} = \frac{\partial \vec{D}}{\partial t} + \vec{j} \quad \text{eq. (2.1 - 4)}$$

The well known Gaussian laws of the magnetic and the electrical field are the constraints to the field equations. The Gaussian law of the electrical field states, that an electrical field may (not must) have sources, whereas the Gaussian law of the magnetic field defines it solenoidal in any case. The Gaussian law of the electrical field may be written as:

$$\oint_F \vec{D} \cdot d\vec{f} = \iiint_V \rho dV \quad \text{eq. (2.1 - 5)}$$

where \vec{f} is the surface vector to the closed surface F and $d\vec{f}$ is oriented away from the enveloped volume for each surface element dF of the closed surface F ; ρ is the charge density inside the volume V . Since the magnetic field is always solenoidal, the Gaussian law of the magnetic field may be expressed as:

$$\oint_F \vec{B} \cdot d\vec{f} = 0. \quad \text{eq. (2.1 - 6)}$$

The corresponding differential forms are:

$$\text{div} \vec{D} = \nabla \cdot \vec{D} = \rho \quad \text{eq. (2.1 - 7)}$$

and:

$$\text{div} \vec{B} = \nabla \cdot \vec{B} = 0. \quad \text{eq. (2.1 - 8)}$$

Considering light propagating in free space or insulators, eq. (2.1 - 7) simplifies to:

$$\text{div} \vec{D} = \nabla \cdot \vec{D} = 0. \quad \text{eq. (2.1 - 9)}$$

The dielectric displacement \vec{D} is related to the electrical field \vec{E} and the magnetic induction \vec{B} is related to the magnetic field \vec{H} according to:

$$\begin{aligned} \vec{D} &= \varepsilon_0 \varepsilon_r \vec{E} \\ \vec{B} &= \mu_0 \mu_r \vec{H} \end{aligned} \quad \text{eq. (2.1 - 10)}$$

with ε_0 as permittivity of the free space, ε_r as relative permittivity, μ_0 as permeability of the free space, and μ_r as relative permeability. The quantities ε_r and μ_r are material parameters.

From Maxwell's equations, the wave equation for electro-magnetic waves can be derived (see standard literature of optics). It has become common practice to consider only the electrical component, which writes for the case of free space:

$$\nabla^2 \vec{E} - \frac{1}{c_0^2} \frac{\partial^2 \vec{E}}{\partial t^2} = 0, \quad \text{eq. (2.1 - 11)}$$

where:

$$c_0 = 1 / \sqrt{\varepsilon_0 \mu_0} \quad \text{eq. (2.1 - 12)}$$

is the propagation velocity of electro-magnetic waves in free space. An important solution of the differential equation eq. (2.1 - 11) is a monochromatic plain wave, which may be expressed

as:

$$\vec{E} = \vec{E}_0 \cos(\omega t \pm \vec{k} \cdot \vec{r} \pm \varphi), \quad \text{eq. (2.1 - 13)}$$

or in complex notation:

$$\vec{E} = \vec{E}_0 e^{i(\omega t \pm \vec{k} \cdot \vec{r} \pm \varphi)}. \quad \text{eq. (2.1 - 14)}$$

with:

$$\omega = 2\pi\nu = 2\pi(c_0/\lambda_0) = kc_0, \quad \text{eq. (2.1 - 15)}$$

where ω , ν , λ_0 and $k = |\vec{k}|$ are the circular frequency, free space wavelength and wave number = modulus of the wave vector, respectively. \vec{E}_0 is the real amplitude of the wave and φ is a phase addend. The plus/minus-signs in eq. (2.1 - 13) and eq. (2.1 - 14) denote arbitrary propagation directions or phasings. Hereafter and throughout the rest of this work complex expressions will be denoted by a subscript tilde as far as the complex character of an expression is not self-evident or irrelevant.

The time derivation in eq. (2.1 - 11) may be eliminated by separating eq. (2.1 - 14) in a time dependent component and a position dependent component according to:

$$\vec{E}(\vec{r}, t) = \vec{E}(\vec{r}) e^{i\omega t} \quad \text{eq. (2.1 - 16)}$$

with:

$$\vec{E}(\vec{r}) = \vec{E}_0 e^{\pm i(\vec{k} \cdot \vec{r} \pm \varphi)}. \quad \text{eq. (2.1 - 17)}$$

Now eq. (2.1 - 11) may be rewritten as:

$$\nabla^2 \vec{E}(\vec{r}) + k^2 \vec{E}(\vec{r}) = 0, \quad \text{eq. (2.1 - 18)}$$

which is known as the *Helmholtz equation* and is commonly applied to problems, which do not require the consideration of the time dependence.

Only the real part of the complex wave according to eq. (2.1 - 14) is physically relevant. The complex notation is only a formalism, which facilitates the mathematical handling for many problems. The physically relevant part of eq. (2.1 - 14) can be extracted by adding the complex conjugate \vec{E}^* according to:

$$\vec{E} = \frac{1}{2}(\vec{E} + \vec{E}^*). \quad \text{eq. (2.1 - 19)}$$

However, only linear operations can be performed using the complex notation. Any operation, which mixes up the real part and the imaginary part is inadmissible, if the problem under consideration has been formulated from the beginning in complex notation. Hence, if nonlinear operations are part of the problem under consideration, the problem initially must not be formulated in complex notation, however, may then be transferred into complex notation using eq. (2.1 - 19).

By inserting eq. (2.1 - 14) and its magnetic equivalent into eq. (2.1 - 2), the relation between the electrical field and the magnetic flux amplitude is obtained to:

$$\vec{B}_0 = \frac{\vec{e}_k \times \vec{E}_0}{c_0}. \quad \text{eq. (2.1 - 20)}$$

When considering the electrical and the magnetic field amplitude:

$$\vec{H}_0 = \frac{\vec{e}_k \times \vec{E}_0}{Z} \quad \text{eq. (2.1 - 21)}$$

is obtained, where \vec{e}_k is the unit vector in propagation direction of the wave and Z is called wave resistance, since it corresponds to the ratio of the electrical and the magnetic field strength (“voltage/current“). The wave resistance is defined by:

$$Z = \sqrt{\frac{\mu_0 \mu_r}{\varepsilon_0 \varepsilon_r}} \quad \text{eq. (2.1 - 22)}$$

and amounts to about 377Ω for the case of free space propagation ($\varepsilon_r = \mu_r = 1$).

The vector product of the electrical and magnetic field vectors defines a vector pointing in propagation direction of the electro-magnetic wave. This vector has the dimension of a power density, represents the energetic flux and is referred to as the *Poynting-vector* \vec{S} :

$$\vec{S} = \vec{E} \times \vec{H} = c^2 \varepsilon_0 \vec{E} \times \vec{B}. \quad \text{eq. (2.1 - 23)}$$

Hereby free space is presumed. The power density emitted by a source is called *specific emission* and the power density incident onto a surface is referred to as (irradiation) *intensity*.

Calculating the Poynting vector for a plain wave according to eq. (2.1 - 13) one obtains from eq. (2.1 - 23):

$$\vec{S} = c^2 \varepsilon_0 \vec{E}_0 \times \vec{B}_0 [\cos(\omega t + \vec{k} \cdot \vec{r})]^2. \quad \text{eq. (2.1 - 24)}$$

According to $(\cos \alpha)^2 = 1/2 - 1/2(\cos 2\alpha)$, the Poynting-vector oscillates in the time domain with twice the frequency of the wave between zero and its maximum value. However, due to the very short oscillation period usually not the current magnitude of the Poynting-vector is of interest, but its time average yielding the intensity I :

$$I = \langle |\vec{S}| \rangle = \frac{c^2 \varepsilon_0}{2} |\vec{E}_0 \times \vec{B}_0| \quad \text{eq. (2.1 - 25)}$$

with $\int_t^{t+\Delta t} [\cos(\vec{k} \cdot \vec{r} + \omega t)]^2 dt = 1/2$ for $\Delta t \gg 2\pi/\omega$. Applying eq. (2.1 - 20) leads to:

$$I = \frac{c \varepsilon_0}{2} E_0^2 = c \varepsilon_0 \langle E^2 \rangle, \quad \text{eq. (2.1 - 26)}$$

where E_0 is the amplitude of the electrical field component.

Calculating the steps from eq. (2.1 - 23) to eq. (2.1 - 26) using the complex notation, one must take into account that the vector product is not a linear operation. Hence, the problem has to be formulated initially in real notation but can then be transferred into complex notation according to eq. (2.1 - 19) as already mentioned before:

$$\vec{S} = \text{Re} \vec{E} \times \text{Re} \vec{H} \quad \text{eq. (2.1 - 27)}$$

with:

$$\vec{E} = \vec{E}_0 e^{i(\omega t + \vec{k} \cdot \vec{r})} \quad \text{eq. (2.1 - 28)}$$

$$\vec{H} = \vec{H}_0 e^{i(\omega t + \vec{k} \cdot \vec{r})}$$

With eq. (2.1 - 19) one obtains:

$$\vec{S} = \frac{1}{4} [(\vec{E} + \vec{E}^*) \times (\vec{H} + \vec{H}^*)]. \quad \text{eq. (2.1 - 29)}$$

For time averaging, it is convenient to introduce a complex amplitude containing the spatial term of the wave as well as the physical (real) amplitude resulting in:

$$\begin{aligned} \vec{E} &= \vec{E}' e^{i\omega t} \\ \vec{H} &= \vec{H}' e^{i\omega t} \end{aligned} \quad \text{eq. (2.1 - 30)}$$

By time averaging according to:

$$\begin{aligned} \langle \vec{E}(t) \times \vec{H}(t) \rangle &= 0 = \langle \vec{E}^*(t) \times \vec{H}^*(t) \rangle && \text{eq. (2.1 - 31)} \\ \langle \vec{E}(t) \times \vec{H}^*(t) \rangle + \langle \vec{E}^*(t) \times \vec{H}(t) \rangle &= 2\text{Re}[\vec{E}^*(t) \times \vec{H}(t)] = 2\text{Re}[\vec{E}(t) \times \vec{H}^*(t)] \end{aligned}$$

one obtains:

$$\langle \vec{S} \rangle = \frac{1}{2}\text{Re}[\vec{E} \times \vec{H}^*] = \frac{1}{2}\text{Re}[\vec{E}' \times \vec{H}'^*]. \quad \text{eq. (2.1 - 32)}$$

This is a general expression, which transfers into eq. (2.1 - 25) when taking the modulus and presuming free space. According to eq. (2.1 - 26) the intensity may be expressed in complex notation as:

$$I = \frac{c\varepsilon_0}{2}\vec{E}\vec{E}^* = \frac{c\varepsilon_0}{2}\vec{E}'\vec{E}'^* = \frac{c\varepsilon_0}{2}E_0^2. \quad \text{eq. (2.1 - 33)}$$

Formulating this relation using the wave resistance Z according to eq. (2.1 - 22) yields:

$$I = \frac{1}{2Z}\vec{E}\vec{E}^*. \quad \text{eq. (2.1 - 34)}$$

Please note that eq. (2.1 - 20) and eq. (2.1 - 21) imply perpendicular orientation of the propagation direction, of the electrical field vector and of the magnetic field vector relative to each other. Therefore, commonly electro-magnetic waves are referred to as TEM-waves (**t**ransversal, **e**lectrical and **m**agnetic). It must be pointed out that only infinitely vast plain waves propagating in free space can be pure TEM waves. Real light beams are always laterally restricted, leading to distortions of the wave fronts and thus to deviations from the TEM nature. However, the assumption of pure TEM waves is a good approximation in many cases, which also applies to all problems considered in the frame of this work.

2.1.2.) Superposition of electro-magnetic waves

This section deals with the superposition of electro-magnetic waves and some related phenomena including polarization, coherence, and the basic concepts of diffraction.

Hereafter, the superposition principle shall be valid, i.e. the electrical field strengths involved shall be small enough to avoid any nonlinear effects, which are discussed later in a separate paragraph. Furthermore ideal TEM waves are presumed.

2.1.2.1.) Polarization

Due to the transversal nature of electro-magnetic waves, the electrical field vector shows time resolved and position resolved a well defined orientation, which is perpendicular to the propagation direction of the wave. This feature is generally described by the concept of the *polarization*. In the frame of this work, the spatial oscillation direction of the electrical field vector will be referred to as the *polarization direction*. (It should be noted, that one can find different definitions in the literature.)

In this context the *polarization plane* of an electro-magnetic wave is defined by the polarization direction and the propagation direction or, in other words, by the wave vector \vec{k} and the real electrical field vector \vec{E} , which oscillates in the polarization plane. As far as there is a clearly defined reference, the polarization state of an electro-magnetic wave is sometimes denoted as “*s-polarized*“, if the polarization plane is oriented perpendicular (germ.: senkrecht)

to the reference plane, and as “*p-polarized*“, if the polarization plane is oriented parallelly to the reference plane. This notation will hereafter always be used in this theses.

Considering the polarization states of an electro-magnetic wave, one has to distinguish basically two limiting polarization states. Any possible polarization state in-between can be formed by suitable superposition of waves in these two states. Furthermore each limiting state can be formed by suitable superposition of two waves in the other limiting polarization state. These limiting polarizations states are:

A) LINEAR polarization

In this case, the polarization direction is neither a function of time nor a function of the position. The electrical field vector oscillates parallelly to a constant straight line perpendicular to the propagation direction of the wave.

B) CIRCULAR polarization

In the case of circular polarization, the electrical field shows a constant modulus but rotates around the propagation direction as a function of the wave propagation.

For an interval of exactly one period of the wave oscillation along the propagation direction, the projection of the end point of the electrical field vector onto a plane perpendicular to the propagation direction forms just a closed circle.

The cases A and B are illustrated in figure (2.1 - 1). All further polarization states are mixed states of A and B and count to the group of elliptic polarization states. For example, the in-phase superposition of two linearly polarized waves propagating in identical directions results in an as well linearly polarized wave (figure (2.1 - 1), left). In contrast, if the superposition is performed phase-shifted by $\pi/2$, a circularly polarized wave (figure (2.1 - 1), right) will result if the amplitudes of the waves are identical. Phase shifts in-between 0 and $\pi/2$ and/or different amplitudes in turn yield some elliptic polarization state. Finally, the superposition of two circularly polarized waves, which are identical, but their polarization vectors rotating in opposite directions, results in a linearly polarized wave.

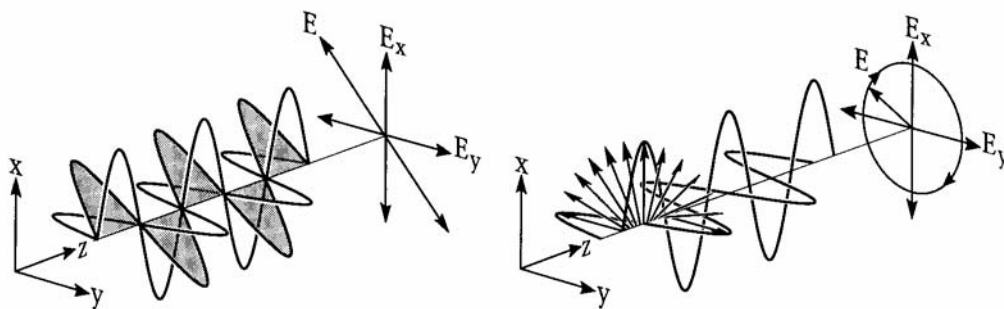


Figure (2.1 - 1): Linear (left) and circular (right) polarization. Redrawn after [B1].

The mathematical procedure of superposing electro-magnetic waves is discussed in the forthcoming section. Mixing of polarization states is not further considered, since the mathematical modelling would be very extensive not revealing new aspects. Please note, that there are particular mathematical formalisms for handling the polarization of electro-magnetic waves. The modern representation of the polarization has been introduced by G.G. Stokes in 1852 and was improved by R. Clark Jones and Hans Müller during the 1940ies.

2.1.2.2.)Interference

As long as the superposition principle is valid, electro-magnetic waves can be superposed by simply adding the electrical field vectors. Since forming a sum is a linear operation, the problem can be formulated initially in complex notation.

Considering two plain electro-magnetic waves of the general complex form:

$$\begin{aligned}\vec{E}_1 &= \vec{E}_{01} e^{i(\omega_1 t + \vec{k}_1 \cdot \vec{r} + \varphi_1)} \\ \vec{E}_2 &= \vec{E}_{02} e^{i(\omega_2 t + \vec{k}_2 \cdot \vec{r} + \varphi_2)}\end{aligned}\quad \text{eq. (2.1 - 35)}$$

where $\varphi_{1,2}$ are phase addends, one obtains for the superposition of the waves:

$$\vec{E}_{12} = \vec{E}_1 + \vec{E}_2 = \vec{E}_{01} e^{i(\omega_1 t + \vec{k}_1 \cdot \vec{r} + \varphi_1)} + \vec{E}_{02} e^{i(\omega_2 t + \vec{k}_2 \cdot \vec{r} + \varphi_2)}.\quad \text{eq. (2.1 - 36)}$$

Depending on the problem under consideration a more or less complicated analytical expression for the sum wave can be extracted from eq. (2.1 - 36), which will here be demonstrated for two simple examples.

At first the superposition of two waves, which differ only slightly in frequency but are otherwise identical will be considered. For this case eq. (2.1 - 35) simplifies to:

$$\begin{aligned}\vec{E}_1 &= \vec{E}_0 e^{i(\omega_1 t)} \\ \vec{E}_2 &= \vec{E}_0 e^{i(\omega_2 t)}\end{aligned}\quad \text{eq. (2.1 - 37)}$$

introducing the complex amplitude \vec{E}_0 with $\vec{E}_0 = \vec{E}_0 e^{i(\vec{k} \cdot \vec{r} + \varphi)}$. For the superposition one obtains after some trigonometric manipulations:

$$\vec{E}_{12} = \vec{E}_1 + \vec{E}_2 = 2\vec{E}_0 e^{i\left(\frac{\omega_1 + \omega_2}{2} t\right)} \cos\left(\frac{\omega_1 - \omega_2}{2} t\right).\quad \text{eq. (2.1 - 38)}$$

This represents a wave with the average frequency $0.5(\omega_1 + \omega_2)$, the amplitude of which, however, is modulated with the average modulation frequency $0.5(\omega_1 - \omega_2)$. This behavior is called “beat“ and characteristic for all wave phenomena.

The second example is of essential importance for this work and will, therefore, be discussed in more detail. Considering the intersection of two linearly polarized plain waves of identical frequency but different propagation directions, a stationary sinusoidal intensity distribution will be observed if some basic conditions are fulfilled. This phenomenon is called *interference*.

According to eq. (2.1 - 35), plain waves of identical frequency but different propagation directions, amplitudes, and phasings may be expressed as:

$$\begin{aligned}\vec{E}_1 &= \vec{E}_{01} e^{i(\omega t + \vec{k}_1 \cdot \vec{r} + \varphi_1)} \\ \vec{E}_2 &= \vec{E}_{02} e^{i(\omega t + \vec{k}_2 \cdot \vec{r} + \varphi_2)}\end{aligned}\quad \text{eq. (2.1 - 39)}$$

The phasings are constant in time. In order to obtain the intensity distribution of the sum of these waves, eq. (2.1 - 33) is applied to the sum of the amplitudes:

$$I(\vec{r}) \propto (\vec{E}_1 + \vec{E}_2) \cdot (\vec{E}_1 + \vec{E}_2)^*\quad \text{eq. (2.1 - 40)}$$

or:

$$I(\vec{r}) \propto E_{01}^2 + E_{02}^2 + (\vec{E}_{01} \bullet \vec{E}_{02}) \left(e^{i[(\vec{k}_1 - \vec{k}_2) \bullet \vec{r} + (\varphi_1 - \varphi_2)]} + cc \right) \quad \text{eq. (2.1 - 41)}$$

where cc stands for the “complex conjugate“. If the intensities of the superposed individual waves are denoted I_1 and I_2 , $I(\vec{r})$ can be expressed by:

$$I(\vec{r}) = I_1 + I_2 + I_{12}, \quad \text{eq. (2.1 - 42)}$$

where I_{12} is referred to as *interference term* and writes:

$$I_{12} = 2\sqrt{I_1 I_2} \cos \alpha_{p12} \cos [(\vec{k}_1 - \vec{k}_2) \bullet \vec{r} + (\varphi_1 - \varphi_2)]. \quad \text{eq. (2.1 - 43)}$$

Here α_{p12} is the angle, which is enclosed by the polarization directions (not the vectors) of the intersecting waves. Please note that the polarization geometry must be read so that $0 \leq \alpha_{p12} \leq 90^\circ$. The observed intensity distribution, called *interference pattern*, is stationary as long as the relative phasing of the intersecting waves is constant in time. I_{12} vanishes for $\alpha_{p12} = \pi/2$, i.e. if the interfering waves are polarized orthogonally.

Thus, the term *interference* is defined as follows:

Any deviation from the additivity of the intensities by considering the superposition of waves is called interference.

“Maximum” interference is observed for $I_1 = I_2$ and $\alpha_{p12} = 0$. The intensity of the so called *interference fringes* varies between zero and two times the total intensity of the two interfering waves. The interference pattern may be considered as an *interference grating* and a grating vector \vec{K} can be assigned according to:

$$\vec{K} = \vec{k}_1 - \vec{k}_2 \quad \text{eq. (2.1 - 44)}$$

and:

$$|\vec{K}| = \frac{2\pi}{\Lambda} \quad \text{eq. (2.1 - 45)}$$

$$\Lambda = \frac{\lambda}{2 \sin(\Theta)},$$

where λ is the wavelength of the interfering waves, Λ is the *grating spacing* (i.e. the wavelength of the grating) and 2Θ is the angle enclosed by the wave vectors of the interfering waves.

The most common expression to describe the interference of two beams is obtained merging eq. (2.1 - 42) to eq. (2.1 - 45) suitably and setting the phasings to zero. This yields:

$$I(\vec{r}) = I_0 [1 + m \cos(\vec{K} \bullet \vec{r})], \quad \text{eq. (2.1 - 46)}$$

with:

$$I_0 = I_1 + I_2$$

$$m = \frac{2\sqrt{I_1 I_2}}{I_1 + I_2} \cos \alpha_{p12} \quad \text{eq. (2.1 - 47)}$$

and \vec{K} according to eq. (2.1 - 44) and eq. (2.1 - 45). The variable m is called *contrast factor* and is a measure for the modulation depth of the interference pattern.

The two beam interference discussed above is representative for any interference phenomenon. As already noted, there are three *interference conditions*, which must be fulfilled by the intersecting waves in order to yield a stationary interference pattern:

- 1) identical frequency
- 2) polarization directions not perpendicular to each other

3) phasing with respect to each other constant in time

The violation of condition 2) leads to vanishing (intensity) contrast of the interference pattern ($m = 0$ due to $\alpha_{p12} = 90^\circ$). Instead of a stationary intensity distribution showing the sequence: “bright-average-dark-average-bright“, then a stationary polarization distribution is formed as long as the other conditions are fulfilled. The corresponding polarization sequence is: “linear1-circularI-linear2-circularII-linear1“, whereby linear1 and linear2 are orthogonal and circularI and circularII rotate in opposite directions. For $0^\circ < \alpha_{p12} < 90^\circ$ both intensity pattern and polarization pattern exist simultaneously in the intersection area. Violation of the conditions 1) and/or 3) leads to an interference pattern changing as a function of time (i.e. spatially moving). Condition 3) is closely related to the concept of *coherence*, which will be outlined in the following section.

2.1.2.3.)Coherence

Coherence is a general term, which concerns the predictionability of phase relations within and in-between waves. The forthcoming discussion will be limited to visible light without loss of generality as far as the basic aspects are concerned. Subsequently, the basic phenomenology and terminology will be explained.

Visible light is usually generated by random electron transitions in atoms, molecules or semiconductors, which by principle are strongly limited in duration. Light sources, in which these processes dominate are called *thermal emitters*. The particular emission events are independent from each other and thus, light generated by thermal emitters consists of many independent individual light wave trains showing randomly distributed phasings. The length of the particular wave trains is determined by the duration of the underlying emission process.

Accordingly, in a light beam emitted by a thermal emitter, prediction of phase relations is only possible within the time scales of a particular emission event. The average length of a particular wave train in the time domain is called *coherence time* Δt_c , the reciprocal of which is the frequency bandwidth $\Delta \nu$ of the wave train. Accordingly, a short coherence time is correlated with a broadband light pulse. In contrast, for hypothetically ideal monochromatic light the coherence time diverges to infinity. The propagation velocity of the wave under consideration links the coherence time with a spatial length, the so called *coherence length*. On this basis, the term *longitudinal coherence* has become generally common for denoting this property in english speaking literature. In contrast, *coherence in time* is more commonly used in german speaking literature. The latter is more general, since it is independent from the propagation medium, which determines the propagation velocity. The coherence length may simply be interpreted as the length of a particular continuous wave train.

Considering a real light source as opposed to the hypothetical point source often used in the literature for simplified discussions, the source has a finite size and consists of a huge number of single emitters, which are again independent from each other, provided that the considered light source is a thermal emitter. Accordingly, a light beam emitted by such a source laterally consists of many independent particular wave trains, showing randomly distributed phasings. In order to denote the phase relations between particular wave trains perpendicular to the propagation direction of a light beam, the terms *spatial coherence* or *lateral coherence* have been commonly adopted. However, this terminology is not clear cut, since it is related to the light source and its properties but it actually depends on the geometry of the considered problem. For example in Young’s double gap experiment interference effects will be observed

if illumination of both gaps is possible by one and the same emitter of a spatially incoherent source. On the other hand, no interference will occur if the light passing through the gaps stems definitely from different lateral areas of the source. For these two cases, the source is one and the same, but the geometry of the experiment defines the result. Hence, definite statements about spatial coherence require deeper insight into the problem under consideration.

The coherence of traditional light sources is poor and accordingly the study of coherence has been neglected for a long time despite the fact, that basic work has already been done about 150 years ago by Emile Verdet. He reported the observation of interference effects with sun light, which before was commonly considered as completely incoherent. However, with the invention of the laser this situation changed dramatically. In a laser, coupled emission of many single emitters is enforced, leading to high grade partial coherence in the light generated. Today, optical coherence theory is a very active research area but beyond the scope of this work.

2.1.2.4.)Phase- and group-velocity

Up to now, the terms “light velocity“ or “propagation velocity of a wave“ have been used several times without looking deeper into their physical meaning, which will be discussed now.

The term “propagation velocity of a wave“ usually refers to the propagation of a state of constant phase angle of the considered wave through space or some medium. Considering a wave e.g. according to eq. (2.1 - 13) or eq. (2.1 - 14), the phase angle ϑ of the wave is defined by the argument of the trigonometric function or the complex exponential function, respectively:

$$\vartheta = \omega t + \vec{k} \bullet \vec{r} + \varphi. \quad \text{eq. (2.1 - 48)}$$

Here φ is a constant and may be disregarded. Accordingly, the propagation of a state of constant phase angle can be expressed as:

$$\left(\frac{\partial \vartheta}{\partial t}\right)_{\vartheta} = -\left(\frac{\partial \vartheta}{\partial t}\right)_{\vec{r}} / \left(\frac{\partial \vartheta}{\partial \vec{r}}\right)_t = \pm \frac{\omega}{\vec{k}} = \pm \vec{v}_p. \quad \text{eq. (2.1 - 49)}$$

by applying the partial derivatives to eq. (2.1 - 48). Accordingly, v_p is the propagation velocity of a wave, referred to as *phase-velocity*.

However, the situation becomes more complicated if the propagation of wave groups or pulses of restricted expansion is considered, which, due to Fourier analysis, can be expressed as superposition of several harmonic waves. The simplest example for this situation is the superposition of two waves, yielding a sum wave according to eq. (2.1 - 38). This wave oscillates with the average frequency of the two superposed waves. The amplitude however, is additionally modulated by the beat frequency. For further consideration eq. (2.1 - 38) is rewritten as:

$$\vec{E} = \vec{E}_0(\vec{r}, t) \cos(\omega_b t + \vec{k}_b \bullet \vec{r}), \quad \text{eq. (2.1 - 50)}$$

where $\omega_b = \frac{1}{2}(\omega_1 - \omega_2)$ is the beat frequency and \vec{k}_b is the corresponding beat wave vector, while

$$\vec{E}_0(\vec{r}, t) = \vec{E}_0 e^{i(\bar{\omega} t + \vec{k} \bullet \vec{r})} \quad \text{eq. (2.1 - 51)}$$

represents the unmodulated wave with the average frequency $\bar{\omega} = 0.5(\omega_1 + \omega_2)$ and with \vec{k} as the corresponding average wave vector.

Obviously, eq. (2.1 - 50) describes a situation containing two different propagation processes, the propagation of the unmodulated wave, which may be considered as carrier wave, and the propagation of the amplitude modulation of the carrier wave. The propagation velocity of the unmodulated wave is $\bar{\omega}/\bar{k}$ according to eq. (2.1 - 49), which is the phase velocity. However, the modulation propagates with a velocity, which depends on the phase angle $(\omega_b t + \vec{k}_b \bullet \vec{r})$ of the modulation function. Therefore, the propagation velocity is:

$$\dot{v}_g = \frac{\omega_b}{\vec{k}_b} = \frac{\omega_1 - \omega_2}{\vec{k}_1 - \vec{k}_2} = \frac{\Delta\omega}{\Delta\vec{k}}. \quad \text{eq. (2.1 - 52)}$$

The parameter v_g is referred to as *group velocity*. The group velocity drops to zero, if $\vec{k}_1 = -\vec{k}_2$ and $\omega_1 = \omega_2$, which corresponds to a standing wave. Please note, that the group velocity corresponds to the actual transport speed of information.

As for the phase velocity, the dispersivity of the propagation medium has to be taken into account. In dispersive media, ω is a function of k (this will be discussed in more detail in section "2.1.3.) Light in linear media" on page 16). If $\Delta\omega$ is small with respect to the average frequency, the group velocity equals the derivative of the dispersion relation:

$$\dot{v}_g = \frac{d\omega}{d\vec{k}}. \quad \text{eq. (2.1 - 53)}$$

This equation is generally valid for each group of superposed waves, provided that $\Delta\omega$ is small with respect to the average frequency. With eq. (2.1 - 49), one obtains:

$$\dot{v}_g = \dot{v}_p + \vec{k} \frac{dv_p}{dk}. \quad \text{eq. (2.1 - 54)}$$

Accordingly, $\dot{v}_g = \dot{v}_p$ in dispersion-free media, since $dk(v_p)/dk = 0$ in this case. However, in dispersive media, $\omega = kc/n$ and one obtains:

$$\dot{v}_g = \dot{v}_p \left(1 - \frac{k}{n} \frac{dn}{dk} \right). \quad \text{eq. (2.1 - 55)}$$

In dispersive optical media and at normal dispersion the refractive index increases as a function of frequency and, hence, $v_g < v_p$. Therefore, sometimes a "group refractive index" is introduced in order to account for the difference of the two propagation velocities.

Finally, it should be noted, that a third kind of velocity occurs in regions of anomalous dispersion, where $dn/dk < 0$ (e.g. in the absorption band of a medium). This velocity is called *signal velocity* and is identical to the group velocity in areas of normal dispersion. The signal velocity accounts for the fact, that information cannot be transported at velocities exceeding vacuum light velocity c_0 . For the same reason, the group velocity never exceeds c_0 in media of normal dispersion, whereas the phase velocity may do, however, without transporting any information.

2.1.2.5.)Diffraction

Diffraction phenomena occur, if parts of a wave are blocked, e.g. by a pin hole, or at the edge of a light beam, even without an obstacle in the beam path. They are due to the superposition of the *elementary waves* existing at the edge of the obstacle or the light beam and, hence, diffraction phenomena may be interpreted as a special class of interference phenomena.

Please note that "Bragg-diffraction" is a special diffraction phenomenon, which will be discussed in context with refraction and reflection.

2.1.2.5.1.)The Huygens-Fresnel principle

Before proceeding, the term “elementary waves“ must be clarified. The concept of the elementary waves is based on a principle first formulated by Christian Huygens and improved by Jean Augustin Fresnel (Huygens-Fresnel principle):

All non-shielded points of a wave-front must at any time be considered as sources of spherical elementary waves of identical frequency as the primary wave. The amplitude of the optical field at any sequencing point is then determined by the superposition of all elementary waves reaching this point and taking into account their individual amplitude and relative phasing.

The meaning of this very important basic optical principle is illustrated in figure (2.1 - 2). The arrow points in the propagation direction of the wave. The elementary waves are indicated for three points on the wave fronts. The dotted circles indicate the elementary waves, generated by the points on the very left wave front, which after a certain time superpose to generate the next wave front in propagation direction. This wave front in turn is origin of elementary waves, which now, after a superposition with each other as well as with the elementary waves of the formal “first“ wave front (all dashed circles) generate the third wave front and so on. Taking into account that there is actually an infinite number of points generating elementary waves on each wave front, plain wave fronts generate plain wave fronts propagating in propagation direction of the wave. However, the components of the elementary waves running into the opposite direction must vanish, which actually is not proposed by the Huygens principle. Fresnel solved this problem proposing obliquity factors making the radiation characteristics of the elementary waves directional. The obliquity factors finally were analytically formulated by Kirchhoff. However, the details of the theoretical validation of the Huygens-Fresnel principle is beyond the scope of this work. Hereafter, the principle is taken for valid and will be applied, disregarding components of the elementary waves propagating in “wrong“ directions. The elementary waves from the edge of the light beam interfere in some way, leading to diffraction effects as mentioned above.

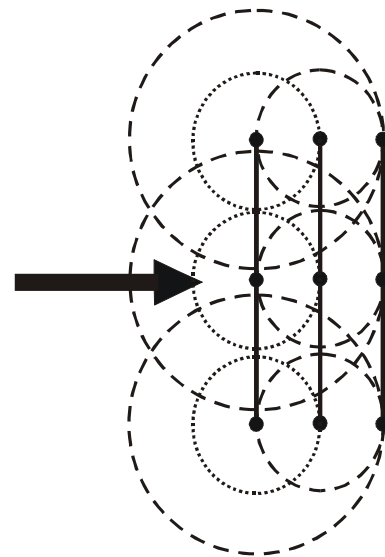


Figure (2.1 - 2)

2.1.2.5.2.)Fraunhofer and Fresnel diffraction

It turned out convenient to distinguish between two subgroups of diffraction phenomena, the *near-field diffraction* (also referred to as *Fresnel's diffraction*) on the one hand, and the *far-field diffraction* (also referred to as *Fraunhofer's diffraction*) on the other. The near-field diffraction concerns the area more or less directly behind and/or before the diffracting object. This applies to either the light source or the observation screen or both. In contrast, the far-field diffraction describes diffraction phenomena observed at sufficient distance from the diffracting object, so that the involved light beams are approximately parallel to the optical axis, which, in simple terms, is the center line connecting the (diffracting) object with the observation plane. The same condition must be met by the distance of the light source to the diffracting object. Note, that ideal far-field diffraction, thus, only occurs for infinite distance between source, object and observation plane and consequently all considerations of real diffraction phenomena

using the far-field diffraction formalism are approximations.

The basic situation is sketched in figure (2.1 - 3), where the source was assumed to be at infinite distance for the sake of simplicity. Hence, the light incident on the obstacle “O” is parallel and “S” is the screen for observation of the transmitted light. In the case of near-field diffraction (no lens), light beams passing through the aperture in the obstacle and meeting in one and the same point on “S” obviously cannot be parallel (dashed lines). If a lens “L” is introduced at focus distance to “S”, parallel beams passing through O meet in one point on S. This represents the situation of far-field diffraction.

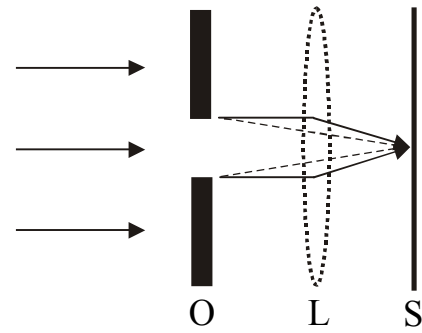


Figure (2.1 - 3): Far- and Near-Field diffraction

It is beyond the scope of this work to discuss the theory of Fraunhofer and Fresnel diffraction in detail as well as to demonstrate the calculation of diffraction patterns and reference is made to the standard literature of optics.

2.1.3.) Light in linear media

In this section, the basic principles of the interaction between light and matter will be outlined. The oscillator model will be worked out as classical consideration of the linear interaction between light and a homogenous, non-conducting and loss-free medium. Then the basic approach for the treatment of wave propagation in loss-free and lossy media will be outlined. Although the concepts outlined here will apply to isotropic as well as anisotropic media, wave propagation in the latter will be discussed in more detail in context with birefringence in section “2.1.4.3.6.) Wave propagation in anisotropic media - the index ellipsoid” on page 35. Furthermore, waves in nonlinear media will be considered separately in section “2.2.1) Nonlinear interaction between light and matter” on page 40. The influence of the homogeneity of the medium will not be considered.

Please note, that this section is restricted to dielectric media, i.e. the presence of free charge carriers shall a priori be excluded and, accordingly, the conductivity $\sigma = 0$ shall be presumed.

2.1.3.1.)Material equations

External electrical and magnetic fields induce associated atomar or molecular dipoles in matter. The dipole moments induced per unit volume are referred to as (complex) electrical $\vec{P}(\vec{E})$ and magnetic $\vec{M}(\vec{H})$ polarization (rarely also “electrization“ and “magnetization“, respectively). Therefore, the dielectric displacement \vec{D} and the magnetic induction \vec{B} in matter is described by:

$$\begin{aligned} \vec{D} &= \epsilon_0 \vec{E} + \vec{P}(\vec{E}) \\ \vec{B} &= \mu_0 \vec{H} + \vec{M}(\vec{H}) \end{aligned} \quad \text{eq. (2.1 - 56)}$$

These relations represent the material equations for arbitrary media.

The polarizations are not proportional to the inducing fields, since the medium will react with a time delay to the inducing fields. However, the magnitude of the material’s response may

be proportional to the inducing fields. In this case, the medium is called linear and it is:

$$\begin{aligned}\vec{P}(t) &= \varepsilon_0 \underline{\chi}_{e,t} \vec{E}(t) \\ \vec{M}(t) &= \mu_0 \underline{\chi}_{m,t} \vec{H}(t)\end{aligned}\quad \text{eq. (2.1 - 57)}$$

where $\underline{\chi}_{e,t}$ and $\underline{\chi}_{m,t}$ are tensorial material constants depending on the particular behavior of the fields as a function of time and are referred to as *dielectric* and *magnetic susceptibility*, respectively. In the case of non-linear media, eq. (2.1 - 57) becomes a virial equation containing terms of higher order in E . This will be discussed later in a dedicated section. Inserting eq. (2.1 - 57) into eq. (2.1 - 56) leads to the relative permittivity $\underline{\varepsilon}_{r,t}$ and permeability $\underline{\mu}_{r,t}$ according to:

$$\begin{aligned}\vec{D}(t) &= \underline{\varepsilon}_{r,t} \varepsilon_0 \vec{E}(t) \\ \vec{B}(t) &= \underline{\mu}_{r,t} \mu_0 \vec{H}(t)\end{aligned}\quad \text{eq. (2.1 - 58)}$$

with:

$$\begin{aligned}\underline{\varepsilon}_{r,t} &= 1 + \underline{\chi}_{e,t} \\ \underline{\mu}_{r,t} &= 1 + \underline{\chi}_{m,t}\end{aligned}\quad \text{eq. (2.1 - 59)}$$

Accounting for the tensorial character of the material constants, eq. (2.1 - 58) may be rewritten in terms of its components as:

$$\begin{aligned}D_a(t) &= \varepsilon_0 \sum_b \underline{\varepsilon}_{ab,t} E_b(t) \\ B_a(t) &= \mu_0 \sum_b \underline{\mu}_{ab,t} H_b(t)\end{aligned}\quad \text{eq. (2.1 - 60)}$$

with $a, b = x, y, z$. Accordingly, $\underline{\varepsilon}_{r,t}$ and $\underline{\mu}_{r,t}$ in general consist of 9 elements.

In linear media, each field as a function of time may be expressed by superposition of monochromatic fields using Fourier transformation. In this case, the material constants become frequency dependent and dispersion has to be taken into account.

In loss-free linear media, the reaction of the medium on the fields occurs simultaneously. In this case, the material constants are independent from time and the $\underline{\varepsilon}_r$ - and $\underline{\mu}_r$ -tensors become real and symmetric, as will be shown later.

2.1.3.2.)The oscillator model (Lorentz-model)

The material constants $\underline{\varepsilon}_{r,t}$ and $\underline{\mu}_{r,t}$ can only be derived correctly by means of a quantum mechanical description of the interaction between light and matter. The Lorentz-model, on the other hand, is a classical model, which only gives a qualitative picture.

The Lorentz-model is based on the perception, that the material response to the interaction with a light wave is due to a displacement of the electron cloud of an atom or molecule with respect to its nucleus or manifold of nuclei, induced by the electrical field component of the wave. The nuclei are considered as fixed due to their large mass relative to the electrons. Thus, an oscillating electrical dipole is induced, which, in turn, is subjected to energy dissipation by electro-magnetic radiation damping the induced oscillation. Without loss of generality, this model can be reduced to the most simple system, which is represented by an electron in the central field of a proton. In order to ensure linear response, small elongation is presumed. Furthermore, relativistic effects shall be excluded.

Taking into account, that the driving force for the oscillation is the Coulomb force F :

$$\vec{F} = e_0 \vec{E}, \quad \text{eq. (2.1 - 61)}$$

with e_0 as elementary charge and presuming an incident monochromatic wave at frequency ω :

$$\vec{E} = \vec{E}_0 e^{i\omega t}, \quad \text{eq. (2.1 - 62)}$$

the vibration equation of the electron with respect to the atomic nucleus will be:

$$m\ddot{u} + m\gamma\dot{u} + m\omega_0^2 u = e\vec{E}_0 e^{i\omega t}. \quad \text{eq. (2.1 - 63)}$$

Here m is the electron mass, γ is the damping constant, ω_0 is the resonance frequency of the system and u is the magnitude of the displacement. The solution of this classical problem is:

$$\dot{u}(\omega, t) = \frac{e}{m(\omega_0^2 - \omega^2) + i\gamma\omega} \vec{E}_0 e^{i\omega t} \quad \text{eq. (2.1 - 64)}$$

Presuming, that the individual dipoles do not interact with each other (i.e. the density of dipole is assumed small), the electrical polarization per unit volume may be expressed as the product of the dipole density n_0 and the induced dipoles:

$$\vec{P} = \frac{n_0 e^2}{m(\omega_0^2 - \omega^2) + i\gamma\omega} \vec{E}_0 e^{i\omega t}. \quad \text{eq. (2.1 - 65)}$$

Comparison of eq. (2.1 - 65) with eq. (2.1 - 57) yields an expression for the complex electrical susceptibility $\chi_{e,t}$:

$$\chi_{e,\omega} = \chi_{e,\omega,1} + i\chi_{e,\omega,2} = \frac{n_0 e^2}{m\epsilon_0(\omega_0^2 - \omega^2) + i\gamma\omega} \quad \text{eq. (2.1 - 66)}$$

with the real part:

$$\chi_{e,\omega,1} = \chi_1 = \frac{n_0 e^2 (\omega_0^2 - \omega^2)}{m\epsilon_0 (\omega_0^2 - \omega^2)^2 + \gamma^2 \omega^2} \quad \text{eq. (2.1 - 67)}$$

and the imaginary part:

$$\chi_{e,\omega,2} = \chi_2 = \frac{n_0 e^2 \gamma \omega}{m\epsilon_0 (\omega_0^2 - \omega^2)^2 + \gamma^2 \omega^2}. \quad \text{eq. (2.1 - 68)}$$

The dependence of χ_1 and χ_2 on the frequency in the region of a resonance point is illustrated in figure (2.1 - 4).

Finally it should be noted that the electrical polarization according to eq. (2.1 - 65) represents a wave by its own, called polarization wave. This polarization wave experiences a phase delay relative to the stimulating electro-magnetic wave, which starts at $\phi = 0^\circ$ for $\omega \rightarrow 0$, is 90° at the resonance point ($\omega = \omega_0$) and ends up at $\phi \rightarrow 180^\circ$ for $\omega \rightarrow \infty$. The phase delay around the resonance point is depicted in the inset of figure (2.1 - 4).

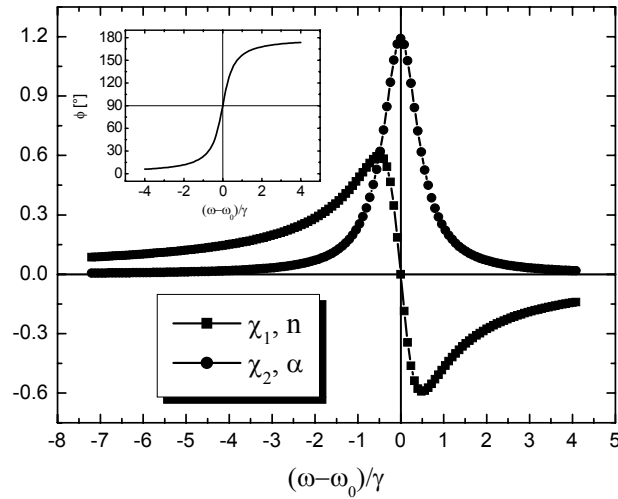


Figure (2.1 - 4): Real part (refractive index) and imaginary part (absorption coefficient) of the electrical susceptibility as a function of frequency near a resonance point. The inset shows the phase delay ϕ between the stimulating wave and the material response.

2.1.3.3.)Loss-free and lossy media

2.1.3.3.1.)Energetic considerations

If an electrical or a magnetic field affects a polarizable medium, the fields perform work. The electro-magnetic work per unit volume w_{em} is identical to the energy density:

$$w_{em} = \int \vec{E} \cdot d\vec{D} + \int \vec{H} \cdot d\vec{B}. \quad \text{eq. (2.1 - 69)}$$

Inserting the material equations eq. (2.1 - 56) yields:

$$w_{em} = \frac{1}{2}[\epsilon_0 \vec{E}^2 + \mu_0 \vec{H}^2] + \int \vec{E} \cdot d\vec{P} + \int \vec{H} \cdot d\vec{M} \quad \text{eq. (2.1 - 70)}$$

and thus, the energy density consists of a field contribution and a contribution of the polarizable medium.

If the medium is linear and the waves involved are monochromatic, eq. (2.1 - 69) yields:

$$w_{em} = \frac{1}{2}\vec{E} \cdot \vec{D} + \frac{1}{2}\vec{H} \cdot \vec{B} = w_e + w_m, \quad \text{eq. (2.1 - 71)}$$

where w_e is the electrical and w_m is the magnetic energy density.

Furthermore, the field energy in a volume V enclosed by the surface F is $\int_V w_{em} dV$ and the energetic flux escaping from V is the surface integral of the Poynting vector.

Thus, applying Gauß' integral law yields:

$$\int_F \vec{S} \cdot d\vec{f} = \int_V \text{div} \vec{S} dV, \quad \text{eq. (2.1 - 72)}$$

where $d\vec{f}$ is the normal vector to an infinitesimal element of the surface F .

If some electro-magnetic field energy in the volume is transformed into another form of energy, power dissipation P_v occurs inside the volume, which can be expressed as the volume integral of the power dissipation density p_v :

$$P_v = \int_V p_v dV = \int_V \text{div} \vec{S} dV + \frac{d}{dt} \int_V w_{em} dV . \quad \text{eq. (2.1 - 73)}$$

Accordingly, the power dissipation density is:

$$p_v = \text{div} \vec{S} + \frac{dw_{em}}{dt} . \quad \text{eq. (2.1 - 74)}$$

Inserting eq. (2.1 - 23) and eq. (2.1 - 71) finally results in:

$$p_v = \frac{1}{2} [\dot{\vec{E}} \cdot \dot{\vec{D}} - \dot{\vec{E}} \cdot \dot{\vec{D}} + \dot{\vec{H}} \cdot \dot{\vec{B}} - \dot{\vec{H}} \cdot \dot{\vec{B}}] - \dot{\vec{E}} \cdot \sigma \dot{\vec{E}} , \quad \text{eq. (2.1 - 75)}$$

where σ is the conductivity of the medium. As already mentioned above this paragraph shall be restricted to dielectric media. Accordingly, the last term is only included for the sake of completeness and will be disregarded hereafter.

2.1.3.3.2.)Loss-free media

If there is no loss of electro-magnetic field energy in the medium, the power dissipation density vanishes, which requires according to eq. (2.1 - 75):

$$\dot{\vec{E}} \cdot \dot{\vec{D}} = \dot{\vec{E}} \cdot \dot{\vec{D}} \quad \text{eq. (2.1 - 76)}$$

$$\dot{\vec{H}} \cdot \dot{\vec{B}} = \dot{\vec{H}} \cdot \dot{\vec{B}}$$

Inserting eq. (2.1 - 62) (i.e. a monochromatic plain wave) into eq. (2.1 - 58), extracting the physically relevant real part and writing the Cartesian components separately results in:

$$D_a = \epsilon_0 \sum_b E_{0b} [Re(\epsilon_{ab}) \cos(\omega_b t) - Im(\epsilon_{ab}) \sin(\omega_b t)] , \quad \text{eq. (2.1 - 77)}$$

with $a = x, y, z$ and $b = x, y, z$. Expressing furthermore eq. (2.1 - 62) in the same way yields:

$$E_b = E_{0b} \cos(\omega_b t) . \quad \text{eq. (2.1 - 78)}$$

Since the requirements according to eq. (2.1 - 76) must be met for loss-free media, it becomes clear, that:

$$Re(\epsilon_{ab}) = Re(\epsilon_{ba}) \quad \text{eq. (2.1 - 79)}$$

$$Im(\epsilon_{ab}) = Im(\epsilon_{ba}) = 0$$

Accordingly, the components of the permittivity tensor ϵ_r are real and symmetric in loss-free media, and a coordinate system (principal axes system) can be found, where:

$$\epsilon_r = (\epsilon_a) = \begin{pmatrix} \epsilon_x & 0 & 0 \\ 0 & \epsilon_y & 0 \\ 0 & 0 & \epsilon_z \end{pmatrix} , (a = x, y, z) . \quad \text{eq. (2.1 - 80)}$$

The same applies for magnetic fields and magnetically polarizable media.

The wave equation and its solution for free space has already been discussed in “2.1.1.) The electro-magnetic theory of light” on page 4. Since the relative permittivity for loss-free media is real, the solution for free space can easily be expanded to loss-free media. Removing the restriction to the free space (however, not allowing for the presence of free charges) the wave equation eq. (2.1 - 11) may be rewritten as:

$$\nabla^2 \vec{E} - \epsilon_r \mu_r \epsilon_0 \mu_0 \frac{\partial^2 \vec{E}}{\partial t^2} = 0 , \quad \text{eq. (2.1 - 81)}$$

with the complex notation already introduced. The solution for the wave equation provided

before will apply here as well (eq. (2.1 - 14)) and will fulfill the wave equation for:

$$k^2 = \varepsilon_r \mu_r \varepsilon_0 \mu_0 \omega^2, \quad \text{eq. (2.1 - 82)}$$

which is the dispersion relation for the wave in the medium.

The propagation velocity c_{ph} of the wave in the medium is according to eq. (2.1 - 12):

$$c_{ph} = \frac{1}{\sqrt{\varepsilon_r \mu_r \varepsilon_0 \mu_0}}, \quad \text{eq. (2.1 - 83)}$$

and is different from the propagation velocity c_0 in free space. The variation of the propagation velocity in the medium relative to the free space is:

$$n = \frac{c_0}{c_{ph}} = \sqrt{\varepsilon_r \mu_r}. \quad \text{eq. (2.1 - 84)}$$

The quantity n is the *refractive index* of the medium. Its frequency dependence is depicted in figure (2.1 - 4). According to eq. (2.1 - 15), it is:

$$k = \frac{\omega}{c_{ph}} = \frac{2\pi}{\lambda} = \frac{2\pi n}{\lambda_0} = nk_0, \quad \text{eq. (2.1 - 85)}$$

where λ_0 is the free space wave length and k_0 is the modulus of the free space wave vector.

The wave resistance of the medium is real and defined by:

$$Z = \sqrt{\frac{\mu_r \mu_0}{\varepsilon_r \varepsilon_0}} \quad \text{eq. (2.1 - 86)}$$

according to eq. (2.1 - 22), which also effects the energy relations, e.g. see eq. (2.1 - 34).

2.1.3.3.)Lossy media

In lossy media power dissipation occurs and the permittivity is complex, as is the susceptibility. According to eq. (2.1 - 84), the refractive index is then complex, too. However, the wave equation (eq. (2.1 - 81)) accounts also for complex material constants. Accordingly, a possible solution is again a plain wave. However, since the refractive index is now complex, according to eq. (2.1 - 85) the wave vector will also be complex (note, that the vacuum wave vector is always real). The plain wave thus writes:

$$\vec{E} = \vec{E}_0 e^{i\vec{k} \cdot \vec{r}}, \quad \text{eq. (2.1 - 87)}$$

with:

$$\vec{k} = n \vec{k}_0. \quad \text{eq. (2.1 - 88)}$$

Here n is the complex refractive index resulting from eq. (2.1 - 84) and the complex material constants. Note, that one may as well formulate a complex wavelength, but (in linear media) not a complex frequency. It depends on the particular problem, which formulation is most appropriate.

According to the equations eq. (2.1 - 84), eq. (2.1 - 68), eq. (2.1 - 67) and eq. (2.1 - 59) the complex refractive index can be expressed as:

$$n = \sqrt{1 + \chi_1 - i\chi_2}, \quad \text{eq. (2.1 - 89)}$$

where $\mu_r = 1$ (i.e. the medium is not magnetizable) was presumed for the sake of simplicity. If the loss is small (i.e. $|\chi_2| \ll 1 + \chi_1$), eq. (2.1 - 89) may be approximated by:

$$n = \sqrt{1 + \chi_1} - i \frac{\chi_2}{2\sqrt{1 + \chi_1}} \quad \text{eq. (2.1 - 90)}$$

and thus be separated into a real and an imaginary refractive index. Inserting eq. (2.1 - 90) into

eq. (2.1 - 87) yields the plain wave:

$$\vec{E} = \vec{E}_0 e^{in_r \vec{k}_0 \cdot \vec{r} + \frac{\alpha}{2} \vec{k}_0 \cdot \vec{r}}, \quad \text{eq. (2.1 - 91)}$$

where \vec{k}_0 is the unit vector in propagation direction of the wave, n_r is the real refractive index:

$$n_r = \sqrt{1 + \chi_1} \quad \text{eq. (2.1 - 92)}$$

and α is the absorption coefficient:

$$\alpha = \frac{2\pi\chi_2}{\lambda_0 \sqrt{1 + \chi_1}}. \quad \text{eq. (2.1 - 93)}$$

The qualitative frequency dependence of n_r and α in the region of a resonance point is depicted in figure (2.1 - 4). Usually, α is positive and the wave according to eq. (2.1 - 91) will decrease exponentially in amplitude while propagating. However, α may be negative in some cases, which are not subject of the present discussion (e.g. in the case of stimulated emission). It should furthermore be pointed out, that the separation of the complex refractive index into the real refractive index and the absorption coefficient performed as above will not hold, if the approximation $|\chi_2| \ll 1 + \chi_1$ is not valid.

The wave resistance of a lossy medium is complex as well:

$$\tilde{Z} = \sqrt{\frac{\tilde{\mu}_r \mu_0}{\tilde{\varepsilon}_r \varepsilon_0}}, \quad \text{eq. (2.1 - 94)}$$

which, according to eq. (2.1 - 21), leads to a dephasing φ of the magnetic component of the electro-magnetic wave relative to the electrical component:

$$\varphi = \text{atan}\left(-\frac{\alpha\lambda_0}{4\pi n_r}\right). \quad \text{eq. (2.1 - 95)}$$

The energy relations (see page 7 ff) are effected as well and the intensity now depends on the penetration depth of the wave in the medium according to:

$$I(\vec{k}_0, \vec{r}) = I_0 e^{-\alpha(\vec{k}_0 \cdot \vec{r})}. \quad \text{eq. (2.1 - 96)}$$

2.1.4.) Reflection and refraction

In this paragraph, the phenomenological and the electro-magnetic treatment of reflection and refraction of light at interfaces will be outlined. Fresnel's equations will be derived, but not interpreted in detail. Thereafter, birefringence will be treated with restriction to uniaxial systems. The special features of inner total reflection as well as reflection and refraction at metallic surfaces will be disregarded.

2.1.4.1.)Phenomenological treatment of reflection and refraction

The phenomenological description of reflection and refraction can be illustrated using the Huygens-Fresnel principle, which has already been formulated above in “2.1.2.5.1.) The Huygens-Fresnel principle” on page 15. Assuming that a plain wave front passes through an interface between two media (which shall be assumed at first to be air and some dielectric) the wave front will be scattered by the atoms at the interface, generating elementary waves at each atom in accordance with the Huygens-Fresnel principle. If the wave front does not pass perpendicularly through the interface, different areas of the wave front will pass at different times through the interface generating delayed elementary waves, which emanate to the outside as well as to the inside of the dielectric. The superposition of the elementary waves outside the dielectric will then form a new wave front propagating outside the dielectric in a different direction than the incident one. This situation is depicted in figure (2.1 - 5). The incident wave front is denoted by “A“ (= “A1 + A2“) and half of the wave front (“A2“) has already passed through the interface generating delayed elementary waves outside the dielectric, which form the emerging wave front “B“. As soon as the rest of front “A“ (i.e. “A1“) has passed through the interface, the new wave front “B“ will be complete. “B“ is the reflected part of “A“. However, the elementary waves inside the dielectric will propagate with reduced velocity (provided the refractive index inside the dielectric is larger than outside) as compared to the elementary waves outside the dielectric. They, in turn, form another wave front “C“ propagating inside the dielectric. Since the elementary waves exhibit a different propagation velocity than the elementary waves outside, the propagation direction of the wave front “C“ is different from the original wave front “A“. “C“ will also be complete as soon as “A“ has completely passed through the interface and is the refracted part of “A“.

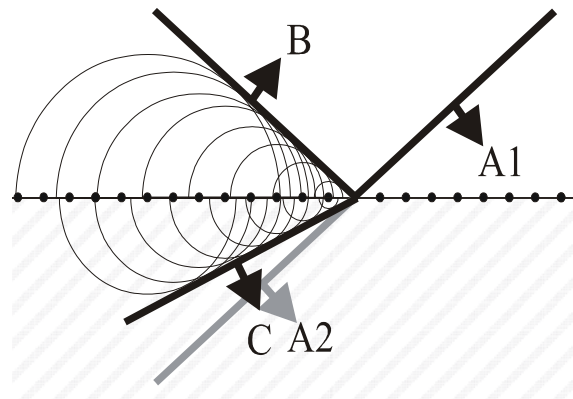


Figure (2.1 - 5): Reflection and refraction of a wave front according to the Huygens-Fresnel principle

2.1.4.1.1.)Fermat’s least-time principle

In order to quantify the relations described above, it is more convenient to apply another fundamental principle of elementary optics, the *least-time principle*, which was already formulated in its present form 1657 by Pierre de Fermat:

The path taken by a light beam between any two points in a system is always the path that takes the least time.

However, this (original) formulation is not unequivocal, since it does not account for the possibility of fundamentally different paths between two points, e.g one direct path and another longer path including reflections. The least time principle in the above formulation would exclude the latter one. This problem is solved by the following (modern) formulation, allowing for different optical paths and defining the “least-time“ condition for each possible path:

A light-beam going from one point to another must traverse an optical path length which is stationary with respect to small variations of that path.

2.1.4.1.2.)Reflection law and Snellius' refraction law

According to Fermat's principle, the time t_{AB} for the light to traverse from A to B and t_{AC} from A to C has to be "stationarized" as a function of x_A and x_B for t_{AB} and x_A and x_C for t_{AC} , respectively. The geometry of the arrangement is illustrated in figure (2.1 - 6). The traversing times may be expressed as:

$$t_{AB} = \frac{\sqrt{x_A^2 + y_A^2}}{c_i} + \frac{\sqrt{x_B^2 + y_B^2}}{c_i} \text{ eq. (2.1 - 97)}$$

and:

$$t_{AC} = \frac{\sqrt{x_A^2 + y_A^2}}{c_i} + \frac{\sqrt{x_C^2 + y_C^2}}{c_t} \text{ eq. (2.1 - 98)}$$

where $c_{i,t}$ are the propagation velocities of the light in the media with the associated refractive index $n_{i,t}$, respectively. In order to eliminate one of the x -components in the above equations:

$$x_B - x_A = a \text{ eq. (2.1 - 99)}$$

$$x_C - x_A = b$$

is introduced and the traversing time is minimized with respect to the remaining x -component, yielding:

$$\frac{dt_{AB}}{dx_B} = \frac{2(a + x_B)}{c_i \sqrt{(a + x_B)^2 + y_A^2}} + \frac{2x_B}{c_i \sqrt{x_B^2 + y_B^2}} = 0 \text{ eq. (2.1 - 100)}$$

and:

$$\frac{dt_{AC}}{dx_C} = \frac{2(a + x_C)}{c_i \sqrt{(a + x_C)^2 + y_A^2}} + \frac{2x_C}{c_t \sqrt{x_C^2 + y_C^2}} = 0. \text{ eq. (2.1 - 101)}$$

Introducing the correlated trigonometric functions, eq. (2.1 - 100) finally results in:

$$\theta_i = \theta_r, \text{ eq. (2.1 - 102)}$$

which is known as the *reflection law* and eq. (2.1 - 101) yields:

$$\frac{\sin \theta_i}{c_i} = \frac{\sin \theta_t}{c_t}. \text{ eq. (2.1 - 103)}$$

With eq. (2.1 - 84) one obtains *Snellius' refraction law* from the above equation:

$$\frac{\sin \theta_i}{\sin \theta_t} = \frac{n_t}{n_i}. \text{ eq. (2.1 - 104)}$$

It becomes clear from the modern formulation of Fermat's principle, that "stationarizing" a light beam path allows for local minima as well as turning points for the traversing time as a function of the path. The original least-time principle in its strict interpretation only refers to the absolute minimum of the traversing time.

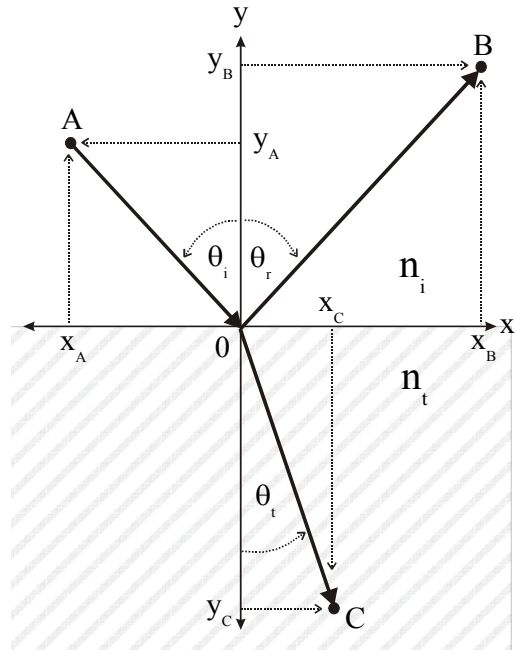


Figure (2.1 - 6): Fermat's least-time principle applied on reflection and refraction.

2.1.4.2.)The electro-magnetic approach to reflection and refraction

The electro-magnetic approach leads to a much more complete description of reflection and refraction known as Fresnel's equations. Based on these equations predictions of the reflected and transmitted relative intensities as well as the phase relations between the incident, the reflected and the refracted wave can be made. Subsequently, the basic equations will be derived and discussed as far as advisable within the frame of this work.

The derivation of Fresnel's equations bases on the continuity conditions for electro-magnetic waves at dielectric interfaces without surface charge density and surface current density, which read:

$$\vec{n} \times (\vec{E}_t - \vec{E}_i) = 0 \quad \text{eq. (2.1 - 105)}$$

$$\vec{n} \cdot (\vec{D}_t - \vec{D}_i) = 0 \quad \text{eq. (2.1 - 106)}$$

$$\vec{n} \times (\vec{H}_t - \vec{H}_i) = 0 \quad \text{eq. (2.1 - 107)}$$

$$\vec{n} \cdot (\vec{B}_t - \vec{B}_i) = 0, \quad \text{eq. (2.1 - 108)}$$

where index "i" denotes the physical quantity incident on a dielectric interface, index "t" denotes the transmitted part of the quantity and \vec{n} is the surface normal vector of the interface under consideration. For a detailed discussion of the continuity conditions reference is made to the standard literature of theoretical electrodynamics.

2.1.4.2.1.)Fresnel's equations

According to the continuity conditions, the electro-magnetic consideration of reflection and refraction must be divided into two parts for the two limiting cases of the orientation of the field vectors relative to the interface considered. A randomly polarized light beam actually will be split into these two components, which then behave differently in refraction as well as reflection. It is common practice to consider only the electrical field component of the electro-magnetic wave. Furthermore, non-absorbing media are assumed for the derivation, however, the results are valid for absorbing media as well if complex refractive indices are used.

Please note, that there are two possible notations, which differ by the reference plane. Usually, the polarization states are referred to the plane of incidence, which is defined as the plane in which the incident and the reflected beams propagate. Referring instead the polarization states to the considered interface is uncommon, since the situation becomes quickly puzzling, if more than one interface is involved. In this work, the plane of incidence serves as reference plane in all cases.

2.1.4.2.1.1.) s-polarization

For s-polarization, the *electrical field vector* of the considered plain wave is oriented tangentially to the interface (figure (2.1 - 7)).

In order to derive Fresnel's equations one has to realize, that this is a problem with two unknown parameters, which are the reflected and the refracted wave, whereas the incident wave is known. Accordingly, two linearly independent equations are required, which can be obtained by using the continuity conditions of eq. (2.1 - 105) to eq. (2.1 - 108). The continuity conditions are linked via eq. (2.1 - 20), which is generally valid:

$$\vec{e}_k \times \vec{E} = c\vec{B}, \quad \text{eq. (2.1 - 109)}$$

where \vec{e}_k is the unit vector of the wave propagation direction and c is the propagation velocity of the wave. For the notation used from now on reference is made to figure (2.1 - 7).

Accounting for the continuity condition eq. (2.1 - 105), the relation between the electrical fields is:

$$\vec{E}_{0i} + \vec{E}_{0r} = \vec{E}_{0t}. \quad \text{eq. (2.1 - 110)}$$

Please note already here, that \vec{E}_{0r} is oriented anti-parallel to \vec{E}_{0t} and \vec{E}_{0i} , which will be shown later. Furthermore, the continuity of the tangential component of the magnetic field \vec{H} (eq. (2.1 - 107)) requires:

$$-\vec{H}_{0i} \cos \theta_i + \vec{H}_{0r} \cos \theta_r = -\vec{H}_{0t} \cos \theta_t \quad \text{eq. (2.1 - 111)}$$

Inserting $\vec{B} = \mu \vec{H}$ and eq. (2.1 - 109) (or eq. (2.1 - 20)) while accounting only for the modula of the field vectors, accounting for $c_i = c_r$, applying eq. (2.1 - 84) and eq. (2.1 - 102), and choosing an appropriate origin for the coordinate system (see figure (2.1 - 7)) finally yields:

$$r_s \equiv \left(\frac{E_{0r}}{E_{0i}} \right)_s = \frac{\frac{n_i}{\mu_i} \cos \theta_i - \frac{n_t}{\mu_t} \cos \theta_t}{\frac{n_i}{\mu_i} \cos \theta_i + \frac{n_t}{\mu_t} \cos \theta_t} \quad \text{eq. (2.1 - 112)}$$

and:

$$t_s \equiv \left(\frac{E_{0t}}{E_{0i}} \right)_s = \frac{2 \frac{n_i}{\mu_i} \cos \theta_i}{\frac{n_i}{\mu_i} \cos \theta_i + \frac{n_t}{\mu_t} \cos \theta_t}, \quad \text{eq. (2.1 - 113)}$$

where r_s and t_s are referred to as *amplitude reflection coefficient* and *amplitude transmission coefficient*, respectively. These equations are generally valid for arbitrary media.

In most cases, dielectrics are considered, which meet the approximation:

$$\mu_i \approx \mu_r \approx \mu_0. \quad \text{eq. (2.1 - 114)}$$

Then, the permeabilities in eq. (2.1 - 112) and eq. (2.1 - 113) fall apart and two equations are obtained, which are referred to as Fresnel's equations (for s-polarized light). By means of Snellius' refraction law (eq. (2.1 - 104)), eq. (2.1 - 112) and eq. (2.1 - 113) finally rewrite as:

$$r_s = - \frac{\sin(\theta_i - \theta_t)}{\sin(\theta_i + \theta_t)} \quad \text{eq. (2.1 - 115)}$$

and:

$$t_s = \frac{2 \sin \theta_t \cos \theta_i}{\sin(\theta_i + \theta_t)}, \quad \text{eq. (2.1 - 116)}$$

respectively.

2.1.4.2.1.2.)p-polarization

For p-polarization, the *magnetic field vector* of the considered plain wave is oriented tangentially to the interface (figure (2.1 - 7) with the polarization of the sketched waves rotated by +90° around the propagation vector).

The continuity condition eq. (2.1 - 105) for the tangential component of the electrical field

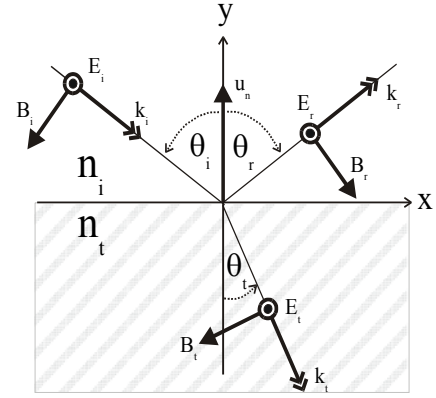


Figure (2.1 - 7): electrical field vector tangential to the interface

vector reads here:

$$\vec{E}_{0i} \cos \theta_i - \vec{E}_{0r} \cos \theta_r = \vec{E}_{0t} \cos \theta_t. \quad \text{eq. (2.1 - 117)}$$

Furthermore, the continuity of the dielectric displacement (eq. (2.1 - 106) requires:

$$\vec{D}_{0i} \sin \theta_i + \vec{D}_{0r} \sin \theta_r = \vec{D}_{0t} \sin \theta_t, \quad \text{eq. (2.1 - 118)}$$

which, with eq. (2.1 - 104), eq. (2.1 - 102) and eq. (2.1 - 84), transforms to:

$$(\vec{E}_{0i} + \vec{E}_{0r}) \sin \theta_i = \frac{\mu_t n_t}{\mu_i n_i} \vec{E}_{0t} \sin \theta_t \quad \text{eq. (2.1 - 119)}$$

where n is the refractive index of the corresponding medium and μ is its permeability. With eq. (2.1 - 117) the amplitude reflection r_p and transmission t_p coefficients are finally given by:

$$r_p \equiv \left(\frac{E_{0r}}{E_{0i}} \right)_p = \frac{\frac{n_t}{\mu_t} \cos \theta_i - \frac{n_i}{\mu_i} \cos \theta_t}{\frac{n_i}{\mu_i} \cos \theta_t + \frac{n_t}{\mu_t} \cos \theta_i} \quad \text{eq. (2.1 - 120)}$$

and:

$$t_p \equiv \left(\frac{E_{0t}}{E_{0i}} \right)_p = \frac{2 \frac{n_i}{\mu_i} \cos \theta_i}{\frac{n_i}{\mu_i} \cos \theta_t + \frac{n_t}{\mu_t} \cos \theta_i}. \quad \text{eq. (2.1 - 121)}$$

These equations are generally valid for arbitrary media.

In analogy to the above, eq. (2.1 - 120) and eq. (2.1 - 121) are strongly simplified if the medium under consideration is purely dielectric, i.e., eq. (2.1 - 114) applies. Then, with eq. (2.1 - 104), eq. (2.1 - 120) and eq. (2.1 - 121) rewrite as:

$$r_p = \frac{\tan(\theta_i - \theta_t)}{\tan(\theta_i + \theta_t)} \quad \text{eq. (2.1 - 122)}$$

and:

$$t_p = \frac{2 \sin \theta_t \cos \theta_i}{\sin(\theta_i + \theta_t) \cos(\theta_i - \theta_t)}, \quad \text{eq. (2.1 - 123)}$$

respectively.

2.1.4.2.2.) Interpretation of Fresnel's equations

Two different situations must be considered, which are the *outer reflection* ($n_t > n_i$) and the *inner reflection* ($n_t < n_i$). A detailed discussion is beyond the scope of this work. The objective of this paragraph is to give a quick and qualitative overview over the basic results, which is best performed graphically. The classical example of an air ($n = 1$) / glass ($n = 1.5$) - interface forms the basis for the graphics.

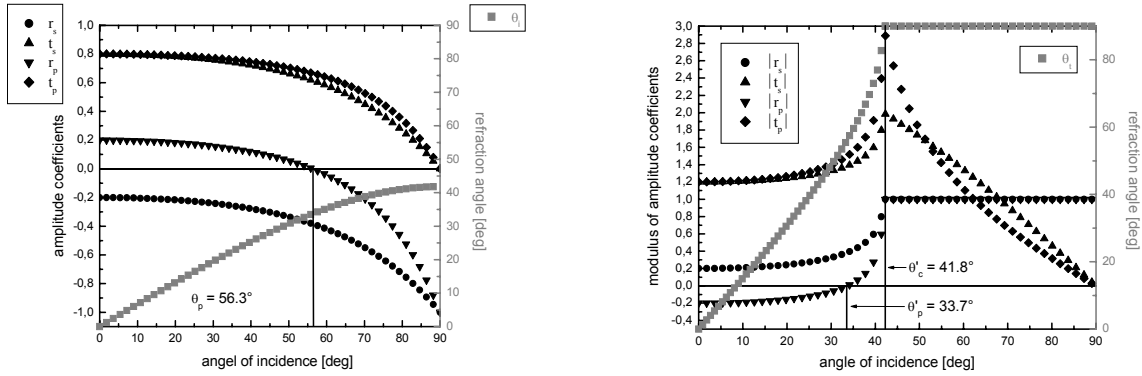


Figure (2.1 - 8): Amplitude coefficients according to Fresnel's equations for an air/glass-interface for outer reflection (left) and inner reflection (right)

At first the amplitude coefficients will be considered, which determine the reflectance and the transmittance of an interface. The amplitude coefficients for outer reflection are real over the whole interval of possible angles of incidence. At the so called *polarization angle* (θ_p) or *Brewster angle* (the latter is the more common notation) the amplitude reflection coefficient for p-polarized light drops to zero, whereas the other coefficients remain finite. This feature can be used for generating polarized light. At an incident angle of 90° (incidence "parallel" to the interface), the light is completely reflected.

The amplitude coefficients for inner reflection are real up to a limiting angle θ_c which marks the onset of *total inner reflection*. For angles of incidence greater than the limiting angle, the amplitude coefficients become complex. There is also a polarization angle, which is smaller than the limiting angle. The fact, that the transmission amplitude coefficients do not drop to zero in the area of total inner reflection is demanded by the electro-magnetic theory (the continuity conditions forbid a singular situation at the interface). However, the transmitted wave "propagates" in the medium of smaller refractive index parallel to the interface (i.e., the refraction angle formally becomes 90°). This wave is called *evanescent wave* (figure (2.1 - 9)). Its amplitude decreases exponentially as a function of the distance from the interface.

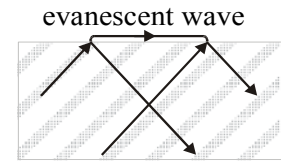


Figure (2.1 - 9): Illustration of an evanescent wave

Please note, that the sum of the amplitude coefficients need not equal one, but rather the sum of the *reflectance* R and *transmittance* T in order to ensure energy preservation.

The reflectance is defined by:

$$R = \frac{I_r}{I_i} = r^2, \quad \text{eq. (2.1 - 124)}$$

where I_i is the incident- and I_r the reflected intensity, and r is the amplitude reflection coefficient. The transmittance is defined by:

$$T = \frac{I_t \cos \theta_t}{I_i \cos \theta_i} = \frac{n_t E_{0t}^2 \cos \theta_t}{n_i E_{0i}^2 \cos \theta_i} = \left(\frac{n_t \cos \theta_t}{n_i \cos \theta_i} \right) t^2, \quad \text{eq. (2.1 - 125)}$$

where t is the transmission amplitude coefficient. The index "t" denotes parameters for the transmitted wave, and θ is the angle, which the wave vector encloses with the normal to the interface.

Secondly, the phase relations between the incident, the reflected, and the transmitted wave

will be discussed. The situation of the total inner reflection will not be elaborated upon, since it is fairly complicated and beyond the scope of this work.

The transmitted wave generally does not experience any phase change with respect to the incident wave, which can readily be derived from the fact, that the amplitude transmission coefficient is never negative.

The phase relation between the incident wave and the reflected wave is illustrated in figure (2.1 - 10) as a function of the incidence angle θ_i .

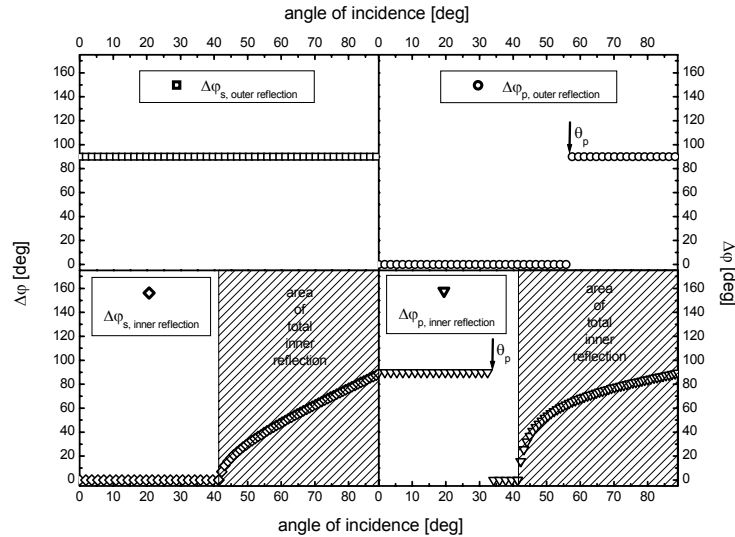


Figure (2.1 - 10): Phase relations for outer and inner reflection. θ_p is the Brewster angle.

2.1.4.3.)Uniaxial birefringence

Birefringence is a phenomenon, which occurs in homogenous, but optically anisotropic media. Optical anisotropy covers the general feature of direction-dependent optical properties of matter. This may refer to various optical parameters, of which the refractive index leads to birefringence. Accordingly, birefringent media feature a direction dependent refractive index. Depending on the symmetry of the medium there are two types of birefringence, uniaxial and biaxial birefringence. While the basic concepts of birefringence apply to both types, biaxial media are less symmetric than uniaxial and, thus, biaxial birefringence is mathematically much more difficult to treat. Since photorefractive polymers only show uniaxial birefringence, biaxial birefringence will be disregarded. Hereafter, all terms concerning birefringence will refer exclusively to uniaxial birefringence unless explicitly noted otherwise.

The birefringence will at first be discussed semi-empirically and in terms of the Huygens-Fresnel principle in order to get a detailed ostensible picture of the wave propagation in birefringent media. After that, a treatment in terms of propagation of plane waves in anisotropic media will be outlined leading to the important general term of the *index ellipsoid*.

2.1.4.3.1.)Optical axis

Uniaxial birefringent media exhibit exactly one at least threefold crystallographic principal axis, which is the axis of highest symmetry of the system. Please note, that the principal axis needs not be purely rotational, but may include translation or inversion. Due to its

symmetry, the crystallographic principal axis defines also a preferred optical direction in the system along of which the medium is optically isotropic. Therefore, this direction is called the *optical axis* of the system. Please note, that the term “axis“ does not refer to a spatially fixed line but rather to a spatial direction.

It should also be noted, that the above conclusion from a crystallographic principal axis to an optical axis cannot be reversed. Thus, biaxial birefringence does not imply the existence of two crystallographic principal axes.

2.1.4.3.2.)Phenomenology of uniaxial birefringence

If a transparent birefringent medium is illuminated with natural light in normal incidence but tilted by $0^\circ < \alpha < 90^\circ$ with respect to the optical axis, the light beam is split into two beams inside the medium, each of which having half of the incident intensity. One beam is transmitted straightly through the medium in accordance with Snellius' refraction law, whereas the other beam is spatially separated from the first as a function of the thickness of the medium violating Snellius' refraction law. By rotating the medium around the incident (and straightly transmitted) beam, the second beam describes an envelope of cone around the incident beam inside the medium and a cylinder casing behind (i.e., outside) the medium without changing the intensity relations.

Checking for the polarization states, the straightly transmitted beam is found to be s-polarized with respect to the plane defined by the optical axis and the incident beam, whereas the spatially separated beam turns out to be p-polarized. Generally, the plane defined by the optical axis and the perpendicular of incidence of the incident beam is called *main section (of the incident beam)* and is of utmost significance for the description of the birefringence. On the basis of this definition, the two beams now can be denoted unequivocally by means of their polarization state relative to the main section:

- s-polarized: *ordinary beam* (o-beam)
- p-polarized: *extraordinary beam* (e-beam)

The two polarization states are sometimes referred to as “eigen polarizations“ of a wave.

2.1.4.3.3.)Wave and beam velocity

The concept of the wave and beam velocity has been developed by Huygens on the basis of his famous principle. He concluded from the experimental observations known at his time (i.e. the polarization states and their relation were not known, yet), that a point source placed in an uniaxial medium will generate two wave fronts, one of which is spherical (o-beam) and the other (e-beam) is an ellipsoid of revolution. The two surfaces touch at two diametrically opposite points, the connection of which coincides with the optical axis of the system. This picture allows for two different geometrical constructions, which are illustrated in figure (2.1 - 11).

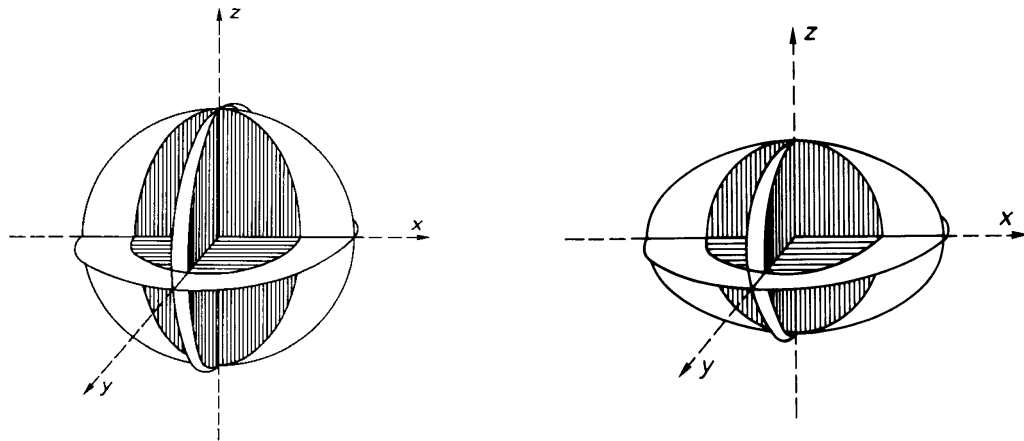


Figure (2.1 - 11): Wave front surface for optical positive (left) and optical negative (right) uniaxial birefringence. The optical axis is the z-axis. Left, the wave front surface of the e-beam is hatched, whereas the wave front surface of the o-beam is hatched in the right figure. Pictures taken from [B1]

In order to get a more detailed insight, an incident wave is considered in terms of this concept in figure (2.1 - 12).

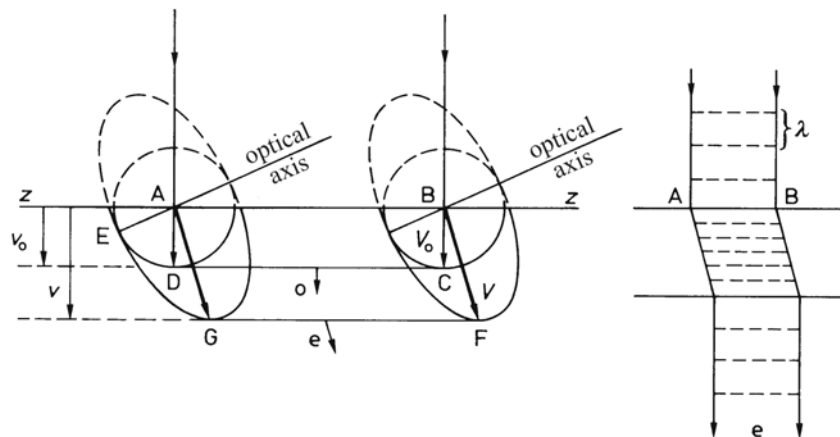


Figure (2.1 - 12): Beam and wave propagation in optical negative birefringent medium for normal incidence onto the medium and tilted incidence with respect to the optical axis in 2-dimensional representation. The main section is the picture plane. Pictures taken from [B1].

From figure (2.1 - 12) it becomes clear that the e-beam experiences a spatial separation from the o-beam in the illustrated case, which also has been described before phenomenologically. The key of the spatial separation in the concept of Huygens is the proposition of two velocities differing in direction as well as magnitude, which describe the propagation of the e-beam. The so called *wave velocity* v describes the actual propagation of a state of constant phase and is oriented normal to the wave fronts of the considered beam, whereas the so called *beam velocity* V describes the propagation of the radiation energy and is oriented along the direction AG (or BF) in figure (2.1 - 12). The latter is as well the direction of the Poynting vector, which, in this case, is no more normal to the wave fronts. Please note, that the electro-magnetic theory explains this by the permittivity tensor applying for anisotropic media, which causes the electrical field vector and the dielectric displacement to be no more parallel. This may be made more ostensible considering a parallel plate capacitor in which a wire is brought in with an angle of e.g 45° relative to the electric field lines. The electrical field

will cause dielectric displacement in the wire, which will basically be oriented along the wire and, thus, not be parallel to the electrical field vector. In contrast, for the o-beam, these two velocities are identical, however, may be separated formally for the sake of consistency, as shown in figure (2.1 - 12).

While the wave and the beam velocity for the o-beam are always identical and not a function of the angel of incidence onto the optical axis, these velocities are always a function of the angel of incidence onto the optical axis for the e-beam and only identical for two important limiting cases:

- a) For incidence parallel to the optical axis, the wave and the beam velocity of the e-beam as well as the o-beam are all identical and the medium is isotropic.
- b) For incidence perpendicular to the optical axis, the wave and the beam velocity of the e-beam are identical, however, different to the corresponding velocities of the o-beam and the medium behaves isotropic but actually is not.

These two limiting cases represent two characteristic constants of a birefringent medium, namely the two *principal propagation velocities* V_o and V_e . V_o is the propagation velocity referring to limiting case a). V_e is the propagation velocity referring to the e-beam in limiting case b).

In terms of the principal propagation velocities, the two *principal refractive indices* n_o and n_e of the medium under consideration are defined according to eq. (2.1 - 84) by:

$$n_{o(e)} = \frac{c_0}{V_{o(e)}}, \quad \text{eq. (2.1 - 126)}$$

where n_o is the ordinary and n_e is the extraordinary principal refractive index.

In terms of the principal refractive indices, the character of the birefringence is commonly defined as:

$$\begin{aligned} n_e - n_o < 0 &\Rightarrow \text{optical negative} \\ n_e - n_o > 0 &\Rightarrow \text{optical positive} \end{aligned}$$

According to the occurrence of two different velocities (beam velocity and wave velocity) in birefringent media, it is possible to derive two types of refractive indices for the e-beam (the refractive index for the o-beam is always n_o).

2.1.4.3.4.)Beam refractive index

According to eq. (2.1 - 126), a beam refractive index n_B may be defined as:

$$n_B = \frac{c_0}{V}, \quad \text{eq. (2.1 - 127)}$$

with the beam velocity V of the e-beam. In order to derive an expression for V , the wave front surfaces according to figure (2.1 - 11) are expressed conjointly in Cartesian coordinates as:

$$\left(\frac{x^2 + y^2 + z^2}{V_o^2} - 1 \right) \left(\frac{x^2 + y^2}{V_e^2} + \frac{z^2}{V_o^2} - 1 \right) = 0. \quad \text{eq. (2.1 - 128)}$$

The rotational symmetry of the problem suggests an expression in polar coordinates:

$$\left(\frac{V^2}{V_o^2} - 1 \right) \left(\frac{V^2}{V_e^2} (\sin \Phi)^2 + \frac{V^2}{V_o^2} (\cos \Phi)^2 - 1 \right) = 0, \quad \text{eq. (2.1 - 129)}$$

with:

$$\begin{aligned}x^2 + y^2 &= V^2(\sin\Phi)^2 \\z^2 &= V^2(\cos\Phi)^2\end{aligned}\quad \text{eq. (2.1 - 130)}$$

where Φ is the elevation angle. Due to the rotational symmetry there is no dependence on the azimuth angle. From eq. (2.1 - 129), an expression for the beam velocity of the e-beam can be deduced:

$$V = \sqrt{\frac{V_o^2 V_e^2}{V_o^2(\sin\Phi)^2 + V_e^2(\cos\Phi)^2}}\quad \text{eq. (2.1 - 131)}$$

which enters into the beam refractive index according to eq. (2.1 - 127). Despite the consideration of the beam refractive index and the beam velocity may be convenient for some problems, it is not possible to derive a simple refraction law from the beam refractive index, since the angle and distance relations are not adaptable to Snellius' refraction law because the propagation direction of the beam in the medium does not coincide with the wave front normal. Employing Fermat's principle to derive the refraction law as performed above, this is not as clear as it is in the derivation using the Huygens principle. However, the problem is similarly essential, since Fermat's principle simply does not apply to the e-beam. Considering figure (2.1 - 12), it becomes ostensibly clear, that the actual e-beam path length is not stationary against small variations of the path. This applies only to the formal path of the wave fronts along their normal, showing on the other hand, that this problem can be solved by considering the wave refractive index.

2.1.4.3.5.)Wave refractive index

In analogy to eq. (2.1 - 127) the wave refractive index n_W is defined as:

$$n_W = \frac{c_0}{v},\quad \text{eq. (2.1 - 132)}$$

with the wave velocity v of the e-beam representing the propagation velocity of the wave fronts along their normal in the medium. Furthermore in analogy to the wave front surfaces in figure (2.1 - 11) representing the beam velocities for the o- and the e-beam in different directions relative to the optical axis, "normal front surfaces" can be defined, which may be interpreted as *phase surfaces* (and will hereafter be called so) representing the corresponding velocities of the wave fronts along their normals (wave velocities). It is easy to see, that the phase surface and the wave front surface are identical for the o-beam and different for the e-beam. The phase surface for the e-beam is a surface of fourth order enveloping the corresponding wave front surface and has the shape of an ovaloid of revolution. The derivation of the mathematical expression for the phase surface of the e-beam is extensive and beyond of the scope of this work. The conjoint expression for the phase surfaces in polar coordinates will turn out to be:

$$\left(\frac{v^2}{V_o^2} - 1\right)(V_e^2(\sin\phi)^2 + V_o^2(\cos\phi)^2 - v^2) = 0\quad \text{eq. (2.1 - 133)}$$

with:

$$\begin{aligned}v^2(\sin\phi)^2 &= x^2 + y^2 \\v^2(\cos\phi)^2 &= z^2\end{aligned}\quad \text{eq. (2.1 - 134)}$$

where ϕ is the elevation angle. Due to the rotational symmetry there is no dependence on the azimuth angle. Please note, that ϕ here and Φ in eq. (2.1 - 130) are different for all $0^\circ < \phi, \Phi < 90^\circ$. Furthermore, the extrema of the radius vectors of the phase surfaces and the wave front

surfaces are identical and, thus, the parameters of the wave front surfaces have already been used in eq. (2.1 - 133).

Inserting eq. (2.1 - 132), an expression for the wave refractive index of the e-beam can be extracted from eq. (2.1 - 133):

$$n_W = \sqrt{\frac{n_o^2 n_e^2}{n_o^2 (\sin \phi)^2 + n_e^2 (\cos \phi)^2}}. \quad \text{eq. (2.1 - 135)}$$

With n_W , Snellius' refraction law can be applied to the e-beam for arbitrary incidence on a birefringent medium:

$$\frac{\sin \theta_i}{\sin \theta_{t,e}} = \frac{n_W}{n_i}, \quad \text{eq. (2.1 - 136)}$$

with θ_i as the angle of incidence relative to the interface normal, $\theta_{t,e}$ as the angle of transmission of the wave front normal of the e-beam and n_i as the refractive index outside the birefringent medium under consideration. It is self-evident, that the wave refractive index and the corresponding angle has to be used for reflection as well as transmission for interfaces between two birefringent media.

In order to solve for the actual beam propagation, a relation between ϕ and Φ must be found. In the x-z-plane in figure (2.1 - 11), the wave front surface for the e-beam will reduce to an ellipse described by:

$$\frac{x^2}{V_e^2} + \frac{z^2}{V_o^2} = 1, \quad \text{eq. (2.1 - 137)}$$

which may be expressed in terms of the principal refractive indices using eq. (2.1 - 126):

$$n_e^2 x^2 + n_o^2 z^2 = c_0^2. \quad \text{eq. (2.1 - 138)}$$

Solving this equation for $z(x)$ and differentiating in x results in:

$$z' = -\frac{x n_e^2}{z n_o^2}. \quad \text{eq. (2.1 - 139)}$$

Since z' is the slope of the wave front WF as sketched in figure (2.1 - 13), it is:

$$z' = \tan(\pi - \phi). \quad \text{eq. (2.1 - 140)}$$

By furthermore accounting for:

$$\frac{x}{z} = \tan \Phi \quad \text{eq. (2.1 - 141)}$$

the desired relation between ϕ and Φ is obtained to:

$$\frac{n_e^2}{n_o^2} = \frac{\tan \phi}{\tan \Phi}. \quad \text{eq. (2.1 - 142)}$$

Furthermore, it follows from figure (2.1 - 13), that:

$$\frac{v}{V} = \cos(\Phi - \phi). \quad \text{eq. (2.1 - 143)}$$

Applying eq. (2.1 - 126) and eq. (2.1 - 132) to eq. (2.1 - 133) yields another pair of characteristic surfaces, the *wave refractive index surfaces* (or in short terms: "index surfaces"):

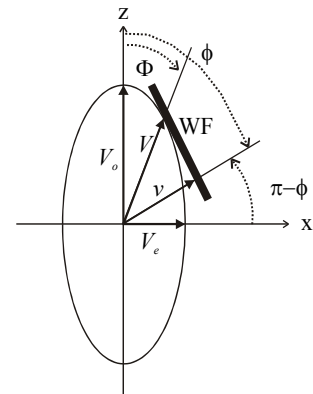


Figure (2.1 - 13): Parameters for the e-beam as discussed in this section. WF is a tangential wave front and the z-axis is the optical axis

$$\left(\frac{n_o^2}{n_w^2} - 1\right)\left(\frac{n_w^2}{n_e^2}(\sin\phi)^2 + \frac{n_w^2}{n_o^2}(\cos\phi)^2 - 1\right) = 0, \quad \text{eq. (2.1 - 144)}$$

or in Cartesian coordinates using eq. (2.1 - 134) and eq. (2.1 - 132):

$$\left(1 - \frac{x^2 + y^2 + z^2}{n_o^2}\right)\left(\frac{x^2 + y^2}{n_e^2} + \frac{z^2}{n_o^2} - 1\right) = 0. \quad \text{eq. (2.1 - 145)}$$

Please note, that the index surfaces have basically the same shape as the wave front surfaces (see eq. (2.1 - 128)) but have exchanged their appearance concerning the optical character due to the reciprocal relation between the wave velocity and its corresponding refractive index. The index surfaces for a birefringent medium of optical negative character will correlate with the left picture in figure (2.1 - 11) and optical positive character will correlate with the right picture. This is also qualitatively illustrated in figure (2.1 - 15).

Since the refractive index surfaces are defined in the “k-space“ (i.e. they refer to the wave propagation direction), a beam propagating “through“ the refractive index surfaces will sense a refractive index which correlates to the RADIUS VECTOR of the particular surfaces, depending on its polarization, i.e. the left (right) term on the left hand side of eq. (2.1 - 144) or eq. (2.1 - 145) accounts for the ordinary (extraordinary) beam. This is a fundamental difference to the so called “index ellipsoid“, which will be discussed in the next section.

2.1.4.3.6.)Wave propagation in anisotropic media - the index ellipsoid

Above, uniaxial birefringence was discussed semi-empirically using the Huygens-Fresnel principle. Now, the wave propagation in (linear) anisotropic media will be outlined more generally in terms of the electro-magnetic approach assuming monochromatic waves and a loss-free medium with $\mu_r = 1$. Please note, that the subsequent discussion is neither restricted to uniaxial birefringent media nor restricted to a special polarization of the considered wave. This is an important point, since in this section another “surface“, the so called “index ellipsoid“ (also: “indicatrix”) will be derived, which exhibits a formal similarity to the refractive index surface according to the above eq. (2.1 - 145), but is defined in “another space“, thus, being different in interpretation.

As already discussed above, wave and beam propagation direction differ in anisotropic media, which will be introduced by the permittivity tensor. Thus, now, $\text{div}\vec{D} = 0$ (eq. (2.1 - 7)) does no more imply $\text{div}\vec{E} = 0$. Rewriting eq. (2.1 - 21) in complex form for arbitrary media and inserting complex plain waves according to eq. (2.1 - 14) for the magnetic field and the dielectric displacement in eq. (2.1 - 4) results in:

$$\partial_k \times \vec{E} = \frac{Z_0}{n} \vec{H} \quad \text{eq. (2.1 - 146)}$$

and:

$$\partial_k \times \vec{H} = -\frac{Z_0}{\mu_0 n} \vec{D}, \quad \text{eq. (2.1 - 147)}$$

respectively, with Z_0 according to eq. (2.1 - 22). Inserting eq. (2.1 - 146) into eq. (2.1 - 147) finally yields:

$$\vec{D} = \varepsilon_0 n^2 [\vec{E} - \partial_k (\partial_k \cdot \vec{E})], \quad \text{eq. (2.1 - 148)}$$

which is known as the *wave equation of crystal optics*. Please note, that this equation refers to the propagation of the wave front normals with ∂_k as the unit propagation vector, not the propagation of the beam and, hence, n is the wave refractive index according to eq. (2.1 - 132).

A corresponding expression for the propagation of the beam can be derived from eq. (2.1 - 148) and would be:

$$\vec{E} = \frac{1}{\epsilon_0 n_B} [\vec{D} - \hat{e}_B (\hat{e}_B \cdot \vec{D})], \quad \text{eq. (2.1 - 149)}$$

with \hat{e}_B as the unit beam propagation vector and n_B as the beam refractive index according to eq. (2.1 - 127). However, this approach will not be pursued any more hereafter. Please recall, that there is a simple refraction law for an arbitrary incident wave on the basis of the wave refractive index. Therefore the wave refractive index will be the parameter of choice for by far most problems concerning wave propagation in anisotropic media.

In principal axes representation and already expressed in terms of its Cartesian components eq. (2.1 - 148) writes:

$$\vec{D}_a = \epsilon_0 n^2 [\vec{E}_a - \hat{e}_a (\hat{e}_a \cdot \vec{E})], \quad \text{eq. (2.1 - 150)}$$

where:

$$\vec{E}_a = \frac{1}{\epsilon_0 n_a} \vec{D}_a \quad \text{eq. (2.1 - 151)}$$

resulting:

$$\vec{D}_a = \epsilon_0 \frac{(\hat{e}_k \cdot \vec{E})}{\frac{1}{n_a^2} - \frac{1}{n^2}} \hat{e}_a, \quad \text{eq. (2.1 - 152)}$$

where \hat{e}_a are the unit vectors in direction of the principal axis with $a = x, y, z$. The refractive indices n_a are the so called *principal refractive indices* and correlate with the permittivity tensor in principal axes representation according to eq. (2.1 - 80) and eq. (2.1 - 84) for $\mu_r = 1$, i.e.:

$$n_a = \sqrt{\epsilon_a}. \quad \text{eq. (2.1 - 153)}$$

According to eq. (2.1 - 9):

$$\vec{D} \cdot \hat{e}_k = \sum_a \vec{D}_a \cdot \hat{e}_a = \sum_a D_a e_a = 0, \quad \text{eq. (2.1 - 154)}$$

which yields together with eq. (2.1 - 152):

$$\sum_a \frac{e_a^2}{\frac{1}{n_a^2} - \frac{1}{n^2}} = 0. \quad \text{eq. (2.1 - 155)}$$

This equation is called *Fresnel's equation of wave normals*. Eq. (2.1 - 155) may be transformed into eq. (2.1 - 133) by replacing the inverse refractive indices by the corresponding velocities of the wave front normals according to eq. (2.1 - 132), multiplying eq. (2.1 - 155) with each denominator in the sum and then (not before!) setting

$$\begin{aligned} v_x &= v_y = v_o \\ v_z &= v_e \end{aligned} \quad \text{eq. (2.1 - 156)}$$

(this correlation is explained by eq. (2.1 - 163)). In accordance with eq. (2.1 - 130) it is furthermore:

$$\begin{aligned} e_x^2 + e_y^2 &= (\sin \phi)^2 \\ e_z^2 &= (\cos \phi)^2 \end{aligned} \quad \text{eq. (2.1 - 157)}$$

which finally results in:

$$(v^2 - v_o^2)[(v^2 - v_e^2)(\sin\phi)^2 + (v^2 - v_o^2)(\cos\phi)^2] = 0, \quad \text{eq. (2.1 - 158)}$$

i.e. eq. (2.1 - 133).

Eq. (2.1 - 155) is a quadratic equation in $1/n^2$ resulting in two refractive indices (the negative solutions are physically meaningless) for a certain given \hat{e}_k , which correspond to the ordinary and the extraordinary refractive index in an uniaxial birefringent system sensed by the beam defined by \hat{e}_k . Please note, that the n_a in eq. (2.1 - 155) are the corresponding principal refractive indices, which, however, must not be inserted ab initio for an uniaxial birefringent system, since then eq. (2.1 - 155) reduces to a simple quadratic form and a part of the solutions will get lost.

Besides the above analytical solution of such a problem based on Maxwell's equations there is a convenient geometric solution, which is more ostensible than the way discussed above. Since the energy density does not depend on the isotropy of the medium, eq. (2.1 - 71) is still valid and thus, the electrical energy density is:

$$w_e = \frac{1}{2} \hat{E} \cdot \hat{D}, \quad \text{eq. (2.1 - 159)}$$

where the real fields must be used, since the scalar product is a nonlinear operation. In principal axes representation eq. (2.1 - 151) applies and, already written in components of the principal axes system, eq. (2.1 - 159) becomes:

$$w_e = \frac{1}{2\varepsilon_0} \left\{ \frac{D_x^2}{n_x^2} + \frac{D_y^2}{n_y^2} + \frac{D_z^2}{n_z^2} \right\}. \quad \text{eq. (2.1 - 160)}$$

By introducing a new normalized vector \vec{d} with:

$$\vec{d} = \frac{\hat{D}}{\sqrt{2\varepsilon_0 w_e}}, \quad \text{eq. (2.1 - 161)}$$

eq. (2.1 - 160) rewrites to:

$$\frac{d_x^2}{n_x^2} + \frac{d_y^2}{n_y^2} + \frac{d_z^2}{n_z^2} = 1, \quad \text{eq. (2.1 - 162)}$$

which represents an ellipsoid in the "d-space" (!), expressing the anisotropic properties of the medium. This construction is called *index ellipsoid* and widespread applied in crystal optics.

Since the index ellipsoid is defined in in the "d-space", its interpretation is different as compared to the refractive index surface discussed before (which is defined in the "k-space") and is illustrated in figure (2.1 - 14). \vec{k} denotes an arbitrarily polarized propagating wave in the principal axis system and n_x, y, z are the principal refractive indices along the corresponding axis. For evaluation, the intersection curve of a plane normal to \vec{k} and the index ellipsoid is taken and the oscillation direction of the electrical field vector (i.e. the polarization) is projected onto the axis of the intersection curve, defining by that the two eigen polarizations of the wave. The length of these axis (n_1 and n_2 in figure (2.1 - 14))

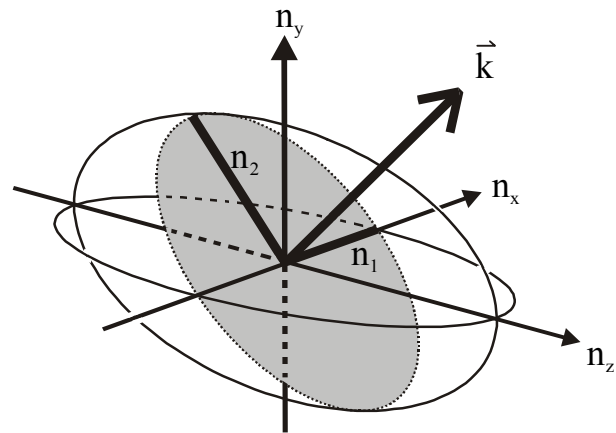


Figure (2.1 - 14): Index ellipsoid for uniaxial medium

denote the refractive indices sensed by the eigen polarizations in the considered geometry.

Applying this concept to an uniaxial birefringent material, it is clear, that

$$\begin{aligned} n_x &= n_y = n_o \\ n_z &= n_e \end{aligned} \tag{2.1 - 163}$$

must apply, so that a wave propagating along z-direction will sense a polarization-independent refractive index, preserving the z-axis as optical axis. Hence, the index ellipsoid for uniaxial birefringent media writes according to eq. (2.1 - 162):

$$\frac{d_x^2}{n_o^2} + \frac{d_y^2}{n_o^2} + \frac{d_z^2}{n_e^2} = 1. \tag{2.1 - 164}$$

Comparing this equation with the ellipse term in eq. (2.1 - 145) reveals, that the ordinary and the extraordinary refractive index in the denominator are exchanged, which is due to the consideration in different “spaces“.

The relations between the beam velocity surface, the index surface (both defined in the “k-space“) and the index ellipsoid (defined in the “d-space“) are depicted as intersections in the x-z-plane for the case of uniaxial birefringence in figure (2.1 - 15). Please note in this context, that eq. (2.1 - 155) as well refers to the “d-space“ but is “transformed“ into the “k-space“ by multiplying with each denominator in the sum and inserting eq. (2.1 - 156), then resulting in eq. (2.1 - 133), which refers to the “k-space“.

The index ellipsoid according to eq. (2.1 - 162) does contain more information than the refractive index surface, which is due to its definition in d-space. Thus, usually the index ellipsoid is used as basis for the consideration of anisotropic media.

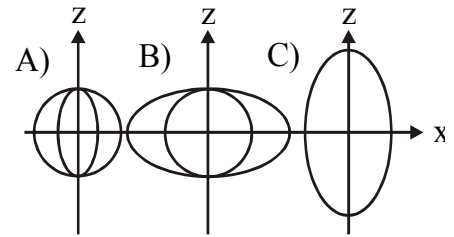


Figure (2.1 - 15): Exemplarily qualitative sketch of a beam velocity surface (A) with the corresponding index surface (B) and the index ellipsoid (C).

2.1.4.4.)Bragg diffraction

Bragg-diffraction is a combined multi-reflection and interference phenomenon and is of essential importance in the framework of this theses. It defines the fundamental geometrical condition for wave mixing experiments in thick hologram gratings. The basic principle is depicted in figure (2.1 - 16). A light beam passes through a periodic phase grating (i.e. refractive index grating), enclosing an angle of

$$0^\circ < \Theta \leq 90^\circ \tag{2.1 - 165}$$

with the grating planes. The beam will experience multiple external and internal reflection and refraction processes as will each individual reflected and transmitted portion of the original beam while passing through the grating. All of these beam portions will finally superimpose. This process may be described accurately applying Fresnel’s equations and considering the occurring interference phenomena. The calculations quickly become fairly cumbersome

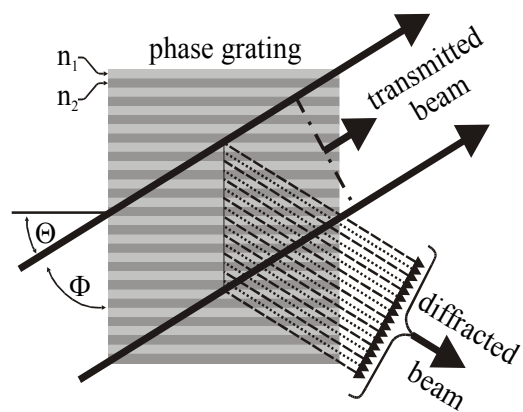


Figure (2.1 - 16): Phenomenology of Bragg diffraction

depending on the demanded accuracy and the number of grating planes to account for. However, such an approach is only necessary for a small number of grating planes and is not referred to as Bragg-diffraction.

The problem simplifies strongly presuming a large number of grating planes. Then, the number of reflected beams is high enough to presume constructive interference of the total number of the reflected beams only for the case when the optical path length difference between neighboring individually reflected beams meets the condition for constructive interference. In any other case the interference will be destructive. If this consideration is valid, the problem is referred to as *Bragg-diffraction*. The condition for constructive interference may be found employing a simple geometrical consideration depicted in figure (2.1 - 17). It is not relevant which individual beams are considered, since the condition will apply to all reflection processes occurring.

Two neighboring beams reflected at similar interfaces (outer reflection *or* inner reflection) may be considered or two neighboring beams reflected at different interfaces (outer reflection *and* inner reflection), however, the phase relations according to figure (2.1 - 10) must be accounted for. Here the reflection at similar interfaces shall be considered. The refractive index modulation of the phase grating is assumed small, i.e.

$$\Delta n = |n_2 - n_1| \ll \frac{1}{2}(n_2 + n_1). \quad \text{eq. (2.1 - 166)}$$

According to figure (2.1 - 17) the optical path length difference between the reflected beams R_1 and R_2 is $2a$ where:

$$a = d \cos \Phi = d \sin \Theta. \quad \text{eq. (2.1 - 167)}$$

Accordingly, the following condition must be met for constructive interference:

$$2nd \cos \Phi = 2nd \sin \Theta = b\lambda_0, \quad \text{eq. (2.1 - 168)}$$

where n is the average bulk refractive index inside the grating, d is the grating spacing (i.e. the grating constant), λ_0 is the wavelength in free space, Θ is the angle between the incident beam and the grating planes, and Φ is the angle between the incident beam and the grating wave vector (by definition perpendicular to the grating planes). The parameter b is an arbitrary integer number. Eq. (2.1 - 168) is called *Bragg-condition*, which must be met in order to observe Bragg-diffraction. If the condition is violated, the incident beam is not diffracted. The Bragg-condition can be very sharp for thick gratings. The question of the grating thickness will be discussed in “2.3.1.2.) Types of holograms” on page 52. Please note, that a Bragg grating need not be holographic, however, the term “thick grating“ as discussed in the before mentioned section is a general definition, which accounts for all types of diffraction gratings.

Additionally it should be mentioned here, that Bragg-diffraction is not a nonlinear optical process. This is important, since wave mixing in thick holograms is often explained in terms of Bragg-diffraction presuming the validity of the nonlinear phase matching condition eq. (2.2 - 39) without notification. However, eq. (2.2 - 39) is not a necessary condition for Bragg diffraction in general although wave mixing in thick hologram gratings obeys eq. (2.1 - 168) as well as eq. (2.2 - 39).

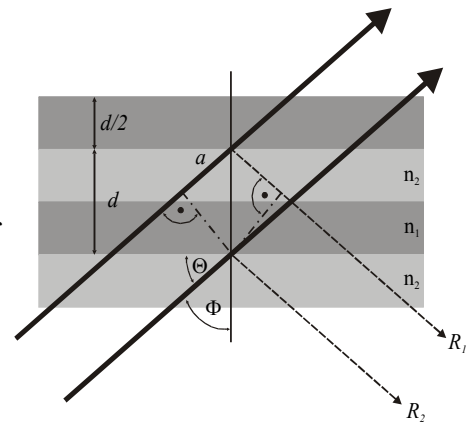


Figure (2.1 - 17): Bragg condition

2.2.)Basic aspects of non-linear optics

The evolution of nonlinear optics (NLO) is closely connected with the development of the laser, since nonlinear phenomena usually require high light intensity. However, most of the theoretical work in NLO has been done before the invention of the laser. Experimental proof so far has only been possible for effects describing the interaction between an electro-magnetic radiation field and an electrical or a magnetic dc-field. The laser with its particular features as a light source, however, enabled the observation of NLO effects based on interaction of pure optical fields and, thus, not only allowed for experimental proof of already theoretically anticipated NLO effects, but even led to the discovery of new effects and promoted the field of NLO from some curious side field into the focus of interest in today's optical sciences.

As discussed in the preceding chapter, propagation of light in matter is described by the frequency dependent optical constants „refractive index“ and „absorption coefficient“, which are not a function of the intensity of the incident light in linear optics. Thus, in linear optics, there are two important principles:

a) Superposition principle

Light waves do not affect each other and, thus, can be distortion-free superposed. A light wave in matter propagates independently of any other light wave existing simultaneously in the same area.

b) Principle of frequency conservation

No new light frequencies are generated by interaction of light with matter. The light frequencies inside and outside the medium are identical. (Exception: Raman effect).

However, both these basic principles of linear optics are no more valid for irradiation with sufficiently high intensities. This paragraph concerns the mutual influence of interacting light waves at high intensities. Subsequently, the phenomenology of the nonlinear interaction between light and matter will be discussed qualitatively for an incident monochromatic plain wave. The basic principles outlined in this context, however, will apply generally. Subsequently the electro-optic effects (Pockels effect and Kerr effect) will be discussed in more detail, since these effects occur in photorefractive polymers. Thereafter, a short consideration of degenerate four wave mixing as an NLO effect will follow, which additionally will serve for the introduction of the NLO phase matching condition. The paragraph will close with a brief discussion of the position of photorefractive in the systematics of nonlinear optics.

The physics of the photorefractive effect as well as four wave mixing in thick hologram gratings will each be discussed in detail in a separate section later on, since these issues concern the core of this work.

2.2.1) Nonlinear interaction between light and matter

The basic material equations for the interaction between light and matter, eq. (2.1 - 56) to eq. (2.1 - 60), as derived in “2.1.3.1.) Material equations” on page 16, will basically hold for nonlinear optics as well.

However, out of this set of equations, eq. (2.1 - 57) will not suffice to describe the polarizations induced by nonlinear interaction between light and matter. This is the fundamental difference between linear and nonlinear optics and will be considered qualitatively in more detail now. In order to illustrate the interaction between light and matter, the oscillator model was first employed in “2.1.3.2.) The oscillator model (Lorentz-model)” on page 17 presuming small elongation in order to ensure linear response of the system. For small elongations, the

potential of an electron in the central field of an atom or molecule may well be approximated by a parabolic potential function resulting in linear response. However, for high irradiance intensity, the elongation of the electron will exceed the area of the parabolic approximation and the response of the system will be nonlinear. This is illustrated in figure (2.2 - 1), where the ideal

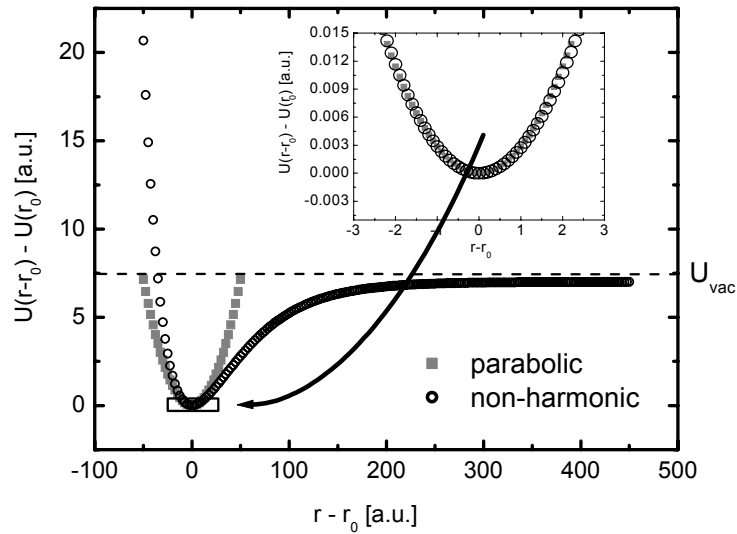


Figure (2.2 - 1): Illustration of the parabolic and a non-harmonic potential function.

parabolic potential function and a more realistic example of a potential function as a function of the elongation from the equilibrium distance r_0 are sketched. The area of linear response is enlarged in the inset. Outside the area of linear response, the characteristic of the induced dipole moment (which is proportional to the electron displacement) as a function of the incident electrical field is nonlinear as illustrated together with the transformation behavior on an incident wave in figure (2.2 - 2). It is clear, that the polarization response must be non-harmonic and that higher harmonics appear in the polarization wave, which results in the polarization to be a complicated function of the electrical field containing terms of higher order.

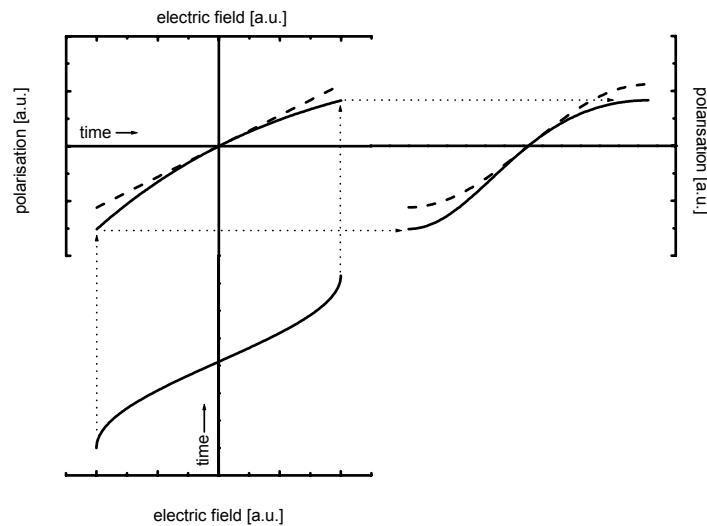


Figure (2.2 - 2): Illustration of linear and non-linear response behavior. The dashed curves depict linear behavior. The lower curve illustrates a branch of the incoming electrical field, the upper left curves illustrate the elongation characteristics of an electron in a central field and the upper right curves depict the resulting branch of the polarization wave in the medium.

2.2.1.1.)Nonlinear polarization

Since terms of higher order in the incident field represent nonlinear operations, the first approach to this problem must be real as discussed in “2.1.1.) The electro-magnetic theory of light” on page 4:

$$\vec{P}(t) = \varepsilon_0[\chi_t^{(1)}\vec{E}(t) + (\chi_t^{(2)}\vec{E}(t))\vec{E}(t) + ((\chi_t^{(3)}\vec{E}(t))\vec{E}(t))\vec{E}(t) + \dots]. \quad \text{eq. (2.2 - 1)}$$

Here $\chi^{(1), (2), (3)}$ are the susceptibilities of first, second and third order, respectively, and their index “ t ” denotes a dependence of the susceptibilities on the particular time history of the electrical field. Usually it is not necessary to consider terms of fourth or even higher order, since the susceptibilities decrease dramatically with increasing order (typically already about 17 orders of magnitude from first to third order). Thus, effects of higher order than three are usually negligible. The above eq. (2.2 - 1), however, only accounts for loss-free media. In lossy media, a phase delay between the polarization and the electrical field will occur, and it would be convenient to express eq. (2.2 - 1) in complex form. This can be achieved by applying eq. (2.1 - 19) to the electrical field as well as to the polarization and taking the non-conjugate complex form of the polarization. Since the resulting expression for the entire eq. (2.2 - 1) is very long, this procedure will be demonstrated on the term of second order:

$$\vec{P}^{(2)}(t) = \frac{1}{2}(\vec{P}^{(2)}(t) + \vec{P}^{(2)*}(t)) = \frac{\varepsilon_0}{4}\left\{\chi_t^{(2)}[\vec{E}(t) + \vec{E}^*(t)][\vec{E}(t) + \vec{E}^*(t)]\right\}. \quad \text{eq. (2.2 - 2)}$$

Please note, that this equation cannot be simplified furthermore without knowing more about the specific problem under consideration, since a n^{th} order susceptibility (here second order) is in general a tensor of $(n+1)^{\text{th}}$ rank (i.e., here of third rank), preventing the electrical field vectors on the right hand side of eq. (2.2 - 2) to be simply multiplied. Therefore, eq. (2.2 - 2) is expressed in terms of its vector components:

$$P_i^{(2)}(t) + P_i^{(2)*}(t) = \frac{\varepsilon_0}{2}\left\{\sum_{j,k} \chi_{ijk,t}^{(2)}[E_j(t) + E_j^*(t)][E_k(t) + E_k^*(t)]\right\}. \quad \text{eq. (2.2 - 3)}$$

This equation can easily be separated in:

$$P_i^{(2)}(t) = \frac{\varepsilon_0}{2}\left\{\sum_{j,k} \chi_{ijk,t}^{(2)}[E_j(t)E_k(t) + E_j^*(t)E_k(t)]\right\} \quad \text{eq. (2.2 - 4)}$$

and:

$$P_i^{(2)*}(t) = \frac{\varepsilon_0}{2}\left\{\sum_{j,k} \chi_{ijk,t}^{(2)}[E_j^*(t)E_k^*(t) + E_j(t)E_k^*(t)]\right\}. \quad \text{eq. (2.2 - 5)}$$

Please note that the susceptibility is not the same for the two types of products in the sum (as indicated by the index „ t ”), since the complete real (or complete complex conjugate) product represents frequency doubling, whereas the mixed products represents optical rectification and the susceptibility depends on the particular time history of the product of the fields.

As an example for higher order polarization equations, the complex third order polarization equation corresponding to the complex second order polarization equation eq. (2.2 - 4) is analogously obtained and writes:

$$P_i^{(3)}(t) = \frac{\epsilon_0}{4} \left\{ \sum_{j,k,l} \chi_{ijkl,t}^{(3)} [E_j(t)E_k(t)E_l(t) + E_j^*(t)E_k(t)E_l(t) + E_j(t)E_k^*(t)E_l(t) + E_j(t)E_k(t)E_l^*(t)] \right\}, \quad \text{eq. (2.2 - 6)}$$

with $(i, j, k = x, y, z)$. The third order susceptibility tensor $\chi_{ijkl,t}^{(3)}$ is of fourth rank and, thus, has 81 element.

Please note that the susceptibility of first order has already been discussed to be a second rank tensor in the context of “2.1.3.) Light in linear media” on page 16.

Combining the nonlinear polarization with Maxwell’s equations leads to the wave equation of nonlinear optics, which writes in general form:

$$\nabla^2 \vec{E} - \frac{1}{c} \frac{\partial^2}{\partial t^2} \vec{E} = \mu_0 \frac{\partial^2}{\partial t^2} \vec{P}_{NL}(\vec{E}). \quad \text{eq. (2.2 - 7)}$$

For its derivation reference is made to the standard literature of nonlinear optics.

2.2.1.2.)Kleinman’s symmetry rule

An important simplification of the second order susceptibility tensor is obtained, if the medium is loss-free for all (!) radiation fields involved in the nonlinear optical process. In this context, loss-free means that the electrical work per period of the light wave vanishes:

$$\oint \vec{P} d\vec{E} = 0. \quad \text{eq. (2.2 - 8)}$$

This closed line integral vanishes for:

$$\text{rot}_{E_k} \vec{P} = \hat{e}_k \left(\frac{\partial P_i}{\partial E_j} - \frac{\partial P_j}{\partial E_i} \right) = 0, \quad \text{eq. (2.2 - 9)}$$

where \hat{e}_k is the unit vector in k -direction and $i, j, k = x, y, z$, which yields for the elements of the susceptibility tensor:

$$\chi_{ijk,t}^{(2)} = \chi_{jik,t}^{(2)}. \quad \text{eq. (2.2 - 10)}$$

Furthermore but trivial, the tensor is real.

Eq. (2.2 - 9) may be applied to all electrical field components, which finally results in three permutation relations, the first of which is eq. (2.2 - 10) and the remaining two of them write:

$$\chi_{ijk,t}^{(2)} = \chi_{ikj,t}^{(2)} \quad \text{eq. (2.2 - 11)}$$

and:

$$\chi_{ijk,t}^{(2)} = \chi_{kji,t}^{(2)}. \quad \text{eq. (2.2 - 12)}$$

This is known as *Kleinman’s symmetry rule*. Usually eq. (2.2 - 11) is applied in order to get a first simplification of the second order susceptibility tensor, since the sequence of the field components in eq. (2.2 - 3) is physically insignificant in the majority of cases. Therefore, eq. (2.2 - 11) does not necessarily require the validity of Kleinman’s symmetry rule. However, the appropriate approach depends on the particular problem considered.

Please note finally that further reduction of the number of independent tensor elements may result from more sophisticated symmetry considerations for a particular system with

respect to a particular problem of nonlinear optics. However, this is too specific to be discussed here. For example, the second order susceptibility vanishes completely for systems exhibiting an inversion center.

2.2.2) Electro-optic effects

The generic term “electro-optic effects“ covers nonlinear optical effects, where a single light wave is affected by static or quasi-electrostatic (see below) electrical fields. These effects can be described by nonlinear polarizations containing an optical field and electrostatic fields. In this context it becomes clear, what is meant by a “quasi-electrostatic“ field. An electrical field can be considered as quasi-electrostatic, when its frequency is sufficiently small to be neglected in mixed terms of the nonlinear polarization, i.e., the sum and difference frequency generation with the optical wave does not change the frequency of the optical wave perceivably.

In more practical terms, electro-optic effects describe the change of an optical anisotropy or the generation of it from optical isotropy by means of an electrostatic field externally applied to the system under consideration. I.e., the refractive indices of the system are affected by an externally applied field. This may be due to deformations of the electron orbitals in the material, induced by the applied field, to orientation of molecular dipoles by the external field or to other mechanisms of similar nature. In this paragraph, the static electrical field is always assumed to be a dc-field without loss of generality.

There are two electro-optic effects. The *Pockels effect* is a quadratic effect which describes the variation of the real part of the permittivity as a linear function of the external field:

$$\Delta Re(\varepsilon_r) \propto E_{ext} \quad \text{eq. (2.2 - 13)}$$

Therefore, the Pockels effect is also referred to as the *linear electro-optic effect*.

The *Kerr effect* is a cubic effect, which describes the variation of the real part of the permittivity as a quadratic function of the external field:

$$\Delta Re(\varepsilon_r) \propto E_{ext}^2 \quad \text{eq. (2.2 - 14)}$$

Therefore, the Kerr effect is also referred to as the *quadratic electro-optic effect*.

Since in general:

$$\Delta \varepsilon_{r, Pockels} \gg \Delta \varepsilon_{r, Kerr} \quad \text{eq. (2.2 - 15)}$$

the Kerr effect is usually negligible in systems, where the Pockels effect occurs.

It is generally possible to consider the electro-optic effects from the point of view of wave propagation. In this case, an expression for the nonlinear polarization $\vec{P}_{NL}(\vec{E})$ in the system considered must be found as a function of the optical wave $\vec{E}(\vec{r}, t)$. This may be necessary for particular applications, however, in many cases it is sufficient to consider simply the spatially resolved refractive index changes as a function of the external field vector, which can be performed on basis of the index ellipsoid (eq. (2.1 - 162)).

Please note, that the Kerr effect is particularly interesting in liquids and solutions, but usually not so much in crystal optics. However, polymeric systems of the kind investigated in the frame of this work consist of low mass molecular components dissolved in a low glass-transition polymer matrix, representing a preferable system for the occurrence of the Kerr effect or of related phenomena. This will be picked up again in the context with the nonlinear optical properties of low glass-transition polymers, which are discussed later in more detail.

2.2.2.1.)Pockels effect

The Pockels effect requires an optically anisotropic medium, the optical behavior of which may be described by the index ellipsoid according to eq. (2.1 - 162), which writes in principal axis representation:

$$\frac{d_x^2}{n_1^2} + \frac{d_y^2}{n_2^2} + \frac{d_z^2}{n_3^2} = 1, \quad \text{eq. (2.2 - 16)}$$

where $n_{1,2,3}$ are the principal refractive indices. By applying an electrical dc-field to the system refractive index changes occur, which result in a new and slightly rotated index ellipsoid as depicted in figure (2.2 - 3), which may be described by:

$$\frac{d_x^2}{n_1'^2} + \frac{d_y^2}{n_2'^2} + \frac{d_z^2}{n_3'^2} + \frac{2d_y d_z}{n_4^2} + \frac{2d_x d_z}{n_5^2} + \frac{2d_x d_y}{n_6^2} = 1, \quad \text{eq. (2.2 - 17)}$$

where the mixed components vanish and the $n_1'^2, n_2'^2, n_3'^2$ become n_1^2, n_2^2, n_3^2 , respectively, for zero external field. Introducing the refractive index changes according to:

$$\Delta \frac{1}{n_i^2} = \begin{cases} \frac{1}{n_i^2} - \frac{1}{n_i'^2} & \forall i = 1, 2, 3 \\ \frac{1}{n_i^2} & \forall i = 4, 5, 6 \end{cases} \quad \text{eq. (2.2 - 18)}$$

and accounting for their linear change as a function of the external field according to eq. (2.2 - 13), the refractive index changes may be expressed as:

$$\Delta \frac{1}{n_i^2} = \sum_j r_{ij} E_j, \quad \text{eq. (2.2 - 19)}$$

with $i = 1, 2, 3$ for the electro-optic coefficients and $j = x, y, z$ for the applied field. The correlation of the index i with Cartesian coordinates can be derived from eq. (2.2 - 17). In terms of a matrix equation eq. (2.2 - 19) writes:

$$\begin{bmatrix} \Delta \frac{1}{n_1^2} \\ \Delta \frac{1}{n_2^2} \\ \Delta \frac{1}{n_3^2} \\ \Delta \frac{1}{n_4^2} \\ \Delta \frac{1}{n_5^2} \\ \Delta \frac{1}{n_6^2} \end{bmatrix} = \begin{bmatrix} r_{11} & r_{12} & r_{13} \\ r_{21} & r_{22} & r_{23} \\ r_{31} & r_{32} & r_{33} \\ r_{41} & r_{42} & r_{43} \\ r_{51} & r_{52} & r_{53} \\ r_{61} & r_{62} & r_{63} \end{bmatrix} \cdot \begin{bmatrix} E_x \\ E_y \\ E_z \end{bmatrix}. \quad \text{eq. (2.2 - 20)}$$

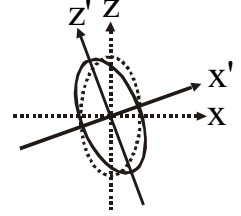


Figure (2.2 - 3)

The r_{ij} -matrix is called the *electro-optic matrix*. Please note, that the electro-optic coefficients depend on the frequency of the light wave as well as on the frequency of the applied field, if the latter is quasi-electrostatic.

For small changes of the refractive indices, eq. (2.2 - 19) may be approximated by:

$$\Delta n_i \approx -\frac{n^3}{2} \sum_j r_{ij} E_j. \quad \text{eq. (2.2 - 21)}$$

2.2.2.2.)Kerr effect

The Kerr effect can be considered the same way as the Pockels effect and, hence, eq. (2.2 - 16) to eq. (2.2 - 18) are valid as well. However, according to eq. (2.2 - 14), the refractive index changes due to the Kerr effect are expressed as:

$$\left(\Delta \frac{1}{n_i} \right)_{Kerr} = \sum_{jk} R_{ijk} E_j E_k, \quad \text{eq. (2.2 - 22)}$$

where the electro-optic tensor R_{ijk} is a third rank tensor and, thus, eq. (2.2 - 22) can not be expressed as a matrix equation according to eq. (2.2 - 20). However, eq. (2.2 - 22) is incomplete, since the Pockels effect may not only contribute as well to the total refractive index changes but usually will be predominant. Hence, the actual refractive index changes are:

$$\Delta \frac{1}{n_i} = \sum_j r_{ij} E_j + \sum_{jk} R_{ijk} E_j E_k. \quad \text{eq. (2.2 - 23)}$$

Since the electro-optic matrix r_{ij} vanishes for media exhibiting an inversion center, only then eq. (2.2 - 22) describes the total refractive index changes.

Considering the Kerr effect for loss-free isotropic media with $\mu_r = 1$ in terms of wave propagation, the third order nonlinear polarization will be:

$$P_{NL,i}^{(3)} = \varepsilon_0 \chi^{(3)} E_i(\omega) \langle \vec{E}_{ext} \bullet \vec{E}_{ext} \rangle, \quad \text{eq. (2.2 - 24)}$$

where $\chi^{(3)}$ is the only remaining independent tensor element of the third order susceptibility tensor for isotropic media. The time average of the external fields depicts their quasi-electrostatic nature as discussed before, and $i = x, y, z$.

Assuming for example a linearly polarized wave running in x -direction:

$$\vec{E}(\omega) = (0, |E_y|, 0) e^{i(\omega t - kx)} \quad \text{eq. (2.2 - 25)}$$

and an external field applied in z -direction (i.e. the wave according to eq. (2.2 - 25) is s -polarized):

$$\vec{E}_{ext} = (0, 0, E_{ext}), \quad \text{eq. (2.2 - 26)}$$

the total field in the system will be the sum of both and yields for the polarization of third order:

$$\vec{P}^{(3)}(\omega) = \left(0, \varepsilon_0 \chi^{(3)} E_y(\omega) \left[\frac{3}{4} |E_y|^2 + E_{ext}^2 \right], 0 \right), \quad \text{eq. (2.2 - 27)}$$

where only components of the frequency ω were considered.

Furthermore, the incident radiation field will generate a polarization of first order according to:

$$\vec{P}^{(1)}(\omega) = (0, \varepsilon_0 \chi E_y(\omega), 0), \quad \text{eq. (2.2 - 28)}$$

where χ is the real linear susceptibility.

Thus, the total polarization in the medium at frequency ω will be:

$$P_y(\omega) = \epsilon_0 E_y(\omega) \left[\chi + \frac{3}{4} \chi^{(3)} |E_y|^2 + \chi^{(3)} E_{ext}^2 \right] = \epsilon_0 \chi_{NL} E_y(\omega), \quad \text{eq. (2.2 - 29)}$$

where χ_{NL} is an intensity dependent nonlinear constant, which allows for the determination of the refractive index (with eq. (2.1 - 59) and eq. (2.1 - 84)) sensed by the wave according eq. (2.2 - 25):

$$n_o = \sqrt{1 + \chi + \frac{3}{4} \chi^{(3)} |E_y|^2 + \chi^{(3)} E_{ext}^2} \text{ for } (\vec{E} \perp \vec{E}_{ext}). \quad \text{eq. (2.2 - 30)}$$

The same procedure performed for a p-polarized wave results in:

$$n_e = \sqrt{1 + \chi + \frac{3}{4} \chi^{(3)} |E_z|^2 + 3\chi^{(3)} E_{ext}^2} \text{ for } (\vec{E} \parallel \vec{E}_{ext}). \quad \text{eq. (2.2 - 31)}$$

Thus, the refractive index is affected by the incident light as well as by the externally applied field. The isotropic medium has become birefringent, as already depicted by assigning eq. (2.2 - 30) and eq. (2.2 - 31) to an ordinary and an extraordinary refractive index. The ‘‘crystal axis’’ of the considered system is the direction of the applied field, i.e. it is the z-axis of the coordinate system chosen here.

For normal light, $|E_z|, |E_y| \ll E_{ext}$ and, furthermore, the variation of the refractive indices as a function of the external field is small due to the in general small third order susceptibility. Thus, approximating $\sqrt{1+x} \approx 1+x/2$ eq. (2.2 - 30) and eq. (2.2 - 31) simplify to:

$$n_o \approx n \left[1 + \frac{\chi^{(3)} E_{ext}^2}{2n^2} \right] \quad \text{eq. (2.2 - 32)}$$

and:

$$n_e \approx n \left[1 + \frac{3\chi^{(3)} E_{ext}^2}{2n^2} \right]. \quad \text{eq. (2.2 - 33)}$$

In order to quantify the quality of the Kerr effect in a particular medium, a characteristic constant, the *Kerr constant*, is defined as:

$$B = \frac{n_o - n_e}{\lambda_0 E_{ext}^2}. \quad \text{eq. (2.2 - 34)}$$

2.2.3) Degenerate four wave mixing and NLO phase matching

NLO effects of third order stand for the interaction of four waves, since the third order polarization will generate a fourth wave. A special case of this situation is the interaction of four waves of identical frequency ω but different propagation vectors \vec{k}_i :

$$\vec{E}_i(\omega) = \vec{E}_{0i} e^{i(\omega t - \vec{k}_i \cdot \vec{r})}, \quad \text{eq. (2.2 - 35)}$$

where $i = 1, 2, 3, 4$ is the running index for the four waves. The polarization states of all four waves shall be identical without loss of generality.

The total field interacting with the nonlinear medium will be:

$$\vec{E}(\omega) = \sum_{i=1-3} \vec{E}_i(\omega) \quad \text{eq. (2.2 - 36)}$$

and the resulting third order polarization regarding only terms in ω will be:

$$\vec{P}^{(3)}(\omega) = \frac{3}{4}\varepsilon_0 e_{11} \vec{E}(\omega) \vec{E}(\omega) \vec{E}^*(\omega). \quad \text{eq. (2.2 - 37)}$$

Subsequently, the most common case of the described situation will be considered, where a weak signal wave \vec{E}_3 interacts with two counterpropagating pump waves of high intensity \vec{E}_1 and \vec{E}_2 (this configuration is known as phase conjugate mirror). In this case the relation between the propagation vectors of the pump waves will be:

$$\vec{k}_1 = -\vec{k}_2. \quad \text{eq. (2.2 - 38)}$$

The interaction can be interpreted ostensibly as diffraction of a signal wave at a periodic refractive index grating resulting from the interference pattern generated by the pump waves. Hence, the diffracted wave must meet the *phase matching condition*. The phase matching condition is the result of the basic law of impulse conservation, with:

$$\vec{p} = \frac{h}{2\pi} \vec{k} \text{ and } \sum \vec{p} = 0 \quad \text{eq. (2.2 - 39)}$$

where p is the photon impulse and h is Planck's constant. In this case, the phase matching condition will write:

$$\vec{k}_1 + \vec{k}_2 + \vec{k}_3 + \vec{k}_4 = 0. \quad \text{eq. (2.2 - 40)}$$

Please note, that the impulse balance must be interpreted correctly to derive the correct phase matching condition accounting as well for energy conservation. Thus, e.g. in frequency doubling the phase matching condition will write $\vec{k}_1 + \vec{k}_1 - \vec{k}_2 = 0$, where the index 2 denotes the generated wave of 2ω .

Accounting for eq. (2.2 - 38), the phase matching condition eq. (2.2 - 39) requires:

$$\vec{k}_4 = -\vec{k}_3, \quad \text{eq. (2.2 - 41)}$$

which yields according to eq. (2.2 - 37) with eq. (2.2 - 36):

$$\vec{P}_4^{(3)}(\omega) = \frac{3}{2}\varepsilon_0 e_{11} \vec{E}_1(\omega) \vec{E}_2(\omega) \vec{E}_3^*(\omega) \quad \text{eq. (2.2 - 42)}$$

and with eq. (2.2 - 35):

$$\vec{P}_4^{(3)}(\omega) = \frac{3}{2}\varepsilon_0 e_{11} \vec{E}_{01} \vec{E}_{02} \vec{E}_{03}^* e^{i(\omega t + \vec{k}_3 \cdot \vec{r})}. \quad \text{eq. (2.2 - 43)}$$

Inserting this equation into the wave equation eq. (2.2 - 7) yields for the diffracted wave:

$$\vec{E}_4(\omega) = \vec{E}_{04} e^{i(\omega t - \vec{k}_4 \cdot \vec{r})} = \mathcal{G} \vec{E}_{03}^* e^{i(\omega t + \vec{k}_3 \cdot \vec{r})}, \quad \text{eq. (2.2 - 44)}$$

with \mathcal{G} as reflection coefficient. Accordingly, the diffracted wave in the discussed case is the phase conjugate to the signal wave, which may be considered as a wave „running back in time“. Hence, the reflection law is not valid here.

The procedure as exemplarily demonstrated above will as well apply to an arbitrary geometry of the setup, not only for counterpropagating pump waves.

Please note that the pump waves and the signal wave need not have the same frequency and even the pump waves themselves may vary in frequency. However, the analytical treatment then becomes much more complicated. In the case of different frequencies of the pump waves, the diffracted signal wave will exhibit another frequency than the signal wave itself. Since eq. (2.2 - 40) accounts for all cases, it may serve for a qualitative estimation of the direction and frequency relations of the involved waves.

Please note furthermore that the mutual interaction between all waves present in the medium taking into account their polarization states may lead to the occurrence of multiple phase gratings. A comprehensive treatment of this problem may become rather cumbersome.

However, some phase gratings may be neglected depending on the intensities of the involved beams as performed above, where the interaction between the pump beams and the signal beam was therefore disregarded. Another way to avoid a multiple phase grating problem would be to use orthogonal polarization states for the pump beams and the signal beam. Furthermore, if the medium is lossy, absorption gratings may occur as well and contribute to the diffraction.

Degenerate four-wave-mixing (DFWM) is one of the key measurement techniques applied in the frame of this work and will be elaborated upon in much more detail in terms of the coupled wave theory in “2.3.2.) Coupled wave theory for thick hologram gratings” on page 53. The treatment of DFWM in terms of the nonlinear optical polarization will not be pursued any longer hereafter.

2.2.4) Photorefraction

The photorefractive (PR) effect will not be discussed here, but elaborated upon in detail in a separate chapter: “2.5.) The photorefractive effect” on page 118. However, here it seems advisable to discuss briefly the position of the photorefractive effect in the systematics of NLO.

Photorefraction is an optical effect representing an outstanding position. The magnitude of the PR effect does not depend on the intensity but on the energy of the involved fields, i.e. the PR effect is an integral effect. By contrast the buildup speed of the effect depends on the intensity. This is unique for a NLO effect and questions the attribution of the PR effect to NLO in general. However, undoubtedly NLO effects are involved in the PR effect, e.g. the Pockels effect. Furthermore, the response of PR media may be described by reasonably applying the physical schemes of nonlinear optics, however, accounting for the nature of the particular experiment to be considered. Thus, the general attribution of the PR effect to nonlinear optics seems reasonable, however, somewhat oblique.

Due to the fact that four-wave-mixing experiments may be carried out in photorefractive media, photorefraction is often referred to as a cubic NLO effect. However, the order of a NLO effect is defined by the number of electrical fields involved. In the case of the PR effect, this number varies between 2 and 5 depending on the type of PR medium and the particular experiment performed (two-wave-mixing or four-wave-mixing). Therefore, a clear attribution of the PR effect to a certain order of nonlinearity is unreasonable. In fact, the PR effect cannot be categorized this way at all. In contrast, the PR effect must be considered as a stand-alone mechanism enabling nonlinear optical response of various order, depending on the particular experiment and medium

2.3.)Holography

The principle of holography has been discovered and demonstrated by D. Gabor in 1948 [14]. However, since there was no sufficiently coherent light source available at this time, the first holograms were realized using mercury vapor lamps in inline recording configuration, which is restricted to at least semi-transparent objects. The initially intolerable technical problems prevented a noticeable further development of holography during the 1950ies. This situation changed with the first realization of an “optical“ Laser by T. Maiman in 1960 [15] based on the work of C. Towns, N. Bassow and A. Prochorow. In 1962, E.N. Leith and J. Upatnieks suggested a significantly improved holographic recording technique known as off-axis recording [16] and, in the same year, J.N. Denijsjuk suggested the recording of holograms in three dimensional media, which is known today as volume holographic recording. Finally, in 1963 Leith and Upatnieks were the first to record an off-axis hologram using Laser beams [17], which initiated intense research in this field, which is still ongoing.

This paragraph deals with the basic principles of holography and its application in holographic data storage. Holography has been utilized basically for the purpose of material characterization in the framework of this theses and not for imaging. Therefore, the holographic process will be outlined only phenomenologically neither considering the extensive field of holographic imaging in detail nor discussing the holographic process in terms of wave mechanics. However, since the diffraction properties of holographic volume gratings are basic characteristics of photorefractive materials, the diffraction properties of thick hologram gratings will be discussed in detail using the coupled-wave theory.

Holography offers a variety of possibilities for application like pattern recognition, data storage, optical correlation, non-destructive characterization of materials, determination of the normal modes of vibrating objects, and others. Out of the various potential applications, holographic multiplexing will be outlined as a technique enabling holographic mass data storage. Different multiplexing techniques will be described and the basic requirements for potential holographic storage media, enabling holographic multiplexing will be discussed.

2.3.1.) The holographic process

The spatial percipience of human beings is due to the stereoscopic parallax, which results in slightly different images of an object observed by each eye. These two images are combined to a stereoscopic picture by the human brain. Nature must use this trick, because there is no way to detect the absolute phasing of an electromagnetic wave. The phasing of a wave can only be defined relative to some reference. This statement is the key to the holographic process. The holographic process enables the recording of both phase and intensity distribution of an optical field in some suitable medium by providing a phase reference and formally recording it together with the optical field. Thus, by reconstructing the optical field from the hologram, the phase normal is as well “reconstructed“ and the phasing of each wave of the optical field relative to the reference is the same as in the original field. Accordingly, also the relative phasings of each wave with respect to one another will be the same as in the original field. Since the absolute phasing of the phase reference is irrelevant, but only the relative phasings of the “individual“ waves of the optical field counts, the original field as a whole is reproduced, containing all its information in phasing and intensity. It is clear, that the a human being observing the reconstructed optical field from a hologram will perceive a stereoscopic picture applying nature’s parallax technique. This recording and retrieval process is subsumed by the term „holography“, originating from the greek term „holos“, which means „the whole“.

2.3.1.1.)Holographic recording and retrieval

As already described above, holographic recording requires basically two optical fields, the optical field of the object, referred to as “object wave (or beam)”, or, more common, as “signal wave (or beam)” and an undisturbed (i.e. carrying no image information) reference wave (or beam) as phase normal. Both waves must be coherent in time with respect to each other for the duration of the recording process. Lateral coherence over the whole beam diameter is presumed.

In order to provide the phase normal for the optical field of the object, the object wave is superimposed with the reference wave yielding an interference pattern. The latter contains the intensity information of the object wave as well as the relative phasing of each individual wave train of the signal wave in form of a specific periodic intensity distribution. Thus, the phase information of the object wave has been transformed into an intensity pattern, which now can be stored together with the basic intensity information in a suitable storage medium. The recording process for off-axis recording is depicted in figure (2.3 - 1).

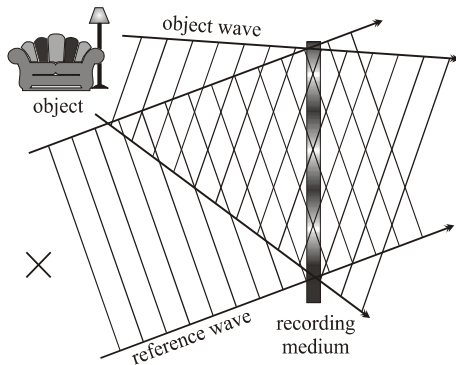


Figure (2.3 - 1): Holographic recording

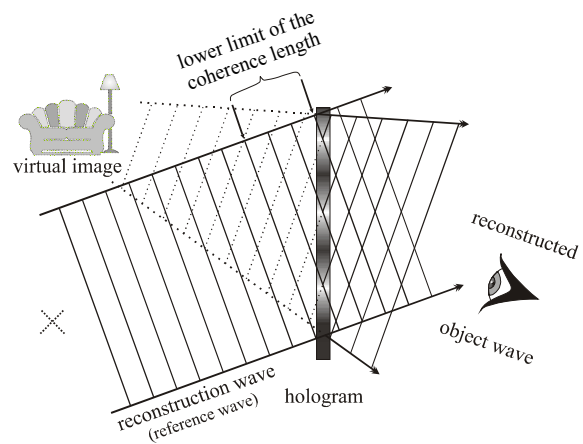


Figure (2.3 - 2): Holographic retrieval

The recorded hologram must be illuminated with a reconstruction wave of equal orientation (relative to the hologram) like the reference wave in order to retrieve the stored information. An observer will then notice a virtual image of the object in the same position relative to the hologram like the object has been for recording (i.e. for the viewer the image occurs “behind” the hologram). Please note, that the reconstruction wave need not fulfill any kind of coherence condition, since the absolute phasing of the reconstruction wave is irrelevant. The projection of its beam diameter onto the hologram normal will be the lower coherence limit, which is very illustrative, since it is necessary to reconstruct at least one complete wave front of the object wave in order to obtain the complete information stored. The retrieval process for an off-axis hologram is depicted in figure (2.3 - 2). Please note, that not the complete hologram is necessary to reconstruct the complete object wave. Theoretically, each infinitesimal volume element carries the complete information of the hologram. However, there is a practical limit due to diffraction at dust, impurities in the material, surface roughness of the medium, and others, which will considerably decrease the reconstruction quality of the object wave if the portion of the hologram for retrieval is chosen too small.

Inline holography will basically follow the same principles as described above. However, the object as well as the virtual image will be positioned in line with the reference beam, which is indicated by a solid line cross and a dotted cross in figure (2.3 - 1) and figure (2.3 - 2), respectively. It is clear, that this technique is not preferable.

2.3.1.2.)Types of holograms

Depending on the recording geometry, basically *transmission holograms* and *reflection holograms* must be distinguished. The determining parameter is the angle 2Θ between the propagation vectors of the object wave, the reference wave, and the conditions write:

$$0 < 2\Theta < 90^\circ \rightarrow \text{transmission geometry} \quad \text{eq. (2.3 - 1)}$$

$$90^\circ < 2\Theta < 180^\circ \rightarrow \text{reflection geometry}$$

There is no fundamental difference between a transmission hologram and a reflection hologram.

The hologram generated in the recording medium may be an *amplitude hologram* or a *phase hologram* or both. Which kind of hologram is dominant depends on the individual medium. Amplitude and phase holograms differ significantly in the achievable diffraction efficiency, which is generally limited to about 6-7% for amplitude holograms, but may reach 100% or even overmodulation for phase holograms.

Furthermore, *plane holograms* and *volume holograms* must be distinguished. The determining parameter in this case is the relation between the fringe spacing of the interference pattern and the thickness of the hologram. A sort of threshold criterion, which defines a volume hologram can be estimated to:

$$d \geq 1.6 \frac{\Lambda^2 n}{\lambda_0}, \quad \text{eq. (2.3 - 2)}$$

where d is the hologram thickness, Λ is the fringe spacing (grating constant) of the interference pattern, n is the average bulk refractive index, and λ_0 is the operating wavelength in vacuum.

There are some fundamental differences between plane holograms and volume holograms. The diffraction properties of plane holograms correlate basically to the diffraction properties of a simple-line grating, whereas the diffraction by volume holograms is of Bragg-type. This has important consequences. Diffraction by plane holograms yields a strong zero order intensity maximum, which carries no information as well as higher positive and negative diffraction orders, carrying the holographically stored information (Raman-Nath regime). The diffraction orders decrease quickly in intensity with increasing order number and usually only diffraction of first order yields significant diffraction efficiency. The diffraction efficiencies of plane holograms are generally strongly limited, since a huge amount of light intensity is lost in the zero order maximum. In contrast, the Bragg-type diffraction by volume holograms yields only one diffraction maximum, which carries the stored information and may achieve high diffraction efficiency. Please note, that ideal Bragg diffraction does not yield “diffraction orders”, which, however, cannot be realized in a real world experiment. Therefore, the diffraction maximum corresponding to ideal Bragg diffraction is sometimes referred to as zero order diffraction, whereas higher order numbers are used to denote additional diffraction maxima, occurring due to deviations of the considered Bragg-type diffraction grating from the ideal case. It is important to understand that this notation does not correspond to Raman-Nath diffraction orders. In fact, the “zero order” Bragg maximum formally corresponds to a first order diffraction maximum in the Raman-Nath regime.

It is important to point out, that an ideal volume hologram is either strictly wavelength or strictly direction selective, but not both of these simultaneously, as may easily be seen from the Bragg condition eq. (2.1 - 168). However, since only holograms with infinite thickness are ideal volume holograms, each real hologram has limited selectivity with respect to direction or wavelength, which worsens increasingly by approaching the condition formulated in eq. (2.3 - 2). Finally, plane holograms are neither wavelength nor direction selective and, therefore, not suitable for multiplexing purposes.

The simplest possible hologram is generated by two undisturbed waves. Provided the waves are ideally plain, the resulting hologram will be an ideal sinusoidal interference pattern according to eq. (2.1 - 46). Such a hologram will suffice to examine the performance and the diffraction properties of some holographic recording medium, since the diffraction properties of a hologram do not depend on its information content.

2.3.2.) Coupled wave theory for thick hologram gratings

In this paragraph, the basic concepts of the coupled-wave theory describing the Bragg diffraction by thick hologram gratings according to [18] will be outlined. This theory predicts the maximum possible diffraction efficiency as well as its angular and wavelength dependence. The theory allows for phase as well as amplitude gratings and additionally for slanted geometry. Strictly speaking, the analysis is restricted to sinusoidal hologram gratings. However, each periodic hologram may be expressed as a superposition of sinusoidal holograms, which allow for the application of the coupled-wave theory.

Subsequently, the derivation of the coupled-wave equations will be summarized, and important solutions will be discussed, which are required for the analytical evaluations performed in the framework of this thesis.

2.3.2.1.)The coupled-wave equations

The theoretical formulation assumes at first s-polarized monochromatic light, incident on the hologram grating at or near the Bragg angle and will be generalized to p-polarization later on.

Only the two waves, which obey the Bragg condition (eq. (2.1 - 168)) at least approximately are assumed to be present in the medium, which limits the analysis to volume holograms. The basic model of a hologram grating used for this analysis is depicted in figure (2.3 - 3). \vec{K} is the grating vector according to eq. (2.1 - 44), Λ is the fringe spacing according eq. (2.1 - 45), \vec{D} and \vec{T} are the diffracted wave and the transmitted wave, respectively, and d is the grating thickness. The slant of the grating is denoted by ψ , and θ_B is the angle of incidence of the transmitted beam. The angles are valid inside the medium. The hologram is assumed to be infinite in y -direction, and the fringes shall be parallel to the y -axis.

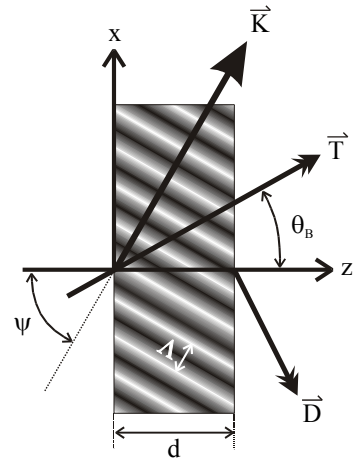


Figure (2.3 - 3): Model of a thick slanted hologram grating.

2.3.2.1.1.)s-Polarization

Since the polarization state of the considered waves has been defined a priori as s-polarized, the wave propagation in the grating may be expressed in scalar form by applying eq. (2.1 - 18):

$$\nabla^2 E(\vec{r}) + k^2 E(\vec{r}) = 0. \quad \text{eq. (2.3 - 3)}$$

A solution for this wave equation taking absorption into account will have a basic form

according to eq. (2.1 - 91), which yields the spatially modulated propagation constant k for a non-resonant situation (see figure (2.1 - 4)) as:

$$k^2(\vec{r}) = k_0^2 n^2 - 2ik_0 n \alpha, \quad \text{eq. (2.3 - 4)}$$

where k_0 is the propagation constant in free space, n is the refractive index, α is the absorption coefficient, and $\mu_r = 1$ is presumed.

By setting:

$$\begin{aligned} n(x, z) &= n_0 + \Delta n \cos(\vec{K} \cdot \vec{r}) \\ \alpha(x, z) &= \alpha_0 + \Delta \alpha \cos(\vec{K} \cdot \vec{r}) \end{aligned} \quad \text{eq. (2.3 - 5)}$$

the fringes of the hologram will be represented by the spatial modulation of n and α with the modulation amplitudes denoted by a preceding “ Δ ” and the average values marked by subscript “0”. The first equation refers to a phase grating and the second term to an amplitude grating. Furthermore, an average propagation constant β describing the propagation in the medium without a phase grating is introduced with:

$$\beta = k_0 n_0 = \frac{2\pi n_0}{\lambda_0}, \quad \text{eq. (2.3 - 6)}$$

where λ_0 is the wavelength in free space. By inserting eq. (2.3 - 5) in eq. (2.3 - 4) one obtains:

$$k^2 = \beta^2 - 2i\alpha_0\beta + 4\kappa\beta \cos(\vec{K} \cdot \vec{r}). \quad \text{eq. (2.3 - 7)}$$

The parameter κ is defined as:

$$\kappa = \frac{1}{4n_0}(k_0\Delta n^2 - 2in_0\Delta\alpha) \quad \text{eq. (2.3 - 8)}$$

and represents the basic parameter of the coupled-wave theory, the *coupling constant*, which describes the coupling between the transmitted and the diffracted wave. For $\Delta n \ll n_0$ the approximation $\Delta n^2 \approx 2n_0\Delta n$ can be applied if Δ is interpreted as total differential of n , and eq. (2.3 - 8) simplifies to:

$$\kappa = \frac{1}{2}(k_0\Delta n - i\Delta\alpha). \quad \text{eq. (2.3 - 9)}$$

The grating formed by Δn and $\Delta\alpha$ couples the two waves \vec{T} and \vec{D} leading to energy exchange between them.

The coordinate system and geometrical configuration depicted in Figure (2.3 - 3) will be used for the subsequent considerations. The waves may then be described by z -dependent complex amplitudes $T(z)$ and $D(z)$ in order to account for the energy interchange as well as for energy loss due to absorption. The total electrical field in the grating is the superposition of the two waves:

$$E = T(z)e^{-i\vec{k}_T \cdot \vec{r}} + D(z)e^{-i\vec{k}_D \cdot \vec{r}}, \quad \text{eq. (2.3 - 10)}$$

where \vec{k}_T is the propagation vector of the freely transmitted wave in absence of a grating and \vec{k}_D is the propagation vector of the diffracted wave. The modulus of the first is the average propagation constant according to eq. (2.3 - 6). The propagation vectors and the grating vector must fulfill the phase matching condition eq. (2.2 - 39), which determines \vec{k}_D . Since the grating has to take on the impulse difference between the two waves, the phase matching condition writes:

$$\vec{k}_T - \vec{k}_D = \vec{K}. \quad \text{eq. (2.3 - 11)}$$

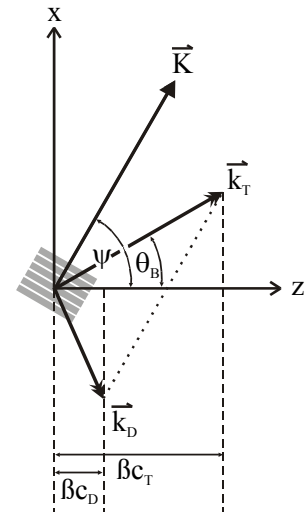


Figure (2.3 - 4): Vector diagram of diffraction by a slanted thick hologram grating

The vectorial representation of the problem considered is depicted in figure (2.3 - 4). Obviously, the components of the individual propagation vectors are given by:

$$\vec{k}_T = \begin{bmatrix} k_{Tx} \\ 0 \\ k_{Tz} \end{bmatrix} = \beta \begin{bmatrix} \sin \theta_B \\ 0 \\ \cos \theta_B \end{bmatrix} \quad \text{eq. (2.3 - 12)}$$

and (applying eq. (2.3 - 11)):

$$\vec{k}_D = \begin{bmatrix} k_{Dx} \\ 0 \\ k_{Dz} \end{bmatrix} = \beta \begin{bmatrix} \sin \theta_B - \frac{K}{\beta} \cos \psi \\ 0 \\ \cos \theta_B - \frac{K}{\beta} \cos \psi \end{bmatrix}, \quad \text{eq. (2.3 - 13)}$$

where $K = |\vec{K}|$.

The Bragg condition eq. (2.1 - 168) can be expressed in terms of the grating vector and the average propagation constant in the medium according to eq. (2.3 - 6):

$$\cos(\psi - \theta_B) - \frac{K}{2\beta} = 0. \quad \text{eq. (2.3 - 14)}$$

It is clear, that the left hand side of eq. (2.3 - 14) will not yield zero, if the Bragg condition is not met. Therefore, it is feasible to account for a deviation from the Bragg condition by introducing a dephasing measure \mathfrak{G} , which refers to this behavior:

$$\frac{\mathfrak{G}}{K} \equiv \cos(\psi - \theta_B) - \frac{K\lambda_0}{4\pi n_0}. \quad \text{eq. (2.3 - 15)}$$

The dephasing measure thus defined is independent from the grating spacing. This can easily be reproduced regarding the derivation of the Bragg condition in section “2.1.4.4.) Bragg diffraction” on page 38. Eq. (2.3 - 15) may be expressed in terms of the waves involved:

$$\mathfrak{G} = \frac{(k_T^2 - k_D^2)}{2k_T} = \frac{(\beta^2 - k_D^2)}{2\beta}. \quad \text{eq. (2.3 - 16)}$$

Any violation of the Bragg condition may occur in terms of an angular mismatch for a fixed wavelength or a wavelength mismatch for a fixed angle of incidence. This may be expressed by writing:

$$\begin{aligned} \theta_B &= \theta_{0B} + \Delta\theta_B \\ \lambda &= \lambda_0 + \Delta\lambda \end{aligned} \quad \text{eq. (2.3 - 17)}$$

Inserting eq. (2.3 - 17) into eq. (2.3 - 15) and performing a Taylor series expansion yields:

$$\mathfrak{G} = \Delta\theta_B K \sin(\psi - \theta_{0B}) - \Delta\lambda \frac{K^2}{4\pi n_0}. \quad \text{eq. (2.3 - 18)}$$

Now eq. (2.3 - 10) is inserted into eq. (2.3 - 3), and eq. (2.3 - 7) is introduced by means of eq. (2.3 - 11). Furthermore, all higher diffraction orders (i.e. all waves not fulfilling eq. (2.3 - 11)) are neglected. Comparing then terms with equal exponential order yields a set of differential equations:

$$\begin{aligned} T''' - 2iT'k_{Tz} - 2i\alpha_0\beta T' + 2\kappa\beta D &= 0 \\ D'' - 2iD'k_{Dz} - 2i\alpha_0\beta D' + (\beta^2 - k_D^2)D + 2\kappa\beta T &= 0 \end{aligned} \quad \text{eq. (2.3 - 19)}$$

which is further simplified by assuming slow energy interchange between $T(z)$ and $D(z)$ as well as “slow” depletion due to absorption, which allows to neglect second derivatives of the

waves' amplitudes. (Please note that “slow” must be understood in the sense of “slowly changing for the waves propagating in z-direction”.) Finally introducing the dephasing measure according to eq. (2.3 - 16) yields the *coupled wave equations*:

$$\begin{aligned} c_T \underline{T}' + \alpha \underline{T} &= -i\kappa D \\ c_D \underline{D}' + (\alpha + i\vartheta) \underline{D} &= -i\kappa \underline{T}' \end{aligned} \quad \text{eq. (2.3 - 20)}$$

with c_T and c_D representing obliquity factors according to figure (2.3 - 4), which account for the slant of the grating:

$$\begin{aligned} c_T &= \frac{k_{Tz}}{\beta} \\ c_D &= \frac{k_{Dz}}{\beta} \end{aligned} \quad \text{eq. (2.3 - 21)}$$

2.3.2.1.2.)p-Polarization

In contrast to s-polarization, the inherent vectorial nature of electromagnetic waves cannot be disregarded considering the interaction of p-polarized waves in the frame of the coupled wave model. Accordingly, eq. (2.1 - 18) must be applied in its vectorial form:

$$\nabla^2 \underline{\vec{E}}(\vec{r}) + k^2 \underline{\vec{E}}(\vec{r}) = 0, \quad \text{eq. (2.3 - 22)}$$

where the constant k is defined by eq. (2.3 - 7). The total electrical field in the grating may be expressed as before, i.e. by the vectorial equivalent of eq. (2.3 - 10). The waves considered are assumed to be ideally transversal, which is expressed by the conditions:

$$\begin{aligned} \underline{\vec{T}} \bullet \underline{\vec{k}}_T &= 0 \\ \underline{\vec{D}} \bullet \underline{\vec{k}}_D &= 0 \end{aligned} \quad \text{eq. (2.3 - 23)}$$

Following now the procedure outlined in the preceding section, one arrives at the vectorial equivalent for eq. (2.3 - 19):

$$\begin{aligned} -2i \underline{\vec{T}}' k_{Tz} + i \underline{\vec{T}}'_z \underline{\vec{k}}_T - 2i\alpha_0 \beta \underline{\vec{T}} + 2\kappa \beta \underline{\vec{D}} &= 0 \\ -2i \underline{\vec{D}}' k_{Dz} + i \underline{\vec{D}}'_z \underline{\vec{k}}_D - 2i\alpha_0 \beta \underline{\vec{D}} + (\beta^2 - k_D^2) \underline{\vec{D}} + 2\kappa \beta \underline{\vec{T}} &= 0 \end{aligned} \quad \text{eq. (2.3 - 24)}$$

Now, the vectorial amplitudes of the transmitted and the diffracted waves are separated into scalar amplitudes, which are a function of z , and corresponding polarization unit vectors $\underline{\vec{e}}_T$ and $\underline{\vec{e}}_D$, which are assumed here to be independent of z :

$$\begin{aligned} \underline{\vec{T}}(z) &= T(z) \underline{\vec{e}}_T \\ \underline{\vec{D}}(z) &= D(z) \underline{\vec{e}}_D \end{aligned} \quad \text{eq. (2.3 - 25)}$$

Multiplying the first equation of eq. (2.3 - 24) with $\underline{\vec{e}}_T$ and the second with $\underline{\vec{e}}_D$ yields:

$$\begin{aligned} 2i T' k_{Tz} - 2i\alpha_0 \beta T + 2\kappa \beta D (\underline{\vec{e}}_D \bullet \underline{\vec{e}}_T) &= 0 \\ -2i D' k_{Dz} - 2i\alpha_0 \beta D + (\beta^2 - k_D^2) D + 2\kappa \beta T (\underline{\vec{e}}_T \bullet \underline{\vec{e}}_D) &= 0 \end{aligned} \quad \text{eq. (2.3 - 26)}$$

and finally the coupled wave equations in analogy to the above:

$$\begin{aligned} c_T T' + \alpha T &= -i\kappa (\underline{\vec{e}}_T \bullet \underline{\vec{e}}_D) D \\ c_D D' + (\alpha + i\vartheta) D &= -i\kappa (\underline{\vec{e}}_T \bullet \underline{\vec{e}}_D) T \end{aligned} \quad \text{eq. (2.3 - 27)}$$

Thus, the coupled wave model yields identical results for s- and p-polarizations of the involved waves, if the coupling constant is adapted to the actually interacting (i.e. parallel) polarization components.

2.3.2.2.)Solution of the coupled wave equations

The solution of the coupled wave equations is obtained by applying the standard approach, which may be written in this case:

$$T(z) = t_1 e^{\gamma_1 z} + t_2 e^{\gamma_2 z} \quad \text{eq. (2.3 - 28)}$$

$$D(z) = d_1 e^{\gamma_1 z} + d_2 e^{\gamma_2 z}$$

In order to determine the constants γ_j ($j = 1, 2$), eq. (2.3 - 28) is inserted into eq. (2.3 - 20), and the coefficients of the different exponentials are compared, finally yielding:

$$\begin{aligned} (c_T \gamma_1 + \alpha) t_1 &= -i \kappa d_1 \\ (c_T \gamma_2 + \alpha) t_2 &= -i \kappa d_2 \\ (c_D \gamma_1 + \alpha + i \vartheta) d_1 &= -i \kappa t_1 \\ (c_D \gamma_2 + \alpha + i \vartheta) d_2 &= -i \kappa t_2 \end{aligned} \quad \text{eq. (2.3 - 29)}$$

Multiplication of equations with identical $j = 1, 2$ from eq. (2.3 - 29) with each other results in two identical quadratic equations:

$$(c_T \gamma_j + \alpha)(c_D \gamma_j + \alpha + i \vartheta) = -\kappa^2, \quad \text{eq. (2.3 - 30)}$$

having the solution:

$$\gamma_{1,2} = -\frac{1}{2} \left(\frac{\alpha}{c_T} + \frac{\alpha + i \vartheta}{c_D} \right) \pm \sqrt{\left(\frac{\alpha}{c_T} - \frac{\alpha + i \vartheta}{c_D} \right)^2 - 4 \frac{\kappa^2}{c_D c_T}}. \quad \text{eq. (2.3 - 31)}$$

In order to determine the constants t_j and d_j , boundary conditions must be introduced into the model. It is clear, that:

$$\begin{aligned} T(0) &= t_1 + t_2 = 1 \\ D(0) &= d_1 + d_2 = 0 \end{aligned} \quad \text{eq. (2.3 - 32)}$$

accounts for a transmission hologram, where the diffracted wave is zero before being diffracted and the transmitted wave is accordingly still undepleted. The undepleted wave is set to unity, since some absolute fields are not of interest here, but rather the relative energy interchange due to diffraction. In order to account for a reflection hologram, the diffracted wave counterpropagates the transmitted wave, which will change the boundary condition for a reflection grating to:

$$\begin{aligned} T(0) &= t_1 + t_2 = 1 \\ D(d) &= d_1 e^{\gamma_1 d} + d_2 e^{\gamma_2 d} = 0 \end{aligned} \quad \text{eq. (2.3 - 33)}$$

where d is the grating thickness. Please note, that the difference between transmission and reflection grating also shows up in the sign of the obliquity factor c_T , which is positive for the first and negative for the latter. Since reflection gratings have not been investigated in the frame of this work, the subsequent considerations will be restricted to transmission gratings.

Entering with eq. (2.3 - 32) into eq. (2.3 - 29) yields:

$$\begin{aligned} d_1 &= -d_2 = -i \frac{\kappa}{c_D (\gamma_1 - \gamma_2)} \\ t_1 &= 1 - t_2 = \frac{c_T \gamma_2 + \alpha}{c_T (\gamma_2 - \gamma_1)} \end{aligned} \quad \text{eq. (2.3 - 34)}$$

The amplitudes of the transmitted and the diffracted wave in a transmission grating are obtained by introducing these constants into eq. (2.3 - 28).

However, usually only the diffracted wave is of interest, the amplitude of which reads:

$$D(d) = i \frac{\kappa}{c_D(\gamma_1 - \gamma_2)} [e^{\gamma_2 d} - e^{\gamma_1 d}]. \quad \text{eq. (2.3 - 35)}$$

The diffraction efficiency of the grating is defined as the diffracted fraction of the incident light power showing up in the diffracted wave:

$$\eta = \frac{DD^*}{|c_{TD}|}, \quad \text{eq. (2.3 - 36)}$$

where the input wave is presumed to have unit amplitude.

The parameter c_{TD} is the slant factor, given by:

$$c_{TD} = \frac{c_T}{c_D}. \quad \text{eq. (2.3 - 37)}$$

2.3.2.3.)Transmission holograms

In order to obtain an analytical expression for the diffraction efficiency, eq. (2.3 - 35) must be combined with eq. (2.3 - 31). This results in a fairly cumbersome expression, which can be expressed more conveniently by separating the coupling constant from the other parameters determining the grating behavior. Therefore, two new parameters ν and ξ are introduced according to:

$$\nu = \frac{\kappa d}{\sqrt{c_D c_T}} \quad \text{eq. (2.3 - 38)}$$

and:

$$\xi = \frac{d}{2} \left(\frac{\alpha}{c_T} - \frac{\alpha + i\vartheta}{c_D} \right), \quad \text{eq. (2.3 - 39)}$$

where d is the grating thickness, κ the coupling constant according to eq. (2.3 - 9), ϑ the dephasing parameter according to eq. (2.3 - 18) and c_T and c_D are the obliquity factors according to eq. (2.3 - 21). These parameters can easily be redefined in order to account for the individual properties of a grating considered.

The amplitude of the diffracted wave in terms of ν and ξ writes:

$$D(d) = -i \sqrt{c_{TD}} e^{-\frac{\alpha d}{c_T}} e^{\xi} \frac{\sin \sqrt{\nu^2 - \xi^2}}{\sqrt{1 - \frac{\xi^2}{\nu^2}}}. \quad \text{eq. (2.3 - 40)}$$

This equation is a general expression for the diffraction efficiency due to phase and absorption gratings and accounts for loss in the medium, slant of the grating and deviations from the Bragg condition. Accordingly, it simplifies dramatically by excluding some of these effects.

The first restriction accounts for the particular properties of the materials investigated within the frame of this work. Although these materials cannot a priori be assumed to be loss-free, the occurrence of a notable absorption grating can safely be excluded. Accordingly, only phase (i.e. dielectric) gratings must be accounted for.

2.3.2.3.1.)Loss-free phase grating

In the case of a loss-free phase grating, the parameters v and ξ may be rewritten as:

$$v = \frac{\pi \Delta n d}{\lambda_0 \sqrt{c_D c_T}} \quad \text{eq. (2.3 - 41)}$$

$$\xi = -i \frac{\mathfrak{g} d}{2 c_D}$$

and the absorption term in eq. (2.3 - 40) becomes unity. Applying eq. (2.3 - 36) yields the diffraction efficiency:

$$\eta = \frac{(\sin \sqrt{v^2 - \xi^2})^2}{1 - \frac{\xi^2}{v^2}}. \quad \text{eq. (2.3 - 42)}$$

Eq. (2.3 - 42) further simplifies by assuming an non-slanted grating and the Bragg condition obeyed:

$$\eta = \left[\sin \left(\frac{\pi \Delta n d}{\lambda_0 \cos \theta_{0B}} \right) \right]^2, \quad \text{eq. (2.3 - 43)}$$

where θ_{0B} is the Bragg angle relative to the grating planes according to the well known form of the Bragg condition according to eq. (2.1 - 168).

2.3.2.3.2.)Lossy phase grating

Eq. (2.3 - 40) is not notably simplified, if a slanted and lossy phase grating is considered allowing for deviations from the Bragg condition. Therefore, Bragg incidence shall be presumed here. Then, the parameters v and ξ may be rewritten as:

$$v = \frac{\pi \Delta n d}{\lambda_0 \sqrt{c_D c_T}} \quad \text{eq. (2.3 - 44)}$$

$$\xi = \frac{d}{2} \left(\frac{\alpha}{c_T} - \frac{\alpha}{c_D} \right)$$

and one obtains for the diffraction efficiency:

$$\eta = \frac{(\sin \sqrt{v^2 - \xi^2})^2}{1 - \frac{\xi^2}{v^2}} e^{-\frac{\alpha d}{2} \left(\frac{1}{c_T} + \frac{1}{c_D} \right)}, \quad \text{eq. (2.3 - 45)}$$

which simplifies for the case of an unslanted grating to:

$$\eta = \left[\sin \left(\frac{\pi \Delta n d}{\lambda_0 \cos \theta_{0B}} \right) \right]^2 e^{-\frac{2\alpha d}{\cos \theta_{0B}}}. \quad \text{eq. (2.3 - 46)}$$

2.3.3.) Holographic data storage

Holographic data storage has been an issue since the invention of the laser, which has promoted holography in general from a barely realizable theoretical concept to actual physical application. The basic concepts of holographic data storage have been established by van Heerden in 1963 [19]. Holographic data storage promises various advantages as compared to other storage techniques.

In this paragraph the basic techniques will be outlined, which may be applied in holographic mass data storage. Therefore, the principles of holographic data storage are described briefly in the frame of optical data storage in general leading to “multiplexing” as a key technique to meet the demand for high storage densities. Subsequently, the different multiplexing techniques are described schematically. The paragraph closes with a consideration of the system metrics for holographic multiplexing. In this context, at first a recording schedule is derived, which allows for holographic multiplexing in erasable media like photorefractives. Secondly, the $M/\#$ (read: „m - number“) is introduced, which currently is on the way to be commonly accepted as a figure of merit, which describes the multiplexing performance of a holographic storage medium. The recording and erasure dynamics of an erasable holographic medium will be shown to have major impact on the possible application in holographic multiplexing. Please note, that this essential question has motivated a great deal of the work presented here.

Technical, engineering and physical aspects concerning the details of holographic memory devices will not be considered, since this work focuses on a particular holographic medium rather than the practical realization of a holographic memory device.

2.3.3.1.)The principle of holographic data storage

Information is stored in today’s commercially available optical storage media (CD and DVD) in terms of a reflection code representing the 1s and 0s of the binary code. In principle, the reflection code is printed or burnt into a rotating medium in the form of one-dimensional strings of longer and shorter reflecting areas arranged in concentric circles around the rotation axis of the medium. Thus, the information is stored two-dimensionally in a serial manner, and the individual bits are spatially located on the data carrier (CD) making them vulnerable to possible damage of the storage medium (e.g. scratches). A very limited number of these information layers may be stacked “mechanically” in a single disc in order to achieve a higher storage density of the complete device (DVD). The principle is depicted in figure (2.3 - 5). The stored data is read out by a focused laser beam, which is modulated in intensity by the string of reflecting dots while the CD or DVD rotates.

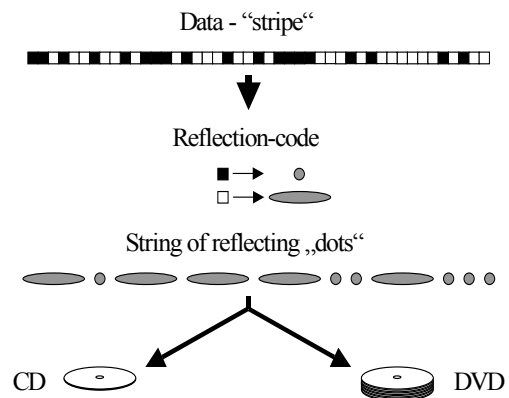


Figure (2.3 - 5): Storage scheme for CD and DVD

For holographic storage, on the other hand, the information is provided in terms of images of two-dimensional pixel arrays. Holograms are formed from these images by means of a spatial light modulator which imprints a corresponding intensity pattern into the signal beam. A hologram is then stored in a holographic medium. For retrieval, the hologram is illuminated solely with the reference beam and the image of the data page will then show up in the diffracted

portion of the reference beam. It can be evaluated by a detector array (charge coupled device, CCD). The information is distributed over the entire recording volume and may be retrieved even from only a small portion of the hologram as already mentioned before. Thus, the information is insensitive against partial damage of the recording medium, which will reduce the signal to noise ratio rather than cause bit errors.

If the recording medium allows for storage of volume holograms, many holograms can be stored in a single volume using slightly different Bragg conditions. This technique is called *multiplexing* and will be discussed subsequently in more detail. Using multiplexing, high storage densities of up to several TBit/cm³ are theoretically possible. During retrieval only the hologram will be detected, which obeys the current Bragg condition. The parallel nature of holography in general shows up in the inherent feature of storage and retrieval of whole pages instead of single bits, which promises high data transfer rates. Holographic data storage moreover offers the possibility of associative retrieval. In this case, the holograms are illuminated with a reference beam carrying some information to compare with the hologram considered. The reference beam will then only be diffracted if the stored hologram is at least very similar to the information imprinted in the reference beam. The diffraction efficiency depends on the quality of the congruence. If the medium carries multiple holograms, all Bragg conditions applied for storage can be tested and, thus, the data page can be found, which correlates best to the information contained in the reference beam.

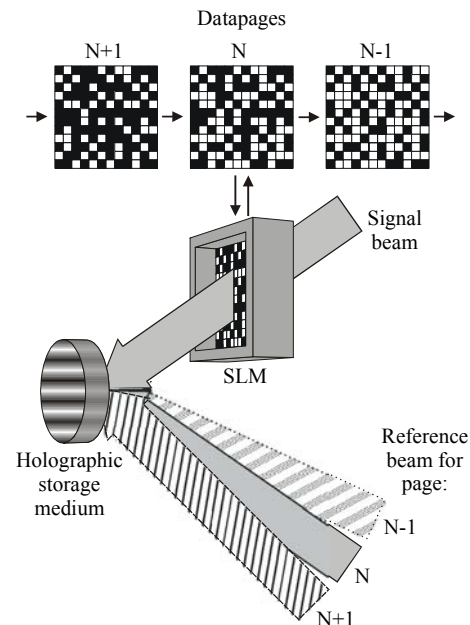


Figure (2.3 - 6): Scheme of holographic data storage. Angular multiplexing of three data pages is depicted.

2.3.3.2.)Holographic multiplexing

Subsequently, the principle of multiplexing will be outlined, followed by a schematic description of the multiplexing methods established today. Finally, the basic scheme will be depicted, which has to be followed in order to reasonably apply the multiplexing methods. In this context, the M-number ($M/\#$) is introduced, which provides a measure to trade off the multiplexing capability of some holographic medium considered in terms of its applicability as holographic mass storage medium.

2.3.3.2.1.)The principle of holographic multiplexing

Holographic multiplexing is based on the inherent property of volume holograms to require a specific geometrical configuration, depending on the wavelength for read-out, which is given by the Bragg condition eq. (2.3 - 14) (or eq. (2.1 - 168)). The diffraction efficiency of a particular hologram vanishes if the Bragg condition is not met, which is referred to as *Bragg selectivity*. The Bragg selectivity is theoretically infinite for an ideal infinitely thick grating, but depends on various factors for a real grating of limited thickness, the most important of which are the grating thickness and the grating spacing. One may get an idea of the relations by

calculating the expected normalized diffraction efficiency as a function of the dephasing with respect to the Bragg condition for various parameters by means of eq. (2.3 - 36) and eq. (2.3 - 40). An example is depicted in figure (2.3 - 7).

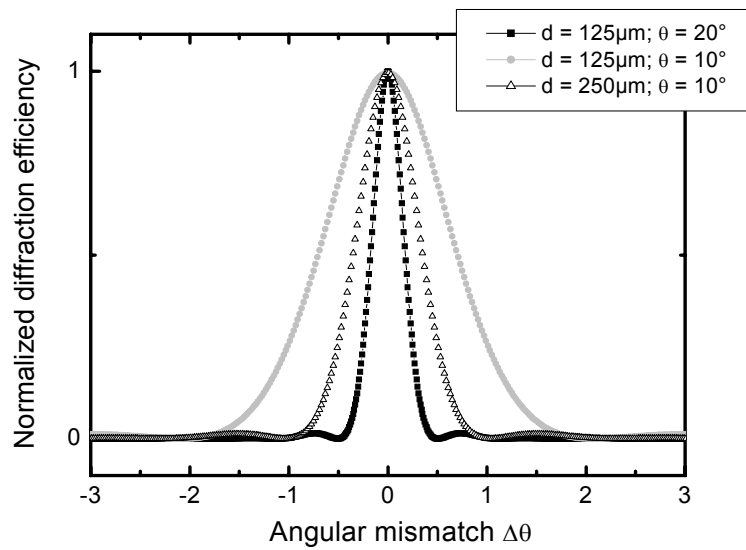


Figure (2.3 - 7): Angular Bragg selectivity of transmission holograms of different thickness d recorded with different intersection angles 2θ of the recording beams (i.e. different grating spacing).

Thus, appropriately applying different Bragg conditions in recording allows to record many holograms in a single volume element of the recording medium, which can be individually retrieved without cross-talk between each other. Consequently, the number of holograms to be multiplexed is in principle limited by the Bragg selectivity of the considered system. The recording of many holograms should not be misconceived as recording of holograms at different depth in the volume. In fact, the holograms are superimposed in the same volume element by intermixing their holographic structures.

While intermixing the holographic structures of many holograms does not affect the information stored in an individual hologram, it is clear, that there will be an effect on the strength of the individual holograms. All holographic recording media actually provide a limited dynamic range, i.e. the achievable absolute refractive index modulation is limited. Thus, by storing a great number of holograms, the refractive index modulation per hologram and accordingly also the diffraction efficiency of each hologram will decrease. Please note, that the diffraction efficiency η is approximately proportional to the square of the index modulation (for $\eta \ll 1$) resulting in a fast decrease of the diffraction efficiency as a function of the multiplexed number of holograms. This is a further limiting factor for the maximum number of holograms to be multiplexed in a system considered.

There are some other factors, which may limit the maximum number of holograms to be multiplexed. However, these factors are related to technical requirements and engineering aspects for real storage devices rather than to physical limitations. In particular, an appropriate control of a storage device requires all stored holograms to exhibit equal or at least very similar diffraction efficiency. These factors will not be discussed here in detail, although they are important as well, if the potential applicability of some holographic medium for multiplexing purposes is considered.

2.3.3.2.2.)Holographic multiplexing methods

In order to multiplex holograms for storage purposes, the Bragg conditions must be varied somehow by varying some physical property of either the signal, or the reference beam, or the storage medium. Furthermore, an appropriate addressing mechanism must be provided, which maps memory addresses to values of the physical properties varied. The physical property used for addressing the Bragg condition for a particular hologram defines the multiplexing method. Please note, that different multiplexing methods may be combined for technical application.

A) Angular multiplexing

Angular multiplexing generally describes all methods to address different Bragg conditions by variation of the angle of incidence of the involved laser beams. This may be performed by changing the angle of incidence of only the reference beam, which is the most common way and already depicted in figure (2.3 - 6). There are alternative possibilities, which are, however, afflicted with unfavorable technical problems. For example the medium may be rotated around its central axis perpendicular to the plane of incidence of the beams, however, the diffracted beam may then move as well due to changing refraction. Angular multiplexing is well established for photorefractive crystals, where a 90° configuration can be applied as sketched in figure (2.3 - 8). When applying angular multiplexing, the holographic grating vector is varied either only by length or by length and direction, the latter which is the case if only the reference beam is manipulated.

Please note, that angular multiplexing may be performed in orthogonal directions, which then is referred to as “in-plane“ and “out-of-plane“. Figure (2.3 - 8) depicts in-plane angular multiplexing. Rotating the variation direction for the angle of incidence of the reference beam by 90° leads to the out-of-plane equivalent.

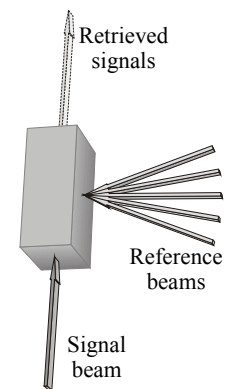


Figure (2.3 - 8):
Angular multiplexing
in 90° configuration

C) Shift multiplexing

Shift multiplexing [20, 21] basically uses the concept of angular multiplexing, however without explicitly changing the angle of incidence of one of the beams. The signal beam is a plane wave, whereas the reference beam is transformed into a spherical wave by a pinhole or a lens of high numerical aperture. Then the beams are intersected inside the medium to record a hologram. The direction and the length of the holographic grating vector in this hologram is not constant but a function of its spatial location in the hologram. Accordingly, this particular hologram can only be read out again, if the position of the spherical reference beam relative to the hologram is exactly reproduced in the lateral position as well as in the distance to the focal point of the reference beam. For recording the next hologram, the medium is then shifted by a portion of the hologram diameter in a plane perpendicular to the plane, which includes the propagation vectors of the signal beam and the

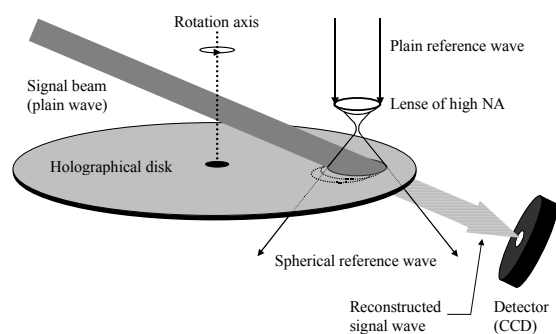


Figure (2.3 - 9): Shift multiplexing

reference beam before its transformation into the spherical reference wave.

Usually the shift is small, so that the holograms overlap significantly. The configuration is depicted in figure (2.3 - 9). Figure (2.3 - 10) illustrates the grating planes, which result from the intersection of the plain signal wave and the spherical reference wave. It is clear, that there is a spatially varying distribution of grating wave vectors, which only can be Bragg-matched by the exact equivalent of the reference wave fronts applied for generating the hologram. Please note, that the shift direction may be chosen arbitrarily, provided it is within the plane described above.

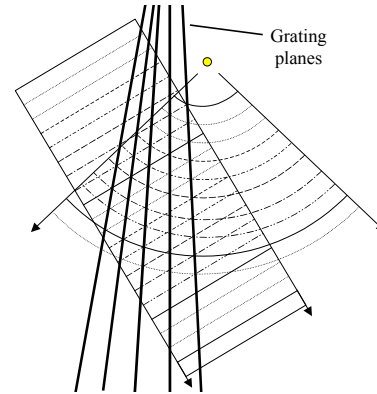


Figure (2.3 - 10): Sketch of some grating planes resulting from interference of a plain with a spherical wave

Shift multiplexing is in particular preferable for disk-shaped holographic media, e.g. organic polymer systems.

B) Wavelength multiplexing

The wavelength of both the signal and the reference beam is varied in wavelength multiplexing. The geometrical configuration of the setup remains unchanged, otherwise, which is in principle favorable. Variation of the wavelength alters the length of the holographic grating vector. Wavelength multiplexing has gained importance during the last years, which is due to the tremendous progress achieved in semiconductor laser technology providing nowadays multi-color tunable semiconductor Lasers at relatively low cost. However, the tunability is still limited which renders wavelength multiplexing still less flexible than other multiplexing methods.

D) Peristrophic multiplexing

Peristrophic multiplexing [22] represents a special case, since the Bragg condition is only altered “spatially“ in this multiplexing method. The individual holograms are recorded in the medium under identical conditions, however, the medium is rotated a bit around its center normal between two recording processes. Thus, the grating vectors of the individual holograms may be interpreted as lying in a conic envelope around the axis of rotation of the medium depending on the particular recording geometry (i.e., the bisector between the recording beams need not coincide with the rotation axis). Therefore, all holograms will be always addressed simultaneously during readout and the reconstructed signal beams will occur as well simultaneously but spatially resolved on a half circle around the axis of rotation. The particularly addressed hologram must then be separated from the others, e.g. by an iris. On the other hand, this feature

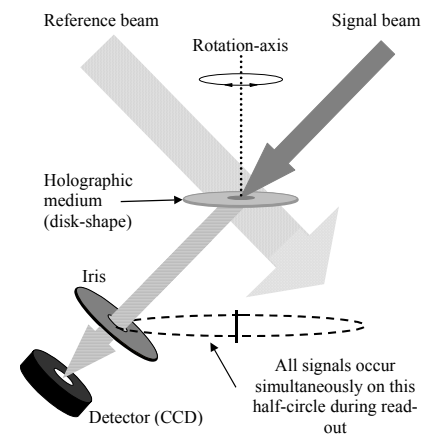


Figure (2.3 - 11): Peristrophic multiplexing

may allow for fast associative retrieval not requiring mechanical repositioning of the holographic recording medium.

Please note, that the axis of rotation is not restricted to be normal to the holographic medium, however, this case is most ostensive. If the axis of rotation is not normal to the medium, the medium will wobble during rotation, which makes the spatial situation more complicated.

In analogy to shift multiplexing, peristrophic multiplexing is in particular preferable for disk-shape holographic media, e.g. organic polymer systems.

E) Phase-encoded multiplexing

Phase-encoded multiplexing [23, 24] does not use a plain reference beam, but a reference beam with modulated phase, i.e. the wave fronts of the reference beam carry some particular pattern. If the functions underlying the phase patterns are orthogonal, holograms can be stored and retrieved without significant cross-talk when applying the different phase patterns to the reference beam. The phase patterns can be imprinted into the reference beam by means of a phase only spatial light modulator (pSLM). The principle may be illustrated by means of the shift multiplexing described before, which may be regarded as a special case of phase multiplexing. By recording a hologram with a reference beam carrying some specific phase pattern, the resulting distribution of holographic grating vectors can only be Bragg-matched by a reference beam carrying an identical phase pattern. However, as mentioned before, the phase pattern functions must be orthogonal, since otherwise portions of the grating vector distributions may coincide for different holograms leading to strong cross-talk.

Phase-encoded multiplexing additionally offers the possibility of arithmetic operations on a stored hologram by means of subsampling of phase codes.

Although this method sounds favorable, since the geometrical configuration of the setup remains unchanged like in wavelength multiplexing and it offers the feature of possible arithmetical operations on stored holograms, it suffers from the lack of high precision pSLM's.

2.3.3.3.)System metrics for holographic multiplexing in erasable media

Technical application of holographic mass data storage by means of holographic multiplexing requires all holograms to exhibit at least very similar diffraction efficiency once the multiplexing recording procedure is finished. This is proximate, since a technical device must not be expected to adapt its detection sensitivity for read out to the individual holograms. Accordingly, it is necessary to multiplex holograms in a way, that the diffraction efficiency of all holograms finally levels off. In erasable media, however, a hologram previously recorded will be partially erased while recording the next hologram. In order to account for this circumstance, an appropriate exposure schedule has to be found, which ensures, that the holograms recorded earlier are erased to just the strength of the last hologram recorded [25]. The derivation of the exposure schedule furthermore results in a figure of merit, which characterizes the dynamic range performance of a holographic memory system, the so called M-number (M/#).

2.3.3.3.1.)The exposure schedule

The particular expression for such an erasure schedule will be recursive and account for the particular recording and erasure dynamics of the medium used. Extensive research efforts have been focused on multiplexing in photorefractive crystals during the last decades, which are regarded as the most promising systems for the application in question. Therefore, photorefractive crystals shall be employed here for discussing the system metrics for holographic multiplexing in erasable media. Photorefractive crystals will be discussed later in more detail. However, in order to proceed in the present considerations, the dynamic behavior of these holographic storage media will be anticipated here. Photorefractive crystals basically exhibit a mono-exponential recording and erasure behavior of the photorefractive space-charge field, which determines the strength of the holographic grating, i.e., the refractive index modulation. Thus, the recording behavior may be expressed by:

$$\sqrt{\eta} \propto A_0 \left(1 - e^{-\frac{t}{\tau_r}} \right), \quad \text{eq. (2.3 - 47)}$$

where A_0 denotes the maximum grating strength, and τ_r is the recording time constant. Eq. (2.3 - 47) assumes, that the diffraction efficiency is small, i.e. $\eta \ll 0.1$, which allows to approximate eq. (2.3 - 43) by $\eta \propto \Delta n^2$. The erasure behavior may be expressed by:

$$\sqrt{\eta} \propto A_0 e^{-\frac{t}{\tau_e}}, \quad \text{eq. (2.3 - 48)}$$

where τ_e is the erasure time constant.

Thus, for multiplexing e.g. $M=10$ holograms, the recording process will look like depicted in figure (2.3 - 12). It is convenient to derive an analytical expression for the schedule starting with the exposure time t_M for the last hologram and calculating the exposure times for the other holograms t_m inversely in a recursive procedure. The choice of the exposure of the last hologram is conducted semi-empirically and will be discussed later in this section.

The derivation of the exposure schedule is straight forward although the indices count backwards, while the reasoning counts forwards. For a very large number of holograms (actually $M \rightarrow \infty$), most of the holograms are recorded to very small strength $\eta \rightarrow 0$. Thus, there will be some hologram number $m_0 > 1$ with $t_{m_0} \ll \tau_r$, which allows for the approximation of eq. (2.3 - 47) by:

$$\sqrt{\eta} \propto A_0 \frac{t_m}{\tau_r} \quad \text{eq. (2.3 - 49)}$$

for $m > m_0$, i.e., the exponential law of growth is linearly approximated by its initial slope.

Now some m th hologram and the corresponding $(m-1)$ th hologram are considered with $m > m_0+1$. The $(m-1)$ th hologram has been recorded for the time t_{m-1} and has subsequently been erased for the time t_m while the m th hologram has been recorded. According to figure (2.3 - 12), both holograms shall end up at the same strength, i.e.:

$$\frac{A_0}{\tau_r} t_m = \frac{A_0}{\tau_r} t_{m-1} e^{-\frac{t_m}{\tau_e}}. \quad \text{eq. (2.3 - 50)}$$

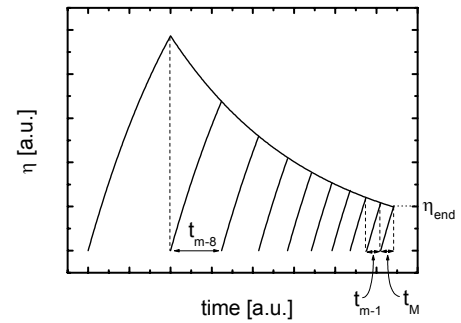


Figure (2.3 - 12): Multiplexing schedule

Accordingly, the inverse recursive expression for the schedule reads:

$$t_{m-1} = t_m e^{t_m/\tau_e} \quad \text{eq. (2.3 - 51)}$$

However, this schedule has been derived applying approximations, which must be accounted for.

This will be done, by choosing an appropriate exposure time for the last hologram and additionally introducing an empirical correction factor. Eq. (2.3 - 51) may be rewritten as:

$$\frac{t_m}{t_{m-1}} = 1 - (1 - e^{-t_m/\tau_e}) \quad \text{eq. (2.3 - 52)}$$

and the approximation used to obtain Eq. (2.3 - 49) can be applied once more yielding:

$$t_m = \frac{t_{m-1}}{1 + \frac{t_{m-1}}{\tau_e}} \quad \text{eq. (2.3 - 53)}$$

Now the recording time for the m th hologram may be defined in terms of the erasure time constant:

$$t_m \equiv \rho_m \tau_e, \quad \text{eq. (2.3 - 54)}$$

where ρ_m is some real number with $\rho_{m_0} \ll 1$ following the constraints preceding eq. (2.3 - 49). Inserting this into eq. (2.3 - 53) results in:

$$\rho_m = \frac{\rho_{m-1}}{1 + \rho_{m-1}} \quad \text{eq. (2.3 - 55)}$$

In order to get rid of the recursive character of eq. (2.3 - 55), the hologram number m_0 is referred to, which is a constant, marking the formal beginning for the validity of the applied approximations. Counting forward from m_0 , i.e. in direction of increasing hologram number, eq. (2.3 - 55) may be rewritten as:

$$\rho_{m_0+1} = \frac{\rho_{m_0}}{1 + \rho_{m_0}} = \frac{1}{1 + 1/\rho_{m_0}} \quad \text{eq. (2.3 - 56)}$$

The next step in the direction of increasing hologram number will read:

$$\rho_{m_0+2} = \frac{1}{1 + 1/\rho_{m_0+1}} = \frac{1}{2 + 1/\rho_{m_0}} \quad \text{eq. (2.3 - 57)}$$

Thus, it follows by induction $m > m_0$:

$$\rho_m = \frac{1}{(m - m_0) + 1/\rho_{m_0}} \quad \text{eq. (2.3 - 58)}$$

As m grows very large with m_0 fixed:

$$\rho_m \approx \frac{1}{m} \quad \text{eq. (2.3 - 59)}$$

and with eq. (2.3 - 54):

$$t_m = \frac{\tau_e}{m} \quad \text{eq. (2.3 - 60)}$$

Referring now to the last hologram M , which shall also define the grating strength finally achieved for all holograms (see figure (2.3 - 12)), the resulting grating strength of the multiplexed holograms will be:

$$\sqrt{\eta_{end}} = A_M = A_0 \left(1 - e^{-\frac{\tau_e}{M\tau_r}} \right) \quad \text{eq. (2.3 - 61)}$$

for $M \gg m_0$ for some m_0 satisfying the constraints preceding eq. (2.3 - 49).

However, applying the last exposure time t_M according to eq. (2.3 - 60) and calculating the previous recording times according to eq. (2.3 - 51) will lead to unreasonably long initial exposure times (and even an infinite first exposure time), which are not practical, and result in too small diffraction efficiencies for the first holograms due to the performed linear approximation of the growth behavior. In turn, this is only valid for small exposure times. Therefore, the exposure of the last hologram must be chosen somewhat smaller than indicated from eq. (2.3 - 60), which is taken into account by introducing an empirical factor f with $f < 1$ and choosing the last exposure according to:

$$t_M = f \frac{\tau_e}{M}. \quad \text{eq. (2.3 - 62)}$$

By reasonable selection of f , the recording sequence will be finite and of practical total length. A reasonable value for f cannot be calculated but has to be identified by trial and error. Typical values for common photorefractive crystals are about $0.5 < f < 0.8$. If f is chosen too small, the dynamic range of the medium is not completely used and if f is chosen too large, the exposure schedule will not be practical as discussed above.

It must be pointed out, that the entire preceding derivation bases on the assumption of a simple mono-exponential dynamic behavior of the holographic medium for both the recording process and the erasure process. Furthermore, both processes are assumed to be independent from each other. If these basic assumptions do not apply, it will be no longer possible to derive an analytical expression for the exposure schedule. As will be shown in the section devoted to the experimental results, both problems apply to PR polymers.

2.3.3.3.2.)The M-number (M/#)

The $M/\#$ is a direct result of eq. (2.3 - 61) [26]. Since M is a very large number, whereas τ_r and τ_e are usually of at least similar magnitude, the exponential growth term in eq. (2.3 - 61) can again be approximated linearly yielding:

$$\eta = \left[\left(\frac{A_0}{\tau_r} \right) \frac{\tau_e}{M} \right]^2. \quad \text{eq. (2.3 - 63)}$$

This expression relates the essential system parameters, i.e. saturation grating strength A_0 , recording time constant τ_r and erasure time constant τ_e to the desired number of holograms M to be multiplexed and the maximum achievable diffraction efficiency η . It is clear, that it would be very convenient to separate the material parameters and merge them into a new parameter, which may serve as figure of merit for the dynamic range performance of a holographic memory system. Therefore, the above expression is rewritten as:

$$\eta = \left[\frac{M/\#}{M} \right]^2 \quad \text{eq. (2.3 - 64)}$$

with $M/\#$ as the desired material parameter, called „M-number“. Accordingly, the $M/\#$ is defined as:

$$M/\# = \left(\frac{A_0}{\tau_r} \right) \tau_e. \quad \text{eq. (2.3 - 65)}$$

The M-number was originally only used in photorefractive crystals. However, it offers more extensive application, since it may be determined on the basis of its original definition according to eq. (2.3 - 65) as well as on basis of eq. (2.3 - 64), which is applicable for arbitrary holographic storage media. To do so, the medium in question must simply be experimentally tested by

multiplexing a sufficiently high number M of holograms (i.e. at least 10; the significance of $M/\#$ increases with increasing hologram number) meeting the condition of similar strength. Then $M/\#$ can be obtained by:

$$M/\# = M\sqrt{\eta} = \sum_{m=1}^M \sqrt{\eta_m}, \quad \text{eq. (2.3 - 66)}$$

where m is the hologram number.

Accordingly, $M/\#$ may serve as an indicator to compare the performance of arbitrary holographic storage media. A higher $M/\#$ directly indicates better system performance. However, the $M/\#$ cannot account for outreaching problems e.g. concerning complicated dynamic behavior of a holographic medium as found in photorefractive polymers. This will be discussed in more detail in the section devoted to the experimental results. Typical values of $M/\#$ for some representative holographic storage systems are given in Appendix A.

2.4.)Physical aspects of organic polymers

This paragraph deals with theoretical aspects of polymer physics. Aspects of relaxation processes in polymers will be outlined. A phenomenological overview over the main transitions in polymers will be given. The glass-transition and the underlying theory will be briefly discussed. Thereafter the oriented gas model describing the electrical poling of organic polymers will be outlined including the nonlinear optical properties of poled polymers. Finally in the last section in this paragraph the electrical properties of organic polymers will be elaborated upon.

2.4.1.) Relaxation and thermodynamics in polymers

Relaxation and thermodynamics in amorphous polymers is a wide field, which covers the entire range of physical states from the glassy state to the melt. Nowadays, polymers are well established materials for an enormous variety of technical applications, and numerous theoretical approaches have been developed to describe the behavior of polymers in their different states. However, all theories developed up to now cover only a small portion of the complete range of physical states a polymer can take on. Moreover, long time scale and short time scale behavior must be distinguished, since the time scale of a particular experiment is a crucial parameter for defining the physical state of the polymer in the experiment. The situation is furthermore complicated by the fact, that on the one hand the physical states of a polymer are not clearly separated and on the other hand different aspects of a particular state may be approached from different points of view. In fact there are solely smooth transitions existing rather than clear limitations and some unifying treatment is still out of sight. Therefore, it is impossible to give a consistent overview in the frame of this work, and the subsequent consideration will only cast spot-lights upon some aspects, which are of major interest for the class of materials under investigation here.

In order to perform a preselection one must anticipate a few points to be discussed later in more detail. Photorefractive polymers are statistically center-symmetric and require poling by an external electrical field in order to become photorefractive, i.e. polar molecules or moieties must be oriented within the polymer matrix. This is the fundamental reason why relaxation and thermodynamics of polymers are important for this class of materials. However, here not the bulk properties shall be focussed upon, but rather the impact of the rigidity of the matrix on the orientational ability of some small molecule. This makes the consideration of some movement or manipulation of whole polymer chains dispensable. In fact, basically the thermodynamical point is of interest, when some tens of chain segments become mobile enabling them to evade when set under stress by the small molecule in its attempt to orient itself along an externally applied field. This leads directly to the glass-transition, which may be considered as the transition from the glassy state, where the matrix is highly rigid to a state, where just some tens of polymer chain segments are mobile enabling some collective motion of the polymer backbone. As soon as this state is reached, the orientational mobility of the small molecule may be considered as approximately unimpeded, which is the basic assumption for the oriented gas model to be discussed in “2.4.2.) Electrical poling of organic polymers - the oriented gas model” on page 83. Furthermore, the case must be considered, when the matrix is still rigid and the small molecule experiences mechanical repulsion from the matrix while attempting to orient. This situation refers to the glassy state, which, however, shows viscoelastic contributions depending on the time scale applied. Therefore, viscoelastic response behavior in non periodic stress-relaxation experiments will be considered. This consideration will be

restricted to the macroscopic phenomenology and will not cover aspects of molecular dynamics, which would go far beyond the scope of this work.

Subsequently a phenomenological overview over the main viscoelastic transitions in polymers is provided. Thereafter, the glass-transition will be elaborated upon followed by a brief discussion of the viscoelastic response behavior. A consideration of the effect of physical aging in amorphous organic polymers will conclude this section.

2.4.1.1.)Phenomenology of viscoelastic transitions

Macromolecular systems like organic polymers usually react viscoelastically on mechanical stress, which means that there is an elastic as well as a viscous response. In first approximation this behavior is described by a serial connection of an elastic and a viscous element, which is called a Maxwell-element.

The elastic element behaves according to Hook's law, which describes a linear proportionality between mechanical stress σ and a resulting deformation ε of a material under the approximation of small deformations. The proportionality factor in the case of linear deformation is Young's modulus of elasticity $E^\#$. (Alternatively and without loss of generality one may consider shearing instead of linear deformation.)

$$\sigma = E^\# \varepsilon \quad \text{eq. (2.4 - 1)}$$

The viscous element is described by Newton's equations, which describes a linear proportionality between mechanical stress and the speed of deformation. The proportionality factor is the viscosity η (Please note that η is typically used in this work for denoting the DFWM diffraction efficiency of a hologram. However, η is commonly used to denote the viscosity in the literature concerning the mechanical properties of materials. Therefore this notation will be adopted here, however, restricted to this section.):

$$\sigma = \eta \frac{d\varepsilon}{dt} \quad \text{eq. (2.4 - 2)}$$

For a serial connection of these elements (then called a Maxwell-element), both contributions to the deformation (eq. (2.4 - 1) has to be derived with respect to the time before) can be added and a mechanical relaxation time τ_{max} of the system can be defined as:

$$\tau_{max} \equiv \eta / E^\# \quad \text{eq. (2.4 - 3)}$$

One ends up with the following relation:

$$\frac{d\varepsilon}{dt} = \frac{1}{E^\#} \frac{d\sigma}{dt} + \frac{\sigma}{\tau_{max} E^\#} \quad \text{eq. (2.4 - 4)}$$

Hence, important basic mechanical properties of an organic polymer may be represented qualitatively by simply considering the modulus of elasticity. This applies especially to the consideration of the temperature dependency of the states of aggregation.

In order to display the different states of aggregation such a system may take on, figure (2.4 - 2) shows qualitatively the modulus of elasticity of a typical organic polymer for a wide range of temperatures. There are five different areas of mechanical relaxation behavior, which are correlated with significantly different behavior in stress-relaxation experiments of any kind and, consequently, are correlated with very different physical states of the system:

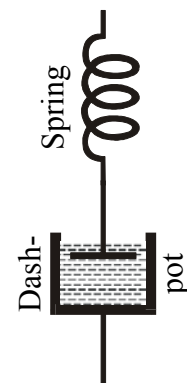


Figure (2.4 - 1): Maxwell-element

1) Range of the glassy state

The modulus of elasticity is high and only slightly temperature dependent. The polymer is hard and brittle. Molecular motions are basically restricted to vibrations and short range rotational motions (typically 1-4 chain atoms).

2) Range of the glass-transition

In the range of the glass-transition the modulus of elasticity is extraordinarily temperature dependent. Typically, area 2 has a width of 20 - 30°C and

while passing over this area by heating up a glassy polymer, $E^\#$ decreases by about three orders of magnitude. For quasi-static measurements the point of maximum slope of this part of the curve is usually defined as the point of the glass-transition. The temperature, which is related to the glass-transition point is defined as the *glass-transition temperature* (T_g). Qualitatively, the glass-transition region can be interpreted as the onset of long range coordinated molecular motion (typically 10-50 chain atoms).

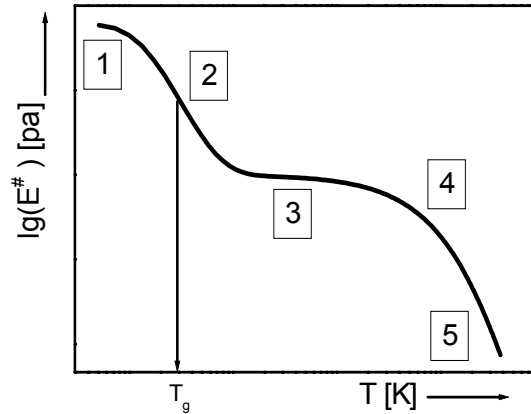


Figure (2.4 - 2): Modulus of elasticity as a function of temperature. T_g indicates the glass-transition „point“.

3) Range of the rubber-like plateau

In this area $E^\#$ depends only weakly on the temperature, if at all, and the polymer is highly elastic. The width of this plateau strongly depends on the molecular mass and/or the degree of crosslinking. Non crosslinked polymers may already show viscoelastic tendencies. Crosslinked systems remain in this state as the temperature further increases until they decompose.

4) Range of the rubber-like flux

At further increasing temperature, the modulus of elasticity starts decreasing again with increasing slope. The polymer starts to flow under the influence of mechanical stress and behaves increasingly viscous. This is the area of dominant viscoelastic behavior.

5) Range of the melt

$E^\#$ is very small (about three orders of magnitude smaller than in area 3), and the polymer behaves like a more or less viscous fluid.

It is important to be aware, that the observed mechanical behavior of the systems depends on the relation between the measurement time and the relaxation times (viscous and elastic) of the system over the entire range discussed above. This will be expressed hereafter by using the term “time scale“ of an experiment. An experiment operating on “short (long) time scale“ is thus correlated to an experiment extending over a short (long) time period as compared to the relaxation times of the system.

For example even in the glassy state viscous behavior may be observed, if the time scale of the applied stress-relaxation experiment is sufficiently long. Hence, the curve in figure (2.4 - 2) refers to an experiment carried out on a constant and relatively short time scale, however, parametric in the temperature. On the other hand, one may determine $E^\#$ as a function of the time scale of the experiment at constant temperature and will obtain a similar curve, where the time increases as well from left to right. It is important to understand, that $E^\#$ at constant temperature is not a function of time, but rather of the time scale of the experiment. Thus, in this case each point of the curve represents the modulus of elasticity determined for a duration of the experiment represented by its corresponding time value in the diagram.

Hence, distinction between a static glass-transition temperature and a dynamic glass transition temperature may be made (however, these are not „different temperatures“ but they rather represent the behavior under different experimental conditions).

2.4.1.2.)Static and dynamic glass-transition temperatures

The static glass-transition temperature refers to the glass-transition temperature obtained by experiments operating on a relatively long time scale, so that the system in question may be approximately considered in thermodynamic equilibrium at any time. Hence, one may also say, that the static glass-transition temperature is basically defined thermodynamically, which as well represents the basis for a theoretical approach to be discussed later in “2.4.1.3.2.) Thermodynamic approaches” on page 78. However, this definition has to be handled with care, since the glass-transition actually is a relaxation process and accordingly of kinetic nature, which is not questioned by the thermodynamic approach. The static glass-transition temperature may be measured for example dilatometrically, by differential scanning calorimetry (DSC), or by mechanical or dielectric loss experiments at very low frequency. It describes the temperature, where slowly charged amorphous matter changes its mechanical behavior from brittle to stringy. As already mentioned before, the experimental results of the static glass-transition temperature will depend on the time scale applied in the particular experiments. However, a thermodynamically well-defined so called ideal glass-transition temperature is implied by the thermodynamic interpretation, which is independent from any measurement parameter. On the other hand, since the ideal glass-transition temperature is only a theoretical parameter, which does not have practical significance in contrast to the experimental value, it is common practice that experimentally determined T_g 's are presented in the literature together with the experimental parameters applied in order to allow for reasonable comparison.

The dynamic glass-transition temperature, on the other hand, is related to the mechanical behavior of amorphous matter, which is changed on short time scale, e.g. by mechanical shots or hits. The dynamic glass-transition temperature can be measured by stress-relaxation experiments like repercussion-elasticity and mechanical or dielectric loss experiments at high frequency. The dynamic glass-transition temperature experimentally obtained will increase with decreasing time scale of the underlying experiment. In classical linear organic polymers (e.g. polystyrene), the increase of T_g amounts to about 5-7° per order of magnitude decrease in time scale of the experiment.

The dynamic and the experimentally obtainable static glass-transition temperatures can be converted into one another by an empirical expression, which is generally valid for arbitrary relaxation processes and known as Williams-Landel-Ferry (WLF) equation, which reads:

$$\log \alpha_T = - \frac{c_1^0 \cdot [T - T_0]}{c_2^0 + [T - T_0]} \quad \text{eq. (2.4 - 5)}$$

The shift factor α_T corresponds to the relation τ / τ_0 of two relaxation times of the system at two different temperatures T and T_0 , whereby T_0 and τ_0 are reference values obtained by any arbitrary measurement technique for the glass-transition temperature. The WLF scaling factors c_1^0 and c_2^0 are empirical values, specific for each type of polymer and a certain reference temperature. The WLF equation is an approximation, which is only reasonably valid within a limited temperature interval around T_0 . The width of this interval is neither well defined, nor necessarily symmetric around T_0 and, accordingly, some experience is required for the WLF scaling to be successfully applied.

The experimental static glass-transition point is often referred to as a proper reference point in the literature, with the validity of the WLF scaling then being restricted to an interval of roughly $T_g < T < T_g + 100K$. According to [B9, p. 300] and [B21, p. 341] average values of $c_1^0 = 17.44K$ and $c_2^0 = 51.6K$ have been found for this case as well as for nearly all polymers.

A conceptual derivation of the WLF equation will be presented in Appendix I in terms of the free-volume theory.

2.4.1.3.)Theoretical approaches to the glass-transition

The theoretical understanding of the glassy state or of the glass-transition, respectively, is still incomplete. Basically, there are three different approaches to this problem, each of which focuses on a different aspect of the phenomenon:

- Free-volume theory
- Kinetic approach
- Thermodynamic approach

It is beyond the scope of this work to discuss all three theoretical approaches to the glass-transition phenomenon in detail. Only the free-volume theory will be outlined in more detail subsequently, since it is more closely related to the problems elaborated upon in the frame of this work than the other approaches. The thermodynamic approach will only be outlined verbally. The kinetic approach will not be discussed separately, since the kinetic elements included in the free volume theory are sufficient for covering the kinetic aspects of interest in this work.

2.4.1.3.1.)Free-volume theory

The free-volume theory (FVT) is based on the perception, that a glass is a supercooled liquid in which the molecular mobility is extremely slowed down as compared to the liquid state. This is assumed to be due to a drastic reduction of the internal free volume available for the molecules to move, preventing the formation of an ordered crystal lattice and freezing in the instantaneous “liquid“ configuration.

Figure (2.4 - 3) qualitatively depicts the total volume V of some matter as a function of the temperature T . For the discussion a sample shall be assumed, which is heated up. The lower

solid curve represents a $V(T)$ -trend of matter in the crystalline state. As soon as the melting temperature T_m is reached, V increases at constant $T = T_m$. The upper curve to the right of T_m represents the $V(T)$ -trend for the corresponding liquid. The upper curve to the left of T_m represents the $V(T)$ -trend of matter in the glassy state. T_g is the “real“ (experimentally obtainable) glass-transition temperature, which depends on the cooling rate previously applied to the liquid (i.e. the history of the sample) as does the $V(T)$ -curve. T_∞ represents the ideal glass-transition temperature. Please note, that the volume of a glass at $T = 0\text{K}$ cannot be as small as the volume of a corresponding crystal at $T = 0\text{K}$, since a state of negative entropy would result. This aspect leads to the ideal glass-transition temperature, which will be discussed in the framework of the thermodynamic theories. $V_g^f(T_g)$ and $V_{fl}^f(T_m)$ are the free volumes of the glass at T_g and of the liquid at T_m , respectively, related to the volume of the crystalline state at T_∞ . This definition of the free volume is derived from the aforementioned entropy problem and will be discussed in the section devoted to the thermodynamic theory.

Generally speaking the total free volume is defined as the excess volume with respect to the volume of the ideal crystalline state at the ideal glass transition temperature.

However, not the total free volume is used for the theoretical treatment of the free-volume conception, but rather the fractional free volume f , which is defined as the free volume V_f normalized by the volume V of the considered phase:

$$f = \frac{V_f}{V}. \quad \text{eq. (2.4 - 6)}$$

Expressing small changes of the fractional free volume in the form:

$$df = \frac{1}{V} dV_f, \quad \text{eq. (2.4 - 7)}$$

one readily concludes from the general thermal expansion coefficient α :

$$\alpha = \frac{1}{V} \cdot \left(\frac{dV}{dT} \right), \quad \text{eq. (2.4 - 8)}$$

that the fractional free volume f increases linearly with temperature, however, for a limited temperature range only, since the total volume of the phase is regarded as constant in eq. (2.4 - 7):

$$f = f_0 + \alpha_f \cdot (T - T_0). \quad \text{eq. (2.4 - 9)}$$

Here, f_0 is the fractional volume at the reference temperature T_0 and α_f may be considered as the thermal expansion factor of the free volume, which, in the case of the liquid to glass transition, is the difference between the thermal expansion coefficients of the liquid phase α_{li} and the glassy phase α_g :

$$\alpha_f = \alpha_{li} - \alpha_g \quad \text{eq. (2.4 - 10)}$$

Accordingly, the free volume can be expressed by the thermal expansion coefficients α_{li} and α_g :

$$V_f = (\alpha_{li} - \alpha_g) \cdot T. \quad \text{eq. (2.4 - 11)}$$

Introducing now P as a measure of the probability that the barrier to some cooperative motion in the system be surmounted, an Arrhenius-type relationship may be assumed for P :

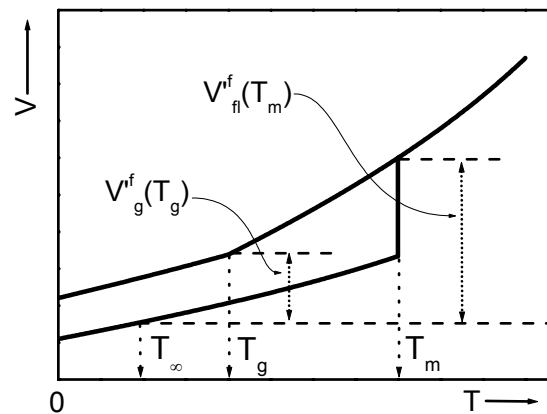


Figure (2.4 - 3): Change of the free volume as a function of temperature

$$P = e^{-\frac{\Delta E_a}{k_B T}}, \quad \text{eq. (2.4 - 12)}$$

where ΔE_a is the activation energy of the process and the denominator of the exponential is the thermal energy.

Furthermore, the time (scale) t of the experiment must be considered as several times mentioned before. The theory assumes, that the product tP must reach a certain value for the collective motion to start and, hence, for the transition to be observed. Thus:

$$tP = te^{-\frac{\Delta E_a}{k_B T}} = \text{const.} \quad \text{eq. (2.4 - 13)}$$

and it follows:

$$\ln t = \text{const.} + \frac{\Delta E_a}{k_B T}, \quad \text{eq. (2.4 - 14)}$$

which correlates the logarithm of time with the inverse of the temperature.

The activation energy ΔE_a will be associated with the free volume and qualitatively may be expected to decrease as the fractional free volume increases. This may be expressed as:

$$\frac{\Delta E_a}{k_B T} = \frac{B'}{f}, \quad \text{eq. (2.4 - 15)}$$

where B' is a constant. Accounting for eq. (2.4 - 3), which correlates the viscosity with a relaxation time, eq. (2.4 - 15) shows similarity with the *Doolittle equation*, which describes the viscosity η as a function of the free volume

$$\ln \eta = \ln A + B \cdot \frac{(V - V_f)}{V_f}. \quad \text{eq. (2.4 - 16)}$$

A and B are empirical factors. Therefore, B' is taken as equal to B and the differential of eq. (2.4 - 14) reads:

$$\Delta \ln t = B \Delta \left(\frac{1}{f} \right), \quad \text{eq. (2.4 - 17)}$$

which correlates the logarithm of time with the inverse of the fractional free volume. Rewriting the differential on the right hand side of eq. (2.4 - 17) as:

$$\Delta \left(\frac{1}{f} \right) = \frac{1}{f} - \frac{1}{f_0} \quad \text{eq. (2.4 - 18)}$$

and inserting eq. (2.4 - 9) yields, after some simple arithmetic manipulations, the WLF equation in log base e form:

$$\ln \alpha_T = - \frac{[B/f_0][T - T_0]}{[f_0/\alpha_f] + [T - T_0]} \quad \text{eq. (2.4 - 19)}$$

with α_T as shift factor according to:

$$\ln \alpha_T = \ln \left(\frac{t}{t_0} \right) = \Delta \ln t. \quad \text{eq. (2.4 - 20)}$$

Comparing eq. (2.4 - 19) with eq. (2.4 - 5) shows, that the WLF scaling factors c_1^0 and c_2^0 can be expressed as:

$$c_1^0 = \frac{B}{e^1 f_0} \quad \text{and} \quad c_2^0 = \frac{f_0}{\alpha_f}, \quad \text{eq. (2.4 - 21)}$$

with $e^1 \approx 2.303$.

As already noted above, the WLF equation is restricted to a limited temperature interval around T_0 , which is due to the linear approximation of α_f according to eq. (2.4 - 9).

Viscosities shift as well with temperature, which may be expressed by the same shift factor as implied by the similarity between the Doolittle equation and eq. (2.4 - 17):

$$\alpha_T = \frac{\eta T_0 \rho_0}{\eta_0 T \rho} = \frac{\tau}{\tau_0} = \frac{t}{t_0} . \quad \text{eq. (2.4 - 22)}$$

The densities ρ_0 (at T_0) and ρ (at T) and the temperatures T_0 and T correct for the thermal expansion and the subscript “0” denotes the reference state. The viscosity is correlated with a relaxation time by eq. (2.4 - 3), which identifies the modulus of elasticity as proportionality factor. For relating the shift factor for the relaxation times to the viscosities, the correction for thermal expansion in eq. (2.4 - 22) is introduced. The relaxation times correspond directly to the time (scale) t of the experiment. It is clear, that the same argumentation applies for the modulus of elasticity, allowing the application of the shift factor as well for $E^\#$. Please note, that the thermal expansion is considered as very small for any kind of solids anyway (as implied already for eq. (2.4 - 7)), making the correction introduced dispensable in most cases.

The WLF equation is well-suited to introduce some kinetic aspects. It was mentioned before, that the measured glass-transition temperature increases with decreasing time scale of the experiment applied for its determination. This relation may be deduced from the WLF equation giving also an indication of the orders of magnitude to be expected. For example one obtains from eq. (2.4 - 5) with the parameter values given subsequent to eq. (2.4 - 5):

$$\lim_{T \rightarrow T_g} \left(\frac{\log \alpha_T}{T - T_g} \right) = -0.338 , \quad \text{eq. (2.4 - 23)}$$

yielding for T near T_g an increase of about 3° in T_g per decade of α_T , however, for α_T covering at maximum a range of about 3 orders of magnitude. For larger changes in the time frame, the average increase in T_g is even higher. For example, solving eq. (2.4 - 5) explicitly for $\alpha_T = 10^{-10}$ yields $T - T_g \approx 69$, i.e. in average about 7° per decade. However, the relation can no longer be approximated as linear for such large changes.

In conclusion, according to the free-volume conception, the glass-point is defined as the point, when the contraction of a melt while rapidly cooling down leads to the subsidence of the free volume below a critical value. Below this value, conformation changes of the molecules are suppressed by a lack of space and the diffusion mobility is frozen.

Expressing this statement in terms of non-crosslinked polymers, one has to account for a possibly significant difference between the diffusion mobility and the ability of conformation changes in polymers around the glass transition due to the relatively large average size of the molecules. Therefore a relative wide plateau area of viscoelastic behavior between the melt and the glassy state occurs, where the diffusion mobility is already almost completely frozen, but a significant ability for conformation changes is still persistent. The latter decreases if the temperature (and free volume) is further reduced until the polymer becomes hard and brittle.

As already mentioned in the introduction above, the free volume conception is a preferable approach for consideration of the problems regarded in the frame of this work, since the free volume may be considered as the determining factor for the orientational mobility of small molecules embedded in the polymer matrix. For temperatures below the glass-transition temperature, the free volume is too small to provide enough space for small molecules to orient freely under the influence of an externally applied field. On the other hand, for temperatures above the glass-transition temperature, the free volume is sufficient for the small molecules to behave approximately like free molecules. In the frame of this work, where the small molecules to be oriented have similar size as about 10 chain segments, the glass-transition may be taken as the onset temperature for approximately free orientational mobility. However, if larger molecules shall be oriented, the onset temperature for approximately free orientational mobility

and the glass transition temperature may differ. The orientation of free (in the sense described above) small molecules by an external field will be discussed in detail in “2.4.2.) Electrical poling of organic polymers - the oriented gas model” on page 83.

2.4.1.3.2.)Thermodynamic approaches

The thermodynamic approach to the glass-transition temperature is known as the Gibbs and DiMarzio theory. Gibbs and DiMarzio took for granted, that kinetic aspects may affect the experimental determination of the glass-transition temperature. However, they argued that the underlying true transitions may be difficult to realize, but nevertheless be of equilibrium nature. This argumentation is based on the observation, that the apparent glass-transition temperature decreases as the experiment for its determination is carried out on longer time scales. Gibbs and DiMarzio postulated, that the material will finally reach equilibrium after infinitely long time, ending up in a true second order transition. According to the Ehrenfest-rule, transitions of second order are defined as transitions involving a discontinuity of the second derivative of the Gibbs free energy to the temperature (and/or the pressure) at the coexistence point of the two phases considered, whereas the first derivative is continuous, i.e., for example, the heat capacity will be discontinuous at the transition point. In contrast, a first order transition (e.g. boiling) is defined by a discontinuity of already the first derivation of the Gibbs free energy and the second derivation (e.g. the heat capacity) will show a singularity at the transition point. Please note, that the transition on limited time scale is only of quasi second order, i.e. the heat capacity will actually not be discontinuous, but will somehow “jump“ significantly. The difference is illustrated in figure (2.4 - 4).

Hence, when cooling the system down infinitely slowly, it will finally reach a glassy state, the configurational entropy of which approaches zero. The temperature, which is correlated to the transition point to zero entropy is the ideal thermodynamic glass-transition temperature T_∞ , which has been mentioned before in the frame of the free volume theory and is depicted in figure (2.4 - 3). The key problem of the Gibbs and DiMarzio theory is to find the appropriate configurational partition function, from which the configurational entropy can be calculated. However, a discussion of this aspect would exceed the frame of this work.

The ideal glass transition temperature may be estimated by means of the Adams and Gibbs theory, which represents some kind of unifying treatment attempting to merge the WLF equation with the Gibbs and DiMarzio theory. A “cooperatively rearranging region“ is defined as the smallest region capable of allowing for conformational changes without being accompanied by changes outside this region. At T_∞ the size of this region is just the size of the sample, since only one conformation per molecule is available. Based on their concept, Adams and Gibbs re-derived the WLF equation suitably and found the following relationship between T_∞ and T_g , valid for a wide range of glass-forming systems [B21, p. 352]:

$$\frac{T_g}{T_\infty} \approx 1.30. \quad \text{eq. (2.4 - 24)}$$

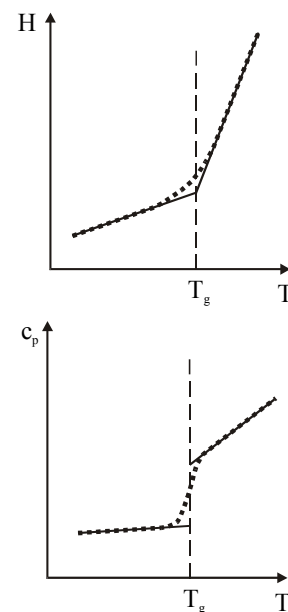


Figure (2.4 - 4): True (solid lines) and quasi (dotted lines) second order transition. H: enthalpy; c_p : heat capacity (const. press.)

2.4.1.3.3.)General trends in influencing the glass-transition temperature

Since the glass transition point is an essential parameter for the class of material investigated in the frame of this work, it seems advisable to give a qualitative overview over possibilities to influence T_g of organic polymer systems. This section is not intended to be comprehensive, but it rather focuses on methods being viable for the systems considered in the frame of this work.

A) Chain length

The influence of the chain length may easily be understood in the context of the free volume conception. The argumentation is based on the reasonable assumption, that a chain end will on the average require a larger free volume for movements than some segment within the chain. On the other hand, when increasing the thermal energy a chain end will rotate sooner than a segment within the chain, i.e. the contribution of the chain ends to the free volume will set on at lower temperature. Thus, the glass-transition temperature will decrease as a function of increasing density of chain ends and accordingly with decreasing chain length, i.e. with decreasing molecular weight. This has been expressed by [B21, p. 352]:

$$T_g = T_g^{(M=\infty)} - \frac{K}{\alpha_f M}, \quad \text{eq. (2.4 - 25)}$$

where M is the molar mass, α_f is the thermal expansion coefficient of the fractional free volume according to eq. (2.4 - 10) and K is a constant given by [B9, p. 303f]:

$$K = \rho N_A \Xi n^{(\Xi)}, \quad \text{eq. (2.4 - 26)}$$

where ρ is the specific density of the polymer, N_A is the Avogadro number, Ξ is the contribution of a chain end to the free volume, and $n^{(\Xi)}$ is the number of chain ends per molecule (i.e. 2 for linear polymers).

B) Internal chain mobility

It is clear, that the internal chain mobility has a tremendous impact on T_g . Making the chain more rigid by introducing e.g. p-phenyle segments, will increase T_g considerably. An extreme case is represented by poly-p-phenylene itself, which does not soften at all for increasing temperature before decomposing.

C) Chemical configuration

The tacticity of a polymer may have a considerable effect on T_g , however, the magnitude of the impact depends on the side group. Generally speaking, a tacticity, which relieves changes of the conformation decreases T_g . Therefore, syndiotactical polymers show higher T_g than isotactical.

A similar trend is observed for cis-trans isomers in polydienes. The isomery affects the internal chain mobility.

D) Sterical effects

Side groups attached to the polymer backbone may have tremendous impact on T_g . As a rule of thumb, T_g increases with size, polarity, and internal rigidity of the side group. The effect of side groups is basically of sterical nature, but may be significantly enhanced by bonding effects like hydrogen bridges. On the other hand, short linear alkyle side groups may even decrease T_g in some cases (see next point).

E) Plasticization

A very common and easy way to control T_g of a polymer system is plasticization by addition of plasticizers, which are small molecules soluble in the polymer matrix, but which do not vaporize easily. This method is referred to as external plasticization or external softening. The effect of the plasticizer may be interpreted in the sense of a lubricant increasing the mobility of the polymer chains by separating them with respect to each other. The resulting degree of reduction in T_g as a function of the plasticizer content may be roughly estimated by [B9, p. 370]:

$$\frac{1}{T_g^{(m)}} = \frac{\phi_p}{T_g^{(p)}} + \frac{\phi_s}{T_g^{(s)}}, \quad \text{eq. (2.4 - 27)}$$

where (m) denotes the mixture, (p) the pure polymer, (s) the plasticizer, and ϕ the corresponding molar fractions. The temperatures must be related to the Kelvin scale. It must be emphasized, that eq. (2.4 - 27) represents only a rule of thumb, which may fail dramatically for particular systems.

In this context is necessary to have some knowledge about the T_g of the plasticizer. Since the plasticizer is often a compound tending to crystallize rather than to form a glass, T_g is often not easily available. However, a very rough relation between the melting temperature T_m and T_g has been experimentally found for linear homopolymers as being “valid“ for about 80% of the systems investigated so far [B9, p. 364; B21, p. 363]:

$$\frac{T_g}{T_m} \approx 0.5 \text{ to } 0.8. \quad \text{eq. (2.4 - 28)}$$

This relation also holds for smaller organic molecules within its inherent „range of validity“. It must be pointed out, that this relation has no physical background, since T_m is correlated with a first order transition and T_g with a second order transition, excluding a simple relation between these two transition temperatures. Nevertheless, together with eq. (2.4 - 27) it may serve as a first rough estimate of what may be expected when adding some plasticizer to a polymer. However, the actual significance of the results must be kept in mind.

A plasticizer need not necessarily be added physically but may as well be attached covalently, then acting as spacers between the polymer chains rather than as a “Lubricant“. These spacers reduce the packing density of the polymer chains leading to plasticization of the material. In contrast to external softening, the latter is referred to as internal softening. It is clear, that these two kinds of plasticization are fundamentally different and that a plasticizer suitable for external softening usually must not be attached covalently (see point D)). Typically, suitable side chain groups for internal softening are simple structures, which are not able to jam with each other.

2.4.1.4.)Viscoelastic response in a creep-relaxation experiment

In the introduction to this section on page 70 it has already been anticipated, that orienting small polar molecules embedded in a polymer matrix under the influence of an electrical dc field will be the problem which this entire section is actually focused upon. In the framework of the above discussion of the glass-transition it has been concluded, that this orientational process may be considered as approximately independent from the surrounding polymer matrix for some temperature at or above the glass-transition temperature, depending on the size of the polar molecule to be oriented (see page 78). Now the case will be considered, that this approximation is definitely not valid, which applies if the orientation is hindered by the polymer matrix. For the materials investigated in the frame of this work this case will occur for ambient temperatures below T_g , i.e. in the glassy state of the polymer matrix. The matrix will then counteract the orientational process. According to the general model of viscoelasticity, this counteraction will be of elastic nature on a short time scale and increasingly viscous when the time scale increases. Thus, it seems reasonable to assume that the orientational process as a function of time will then contain contributions as encountered in a simple creep-relaxation experiment. Therefore, the basic behavior of a viscoelastic system in such an experiment will be outlined subsequently.

The Maxwell element according to eq. (2.4 - 4) is usually much too simple to describe viscoelastic behavior. Therefore a more complex system is usually employed, which is represented by the four-element model (also called “Burger’s element“ [B7, p. D45f]). Please note, that the four element model is in most cases actually also too simple for quantitative considerations, however, it provides all contributions of the viscoelastic response in qualitative manner. The four-element model is depicted in figure (2.4 - 5). If some constant stress σ is applied to Burger’s element, the resulting elongation will basically have three contributions, an elastic ε_e , a viscoelastic ε_r , and a viscous contribution ε_v . The first writes according to eq. (2.4 - 1):

$$\varepsilon_e = \frac{\sigma}{E^\#} \quad \text{eq. (2.4 - 29)}$$

and the third results from eq. (2.4 - 2):

$$\varepsilon_v = \frac{\sigma}{\eta} t. \quad \text{eq. (2.4 - 30)}$$

Both the above contributions are due to the “Maxwell part“ of the four-element model. The viscoelastic contribution is represented by the parallel connection of a spring and a dash-pot, which is called Voigt-Kelvin-element. The elongation due to the Voigt-Kelvin-element is:

$$\varepsilon_r = \frac{\sigma}{E_r^\#} (1 - e^{-t/\tau_r}), \quad \text{eq. (2.4 - 31)}$$

where $E_r^\#$ is a modulus of relaxation and τ_r , a correlated relaxation time, called retardation time, both of which may experimentally obtained by from measurements of the strain as a function of time. Please note, that the modulus of relaxation is different from the modulus of elasticity and that the correlated relaxation time is not the relaxation time defined by eq. (2.4 - 3). Please note furthermore, that in practice a viscoelastic system will show numerous retardation times, which may be expressed by a distribution function as discussed in the section devoted to the experimental results.

Merging all three contributions, the total deformation writes:

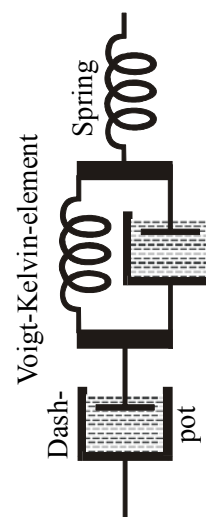


Figure (2.4 - 5):
Burger’s element

$$\varepsilon_{tot} = \sigma \left(\frac{1}{E^{\#}} + \frac{t}{\eta} + \frac{1}{E_r^{\#}} (1 - e^{-t/\tau_r}) \right) \quad \text{eq. (2.4 - 32)}$$

and, depicted as a function of time, will qualitatively look like illustrated in figure (2.4 - 6).

Deformations due to viscous behavior (eq. (2.4 - 30), ε_v) are usually irreversible. However, if a counter force is applied, the deformation may be completely reversed.

It should be noted, that the viscoelastic behavior of polymers may be described in terms of molecular dynamics, which leads to the Rouse-Zimm-Bueche theory and the reptation model. These modern approaches have been successfully applied to describe in detail several aspects of the viscoelastic behavior of organic polymers. However, there are still a lot of open questions. A reasonably detailed consideration of these theories by far exceeds the frame of this work.

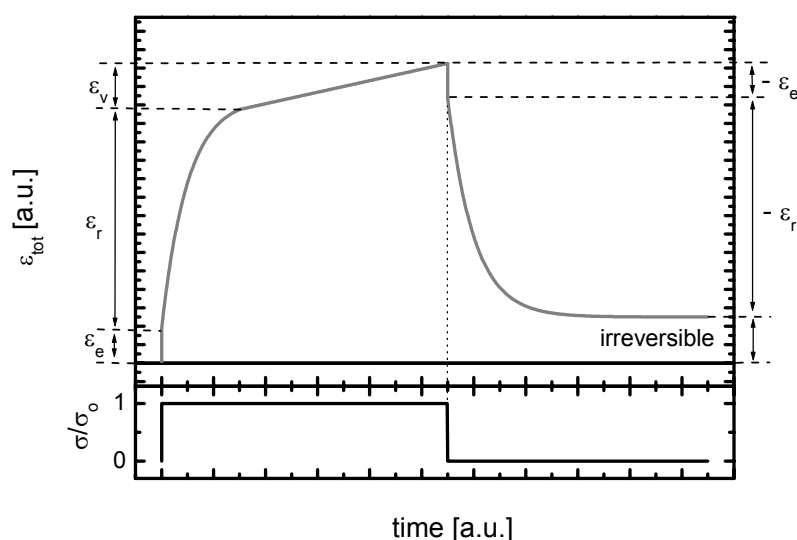


Figure (2.4 - 6): Scheme of a typical macroscopic viscoelastic behavior

2.4.1.5.)Physical aging

According to the free volume theory, the extent of molecular motion in a polymer in the glassy state depends on the free volume. On the other hand, it is clear, that the free volume in the glassy state will depend on the thermal history of the polymer. By cooling down a polymer below T_g , the instantaneous configuration will be frozen. If the cooling process is performed with a very high cooling rate, a high degree of conformational disorder will be frozen and, thus, the free volume will be accordingly high. In contrast, if the polymer is cooled down very slowly (in the limiting case infinitely slowly), the system will have enough time to approach its equilibrium state and the conformational disorder will be small (the conformational entropy will approach zero in the limiting case of infinitely slow cooling rate - see "2.4.1.3.2.) Thermodynamic approaches" on page 78) and so will be the free volume.

However, even in the glassy state, there is some molecular mobility, enabling the system to further relax slowly after the cooling process is completed, i.e. when the system is held at constant temperature below T_g . Hence, as long as the extent of the free volume is higher than it would be in the case of infinitely slow down-cooling, it will slowly decrease further on even in

the glassy state, which affects the mechanical properties of the system. This process is referred to as *physical aging* since it does not involve any chemical degradation. Physical aging basically leads to a densification of the system and, thus, will cause a considerable change of all the relevant mechanical parameters like viscosity or some mechanical modulus slowly in time. In general, the viscosity and the elasticity will decrease by physical aging. The rate of change will decrease with decreasing temperature below T_g and increase with increasing free volume (i.e. with increasing cooling rate in the thermal history of the system). The range of the change depends as well on the amount of the free volume.

Figure (2.4 - 7) exemplarily illustrates the relations described above for poly(vinyl chloride). The material was annealed at a temperature of 10° above T_g and thereafter quenched to 40° below T_g and stored at this temperature for at maximum 4 years. The curves are the results of creep-relaxation experiments obtained for different times after the elapsed quench. 0.03 days after the quench a tensile creep compliance (this may be interpreted as the inverse of the modulus of relaxation in eq. (2.4 - 31)) of $5 \times 10^{-10} \text{ m}^2\text{N}^{-1}$ was reached after about 10^3 sec and 1000 days after the quench 10^7 sec were required to reach the same value.

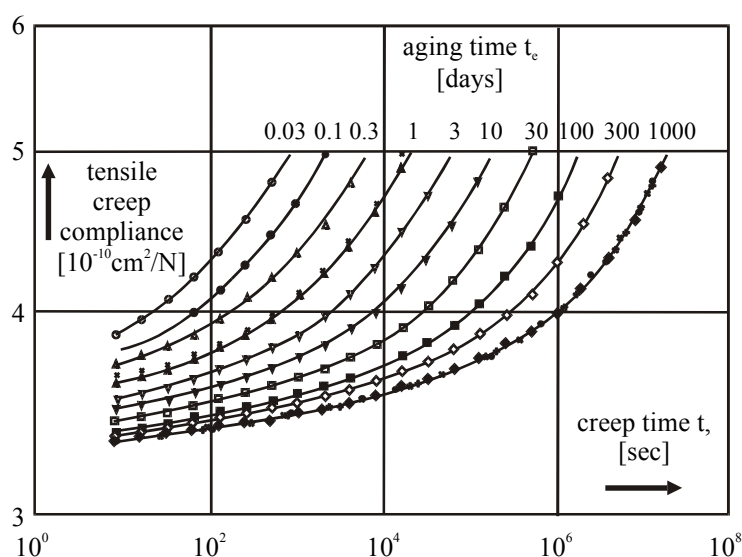


Figure (2.4 - 7): Small-strain tensile creep curves for glassy PVC. Partly redrawn after [B21, p. 478]

2.4.2.) Electrical poling of organic polymers - the oriented gas model

The oriented gas model to be elaborated upon in this section is a relatively simple model describing the linear and second order optical properties of glassy polymer systems doped with nonlinear optical molecules [27, 28]. Classical representatives of the latter are intramolecular charge-transfer (CT) molecules, which usually exhibit a large permanent dipole moment and highly anisotropic polarizability. A general scheme of the structure of a CT-molecule consisting of an electron-accepting group "A" and an electron-donating group "D" connected by a π -bridge is depicted in figure (2.4 - 8). The basic geometry of this structure, i.e. rod-like shape and rotational symmetry around the long molecule axis, will be used for the forthcoming discussions. The inherent statistical centro-symmetry of glassy polymers doped with CT-molecules, which prevents second order nonlinear optical response, may be broken by applying an external dc-field. This interacts with the dipole moment of the nonlinear optical dopants forming a torque, which forces the dopants to take on a preferred orientation component on the average. This process is referred to as „*electrical poling*“. The orientational process is counteracted by the thermal energy and the repulsion of the glassy matrix. For the oriented gas

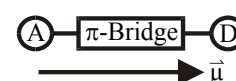


Figure (2.4 - 8): CT-molecule, A = acceptor, D = donor

model the latter is considered negligible, if the poling is performed at temperatures at least at, or even better, above the glass-transition temperature of the system. The macroscopic system thus emerging will usually be uniaxial birefringent with the direction of the external field representing the optical axis.

The oriented gas model enables the deduction of the macroscopic optical nonlinearity of the considered electrically poled system from the molecular optical nonlinearity of the dopants, their orientational distribution for a given field and their density. The molecular polarization p in the dipole approximation may be described by:

$$p_i = \mu_i + \alpha_{ij}E_j + \beta_{ijk}E_jE_k + \dots, \quad \text{eq. (2.4 - 33)}$$

where the indices $i, j, k = 1, 2, 3$ refer to coordinates of the molecular frame, α_{ij} and β_{ijk} are tensor quantities commonly referred to as “(molecular) polarizability“ and “(molecular) hyper-polarizability“, respectively, and E_j and E_k are components of the electrical field. The macroscopic polarization P may be expressed according to eq. (2.2 - 1):

$$P_I = \chi_{IJ}^{(1)}E_J + \chi_{IJK}^{(2)}E_JE_K + \dots, \quad \text{eq. (2.4 - 34)}$$

where the indices $I, J, K = x, y, z$ refer to coordinates of the laboratory frame, E_J and E_K are components of the electrical field and $\chi_{IJ}^{(1)}$ and $\chi_{IJK}^{(2)}$ denote the susceptibility tensors of first and second order, respectively.

The correlation between the molecular frame and the laboratory frame is illustrated in figure (2.4 - 9).

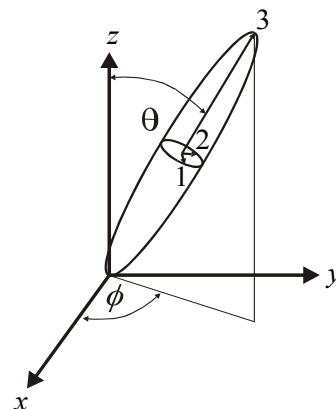


Figure (2.4 - 9): Molecular and laboratory frame

As will be shown later in this section, the orientational order can be described by average quantities of the form:

$$\langle (\cos\theta)^n \rangle = \frac{\int (\cos\theta)^n f(\Omega) d\Omega}{\int f(\Omega) d\Omega} = \frac{\int_0^\pi (\cos\theta)^n e^{a\cos\theta} d\cos\theta}{\int_0^\pi e^{a\cos\theta} d\cos\theta} = L_n(a) \quad \text{eq. (2.4 - 35)}$$

where θ is the angle according to figure (2.4 - 9), $f(\Omega)$ is an orientational distribution function to be discussed later in this section, Ω is the steradian corresponding to θ , a is a dimensionless parameter to be discussed later in this section as well, and n is a natural number. $L_n(a)$ are the Langevin functions. The (first, i.e. $n = 1$) Langevin function, after which the whole group of functions is named is defined as:

$$L(a) = \coth a - \frac{1}{a}. \quad \text{eq. (2.4 - 36)}$$

The higher Langevin functions may be found by solving the integral ratio:

$$\frac{\int_{-1}^1 x^n e^{ax} dx}{\int_{-1}^1 e^{ax} dx} = L_n(a), \quad \text{eq. (2.4 - 37)}$$

which yields e.g. for $n = 2$:

$$L_2(a) = 1 + \frac{2}{a^2} - \frac{2}{a} \coth a. \quad \text{eq. (2.4 - 38)}$$

Expanding the exponentials in eq. (2.4 - 37) up to the second term one obtains as approximation for $n = 1$ valid for $a \ll 1$:

$$L_1(a) \approx \frac{a}{3} . \quad \text{eq. (2.4 - 39)}$$

By expanding the exponentials to the third term (this is necessary, since the second term will vanish by solving the resulting integral making the approximating too crude), one obtains for $n = 2$:

$$L_2(a) \approx \frac{\frac{1}{3} + \frac{a^2}{10}}{1 + \frac{a^2}{6}} , \quad \text{eq. (2.4 - 40)}$$

which may be rewritten by means of polynomial division:

$$L_2(a) \approx \frac{\frac{1}{3}\left(1 + \frac{a^2}{6}\right)}{1 + \frac{a^2}{6}} + \frac{\frac{2a^2}{45}}{1 + \frac{a^2}{6}} \approx \frac{1}{3} + \frac{2a^2}{45} , \quad \text{eq. (2.4 - 41)}$$

where the second term of the sum in the denominator to $2a^2/45$ was neglected.

In order to obtain an approximation for the third Langevin function, the first two terms of the expansion of the exponentials will again be sufficient yielding:

$$L_3(a) \approx \frac{a}{5} . \quad \text{eq. (2.4 - 42)}$$

The above approximations actually will lead to an acceptable agreement with the original Langevin functions for up to $a \leq 1$. For example, this corresponds to about 125V/ μm poling field strength applied to a system containing a nonlinear optical dopant with a permanent dipole moment of $\mu = 10$ Debye = 3.3336×10^{-29} Cm. The admissible poling field strength is an inverse function of the dopant's dipole moment, thus, the admissible field increases with decreasing dipole moment.

Hereafter and throughout the rest of this work the dopant will simply be referred to as (NLO) „chromophore“.

2.4.2.1.)Steady-state solutions of the oriented gas model

2.4.2.1.1.)Steady-state distribution function

A random orientational distribution of the chromophores will result in a centro-symmetric system showing isotropic macroscopic susceptibility, i.e. the material is not birefringent. However, in the presence of an electrical dc-field, the chromophores will take on a preferred orientational component along the applied field, and the orientational distribution will no more be random. Assuming, that the orientational mobility of the chromophores in the glassy polymer matrix is not restricted by the matrix, the statistical orientational distribution may then be described by a Maxwell-Boltzmann distribution. This assumption is considered a valid approximation for sufficiently high temperature, i.e. in particular $T \geq T_g$. Conveniently, the orientational distribution function $G(\Omega)$ may then be written in normalized form:

$$G(\Omega) = \frac{f(\Omega)}{\int f(\Omega) d\Omega} \quad \text{eq. (2.4 - 43)}$$

with Ω as the steradian from a given axis defined by the external field direction, which usually

is chosen to be oriented along the z -axis of the laboratory frame (see figure (2.4 - 9)).

The function $f(\Omega)$ is the Maxwell-Boltzmann distribution:

$$f(\Omega) = e^{-\frac{U_{tot}}{k_B T}}, \quad \text{eq. (2.4 - 44)}$$

where $k_B T$ is the thermal energy and U_{tot} is the total dipole interaction energy of the polarizable dipoles, which is given by:

$$U_{tot} = U_E + U_{\mu^*} = -\vec{\mu} \cdot \vec{E} - \frac{1}{2} \vec{\mu}^* \cdot \vec{E}. \quad \text{eq. (2.4 - 45)}$$

The total dipole interaction energy consists of two contributions, resulting from the interaction of the externally applied field \vec{E} with the permanent dipole moment $\vec{\mu}$ of the chromophores on the one hand (U_E) and with the field induced dipole moment $\vec{\mu}^*$ of the chromophores (U_{μ^*}) on the other. Assuming, as mentioned before, that the external field is oriented along the z -axis of the laboratory frame:

$$\vec{E} = E \hat{e}_z, \quad \text{eq. (2.4 - 46)}$$

where \hat{e}_z is the unit vector along this axis, the field components must be projected into the molecular frame in order to calculate the induced dipole moment. The field components of the external field in the molecular frame then induce a dipole moment according to

$$\vec{\mu}^* = \sum_{m=1}^3 \mu_m^* \hat{e}_m \quad \text{eq. (2.4 - 47)}$$

and (according to eq. (2.4 - 33)):

$$\mu_i^* = \alpha_{ij} E_j, \quad \text{eq. (2.4 - 48)}$$

where α_{ij} are components of the polarizability tensor $\tilde{\alpha}$. In the molecular principal axis system (which is identical to the molecular frame "1, 2, 3" by convenient choice of the latter) the latter writes:

$$\tilde{\alpha} = \begin{pmatrix} \alpha_{11} & 0 & 0 \\ 0 & \alpha_{22} & 0 \\ 0 & 0 & \alpha_{33} \end{pmatrix} = \begin{pmatrix} \alpha_{\perp} & 0 & 0 \\ 0 & \alpha_{\perp} & 0 \\ 0 & 0 & \alpha_{\parallel} \end{pmatrix}, \quad \text{eq. (2.4 - 49)}$$

where α_{\perp} and α_{\parallel} are the polarizability perpendicular and parallel to the molecular principal axis (3), respectively, according to the presumed geometry of the chromophore as mentioned before (figure (2.4 - 8)). The field components along the molecular principal axis result from eq. (2.4 - 46) considering figure (2.4 - 9) and write:

$$\begin{aligned} E_1 &= E \sin \theta \cos \phi \\ E_2 &= E \sin \theta \sin \phi, \\ E_3 &= E \cos \theta \end{aligned} \quad \text{eq. (2.4 - 50)}$$

where θ is the elevation angle and ϕ is the azimuth angle according to figure (2.4 - 9). Then, one obtains for the induced dipole moment in the molecular frame:

$$\vec{\mu}^* = \hat{e}_1 \alpha_{\perp} E \sin \theta \cos \phi + \hat{e}_2 \alpha_{\perp} E \sin \theta \sin \phi + \hat{e}_3 \alpha_{\parallel} E \cos \theta. \quad \text{eq. (2.4 - 51)}$$

Please note, that the projection according to eq. (2.4 - 50) may as well be expressed by employing direction cosines, reading then:

$$\begin{aligned} E_1 &= E \cos(1, z) \\ E_2 &= E \cos(2, z), \\ E_3 &= E \cos(3, z) \end{aligned} \quad \text{eq. (2.4 - 52)}$$

which may be more convenient to handle in some cases. The relation between the direction cosines and the angular expressions according to eq. (2.4 - 50) results from the comparison with eq. (2.4 - 52).

In the molecular (principal axes) frame, the permanent dipole moment of the chromophore will be:

$$\vec{\mu} = \mu \hat{e}_3 \quad \text{eq. (2.4 - 53)}$$

and the total dipole interaction energy may be expressed as:

$$U_{tot} = -\mu E_3 - \frac{1}{2}[\mu_1^* E_1 + \mu_2^* E_2 + \mu_3^* E_3]. \quad \text{eq. (2.4 - 54)}$$

In order to express U_{tot} in the laboratory frame, the components of the dipole moments according to eq. (2.4 - 51) and eq. (2.4 - 47) and the field components according to eq. (2.4 - 50) are inserted into eq. (2.4 - 54) yielding:

$$\begin{aligned} U_{tot} &= -\mu E \cos \theta - \frac{1}{2}[\alpha_{\perp}(\sin \theta \cos \phi)^2 + \alpha_{\perp}(\sin \theta \sin \phi)^2 + \alpha_{\parallel}(\cos \theta)^2]E^2 \\ &= -\mu E \cos \theta - \frac{1}{2}[\alpha_{\perp}(\sin \theta)^2 + \alpha_{\parallel}(\cos \theta)^2]E^2 \\ &= -\mu E \cos \theta - \frac{1}{2}[\alpha_{\perp} + (\alpha_{\parallel} - \alpha_{\perp})(\cos \theta)^2]E^2 \end{aligned} \quad \text{eq. (2.4 - 55)}$$

Please note, that the dependence on the azimuth angle vanishes here for mathematical reasons. However, accounting for the rotational symmetry of the chromophore the azimuth angle may be freely chosen. Choosing $\phi = \pi/4 = \text{constant}$ will therefore yield identical results in a more straight forward manner. This procedure will be applied hereafter.

The expression may be rewritten in terms of two dimensionless quantities a and b :

$$U_{tot} = \frac{1}{2}\alpha_{\perp}E^2 - akT \cos \theta - bkT(\cos \theta)^2 \quad \text{eq. (2.4 - 56)}$$

with:

$$a = \frac{\mu E}{kT} \quad \text{eq. (2.4 - 57)}$$

and:

$$b = \frac{(\alpha_{\parallel} - \alpha_{\perp})E^2}{2kT}. \quad \text{eq. (2.4 - 58)}$$

Parameter a corresponds to the interaction of the permanent dipole of the chromophore with the external field and b corresponds to the interaction of the induced dipole of the chromophore with the external field. The relation between a and b is basically a question of the chromophore structure. In all cases considered in the frame of this work, the approximation

$$a \gg b \quad \text{eq. (2.4 - 59)}$$

will hold.

Please note, that the quantity a according to eq. (2.4 - 57) is identical to the a occurring in the equations eq. (2.4 - 35) to eq. (2.4 - 42).

2.4.2.1.2.)Linear optical properties of poled polymers

In order to calculate the linear optical properties of a poled polymer, the macroscopic polarization in the system induced by an optical field must be considered. The basic approach will be similar to the procedure outlined in the previous section for the induced dipole moment, however, the quantities involved may now be frequency dependent, which will be indicated by

superscripting (ω) in the case of possible confusion.

Presuming at first an optical field polarized in z -direction in the laboratory frame, i.e.

$$\vec{E}^{(\omega)} = E_z^{(\omega)} \hat{e}_z, \quad \text{eq. (2.4 - 60)}$$

the macroscopic polarization along the z -axis of the laboratory frame $P_z^{(\omega)}$ will be the projection of the orientationally averaged induced dipole moments of the chromophores into the laboratory frame:

$$\frac{P_z^{(\omega)}}{E_z^{(\omega)}} = N \int [\alpha_{\perp}^{(\omega)} + (\alpha_{\parallel}^{(\omega)} - \alpha_{\perp}^{(\omega)}) (\cos(3, z))^2] G(\Omega) d\Omega = \chi_{zz}^{(1)}. \quad \text{eq. (2.4 - 61)}$$

Here N is the number density of chromophores, $\chi_{zz}^{(1)}$ is the corresponding macroscopic susceptibility and $G(\Omega)$ is the orientational distribution function according to eq. (2.4 - 43). It is clear that the macroscopic susceptibility is as well frequency dependent, which is often indicated by writing $\chi_{zz}^{(1)}(-\omega; \omega)$ in order to express the “incoming“ frequency (positive) and the frequency of the “outgoing“ polarization wave (negative), however, this notation will not be used here. Please note, that the laboratory frame is conveniently chosen to be identical to the principal axis frame of the macroscopic system.

In a similar way one will obtain a corresponding expression for the macroscopic polarization along the x -axis of the laboratory frame $P_x^{(\omega)}$ for an optical field polarized in x -direction of the laboratory frame, i.e.

$$\vec{E}^{(\omega)} = E_x^{(\omega)} \hat{e}_x, \quad \text{eq. (2.4 - 62)}$$

while the external field is still given by eq. (2.4 - 46). An accurate coordinate transformation in this case would be rather cumbersome, however, may be avoided when accounting for the rotational symmetry of the chromophores, which allows a free choice of the azimuth angle as already mentioned before. Choosing $\phi = \pi/4 = \text{constant}$, the direction cosines involved may be expressed as:

$$\begin{aligned} \cos(1, x) &= \frac{1}{\sqrt{2}} \cos \theta \\ \cos(2, x) &= \frac{1}{\sqrt{2}} \cos \theta. \\ \cos(3, x) &= \frac{1}{\sqrt{2}} \sin \theta \end{aligned} \quad \text{eq. (2.4 - 63)}$$

and the polarization reads:

$$\frac{P_x^{(\omega)}}{E_x^{(\omega)}} = N \int [\alpha_{\perp}^{(\omega)} + (\alpha_{\parallel}^{(\omega)} - \alpha_{\perp}^{(\omega)}) (\cos(3, x))^2] G(\Omega) d\Omega = \chi_{xx}^{(1)}. \quad \text{eq. (2.4 - 64)}$$

According to eq. (2.1 - 59) and eq. (2.1 - 84), the refractive index n may be expressed as:

$$n = \sqrt{1 + \chi^{(1)}}. \quad \text{eq. (2.4 - 65)}$$

The change in the refractive index due to electrical poling will be due to a change in the orientational distribution function and therefore:

$$\Delta [n_z^{(\omega)}]^2 = N \Delta \alpha^{(\omega)} \left[\int (\cos(3, z))^2 G(\Omega) d\Omega - \int (\cos(3, z))^2 G_0(\Omega) d\Omega \right] \quad \text{eq. (2.4 - 66)}$$

with:

$$\Delta \alpha^{(\omega)} = \alpha_{\parallel}^{(\omega)} - \alpha_{\perp}^{(\omega)}. \quad \text{eq. (2.4 - 67)}$$

$G_0(\Omega)$ is the distribution function without external field where $a = 0$. Therefore, the second term of the difference in eq. (2.4 - 66) yields according to eq. (2.4 - 35):

$$\frac{\int_0^\pi (\cos\theta)^2 e^{a\cos\theta} d\cos\theta}{\int_0^\pi e^{a\cos\theta} d\cos\theta} = \frac{\int_0^\pi \frac{1}{3} d(\cos\theta)^3}{\int_0^\pi d\cos\theta} = \frac{1}{3}. \quad \text{eq. (2.4 - 68)}$$

With eq. (2.4 - 35) one obtains finally:

$$\Delta[n_z^{(\omega)}]^2 = N\Delta\alpha^{(\omega)}\left(\langle(\cos\theta)^2\rangle - \frac{1}{3}\right). \quad \text{eq. (2.4 - 69)}$$

In order to solve eq. (2.4 - 64), eq. (2.4 - 63) is taken into account as well as a relation equivalent to eq. (2.4 - 35) in terms of the sinus function:

$$\langle(\sin\theta)^n\rangle = \frac{\int(\sin\theta)^n f(\Omega) d\Omega}{\int f(\Omega) d\Omega} = \frac{\int_{-\pi/2}^{\pi/2} (\sin\theta)^n e^{a\sin\theta} d\sin\theta}{\int_{-\pi/2}^{\pi/2} e^{a\sin\theta} d\sin\theta} = L_n(a), \quad \text{eq. (2.4 - 70)}$$

yielding in analogy to eq. (2.4 - 69):

$$\Delta[n_x^{(\omega)}]^2 = N\Delta\alpha^{(\omega)}\left(\frac{1}{2}\langle(\sin\theta)^2\rangle - \frac{1}{3}\right) = N\Delta\alpha^{(\omega)}\left(\frac{1}{6} - \frac{1}{2}\langle(\cos\theta)^2\rangle\right) \quad \text{eq. (2.4 - 71)}$$

which may be rewritten as:

$$\Delta[n_x^{(\omega)}]^2 = -\frac{1}{2}\left[N\Delta\alpha^{(\omega)}\left(\langle(\cos\theta)^2\rangle - \frac{1}{3}\right)\right]. \quad \text{eq. (2.4 - 72)}$$

In conclusion, by application of an external electrical dc field the system has become uniaxial birefringent. The relation between the refractive index changes for the extraordinary and for the ordinary beam relative to the isotropic refractive index with no field applied is obtained from comparing eq. (2.4 - 69) and eq. (2.4 - 72). Assuming furthermore small index changes, which allows for the approximation (i.e., the difference is considered as a differential expression):

$$\Delta n^2 = 2n\Delta n \quad \text{eq. (2.4 - 73)}$$

and applying eq. (2.4 - 35), eq. (2.4 - 41), and eq. (2.4 - 57), finally yields:

$$\Delta n_x^{(\omega)} = \Delta n_y^{(\omega)} = -\frac{1}{2}\Delta n_z^{(\omega)} \quad \text{eq. (2.4 - 74)}$$

with:

$$\Delta n_z^{(\omega)} = \frac{N\Delta\alpha^{(\omega)}\mu^2 E^2}{45n^{(\omega)}k^2 T^2}. \quad \text{eq. (2.4 - 75)}$$

Please note, that E in eq. (2.4 - 75) is the external electrical dc field oriented in z -direction, which is self-evident since the direction of this field defines the z -direction.

2.4.2.1.3.)Nonlinear optical properties of poled polymers

In this section the second order nonlinear properties of a poled polymer system will be considered. The discussion will be restricted to the linear electro-optic response, since only this is the relevant one for this work. Frequency dependent quantities will again be indicated by a superscript (ω) if confusion may be caused otherwise. According to eq. (2.4 - 33), the second order nonlinear molecular polarization p is described by:

$$p_i^{(\omega)} = \beta_{ijk}^{(\omega)} E_j^{(\omega)} E_k, \quad \text{eq. (2.4 - 76)}$$

where $i, j, k = 1, 2, 3$ denote coordinates of the molecular principal axis system and E_k represents some electrical dc field determining the electro-optic response. For the subsequent considerations shall be assumed, that E_k is not the poling field and the poling process and the electro-optic process will be treated independently. The corresponding macroscopic polarization P writes according to eq. (2.4 - 34):

$$P_I^{(\omega)} = \chi_{IJK}^{(2)} E_J^{(\omega)} E_K, \quad \text{eq. (2.4 - 77)}$$

where $I, J, K = x, y, z$ denote coordinates of the laboratory frame, which are chosen to be identical with the principal axis frame of the macroscopic system. Please note, that the second order nonlinear susceptibility $\chi^{(2)}$ and the hyperpolarizability β depend on the particular effect considered and that the complete notation usually applied for the linear electro-optic response would be $\chi^{(2)}(-\omega; \omega, 0)$ and $\beta(-\omega; \omega, 0)$. However, since no other second order effect is considered, this notation will not be used here.

In order to simplify the forthcoming discussion, the only non vanishing component of the hyperpolarizability tensor is assumed to be β_{333} , which is in fact a good approximation for rod-like chromophores. Hence, only a molecular polarization along the 3-direction will remain:

$$p_3^{(\omega)} = \beta_{333}^{(\omega)} E_3^{(\omega)} E_3. \quad \text{eq. (2.4 - 78)}$$

Accordingly, for some dc field according to eq. (2.4 - 46) (still not the poling field as mentioned before) and an optical field according to eq. (2.4 - 60) one obtains for the macroscopic polarization:

$$\begin{aligned} \frac{P_z^{(\omega)}}{E_z^{(\omega)} E_z} &= \frac{N}{E_z^{(\omega)} E_z} \int p_3^{(\omega)} \cos(3, z) G(\Omega) d\Omega \\ &= N \int \beta_{333}^{(\omega)} (\cos(3, z))^3 G(\Omega) d\Omega = \chi_{zzz}^{(2)} \end{aligned} \quad \text{eq. (2.4 - 79)}$$

whereby eq. (2.4 - 52), eq. (2.4 - 77) and eq. (2.4 - 78) have been used as well.

Applying the same procedure for the case of some dc field according eq. (2.4 - 46) and an optical field according to eq. (2.4 - 62) yields:

$$\frac{P_z^{(\omega)}}{E_x^{(\omega)} E_z} = N \int \beta_{333}^{(\omega)} (\cos(3, x))^2 \cos(3, z) G(\Omega) d\Omega = \chi_{xxz}^{(2)}. \quad \text{eq. (2.4 - 80)}$$

Please note that the second order nonlinear optical susceptibility, which is the quantity in question, does not depend on the electrical dc field introduced before in order to formulate the electro-optic response. Hence, this field is now identified as being only a supplement quantity for the discussion on hand.

As before, the change of the second order nonlinear susceptibility will be the result of a changing orientational distribution function due to the applied field. Therefore, one obtains from eq. (2.4 - 79):

$$\Delta \chi_{zzz}^{(2)} = N \beta_{333}^{(\omega)} \left[\int (\cos(3, z))^3 G(\Omega) d\Omega - \int (\cos(3, z))^3 G_0(\Omega) d\Omega \right], \quad \text{eq. (2.4 - 81)}$$

where $G_0(\Omega)$ is the distribution function for zero external dc-field (i.e. $a = 0$). The second term of the sum to the right hand side of the above equation will be zero according to:

$$\frac{\int_0^\pi (\cos\theta)^3 e^{a\cos\theta} d\cos\theta}{\int_0^\pi e^{a\cos\theta} d\cos\theta} = \frac{\int_0^\pi \frac{1}{4} d(\cos\theta)^4}{\int_0^\pi d\cos\theta} = 0 \quad \text{eq. (2.4 - 82)}$$

and one finally obtains with eq. (2.4 - 35) for the term with $a \neq 0$:

$$\chi_{zzz}^{(2)} = N\beta_{333}^{(\omega)} \langle (\cos\theta)^3 \rangle = \frac{N\beta_{333}^{(\omega)} \mu E}{5kT}, \quad \text{eq. (2.4 - 83)}$$

where E is the poling field and μ the permanent dipole moment of the chromophore.

When solving eq. (2.4 - 80) analogously, an expression similar to eq. (2.4 - 81) will be obtained, which contains the product of the two direction cosines from eq. (2.4 - 80). According to eq. (2.4 - 63) this product may be rewritten as:

$$(\cos(3, x))^2 \cos(3, z) = \frac{1}{2}(\sin\theta)^2 \cos\theta = \frac{1}{2}\cos\theta - \frac{1}{2}(\cos\theta)^3. \quad \text{eq. (2.4 - 84)}$$

Accounting for eq. (2.4 - 82), which will solve identically for $\cos\theta$ to the power one, from eq. (2.4 - 80) with eq. (2.4 - 35) for the term with $a \neq 0$ one finally obtains:

$$\chi_{xxz}^{(2)} = N\beta_{333}^{(\omega)} \frac{1}{2} [\langle \cos\theta \rangle - \langle (\cos\theta)^3 \rangle] = \frac{N\beta_{333}^{(\omega)} \mu E}{15kT}, \quad \text{eq. (2.4 - 85)}$$

with E being the poling field.

Having found expressions for the susceptibility, it is straight forward to relate them to the corresponding elements of the second order susceptibility tensor. Poled polymers belong to the $C_{\infty v}$ symmetry group, which reduces the number of independent tensor elements to three. If Kleinman's symmetry rule ("2.2.1.2.) Kleinman's symmetry rule" on page 43) applies additionally, the third rank second order susceptibility tensor may be expressed as a 3 x 6 matrix, which will read:

$$\chi^{(2)} \Rightarrow \begin{bmatrix} 0 & 0 & 0 & 0 & d_{15} & 0 \\ 0 & 0 & 0 & d_{24} & 0 & 0 \\ d_{31} & d_{32} & d_{33} & 0 & 0 & 0 \end{bmatrix} \quad \text{eq. (2.4 - 86)}$$

with:

$$d_{31} = d_{32} = d_{24} = d_{15} = \frac{\chi_{xxz}^{(2)}}{2} \quad \text{eq. (2.4 - 87)}$$

$$d_{33} = \chi_{zzz}^{(2)}$$

and is related to the electro-optic (i.e. r_{ij} -) matrix (often misleadingly called electro-optic tensor, however, it does not represent a vector operation and, thus, is a matrix) according to eq. (2.2 - 20) by:

$$r_{ij} = -\frac{d_{ji}}{n^4}. \quad \text{eq. (2.4 - 88)}$$

2.4.2.1.4.)Local field correction

The above discussion presumed without explicit notation, that the polymer matrix surrounding the chromophores will not affect the electrical fields at the location of the chromophores in the matrix. It is clear, that this cannot be true. Since this influence of the matrix

simply acts on the fields sensed by the chromophores, this problem may be accounted for by introducing *local field correction factors*.

The local field correction factor for a dc or a low frequency electrical field is:

$$F_0 = \frac{\varepsilon(\varepsilon_\infty + 2)}{2\varepsilon + \varepsilon_\infty} \quad \text{eq. (2.4 - 89)}$$

and the local field correction factor for an optical electrical field is:

$$F_\infty = \frac{\varepsilon_\infty + 2}{3}, \quad \text{eq. (2.4 - 90)}$$

where ε is the static dielectric constant of the system and ε_∞ is the dielectric constant at the frequency of the optical field involved, which determines the refractive index of the system.

In order to introduce the local field correction factors correctly into eq. (2.4 - 75), eq. (2.4 - 83) and eq. (2.4 - 85), one simply must consider, that these factors are meant to correct for the electrical fields which polarize optical chromophores for the optical response. In other words, one may as well correct the polarizability or the hyperpolarizability for the local fields beforehand performing the discussion in the above two sections instead of introducing correction factors afterwards. This means, that only the fields responsible for the optical response in question must be considered by having a look at eq. (2.4 - 33).

In the case of the linear optical properties (eq. (2.4 - 75)) only the optical field must be corrected and accordingly, the corrected form of eq. (2.4 - 75) will be:

$$\Delta n_z^{(\omega)} = F_\infty \frac{N\Delta\alpha^{(\omega)}\mu^2 E^2}{45n^{(\omega)2}k^2 T^2}. \quad \text{eq. (2.4 - 91)}$$

In the case of the considered nonlinear optical response, i.e. electro-optic response, there is an optical field to be corrected and a dc field. However, since the local field correction is actually related to the dielectric displacement vector, which responds to the optical as well as the static electrical field, the local field correction for the second order susceptibility is additionally superposed with the local field correction for the linear response. Hence, F_∞ appears to the square and the corrected forms of eq. (2.4 - 83) and eq. (2.4 - 85) are respectively:

$$\chi_{zzz}^{(2)} = F_\infty^2 F_0 \frac{N\beta_{333}^{(\omega)}\mu E}{5kT} \quad \text{eq. (2.4 - 92)}$$

and:

$$\chi_{xxz}^{(2)} = F_\infty^2 F_0 \frac{N\beta_{333}^{(\omega)}\mu E}{15kT}. \quad \text{eq. (2.4 - 93)}$$

2.4.2.2.) Transient solutions of the oriented gas model

The mathematical efforts to obtain the transient solutions are extensively high and will not be elaborated upon in similar detail as conducted before for the steady state solutions. Subsequently, the basic approach will briefly be outlined and then the results will be presented.

The treatment of the transients for the linear and the nonlinear optical properties is based on the rotational diffusion equation for a system with axial symmetry, which is given by:

$$\frac{\partial}{\partial t} G(\theta, t) = \frac{D}{\sin\theta} \frac{\partial}{\partial\theta} \left\{ \sin\theta \left[\frac{\partial}{\partial\theta} G(\theta, t) + \frac{1}{kT} \frac{\partial U}{\partial\theta} G(\theta, t) \right] \right\}, \quad \text{eq. (2.4 - 94)}$$

where D is the diffusion constant and U is the dipole interaction energy, which is approximated

the same way as for the steady state solutions, i.e.:

$$U = -akT \cos \theta \quad \text{eq. (2.4 - 95)}$$

with a given by eq. (2.4 - 57). Eq. (2.4 - 95) is the steady-state solution for eq. (2.4 - 94).

The distribution function $f(\theta)$ according to eq. (2.4 - 44) may be expanded in terms of Legendre polynomials, which is proximate, since rotational diffusion in an axially symmetric system is considered with the symmetry axis defined by the direction of the external field. Hence, Legendre polynomials will be the eigen functions of the system. The (first four) Legendre polynomials are given by:

$$\begin{aligned} \Pi_0(x) &= 1 \\ \Pi_1(x) &= x \\ \Pi_2(x) &= \frac{1}{2}(3x^2 - 1) \\ \Pi_3(x) &= \frac{1}{2}(5x^3 - 3x) \end{aligned} \quad \text{eq. (2.4 - 96)}$$

After inserting eq. (2.4 - 95) into eq. (2.4 - 44) the expansion in terms of Legendre polynomials results in:

$$f(\theta) = e^{a \cos \theta} = \sum_0^{\infty} (2n + 1) i_n(a) \Pi_n(\cos \theta), \quad \text{eq. (2.4 - 97)}$$

where the expansion coefficient $i_n(a)$ is the spherically modified Bessel function of n -th order satisfying the following recurrence relation:

$$i_{n-1}(a) - i_{n+1}(a) = \frac{2n+1}{a} i_n(a) \quad \text{eq. (2.4 - 98)}$$

The number index n here stands for a natural number. The refractive index (which is usually denoted by n in the frame of this work) is identified by a superscript (ω) in this section. Normalization of the distribution function eq. (2.4 - 97) yields:

$$G(\theta, t) = \sum_0^{\infty} g_n(t) (2n + 1) \frac{i_n(a)}{i_0(a)} \Pi_n(\cos \theta), \quad \text{eq. (2.4 - 99)}$$

where $g_n(t)$ was introduced in order to account for the time dependence. The average value of each Legendre polynomial is thus given by:

$$\langle \Pi_n(\cos \theta) \rangle = \frac{i_n(a)}{i_0(a)} \quad \text{eq. (2.4 - 100)}$$

and the time dependence of the average value is accounted for by $g_n(t)$, hence:

$$\langle \Pi_n(\cos \theta) \rangle(t) = g_n(t) \frac{i_n(a)}{i_0(a)}. \quad \text{eq. (2.4 - 101)}$$

The behavior of $g_n(t)$ will be determined by the boundary conditions of the particular cases considered below (i.e turning on or off the poling field). Inserting eq. (2.4 - 99) into the rotational diffusion equation eq. (2.4 - 94) will result in a differential equation for $g_n(t)$, which then can be solved taking the particular boundary conditions into account. The transient solutions are obtained by expressing the steady state solutions for the linear and the nonlinear optical response, eq. (2.4 - 69), eq. (2.4 - 83) and eq. (2.4 - 85) also in terms of Legendre polynomials by means of eq. (2.4 - 96):

$$\frac{2n^{(\omega)} \Delta n_z^{(\omega)}}{N \Delta \alpha^{(\omega)}} = \langle (\cos \theta)^2 \rangle - \frac{1}{3} = \frac{2}{3} \langle \Pi_2(\cos \theta) \rangle, \quad \text{eq. (2.4 - 102)}$$

$$\frac{\chi_{zzz}^{(2)}}{N\beta_{333}^{(\omega)}} = \langle (\cos\theta)^3 \rangle = \frac{3}{5}\langle \Pi_1(\cos\theta) \rangle + \frac{2}{5}\langle \Pi_3(\cos\theta) \rangle, \text{ and} \quad \text{eq. (2.4 - 103)}$$

$$\frac{\chi_{xxz}^{(2)}}{N\beta_{333}^{(\omega)}} = \frac{1}{2}[\langle \cos\theta \rangle - \langle (\cos\theta)^3 \rangle] = \frac{1}{5}[\langle \Pi_1(\cos\theta) \rangle - \langle \Pi_3(\cos\theta) \rangle], \quad \text{eq. (2.4 - 104)}$$

and inserting eq. (2.4 - 101) into these expressions.

2.4.2.2.1.)Turning on the poling field

Since without poling field, i.e. at $t=0$ the distribution must be isotropic, and, after turning the poling field on, must become Boltzmannian for $t \rightarrow \infty$, the boundary conditions for $g_n(t)$ for $n \neq 0$ are:

$$\begin{aligned} g_n(t=0) &= 0 \\ g_n(t \rightarrow \infty) &= 1 \end{aligned} \quad \text{eq. (2.4 - 105)}$$

The condition for $n=0$ is trivial; the expression in the sum to the right of eq. (2.4 - 99) must be the first expansion term of the exponential function, i.e. unity. Accordingly, $g_n(t)$ for $n=0$ is:

$$g_0(t) = 1. \quad \text{eq. (2.4 - 106)}$$

Substitution of eq. (2.4 - 99) into eq. (2.4 - 94) leads to the differential equation to be satisfied by $g_n(t)$:

$$\frac{1}{D} \frac{\partial}{\partial t} g_n(t) + n(n+1)g_n(t) = \frac{an(n+1)}{2n+1} \left[g_{n-1}(t) \frac{i_{n-1}(t)}{i_n(t)} - g_{n+1}(t) \frac{i_{n+1}(t)}{i_n(t)} \right] \quad \text{eq. (2.4 - 107)}$$

Approximate solutions for $g_n(t)$ associated with some low orders of Legendre polynomials and satisfying the conditions defined in eq. (2.4 - 105) and eq. (2.4 - 106) are:

$$g_1(t) = 1 - e^{-D_1 t} + \frac{ai_2(a)}{6i_1(a)} \left[e^{-D_1 t} - e^{-D_2 t} \right], \quad \text{eq. (2.4 - 108)}$$

$$g_2(t) = 1 - e^{-D_2 t} - \frac{3ai_1(a)}{10i_2(a)} \left[e^{-D_1 t} - e^{-D_2 t} \right] + \frac{ai_3(a)}{5i_2(a)} \left[e^{-D_2 t} - e^{-D_3 t} \right] \text{ and} \quad \text{eq. (2.4 - 109)}$$

$$g_3(t) = 1 - e^{-D_3 t} - \frac{2ai_2(a)}{7i_3(a)} \left[e^{-D_2 t} - e^{-D_3 t} \right] + \frac{3ai_4(a)}{14i_3(a)} \left[e^{-D_3 t} - e^{-D_4 t} \right], \quad \text{eq. (2.4 - 110)}$$

where:

$$D_n = n(n+1)D, \quad \text{eq. (2.4 - 111)}$$

with D as the rotational diffusion coefficient. Please note, that the related time constants for the exponentials will be:

$$\tau_n = \frac{1}{D_n}. \quad \text{eq. (2.4 - 112)}$$

Hence, since $n > 0$ (and a natural number), the process is slower for higher n .

Now it is straightforward to obtain the transients of the optical properties by combining eq. (2.4 - 101) to eq. (2.4 - 104) with eq. (2.4 - 108) to eq. (2.4 - 110), which results for the case of the linear properties in:

eq. (2.4 - 113)

$$\Delta n_z^{(\omega)}(t) = \frac{N\Delta\alpha^{(\omega)}i_2(a)}{3n^{(\omega)}i_0(a)} \left\{ 1 - e^{-D_2t} - \frac{3ai_1(a)}{10i_2(a)} \left[e^{-D_1t} - e^{-D_2t} \right] + \frac{ai_3(a)}{5i_2(a)} \left[e^{-D_2t} - e^{-D_3t} \right] \right\}$$

Please note, that a in eq. (2.4 - 113) accounts for the state of the system to be approached *after* turning on the poling field!

2.4.2.2.2.)Turning off the poling field

For turning off the poling field, the situation is opposite to turning on the poling field. For $n \neq 0$ and $t = 0$, the distribution may be assumed to be Boltzmannian and for $t \rightarrow \infty$ the distribution approaches the isotropic case, hence:

$$\begin{aligned} g_n(t=0) &= 1 \\ g_n(t \rightarrow \infty) &= 0 \end{aligned} \quad \text{eq. (2.4 - 114)}$$

For $n = 0$, eq. (2.4 - 106) holds. Furthermore, the rotational diffusion equation simplifies considerably when taking into account, that the dipole interaction energy is zero without poling field as is its time derivative. For $n \neq 0$, one obtains the differential equation to be satisfied by $g_n(t)$:

$$\frac{1}{D} \frac{\partial}{\partial t} g_n(t) + n(n+1)g_n(t) = 0 \quad \text{eq. (2.4 - 115)}$$

and its simple solution:

$$g_n(t) = e^{-D_n t} \quad \text{eq. (2.4 - 116)}$$

The combination of eq. (2.4 - 101) to eq. (2.4 - 104) with eq. (2.4 - 116) yields the expressions for the decay of the optical properties, which writes for the linear case:

$$\Delta n_z^{(\omega)}(t) = \frac{N\Delta\alpha^{(\omega)}i_2(a)}{3n^{(\omega)}i_0(a)} e^{-D_2 t} \quad \text{eq. (2.4 - 117)}$$

Please note, that a in eq. (2.4 - 117) accounts for the initial state of the system *before* turning off the poling field!

2.4.3.) Electrical conduction in organic polymers

The electrical conduction in disordered organic solids has been in the focus of interest for nearly three decades now and a variety of models and interpretations has been presented during this period. All in common are characterized by a more or less empirical nature supported by an extensive set of experimental data as well as numerical simulations. Today, the electrical conduction in disordered organic solids is considered as fairly well understood in principle, however, no model up to date proved to hold generally and in detail. Any attempt to give a comprehensive picture of this topic would by far go beyond the scope of this work, however, the significance of the electrical conduction properties of organic polymers in particular for this work requires at least to give a brief outline of the most common basic concepts.

2.4.3.1.)Space-charge-limited currents

The concept of the space-charge limited currents (SCLC's) does not directly concern photorefractivity in polymers, since it describes the bulk current flowing through a system of finite electrical resistance and low charge carrier mobility when an electrical field is applied. However, there is always (in the dark as well as under illumination) some current flowing through a photorefractive polymer with an external field applied, which must be expected to be space-charge limited. This current may easily be measured by a source-measure unit and is usually determined by an electrical resistance typically in the $G\Omega$ (under illumination) to $T\Omega$ (in the dark) regime. This bulk current has barely been paid attention to up to now in the direct context with photorefractivity in polymers, but it is reasonable to assume that it may have a major impact on basic properties of polymeric photorefractive media.

In order to address the possible importance of SCLC's in PR polymers, subsequently some aspects will be discussed in advance to the chapter dealing with the photorefractive effect in particular. A permanent current flowing through the system may be assumed to assist the dark decay of photorefractive gratings in polymers. Furthermore, it will fill up all inactive deep charge carrier traps in the system blocking these traps for the photorefractive process. Moreover, since PR systems are photoconductors, nonuniform illumination will result in an electrical resistance grating, which is in anti-phase to the illumination pattern. Accordingly, a current flowing permanently through a nonuniformly illuminated PR polymer will cause some spatially modulated field distribution inside. This can be especially important if the real dynamics of photorefractive grating build-up is considered. For more details see "2.5.) The photorefractive effect" on page 118.

Although, this work actually does not consider the possible impact of SCLC's on the photorefractive properties of organic polymers in detail, the basic concept of space-charge limited currents is outlined subsequently.

Assuming more or less ohmic contacts between the polymer and the electrical source unit U , charge carriers are easily injected into the polymer at $x = 0$ but cannot be transported rapidly enough to the countercontact at $x = d$ due to the low charge carrier mobility in the polymer. Accordingly, the charge carriers will accumulate close to the injection contact forming a space-charge region, which counteracts the electrical field between the contact interfaces near the injection contact. Thus, the field driving the injection will be reduced to form an equilibrium state, which finally adapts the number of injected carriers to the number which can be transported by the polymer. The overall current is then determined by the bulk transport properties. The situation assuming hole transport is illustrated in Figure (2.4 - 10); the dotted line illustrates the electrical field as a function of x and sc indicates the depth of the space-charge region.

Charge carrier transport in general can be described by the current density equation, Poisson's equation and the continuity condition of the charge carriers. Without loss of generality, the problem may be considered one-dimensionally and the named equations for hole conducting polymers may be written as:

$$j(x) = -qn(x)\mu E(x) + k_B T \mu \frac{dn}{dx}, \quad \text{eq. (2.4 - 118)}$$

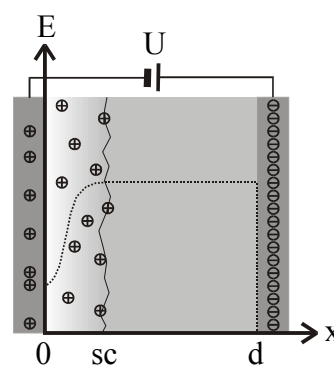


Figure (2.4 - 10): Sketch of the situation leading to SCLC

$$\varepsilon \frac{d}{dx} E(x) = \rho(x) = q(n(x) + N_T^i(x)), \text{ and} \quad \text{eq. (2.4 - 119)}$$

$$\frac{\partial}{\partial t} n(x) = \frac{1}{q} \frac{d}{dx} j(x) . \quad \text{eq. (2.4 - 120)}$$

Here, q is the elementary charge, n is the hole number density, E is the electrical field, j is the current density, μ is the charge carrier mobility, ε is the effective permittivity, and N_T^i is the density of ionized charge carrier traps in the polymer. Einstein's relation is presumed to be valid and is already inserted into eq. (2.4 - 118).

Steady-state solutions (i.e. eq. (2.4 - 120) equals zero) for the above set of equations are easily found assuming predominant drift transport of holes, which is true for sufficiently high fields in arbitrary conductors and (almost) generally in polymers, where charge carrier diffusion is (almost) always negligibly small. Thus, the second term on the right hand side of eq. (2.4 - 118) may be ignored. Furthermore assuming at first, that no charge carrier traps are present ($N_T^i = 0$), eq. (2.4 - 118) can be inserted into eq. (2.4 - 119), which then is integrated yielding:

$$E(x) = \sqrt{\frac{2j(x)}{\mu\varepsilon}x} + C. \quad \text{eq. (2.4 - 121)}$$

For an ideal ohmic contact at $x = 0$, the boundary condition $E(0) = 0$ yields $C = 0$. Please note, that this might not be strictly valid for an ITO (indium tin oxide) - polymer contact. The electrical potential $\varphi(x)$ is defined as:

$$\varphi(x) = \int_0^x E(x) dx = \sqrt{\frac{8j(x)x^3}{9\varepsilon\mu}} \quad \text{eq. (2.4 - 122)}$$

and the voltage applied to the device is $U(d) = \varphi(d) - \varphi(0)$ yielding *Child's law*:

$$j = \frac{9}{8} \varepsilon \mu \frac{U^2}{d^3}. \quad \text{eq. (2.4 - 123)}$$

Please note, that the charge carrier mobility is here assumed to be field independent.

In some systems (especially crystals and inorganic semiconductors), internal thermal charge generation may significantly contribute to the total density of charge carriers in the system at low fields applied, since the injected number of carriers is then relatively small. The current density will in this case follow Ohm's law:

$$j = q\mu n_{th} \frac{U}{d}, \quad \text{eq. (2.4 - 124)}$$

where n_{th} is the thermally generated intrinsic charge carrier density. However, thermal charge generation is usually of minor impact in amorphous organic polymers.

If the charge carrier mobility is field dependent, according to [B5, p. 60f] eq. (2.4 - 123) may be expressed as:

$$j = \frac{(P_m + 3)^{P_m+2}}{(P_m + 2)^{P_m+3}} \varepsilon \mu \frac{U^2}{d^3}, \quad \text{eq. (2.4 - 125)}$$

where an empirical field dependence of the mobility of:

$$\mu = \mu_0 \left(\frac{U}{U_0} \right)^{P_m} \quad \text{eq. (2.4 - 126)}$$

is assumed. Here P_m and U_0 are empirical constants, which can be obtained experimentally. Eq. (2.4 - 126) provides a reasonable approximation for the field dependence of the mobility for

most polymers in the experimentally relevant range of applied fields. A more accurate description of the field (and temperature) dependence of the mobility will be focused upon in the subsequent sections.

The above assumption of a trap free medium will usually not account for polymers. In the presence of shallow traps (i.e. traps, which may be detrapped thermally as well as optically) and assuming iso-energetic traps (which again will not account for polymers), the current density may be expressed by means of an effective charge carrier mobility:

$$\mu_{eff} = \Upsilon \mu, \quad \text{eq. (2.4 - 127)}$$

since intermediate trapping processes during the charge transport may be interpreted as a reduced mobility. Here, the parameter Υ is the fraction of untrapped charge carriers:

$$\Upsilon = \frac{n_{untrapped}}{n_{untrapped} + n_{trapped}} \quad \text{eq. (2.4 - 128)}$$

The effective mobility will then replace the mobility in eq. (2.4 - 123) or eq. (2.4 - 125). In the so called *trap-filled-limit*, which may be approached for high applied fields, all shallow traps in the system will be filled, and the current density behavior then approaches child's law.

Dropping the assumption of iso-energetic traps and an exponential energetic distribution for the traps of the general form may be assumed:

$$f(E) = \frac{N_T}{k_B T_T} e^{\frac{E - E_C}{k_B T_T}}, \quad \text{eq. (2.4 - 129)}$$

where $k_B T_T$ is an average energetic trap depth (or T_T the required temperature to thermally empty such an average trap, respectively), N_T is the total number of available traps, and E_C is the energy level of the conduction band. For disordered organic solids the latter may be interpreted as the center of the energetic distribution of conducting sites. Please see subsequent section for the underlying models. The current density for an energetic distribution of trapping levels according to eq. (2.4 - 129) may then be expressed as:

$$j = q^{1-l} \mu N_C \left(\frac{2l+1}{l+1} \right)^{l+1} \left(\frac{l}{l+1} \frac{\varepsilon}{N_T} \right)^l \frac{U^{l+1}}{d^{2l+1}}, \quad \text{eq. (2.4 - 130)}$$

where N_C is the effective density of states of charge carriers in the conduction band, which may be interpreted as the effective density of states at the center of the distribution of conduction sites in polymers. The parameter l is defined by:

$$l = T_T / T \quad \text{eq. (2.4 - 131)}$$

and usually $l \geq 1$.

If there are only deep traps, the traps are usually filled completely all over the system and the aforementioned trap-filled-limit will be reached already at low fields. Thus, in this case, the behavior corresponds to *child's law*.

It is necessary to point out, that the theoretical models of space charge limited currents have been developed for systems obeying the band transport theory and, hence, cannot account for the particular charge transport properties of polymers. Nevertheless, SCLC has been widely used to characterize the electrical properties of organic materials. From current-voltage characteristics obeying child's law, for example, the charge carrier mobility may be estimated and, if μ has been obtained independently, the fraction of not trapped charge carriers may be estimated. From this, conclusions on the depth of shallow traps may be drawn. In the trap-filled-limit, N_T^i in eq. (2.4 - 119) equals N_T and integration over the applied voltage yields:

$$U_{tfl} = \frac{qN_T d^2}{2\varepsilon}. \quad \text{eq. (2.4 - 132)}$$

Therewith the maximum trapped charge density and, accordingly, the trap density in the system can be estimated. However, the trap-filled-limited regime is hard to reach experimentally, since most systems suffer from dielectric breakdown before this regime is approached. Last not least, it should be mentioned, that the transitions between some particular SCLC behavior may reveal important aspects about the principal nature of the conduction process in a system. For example, the thermally generated intrinsic charge density may be obtained considering the transition from ohmic to standard SCLC behavior. The transition points, once identified, are treated theoretically by equalizing the expressions describing the flanking transport regimes. However, this requires the correct identification of the involved regimes beforehand, which may be problematic and ambiguous.

2.4.3.2.)Basic charge transport models for organic polymers

Charge transport in disordered organic solids (i.e. polymers and glasses) cannot be described by the common band transport model, which is well established to describe the electrical conduction properties of periodic structures (i.e. crystals including metals). This is due to the basic model of band transport, which is inapplicable for disordered amorphous systems in general. The periodicity has important consequences for the macroscopic electronic structure of a system, since the energy levels of the HOMO (highest occupied molecular orbital) and the LUMO (lowest unoccupied molecular orbital) of the moieties of the system (which may be molecules or atoms) are identical due to the identical environment as a result of the periodicity. Thus, the energy levels overlap (and split) to form quasi continuous bands of quantum-mechanic energy levels with a degeneracy approaching to infinity as long as the macroscopic dimensions of the crystal are large enough to neglect surface contributions to the bulk electrical properties. For more details about the quantum-mechanical background, reference is made to any standard literature in solid state physics, basic quantum physics or physical chemistry.

On the other hand, in amorphous systems, there is neither periodicity nor any long range order. Therefore, the moieties of such systems exist in slightly different environments at least in short range distances, leading to slightly different energy levels of the HOMO and the LUMO of adjacent moieties. Accordingly, any overlap of many molecular orbitals leading to formation of energy bands is inhibited. Therefore, charge transport in disordered organic solids cannot be described by band transport mechanisms. This is experimentally confirmed by the fact, that the observed charge carrier mobilities μ in polymers are at least two orders of magnitude smaller ($\mu \approx 10^{-2}$ to 10^{-10} cm²/Vs) than found for systems exhibiting band transport ($\mu > 10^0$ cm²/Vs). Furthermore, a dependence of μ on an applied electrical field is only found in systems exhibiting band transport, if the electrical conduction involves the Poole-Frenkel effect, and then always leads to an increase of the mobility with increasing field. In contrast, the charge carrier mobility in polymers always depends strongly on an applied field and may even decrease with increasing field. Please note, that especially the latter observation excludes a Poole-Frenkel mechanism to account for the charge carrier mobility in polymers, which (amongst others) has initially been proposed. Furthermore, the implication of Poole-Frenkel behavior in organic solids requires unphysical assumptions. This question is discussed in more detail in [B5, p. 154f]. Finally, the charge carrier mobility will decrease in band transport systems as a function of increasing temperature, since augmented collisions with phonons and interaction with an increasing

number of lattice defects will decelerate the charge carriers. On the contrary, μ in polymers is usually increased with increasing temperature, which indicates some activated process. It is assumed today, that charge carrier transport in disordered organic solids follows some hopping transport mechanism of the charge carriers between localized discrete transport sites as illustrated in figure (2.4 - 11). Hopping transport may be understood as a series of subsequent redox-reactions between identical reactants, the one being in the neutral state, the other being a radical ion. Hopping basically (but not stringently, as discussed later) occurs in the direction defined by the externally applied field so that the charge carrier gains energy and may be thermally activated or be due to tunneling. The gain in energy due to the motion in the direction of the externally applied field also allows for “up-hill“ jumps into a state of higher energy than the original state. Established models to describe hopping transport in disordered organic solids are the (small) Polaron model, the theoretical basis of which has been provided by Holstein et. al. [29] and Emin et. al. [B12] and the so called Baessler formalism, developed by Baessler et. al. [30] (review). Nowadays, the latter is the most widely used formalism and commonly accepted as being the most powerful and realistic model to describe electrical conduction in non-conjugated polymers.

Please note finally, that molecular organic crystals represent some special case, since they exhibit periodicity but usually only form small bands due to the small intermolecular interactions occurring in molecular crystals. The charge carrier mobilities in these systems are fairly small, and coherent charge transport as predicted by the band transport model is not observed in most cases. Thus, there is a tendency that the conduction properties of these systems must also be attributed to hopping transport mechanisms although they are crystals.

The history of the research activities in the field of electrical conduction in disordered organic solids is marked by a considerable delay between the recognition of a relatively comprehensive empirical description of the process and the development of some theory, which fits the trends empirically found at least for an acceptable range. Therefore, the empirically found expression describing charge carrier hopping mobility in disordered organic solids will be shown subsequently and interpreted in short terms. Thereafter, the basic concepts of both the aforementioned hopping models will briefly be outlined and correlated with the empirical formula. A comprehensive analysis and comparison with the experiment, which would be advisable in order to allow a judgement of the ranges of validity of the models established nowadays and to interpret experimental data correctly in the context of these models cannot be provided in the frame of this work. For the very details reference is made to the specialized literature, see e.g. [30] - [36] and references therein.

2.4.3.2.1.) Empirical description of the electrical conduction in disordered organic solids

The empirical description of the charge carrier hopping mobility μ in disordered organic solids is based on an expression of the general form [36]:

$$\mu = a_0 \bar{\delta}^2 e^{f_1(\bar{\delta})} e^{f_2(\bar{\delta}, T)} e^{f_3(\bar{\delta}, T, E)}, \quad \text{eq. (2.4 - 133)}$$

where a_0 is an experimental constant, T is the (absolute) temperature, E is the electrical field,

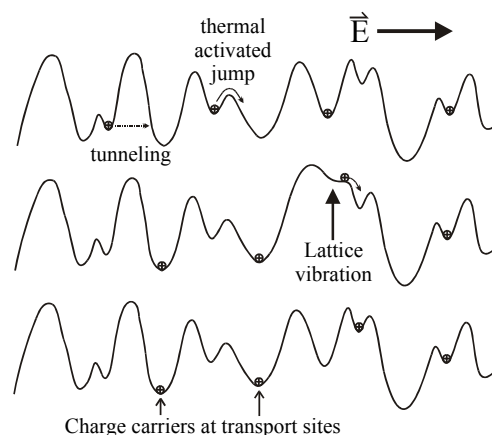


Figure (2.4 - 11): Illustration of hopping of charge carriers in disordered organic solids

and $\bar{\delta}$ is the average inter-site distance between transporting moieties, i.e. it depends on the concentration of transport moieties in molecularly doped polymers as well as on their structure. The exponentials in eq. (2.4 - 133) may physically be interpreted as follows (the list is enumerated corresponding to the number indices in the exponential arguments):

→ 1)

The first exponential accounts for quantum-mechanical interactions between particular transporting sites and, thus, stands for the overlap of their molecular wave functions. For sufficient distance from the core of the considered molecule, the molecular wave function will decay exponentially as a function of the distance as known from quantum mechanics, which suggests to express the wave function overlap in terms of:

$$f_1(\bar{\delta}) = -2\gamma\bar{\delta}, \quad \text{eq. (2.4 - 134)}$$

where γ stands for the inverse of the wave function's decay radius, which may be taken as a measure for the length of the offshoot of the molecular electronic wave function surpassing a fictive shell of the molecule, which represents the „classical size“ of the molecule.

→ 2)

The second term reflects the temperature dependence of the charge carrier mobility, however, afflicted with an inherent dependence on the average inter-site distance as well, and accounts for its experimentally observed activated behavior. Arrhenius relationship as well as stretched exponential behavior has been proposed:

$$f_2(\bar{\delta}, T) = -\frac{\Delta E_A(\bar{\delta})}{k_B T} \quad \text{eq. (2.4 - 135)}$$

$$f_2(\bar{\delta}, T) = -\left(\frac{T_B(\bar{\delta})}{T}\right)^2, \quad \text{eq. (2.4 - 136)}$$

where ΔE_A is the activation energy and T_B a parameter, which will be clarified in context with the Baessler formalism. Up to date, unambiguous experimental evidence for one or the other version could not be supplied. Fits to experimental data plotted as $\ln\mu \propto T^{-1}$ and $\ln\mu \propto T^{-2}$ gave comparably good correlation for both versions, however, the latter being slightly better if the entire range of temperatures is considered [36]. The Baessler formalism favours the latter version as well, which supports a general acceptance.

→ 3)

The third exponential reflects the field dependence of the charge carrier mobility, however, afflicted with an inherent dependence on the temperature and on the average inter-site distance as well. Functions of the form:

$$f_3(\bar{\delta}, T, E) = \frac{\beta(\bar{\delta})\sqrt{E}}{k_B\left(\frac{1}{T} - \frac{1}{T_0(\bar{\delta})}\right)} \quad \text{and} \quad \text{eq. (2.4 - 137)}$$

$$f_3(\bar{\delta}, T, E) = \frac{\beta(\bar{\delta})\sqrt{E}}{k_B\left(\frac{1}{T} - \frac{1}{T_0(\bar{\delta})}\right)^2} \quad \text{eq. (2.4 - 138)}$$

have been empirically found, where β and T_0 are constants in T and E . The problem of the temperature occurring with different exponents has already been discussed above, and applies here in a similar way. A physical interpretation of the third exponential

can only be provided on the basis of the Baessler formalism, which will be discussed in the corresponding section.

Since the functional dependencies according to eq. (2.4 - 133) with eq. (2.4 - 134), eq. (2.4 - 135) and eq. (2.4 - 137) or eq. (2.4 - 134), eq. (2.4 - 136) and eq. (2.4 - 138) inserted represent the experimental reality, theoretical models describing the charge transport must agree consistently.

2.4.3.2.2.)The polaron model

In the polaron theory, not only the charge carrier itself is considered for the charge carrier mobility, but the entire polaron.

Some charge carrier in a polarizable solid environment will polarize its proximity and the polarized surrounding, in turn, will reduce the energy of the charge carrier. The complete system formed by the charge carrier and the associated polarization in its proximity is called a polaron, which is a quasi particle and represents the total energy quantum of this state. The term “polaron“ includes all effects of a charge carrier on its environment in a solid. Hence, in the case of some molecular system (polymer, glass or molecular crystal), where a charge carrier is localized at some molecule, it will not only polarize its surrounding but also affect the equilibrium values of basic molecular parameters of the transporting site like bond lengths and bond angles as compared to the values found in the neutral molecule.

It is clear, that the “size“ of a polaron (i.e. its energy) will strongly depend on the “velocity“ of the charge carrier motion in the system with respect to the typical relaxation times of the system itself, since by that the degree of interaction between the charge carrier and its surroundings is determined. This relationship will be expressed hereafter by using the term “time scale (of the charge carrier motion)“. Hence, e.g. “motion on short time scale“ means that the motion is fast with respect to the relaxation behavior of the system. In particular, four times and their relation to each other must be considered for organic systems following hopping transport mechanisms:

- a) The average dwell time τ_{dwell} of a charge carrier on a transporting site
- b) The period of intramolecular vibrations (typical: $\tau_{ia} > 10^{-14}$ sec)
- c) The period of intermolecular vibrations (typical: $\tau_{ie} < 10^{-12}$ sec)
- d) The response time for deformation of neighboring molecular orbitals as a result of the presence of the charge carrier (typical: $\tau_{\pi} \sim 10^{-16}$ sec). It is clear for organic systems, that the main contribution stems from π -orbitals.

There are basically two limiting cases representing very different charge transporting properties. For $\tau_{\text{dwell}} \leq \tau_{\pi}$ ($< \tau_{\text{vibrations}}$), the charge carriers move too fast through the crystal lattice to induce notable changes in its environment and will exhibit long free path lengths before being decelerated (e.g. scattered at a phonon). This is the case of band transport. For $\tau_{\text{dwell}} \geq \tau_{ie}$, a charge carrier moves only slowly through the system allowing its environment to relax and form a potential well, which traps the charge carrier („self-trapping“). Thus, the charge carrier will be localized on the current transporting site and only be released if the local neighborhood is changed from „outside“, i.e. by a phonon. Once the charge carrier has hopped to another transporting site, it will be self-trapped again as described above. Thus, the hopping process will be supported by phonons and the whole polaron will be displaced.

In the simplest case, the polaron theory may be considered only one-dimensionally, i.e. the charge carriers are assumed to be transported along a straight line through the system. This

point of view will suffice here. According to [B12], the one-dimensional polaron theory predicts the charge carrier mobility by:

$$\mu = \frac{q\bar{\delta}^2}{k_B T} P v_{ph} e^{-\frac{E_p - 2J(\bar{\delta})}{2k_B T}} \quad \text{eq. (2.4 - 139)}$$

The Boltzmann term accounts for the activation energy, which must be expended in order to generate energetic coincidence between the polaron and a neighboring transportation site. The activation energy itself consists of the polaron binding energy E_p reduced by the overlap integral J since the thermal energy required to generate energy coincidence is reduced for increasing overlap of the wave functions of neighboring transportation sites (the factor of two stems from the relation between polaron binding energy and the reorganization energy = 2:1). Please note, that the polaron theory assumes the charge carriers to hop to nearest neighbors, which are inside the polarization cloud.

The parameter P describes the probability of charge transfer once energy coincidence is at hand. The phonon frequency v_{ph} is included, since a charge carrier has only one chance to hop per phonon oscillation period and thus v_{ph} may be taken as a measure for a maximum hop frequency, which is equivalent to the interpretation as an ‘‘attempt-to-escape’’ frequency. The hopping probability P may be related to the diffusion coefficient D by:

$$D = P\bar{\delta}^2 \quad \text{eq. (2.4 - 140)}$$

and the diffusion coefficient can be expressed in terms of the charge carrier mobility by means of the Einstein relation:

$$\mu = \frac{qD}{k_B T} \quad \text{eq. (2.4 - 141)}$$

Merging eq. (2.4 - 140) and eq. (2.4 - 141) reveals, that the ratio $q\bar{\delta}^2 / k_B T$ converts a hopping frequency to a mobility, provided the Einstein relation holds, which will be discussed below in the context with dispersive charge transport.

Interpreting eq. (2.4 - 139) in terms of eq. (2.4 - 133), the correlations are as follows:

$$a_0 = \frac{q v_{ph}}{k_B T}, \quad \text{eq. (2.4 - 142)}$$

$$f_1(\bar{\delta}) = \ln P \quad \text{and} \quad \text{eq. (2.4 - 143)}$$

$$f_2(\bar{\delta}, T) = -\frac{E_p - 2J(\bar{\delta})}{2k_B T} \quad \text{eq. (2.4 - 144)}$$

Comparison with the experiment [34] shows a good agreement of the polaron model with experimental data at zero external field without considering disorder.

However, the polaron theory fails to describe the field dependence of the charge carrier mobility correctly. The field dependence is usually described by an expression given by Marcus et. al. [37]:

$$\mu(E) \propto \frac{1}{E} \sinh\left(\frac{q\bar{\delta}E}{2k_B T}\right) \quad \text{eq. (2.4 - 145)}$$

This expression is basically derived from the idea, that an applied field will support hopping in one field direction, since it reduces the activation energy, and will hamper hopping in the opposite direction by rising the activation energy. When expressing both the contributions Arrhenius-like, taking the sign of the field into account (i.e. the exponential arguments will have opposite signs) and subtracting these two rates one obtains the form of the field term given

above. Eq. (2.4 - 145) predicts almost field independent mobility at low fields and strong dependence at high fields, whereas the contrary is observed experimentally, namely saturation or even a decrease of the mobility at high fields. Even if the one-dimensional model is expanded to three dimensions, tunnelling is allowed for, and a small disorder term is introduced only some gradual improvement of congruence between theory and experiment is achieved but not a reasonable agreement [38]. The resulting expression is very complicated and will not be reproduced here.

Thus, in conclusion, there is currently strong indication, that charge carrier transport in disordered organic solids is not (notably) due to polaronic effects, since the polaron model cannot account for the field dependence experimentally found.

2.4.3.2.3.)The Baessler formalism (disorder model)

In the disorder model fluctuations of the molecular energy levels and of the intermolecular distance and mutual orientation in amorphous organic solids are considered as determining the charge carrier mobility. Polaronic effects are neglected. The formalism has been developed largely by means of Monte Carlo (MC) simulation techniques. Subsequently only the basic concept of the model will be outlined and the resulting expression for the charge carrier mobility will be shown. A more comprehensive review is provided in Appendix E and in [30].

A fundamental assumption of the Baessler formalism is that the transport manifold of a disordered organic system abandoning long range order is smeared out into a Gaussian distribution of localized states. The origin of the distribution is attributed to fluctuations of the entire variety of intermolecular potentials existing in an organic system containing ions, i.e. the interaction of ions, dipoles and induced dipoles with themselves and each other, whereby ion - ion and ion - dipole interactions contribute most. The distribution of localized energetic states is referred to as *diagonal disorder*, since the eigen-energies of the sites thus modified would occur as diagonal elements in the energy matrix.

Another fundamental assumption of the Baessler formalism is based on model calculations in [40], which showed that the transfer integrals for charge carrier exchange between two adjacent transport sites may vary by several orders of magnitude as a function of the mutual orientation of the transport sites. Thus, it must be expected that the wave function overlap between adjacent transporting sites, which determines the probability of a charge carrier exchange (i.e. the jump rate), is subjected to a distribution. Furthermore but less important (except for fullerene systems), the inter-site distance will not be constant but subjected to a distribution as well. The subsumption of these distributions is referred to as positional disorder or *off-diagonal disorder*.

Based on the above assumptions and by means of MC simulation techniques Baessler et. al. derived the following expression for the charge carrier mobility in disordered organic solids:

$$\mu = \mu_0 e^{-\left(\frac{2}{3}\hat{\sigma}\right)^2} e^{C[\hat{\sigma}^2 - \Sigma^2]\sqrt{E}} \quad \forall(\Sigma \geq 1.5) \quad \text{eq. (2.4 - 146)}$$

$$\mu = \mu_0 e^{-\left(\frac{2}{3}\hat{\sigma}\right)^2} e^{C[\hat{\sigma}^2 - 2.25]\sqrt{E}} \quad \forall(\Sigma < 1.5)$$

with:

$$\hat{\sigma} = \frac{\sigma}{k_B T}, \quad \text{eq. (2.4 - 147)}$$

where σ is the (1/e -) width of the DOS of transporting sites, Σ is the positional disorder parameter, $C = 2.9 \times 10^{-7} (\mu\text{m}/\text{V})^{1/2}$, and μ_0 is an experimental constant.

The disorder model is the first model in several decades of research on electrical conduction in disordered organic solids, which is able to describe the particular features of this phenomenon consistently and at least qualitatively over a wide range of possible variations of experimental parameters. Unfortunately, also the disorder formalism utilizes parameters, which are not or at least not directly accessible by the experiment. The problem in determining the width of the DOS of transport sites has already been discussed above. The off-diagonal disorder parameter is even more problematic, since up to date there is no really independent method to obtain this parameter. Thus, Σ must be gained by fitting experimental data on conductivity and charge carrier mobility measurements to the equations eq. (2.4 - 146).

Nevertheless, the Baessler formalism has been a great progress, since it provides a qualitative idea of the physical processes behind the electrical conduction in disordered organic solids and it supplies the people working in this field with analytical expressions applicable to fit experimental data. Since the model was presented first around 1990, it has been applied to a big variety of different systems and has proven its solid groundwork impressively.

2.4.3.2.4.)Concentration and matrix dependence

The charge carrier mobility in general depends strongly on the concentration of transport sites in the medium and the type of the polymer matrix in molecularly doped polymer systems, i.e. in systems, where the transport sites are diluted in an inert polymer matrix. Experimentally, an increase of the charge carrier mobility by several (i.e. some five to more than seven) orders of magnitude is observed within a concentration range of about $10\%wt \leq c \leq 100\%wt$ of transport sites [46] and no general trend can be formulated for the matrix dependence, but it is clear that the polarity plays an important role. Neither the concentration dependence of the charge carrier mobility nor the matrix dependence can be described analytically. However, there have been attempts to develop some models to describe the concentration dependence. These are the homogenous lattice gas model [47] and considerations based on the percolation concept [48]. Although both the models turned out to show considerable deviations from simulation and experimental data, they may serve as a guideline for understanding the basic relations between the concentration of transport sites and the charge carrier mobility. Subsequently, the homogenous lattice gas model and the percolation concept will be briefly outlined. The influence of the polymer matrix will not be elaborated upon, since the systems investigated in the frame of this work (PVK as polymer matrix) are not classical molecularly doped polymers but may rather be considered as systems, where the matrix itself is conductive. Hence, the influence of the matrix on the conduction properties of these systems becomes a question of the concentration dependence.

2.4.3.2.4.1.)Homogenous lattice gas concept

Assuming cubic shape of the molecules as well as their homogenous distribution in zero order approximation, the average inter-site distance $\bar{\delta}$ between two transport molecules or moieties may be expressed as:

$$\bar{\delta} = \sqrt[3]{\frac{M}{N_A \rho_M c}} = \frac{\bar{\delta}_0}{\sqrt[3]{c}}, \quad \text{eq. (2.4 - 148)}$$

where M is the molar mass of the transport moieties and ρ_M is their density (in pure form), N_A is Avogadro's constant, and c is the fractional concentration (i.e. dimensionless) of transport moieties in the system. The parameter $\bar{\delta}_0$ may then be interpreted as mean nearest neighbor distance in the undiluted system. The average inter-site distance $\bar{\delta}$ will decrease as a function of increasing concentration, which will result in an increase of the wave function overlap as well

as a decrease of the average quadratic distance to be covered per jump. Hence, the concentration dependence of the charge carrier mobility may be expressed according to eq. (2.4 - 133) (disregarding the last two exponentials) and eq. (2.4 - 134) as:

$$\mu_0(c) = \frac{a_0'}{\sqrt[3]{c^2}} e^{-2\gamma\bar{\delta}_0\sqrt[3]{c}}, \quad \text{eq. (2.4 - 149)}$$

where a_0' can be identified according to eq. (2.4 - 139) to eq. (2.4 - 142) (conversion of a jump frequency into a mobility) resulting in:

$$a_0' = \frac{q\bar{\delta}_0^2 v_0}{6k_B T}. \quad \text{eq. (2.4 - 150)}$$

Here v_0 is the prefactor in the jump rate eq. (E - 2) and the factor 6 in the denominator stems from the consideration of in principle three spatial jump directions with the possibility of forward and backward jumps. Please note, that v_0 and v_{ph} in eq. (2.4 - 139) are closely related to each other and have very similar physical meaning and value.

The model ignores diagonal and off-diagonal disorder and takes the hopping sites as an array of points, whereas the average hopping distances may be estimated as being comparable to the typical physical dimensions of the hopping sites. Accordingly, it does not surprise, that comparison of eq. (2.4 - 149) with MC simulations revealed partly considerable deviations, however, the general trend is reproduced. Thence, it may serve as zero order approximation of the real behavior.

Please note, that the second and the third exponential in eq. (2.4 - 133) are derived according to the polaron model as well as the Baessler formalism, tacitly presuming the absence of any concentration dependence. This is obviously not true, since the width of the DOS of transport sites depends on the concentration of transport moieties as shown in [33] for a representative system. The DOS was found to increase as a function of decreasing concentration, which was attributed to an increase of the fluctuations of the intermolecular dipole interactions for smaller concentrations. Most probably, this finding represents a general trend, which suggests, that both the second exponential (temperature dependence) and the third exponential (field (and temperature) dependence) in the general form of the mobility equation (see eq. (2.4 - 133) and especially eq. (2.4 - 146)) may depend considerably on the concentration of transport moieties.

2.4.3.2.4.2.)The percolation model

The percolation model was proposed by Silver et. al. [49] as an alternative to the lattice gas model described above. The percolation theory in general deals with the effects of varying richness of interconnections present in a random network system. A simple picture illustrating the basic concept is shown in figure (2.4 - 12). In a network of conducting connections, the connecting links are cut one after the other and at random. The question is what fraction of links must be cut in order to cut off the macroscopic conductivity of the whole system. Percolation theory tries to answer this question. It can be shown, that there is a definite answer to this question for a network size approaching infinity. For the case of a 2D network as illustrated in figure (2.4 - 12), the threshold point, referred to as *percolation threshold*, is $c_0 = 0.5$. Accordingly, there is a sharp transition at which some long-range connectivity appears or disappears and which occurs abruptly. Percolation theory is an active field of mathematical research finding application especially in theoretical physics and polymer chemistry (sol-gel processes). It is beyond the scope of this work to proceed to a more detailed consideration of the mathematics behind this theory.

It is obvious to try to apply the percolation concept to the concentration dependence of the charge carrier mobility in molecularly doped polymers. Assuming that the transport sites occupy positions in a lattice, for a fractional concentration of unity all positions are occupied. For decreasing concentration, transport sites are withdrawn randomly from the lattice leaving open positions behind. In the absence of energetic and positional disorder (according to the Baessler formalism; please note, that percolation itself is a statistical problem and thus subject to disorder considerations as well, e.g. the lattice disorder covering the randomness of the condition “unoccupied position“ and “occupied position“, which is not meant here), the percolation model predicts the concentration dependence of the charge carrier mobility to be:

$$\mu \propto (c - c_0)^\alpha \quad \text{eq. (2.4 - 151)}$$

The parameter α is a constant, which amounts to $\alpha = 1.5$ for site percolation (i.e. site existent or missing) and $\alpha = 1.6$ for bond percolation (i.e. „connection“ between sites existent or missing) and c_0 is the percolation threshold, which is $c_0 = 0.312$ for a simple cubic structure. Please note, that the model presumes hops of charge carriers only to nearest neighbors and hence no hop is implied, if the considered neighboring position is empty.

MC simulations of the concentration dependence of the charge carrier mobility, however, did not show a well defined percolation threshold and a much stronger concentration dependence than predicted from the percolation model. Increasing the overlap parameter $2\gamma\bar{\delta}$ (i.e. the spatial extent of the wave function is reduced) in the simulations leads to improved agreement between theory and simulation. This shows, that the above approximation of only nearest neighbor jumps is not acceptable. In conclusion, the MC simulation results tend to support the lattice gas model rather than the percolation model. Nevertheless, the percolation model takes proper account of the discrete molecular structure of the system and thus may be developed to a more powerful concept in the future.

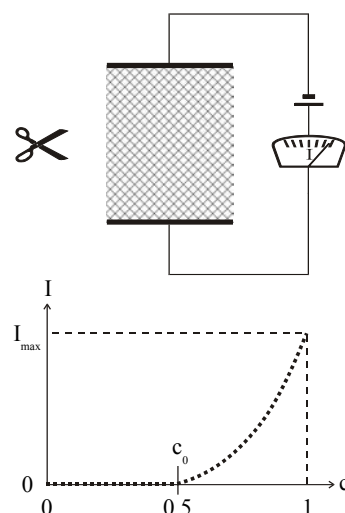


Figure (2.4 - 12): Illustration of the percolation concept. c is the fraction of uncut connections, I is the flux through the network system

2.4.3.3.)Dispersive charge transport

Conducting polymers are subjected to dispersive charge transport. The term “dispersive charge transport“ describes the phenomenon, that a charge carrier packet diverges considerably more than predicted from normal diffusion during its field-driven motion through a disordered organic solid. This results in anomalous broadening of the signals obtained by time of flight (TOF) experiments, which is the typical experiment to determine conduction properties. In TOF, a sheet of charge carriers is generated by flash excitation in a photosensitive layer and its motion through a conduction layer to be experimentally tested is measured by monitoring the displacement current flowing through the setup. The working principle and the typical signal shape are depicted in figure (2.4 - 13). The so called *transit time* t_T (the time the charge carrier packet takes to traverse the conducting layer) is a measure for the charge carrier mobility. If the charge carrier packet divergence is anomalously strong, the transit time is no longer a well defined point. In the limiting case of “extremely“ dispersive transport, a transit time cannot be defined.

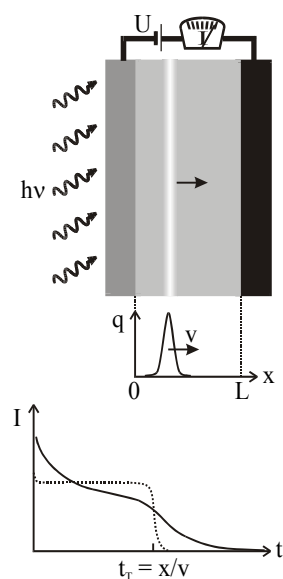


Figure (2.4 - 13): TOF experiment and typical signals: dotted line → non-dispersive; solid line → strongly dispersive.

Phenomenologically, dispersive charge transport may be understood in the sense of a broad distribution of propagation velocities of the single charge carriers. Thus, a clear definition of a charge carrier mobility is difficult and eventually becomes impossible when the distribution becomes too broad to clearly define a maximum in a physical sense. The fortune of a charge carrier packet traversing a conducting layer at non-dispersive and dispersive transport is illustrated in figure (2.4 - 14). The original charge carrier packet is transported along x at velocity v_{nd} for a certain time not remarkably changing its shape for the case of non-dispersive transport. In contrast, in the case of strongly dispersive transport, the carrier packet is smeared out in transport direction due to a broad distribution of propagation velocities rather than transported.

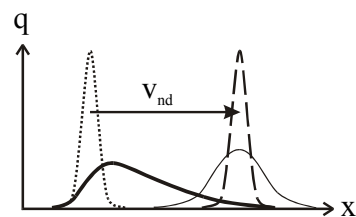


Figure (2.4 - 14): Illustration of dispersive transport. Dotted line: original charge carrier packet. Dashed line: non-dispersive transport. Thick solid line: strongly dispersive transport. Thin solid line: moderately dispersive transport.

Dispersion in charge transport has an important impact on the Einstein relation eq. (2.4 - 141), which will be discussed below. A more comprehensive discussion of dispersive charge transport will be provided in Appendix F.

2.4.3.3.1.)The Einstein relationship

As mentioned before, for non-dispersive media the field-driven motion of a well defined packet of charge carriers gives rise to a constant displacement current in TOF experiments until the carriers reach the electrode on the right hand side of the sketch in figure (2.4 - 13). There will be some diffusive spreading of the packet, broadening the trailing edge of the photo current transients as depicted by the dotted line in the diagram at the bottom of figure (2.4 - 13). In a homogeneous medium and for fields small enough to ensure, that the gain in energy for a charge carrier travelling along the electrical field vector is significantly smaller than the thermal energy

(i.e. $qE\bar{\delta}/2k_B T \ll 1$, for the parameters see above), Einstein's relation eq. (2.4 - 141) will hold, relating charge carrier diffusion and drift mobility. Then, the mean spatial width Δx of an initially δ -shaped (δ in this case: Kronecker symbol) charge carrier packet will evolve according to:

$$\frac{\sqrt{\langle \Delta x^2 \rangle}}{\langle x \rangle} = \frac{k_B T}{qE} \sqrt{\frac{2}{Dt}}, \quad \text{eq. (2.4 - 152)}$$

where x is the traversing direction of the carrier packet through the medium, D is the diffusion coefficient and t is the time. This yields for the relative spread of the photocurrent transient:

$$\frac{\Delta t_T}{\Delta t} = \sqrt{\frac{2k_B T}{qEL}}, \quad \text{eq. (2.4 - 153)}$$

where L is the thickness of the sample conducting layer according to figure (2.4 - 13).

In polymers, however, it is always observed, that the packet of charge carriers spreads considerably faster with time relative to the transit time as predicted by eq. (2.4 - 152). Accordingly, the apparent diffusivity exceeds the zero field diffusivity as predicted by the Einstein relation. It has been shown by MC simulations in [50], that the ratio $qD/\mu k_B T$, equaling unity if the Einstein relation holds (see eq. (2.4 - 141)) may reach values as large as of order 10^3 in disordered systems and depends strongly on the bias field as well as the disorder in the system (for more details, see Appendix F). As already mentioned before, this is referred to as *dispersive charge transport* and proves the Einstein relation not being valid in disordered organic systems. The deviation of the real behavior from the Einstein relation increases with increasing dispersity of the charge transport.

2.4.4.) Charge generation and recombination in organic polymers

Apart from charge transport in disordered organic solids, photoinduced charge generation and recombination is the second major issue within the frame of electrical properties of organic polymers. In inorganic semiconductors band-to-band excitation leads to the photogeneration of free charge carriers. In contrast, bound geminate electron - hole pairs (excitons) are involved in this process in organic materials. The models by far most widely used to describe charge generation in organic solids are all based on the Onsager formalism [59]. Free carriers are assumed to be generated by a multi-step process beginning with photon absorption and creation of a localized hole and a hot (i.e. having considerable kinetic energy) electron, provided electrons are the mobile charge carrier species. The hot electron then becomes thermalized after having travelled a certain distance, which is called thermalization radius r_0 , creating a charge-transfer (CT) state. This initial process is described by a primary quantum yield Φ_0 . In this state, the Coulomb energy associated with the thermalization distance is comparable to the thermal energy. Eventually, the charge transfer state can either dissociate resulting in a free electron and a free hole or undergo geminate recombination, i.e. the electron recombines with its parent cation. The dissociation probability is described by the theory due to Onsager. Accordingly, the photogeneration efficiency is then given by the product of the efficiency of creating a bound electron - hole pair and the probability that the pair dissociates. Please note, that the theory is not restricted to a certain type of charge carrier to be mobile or not and, thus, applies to electron conductors as well as hole conductors.

Subsequently, the Onsager formalism will briefly be outlined without elaborating on the complicated mathematics behind it. The situation found in polymers will be discussed separately. A short discussion of closely related models based on the Onsager theory will follow. This includes the discussion of a more recent model especially focusing on the hole conducting

polymer poly(N-vinylcarbazole), which is of particular interest for this work. Models using other approaches will not be considered. The paragraph will close with a short note about the repeatedly cited „Langevin recombination“.

2.4.4.1.)Onsager formalism

The Onsager formalism is derived from the time independent Smoluchowski equations [60], which are:

$$\operatorname{div} j = \delta(r - r_0) \quad \text{eq. (2.4 - 154)}$$

and:

$$j = -De^{-W}\nabla\rho e^W. \quad \text{eq. (2.4 - 155)}$$

Here, j is the current density, r is the relative position of the charge carrier with respect to its counter-ion, r_0 is the initial separation, ρ is the particle distribution function, D is the sum of the diffusion coefficients and W is the potential energy normalized by the thermal energy according to:

$$W(r, \theta, E, T) = -\left(\frac{r_C}{r} + 2Br \cos\theta\right), \quad \text{eq. (2.4 - 156)}$$

where θ is the polar angle and:

$$B = \frac{qE}{2k_B T}. \quad \text{eq. (2.4 - 157)}$$

The corresponding reference frame is defined such that the direction of the applied field coincides with the z -axis and the equations are expressed in polar coordinates. The quantity r_C is the distance, where the Coulomb potential equals the thermal energy, commonly referred to as „Coulomb radius“ or, less common, but sometimes used in older literature, „Onsager radius“ and thus given by:

$$r_C = \frac{q^2}{4\pi\epsilon k_B T} \quad \text{eq. (2.4 - 158)}$$

with $\epsilon = \epsilon_r\epsilon_0$ being the total permittivity. The Smoluchowski equations may easily be understood. Eq. (2.4 - 154) is the mathematical formulation of the condition, that the charge carriers contributing to the considered current density are actually generated in the respective area and do not come from outside. Eq. (2.4 - 155) is Fick's first law with the particle distribution function being the concentration. The exponential arguments (eq. (2.4 - 156)) account for the influence of the Coulomb interactions (left term of the exponential argument W) counteracting the diffusion process and for the applied field (right term of the exponential argument W) „promoting the diffusion“ by adding a drift component (please note, that the current density may be expressed as $j = s\rho$, s being the propagation velocity of the particles, i.e., the charge carriers, whose distribution is given by ρ). Please note, that the application of the Smoluchowski equations demands the mean free path length of the diffusing particles to be much smaller than the Coulomb radius.

Onsager gave a solution for eq. (2.4 - 154) and eq. (2.4 - 155) presuming the boundary conditions:

$$\rho(0|r_0) \neq \infty \quad \text{eq. (2.4 - 159)}$$

and:

$$\lim_{r \rightarrow \infty} \rho(r|r_0) \rightarrow 0, \quad \text{eq. (2.4 - 160)}$$

where the notation “ $a|b$ ” usually refers to probability considerations for „parameter a out of ensemble b “. In the current context, $\rho(r|r_0)$ must be understood as the conditional probability of finding a particle at r , if initially at r_0 . Eq. (2.4 - 159) thus reflects the demand, that a charge carrier may escape from its origin, whereas eq. (2.4 - 160) ensures, that it does not vanish. In other words, the boundary conditions require the particle to exist somewhere between $r = 0$ and $r \rightarrow \infty$, but not only at 0. He obtained the following expression for the probability $f(r, \theta, E, T)$ of escaping geminate recombination for an isolated thermalized charge pair at temperature T separated by distance r , with the distance (vector) oriented at an angle of θ with respect to the applied field E :

$$f(r, \theta, E, T) = e^{-\left[\frac{r_C}{r} + Br(1 + \cos\theta)\right]} \sum_{n=0}^{\infty} \sum_{m=0}^{\infty} \frac{(B + B \cos\theta)^{n+m} r^n}{m!(n+m)! r_C^{-m}} \quad \text{eq. (2.4 - 161)}$$

Thus, with the aforementioned primary quantum yield Φ_0 , the photogeneration efficiency can be expressed as:

$$\Phi(E, T) = \Phi_0 \int g(r, \theta) f(r, \theta, E, T) r^2 \sin\theta d\theta d\phi dr, \quad \text{eq. (2.4 - 162)}$$

where ϕ is the azimuth angle and $g(r, \theta)$ is the distribution function of the initial distribution of the thermalized charge pair configurations.

The different models of photogeneration based on the Onsager formalism basically differ by the employed distribution function $g(r, \theta)$. Most often it is assumed, that the distribution of thermalized pairs may be described by an isotropic (i.e. no dependence on θ) delta function $\delta(r - r_0)$ according to:

$$g(r) = \frac{\delta(r - r_0)}{4\pi r_0^2}, \quad \text{eq. (2.4 - 163)}$$

which represents a perfectly absorbing sphere with vanishing radius at the origin. With eq. (2.4 - 163) and completing the integration of eq. (2.4 - 162), a good numerical approximation for the photoinduced charge generation has been presented by Mozumder [61]:

$$\Phi(r_0, E, T) = \Phi_0 F(r_0, E, T) = \Phi_0 \left[1 - \frac{1}{2Br_0} \sum_{l=0}^{\infty} Y_l\left(\frac{r_C}{r_0}\right) Y_l(2Br_0) \right], \quad \text{eq. (2.4 - 164)}$$

with r_0 according to the definition preceding eq. (2.4 - 156) and the functions $Y_l(a)$ (modified Bessel-functions of the first kind) given by the recursive formula:

$$Y_l(a) = Y_{l-1}(a) - \frac{a^l e^{-a}}{l!} \quad \text{eq. (2.4 - 165)}$$

with the initial element:

$$Y_0(a) = 1 - e^{-a}. \quad \text{eq. (2.4 - 166)}$$

Please note, that the primary quantum yield is considered as independent from the applied field E and the ambient temperature T .

2.4.4.2.)The situation in organic polymers

As mentioned before, a key assumption in the Onsager formalism is the distribution function describing the charge transfer radii. However, taking the inherent disorder of organic polymers into account, it is scarcely imaginable that the distribution of CT states is described realistically by eq. (2.4 - 163). In fact, comparison between experimental data on the electric field dependence of the charge carrier photogeneration efficiency with theoretical fits applying eq. (2.4 - 163) reveal considerable deviations especially for high applied fields exceeding $100\text{V}/\mu\text{m}$ [62] - [64]. In contrast, the classical model appeared to hold for moderate fields, however, depending on the material. The low field behavior turned out to be dubious in all cases, however, is afflicted with very high experimental error, making the results experimentally obtained less significant. Considering the success of the Baessler formalism in the description of the charge carrier mobility by applying Gaussian distributions for energetic and positional disorder of transport sites, it seems proximate to assume a distribution of CT radii, which is as well Gaussian. However, it must be pointed out, that this is not causal a conclusion but rather a backwards illustration, since various distribution functions have been tested more or less successfully before the Baessler formalism has been developed [62]. In the most recent works [63] and [64], the CT radii distribution function:

$$g(r) = \frac{\beta^3}{\sqrt{\pi^3}} e^{-\frac{r^2}{\beta^2}} \quad \text{eq. (2.4 - 167)}$$

has been found to yield best theoretical fits to experimental data on the field dependence of photogeneration efficiencies, where β is an adjustable field dependent parameter describing the distribution of CT radii ($\beta \approx r_0/2$ at low fields and approaches r_0 for high fields). This parameter accounts for the fact, that the accessibility of the distribution of CT radii for dissociation depends on the applied field. CT states with smaller thermalization distance tend to recombine strongly at low fields, whereas they contribute notably to the dissociation at high fields. Figure (2.4 - 15) gives an example plot obtained for a crystalline PVK film at $\lambda_0 = 254\text{nm}$ [64]. Very similar data were obtained with amorphous PVK films and for $\lambda_0 = 355\text{nm}$ [64]. In all cases, within the field range relevant in the frame of this work ($\approx 10 - 100\text{V}/\mu\text{m}$), the field dependence of Φ is described well by the classical Onsager theory using eq. (2.4 - 163). Therefore, data and references concerning $\Phi(E)$ given later in the section devoted to the experimental results will generally refer to eq. (2.4 - 164), which is derived on the basis of eq. (2.4 - 163).

Although the classical Onsager theory turns out to be well applicable to describe the field dependence of Φ for by far most of the practical cases, there is a significant weakness of this theory, if the temperature dependence as well as the dependence on the photon energy of the exciting radiation in polymers is considered. For the sake of completeness, the reason for and solution of this problem will be outlined subsequently.

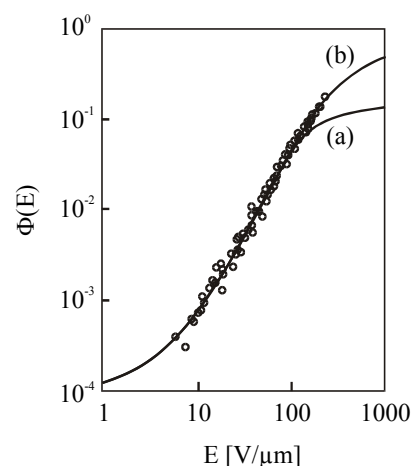


Figure (2.4 - 15): exp. $\Phi(E)$ fitted with (a): eq. (2.4 - 163), (b): eq. (2.4 - 167). Redrawn after [64].

2.4.4.2.1.) Important Onsager based models

The Onsager model assumes thermalization of the charge carrier initially ejected from the generation site by absorption of a photon with an excess kinetic energy, which is then assumed to be dissipated by means of numerous collisions with the medium. After the dissipation process, the carrier has travelled a certain thermalization length from its parent countercharge and the diffusion process begins. This ballistic nature of the Onsager model implies, that Φ depends considerably on the energy of the absorbed photon and increases with increasing exciting radiation frequency, since longer thermalization length facilitates diffusive dissociation of the bound electron - hole pair. In fact, such a behavior is observed in certain organic solids, e.g. in PPV derivatives and polysilanes [63, 65]. However, many organic materials do not show a wavelength dependence of the photogeneration efficiency of charge carriers [B20], which contradicts the classical Onsager model. The first to account for these deviations were Noolandi and Hong [66]. They assumed the photoexcited molecules to lose their energy via internal conversion rather than ballistically and thus to drop from the virtual (singlet) state S^* to the first excited singlet state S_1 without involving some thermalization distance. This is followed by some radiative (rate constant k_R) or non-radiative (rate constant k_N) relaxation to the ground state S_0 , or by the formation of a bound electron - hole pair (rate constant k). The latter then may dissociate according to the Onsager model. Recombination (R) of an electron - hole pair will at first regenerate S_1 , which then may again follow the processes described above. Please note, that a recombining pair is assumed to solely relax to the ground state in the classical Onsager model. The two models are compared in figure (2.4 - 16) and figure (2.4 - 17). L. B. Braun applied the Noolandi-Hong model for the special case that the electron - hole distance in the bound pair is larger than the recombination length of the bound pair, i.e. he assumed direct formation of the free carriers from the S_1 state [67]. The latter model has been experimentally verified by Goliber and Perlstein for an acceptor doped Triphenylamine/Lexan system [62]. However, Cimrová and Nešpurek reported, that this model fails for Poly(n-vinylcarbazole) (PVK) [64] and developed another model based on the idea of Noolandi and Hong in order to explain the behavior found in PVK. Since PVK is a key material in the frame of this work, the model worked out by Cimrová and Nešpurek will be considered in more detail now.

Cimrová and Nešpurek extended the model of Noolandi and Hong (depicted in figure (2.4 - 17)) by the assumption, that the molecule in its S_1 state (besides the other relaxation processes described above) may directly form a bound electron - hole pair like proposed by Noolandi and Hong on the one hand, or that the entire exciton may diffuse to an exciton trapping site Cz^* first, and form a bound electron - hole pair later, on the other hand. Two types of exciton trapping centers were proposed, the one type being active for charge carrier generation (Cz_a^* , corresponding trapping rate constant k_a) and the other type being inactive (Cz_b^* , corresponding trapping rate constant k_b). According to [68], monomer fluorescence of solid PVK is strongly quenched and only excimer fluorescence is observed. This allows for the neglect of radiative relaxation of S_1 ($k_R = 0$) and the assumption of a very small probability for a direct formation

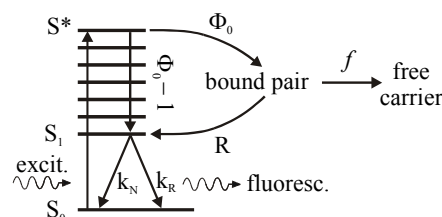


Figure (2.4 - 16): Classical Onsager model and ...

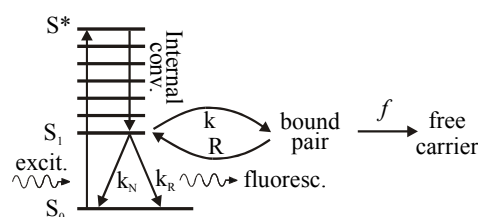


Figure (2.4 - 17): ... Noolandi-Hong-model. The notation is defined in the allotted text.

of bound electron - hole pairs. Thus, the formation of bound electron - hole pairs is restricted to the case of previous exciton trapping by active sites and the rate constant for the formation, k_i , is assumed to be field independent. Furthermore, non-radiative (rate constant k_N^*) and radiative (rate constant k_R^*) relaxation of Cz_a^* to the groundstate may occur. The formed pair may dissociate following Onsager's formalism (rate constant k_d) or recombine back to Cz_a^* (rate constant k_r), which then open again all possible ways as just described. Furthermore, intersystem crossing of S_1 and Cz_a^* to the triplet manifold may happen. The processes relevant for generation of free charge carriers in PVK are schematically illustrated in figure (2.4 - 18).

The photogeneration process described above can be expressed by the following first-order kinetic equations:

$$\frac{[S_1]}{\tau} = \alpha I, \quad \text{eq. (2.4 - 168)}$$

$$\frac{[Cz_a^*]}{\tau_a} = k_a[S_1] + k_r[CT] \quad \text{eq. (2.4 - 169)}$$

and

$$\frac{[CT]}{\tau_{CT}} = k_i[Cz_a^*], \quad \text{eq. (2.4 - 170)}$$

where $[S_1]$, $[Cz_a^*]$ and $[CT]$ are stationary concentrations of the singlet state, the excitons trapped by active sites and bound electron - hole pairs and τ , τ_a and τ_{CT} are the corresponding lifetimes of these states, respectively. The parameters α and I are the absorption coefficient and the radiation intensity. The photogeneration efficiency Φ may be expressed as:

$$\Phi = \frac{k_d[CT]}{\alpha I}. \quad \text{eq. (2.4 - 171)}$$

The lifetimes in eq. (2.4 - 168) to eq. (2.4 - 170) may be expressed as:

$$\tau = \frac{1}{k_a + k_b + k_N}, \quad \text{eq. (2.4 - 172)}$$

$$\tau_a = \frac{1}{k_N^* + k_R^* + k_i}, \quad \text{and} \quad \text{eq. (2.4 - 173)}$$

$$\tau_{CT} = \frac{1}{k_d + k_r}, \quad \text{eq. (2.4 - 174)}$$

where the first two are assumed to be field independent, whereas τ_{CT} is field dependent due to the field dependent dissociation rate constant $k_d(E)$. With eq. (2.4 - 168) to eq. (2.4 - 170) and eq. (2.4 - 172) to eq. (2.4 - 174), eq. (2.4 - 171) may be rewritten as:

$$\Phi = \frac{k_a k_d \tau_{CT}}{(k_a + k_b)(K + k_d \tau_{CT})} \quad \text{eq. (2.4 - 175)}$$

with:

$$K = \frac{k_N^* + k_R^*}{k_i}. \quad \text{eq. (2.4 - 176)}$$

The dissociation rate constant can be expressed in terms of the Onsager dissociation probability $f(r, \theta, E, T)$ according to eq. (2.4 - 161):

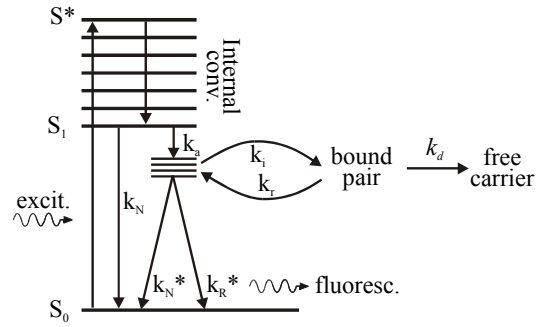


Figure (2.4 - 18): Charge carrier photogeneration model for PVK. The notation is defined in the allotted text.

$$k_d(r, \theta, E, T) = \frac{f(r, \theta, E, T)}{\tau_{CT}} \quad \text{eq. (2.4 - 177)}$$

Presuming a distribution of CT radii according to eq. (2.4 - 163), Cimrová et. al. obtained for the charge carrier photogeneration efficiency:

$$\Phi(r_0, E, T) = \Phi_0 \frac{F(r_0, E, T)}{K + F(r_0, E, T)}, \quad \text{eq. (2.4 - 178)}$$

where $F(r_0, E, T)$ is defined by eq. (2.4 - 164) and Φ_0 is given by:

$$\Phi_0 = \frac{k_a}{k_a + k_b + k_N}. \quad \text{eq. (2.4 - 179)}$$

According to Cimrová et. al., best theoretical fits are obtained for a distribution function of Ct radii according to eq. (2.4 - 167). The corresponding expression for the charge carrier photogeneration efficiency is then:

$$\Phi(\beta, E, T) = \frac{\Phi_{0\beta}}{\beta^3 \sqrt{\pi}} \int \frac{F(r_0, E, T)}{K + F(r_0, E, T)} e^{-\frac{r^2}{\beta^2}} 4r^2 dr. \quad \text{eq. (2.4 - 180)}$$

Here $\Phi_{0\beta}$ is the fraction of excitons becoming trapped in trapping sites active for charge carrier generation and the meaning of β is clarified subsequent to eq. (2.4 - 167).

Using this model, both the field and the temperature dependence of the charge carrier photogeneration can be explained with the same set of parameters $\Phi_{0\beta}$, β and K , as presented in [64].

2.4.4.3.)Langevin theory of geminate recombination

The Langevin theory of geminate recombination [69] is based on the assumption, that the mean distance between two oppositely charged particles is very large as compared to the mean free path length. Furthermore, the mean distance is assumed to be large enough, so that the electrostatic interaction between the particles is too small to effect their mutual trajectories. This requires, that two particles must considerably approach each other by random in order to result in a notable attractive electrostatic interaction. Since the mean distance is assumed to be much larger than the minimum distance resulting in some attractive interaction, it may safely be assumed that in average no third charged particle will be present in the case, when two oppositely charged particles happen to approach sufficiently to be attracted by one another. Thus, in the Langevin theory the problem of geminate recombination is basically reduced to a problem of two particles.

For an analytic treatment of this problem, one of the particles is assumed to be enclosed in a spherical surface S with the radius r being one tenth of the mean distance between the particles. The radius is thus chosen small as compared to the mean distance and large as compared to the mean free path length. The other (oppositely charged) particle is assumed to be in the immediate proximity of the enveloping surface. Furthermore it is assumed that geminate recombination occurs if the latter particle passes through S . Under these conditions, the particles may be assumed to move under the influence of their mutual electrostatic interaction, whereby their mobilities are the same as for some motion under the influence of some arbitrary external electrical field. The quantity in question now is the number of particles of the one sign enclosed by S , which are approached by a particle of the opposite sign passing through S in the time interval dt . This number of particles will solely depend on the relative velocity of the two

considered neighboring particles with respect to each other.

The velocities of the two considered particles are determined by their mobility, the sum of external electrical fields and the electrical field resulting from the neighboring oppositely charged particle. Thus, provided the electrical charge of the particles is one unit elementary charge, these velocities may be expressed as:

$$\dot{v}_1 = \mu_1 \left(\vec{E}_1 + \frac{q}{4\pi\epsilon r^2} \vec{e}_r \right) \quad \text{eq. (2.4 - 181)}$$

and:

$$\dot{v}_2 = -\mu_2 \left(\vec{E}_2 + \frac{q}{4\pi\epsilon r^2} \vec{e}_r \right). \quad \text{eq. (2.4 - 182)}$$

Here $E_{1,2}$ are the total local external electrical fields, $\mu_{1,2}$ are the mobilities, \vec{e}_r is the distance unit vector of the particles pointing towards the negative charge, q is the (modulus of the) elementary charge and ϵ is the total permittivity of the medium. The relative velocity of the particles with respect to one another thus will be:

$$\dot{v} = \dot{v}_1 - \dot{v}_2 = \mu_1 \vec{E}_1 + \mu_2 \vec{E}_2 + (\mu_1 + \mu_2) \frac{q}{4\pi\epsilon r^2} \vec{e}_r. \quad \text{eq. (2.4 - 183)}$$

Without loss of generality, one may now assume that the particle enclosed by S is locally fixed and assign the number density N to these particles. The other particle (assigned density P), which is about to pass through S within the time interval dt may then be considered to be inside a cylinder of volume $(\dot{v} \cdot \vec{dS})dt$, which may be interpreted as the flux through the infinitesimal surface element \vec{dS} . Summing up all these cylinders within an infinitesimal volume element dV of the overall medium considered and multiplying with the number density P yields the total flux of particles within dV through \vec{dS} approaching in order to recombine. In order to obtain the corresponding flux quantity through the complete enveloping surface S one has to integrate:

$$\begin{aligned} & P dt \sum_S \int \dot{v} \cdot \vec{dS} \\ &= P dt \sum \left[\mu_1 \int_S \vec{E}_1 \cdot \vec{dS} + \mu_2 \int_S \vec{E}_2 \cdot \vec{dS} + \frac{(\mu_1 + \mu_2)q}{4\pi\epsilon} \int_S \frac{\vec{e}_r}{r^2} \cdot \vec{dS} \right] \end{aligned} \quad \text{eq. (2.4 - 184)}$$

The term to the left hand side of eq. (2.4 - 184) may be interpreted as the relative number density of particles “ P ” in a spherical shell around one particle “ N ” passing through S in the interval dt . The first two integrals at the right hand side of eq. (2.4 - 184) yield zero according to eq. (2.1 - 5) (Gauss’s law), since neither E_1 nor E_2 are correlated with some charge enclosed by S and the third integral yields just 4π . The complete term in square brackets is moreover identical for each particle “ N ” and thus occurs N times in the volume element dV . Accordingly, one obtains eventually:

$$P dt \sum_S \int \dot{v} \cdot \vec{dS} = P dt \sum \frac{(\mu_1 + \mu_2)q}{\epsilon} = \frac{(\mu_1 + \mu_2)q}{\epsilon} NP dt dV. \quad \text{eq. (2.4 - 185)}$$

Langevin referred to the term on the right hand side of eq. (2.4 - 185) as the “number of collisions resulting in geminate recombination within the time interval dt in the volume dV ”. It is straight forward, that the number of particles per unit volume recombining in the interval dt is given by:

$$dN = dP = -\frac{(\mu_N + \mu_P)q}{\epsilon} NP dt, \quad \text{eq. (2.4 - 186)}$$

where N and P are the number densities of the involved charged particles, μ_N and μ_P are their mobilities, respectively, q is the elementary charge and ε is the total permittivity of the medium. Eq. (2.4 - 186) is Langevin's law for geminate recombination and may be rewritten as:

$$dN = dP = -\gamma_R NP dt \quad \text{eq. (2.4 - 187)}$$

with:

$$\gamma_R = \frac{(\mu_N + \mu_P)q}{\varepsilon} \quad \text{eq. (2.4 - 188)}$$

as (geminate) recombination coefficient γ_R .

2.5.)The photorefractive effect

2.5.1.) Phenomenology of the photorefractive effect

The photorefractive effect was discovered in 1966 by A. Ashkin et. al. [8], who observed a refractive index change in LiNbO_3 as a result of intensive laser irradiation. However, this observation was initially misinterpreted as optical damage instead of a new nonlinear optical effect. During the subsequent 5 years basic work by F.S. Chen [9] and J.J. Amodi [70] was done on the identification of the photorefractive (PR) effect as a new effect of nonlinear optics with high application potential and on the enlightenment of its fundamental mechanism. The PR effect has been recognized as a reversible photoinduced refractive index change in certain materials opening the way to reversibly store optical interference fields, i.e. holograms. In order to be photorefractive, a material must show the subsequent essential properties besides the trivial demand for high transparency at the operating wavelength:

- ➔ The material must be photoconducting, which demands a minimum of absorption at the operating wavelength. The photogenerated charges must have different mobility, i.e. ideally the photoconduction should be monopolar.
- ➔ The material must exhibit some electro-optic effect (Pockels- and/or electrical Kerr effect), i.e. it must be optically nonlinear.

The build-up of a PR refractive index grating in a suitable medium as a result of nonuniform illumination may formally be divided into four subsequent steps, which, however, actually take place simultaneously. These steps are illustrated in figure (2.5 - 1). The diagram must be read from top to bottom and covers the following steps:

- ➔ Nonuniform illumination of the PR material with an optical interference field. The simple case of an sinusoidal pattern is assumed without loss of generality. I_1 is the modulation amplitude of the interference field and I_0 the average intensity. A surplus of free charge carriers is photogenerated in the bright(er) areas as compared to the dark(er) areas. Without loss of generality their countercharges are assumed to be immobile.
- ➔ The mobile charge carriers are redistributed from the bright(er) areas in the medium to the dark(er) areas by means of diffusion or drift under the influence of an externally applied field and eventually will be trapped in the dark(er) areas. This yields a spatially varying space-charge distribution, which reproduces the shape of the interference pattern. In the case of pure diffusion, the space-charge distribution will be in-phase or anti-phase to the interference pattern, whereas there will be

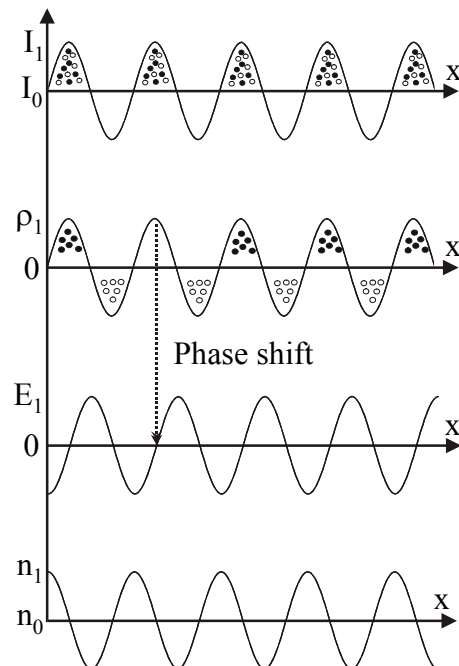


Figure (2.5 - 1): Formal steps of the photorefractive grating build-up

some dephasing in-between these limits if charge carrier drift contributes notably to the redistribution process.

- ➔ Some space-charge distribution will give rise to a space-charge field according to Poisson's equation (eq. (G - 5)), which is dephased with respect to the space-charge distribution. The dephasing will amount to $\pi/2$ (90°) for the case of a sinusoidal space-charge distribution. Hence, depending on the dominant charge transport mechanism (diffusion or drift) an overall phase shift of the space-charge field with respect to the interference pattern in-between 0 and $\pm\pi/2$ will occur.
- ➔ The space-charge field modulates the refractive index of the material by means of the linear and/or the quadratic electro-optic effect. Depending on the mechanism, which modulates the refractive index as a function of the space-charge field, the resulting refractive index pattern will be in-phase or anti-phase to the space-charge field. Thus, the refractive index grating will be out of phase with respect to the interference pattern, which is a unique feature of the photorefractive effect. This inherent phase shift between the index grating and its generating interference pattern leads to coherent energy exchange between the beams generating the interference field, which is referred to as "two-beam coupling". The recorded hologram may be read out by standard holographic methods.

2.5.2.) The photorefractive effect in inorganic crystals

As mentioned before, the photorefractive effect was first discovered in inorganic crystals, which was the only class of materials known to be possibly photorefractive for the succeeding two decades. Fundamental work therefore focused upon systems, the electrical conduction properties of which can be described by the band transport mechanism. The band transport model of the photorefractive effect, however, cannot be transferred to amorphous organic PR polymers, which this work is mainly focused upon and which follow a completely different electrical conduction mechanism as discussed before in "2.4.3.) Electrical conduction in organic polymers" on page 95. Nevertheless, the basic concepts of the band transport model developed by Kukhtarev et.al. [71] are still essential in understanding photorefractivity. Thus, the basic results of the band transport model will be depicted below, however, excluding special aspects, which are absent or at least negligible in PR polymer. For example photovoltaic effects, which can be very important in crystals, are negligible in polymers due to the strong external electric field usually applied to these systems. The derivation of the below presented results is outlined in Appendix G.

2.5.2.1.) The band-transport model of the photorefractive effect (Kukhtarev-model)

The Kukhtarev-model presumes, that there is a fixed and constant number of impurities and/or defects in the PR medium, which may serve as charge carrier sources or traps depending on their initial ionization state. The redox-system $\text{Fe}^{2+}/\text{Fe}^{3+}$ in a LiNbO_3 crystal is a typical example, where the Fe^{2+} ions may act as donor-impurities (referred to hereafter simply as „donors“) capable of releasing an electron into the conduction band upon optical excitation and the Fe^{3+} ions may act as acceptor-impurities (referred to hereafter as acceptors) capable of

trapping a free electron from the conduction band.

A system as described above will always contain donors as well as traps (i.e. even in the dark, when there are no photoinduced traps and charges) as implied by the electro-chemical equilibrium of such a system in sufficiently polar solution. Donors and acceptors are presumed to be of identical species, having identical energy levels located somewhere in the band gap of the system. This, in turn, implies that only ionized donors are considered as traps, which requires the introduction of fictive acceptor sites ensuring a non vanishing trap density in the dark without violating the demand for macroscopic electrical neutrality of the system. These acceptor levels are often referred to as “compensating charges” since they “compensate” the “excess charges”, which arise from the existence of ionized donor levels without having donated a charge carrier into the conduction band. The “compensating charges” themselves do not take an active part in the photorefractive effect (the allotted traps, however, do). Figure (2.5 - 2) illustrates the model.

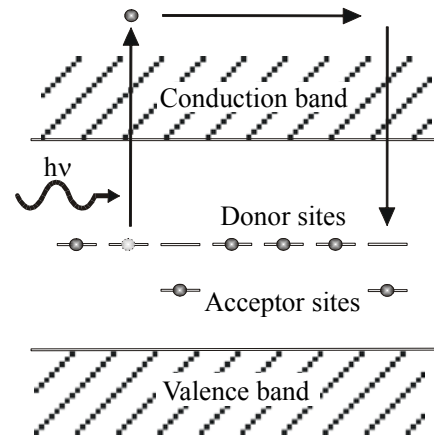


Figure (2.5 - 2): Kukhtarev's band transport model of the photorefractive effect

Upon non-uniform illumination charge carriers are excited from Donor sites in the bright areas and diffuse or drift in the dark areas, where they get trapped by acceptor sites. This gives rise to a non-uniform space-charge distribution, which entrains a corresponding space-charge field, the photorefractive space-charge field. A more detailed discussion of this process as well as its theoretical description is provided in Appendix G. Subsequently, only the resulting expressions for the space-charge field and the photorefractive phase shift will be presented.

2.5.2.1.1.)Steady-state solution for the space-charge field

Neglecting photovoltaic contributions, from Kukhtarev's model the following expression for steady-state photorefractive space-charge field E_{sc} is obtained:

$$E_{sc}(\vec{r}) = -M \left[\frac{E_0 E_q^2}{(E_q + E_d)^2 + E_0^2} \cos(\vec{K} \cdot \vec{r}) + \frac{E_d E_q^2 + E_q E_0^2 + E_q E_d^2}{(E_q + E_d)^2 + E_0^2} \sin(\vec{K} \cdot \vec{r}) \right] \quad \text{eq. (2.5 - 1)}$$

where E_0 is the projection of an externally applied dc field onto the grating wave vector K and the field quantities E_d and E_q are given by:

$$E_d \equiv K \frac{k_B T}{q} \quad \text{eq. (2.5 - 2)}$$

and

$$E_q \equiv q \frac{N_A}{\langle \epsilon \rangle K}. \quad \text{eq. (2.5 - 3)}$$

Here, k_B is the Boltzmann factor, T is the temperature, q is the elementary charge, N_A is the density of charge carrier traps (acceptor sites) and $\langle \epsilon \rangle$ is the average permittivity. E_d is called “diffusion field” and may be taken as the field strength, which arises, if charge separation solely due to diffusion takes place between the bright and the dark areas along the grating vector until steady-state is achieved, i.e. until the formed electrical field suppresses further charge separation. E_q is called “saturation field” and represents the hypothetical field strength, which may be achieved, if the maximum available charge carriers are separated between the bright and

the dark areas. This state would correspond to a situation in which “all traps are filled”, i.e., more exactly, the number density of ionized donor/acceptor levels in the bright area has taken on its inherent maximum value, whereas in dark area all these sites are occupied, and the charge carrier concentration in the conduction band is zero.

The quantity M is a contrast factor given by:

$$M = m \frac{\sigma_{ph}}{\sigma_d + \sigma_{ph}}. \quad \text{eq. (2.5 - 4)}$$

where m is the contrast factor of the light fringe pattern according to eq. (2.1 - 47) and σ_{ph} and σ_d are the photoconductivity and the dark conductivity of the medium, respectively. The latter is due to thermal excitation of charge carriers. The quotient to the right hand side of eq. (2.5 - 4) is commonly referred to as „conductivity contrast“.

The phase shift ϕ between the interference pattern and the space-charge field is given by:

$$\phi = \text{atan} \frac{E_d(E_d + E_q) + E_0^2}{E_0 E_q}. \quad \text{eq. (2.5 - 5)}$$

Please note that ϕ approaches $\phi = 90^\circ$ for $E_0 = 0$ and $\phi < 90^\circ$ for $E_0 > 0$.

2.5.2.1.2.) Dynamics of the space-charge field

2.5.2.1.2.1.)Build-up dynamics

Kukhtarev’s model provides the following expression for the build-up of the physical space-charge field E_{sc} :

$$E_{sc}(\vec{r}, t) = E_{sc}[-\cos(\vec{K} \cdot \vec{r} + \phi) + \cos(\vec{K} \cdot \vec{r} + \phi + \omega_g t) e^{-t/\tau_g}], \quad \text{eq. (2.5 - 6)}$$

where E_{sc} is the amplitude of the steady-state space-charge field according to eq. (2.5 - 1), given by:

$$E_{sc} = M \sqrt{\frac{E_q^2 (E_0^2 + E_d^2)}{E_0^2 + (E_d + E_q)^2}}, \quad \text{eq. (2.5 - 7)}$$

with M and the characteristic fields as defined before, and ϕ is the phase angle according to eq. (2.5 - 5). The time constant for the build-up of the space-charge field τ_g is given by:

$$\tau_g = t_0 \frac{(E_\mu + E_d)^2 + E_0^2}{E_d^2 + E_d E_\mu + E_\mu E_q + E_d E_q + E_0^2} \quad \text{eq. (2.5 - 8)}$$

and the phase addend ω_g reads:

$$\omega_g = \frac{1}{t_0} \cdot \frac{E_\mu E_0 - E_q E_0}{(E_\mu + E_d)^2 + E_0^2}. \quad \text{eq. (2.5 - 9)}$$

The quantity E_μ is another characteristic field quantity referred to as drift field:

$$E_\mu = \frac{\gamma_R N_A}{\langle \mu \rangle K} \quad \text{eq. (2.5 - 10)}$$

and the parameter t_0 is a characteristic time constant defined by:

$$t_0 = \frac{N_A}{f_0 N_D}. \quad \text{eq. (2.5 - 11)}$$

Please note that ω_g represents an important feature of PR crystals. It implies an oscillation superposing the exponential part during the build-up of the PR grating in the presence of an externally applied field. The oscillation may be considered as the result of a moving grating with respect to the stationary intensity pattern during build-up. The significance of this feature will be discussed in short terms at the end of the following section.

2.5.2.1.2.2.)Erasure dynamics

In analogy to eq. (2.5 - 6) the erasure dynamics of the space-charge field may be expressed as:

$$E_{sc}(\vec{r}, t) = E_{sc}[\cos(\vec{K} \cdot \vec{r} + \phi + \omega_g t)e^{-t/\tau_g}]. \quad \text{eq. (2.5 - 12)}$$

Here, E_{sc} represents the initial value of the photorefractive space-charge field when the erasure process starts and, thus, is only defined by eq. (2.5 - 7), if the space-charge field has been recorded to steady-state prior to the erasure process. In contrast, the quantities ϕ , τ_g and ω_g are defined by eq. (2.5 - 7), eq. (2.5 - 8), and eq. (2.5 - 9) independently from the initial grating strength. Accordingly, the time history of grating erasure does not depend on the initial grating strength.

Please note that eq. (2.5 - 12) does NOT imply an oscillation but rather only the grating spatially moving by $-\vec{K} \cdot \vec{r} = \omega_g t$. Since there is no “phase reference“ (i.e. the term “ $-\cos(\vec{K} \cdot \vec{r} + \phi)$ “ at the right hand side of eq. (2.5 - 6)) during erasure, no oscillation of $E_{sc}(t)$ will be observed, whereas the basic mechanism causing the oscillation remains unchanged. Accordingly, the erasure process will be simply mono-exponential even with an external field applied.

The oscillation during the formation of the PR grating and its absence during erasure has important consequences. In suitable PR crystals, the grating build-up may be considerably faster than the grating erasure as a result of the superposition of the oscillation and the exponential growth term. PR media showing this feature are preferable candidates for potential application in holographic storage, especially utilizing holographic multiplexing techniques as discussed in “2.3.3.) Holographic data storage” on page 60.

2.5.3.) Photorefractivity in amorphous organic polymers

Some of the basic assumptions Kukhtarev presumed for the development of his famous model are inadmissible for amorphous organic materials. Therefore, strictly speaking, Kukhtarev’s model cannot be applied to PR polymers, even so it is still pretty common to discuss organic PR polymers on the basis of this model. Although many conclusions drawn from the application of Kukhtarev’s model to photorefractive polymers seem somehow reasonable, it is quite unsatisfying to argue on the basis of a model, which is well-known to be in fact not applicable. Subsequently, the main deviations of PR polymers from Kukhtarev’s model are outlined and a more suitable model to describe photorefractivity in disordered organic solids is presented. This model, basically developed by Schildkraut et.al., yields a steady-state solution for the space-charge field as well as transient solutions, which are presented as well. Finally, the orientational enhancement effect is described, which accounts for the particular orientational effects observable in low-glass-transition PR polymers and their extraordinary steady-state performance.

Please note, that photorefractive polymers require an external field not only for breaking the inherent statistical centrosymmetry, but also to support the charge generation and to enable charge carrier redistribution by charge carrier drift. The latter requires that the external field has a non-vanishing projection onto the grating wave vector of the interference pattern. Therefore, photorefractive polymers are usually operated in a tilted geometrical configuration, which is depicted in figure (2.5 - 3). Hereafter the tilted geometry will generally be presumed when considering PR polymers unless explicitly noted otherwise. In figure (2.5 - 3), K denotes the grating wave vector, I_{01} and I_{02} are the recording beams for the grating and E_{ext} is the externally applied field. The angles are self-evident. Hereafter, this notation will be maintained as consistent as possible throughout this work.

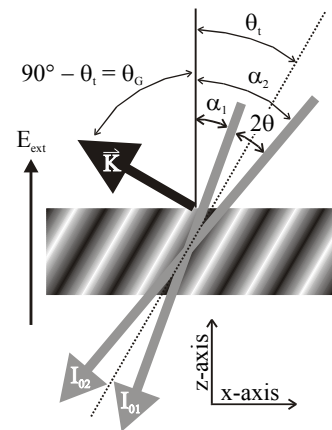


Figure (2.5 - 3): Typical geometry for PR polymers.

2.5.3.1.) Limitations of Kukhtarev's model

An obvious limitation is the premise of a field independent charge carrier photogeneration efficiency. Twarowski [72] already introduced an Onsager type field dependence for the photogeneration efficiency into Kukhtarev's model in order to describe the influence of geminate recombination in PR crystals. This resulted in the prediction of a considerable slow down of the grating formation speed in materials exhibiting a low dielectric constant, whereas the steady-state space-charge field is only affected to a minor extent.

It is furthermore clear, that the assumption of a field independent charge carrier mobility can not account for the situation found in disordered organic solids, as described in "2.4.3.) Electrical conduction in organic polymers" on page 95.

Finally, Kukhtarev's model presumes a dedicated nature of the traps inherent in the system, which are represented by the compensating sites as depicted in figure (2.5 - 2). However, the physical nature of the traps is not yet clear in organic materials. It seems reasonable to assume, that the charge carrier generation sites (donors) may act as traps once they have generated a charge carrier, thus being then charged themselves, like an acceptor site in a PR crystal. On the other hand, there is very strong indication, that there are several other neutral potential trapping sites in addition to the ionized donors, the nature of which is still unclear and the number density of which is not directly accessible.

There are several more complications in disordered organic systems, which may have impact on the PR behavior. For example, the Einstein relation between drift and mobility is not valid in polymers subject to a strong external field applied as discussed in "2.4.3.3.1.) The Einstein relationship" on page 108. A field enhanced diffusion process has been postulated to explain the experimentally found discrepancies [52, 73]. Moreover, there is some indication, that the trap density in PR polymers may vary on several parameters like light irradiance [74, 75, 76], glass-transition temperature and others.

In conclusion, it seems quite impossible to try to account for all implications, which may occur in PR polymers. However, there is a model derived by Schildkraut et. al., which approaches the conditions found in PR polymers much closer than Kukhtarev's model.

2.5.3.2.) Schildkraut's model

In its basics Schildkraut's model [77, 78] is fairly similar to Kukhtarev's model. The mobile charge carriers are assumed to be holes and to be photogenerated from neutral electron accepting moieties. The negative countercharges are assumed to be fixed at the ionized sensitizer moieties. A shallow trap level is taken into account as was introduced by Tayebati et al. for PR crystals [79]. Finally, the charge carrier photogeneration efficiency and the hole mobility are allowed to be field dependent.

The field dependency of the photogeneration efficiency $\Phi(E)$ is basically described by the Onsager theory (page 110). Twarowski already introduced a field dependency of the photogeneration efficiency into Kukhtarev's model [72]. He used Onsager's expression for the quantum yield expanded to the first order in the electrical field [80]:

$$\phi(E) = \phi_0 \left(1 + \frac{E}{2E_C} \right) e^{-\frac{r_C}{r_0}}, \quad \text{eq. (2.5 - 13)}$$

where r_0 is the initial separation length of the thermalized charge carrier from its generation site, r_C is the Coulomb radius according to eq. (2.4 - 158) and E_C is a characteristic field reading:

$$E_C = \frac{k_B T}{q r_C}. \quad \text{eq. (2.5 - 14)}$$

In contrast, Schildkraut et al. assumed that the field dependency of the photogeneration efficiency within the interval of external fields typically applied to PR polymers (about 10V/ μm - 100V/ μm) may be approximated with sufficient accuracy by a simple power law [78]:

$$\Phi(E) = \Phi_i E^p, \quad \text{eq. (2.5 - 15)}$$

where Φ_i is a constant and p is a system dependent empirical parameter to be determined experimentally. However, according to [78] this relation was derived from a plot depicted in [67] by sense of proportion and, thus, is not an experimentally confirmed relationship. It should rather be considered as a rule of thumb, which has been widely accepted as some reasonable approximation as PR polymers have moved into the focus of interest. In fact, the validity of eq. (2.5 - 15) appears rather arguable.

The field dependency of the hole mobility $\mu(E)$ is described using the hopping transport formalism in disordered organic systems [81]:

$$\mu(E) = \mu_i e^{C(\sqrt{E}-1)}, \quad \text{eq. (2.5 - 16)}$$

where μ_i is a constant and C is an experimentally obtained characteristic parameter. A charge carrier once generated may recombine with one of the fixed countercharges, i.e. an ionized sensitizer N_G^+ , or be trapped in a neutral trap N_T . Recombination is assumed to follow the Langevin theory (page 115), whereas this assumption is relaxed for trapping, since traps are not required to be charged. Eventually, charge carriers trapped in shallow traps may thermally be detrapped again and further participate in the overall process. A schematic of Schildkraut's model is depicted in figure (2.5 - 4). Subsequently, the results of Schildkraut's model are presented in SI units. A detailed derivation of the given expressions is provided in Appendix H.

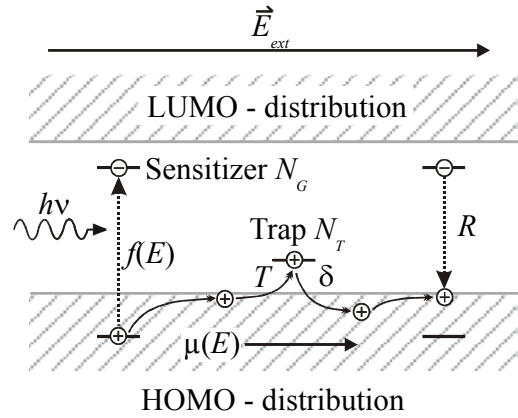


Figure (2.5 - 4): Energy level scheme of Schildkraut's model. $f(E)$ is the generation rate, T represents trapping and R recombination and δ stands for detrapping.

2.5.3.2.1.)Steady state solutions for the space-charge field in polymers

Schildkraut et. al. considered the limiting case of deep traps, i.e. detrapping is considered negligible. All traps can then be considered as filled if the system has reached its steady-state. Based on these perceptions, Schildkraut et. al. obtained the following expression for the modulus of the steady state photorefractive space-charge from their model:

$$|E_{sc}| = \frac{m\Upsilon E_q \sqrt{E_0^2 + E_D^2}}{\sqrt{\left[E_D + E_q(1 + \Upsilon p) + E_I \left(\frac{E_m}{E_0} + 1 \right) \right]^2 + \left[E_0 + \frac{E_D E_q}{E_0} \left(\frac{E_m}{E_0} - \Upsilon p \right) \right]^2}}, \quad \text{eq. (2.5 - 17)}$$

where p stems from eq. (2.5 - 15) and the parameter Υ given by:

$$\Upsilon = f_0 \frac{(N_{G,i} - N_{T,i} - n_0)}{\gamma_{R0} n_0 (n_0 + N_{T,i})}. \quad \text{eq. (2.5 - 18)}$$

Here, $N_{G,i}$ and $N_{T,i}$ are the initial densities of neutral sensitizers and traps, respectively. n_0 , γ_{R0} , and f_0 are the zero hole density, the zero order recombination rate, and the zero order charge generation rate, respectively, analytical expressions for which are provided in Appendix H. The field quantities are defined as:

$$E_D = \frac{k_B T}{q} K, \quad \text{eq. (2.5 - 19)}$$

$$E_q = \frac{\gamma_{R0} (n_0 + N_{T,i}) q n_0}{(f_0 + \gamma_{R0} n_0) K \varepsilon}, \quad \text{eq. (2.5 - 20)}$$

$$E_I = \frac{q n_0}{\varepsilon K}, \quad \text{and finally} \quad \text{eq. (2.5 - 21)}$$

$$E_m = \frac{C}{2} \sqrt{E_0} E_0. \quad \text{eq. (2.5 - 22)}$$

Here, k_B is the Boltzmann factor, T is the temperature, q is the elementary charge, K is the grating wave vector, ε is the permittivity, E_0 is the projection of the externally applied onto K and the parameter C stems from eq. (2.5 - 16). Please note, that the ‘‘field’’ in the square root carries no dimension, but has the value of E_0 .

E_D obviously is the diffusion field. The other fields do not correlate directly to some classical field quantities known from Kukhtarev’s model. However, E_I may be interpreted as a kind of general current saturation field, since it may be taken as the maximum field achievable by separating the zero order charge carrier density determining the current flowing through the sample in the steady-state case over one grating period of the PR grating. E_q may then be taken as E_I normalized by the ratio of hole recombination and generation, which may be interpreted as correction by some contrast factor depending on a particular system. Accordingly, E_q may be taken as some ‘‘real’’ current saturation field. E_m may be taken as a ‘‘mobility’’ field, i.e. a field due to different charge carrier mobilities. In a sense, this has some phenomenological similarity to the drift field in Kukhtarev’s model.

For the phase shift ϕ of the space-charge field with respect to the interference pattern Schildkraut et. al. obtained:

$$\tan \phi = \frac{E_0^2 + E_D(E_D + E_I + E_q) + \frac{E_D E_m}{E_0} (E_I + E_q)}{\frac{E_D^2 E_q}{E_0} \left(\frac{E_m}{E_0} - \Upsilon p \right) - E_0 E_q (1 + \Upsilon p) - E_0 E_I \left(1 + \frac{E_m}{E_0} \right)}. \quad \text{eq. (2.5 - 23)}$$

If the density of deep traps $N_{T,i}$ is assumed to be much smaller than the zero order hole

density n_0 and if the photogeneration efficiency is assumed to be much smaller as compared to the initial hole trapping rate, E_I in eq. (2.5 - 17) and in eq. (2.5 - 23) becomes negligible and Y approaches unity. In this case, the expressions eq. (2.5 - 17) and eq. (2.5 - 23) become similar to the corresponding results obtained from Kukhtarev's model.

Eventually, it is particularly important to point out, that the results of Schildkraut's model imply a steady-state situation in the sense of an equilibrium state with a considerable current flowing permanently through the system. This is fundamentally different from Kukhtarev's model, which basically assumes vanishing charge carrier concentration in the conduction band once the steady-state is reached and, hence, no current flowing through the sample even with an external field applied. On the other hand, the Schildkraut model does not account for thermal generation of charge carriers as introduced for the Kukhtarev model. However, thermal generation of holes will simply increase the zero order hole density n_0 as will do any other process different from photogeneration, which supplies the system with mobile charge carriers (e.g. by injection from the electrodes). An increase of n_0 results in a reduction of the space-charge field amplitude.

2.5.3.2.2.) Build-up dynamics for the space-charge field in polymers

Based on Schildkraut's model, Yuan et. al. derived an analytical expression for the build-up dynamics of the space-charge field in polymers [82]. Subsequently, their results are presented in SI units. A detailed derivation of the given expressions is provided in Appendix H. The physically relevant real part of the complex space-charge field may be expressed in similar form like eq. (2.5 - 6). Without loss of generality, the problem is expressed one-dimensional:

$$E_{sc}(x, t) = R_1[\cos(Kx + \phi_1) - R_2 \cos(Kx + \omega_1 t + \phi_1 + \phi_2) e^{-\frac{t}{\tau_{sc1}}} - R_3 \cos(Kx + \omega_2 t + \phi_1 + \phi_3) e^{-\frac{t}{\tau_{sc2}}}] \quad \text{eq. (2.5 - 24)}$$

where R_1 and ϕ_1 , R_2 and ϕ_2 , and R_3 and ϕ_3 are the amplitudes and phases of corresponding complex expressions, the explicit form of which is given in Appendix H. The time constants $\tau_{sc1,2}$ are:

$$\tau_{sc1} = -\frac{1}{Re\left(\frac{-b + \sqrt{b^2 - 4ac}}{2a}\right)} \quad \tau_{sc2} = -\frac{1}{Re\left(\frac{-b - \sqrt{b^2 - 4ac}}{2a}\right)} \quad \text{eq. (2.5 - 25)}$$

For the meaning of the parameters a , b , and c reference is made to Appendix H. The circular frequencies ω_1 and ω_2 add a phase to the two decaying waves of the amplitudes R_2 and R_3 , which may be interpreted as some spatial shift of corresponding grating components during build-up of the space-charge field, as discussed before for PR crystals. This may or may not result in an oscillation observable during grating build-up depending on the numerical values of the involved quantities. The parameters ω_1 and ω_2 read:

$$\omega_1 = \text{Im} \left(\frac{-b + \sqrt{b^2 - 4ac}}{2a} \right)$$

$$\omega_2 = \text{Im} \left(\frac{-b - \sqrt{b^2 - 4ac}}{2a} \right)$$

eq. (2.5 - 26)

For the meaning of the parameters a , b , and c again reference is made to Appendix H.

Please note in particular, that this theory predicts a possible oscillation of the PR grating. Such an oscillation would be an important feature since it may accelerate the grating build-up relative to the erasure, which is helpful (however, not essential) for successfully applying holographic multiplexing techniques, as already mentioned before for PR crystals. However, in contrast to PR crystals, such an oscillation has not been observed experimentally in polymers so far. This may be due to the fact, that real systems are believed to always contain a considerable amount of shallow traps, even if doped with deep traps, which may suppress such an effect.

2.5.3.2.3.)Erasure dynamics of the space-charge field in polymers

The erasure dynamics of PR polymers may be considered in two ways. The first and most proximate way is to invert the boundary conditions applied for deriving the build-up dynamics (see Appendix H). However, this approach suffers from the basic limitation to a system with solely deep traps, which has been applied in order to obtain an analytical solution for Schildkraut's model.

On the other hand, Cui et. al. recently presented a more detailed analysis of the erasure process in PR polymers [83] taking into account different levels of traps. This analysis focusses on the intensity dependence of the erasure rate rather than the general erasure behavior and therefore uses a simplified approach, not accounting for a particular field dependency of the charge carrier generation efficiency and the charge carrier mobility as in Schildkraut's model. The dependence of the erasure rates on the erasing intensity has been found to be sublinear in PR polymers by several working groups [84 - 86] which may be expressed as:

$$\frac{1}{\tau} \propto I^\alpha$$

eq. (2.5 - 27)

and Cui et. al. include the aforementioned field dependencies in a field dependency of the power index in eq. (2.5 - 27).

Both approaches enumerated above will be outlined below and are discussed in more detail in Appendix H. As will be shown, the basic results are similar, however, not really identical. The approach by Cui et. al. provides a more detailed insight into the erasure process in PR polymers, whereas the first of the above noted approaches is important, since it is a direct consequence of Schildkraut's model. Both approaches can only be approximations and reflect the problem, that there is still no satisfyingly consistent theoretical basis for the photorefractive effect in polymers.

2.5.3.2.3.1.)Erasure dynamics in Schildkraut's model

As mentioned before, the erasure dynamics of the space-charge field in PR polymers may be described on the basis of Schildkraut's model. This analysis basically follows the same path as in "2.5.3.2.2.) Build-up dynamics for the space-charge field in polymers" on page 126 applying different boundary conditions. For details reference is made to Appendix H. The physically relevant real part of the complex space-charge field can be expressed in a form

similar to eq. (2.5 - 6):

$$E_{sc}(x, t) = R_1' \cos(Kx + \omega_1 t + \phi_1') e^{-\frac{t}{\tau_{sc1}}} + R_2' \cos(Kx + \omega_2 t + \phi_2') e^{-\frac{t}{\tau_{sc2}}} \quad \text{eq. (2.5 - 28)}$$

where R_1' and ϕ_1' and R_2' and ϕ_2' are the amplitudes and phases of corresponding complex expressions, the explicit form of which is given in Appendix H. The time constants $\tau_{sc1,2}$ are given by eq. (2.5 - 25). The circular frequencies ω_1 and ω_2 are given by eq. (2.5 - 26).

Please note, that the general law represented by eq. (2.5 - 28) will be universal, provided the terms of the sum are independent. However, the analytic expressions for the coefficients will depend on the boundary conditions for $t = 0$. Please note furthermore, that the circular frequencies add phases to the erasure components as already described above. This may be interpreted as some spatial shift of corresponding grating components during erasure of E_{sc} , as discussed for PR crystals. Since the circular frequencies are different, the relative weighting of the erasure components should be expected to change in time. Hence, despite there is no more a phase reference being constant in time like in eq. (2.5 - 24), the phases should affect the erasure behavior as opposed to the situation found in PR crystal and discussed before in “2.5.2.1.2.) Dynamics of the space-charge field” on page 121. Thus, some kind of oscillation is implied in PR polymers for the erasure process as well.

2.5.3.2.3.2.)Cui's approach to the erasure dynamics

According to Cui et. al. [83], the main factors affecting the dynamics of the space-charge field in some PR material are the generation, transportation, and trapping of charge carriers. The field dependency of the quantum efficiency of charge generation, the charge trapping rate and the charge carrier mobility result from the positional and energetic disorder of the charge transporting and trapping sites in the polymer matrix. Presumed that holes are the only free charge carriers present in the medium and that their negative countercharges are fixed at the generation sites, the energy levels of the trapping sites should follow some particular distribution, and there will be a certain density of traps for a given energy level E . Trapped holes may be detrapped thermally and/or optically with different detrapping rates depending on the energy levels of the involved trapping sites. Thus, integrating over all energy levels at a given external field results in rate equations taking into account the non-discrete character of the involved parameters. By means of the mean value theorem of integrals, the set of rate equations involving integrals of non-discrete parameters can then be reduced to a set of rate equations containing characteristic discrete values of the parameters in question for the particular system considered. For more details reference is made to Appendix H. As a solution for the latter set of rate equations, Cui et. al. obtained for the complex space-charge field $E_1(t)$ in terms of the rate constants:

$$E_1(t) = -\frac{iq}{\varepsilon K} \left[\Xi e^{-\frac{t}{\tau_1}} + \frac{(DK^2 + iK\mu E_0)N_{T10}^i}{1/\tau_1 - 1/\tau_2} e^{-\frac{t}{\tau_2}} - \frac{(DK^2 + iK\mu E_0)N_{G10}^i}{1/\tau_1 - 1/\tau_3} e^{-\frac{t}{\tau_3}} \right] \quad \text{eq. (2.5 - 29)}$$

where μ is the charge carrier mobility, ε is the total (effective) permittivity, and D is the diffusion coefficient. N_{G10}^i and N_{T10}^i are the initial values of the first order spatial Fourier components of the densities of ionized charge generators and filled traps, respectively, q is the elementary

charge. K is the grating wave vector, E_0 is the projection of the externally applied field onto the grating wave vector, and Ξ is a constant, which can be found by setting $E_1(t) = E_1(t=0)$. $N_{T10}^i = N_{T1}(t=0)$ and $N_{G10}^i = N_{G1}(t=0)$, and the three decay rate constants are:

$$\frac{1}{\tau_1} = \frac{q\mu}{\varepsilon}n_0 + DK^2 + iK\mu n_0, \quad \text{eq. (2.5 - 30)}$$

$$\frac{1}{\tau_2} = \alpha_G + \gamma_R n_0, \text{ and} \quad \text{eq. (2.5 - 31)}$$

$$\frac{1}{\tau_3} = \delta + \gamma_T n_0. \quad \text{eq. (2.5 - 32)}$$

Here, n_0 is the zero order hole density and α_G , γ_R , γ_T and δ are the characteristic, discrete values of the system for the charge generation rate, the charge carrier recombination rate, the trapping rate and the detrapping rate, respectively, and α_G and δ are given by:

$$\begin{aligned} \alpha_G &= s_G I \\ \delta &= s_T I + \beta \end{aligned} \quad \text{eq. (2.5 - 33)}$$

with the characteristic, discrete values of s_G , s_T , and β . These parameters are the cross section for light excitation of the charge generating sites, the cross section for optical detrapping of charges from filled trapping sites and the thermal detrapping rate, respectively.

Among these above rate constants, $1/\tau_3$ is the smallest one and is attributed to the existence of traps. $1/\tau_1$ is complex implying an oscillation as already derived and discussed above.

For a case of low light intensity, which is usually typical for holographic experiments in photorefractives, the photogeneration rate (i.e. the rate of generation of holes from neutral sensitizers) will be small as compared to the geminate recombination rate (i.e. the product of the zero order hole density and the geminate recombination coefficient). This may ostensibly be explained considering the fact, that there is already a considerable amount of holes distributed in the system stemming from the previous recording process, thus, decoupling the zero order hole density from the photogeneration process. Hence, the approximation of low light intensity also refers to some extent to the recording intensity and will be valid as long as the erasure intensity is not markedly higher than the spatial average of the recording intensity has been. However, it is clear, that this point of view requires as well, that the system is operated in the range of non-saturation, i.e. in this case that the trap density in the system is sufficiently high as compared to the density of photogeneration centers. This condition is usually fulfilled in organic amorphous PR systems, since a high trap density may be implied by principle due to the mechanism underlying the hopping transport model [87]. Thus, the explicit demand for non-saturation actually refers to inorganic PR crystals rather than to PR polymers. Furthermore, uniform illumination will cause a small average hole trapping rate as compared to the detrapping rate, which may be understood when considering, in contrast, the recording process, where the average hole trapping rate will be higher due to the higher trapping rate in the dark areas. Hence, one may conclude that the detrapping rate δ dominates in eq. (2.5 - 32), which is proposed in the original literature without reasoning.

Taking furthermore only the real part of eq. (2.5 - 30) and assuming Langevin mechanism for the recombination (see "2.4.4.3.) Langevin theory of geminate recombination" on page 115), the rate constants simplify to:

$$Re\left(\frac{1}{\tau_1}\right) = \gamma_R n_0 + DK^2, \quad \text{eq. (2.5 - 34)}$$

$$\frac{1}{\tau_2} = \gamma_R n_0, \text{ and} \quad \text{eq. (2.5 - 35)}$$

$$\frac{1}{\tau_3} = \delta. \quad \text{eq. (2.5 - 36)}$$

Moreover, charge carrier diffusion usually is negligible in amorphous organic polymers. Thus, eq. (2.5 - 34) and eq. (2.5 - 35) equalize and the decay becomes bi-exponential as found from Schildkraut's model.

The model outlined above allows for some rough correlation of the grating decay rates to the involved trap types. Introducing appropriate approximations for the different trap types (i.e. no traps, shallow traps, deep inactive traps, and deep optically active traps) into the expressions eq. (H - 60) allows for the derivation of a trap type specific expression for n_0 , which then allows for some conclusion on the behavior of the related decay rates to be expected.

The case of *no traps* leads to the condition $n_0 = N_{G0}^i$ and one obtains:

$$n_0 = \sqrt{\frac{s_G N_G I}{\gamma_R}}. \quad \text{eq. (2.5 - 37)}$$

Thus, for the fast decay rate the power index in eq. (2.5 - 27) may be expected to be $\alpha = 1/2$.

The case of *deep inactive traps* (i.e. a hole once trapped cannot be re-excited) will be represented by the condition $n_0 = N_{G0}^i - N_T$ yielding:

$$n_0 = \frac{\gamma_R N_T + \sqrt{(\gamma_R N_T)^2 + 4\alpha_G \gamma_R (N_G - N_T)}}{2\gamma_R}. \quad \text{eq. (2.5 - 38)}$$

Expanding the square root of the above expression accounting only for the zero and the first order term and applying eq. (2.5 - 33) results in:

$$n_0 = N_T + \frac{s_G (N_G - N_T) I}{\gamma_R N_T}. \quad \text{eq. (2.5 - 39)}$$

Thus, for the fast decay rate the power index in eq. (2.5 - 27) may be expected to be $\alpha = 1$.

For the case of *deep optically active traps* the approximation $N_{T0}^i \ll N_T, N_G$ yields:

$$n_0 = \sqrt{\frac{\alpha_G \delta N_G}{\gamma_R (\delta + \gamma_T N_T)}} \quad \text{eq. (2.5 - 40)}$$

and, since only optical detrapping shall be admitted, β in eq. (2.5 - 33) can be neglected, resulting in:

$$n_0 = \sqrt{\frac{s_G s_T N_G I^2}{\gamma_R (s_T I + \gamma_T N_T)}}. \quad \text{eq. (2.5 - 41)}$$

Thus, for the fast decay rate the power index in eq. (2.5 - 27) may be expected to be $1/2 < \alpha < 1$.

In the case of *shallow traps*, the charge carriers may be detrapped thermally and optically. Otherwise, this case is basically similar to the case of deep optically active traps and eq. (2.5 - 41) will be valid as well, however, completed by the thermal detrapping rate β :

$$n_0 = \sqrt{\frac{(s_T I + \beta) s_G N_G I}{\gamma_R (s_T I + \beta + \gamma_T N_T)}}. \quad \text{eq. (2.5 - 42)}$$

The fast erasure rate, thus, will depend sublinearly on the intensity as well, however, the power index will, in turn, depend on the intensity. Combining eq. (2.5 - 27) and eq. (2.5 - 42) results in:

$$\alpha = \frac{d}{d \ln I} \ln\left(\frac{1}{\tau}\right) = \frac{1}{2} + \frac{\gamma_T N_T s_T I}{2(s_T I + \beta)(s_T I + \beta + \gamma_T N_T)}. \quad \text{eq. (2.5 - 43)}$$

Despite the obvious fact, that α shows a more complicated behavior in this case, it will remain in the range $1/2 < \alpha < 1$.

It seems problematic to try to draw some definite conclusions concerning the trap species dominant in a PR polymer from experimentally obtained values of α on the basis of eq. (2.5 - 37) to eq. (2.5 - 43), since the correlation between the possible ranges for α and a particular trap species seems to be too ambiguous. Cui et. al. tried to find a second argument by considering the field dependence of the light excitation cross section of filled traps. However, their discussion is barely comprehensible. For details reference is made to the original literature.

Nevertheless, eq. (2.5 - 37) to eq. (2.5 - 43) indicate, that a changing trap situation in some material for different experimental conditions may show up in some systematic change of the power index for the intensity dependency of the erasure rate. However, interpreting an observed systematic change of the power index unambiguously may not be possible.

This issue will be picked up again in the section devoted to the experimental results, when discussing the erasure behavior of PVK based PR polymers.

2.5.3.3.) *Orientalional enhancement effect*

Any model of the photorefractive effect taking into account the influence of a strong external electrical field predicts that the PR space-charge field will not exceed notably the projection of the external field onto the grating vector K of the holographic grating. This is obvious, since the PR space-charge field results from redistribution of generated charge carriers due to drift and diffusion, giving rise to the spatially modulated space-charge field, which spatially resolved acts as a counter field or a supplement field to the external field depending on the considered spatial location along the direction of K . In the location, where the space charge field acts as a counter field, the drift-driven charge carrier redistribution will be suppressed as soon as the space-charge field reaches the strength of the external field, cancelling the latter. Thus, a possible excess space-charge field can only be due to diffusion, which, in polymers, is negligibly small not contributing notably to the space-charge field. However, in today's high performance PR polymers, the achieved refractive index modulations would require a space-charge field being more than one order of magnitude higher than the projection of the external field onto K , if only the electro-optic response of a uniformly poled polymer is taken into account. Accordingly, there must be some considerable enhancement effect for the PR effect in today's high performance PR polymers, which explains this contradiction. The explanation has been given by Moerner et. al. in [88] and is well-known today as the so called *orientational enhancement effect*, which will be discussed in this paragraph.

The orientational enhancement effect arises from the inherent property of all high performance PR polymers known up to date to be electrically poled *in situ*. Thus, the NLO chromophores will not only be aligned by the externally applied electrical field but by the total internal electrical poling field E_T , i.e. by the sum of the external field and the internal space-charge field. Since the PR space-charge field is spatially modulated, the total field in the system will as well be modulated spatially. Depending on the particular geometry applied, the total field will be modulated in amplitude, if the external field is aligned parallel to the grating wave vector K or will be modulated in direction if the external field is oriented perpendicular to K or will be modulated both in direction and in amplitude for the typical tilted geometry applied to PR

polymers, which is a geometric configuration in-between the aforementioned limiting cases and is depicted in figure (2.5 - 5). Please note, that the latter of the limiting cases is hypothetical, since no notable PR space-charge field will be formed if the projection of the external field onto K is zero, since then there will be no charge carrier drift along K . Hereafter, the general case of some tilted geometry will be considered.

The spatial modulation of the total internal poling field E_T in amplitude and direction results in a corresponding spatial modulation of the electrical poling direction in the system, which may as well be considered as a spatial modulation of the direction of the optical axis of the macroscopic system and of the poling strength. Furthermore there will be a spatial modulation of the degree of the electrical poling. Both affect the linear as well as the nonlinear optical properties of the system. Please note, that steady-state is assumed, i.e. the space-charge field is constant in time, and that the external field is presumed to be a dc electrical field.

The linear optical properties are spatially modulated as a function of the square of the total poling field. In the local (molecular) principal axis system (for a detailed definition see “2.4.2.) Electrical poling of organic polymers - the oriented gas model” on page 83), where the susceptibility and permittivity tensors are diagonal, the changes of the first order susceptibility and the refractive index from the isotropic case (non-poled system) to the anisotropic case (poled system) are given by:

$$\Delta\chi_{zz,loc}^{(1)} = \Delta\{[n_{z,BR,loc}]^2 - 1\} \approx 2n\Delta n_{z,BR,loc} = C_{BR}E_{T,loc}^2 \quad \text{eq. (2.5 - 44)}$$

and analogously:

$$\Delta\chi_{xx,loc}^{(1)} \approx 2n\Delta n_{x,BR,loc} = -\frac{1}{2}C_{BR}E_{T,loc}^2 = A_{BR}E_{T,loc}^2 \quad \text{eq. (2.5 - 45)}$$

with:

$$C_{BR} = \frac{2N\Delta\alpha\mu^2}{45k_B^2T^2} \quad \text{eq. (2.5 - 46)}$$

and:

$$\Delta\alpha = \alpha_{\parallel} - \alpha_{\perp}, \quad \text{eq. (2.5 - 47)}$$

according to eq. (2.4 - 65), eq. (2.4 - 67), eq. (2.4 - 69), eq. (2.4 - 73), eq. (2.4 - 74) and eq. (2.4 - 75). The notation “BR“ refers to “birefringent“ and will be used hereafter to denote the contribution due to linear optical properties. The first order susceptibilities (i.e. the polarizabilities) α and the ground state dipole moment are taken as dressed values, i.e. already corrected by local field factors according to “2.4.2.1.4.) Local field correction” on page 91. For the meaning of the other parameters reference to the oriented gas model (page 83) is made. Please note explicitly, that eq. (2.5 - 44) and eq. (2.5 - 45) do not yet describe some photorefractive index modulation, but rather the electrical poling induced optical anisotropy of the system in the local frame. It must be pointed out, that $E_{T,loc}$ is the total internal poling field in the molecular (i.e. local) principal axis system, i.e. the magnitude of the vector sum of the externally applied bias field $E_{B,loc}$ and the PR space-charge field $E_{sc,loc}$ in the local frame. Thus,

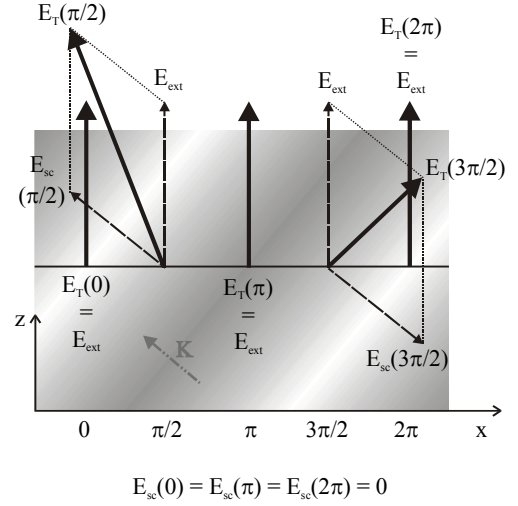


Figure (2.5 - 5): Illustration of the orientational enhancement effect (the denoted phase in x -direction is related to the interference pattern, the space-charge field is assumed to phase-shifted by $\pi/2$ and the initial phasing is chosen arbitrarily; all quantities are vectors).

the results for the macroscopic susceptibility changes from the oriented gas model on page 83 are related to the fields, which are considered as transformed into the local frame before.

The nonlinear optical properties are considered analogously. According to eq. (2.4 - 83) and eq. (2.4 - 85), the macroscopic second order susceptibilities, which arise from poling the system (this is taken here as a change starting at zero for the isotropic case) are given by:

$$\Delta\chi_{zzz,loc}^{(2)} = \frac{N\beta_{333}\mu E_{T,loc}}{5k_B T} = C_{EO}E_{T,loc} \quad \text{eq. (2.5 - 48)}$$

and:

$$\Delta\chi_{xxz,loc}^{(2)} = \frac{N\beta_{333}\mu E_{T,loc}}{15k_B T} = A_{EO}E_{T,loc} = \frac{1}{3}C_{EO}E_{T,loc}^2, \quad \text{eq. (2.5 - 49)}$$

The notation ‘‘EO’’ refers to ‘‘electro-optic’’ and will be used hereafter to denote the contribution due to nonlinear optical properties. In order to get the (local) refractive index as a result from the linear electro-optic effect sensed by an optical field, now the dc field for the electro-optic response must be accounted for yielding:

$$\Delta n_{z,EO,loc} = \frac{1}{2n}\Delta\chi_{zzz,loc}^{(2)}E_{T,loc} = \frac{1}{2n}C_{EO}E_{T,loc}^2 \quad \text{eq. (2.5 - 50)}$$

and analogously:

$$\Delta n_{x,EO,loc} = \frac{1}{6n}C_{EO}E_{T,loc}^2 = \frac{1}{2n}A_{EO}E_{T,loc}^2. \quad \text{eq. (2.5 - 51)}$$

As for the linear optical properties, $E_{T,loc}$ is the total internal poling field in the local frame and the hyperpolarizability β is taken as dressed value. Please note, that the refractive index change depends on the square of the total poling field, like in the case of the linear optical properties. This is due to the fact, that the property ‘‘Pockels effect’’ itself in poled polymers depends on the applied field.

Please note, that the relations expressed above:

$$C_{BR} = -2A_{BR} \quad \text{and} \quad \text{eq. (2.5 - 52)}$$

$$C_{EO} = 3A_{EO} \quad \text{eq. (2.5 - 53)}$$

will also account for situations where the system can no more be approximated by the oriented gas model, provided it still has $C_{\infty v}$ symmetry. This accounts for the case when the chromophores are hindered in rotational mobility e.g. if the glass transition temperature of the system is well above the ambient temperature or if the chromophores are attached to the polymer backbone by some spacer groups, flexible enough to enable some rotational mobility at all. Furthermore, A and C are microscopic constants, which do not depend on the chosen frame, i.e. they are not restricted to the local frame.

Since both the birefringent response according to eq. (2.5 - 44) and eq. (2.5 - 45) and the electro-optic response according eq. (2.5 - 50) and eq. (2.5 - 51) depend on the square of the total poling field (in the local frame), the total susceptibility change may be expressed as:

$$\Delta\chi_{loc} = \begin{bmatrix} A & 0 & 0 \\ 0 & A & 0 \\ 0 & 0 & C \end{bmatrix} E_{T,loc}^2, \quad \text{eq. (2.5 - 54)}$$

where:

$$A = A_{BR} + A_{EO} \quad \text{and} \quad \text{eq. (2.5 - 55)}$$

$$C = C_{BR} + C_{EO}. \quad \text{eq. (2.5 - 56)}$$

The PR space-charge field may be written as:

$$\vec{E}_{sc}(\vec{r}) = E_{sc}(\vec{r})\vec{e}_K = E_{sc0}e^{i\vec{K}\cdot\vec{r}}, \quad \text{eq. (2.5 - 57)}$$

where E_{sc0} is the amplitude and \vec{e}_K is the unit PR grating vector. Thence, the total internal electrical field in the laboratory frame can then be expressed as:

$$\vec{E}_T(\vec{r}) = (E_{sc}(\vec{r})\sin\theta_G)\vec{e}_x + (E_{ext} + E_{sc}(\vec{r})\cos\theta_G)\vec{e}_z, \quad \text{eq. (2.5 - 58)}$$

where θ_G is the angle between the grating wave vector K and the laboratory z -axis, which is the direction of the applied external field E_{ext} in the laboratory frame. Defining, on the other hand, θ_p as the local tilt angle of the total internal poling field E_T with respect to the laboratory z -axis, θ_p will be:

$$\theta_p = \text{atan}\left(\frac{E_{sc}(\vec{r})\sin\theta_G}{E_{ext} + E_{sc}(\vec{r})\cos\theta_G}\right). \quad \text{eq. (2.5 - 59)}$$

Please note, that quantities expressed in the laboratory frame are not explicitly denoted here. On the other hand, quantities in the local frame carry the subscript ‘‘loc’’.

In order to obtain the susceptibility matrix according to eq. (2.5 - 54) in the laboratory frame, the laboratory frame is transformed into the local frame so that E_T coincides with the molecular z -axis (i.e. the 3-axis in the notation used for the oriented gas model). This may be performed applying the transposed rotation matrix U^T . Then the susceptibility change is considered in the local frame and is finally transformed back into the laboratory frame by the rotation matrix U , which reads in summary:

$$\Delta\chi = U^T \Delta\chi_{loc} U \quad \text{eq. (2.5 - 60)}$$

with the rotation matrix given by:

$$U = \begin{bmatrix} \cos\theta_p & 0 & -\sin\theta_p \\ 0 & 1 & 0 \\ \sin\theta_p & 0 & \cos\theta_p \end{bmatrix}. \quad \text{eq. (2.5 - 61)}$$

The rotation matrix is chosen here as representing a rotation by θ_p around the laboratory y -axis; however, this is arbitrary due to the rotational symmetry of the problem around the z -axis. Solving eq. (2.5 - 60) with eq. (2.5 - 61) yields:

$$\Delta\chi = \begin{bmatrix} A(\cos\theta_p)^2 + C(\sin\theta_p)^2 & 0 & (C-A)\sin\theta_p\cos\theta_p \\ 0 & A & 0 \\ (C-A)\sin\theta_p\cos\theta_p & 0 & A(\sin\theta_p)^2 + C(\cos\theta_p)^2 \end{bmatrix} E_T^2. \quad \text{eq. (2.5 - 62)}$$

In order to solve for eq. (2.5 - 62), the situation of the poling field must be considered in more detail as depicted in figure (2.5 - 6). It becomes clear, that:

$$\sin\theta_p = \frac{E_{sc}(\vec{r})}{E_T(\vec{r})}\sin\theta_G \quad \text{eq. (2.5 - 63)}$$

and:

$$\cos\theta_p = \frac{E_{ext} + E_{sc}(\vec{r})\cos\theta_G}{E_T(\vec{r})} \quad \text{eq. (2.5 - 64)}$$

which are merged to form eq. (2.5 - 59).

Inserting eq. (2.5 - 63) and eq. (2.5 - 64) into eq. (2.5 - 62) eventually results in:

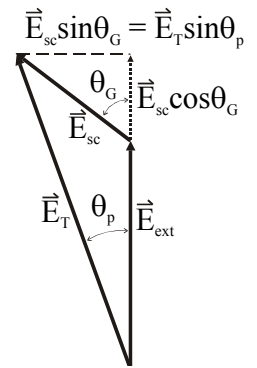


Figure (2.5 - 6): total poling field

$$\Delta\chi = \begin{bmatrix} AE_{ext}^2 + 2AE_{ext}E_{sc}\cos\theta_G + E_{sc}^2(A - (A - C)(\sin\theta_G)^2) & 0 & (C - A)\left[E_{ext}E_{sc}\sin\theta_G + \frac{E_{sc}^2}{2}\sin 2\theta_G\right] \\ 0 & AE_T^2 & 0 \\ (C - A)\left[E_{ext}E_{sc}\sin\theta_G + \frac{E_{sc}^2}{2}\sin 2\theta_G\right] & 0 & AE_{ext}^2 + 2AE_{ext}E_{sc}\cos\theta_G + E_{sc}^2(C - (C - A)(\sin\theta_G)^2) \end{bmatrix} \quad \text{eq. (2.5 - 65)}$$

where “ (\hat{r}) ” is set aside for the sake of a short notation and E_T^2 follows from eq. (2.5 - 58):

$$E_T^2 = E_{ext}^2 + E_{sc}^2 + 2E_{ext}E_{sc}\cos\theta_G. \quad \text{eq. (2.5 - 66)}$$

Eq. (2.5 - 65) may be separated into components of (zero,) first and second order PR gratings by inserting eq. (2.5 - 57) and comparing coefficients of exponential terms of corresponding grating order.

2.5.3.3.1.)First order grating

The first order Fourier component of the susceptibility change writes according to eq. (2.5 - 65) with eq. (2.5 - 57):

$$\Delta\chi_{1K} = \begin{bmatrix} 2A\cos\theta_G & 0 & (C - A)\sin\theta_G \\ 0 & 2A\cos\theta_G & 0 \\ (C - A)\sin\theta_G & 0 & 2C\cos\theta_G \end{bmatrix} E_{ext}E_{sc0}e^{i\vec{K}\cdot\hat{r}} \quad \text{eq. (2.5 - 67)}$$

which yields for the first order Fourier component of the photorefractive refractive index modulation, sensed by s-polarized light (i.e. polarized perpendicular to the x,z -plane in the laboratory frame):

$$\Delta n_{1K}^{(s)} = \frac{A}{n}E_{ext}E_{sc}(\hat{r})\cos\theta_G \quad \text{eq. (2.5 - 68)}$$

and sensed by p-polarized light (i.e., polarized in the x,z -plane):

$$\begin{aligned} \Delta n_{1K}^{(p)} = \frac{1}{2n}E_{ext}E_{sc}(\hat{r})[& 2A\cos\alpha_1\cos\alpha_2\cos\theta_G + \\ & + (C - A)\sin(\alpha_1 + \alpha_2)\sin\theta_G \cdot \\ & + 2C\sin\alpha_1\sin\alpha_2\cos\theta_G] \end{aligned} \quad \text{eq. (2.5 - 69)}$$

The angles α_1 and α_2 are the incident angles of the recording beams for the interference pattern, according to figure (2.5 - 3). It is obvious, that a non-zero, externally applied field is required in order to obtain a photorefractive refractive index modulation, independent from other points of view, which as well demand an external field (i.e. charge carrier generation and drift).

2.5.3.3.2.)Second order grating

The second order Fourier component of the susceptibility change is:

$$\Delta\chi_{2K} = \begin{bmatrix} A - (A - C)(\sin\theta_G)^2 & 0 & (C - A)\frac{1}{2}\sin 2\theta_G \\ 0 & A & 0 \\ (C - A)\frac{1}{2}\sin 2\theta_G & 0 & C - (C - A)(\sin\theta_G)^2 \end{bmatrix} E_{sc0}^2 e^{i2\vec{K} \cdot \vec{r}}, \quad \text{eq. (2.5 - 70)}$$

which yields for the corresponding Fourier component of the photorefractive refractive index modulation sensed by s-polarized light:

$$\Delta n_{2K}^{(s)} = \frac{A}{2n} E_{sc}^2(\vec{r}) \quad \text{eq. (2.5 - 71)}$$

and sensed by p-polarized light:

$$\begin{aligned} \Delta n_{2K}^{(p)} = \frac{1}{2n} E_{sc}^2(\vec{r}) [& A \cos\alpha_1' \cos\alpha_2' + \\ & + (C - A) \cos(\alpha_1' + \alpha_2') (\sin\theta_G)^2 \\ & + \frac{(C - A)}{2} \sin(\alpha_1' + \alpha_2') \sin 2\theta_G \\ & + C \sin\alpha_1' \sin\alpha_2'] \end{aligned} \quad \text{eq. (2.5 - 72)}$$

The angles α_1' and α_2' are the incident angles of the virtual recording beams for a $2K$ interference pattern. Beams exhibiting these incident angles, thus, fulfill the Bragg-condition for the second order Fourier component of the PR refractive index grating. Please note, that the second order PR refractive index grating is independent from the existence of an external field, opposed to the first order grating. (However, an external field is nevertheless required to build up the space-charge field.)

2.5.3.3.3.)The enhancement - a comparison

In order to get an idea of the outstanding importance of the above discussed enhancement mechanism, in this section the quantitative relations will be regarded more closely. However, the consideration will be restricted to the first order grating, since the $2K$ grating has not been investigated in the frame of this work and has only been noted above for the sake of completeness.

For comparison, an expression for the refractive index modulation for the case of a pure electro-optic polymer will be given below. The case of a pure electro-optic polymer may be understood as the limiting case of a system of very high glass-transition temperature, which has been electrically poled at elevated temperature and then cooled down with the poling field applied. Accordingly, the orientational order generated at high temperature, when the chromophores exhibited approximately free orientational mobility, is frozen and cannot be altered any more. The orientational enhancement effect, thus, will not occur in such a system.

Poled polymers in general belong to the $C_{\infty v}$ symmetry group, the electro-optic tensor \hat{r} of which writes in contracted notation (Kleinman symmetry applies):

$$\hat{r} = \begin{bmatrix} 0 & 0 & r_{13} \\ 0 & 0 & r_{13} \\ 0 & 0 & r_{33} \\ 0 & r_{13} & 0 \\ r_{13} & 0 & 0 \\ 0 & 0 & 0 \end{bmatrix}. \quad \text{eq. (2.5 - 73)}$$

For a certain geometry, an effective electro-optic coefficient may be calculated according to the expression:

$$r_{eff} = \hat{e}_{p1} \bullet \{ \hat{\epsilon} \bullet [\hat{r} \bullet \hat{e}_K] \bullet \hat{\epsilon} \} \bullet \hat{e}_{p2}, \quad \text{eq. (2.5 - 74)}$$

where \hat{e}_{p1} and \hat{e}_{p2} are the polarization unit vectors of the recording beams, $\hat{\epsilon}$ is the second rank permittivity tensor and \hat{e}_K is the unit grating wave vector. By means of figure (2.5 - 3), the vectors involved can easily be identified to (the polarization unit vectors are oriented perpendicular to the propagation direction):

$$\hat{e}_{p1}^{(s)} = \hat{e}_{p2}^{(s)} = \begin{bmatrix} 0 \\ 1 \\ 0 \end{bmatrix}, \quad \text{eq. (2.5 - 75)}$$

$$\hat{e}_{p1,2}^{(p)} = \begin{bmatrix} \cos \alpha_{1,2} \\ 0 \\ \sin \alpha_{1,2} \end{bmatrix} \text{ and} \quad \text{eq. (2.5 - 76)}$$

$$\hat{e}_K = \begin{bmatrix} \sin \theta_G \\ 0 \\ \cos \theta_G \end{bmatrix}, \quad \text{eq. (2.5 - 77)}$$

where the superscripts (s) and (p) denote s-polarization and p-polarization. Neglecting some small contribution due to the uniform background birefringence (please note, that this has already been presumed for eq. (2.5 - 74)), presuming a PR space-charge field according to eq. (2.5 - 57) and using eq. (2.2 - 21) rewritten to the form:

$$\Delta n \approx -\frac{n^3}{2} r_{eff} E_{sc}(\hat{r}), \quad \text{eq. (2.5 - 78)}$$

the PR refractive index modulation will be:

$$\Delta n_{1K,pp}^{(s)} = -\frac{n^3}{2} r_{13} E_{sc}(\hat{r}) \cos \theta_G \quad \text{eq. (2.5 - 79)}$$

and:

$$\begin{aligned} \Delta n_{1K,pp}^{(p)} = -\frac{n^3}{2} E_{sc}(\hat{r}) [& r_{13} \cos \alpha_1 \cos \alpha_2 \cos \theta_G + \\ & + r_{13} \sin(\alpha_1 + \alpha_2) \sin \theta_G + \\ & + r_{33} \sin \alpha_1 \sin \alpha_2 \cos \theta_G] \end{aligned} \quad \text{eq. (2.5 - 80)}$$

The subscript ‘‘pp’’ refers to ‘‘prepoled’’. Calculating back the electro-optic coefficients by means of eq. (2.4 - 88) reveals, that:

$$-\frac{n^3}{2}r_{13} = \frac{1}{2n}E_{ext}A_{EO} \text{ and} \quad \text{eq. (2.5 - 81)}$$

$$-\frac{n^3}{2}r_{33} = \frac{1}{2n}E_{ext}C_{EO}. \quad \text{eq. (2.5 - 82)}$$

Extracting the electro-optic contribution from eq. (2.5 - 68) and eq. (2.5 - 69) by means of eq. (2.5 - 55) and eq. (2.5 - 56) and accounting for eq. (2.5 - 53) shows eventually that the electro-optic contribution to the PR refractive index modulation is enhanced by a factor of two. This relation was experimentally verified e.g. by Sandalphon et.al. [198].

A corresponding relation for the birefringence contribution cannot be derived, since there is no such contribution in a prepoled system. However, the birefringence contribution adds to the electro-optic contribution taking into account the signs of both the contributions. This may lead to a significantly stronger enhancement, than implied from only considering the electro-optic contribution.

2.5.3.4.)PR refractive index modulation in low- T_g PR polymers

As discussed in the preceding section, in a PR polymer featuring in situ poling, the total PR refractive index modulation will result from two contributions, the electro-optic contribution and the birefringent contribution:

$$\Delta n_{tot} = \Delta n_{EO} + \Delta n_{BR}. \quad \text{eq. (2.5 - 83)}$$

The electro-optic contribution is additionally enhanced by a factor of two with respect to the electro-optic response in a comparable system not featuring in situ poling.

In today's high performance PR polymers, the birefringence contribution is the dominant or even the only contribution. It leads to very high achievable PR refractive index modulations of up to 10^{-2} , which is on the average more than one order of magnitude higher than in common PR crystals (in photoconductive PR recording).

2.5.4.) Photorefractive two-wave mixing

Wave mixing in thick hologram gratings is described by the coupled wave theory, which has already been elaborated upon in "2.3.2.) Coupled wave theory for thick hologram gratings" on page 53. The concepts outlined in this section are generally valid and important solutions, which are relevant in the frame of this work, have already been discussed. Furthermore, in "2.2.3) Degenerate four wave mixing and NLO phase matching" on page 47, wave mixing has been identified as an NLO effect in general, however, considered only for the particular example discussed there. This may seem sufficient to obtain some overview over the issue of wave mixing in thick hologram gratings. However, there is good reason to pick up this subject once more in the particular context of the photorefractive effect generating the considered hologram grating. As mentioned before, the mechanism of the photorefractive grating build-up leads to a dephasing between the eventually resulting refractive index grating and the original holographic interference pattern. This phase shift results in a coherent energy exchange between the recording beams, referred to as "two-beam coupling" (2BC). 2BC is a unique feature of the photorefractive effect and, thus, deserves a separate discussion in order to emphasize the outstanding significance of this special case of wave mixing in photorefractive nonlinear optics. In this section, 2BC will at first be ostensibly explained and then treated in terms of a coupled

wave formalism. However, it is beyond the scope of this work to give a comprehensive overview over the variety of particular physical applications of 2BC and closely related effects in photorefractives. For this wide field, reference is made to the literature [B8, B13, B16, B22, B24 - B26, and references therein].

The details of the subsequent discussion will be restricted to transmission holograms and degenerate wave mixing. The presented principles, however, apply to the general case.

2.5.4.1.)Phenomenology of two-beam coupling

In order to understand 2BC phenomenologically, the intersection of two plane waves I_{01} and I_{02} in a PR medium shall be considered, as depicted in figure (2.5 - 7) (A). At first, the resulting interference pattern shall be assumed to have generated a local refractive index grating. Both the intersecting beams will be partially diffracted and transmitted by “their own“ grating. For the sake of simplicity the refractive index profile shall not be considered as sinusoidal as depicted by the solid line in figure (2.5 - 7) (B), but as rectangular with the interfaces between the fringes of different refractive indices located at “-0.5“ and “+0.5“ as hinted by the hatched areas. As can be seen from figure (2.5 - 7) (A), the phase shift between I_{01} and I_{02} will be 90° at the interfaces “-0.5“ and “+0.5“. One point where this can be seen is highlighted by a circle in figure (2.5 - 7) (A). Thus, independently from considering outer or inner reflection (excluding the case of total reflection), the phase shift between a reflected portion of the one beam and the transmitted portion of the other beam will always be shifted against one another by $\pm 90^\circ$. For now a diffraction efficiency of 50% shall be assumed. Please note that the diffraction efficiency is the same for each beam in any case. Then, the beams leaving the medium to the right of figure (2.5 - 7) (A) will consist half by half of a transmitted part of the one beam and a diffracted part of the other beam, which superpose to form the overall transmitted beams. If these contributions are phase shifted by 90° , their superposition will have a phase in-between (figure (2.5 - 7) (C) upper diagram) but will not be altered in amplitude with respect to the incident beams.

However, if the interfaces at ± 0.5 are now displaced by 90° (the direction does not matter) as depicted in figure (2.5 - 7) (A) (illustrated only for one interface (+0.5)), the mutual phase shifts of the contributions forming an overall transmitted beam will drop to 0° in the one case and increase to 180° in the other case. Hence one beam will vanish through destructive interference while the other will be doubled in intensity. For illustration, consider the interface “+0.5“ and the encircled point, which represents zero displacement of the interface. Shift the interface e.g. by $+90^\circ$ as depicted in the figure. One can see now that a “ 180° phase state“ of I_{02} (dotted line) coincides with a “ 0° (or 360°) phase state“ of I_{01} (solid line) at the shifted interface resulting in a mutual phase shift of 180° . It follows that I_{01} will be depleted in this situation since the reflected portion of I_{02} and the transmitted portion of I_{01} interfere destructively (figure (2.5 - 7) (C), lower diagram to the right). Consider now what happens to I_{02} behind the grating. For this purpose, the interface “-0.5“ shall be chosen in order to keep consistent in the considered reflection process (choosing “+0.5“ would require to account for the inner reflection introducing an additional phase change of 180°). At zero displacement a mutual shift of 90° between the beam portions forming I_{02} behind the grating results as expected. If now the interface is also shifted by $+90^\circ$ and the phase relations of the beams at the shifted interface are considered, the dotted or solid lines coincide indicating a mutual phase shift of 0° . Thus I_{02} will be doubled in intensity by constructive interference in the described case.

This effect is referred to as 2BC and requires a dephasing of the refractive index pattern with respect to the interference pattern, as just explained.

Please note, that the above phenomenological explanation is not purely formal, but may be considered as ostensible model for the actual process, if the assumption of a constant diffraction efficiency of 50% is dropped. The energy exchange then will depend on the diffraction efficiency (i.e. the refractive index modulation amplitude) of the grating as well as the PR phase shift (i.e. the dephasing between the interference and the index pattern), which in fact can be verified experimentally and will subsequently be derived theoretically.

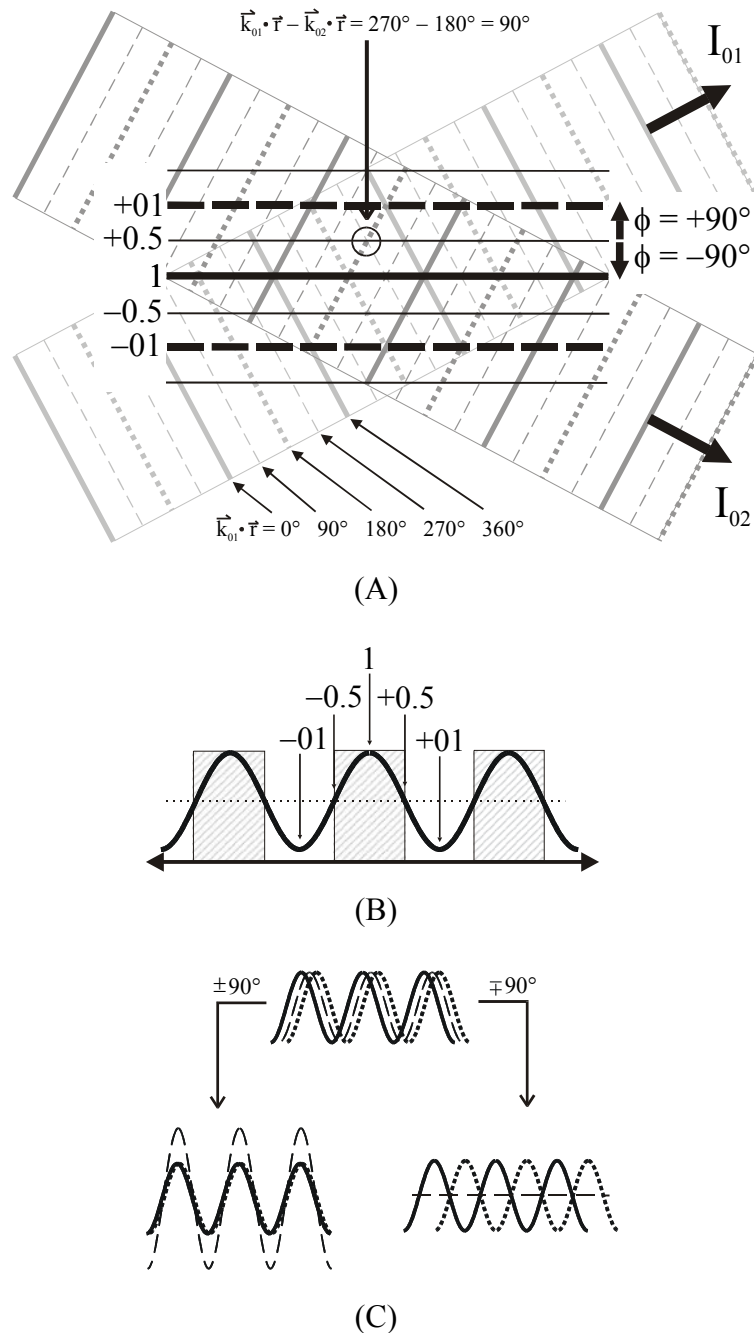


Figure (2.5 - 7): Phenomenology of 2BC. (C): Components of a transmitted wave. If the solid line represents the transmitted component of the one beam, the dotted line will be the diffracted component of the other beam. The dashed line depicts the sum, which will be observed behind the grating. (A): Wave front scheme of the process. (B): Schematic of the grating. For more details see text.

2.5.4.2.)Theoretical formulation of two-beam coupling

The theoretical consideration of 2BC will lead to the photorefractive gain, which is the key parameter to describe the energy exchange between the recording beams by means of the mechanism phenomenologically described before.

For the sake of simplicity, an isotropic medium shall be presumed, the beams are taken as s-polarized and absorption is set to zero. Corrections accounting for p-polarized beams and non vanishing absorption will be discussed later in this section. The underlying geometry is depicted in figure (2.5 - 8): Two infinite plain waves intersect in order to generate an interference pattern in the photorefractive medium. Since the beams are taken as s-polarized, vectorial notation of the field components is dispensable. According to eq. (2.1 - 17), the waves may be expressed as:

$$E_{1,2}(\vec{r}) = E_{01,02} e^{i(\vec{k}_{1,2} \cdot \vec{r} + \varphi)} = A_{1,2} e^{i\vec{k}_{1,2} \cdot \vec{r}}, \quad \text{eq. (2.5 - 84)}$$

where $E_{01,02}$ are the real and $A_{1,2}$ are the complex amplitudes of the waves. The interference pattern generated by the two waves may be written according to eq. (2.1 - 40) as follows

$$I(\vec{r}) = |A_1|^2 + |A_2|^2 + A_1^* A_2 e^{i\vec{K} \cdot \vec{r}} + A_1 A_2^* e^{-i\vec{K} \cdot \vec{r}}, \quad \text{eq. (2.5 - 85)}$$

where the wave resistance according to eq. (2.1 - 35) has been disregarded, and \vec{K} is the grating wave vector according eq. (2.1 - 44).

In order to account for the fact that the refractive index grating, which will result in the coupling of the two waves has been generated by just these two waves and may be dephased by ϕ with respect to the interference pattern, the refractive index modulation conveniently is expressed in terms of the normalized interference grating including an offset phase ϕ . Thus the refractive index of the medium reads:

$$n = n_0 + \frac{\Delta n_m}{2} \left[\frac{A_1^* A_2}{I_0} e^{i(\vec{K} \cdot \vec{r} - \phi)} + cc \right], \quad \text{eq. (2.5 - 86)}$$

where cc denotes the complex conjugate of the preceding term and Δn_m is the material response to a light intensity modulation of unit contrast. Kukhtarev's as well as Schildkraut's model predict a linear dependence of the PR space-charge field on m (eq. (2.5 - 1), eq. (2.5 - 4), and eq. (2.5 - 17)). Furthermore, the EO mechanisms translating E_{sc} into a first order refractive index grating depend linearly on E_{sc} (for low- T_g PR polymers according to eq. (2.5 - 68) and eq. (2.5 - 69), for PR crystals and high- T_g PR polymers see eq. (2.5 - 78)). Hence, Δn_m is the (real) PR refractive index modulation amplitude Δn which has been dealt with several times before in this paragraph, but normalized by the contrast factor m :

$$\Delta n_m = \frac{\Delta n}{m}. \quad \text{eq. (2.5 - 87)}$$

I_0 is the total average intensity, given by:

$$I_0 = I_1 + I_2 = |A_1|^2 + |A_2|^2. \quad \text{eq. (2.5 - 88)}$$

In order to investigate the wave coupling, the total electrical field according to

$$E(\vec{r}) = E_1(\vec{r}) + E_2(\vec{r}) \quad \text{eq. (2.5 - 89)}$$

and the refractive index according to eq. (2.5 - 86) are inserted into the Helmholtz-equation eq. (2.1 - 18), which is rewritten into the form:

$$\nabla^2 E + k_0^2 n^2 E = 0, \quad \text{eq. (2.5 - 90)}$$

where k_0 denotes wave propagation in free space. Since the considered waves are taken as

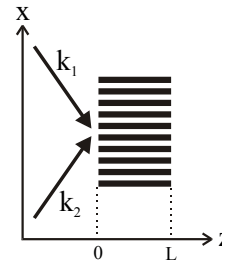


Figure (2.5 - 8):
2BC geometry

infinite, merely the components of the waves perpendicular to the grating vector must be accounted for (i.e. in z -direction in the discussed geometry according to figure (2.5 - 8)). Furthermore applying the common approximation of slowly varying amplitude (see also “2.3.2.1.) The coupled-wave equations” on page 53), which allows for disregarding the second order derivative of the wave amplitude with respect to z finally yields the coupled wave equations by means of comparing coefficients of equal exponentials:

$$2i\beta_1 \frac{dA_1}{dz} = \frac{n_0 \Delta n_m}{I_0} k_0^2 A_2^* A_2 A_1 e^{i\phi} \quad \text{eq. (2.5 - 91)}$$

and:

$$2i\beta_2 \frac{dA_2}{dz} = \frac{n_0 \Delta n_m}{I_0} k_0^2 A_1^* A_1 A_2 e^{-i\phi}, \quad \text{eq. (2.5 - 92)}$$

where β_1 and β_2 are the projections of the wave propagation vectors \vec{k}_1 and \vec{k}_2 onto the z -direction, respectively, and ϕ is the phase shift between the interference pattern and the refractive index pattern.

The coupled wave equations will now be solved exemplarily for the geometry depicted in figure (2.5 - 8). Symmetric incidence may be presumed without loss of generality. Considering a tilted geometry would require to the introduction of obliquity factors as discussed in section “2.3.2.) Coupled wave theory for thick hologram gratings” on page 53, which would only make the subsequent expressions more complicated without altering their general proposition. Please note, that both the recording beams in 2BC will always ideally obey the Bragg-condition, since 2BC is a dynamic self diffraction process, i.e. any perturbation of the Bragg-condition will lead to the formation a new grating matching the “new“ Bragg-condition.

The components of the wave propagation vectors along the z -direction write for the case of symmetric incidence:

$$\beta_1 = \beta_2 = k_0 n_0 \cos \theta = \frac{2\pi}{\lambda_0} n_0 \cos \theta, \quad \text{eq. (2.5 - 93)}$$

where 2θ is the intersection angle of the recording beams in the medium, n_0 is the average refractive index of the medium and λ_0 is the wave length of the beams in free space. Inserting eq. (2.5 - 93), one obtains from the coupled wave equations eq. (2.5 - 91) and eq. (2.5 - 92):

$$\frac{dA_1}{dz} = \frac{1}{2I_0} \Gamma_{\sim}^* |A_2|^2 A_1 \quad \text{eq. (2.5 - 94)}$$

and

$$\frac{dA_2}{dz} = -\frac{1}{2I_0} \Gamma_{\sim} |A_1|^2 A_2 \quad \text{eq. (2.5 - 95)}$$

with the complex coupling constant Γ_{\sim} , called the photorefractive *gain*, given by:

$$\Gamma_{\sim} = i \frac{2\pi \Delta n_m}{\lambda_0 \cos \theta} e^{-i\phi}, \quad \text{eq. (2.5 - 96)}$$

The photorefractive gain is the key parameter for describing 2BC. Please note, that the case of p-polarization of the beams may be accounted for at this point by introducing the scalar product of the polarization unit vectors as multiplicative correction to the complex coupling constant as discussed in the context of the coupled wave theory for thick hologram gratings in “2.3.2.1.2.) p-Polarization” on page 56.

According to eq. (2.5 - 84) the complex amplitudes may be replaced by:

$$A_1(z) = \sqrt{I_1(z)}e^{-i\varphi_1(z)} \text{ and} \quad \text{eq. (2.5 - 97)}$$

$$A_2(z) = \sqrt{I_2(z)}e^{-i\varphi_2(z)} \quad \text{eq. (2.5 - 98)}$$

and one obtains from eq. (2.5 - 94) and eq. (2.5 - 95):

$$\frac{dI_1}{dz} - i2I_1 \frac{d\varphi_1}{dz} = \tilde{\Gamma}^* \frac{I_1 I_2}{I_0} \text{ and} \quad \text{eq. (2.5 - 99)}$$

$$\frac{dI_2}{dz} - i2I_2 \frac{d\varphi_2}{dz} = -\tilde{\Gamma} \frac{I_1 I_2}{I_0}. \quad \text{eq. (2.5 - 100)}$$

It is obvious, that these expressions can be separated into an intensity and a phase contribution by rewriting the complex photorefractive gain $\tilde{\Gamma}$ into the form:

$$\tilde{\Gamma} = \Gamma + 2i\xi \quad \text{eq. (2.5 - 101)}$$

where Γ is the real PR gain, responsible for the coherent energy exchange between the recording beams and ξ is related to the imaginary part of the complex gain, causing a phase shift of the recording beams with respect to each another. These coupling parameters thus read:

$$\Gamma = \frac{2\pi\Delta n_m}{\lambda_0 \cos\theta} \sin\phi \quad \text{eq. (2.5 - 102)}$$

and:

$$\xi = \frac{\pi\Delta n_m}{\lambda_0 \cos\theta} \cos\phi \quad \text{eq. (2.5 - 103)}$$

and the corresponding particular differential equations are:

$$\frac{dI_1}{dz} = \Gamma \frac{I_1 I_2}{I_0}, \quad \text{eq. (2.5 - 104)}$$

$$\frac{dI_2}{dz} = -\Gamma \frac{I_1 I_2}{I_0}, \quad \text{eq. (2.5 - 105)}$$

$$\frac{d\varphi_1}{dz} = \xi \frac{I_2}{I_0} \text{ and} \quad \text{eq. (2.5 - 106)}$$

$$\frac{d\varphi_2}{dz} = \xi \frac{I_1}{I_0}. \quad \text{eq. (2.5 - 107)}$$

Solving the first two differential equations results in expressions for the intensities as a function of z :

$$I_1(z) = I_1(0) \frac{1+b}{1+be^{-\Gamma z}} \quad \text{eq. (2.5 - 108)}$$

and:

$$I_2(z) = I_2(0) \frac{1+\frac{1}{b}}{1+\frac{1}{b}e^{\Gamma z}} \quad \text{eq. (2.5 - 109)}$$

with b as the initial intensity ratio of the recording beams given by:

$$b = \frac{I_2(0)}{I_1(0)}. \quad \text{eq. (2.5 - 110)}$$

Please note, that eq. (2.5 - 108) and eq. (2.5 - 109) may be corrected for some absorption of the

medium by multiplying the right hand side with “ $\exp(-\alpha z)$ “, where α is the absorption coefficient.

Knowing the analytic expressions for the intensities, eq. (2.5 - 106) and eq. (2.5 - 107) can be solved by direct integration after inserting eq. (2.5 - 108) and eq. (2.5 - 109), respectively, yielding:

$$\varphi_1(z) = \varphi_1(0) + \frac{\xi}{\Gamma} \ln\left(\frac{1+b}{1+be^{-\Gamma z}}\right) \quad \text{eq. (2.5 - 111)}$$

and:

$$\varphi_2(z) = \varphi_2(0) + \frac{\xi}{\Gamma} \ln\left(\frac{1+b}{b+e^{\Gamma z}}\right). \quad \text{eq. (2.5 - 112)}$$

It is important to understand, what happens to the PR grating as a result of the energy exchange and the relative dephasing of the recording beams.

The first will result in a change of the contrast of the interference pattern as a function of the propagation of the recording beams through the PR medium. It depends on the particular initial intensity ratio and the sign of Γ , whether the contrast of the interference pattern will improve or decay. In any case, a change of the optical grating contrast will influence the space-charge field according to eq. (2.5 - 4) or eq. (2.5 - 17), which, in turn, will affect the PR gain. Finally there will be some equilibrium, which may deviate considerably from what might be expected from the basic equations for the space-charge field. This is a particular problem in PR media showing high net gain, i.e. in high-performance PR polymers. Note that the gain coefficient in theory is not altered by a change of the grating contrast, due to the normalization of the refractive index modulation by m (eq. (2.5 - 97) with eq. (2.5 - 86)). Furthermore, the derivation as depicted above assumes a “slowly varying amplitude” of the involved beams in order to allow for the neglect of the second order derivative of the wave amplitude with respect to z as already noted before. It is important to point out, that this approximation can become poor or even insufficient in high-performance PR polymers.

The relative dephasing of the recording beams, on the other hand, will result in a continuous displacement of the optical grating planes as a function of z . Thus, the grating will be bent as a function of z . At first sight, it seems reasonable to imply, that this may affect the diffraction efficiency in wave mixing experiments operating with separate read-out beams, since the Bragg-condition will be a function of z , which cannot be matched all over the grating by a single wave. However, as will be shown in the section “5.1.) Influence of hologram bending on the diffraction efficiency in PR thin film devices: A simple model calculation” on page 214, this effect is insignificant for today’s high-performance PR polymers. Please note, that the bending of the grating will not affect the dynamic self-diffraction, since the Bragg condition will be matched for any infinitesimally thin volume sheet perpendicular to the z -axis. This kind of grating distortion, nevertheless, may become important for PR crystals, since these are usually much thicker than PR polymer devices and, thus, exhibit significantly higher Bragg-selectivity. However, PR crystals are beyond the scope of this work and, hence, issues concerning this PR material class will not be discussed in detail.

All investigations within the frame of this work were carried out using a contrast factor of the recording beams of the PR grating close to unity. Thus, hereafter the notation Δn_m will be replaced by Δn , i.e., the actual PR refractive index modulation will be used in the sense of Δn_m as long as the PR gain is concerned. However, one should keep in mind that this is matter of the experimental conditions applied here.

2.5.5.) Photorefractive characterization parameters and figures of merit

Photorefractive materials are usually characterized by means of their steady-state and dynamic performance, i.e the achievable refractive index modulation for a given experimental configuration, the PR gain, and the response times for grating recording and erasure. Furthermore, the sensitivity of a PR material is important, which is a measure for the optical energy, which has to be expended in order to achieve a certain refractive index modulation. However, one must keep in mind, that the interpretation of the PR characteristics will depend on the demands of a particular application considered. A complication in comparing PR materials on the basis of the characteristics enumerated above may be due to the fact that most of these characteristics depend on the geometrical configuration of the setup used for determination, as well as a number of extrinsic and intrinsic parameters like the operating wavelength in general and the relation between glass-transition temperature and ambient temperature for amorphous organic systems. A question often also disregarded is the thickness of a hologram. Especially in the case of organic PR thin film devices, many data have been obtained in the past at the edge of the term „thick hologram grating“. For example, the most common applied geometry is (referring to figure (2.5 - 3)) $\theta_t \approx 30^\circ$ and $2\theta \approx 7^\circ$, resulting in a grating spacing of $\Lambda \approx 3\mu\text{m}$. Operating such a system at 633nm operating wavelength will require a sample thickness of at least $20\mu\text{m}$ to obey eq. (2.3 - 2). Thus any comparison of PR performance data has to be considered with special care with respect to the actual comparability of the data to be compared.

In an attempt to systemize the performance of PR materials, some criteria have been proposed, which focus on the achievable refractive index modulation of PR materials, i.e. on the so called *dynamic range*. These criteria shall allow to compare PR materials most independently from particular experimental parameters or at least allow for quick transformation of some performance data into a particular experimental configuration. A general requirement for such *figures of merit* is, that they contain basically only material parameters. Subsequently, the common expressions for figures of merit for PR crystals are derived, which apply as well for PR semiconductors, PR organic crystals, and purely electro-optic PR polymers. Since the mechanism of the refractive index modulation by the PR space-charge field is different for organic PR materials, which allow for orientational enhancement, these figures of merit will be invalid for such systems. Therefore, another figure of merit has been proposed to account for the special feature of in-situ poling of such system, which will also be derived below. Finally the sensitivity of PR materials is discussed in short terms.

Please note, that one may derive various figures of merit taking into account different parameters or focusing on particular applications. A specialized parameter in this sense, which counts as well to the term “figure of merit“ is for example the M/#, describing the multiplexing capability of a holographic medium for mass data storage as discussed in “2.3.3.3.) System metrics for holographic multiplexing in erasable media” on page 65.

2.5.5.1.) Figures of merit for purely electro-optic PR materials

The refractive index modulation as a function of the PR space-charge field of purely electro-optic PR materials is given by eq. (2.5 - 78). Considering the space-charge field amplitude according to eq. (2.5 - 7), two limiting cases can be distinguished. At first, for small grating spacing Λ , the grating vector K becomes large and the saturation field according to eq. (2.5 - 3) correspondingly small. Hence, eq. (2.5 - 7) may then be rewritten as:

$$E_{sc} = mE_q \sqrt{\frac{E_0^2 + E_D^2}{E_0^2 + (E_D + E_q)^2}} \approx mE_q, \quad \text{eq. (2.5 - 113)}$$

since the diffusion field becomes large according to eq. (2.5 - 2). On the other hand, if Λ is large, E_q is also large, and E_D is small. Hence, eq. (2.5 - 7) may be approximated by:

$$E_{sc} = mE_q \sqrt{\frac{E_0^2 + E_D^2}{E_0^2 + (E_D + E_q)^2}} \approx mE_q \sqrt{\frac{1}{1 + \left(\frac{E_q}{E_0}\right)^2}}, \quad \text{eq. (2.5 - 114)}$$

which may be series-expanded to:

$$E_{sc} \approx mE_q \left(1 + \frac{E_q^2}{2E_0^2}\right). \quad \text{eq. (2.5 - 115)}$$

This approaches direct proportionality in E_q with increasing E_0 exceeding E_q .

Hence, for both of these cases, the maximum achievable refractive index modulation of some electro-optic PR material may be (more or less) roughly approximated by:

$$\Delta n_{max} \approx -\frac{n^3}{2} r_{eff} E_q. \quad \text{eq. (2.5 - 116)}$$

From this and according to eq. (2.5 - 3), a photorefractive figure of merit Q may be defined by extracting the material dependent quantities:

$$Q = \frac{n^3 r_{eff}}{\epsilon_{eff}} N_{eff}. \quad \text{eq. (2.5 - 117)}$$

Please note, that the effective electro-optic coefficient still depends on the geometrical configuration of some particular setup. However, r_{eff} can be calculated unambiguously for a particular experimental setup by means of eq. (2.5 - 74) and also recalculated for another setup allowing to adapt Q to any setup configuration.

On the basis of eq. (2.5 - 117), a variety of slightly different figures of merit have been established, which are more and more reduced in the number of included parameters. The most common form is:

$$Q' = \frac{n^3 r_{eff}}{\epsilon_{eff}}, \quad \text{eq. (2.5 - 118)}$$

since the effective trap density is a parameter in PR crystals, which still successfully defies efficient control. Thus, by simply ignoring N_{eff} , this does not find reflection in Q , which is often found convenient, since it makes experimental data „more reproducible“. However, this is a problem typically found in PR crystals and not in PR polymers.

Some inorganic PR crystals exhibit sufficiently large electro-optic coefficients in order to achieve reasonable nonlinearities already for moderate space-charge fields, which do not approach E_q . Then the experiments can be designed not to approach one of the aforementioned limiting cases, i.e. intermediate fringe spacings and/or only moderate external fields may be applied. In these cases, the space charge field will depend on E_D and/or E_0 , which do not depend on the material parameters and the figure of merit may be written:

$$Q'' = n^3 r_{eff}. \quad \text{eq. (2.5 - 119)}$$

Please note, that it is stated in [B13] on p. 348, that polymers are often operated in regimes, where Q and Q' are the limiting factors, whereas PR crystals often rely on Q'' . This is

not correct, basically due to two reasons. At first, Q is the wrong figure of merit not reflecting the particular properties of high-performance PR polymers as will be shown later. Secondly, there is no saturation field in PR polymers in the sense as found in PR crystals. If such a saturation field would be postulated, the effective trap density would be dynamic. This may easily be understood considering eq. (2.5 - 20) and eq. (2.5 - 21), which represent the parameter being closest to something, which may be interpreted as saturation field. It is obvious, that this “saturation field“ will depend on the external field and the irradiation intensity via the zero order hole density. It is incomprehensible, which kind of reasoning may attribute PR polymers to some regime according to eq. (2.5 - 117) to eq. (2.5 - 119), if there is no reference as discussed preceding to eq. (2.5 - 119) above.

Last not least, even if someone insists on attributing PR polymers to a regime, where Q and Q' are relevant, this does not matter also due to two reasons. At first, the effective permittivity of polymers is rather small, so it does not notably lower the value of Q' especially as compared to PR crystals. Secondly, as already noted above, experimental data on PR polymers are usually excellently reproducible. This includes reproduction of data obtained from different samples containing material prepared on different days at different atmospheric conditions (humidity, ambient temperature and more) and so on.

2.5.5.2.)A figure of merit for orientationally enhanced PR materials

As for the figure of merit for purely electro-optic PR materials, the achievable refractive index modulation as a function of the space-charge field is considered in order to find a figure of merit for orientationally enhanced PR materials (especially polymers, however, also liquid crystals and polymer dispersed liquid crystals may be accounted for). According to the orientational enhancement effect, the index modulation is given by eq. (2.5 - 68) and eq. (2.5 - 69). In contrast to purely electro-optic PR materials, all orientationally enhanced PR materials are of the same symmetry group, and refer their inherent optical nonlinearity not to a bulk effect like crystals but to molecular nonlinearities. This makes the consideration of some “effective“ quantities dispensable and offers the possibility of defining a microscopic figure of merit, which does not depend on any parameter associated with the space-charge field. In order to find such a figure of merit, simply the parameters A and C in eq. (2.5 - 68) and eq. (2.5 - 69) according to eq. (2.5 - 55) and eq. (2.5 - 56) must be considered:

$$A = A_{EO} + A_{BR} = N \frac{\beta_{333}\mu}{15k_B T} - 2N \frac{\Delta\alpha\mu^2}{90k_B^2 T^2} \quad \text{eq. (2.5 - 120)}$$

and:

$$C = C_{EO} + C_{BR} = N \frac{\beta_{333}\mu}{5k_B T} + 2N \frac{\Delta\alpha\mu^2}{45k_B^2 T^2}. \quad \text{eq. (2.5 - 121)}$$

Replacing N by $w\rho N_A/M$, where w is the concentration of the chromophore in the material (in %wt), ρ is the density, N_A is the Avogadro number and M is the molecular weight of the chromophore, these expressions may be rewritten as:

$$F_A = \frac{90k_B T}{w\rho N_A} A = \frac{6k_B T\beta_{333}\mu - 2\Delta\alpha\mu^2}{k_B T M} \quad \text{eq. (2.5 - 122)}$$

and:

$$F_C = \frac{45k_B T}{w\rho N_A} C = \frac{9k_B T\beta_{333}\mu + 2\Delta\alpha\mu^2}{k_B TM} \quad \text{eq. (2.5 - 123)}$$

The right hand side of these expressions only contains molecular parameters. F_A is the molecular figure of merit for photorefractive polymers for s-polarized beams and F_C for p-polarized beams. Commonly only the latter is considered, since it represents the higher nonlinearity. Consequently, operating a PR polymer with s-polarization leads in general to a significantly smaller effect (i.e. PR gain in 2BC and diffracting efficiency in four-wave-mixing), which is a well-known experimental fact.

It must be pointed out, that F_A as well as F_C basically may serve for comparison of the potential PR capability of different NLO chromophores to be used as dopant in a PR polymer. It is not possible to conclude an estimate of the performance of a real polymer containing the chromophore from F_A or F_C , since a manifold of further parameters will have significant impact on the eventually obtained system. However, these figures of merit are not intended to describe a PR material comprehensively, but rather give an idea of the basic capability, which may be achieved, if the general framework fits.

Please note, that F_A and F_C are formally related to Q'' (eq. (2.5 - 119)) and not to Q , or to Q' , since they do not contain any parameter of the bulk system. However, direct comparison between PR crystals and orientationally enhanced polymers is neither possible by means of any of the presented figures of merit, nor can the figures of merit themselves be compared. Both the purely electro-optic and the orientationally enhanced PR systems represent a class of materials by themselves, having in common the basic mechanism of the formation of a displaced space-charge field, but differing significantly by the mechanism, which modulates the refractive index.

For the sake of completeness, it should be noted, that this led to some dispute about the attribution of orientationally enhanced PR systems to the „pure photorefractive effect“. However, the basic mechanism, which leads to the formation of a displaced space-charge field, is the same. Since this feature marks the photorefractive effect unequivocally, the aforementioned dispute appears dispensable.

2.5.5.3.)Photorefractive sensitivity

For many holographic applications, not only the dynamic range of a PR material is important but as well the optical energy, which must be expended to achieve a desired PR response. Therefore, the sensitivity of a PR medium is of major interest, i.e. the achievable refractive index change per unit incident or absorbed optical energy. In the literature, two different measures for the sensitivity have been defined:

$$S_{n1} = \frac{1}{\alpha} \frac{\partial}{\partial J_0} \Delta n \quad \text{eq. (2.5 - 124)}$$

and:

$$S_{n2} = \frac{\partial}{\partial J_0} \Delta n, \quad \text{eq. (2.5 - 125)}$$

where J_0 is the incident fluency of optical energy per unit area and α is the absorption coefficient. Instead of Δn , $(\sqrt{\eta})/d$ may be used as a measure for the grating strength and the corresponding sensitivities are then defined as:

$$S_{\eta 1} = \frac{1}{\alpha d} \frac{\partial}{\partial J_0} \sqrt{\eta} \quad \text{eq. (2.5 - 126)}$$

and:

$$S_{\eta_2} = \frac{1}{d} \frac{\partial}{\partial J_0} \sqrt{\eta} . \quad \text{eq. (2.5 - 127)}$$

For determination of the sensitivities, the derivatives in the above expressions are taken at the beginning of the recording process, which usually avoids a possible influence of the experimental configuration. However, the sensitivities depend on the operating wavelength, a possibly applied external field, and on the recording scheme, if the latter impacts the dynamic response behavior. The latter is especially important in polymers as discussed in [92]. Furthermore, the complicated dynamics of PR polymers in general reduces the significance of the sensitivity obtained in the way described above.

3.)Photorefractive polymers

In this paragraph, the basic concepts for photorefractive amorphous organic materials will be outlined. Photorefractive polymer composites, which are subject of this work are considered in detail, whereas other approaches are only reviewed briefly. It will be abstained from discussing photorefractive crystalline systems and comparing them with amorphous photorefractive polymers. A comparative discussion of this kind may be found in [B13, p. 349ff].

Systems, which are closely related to nowadays common materials, but show only minor variations not resulting in significant different properties as compared to the basic system will not be considered explicitly. Furthermore, the very first photorefractive organic polymers usually showing poor performance are not considered as well.

Please note, that the chemical structures of subsequent particularly cited materials and molecules will be listed alphabetically in Appendix D, whereas only abbreviations will be used in the text of this chapter. Explicit reference to the mentioned overview will not be provided in the text with the used abbreviations hereafter.

Some material will have to meet a couple of basic requirements in order to be photorefractive at all, on the one hand, and in order to be potentially applicable as optically nonlinear material on the other. It is clear that the requirements, which must be met to be potentially suitable for certain applications, will depend on the particular application envisaged whereas the basic requirements for PR response have to be met in any case. The general features some material must exhibit in order to observe PR response have already been discussed in “2.5.1.) Phenomenology of the photorefractive effect” on page 118 but will subsequently be summarized once more and extended by some more technical demands, which, however, are not necessarily required for the purely physical occurrence of the PR effect. Thereafter performance issues will be discussed in order to provide a basis for the discussion of the different approaches and concepts to realize amorphous organic photorefractive materials.

3.1.)General requirements

In order to be photorefractive some (arbitrary) material must:

- be photoconductive
- exhibit monopolar electrical conduction (i.e., disparate mobility for electrons and holes)
- be photosensitive (i.e. photoinduced charge generation must be possible)
- exhibit the linear and/or quadratic electro-optical effect (i.e. Pockels-effect and/or (orientational) Kerr-effect).
- be transparent to some degree at operating wavelength.

In order to exhibit photorefractivity in a useful manner, some photorefractive material meeting the above listed general requirements should furthermore:

- be as transparent as possible at operating wavelength without sacrificing the photosensitivity
- show excellent optical quality (→ minimal scattering, maximum homogeneity, etc.)
- be stable against degradation of any kind (e.g. phase separation in multi-component systems, chemical reaction under the influence of an externally applied field or due to optical irradiation, physical aging in low- T_g systems (see page 82), etc.).

Furthermore, easy processability, low cost and the possibility to tune the general properties in an uncomplicated way would be preferable properties for any kind of material in question for technical and commercial application. However, these are not basic requirements.

3.1.1.) Performance issues

The performance of photorefractive materials is determined by four features, which, however, must be judged having in mind what a particular material is intended to be used for. Hence, performance properties useful for the one application may be unfavorable for another and „good performance“ is not necessarily a question of achieving best numerical performance values in all features. The four performance features of PR materials are subsequently listed and discussed in a general way.

Please note, that figures of merit as discussed in “2.5.5.) Photorefractive characterization parameters and figures of merit” on page 145 are barely considered in the photorefractive literature concerning polymers.

3.1.1.1.)Dynamic range

The achievable refractive index modulation is usually referred to as the dynamic range of a PR material. High dynamic range corresponds to high achievable PR refractive index modulation and is preferable in general. The achievable refractive index modulation is directly related to the achievable diffraction efficiency of some hologram stored in PR material. The dynamic range in general depends on various extrinsic parameters, which are in particular the

setup configuration, the operating wavelength, the polarization of the incident light, and the applicable maximum field limited by dielectric breakdown of the sample. If the diffraction efficiency alone is employed to discuss the dynamic range, the thickness of the sample must be included in the considerations according to “2.3.2.1.) The coupled-wave equations” on page 53.

Today’s high performance PR polymers in general exhibit relatively high dynamic ranges and, thus, the question of the dynamic range as a performance indicator is now focused on the physical operating conditions required to achieve a certain refractive index modulation. In this context, the required external field at a certain setup configuration (grating spacing, tilt angle and polarization of the incident light) becomes the crucial question in the sense, that lower required field means better performance. Typically, the index modulation related to the first diffraction maximum in degenerate four-wave-mixing (DFWM) experiments is taken as reference. Please note, that usually the external field for the first diffraction maximum is referred to, which may lead to misinterpretations. One must be aware, that the refractive index modulation necessary to achieve the first diffraction maximum depends on the sample thickness even under otherwise identical conditions (especially identical geometrical holographic setup configuration). Thus, external field data related to the first diffraction maximum but obtained for samples of different thickness cannot be compared directly, since they refer to different index modulations. Unfortunately, the exact field dependence of the refractive index modulation cannot be derived theoretically and thus comparison of data obtained under different conditions is barely possible. The common model according to “2.5.3.3.) Orientational enhancement effect” on page 131 predicts a quadratic field dependence. However, experimental determination of the power index yields values deviating from this prediction and varies moreover for different materials. For the material type investigated in frame of this work, the index modulation was found to be proportional to the applied field to the power of about 1.7 in the low- T_g regime. The power index was furthermore found to depend on the glass transition temperature [89].

Nevertheless, the dynamic range is the most general performance indicator. However, detailed comparison of the dynamic range of PR systems requires explicit knowledge of the conditions applied for determining the dynamic range. Thus, the general statement „high -“ or „higher dynamic range“ must always be considered carefully.

3.1.1.2.)Photorefractive response time

The response time of a holographic material is important for any kind of holographic application. One has to distinguish three dynamic processes, the proper combination of which determines the performance of a PR material for a particular application.

The build-up dynamics of the PR grating has been most widely elaborated upon since the discovery of the first high performance PR polymer in 1994. In general, fast grating build-up is favorable. This may be of minor importance for some applications, but slow grating build up is nevertheless undesirable.

The erasure dynamics of a PR grating has not been paid attention to very much up to now, but is a major issue of this work. The erasure dynamics must be seen in the context with the application intended. For example for fast associative memories, fast erasure is favorable, whereas relatively slow erasure is preferable for holographic mass data storage using multiplexing techniques.

Another dynamic feature of photorefractive systems is the dark decay dynamics. The dark decay dynamics has so far not been investigated in detail, however, considered superficially e.g in [90] and [91]. This work presents a much more detailed investigation of this aspect.

Generally, slow dark decay is preferable, and the ideal case would be a grating not decaying in the dark at all.

The PR response time for grating build-up is a parameter widely misused for the straining after effect in the field of PR polymers. The first high performance PR polymers exhibited rather slow PR response of roughly one order of magnitude slower than video rate (25fps for NTSC coding, or 30fps for PAL coding). Therefore, there have been great research efforts to make PR polymers faster, which led to a number of abstruse publications reporting “significant improvement“. For example, response rates of more than one order of magnitude smaller than video rate have been claimed as “world record“ for a PR polymer at an extremely high operating intensity being more than one order of magnitude higher than commonly applied. Since the PR effect is an integral effect, the dynamics of which necessarily depends on the irradiation intensity, this is not really striking. Reading the corresponding publication more carefully finally reveals, that operating the same system at (the commonly applied) moderate intensities results in a photorefractive response dynamics which is more than one order of magnitude slower, however, still well below video rate, which has nevertheless been a considerable improvement.

In another case, not the build-up rate of the PR grating was reported as measure of the response dynamics but the evolution of the PR gain, which includes the evolution of the PR phase shift. The response dynamics thus obtained is simply not meaningful for most holographic applications and not representative for the PR grating build up dynamics. The latter may be derived from the evolution of the refractive index grating obtainable by four-wave-mixing experiments. Furthermore, it has become common practice to consider only the fastest build up rate for judging the PR dynamic performance, whereas the PR grating build-up dynamics in polymer systems has been shown to consist of at least two rates. Although this is partly justified by the fact, that the fast component mostly covers a significant part of the build up process which is most relevant for many applications, in some cases only the first response rate was presented neither showing what happens on longer time scale, nor stating the contribution of the fast component to the overall dynamics, nor naming the total number of response rates observed. Such a practice is highly questionable. Eventually it is important to note, that the PR grating build-up depends on the recording scheme as shown in [92] and on the applied electrical field due to field dependent charge carrier mobility and photogeneration efficiency. It is understood, that the geometrical setup configuration shows considerable influence on the response dynamics as well.

The erasure dynamics of the gratings in some PR material is a crucial question for the potential applicability as mass data storage devices using multiplexing. For this purpose, slow erasure and fast recording are the favorable combination. On the other hand in fast erasable memories like associative memories or RAM's, slow erasure dynamics is unfavorable. A major issue in considering the erasure time as a performance parameter is the way, how the erasure process is performed. Generally, only erasure experiments conducted by a non Bragg-matched erasure beam yield correct results. If the grating is erased by some Bragg-matched light beam, the grating to be erased will be refreshed by the „erasure“-beam and its diffracted beam resulting in a slower grating decay than correlated to the actual erasure dynamics of the investigated system. For high performance holographic erasable media exhibiting high diffraction efficiency, the error thus made may well exceed a factor of 2. Besides the erasure scheme, the PR erasure dynamics depends on the same parameters as the grating build-up dynamics. However, a major result of the work at hand is that the erasure dynamics depends moreover on the recording time, which is a new effect not considered before. Accordingly, erasure time constants presented in the literature so far are often not clearly assigned to a recording time thus questioning comparability. Furthermore, the erasure dynamic behavior has been employed several times to discuss the general dynamics of organic PR systems. It is clear, that this may be

very problematic according to the circumstances discussed above.

3.1.1.3.)The PR sensitivity

The photorefractive sensitivity has been discussed in detail in “2.5.5.3.) Photorefractive sensitivity” on page 148. Basically, higher sensitivity is preferable. The PR sensitivity has not extensively been discussed in the literature about amorphous organic PR solids, which may be due to the complicated dynamic behavior of PR polymers reducing the significance of the sensitivity for these systems determined in the conventional way. However, it is a parameter usually presented in the literature about inorganic crystals.

3.1.1.4.)The PR phase shift and the PR gain

The photorefractive phase shift is actually not a performance parameter. However, besides the refractive index modulation, it is the second of these two intrinsic parameters of the photorefractive effect determining the PR gain. The PR gain, on the other hand, due to its uniqueness is often referred to in the literature as some kind of performance parameter or at least as an experimental proof or disproof for the photorefractive nature of a holographic grating. Often, high PR gain is correlated with better performance in the literature, but actually this is problematic. Disregarding the question whether the PR gain may be useful, useless or even objectionable for some application considered, one cannot deduce a clear idea about a material's performance from the gain coefficient alone. Only if the gain coefficient (usually the real gain according to eq. (2.5 - 102) is referred to) is reported together with some data on the refractive index modulation enabling the estimation of the PR phase shift, one may state about PR material's performance by considering the gain. Furthermore, the gain coefficient is counteracted by absorption and thus the net gain (i.e. gain minus absorption coefficient) is an important parameter as well. Large gain coefficients and no net gain is an unfavorable situation in general.

In this context it is particularly important to point out, that the PR gain is a parameter, which can only have physical meaning for volume holographic gratings. One may calculate something for thin holographic gratings using the typical evaluation techniques for the PR gain (to be discussed later), but this „something“ is basically meaningless. This mistake has been pretty commonly made at the early stage of research on PR organic thin film devices, and even today there are publications discussing the PR gain while referring to holographic gratings at the lower edge of a volume grating not pointing out the limitation discussed above.

Furthermore it should be noted, that the refractive index modulation for s- and p-polarized beams is different in amorphous organic systems (see eq. (2.4 - 74)). Since it has become common to probe the refractive index modulation using DFWM technique with s-polarized recording beams and p-polarized probe beam (to be discussed later in detail), the index modulation thus probed cannot be used directly for calculating the phase shift from concomitant gain measurements. In fact, eq. (2.4 - 74) must be used to correct for the polarization anisotropy and the phase shift thus obtained can only be an estimation, since eq. (2.4 - 74) is only an approximation. This issue will be discussed later on in “4.2.1.4.) Polarization anisotropy for PR wave mixing experiments” on page 199 in more detail and more accurate ways of taking into account the polarization anisotropy will be shown.

3.2.)Material concepts and approaches - a brief survey

A variety of different approaches for developing amorphous organic photorefractive system have been presented during the last years of intensive research in this relatively new field. Three basically different concepts must be distinguished, which are the *polymer* concept, the *glass* concept and the *liquid crystal* concept. Furthermore, the polymer concept can be divided formally into two groups which are the polymer composites consisting of some polymer matrix not actively participating in the PR effect at all and various low molecular mass components incorporated in the matrix and the monolithic polymers carrying all functional moieties covalently attached to and/or directly included in the polymer backbone. However, these are limiting cases and there is a broad spectrum of systems consisting of more or less multifunctional polymer matrices with some functionalities being additionally incorporated as low molecular mass components. Hereafter, a PR polymer system will be referred to as composite if more than about 1-2%wt of the system corresponds to an added low molecular mass component. Otherwise, the system shall be regarded as monolithic. This convention is intended to allow for the sensitizer to be added as molecular component to an otherwise fully functionalized polymer. Eventually, there have been attempts to develop photorefractive *gels*. However, this approach has not been elaborated upon very much up to now.

Subsequently all the above mentioned concepts will be briefly reviewed. However, discussing the manifold of developed systems will by far exceed the frame of this work. Hence, in most cases the systems will only be described superficially without discussing their particular properties and reference will be made to the original literature. Furthermore, a selection of the systems to be reviewed will be made, if the number of known systems is too large. This applies especially for the PR polymers (monolithic polymers as well as composites) whereas gels, liquid crystalline systems and even low molecular mass glasses investigated up to now are less in number and, thus, can be summarized more comprehensively. In general, photorefractive polymeric composites will be considered in more detail as compared to the other approaches, since this class of materials includes the system, which has been subject of this work.

3.2.1.) Gels

Photorefractive gels have been reported upon by Chaput et. al. and Darracq et. al. [93, 94]. The materials consisted of a silica oxide backbone with carbazole moieties (charge transporting moieties, referred to hereafter as “CTA”) and DR moieties (NLO chromophore) covalently attached via alkyl spacer groups in order to introduce charge transporting and nonlinear optical properties. For sensitization small amounts of TNF were added. The system was corona poled in order to break the statistical centro-symmetry. Photorefractivity was proven by 2BC experiments yielding gain coefficients of up to $\Gamma = 450\text{cm}^{-1}$ for a grating spacing of $0.81\mu\text{m}$ in $3.5\mu\text{m}$ thick samples [94], however, no net gain was achieved since the absorption was $\alpha = 560\text{cm}^{-1}$ at 628nm operating wavelength. Neither refractive index modulation data nor PR phase shift data have been given. The response time was reported to be 320sec to achieve 90% of the saturation value of the gain coefficient. A comparable system was also presented by Burzynski et. al. [95] using a push-pull substituted stilbene derivative as NLO chromophore. They reported a diffraction efficiency of $\eta = 0.01\%$ and a gain coefficient of $\Gamma = 0.3\text{cm}^{-1}$. The authors stated the excellent optical quality and a trend of retaining the second order NLO character for a long time after corona poling as major advances of their systems. However, this approach seems not to be persecuted thereafter anymore.

Please note, that the systems described above must be taken as hybrid systems due to the

inorganic character of the backbone and the organic functional moieties providing the PR character.

3.2.2.) Liquid crystalline systems

Photorefractive liquid crystalline systems have been focussed upon as it became clear, that the PR effect in organic amorphous systems is significantly enhanced by orientational effects (see “2.5.3.3.) Orientational enhancement effect” on page 131). At first sight this seems obvious, because liquid crystals are well known to exhibit large Kerr effects. Due to their collective orientational properties, this material class promises PR response at very low externally applied field, since the electrical poling in order to give rise to second order nonlinearity is very easy. On the other hand, small fields applied are unfavorable for charge transport and generation, both of which are essential for the PR effect. Furthermore, the charge transport in these systems is due to diffusive motion of ions causing hydrodynamic turbulences, if the applied fields are too high. Using liquid crystal cells faces moreover the problem, that the inherent long range orientational interaction requires very large grating spacing of several tens up to hundreds of microns to take place to a sufficient degree. For smaller grating spacings, the elastic energy counteracting a periodic modulation of the birefringence increases dramatically, eventually almost suppressing PR response completely. The large grating spacings result in slow response times on the one hand and operation in the Raman-Nath regime (thin holographic grating) on the other. Furthermore, the spatial resolution of a hologram written at large grating spacings is unsatisfactory.

Photorefractive response has been proven in commercial nematic liquid crystals (e.g. 5CB) doped with small amounts of Rhodamine 6G [96], C₆₀ [97, 98] or perylene and NI (N,N'-di-(n-octyl)-1,4,5,8-naphthalin-diimide) [99, 100] for generating mobile ions. The latter system was also reported with the naphthalin-diimide moieties covalently attached to an acrylic polymer backbone [101], which the authors referred to as polymer stabilized liquid crystals. Up to 8 diffraction orders have been observed [99] and diffraction efficiencies of up to 12% [97] were obtained for PR liquid crystalline systems. Gain coefficients of no less than 2890cm⁻¹ were stated [98], however, for operation in the Raman-Nath regime. Thus the physical significance of this number is strongly reduced. On the other hand, a gain coefficient of $\Gamma = 15\text{cm}^{-1}$ was reported for polymer stabilized liquid crystals operating at the edge of the condition for considering a photorefractive grating as a volume grating [101]. Generally all the authors point out, that the mechanism of the formation of the space-charge field is actually not classically photorefractive but at least partly due to the Carr-Helfrich effect [102, 103]. Please note finally, that the holographic diffraction properties of pure liquid crystalline systems are two-dimensional, i.e. diffraction is only observed for p-polarization. This is due to the fact, that the relaxed phase of liquid crystals is not isotropic like in polable polymers and thus, the relation eq. (2.4 - 74) is not applicable.

A very promising approach to realize photorefractive liquid crystalline systems has been followed by Ono et. al.. They showed, that mixing high and low molecular mass liquid crystals leads to nematic phase systems operable at the low external electrical dc fields characteristic for liquid crystalline systems, but in the volume grating regime with grating spacings in the order of few microns [104]. The first system reported was composed of a typical commercially available liquid crystal (4-pentyl-4'-cyano-triphenyl, E44) and a side chain liquid crystalline polymer (SLCP) carrying a liquid crystal covalently attached to an acrylic polymer backbone by an alkyle spacer. The authors refer to their material class as polymer dissolved liquid crystals (PDSLCS). The systems in general are doped with a small amount of common sensitizers, in

this case C_{60} . Net gain of up to $\Gamma = 43\text{cm}^{-1}$ and a diffraction efficiency of $\eta = 9\%$ with a response time constant of 200ms was obtained for a $50\mu\text{m}$ thick device at an applied field of $4\text{V}/\mu\text{m}$ and a grating spacing of $4\mu\text{m}$. Further optimization of these PDSLCS basically by varying the molar mass of the high molar mass component and using an appropriate mixture of slightly different low molecular mass liquid crystals (commercial name: E7) finally yielded composites showing response times down to 15ms while maintaining gain coefficients of $\Gamma = 270\text{cm}^{-1}$ at $0.1\text{V}/\mu\text{m}$ field applied to samples of $50\mu\text{m}$ thickness and at a grating spacing of $2.4\mu\text{m}$ [105]. However, it must be pointed out, that the response times reported refer to the evolution of the gain coefficient and thus are not directly comparable to the response times usually published for amorphous PR polymers, which are commonly obtained from the evolution of the refractive index modulation. Nevertheless, these are impressing performance data. For the same class of materials, world record values of up to $\Gamma = 600\text{cm}^{-1}$ for volume gratings have as well been reported for $50\mu\text{m}$ thick samples, a grating spacing of $2.8\mu\text{m}$ and an applied field of $0.7\text{V}/\mu\text{m}$ [106]. Recently, the concept has been extended by introducing “real“ photoconduction to this material class. Please recall, that the PDSLCS reviewed above are photoconductive due to ionic diffusion and drift. For this purpose a 1:1 copolymer carrying the same mesogenic group as SLCP as well as carbazole covalently attached to the acrylic backbone and TNF as sensitizer have been used at otherwise identical composition as described above. The PR liquid crystalline composite thus obtained showed DFWM diffraction efficiencies of up to $\eta = 39\%$ in a $50\mu\text{m}$ thick sample at an applied field of $0.3\text{V}/\mu\text{m}$ and for a grating spacing of $2.8\mu\text{m}$. Response times of these systems obtained from DFWM down to 1sec for grating build-up have been reported [107, 108]. The grating erasure, however, is roughly twice as fast as the build-up. Accounting, on the other hand, for the early stage of research on this very promising class of photorefractive organic composites, one may expect significant progress in the future. In fact it has to be admitted, that PDSLCS may be about to drive out PR polymers and glasses since they don't require application of such high external fields as necessary for polymers and glasses at meanwhile competing performance.

Eventually it should be noted, that there has been a third approach to utilize liquid crystals for photorefractive amorphous organic materials, namely polymer dispersed liquid crystals (PDLC's) [109, 110]. In these systems, the liquid crystal is dispersed in a photoconducting polymer matrix forming small droplets, which are in the mesophase. The polymer matrix decouples the droplets, which breaks the long range orientational order and thus the droplets exhibit random director of their individual mesophase. This material class may be understood as an intermediate stage on the way from liquid crystals to PDSLCS, utilizing liquid crystals and allowing for the operation in the volume grating regime of holography. The basic operating conditions of these systems are in-between PR polymers or glasses and PDSLCS, i.e. a relatively strong electrical field is necessary for operation, not as strong as required for polymers, but nevertheless discounting the major advantage of liquid crystalline systems. The performance of PDLC's was found to be comparable to PR polymers and glasses. However, the inherent inhomogenous character of a dispersion results in bad optical quality (strong scattering), which makes these systems unfavorable in general. Except in [111] this approach has not been pursued any more after the initial works.

3.2.3.) Low molecular mass glasses

Strictly speaking, low molecular mass glasses consist solely of one or more low molecular mass components forming an amorphous glassy solid. However, this definition will be

expanded to the case of composites containing up to about 10%wt high molecular mass polymeric compounds. This is reasonable, since the low molecular mass component will dominate the bulk properties and the polymeric component may be considered as some sort of stabilizing matrix. Materials with more than 10%wt polymer content will be considered as polymer composites, which will be discussed later on.

Low molecular mass glasses (referred to as LMMG hereafter) commonly consist of bifunctional molecules acting as NLO chromophore as well as charge transporting matrix. These properties may be combined in one moiety or may be linked by covalently binding transporting moieties with NLO chromophores so that these two properties are combined in one molecule but are intramolecularly decoupled to some degree. The latter approach has the apparent advantage, that the NLO chromophore changes its optical properties less significantly when the molecule acts as charge transporting moiety and that the charge transporting properties can be optimized independently by using transporting agents known to show deliberate charge carrier mobility. LMMG's have first been taken into consideration as potential photorefractive materials by Lundquist et. al. [91] as a way to increase the NLO chromophore content in a PR amorphous organic system above a certain threshold concentration, which, in polymer composites, basically is determined by the solubility of the low molecular mass components in the polymer matrix, the thermodynamic stability of the resulting system and its dielectric strength. In contrast to the second way of overcoming this problem, which is the monolithic polymer approach discussed below, the LMMG approach usually requires less synthetic efforts and inherently allows for the occurrence of the orientational enhancement effect, provided the glass-transition temperature is sufficiently low. A major draw back of LMMG's, however, is the inherently fairly slow PR response basically due to mutual orientational hindrance of the glass forming molecules even at low T_g 's. This problem may be solved by adding plasticizers or small amounts of inert polymers as "lubricants" for the orientational motion. This naturally reduces the chromophore concentration, which is, however, still considerably higher than achievable in typical polymer composites. The major advantage of low molecular mass glasses as PR materials is the stability against phase separation, which is still a major problem in polymer composites. However, there may be a problem concerning crystallization inherent in low molecular mass systems. Furthermore, the bulk properties of such systems mostly cannot be altered as simply as in polymer composites. Especially the tuning of the properties of systems containing multifunctional components usually requires considerable synthetic efforts.

One of the first LMMG's was presented by Lundquist et. al. [91]. The system was based on the NLO chromophore 2BCNM and solely consisted of the glass forming chromophore doped with small amounts of sensitizer (0.3%wt TNF). A glass-transition temperature of $T_g \approx 25^\circ\text{C}$ and a very high refractive index modulations of up to $\Delta n = 10^{-2}$ at $90\text{V}/\mu\text{m}$ external field was reported, however, also dramatically slow response behavior (the authors abstained from quoting numerical values). The authors found out that doping this system furthermore with 10%wt PMMA decreases the holographic response time significantly to $\tau = 83\text{sec}$ at an applied field of $40\text{V}/\mu\text{m}$ obtained by stretched exponential (KWW) fitting using a stretch exponent of $\beta = 2$. The first diffraction maximum in DFWM for a sample thickness of $150\mu\text{m}$ using an operating wavelength of 676nm , a recording intensity of $1\text{W}/\text{cm}^2$ and otherwise a standard setup geometry (external tilt angle 60° , inter-beam angle 20° , p-polarized read-out, recording polarization not addressed) was determined at $40\text{V}/\mu\text{m}$ in the quasi steady-state regime with a corresponding PR gain of $\Gamma \approx 70\text{cm}^{-1}$.

A different approach has been followed by Wang et. al. [112]. The authors reported on the PR properties of a novel carbazole trimer hereafter referred to as TRC1. The TRC1 glass was solely doped with different amounts of TNF (0.05%wt up to 0.5%wt) for sensitizing and the material showed a glass-transition temperature of $T_g = 29^\circ\text{C}$. DFWM diffraction efficiencies of up to $\eta \approx 24\%$ in $130\mu\text{m}$ thick samples were measured at 633nm operating wavelength with s-

polarized recording beams at an intensity of $0.4\text{W}/\text{cm}^2$, $3.9\mu\text{m}$ grating spacing and for about $40\text{V}/\mu\text{m}$ applied field. For p-polarized recording at an intensity of $0.5\text{W}/\text{cm}^2$ a net PR gain of up to 76cm^{-1} was as well reported for about $40\text{V}/\mu\text{m}$ applied field. The PR phase shift obtained from grating translation technique was found to approach 90° for fields exceeding $20\text{V}/\mu\text{m}$, which is a questionable result, since it implies diffusion controlled grating build-up according to the standard theory of photorefractivity. Accounting for the strong applied field, this seems not realistic. The dynamic response behavior was not addressed.

Li et. al. reported on a PR organic glass based on a functionalized oligothiophene [113]. The material is referred to as OT1 hereafter. The authors found a net optical gain of 83cm^{-1} at $71\text{V}/\mu\text{m}$ applied field and for an operating wave length of 633nm applying p-polarized recording. The external tilt angle of the sample normal with respect to the bisector between the recording beams was 30° . Under identical conditions the authors obtained a non-degenerate four-wave-mixing diffraction efficiency of $\eta = 40\%$ correlated to a refractive index modulation of $\Delta n = 2.55 \times 10^{-3}$ using a p-polarized read-out beam. A response time for grating build-up of 42ms was obtained from the initial growth of the grating using the uncommon growth function $\eta(t) \sim e^{-2t/\tau}$ and at $62\text{V}/\mu\text{m}$ applied field. The sample thickness was reported as „typically in-between $60\mu\text{m}$ to $75\mu\text{m}$ “. Data on the glass-transition temperature, the actual beam intensities and the detailed setup geometry were not provided. A conceptually similar material was described by Wang et. al. and comprehensively investigated [114]. The system showed uncommon behavior due to bipolar charge transport leading to undesired side effects.

A siloxane based PR glass has been reported by Mager et. al. [115]. An unsubstituted and an acceptor substituted carbazole moiety have been N,N-covalently connected by short siloxane spacers. The materials $\text{Si}_2(\text{Cz-Cz}/\text{TCNE})$ and $\text{Si}_3(\text{Cz-Cz}/\text{Stilbene})$ showed glass-transition at $T_g = 26^\circ\text{C}$ and $T_g = 5^\circ\text{C}$, respectively, and acted as excellent glass-formers, the glass showing high optical quality. Doped with TNFM, $\text{Si}_2(\text{Cz-Cz}/\text{TCNE})$ was reported to show a net optical gain of 14cm^{-1} at a gain coefficient of $\Gamma = 38\text{cm}^{-1}$ at $50\text{V}/\mu\text{m}$ applied to a $100\mu\text{m}$ thick sample and at an operating wavelength of 514nm . $\text{Si}_3(\text{Cz-Cz}/\text{Stilbene})$ was found to exhibit a gain coefficient of $\Gamma = 180\text{cm}^{-1}$ at $60\text{V}/\mu\text{m}$, however doped with some soluble fullerene derivative similar to PCBM and at 633nm operating wavelength. The latter material did not yield net gain. The figures of merit according to eq. (2.5 - 123) were quoted as well. Both materials were not optimized and appear to be very promising.

A group of triphenylamine (TPA) based PR organic glasses was developed by Hohle et. al. [116] and was characterized by Hofmann et. al. [117] and Grasruck et. al. [118]. For DRDCTA plasticized with EHMPA and sensitized with C_{60} , initial response times in DFWM experiments of down to $\tau = 0.5\text{ms}$ at $92\text{V}/\mu\text{m}$ applied field, $10.8\text{W}/\text{cm}^2$ recording intensity at 645nm operating wavelength, $22.3\mu\text{m}$ thick samples and a grating spacing of $3.5\mu\text{m}$ were reported. For $180\text{mW}/\text{cm}^2$ intensity at 670nm wavelength and otherwise identical conditions as described above the authors found an initial response time of $\tau \approx 10\text{ms}$. The authors furthermore reported on refractive index modulations of up to $\Delta n \approx 6 \times 10^{-3}$ for p-polarized read-out and s-polarized recording at $110\text{V}/\mu\text{m}$ external field and maximum gain coefficients of up to $\Gamma \approx 140\text{cm}^{-1}$ for p-polarized recording which, however, is counteracted by a considerable absorption of $\alpha = 42\text{cm}^{-1}$ at 670nm and $\alpha = 93\text{cm}^{-1}$ at 645nm operating wavelength. The same system plasticized with DOP showed considerably slower response behavior and otherwise comparable performance data. The glass-transition temperature of both systems has been estimated to about 20°C . The system furthermore has been altered by replacing the NLO chromophore moiety (DR) in DRDCTA by stilbenes. However, no holographic data for these systems have been presented yet, but solely investigations on the charge carrier transport behavior [118].

Another PR molecular glass based on TPA has been presented by Ogino et. al. [119]. The materials TPA-NA and TPA-DCVA are composed of acceptor substituted anilines covalently

attached to TPA via a diester spacer and showed glass-transition temperatures of $T_g = 28^\circ\text{C}$ and $T_g = 34^\circ\text{C}$, respectively. For sensitization 0.2%wt C_{60} was used. The holographic characterization was performed with a standard setup working at a wavelength of 633nm and external recording beam angles of 50° and 70° , each of which having an intensity of $130\text{mW}/\text{cm}^2$. For TPA-DCVA a steady-state diffraction maximum of 66% for p-polarized read-out and s-polarized recording in DFWM was observed at $65\text{V}/\mu\text{m}$ external field applied to a $100\mu\text{m}$ thick sample, whereas the diffraction efficiency in TPA-NA was reported to be about 33% at $80\text{V}/\mu\text{m}$ not showing a maximum at lower fields. For p-polarized recording net gains of 58cm^{-1} for TPA-NA and 182cm^{-1} for TPA-DCVA at $60\text{V}/\mu\text{m}$ were quoted. DFWM response times of about 3 to 5sec for TPA-NA and 5 to 9sec for TPA-DCVA depending on the applied field were obtained from single exponential fits. The obviously bad agreement of the fits with the experimental curves as shown in a presented example plot, however, indicates the obtained response times to be only rough estimates. Considering the glass transition temperatures in context with the reported ambient temperature of 20°C , it should be possible to accelerate the dynamic response by adding plasticizers.

Recently Wang et. al. have reported on an exciting novel multifunctional glass-forming PR material based on methine dyes [120]. These materials combine all functionalities (including charge generation) necessary for photorefractivity in one molecular moiety, which was only slightly modified to provide glass-forming properties. The molecules are referred to hereafter as MG1 ($T_g \approx 6^\circ\text{C}$) and MG2 ($T_g \approx 26^\circ\text{C}$). The authors point out, that the materials are electron conducting and thus the first of this kind utilized for PR application in organic materials. DFWM experiments were carried out with 633nm operating wavelength for MG1 and 780nm for MG2, both the setups having otherwise similar configuration with 54° (53°) external tilt angles and 19.8° (19.6°) inter-beam angles and $2.9\text{W}/\text{cm}^2$ ($3\text{W}/\text{cm}^2$) total intensities with beam ratios of 0.98 (1.09) for 633nm (780nm) in s-polarization. For p-polarized read-out, the authors obtained diffraction maxima of 74.3% (87.6%) at $53\text{V}/\mu\text{m}$ ($44\text{V}/\mu\text{m}$) fields applied to $130\mu\text{m}$ thick material films and maximum refractive index modulations of 5.6×10^{-3} (1.0×10^{-2}) achieved for the highest fields applied (not specified) for MG1 (MG2). For MG2 the authors reported bi-exponential dynamic build-up behavior for the refractive index change with the time constants 16.6ms and 1.2s obtained at $84\text{V}/\mu\text{m}$. However, the authors did not explain how they determined the time constants at a field considerably higher than required for the first diffraction maximum, which reduces the physical significance of the presented results on the PR dynamics. The gain coefficients were obtained on the setups described above, however with total intensities of $2.83\text{W}/\text{cm}^2$ ($3.655\text{W}/\text{cm}^2$) at beam ratios of 1.02 (3.78) and with p-polarized recording beams at 633nm (780nm). Gain coefficients of $\Gamma = 116.1\text{cm}^{-1}$ and $\Gamma = 215.9\text{cm}^{-1}$ were measured at $89\text{V}/\mu\text{m}$ applied field, and the absorption coefficients were specified as $\alpha = 1.64\text{cm}^{-1}$ and $\alpha = 5.54\text{cm}^{-1}$ for MG1 and MG2, respectively.

3.2.4.) Monolithic polymers

Numerous monolithic PR polymers have been developed since the first observation of the PR effect in a polymer in 1991 [12]. In contrast to the PR liquid crystalline systems and the PR low molecular glasses, both of which are comparatively young material classes and thus could be reviewed rather comprehensively above, this is not appropriate in the case of monolithic PR polymers. Hence, subsequently only a selection of important systems recently presented will be summarized.

For the subsequent review monolithic polymers shall be defined by the condition, that all the functional moieties required for the PR effect except the sensitizer are attached to a

collective polymer backbone. The sensitizer as very low amount dopant will be allowed for being added to the system as low molecular mass component. An advantage of monolithic polymers as PR materials is their phase stability. Phase separation cannot occur and crystallization is strongly hindered, however, cannot be excluded completely especially on short length scales (formation of micro-crystalline structures and/or domains) and/or long time scales. Partial crystallization may be especially a problem in strongly polar materials and in systems allowing for the formation of hydrogen bridges. The advantage of high phase stability, however, is counteracted by the fact, that tuning of the bulk properties of these systems can only be performed making significant synthetic efforts. Furthermore, the general processibility is usually considerably worse than in the case of low molecular mass glasses and PR polymer composites. Accordingly, monolithic PR polymers are comparatively “expensive” systems.

The search for fast responding PR polymers has been another driving force for the development of fully functionalized PR polymers. This material class offers the possibility of incorporating large amounts of chromophore without lowering the glass transition temperature, thus opening a way to purely electro-optic systems of high nonlinearity. Furthermore, the orientation of the NLO chromophores in low- T_g systems was regarded as a dominant factor limiting the response time of PR polymers [121 - 123]. Thus, purely electro-optic system have been expected to be faster than systems showing orientational enhancement. However, as will be shown in “5.2.3.) The relation between the glass-transition temperature and the dynamic performance in PVK based PR polymers” on page 243 ([124]), the build-up dynamics of the PR grating in low- T_g PR polymers is limited by the build-up dynamics of the PR space-charge field rather than by the orientational dynamics of the chromophores whereas the latter is the limiting factor in high- T_g systems still showing orientational enhancement. On the other hand, Herlocker et. al. proved, that the orientational dynamics may be insignificant even in high- T_g systems [125]. It turned out, that the dominant aspect in the search for fast PR polymer systems is actually the question of the electrical properties, i.e. charge carrier mobility and generation efficiency, rather than the type of the nonlinear optical response. Accordingly, the fully functionalized electro-optic PR polymers, which have mostly been developed on the basis of the same organic photoconductors as the low- T_g PR polymer composites did not meet the high expectations.

The steady-state PR performance of monolithic polymers is dominantly determined by the question of the extent to which the orientational enhancement effect can contribute to the overall PR effect. Since also the NLO chromophores are attached to the polymer backbone, their orientational mobility is restricted. Orientational mobility in general may be allowed for to some extent by introducing sufficiently long and flexible spacer groups between the chromophore moieties and the polymer backbone. However, this action usually adversely affects the charge transporting properties, since the introduction of such spacer groups rises the portion of inert material in the overall system. The dynamic performance of monolithic systems is limited by their electrical properties on the one hand and, depending on the system, by the orientational dynamics of the chromophores on the other. In general, up to now the steady-state as well as the dynamic PR performance of all the known monolithic PR polymers is inferior to today’s high-performance polymer composites, low molecular glasses and polymer dissolved liquid crystals.

Please note, that the systems reviewed subsequently will not be described in detail in the text. Instead, the materials will be numbered systematically as P# and their structures will be shown in section Appendix D. If polymer systems are presented, where the same basic system has been combined with various functional groups, the functional groups are numbered systematically as well using CHR# for chromophores or CT# for charge transporting moieties. The same principle applies if different spacer groups have been used for one and the same moiety. The number scheme then refers to the attached moiety.

Van Steenwinckel et. al. have presented a group of fully functionalized polymethacrylates

utilizing carbazole as charge transporting moiety (P1) and three different stilbenes as NLO chromophores (CHR1 - 3) [126]. The systems were sensitized with 1%wt TNFM and were characterized holographically at 780nm operating wavelength. The glass transition temperatures of the different systems were determined to $T_g(\text{P1CHR1a}) = 66^\circ\text{C}$, $T_g(\text{P1CHR1b}) = 48^\circ\text{C}$, $T_g(\text{P1CHR2}) = 47^\circ\text{C}$, $T_g(\text{P1CHR3}) = 52^\circ\text{C}$, where “P1CHR1a” and “P1CHR1b” denote systems of different molecular mass and component ratio. For photorefractive characterization a setup with an external inter-beam angle of the recording beams of 14° and an external tilt angle of 50° was used, and the sample thickness was $125\mu\text{m}$. For DFWM experiments s-polarized recording and p-polarized read-out and for 2BC p-polarized recording was used. The correlated intensities have not been reported but rather beam power and some beam diameter, which is not referred to the beam profile. This makes it difficult to compare the reported results with data presented elsewhere. The diffraction efficiency and the gain coefficient have been reported for different ambient temperatures. Best performance values were found for P1CHR3 at the highest applied ambient temperature of 54°C . A DFWM diffraction efficiency of $\eta = 60\%$ was obtained and a gain coefficient of $\Gamma = 57\text{cm}^{-1}$, both at $58\text{V}/\mu\text{m}$ applied field. A DFWM diffraction maximum was not observed within the reported field interval. At 20°C ambient temperature diffraction efficiencies of up to about $\eta \approx 11\%$ and gain coefficients of up to about $\Gamma \approx 12\text{cm}^{-1}$ at $E_{\text{ext}} \approx 62\text{V}/\mu\text{m}$ were found for the same system. The response times have been considered. The authors furthermore report on significant improvement of the PR performance if a substantial amount of plasticizer is added [127]. However, the resulting systems then are no more monolithic PR polymers. Dynamic data have not been presented for these systems as well. The authors point out, that their polymers contain only about 20%wt carbazole moieties.

Yu et. al. recently reported on numerous fully functionalized PR polymers [128 - 131] among of which conjugated systems are outstanding, which contain the transition metal complexes. The conjugated polymer backbone exhibits the required charge transporting properties, whereas the metal complexes incorporated in the polymer backbone by copolymerization act as sensitizers. The thus provided amount of sensitizer is much larger than typically used in PR polymers. The NLO properties were introduced by covalently attaching stilbenes. In [131] the development of these systems is reviewed in chronological order. The first systems containing ionic $\text{Ru}(\text{bpy})_3(\text{PF}_6)_2$ moieties were systems showing high glass-transition temperature (high- T_g) and proved high photorefractivity with net optical gains of up to almost 200cm^{-1} without external field. However, the system has been corona poled and operated at the edge of the Raman-Nath regime due to the small film thickness ($\approx 10\mu\text{m}$) achievable with the high- T_g systems. In contrast, corresponding low- T_g systems allowed for films of more than $100\mu\text{m}$ thickness and the orientational enhancement effect, however, in general showed unusual behavior (saturation of the gain coefficient as a function of the applied field) and no net gain, which the authors attribute to an alignment of the Ru- PF_6 dipoles under the influence of the poling field screening the actual field sensed by the charge generating metal complexes. In order to avoid this screening effect, neutral phtalocyanine and porphyrine complexes were used as charge generators incorporated in low- T_g fully functionalized PR polymers (P2, P3), which then exhibit high photorefractivity. The obtained performance data [130] are among the best found in monolithic PR polymers up to now. The authors report glass-transition temperatures of $T_g \approx 16^\circ\text{C}$ for all systems investigated. Net optical gains of up to 53.3cm^{-1} (P2) and 66.5cm^{-1} (P3) at an external field of $60\text{V}/\mu\text{m}$ applied to $104\mu\text{m}$ thick films were achieved at 633nm operating wavelength and with p-polarized recording beams intersecting at an internal angle of 7.5° . Tilt angle and beam intensities have not been specified. DFWM diffraction efficiencies of 12% (P2) and 18% (P3) have been obtained for $60\text{V}/\mu\text{m}$ applied field and p-polarized read-out. The authors report strongly field dependent PR grating build up dynamics yielding time constants down to 4.7sec (P2) and 450ms (P3) determined

from fitting the experimental data to the uncommon expression $\eta(t) \sim e^{-2t/\tau}$ for the initial growth of the DFWM diffraction signal for an external field of $60\text{V}/\mu\text{m}$ and an incident light intensity of $830\text{mW}/\text{cm}^2$.

Hwang et. al. presented a fully functionalized low- T_g single component PR polymer (P4) showing photorefractive response even without adding small amounts of sensitizer [132]. The system showed a T_g of 15°C . A gain coefficient of $\Gamma = 9.7\text{cm}^{-1}$ (absorption coefficient $\alpha = 6.7\text{cm}^{-1} \Rightarrow 3\text{cm}^{-1}$ net gain) at $50\text{V}/\mu\text{m}$ external field and using p-polarized recording beams, and a DFWM diffraction efficiency of more than $\eta = 3\%$ at $85\text{V}/\mu\text{m}$ external field using s-polarized recording beams and a p-polarized reading beam were obtained. In both experiments identical beam intensities of $60\text{mW}/\text{cm}^2$ were applied, the sample was tilted by an external angle of 60° , the external angle enclosed by the recording beams was 11° , and the film thickness was $100\mu\text{m}$. The operating wavelength has been reported as $\lambda_0 = 633\text{nm}$. It is important to emphasize once more, that these performance data refer to a real single component monolithic polymer, which, thus, is the first material of this kind showing notable photorefractivity reported on up to date. Please note, however, that there are PR single component monolithic glasses, as described in the preceding section. Furthermore, the authors have reported that adding up to 1%wt TNF as sensitizer improves the PR performance up to $\Gamma = 27.4\text{cm}^{-1}$ (15cm^{-1} net gain) and $\eta = 5.2\%$ at $60\text{V}/\mu\text{m}$ external field each and otherwise identical conditions as mentioned above. At $50\text{V}/\mu\text{m}$, the gain coefficient amounts to about $\Gamma = 12.5\text{cm}^{-1}$, not yielding net gain.

Hattermer et. al. presented a variety of novel fully functionalized purely electro-optic (i.e., high- T_g) PR polymers in [133]. Having focused on the synthesis, the authors only report on a proof of principle of the photorefractivity of their systems for a particular model system (P5). However, the PR performance presented is outstanding for this class of materials. In order to fabricate dielectric stable thin films of the necessary thickness, the authors added a small amount of ethylcarbazole as a plasticizer. Therefore, one can argue about whether this system is still monolithic. However, the authors quote a glass transition temperature of $T_g = 79^\circ\text{C}$, high stability of the optical nonlinearity after poling the system at elevated temperatures and cooling down with the poling field applied, and proved the purely electro-optic nature of the PR effect by relating the sign of the gain to the field direction in comparison to a low- T_g system (see below). Therefore, in this case the plasticizer may be taken as a means for improving dominantly the processability of the material rather than altering the PR properties and the system may be considered as basically monolithic. The material was prepoled at an ambient temperature of $T = 80^\circ\text{C}$ applying an external field of $76\text{V}/\mu\text{m}$ to the film. The PR measurements were carried at 633nm operating wavelength with s-polarized recording beams for both the 2BC and the DFWM experiment showing a total external intensity of $205\text{mW}/\text{cm}^2$ and equal internal intensity ratio. The external inter-beam angle was 20° and the sample was tilted by 60° . P-polarized read-out was applied in the DFWM experiments. A steady-state gain coefficient of $\Gamma = 7\text{cm}^{-1}$ and a steady-state diffraction efficiency of $\eta = 1.3\%$ are reported for an applied field of $95\text{V}/\mu\text{m}$. The response time constants were obtained from dynamic experimental data of η and Γ (both at $E_{ext} = 95\text{V}/\mu\text{m}$) by fitting to a bi-exponential associative growth function. Time constants of $\tau_1 = 100\text{ms}$ (40ms) and $\tau_2 = 1.5\text{sec}$ (660ms) and relative weighting factors of $A_1 = 0.77$ (0.81) and $A_2 = 0.23$ (0.19), respectively, were determined for the evolution of η (Γ). The authors point out that the external field had to be applied in order to observe the PR effect despite the system has been prepoled. The DFWM diffraction efficiency is the highest and the PR response is the fastest reported up to date for this class of materials. The purely electro-optic nature of the observed PR response has been proven by comparing the sign of the gain coefficient for a well-known low- T_g system showing dominant birefringence contribution to the refractive index modulation with the sign of the gain coefficient for the currently discussed system under identical experimental conditions. This argumentation bases on the fact that for s-polarized recording, the electro-optic and the birefringence contribution to

the refractive index modulation will have opposite sign according to eq. (2.5 - 45) and eq. (2.5 - 51). Thus, according to eq. (2.5 - 102), the gain coefficient obtained for a (dominantly) electro-optic system must have the opposite sign as compared to the gain coefficient obtained for the reference system with dominant birefringence contribution to the refractive index modulation. Please note, that this is a proof of principle and does not exclude a birefringence contribution to the electro-optic system, which, however, then counteracts the electro-optic response according to orientational enhancement model (see page 131 ff).

Eventually, Park et. al. presented a multifunctional PR polymer based on TPA (TDPANA-FA) [134] and carrying NPP as NLO chromophore incorporated in the polymer backbone. The polymer showed a glass-transition temperature of $T_g = 204^\circ\text{C}$ and required a substantial amount of plasticizer in order to observe PR response. Therefore, this system actually cannot be considered as a monolithic PR polymer. However the concept may be developed to a monolithic system in the future and thus will be treated in this context. The PR properties were examined at 100 μm thick films of TDPANA-FA plasticized by 40%wt TCP and sensitized by C₆₀. For the 2BC experiments p-polarized recording beams were used and for the DFWM experiments s-polarized recording beams and a p-polarized reading beam. The recording beams intersected at an external angle of 20° and the sample was tilted by 50°. The total recording intensity was 300mW/cm² at a beam ratio of 1:1. A DFWM diffraction efficiency of $\eta = 0.92\%$ and a response time of $\tau_1 = 4\text{ms}$ (fast component) obtained from fitting the evolution of the refractive index modulation bi-exponentially (the slow component was not presented) were reported for an external field of $E_{ext} = 80\text{V}/\mu\text{m}$. A gain coefficient of $\Gamma = 36\text{cm}^{-1}$ has been achieved at the same external field. The actual T_g of the examined composite is not mentioned. This system may be expected to be further developed to the first monolithic PR polymer operating below video rate in the future.

3.2.5.) Polymer composites

Most PR polymers developed up to date are polymer composites. PR polymer composites basically consist of a more or less inert polymer backbone which may or may not carry some functional moieties required for PR response covalently attached. The other functionalities required are incorporated in the system as low molecular mass components. It is clear that this „mixing“ technique has the inherent advantage that the systems can be tuned very easily by simply altering the composition or using different components. On the other hand, PR polymer composites tend to lack compositional stability. Especially the typically highly polar NLO chromophores being mobile in low- T_g systems tend to crystallize on relatively short time scales in the usually only little polar polymer matrix. The system then becomes opaque and brittle.

The great variety of sometimes even only slightly different PR polymer composites developed up to now requires a different approach for a review as compared to the PR systems discussed in the preceding sections. Therefore, this section will be structured as follows. Firstly, two high-performance PR polymer composites will be discussed, which may be regarded as milestones in this field. In this context typical performance data of high-performance PR polymer composites will be shown. Secondly, general problems will be discussed, which have to be taken into account in order to compose a PR polymer composite. Thereafter, the groups of components will be discussed separately.

Performance data of some more important PR polymer composites, which are not discussed in the following section “3.2.5.1.) Milestones” will be reviewed in context with the discussion of the NLO chromophore in “3.2.5.5.2.) Characteristic examples” on page 173.

3.2.5.1.)Milestones

The first high performance PR polymer composite was presented in 1994 by Meerholz et. al. [13]. Consisting of PVK (hole conductive matrix), ECZ (plasticizer), TNF (sensitizer), and DMNPAA (NLO chromophore) in the ratio of 33:16:1:50%wt, the polymer composite exhibited a glass-transition temperature of $T_g \approx 5^\circ\text{C}$. For the holographic characterization s-polarized as well as p-polarized recording beams of 675nm wavelength and $1\text{W}/\text{cm}^2$ total intensity were used in the 2BC experiments and s-polarized beams of identical total intensity in the DFWM experiments. The sample was tilted by 60° and the external intersection angle of the recording beams was 22° . The DFWM diffraction efficiency was determined for s-polarized as well as p-polarized read-out. The film thickness was $105\mu\text{m}$. Gain coefficients of $\Gamma_p = 220\text{cm}^{-1}$ and $\Gamma_s = -40\text{cm}^{-1}$ were achieved at $90\text{V}/\mu\text{m}$ applied field (total absorption coefficient at this field: $\alpha = 13\text{cm}^{-1}$). In the DFWM experiments, the first diffraction maximum occurred at an applied external field of $56\text{V}/\mu\text{m}$ for p-polarized read-out and for s-polarized read-out a diffraction efficiency of $\eta_s = 60\%$ has been achieved for an external field of $90\text{V}/\mu\text{m}$ not showing a maximum in the range of external fields applied. The dynamic response behavior has not been investigated at that time. However, the dynamics of a system with identical composition was determined later in [124] for a total recording intensity of $45\text{mW}/\text{cm}^2$ and 633nm operating wavelength on a setup of very similar configuration. Fitting the growth of the DFWM diffraction signal to a bi-exponential associative growth function yielded the time constants $\tau_1 = 1.5\text{sec}$ and $\tau_2 = 10\text{sec}$ with relative weighting factors of $A_1 = 0.73$ and $A_2 = 0.26$ at $56\text{V}/\mu\text{m}$ applied field. A closely related system containing less NLO chromophore and showing lower glass transition temperature yielded time constants of down to $\tau_1 = 200\text{ms}$ at $87.5\text{V}/\mu\text{m}$ applied field. These results will be discussed later in detail in the section devoted to the experimental results. The first high-performance PR polymer substantially suffered from the before mentioned lack of compositional stability. The stability of the systems could be improved significantly by using eutectic mixtures of the NLO chromophores 2,5-DMNPAA and 3,5-DMNPAA [135] and 2,5-DMNPAA and MNPAA [136]. Especially the latter system showed not only significantly improved shelf life time but as well markedly improved PR performance. The family of PR polymer composites described in the current section still counts to the best performing organic PR materials and is, moreover, the best characterized as well. Many systems have been developed as novel PR polymer composites, which actually may be regarded as closely related derivatives of the first high-performance PR polymer.

The first report of a high speed PR polymer utilized the build-up dynamics of the PR gain in order to discuss the PR response time [137]. The authors obtained a single response time of $\tau_g = 7.5\text{ms}$ for the build-up of the PR gain at $70\text{V}/\mu\text{m}$ external field applied to a $100\mu\text{m}$ thick sample and $500\text{mW}/\text{cm}^2$ total recording intensity. The system was a TPD based PR polymer utilizing DEANST as NLO chromophore (15%wt, which is fairly low) and C_{60} as sensitizer and exhibited $T_g \approx 30^\circ\text{C}$. The concomitant gain coefficient was reported as $\Gamma = 40\text{cm}^{-1}$ (net gain 33.5cm^{-1}) and the setup configuration was characterized by an external tilt angle of 50° and an external inter-beam angle of 22.6° . The authors missed to report the beam polarization. DFWM experiments were not reported. It has already been discussed, that fitting the evolution of the PR gain does not yield response times, which can be compared reasonably with results obtained on the basis of the DFWM diffraction efficiency, which is by far the more common procedure. Nevertheless, the reported system represents the very first PR polymer composite stated to be operable at frequencies below video rate.

The first reliable report of a PR polymer composite exhibiting fast response in DFWM experiments has been provided by Herlocker et.al. [125]. The system investigated consisted of PVK (hole conducting matrix), ECZ (plasticizer), TNFM (sensitizer), and the tolane FTCN (NLO chromophore) in the ratio of 56:28:0.8:15.2%wt and exhibited a glass-transition

temperature of $T_g = 39^\circ\text{C}$. The PR properties were determined by 2BC utilizing p-polarized recording beams of 633nm wavelength, $500\text{mW}/\text{cm}^2$ total intensity and a beam ratio of 6.3:1, and by DFWM experiments utilizing s-polarized recording beams at identical total intensity as for 2BC but a beam ratio of 1:1 and p-polarized read-out. The setup was described as applying an external tilt angle of 60° and an external inter-beam angle of 20.5° resulting in $3.1\mu\text{m}$ grating spacing. The film thickness was reported as $105\mu\text{m}$. No net gain ($\Gamma = 35\text{cm}^{-1}$, $\alpha = 98\text{cm}^{-1}$) was achieved for external fields of up to $E_{\text{ext}} = 95\text{V}/\mu\text{m}$ due to strong absorption of the sensitizer at the applied operating wavelength. An internal DFWM diffraction efficiency of $\eta = 24\%$ was obtained not yet showing a diffraction maximum at the aforementioned field. The authors reported response times of $\tau_1 = 4\text{ms}$ (weighting 0.8) and $\tau_2 = 50\text{ms}$ (weighting 0.2) for the build-up of the refractive index grating obtained from fitting the evolution of the refractive index modulation calculated from DFWM diffraction data to a bi-exponential associative growth function. However, these performance data were obtained on the expense of strong absorption, which was induced by using a sensitizer at an operating wavelength in the visible, which is commonly applied in the infrared. Using TNF instead like in the aforementioned PVK:ECZ:DMNPAA:TNF-system, the system would be sufficiently transparent to possibly show a net gain, but also must be expected to response considerably slower in the PR dynamic experiments.

Please note, that a variety of fast PR polymer systems has been presented during the past two years, which exhibit more or less comparable speed at the expense of some other PR property. In particular, these systems often show large absorption which is extremely unfavorable for most potential applications. Furthermore, the “high-speed“ PR polymers are often doped with low amounts of chromophore in order to improve the electrical conduction properties of the system and, hence, must be operated at very high fields in order to obtain a reasonable dynamic range. Another method to speed up PR polymers is the application of high intensities of several W/cm^2 , which are not practicable or at least undesired in many potential applications. In conclusion, the dynamic performance of PR polymers and polymer composites is still a field of extensive research efforts and publications in this field must be considered with special care in order to reasonably trade off the properties reported.

3.2.5.2.)General problems

In this section, general considerations to be taken into account when designing some PR polymer composite system are discussed. Please note, that these considerations apply to PR low molecular glasses and monolithic polymers as well, and even to liquid crystalline systems, however, with some restrictions, which will not be discussed here.

In order to obtain PR response from an amorphous organic polymer system, generally three functionalities must be incorporated:

- a) photoconductivity
- b) photosensitivity
- c) optical nonlinearity.

This list must be extended by:

- d) in-situ polability

if a large PR effect is desired. These four functionalities may be incorporated in the polymer by

means of appropriate monofunctional or multifunctional moieties. The following general points must be taken into account:

3.2.5.2.1.)Miscibility

PR polymer composites are thermodynamically metastable systems inherently suffering from possible phase separation and crystallization of the contained low molecular mass components. Accordingly, the thermodynamic stability of PR polymer composites will strongly depend on the miscibility of low molecular mass components with the polymer matrix.

Thereby, special care must be taken of the compatibility of the polymer matrix and the NLO chromophore, since the latter is inherently rather polar, whereas the polymer matrix usually is not, and a substantial amount of chromophore must be incorporated into the system in order to obtain large nonlinearity. Since the mixing of components showing markedly different polarity is unfavorable in principle, the compatibility of the chromophore with the matrix is the major issue leading to often poor thermodynamic stability of PR polymer composites. The miscibility of a NLO chromophore with the polymer matrix may be improved by aliphatic side groups attached to the chromophore.

If a substantial amount of plasticizer shall be incorporated as well, similar considerations will apply. However, the plasticizer need not be strongly polar and thus the compatibility problem is less pronounced and more easy to solve.

It is clear, that components added in only small amounts (e.g. the sensitizer) must at least be soluble in the system in the amount desired.

3.2.5.2.2.)Absorption and the problem of isomerization gratings

The absorption spectra of the components with respect to the desired operating wavelength are of significant importance. On the one hand, a minimum absorption must be provided in order to generate free charge carriers, which then give rise to the PR space-charge field. This minimum absorption is typically introduced in a PR polymer composite by means of a sensitizer added in small amounts to the system. However, the other components of the system should not show notable absorption at the operating wavelength. Although this is a trivial demand, it often requires a trade-off between the nonlinear properties of the NLO chromophore and its absorption coefficient at the operating wavelength of the system. Unfortunately, the chromophores showing high molecular optical nonlinearity usually also absorb strongly in the visible or even in the near infrared, which often prevents their application in PR polymer composites. A further problem may arise from the ability of some very common NLO chromophores (especially azo-dyes) to undergo photoinduced isomerization. This may lead to an undesired local refractive index grating (i.e. shifted by 180° with respect to the interference pattern) behaving very differently as compared to the PR grating. The isomerization process may even occur at very small absorption (however, slowly).

Please note, that a PR polymer composite may be made faster in PR response by adding a strongly absorbing and/or a relatively large amount of sensitizer. Thus, a compromise must be found in this case as well.

3.2.5.2.3.)Relation of the energy levels of the components

The relevant energy levels in question are the highest occupied molecular orbital (HOMO) and the lowest unoccupied molecular orbital (LUMO) of the components. The relations of these energy levels must be coordinated correctly.

Subsequently, the relations of the HOMO's and the LUMO's of the chromophore and the

sensitizer will be discussed qualitatively with respect to the HOMO and the LUMO of the charge conducting moieties, hereafter referred to as “CTA“ (charge transporting agent). Hole conduction shall be presumed, but the general considerations to be discussed below will apply to electron conducting systems as well.

The charge transport in organic polymers takes place by means of subsequent redox steps, i.e. the hole transport results from exchange of holes between HOMO's of the CTA. Disregarding charge carrier injection from the electrodes, this requires previous photo-generation of the holes. By optical excitation, an electron is promoted from the HOMO of the sensitizer to its LUMO, leaving an empty place (hole) in the HOMO behind. This hole must be transferred to an adjacent CTA. In order to facilitate this process, the HOMO of the sensitizer thus should be of lower energy than the HOMO of the CTA so that the system gains energy by the transfer (i.e. the hole jumps upwards in energy (figure (3 - 1))). In the worst case the HOMO's in question may be of similar level, which however is not preferable. The HOMO of the CTA must not be lower than the HOMO of the sensitizer. The NLO chromophore should possess the lowest HOMO of all components in order to avoid its involvement in the charge transporting process. If the chromophore is involved in the charge transporting process, it may be charged temporarily and possibly no more contribute to the NLO response of the system during these time periods, which is not desired. Finally, if the system contains extrinsic traps, it is self-evident that their HOMO must be of higher energy than the CTA (otherwise, the functional moiety considered will not act as a trap).

Considering the LUMO's, there is only one condition to be fulfilled. The sensitizer carries a single electron in its LUMO and will be a radical anion after the hole has been transferred to a CTA. In order to keep the electron fixed at the sensitizer moiety its LUMO should be the lowest of all components in the system.

For an electron conducting system, analogous relations will apply, however, HOMO's and LUMO's must be interchanged in the above considerations.

3.2.5.3.)The polymer matrix

The polymer matrix in today's high performance PR polymer composites usually consists of some polymer backbone being photoconductive itself or being inert and carrying charge transporting moieties covalently attached. Completely inert polymers (e.g. PMMA, PS) have been used previously, but are at a discount today, since a large amount of inert matter reduces the performance of the system.

By far most high performance PR polymer composites reported up to now utilize carbazole as CTA and among these, the PVK based systems are by far the largest group. PVK has been known to be photoconductive for about 30 years now and, thus, is well characterized, showing a charge carrier mobility of $\mu = 10^{-6} \text{cm}^2/\text{Vs}$ in its pristine state [47]. PVK shows excellent film forming properties, is easily processable, and commercially available at low cost, since it has already found widespread application in xerography and is produced in large amounts. It furthermore has the advantage of offering its formal monomer as plasticizer, which

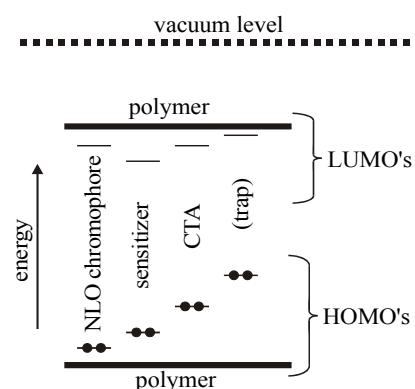


Figure (3 - 1): Diagram of energy levels for PR polymer composites. The scheme depicts the energetic situation as sensed by an electron. Accordingly, electrons relax downhill and holes uphill with respect to the indicated direction of increasing energy. (CTA: charge transporting agent)

will be discussed below. The best performing PR polymer composites known up to date are PVK based. PVK based systems have been investigated intensively, e.g. in [138 - 144], and are furthermore subject of this work. The aforementioned literature refers basically to issues of the PVK matrix. Literature dealing with PVK based systems but focusing on other components of PR composites will be noted in the corresponding sections.

A carbazole based polysiloxane (PSX) carrying carbazole covalently attached to a polysiloxane backbone by means of aliphatic spacer groups has first been used in PR polymer composites by Zobel et. al. [145]. Like PVK, PSX shows a charge carrier mobility of $\mu = 10^{-6} \text{cm}^2/\text{Vs}$ in pristine state [146], has excellent film forming properties and is easily processable. The glass transition temperature of PSX based systems may be adjusted by varying the length of the aforementioned spacer groups. This avoids the use of low molecular mass plasticizers and thus increases the stability of the composite. The performance of the PSX based systems compares to PVK based systems. PSX based PR polymer composites were investigated in more detail in [147 - 150].

Ogino et. al. presented a polymer matrix (PTPD-ac) suitable for PR polymer composites, which is based on TPD moieties covalently attached to a polyacrylic backbone [137]. PTPD-ac shows a charge carrier mobility of $\mu = 10^{-4} \text{cm}^2/\text{Vs}$ in pristine state, two orders of magnitude higher than PVK. The glass transition temperature of this system can be adjusted by incorporating n-butyl acrylate into the polymer backbone by means of copolymerization with the TPD-ac monomer, however, at the expense of the charge carrier mobility, which drops by one order of magnitude if the copolymer contains 50% n-butyl acrylate. This system shows relatively fast IR response, which has been attributed to its comparatively high charge carrier mobility.

Mecher et. al. presented a comprehensive study of PR polymer composites based on a poly(phenylene vinylene) homopolymer (DBOP-PPV) showing long-range π -conjugation, therefore promising high charge carrier mobility and fast PR response [151]. However, the charge carrier mobility in pristine DBOP-PPV of $\mu = 10^{-5} \text{cm}^2/\text{Vs}$ is only one order of magnitude higher than in pristine PVK and smaller than in PTPD-ac [152]. The PR polymer composites based on DBOP-PPV showed similar steady-state PR performance as comparable systems based on PVK and slightly better dynamic PR performance, however, did not fulfill the high expectations. This was attributed to low charge carrier generation efficiency achieved with the fullerene derivative PCBM used as sensitizer.

A fluorene-triarylamine copolymer (TFB) was reported upon by Hofmann et. al. showing a charge carrier mobility of $\mu = 10^{-5} \text{cm}^2/\text{Vs}$ in pristine state [153]. PR response times down to $\tau_1 = 1 \text{ms}$ for the fastest time constant have been determined in a composite utilizing DMNPAA as NLO chromophore and C_{60} as sensitizer, however, the dynamic behavior of this system proved to be very complicated and the significance of the presented response time is questionable. Moreover, the steady-state performance of this system is very poor questioning the attribution of this system to high performance PR polymers.

Please note, that all matrix polymers discussed in this section show maximum optical absorption at wavelengths shorter than 400nm and thus are operable in the red color spectrum ($\lambda > 633 \text{nm}$) without restrictions.

3.2.5.4.)The plasticizer

The glass-transition temperature T_g of any PR polymer is of substantial significance for the PR performance according to the orientational enhancement effect (“2.5.3.3.) Orientational enhancement effect” on page 131). In order to reduce T_g and to let the orientational

enhancement effect take place efficiently, very often plasticizers are added to PR polymer composites. The choice of a suitable plasticizer is at first determined by the question of its compatibility with the polymer matrix. Secondly, it would be favorable if the plasticizer contributes constructively to the functionalities required for PR response, since otherwise it will only be some inert ballast reducing intrinsic performance parameters, in particular the charge carrier mobility. Thus, the plasticizer of choice for PVK based systems will be the formal monomer of PVK, i.e., ECZ, which in fact has most widely been used up to now for this purpose. In this case the plasticizer acts as CTA. However, despite ECZ and PVK are widely miscible, the maximum amount of ECZ in a PR polymer composite will be limited, since pristine ECZ is crystalline and, hence, too much ECZ added will increase the inherent tendency of the composite to crystallize. A comprehensive study of the influence of varying ECZ concentration in PVK based PR polymers will be presented in the section devoted to the experimental results.

Furthermore, derivatives of phthalic acid have been widely used as plasticizer. BBP has been used in PVK based systems. Since pristine BBP is liquid at room temperature, the thermodynamic stability of the composite is improved [155, 156]. For plasticizing the aforementioned DBOP-PPV matrix DPP was used. The authors stated, that this plasticizer turned out to be highly compatible with the polymer matrix. A TFB matrix has been plasticized with another derivative of phthalic acid, DOP. However, none of these plasticizers contributes directly to the PR effect like ECZ. The matrices have already been discussed above in “3.2.5.3.) The polymer matrix”.

Furthermore, TCP has previously been used sometimes for plasticizing a PVK matrix [157, 158]. TCP does not contribute to the formation of the space-charge field, is highly toxic, and potentially cancerogene. Hence, this plasticizer is now at a discount.

Please note, that the chromophore will also act as a plasticizer, however only to some extent, since the chromophore usually is a strongly polar molecule showing limited softening capabilities. Nevertheless, low molecular mass NLO chromophores (or liquid crystals) have successfully been used as plasticizers in PR polymers, e.g. in [127] for plasticizing a fully functionalized PR polymer.

3.2.5.5.)The chromophore

The PR quality of some NLO chromophore to be used in high performance (and accordingly in-situ polable) PR polymer composite can be estimated based on the PR figure of merit according to eq. (2.5 - 123). In order to determine favorable combinations of the molecular constants in eq. (2.5 - 123) for achieving a high figure of merit, the bond-length alternation (BLA) model developed by Marder et. al. [159, 160] is very helpful. A model very similar to the BLA model has been developed by Meyers et. al. [160]. In this model not the bond length alternation is considered but the bond order alternation (BOA). The BOA considers the relative difference of the π -bond orders of adjacent carbon-carbon bonds in a π -conjugated system. In fact, both these models differ only in their methodology and yield identical results. Another model similar but significantly more accurate than the BLA model has been formulated by Wortmann et. al. [161, 162] and Barzoukas et. al. [163, 164]. It relates the electronic and the geometrical structure of some NLO chromophore to its molecular constants of interest, which are in particular the polarizability and the first hyperpolarizability.

Subsequently, the theoretical models will be briefly outlined and correlated with the PR figure of merit (FOM). The quantum mechanical basics are beyond the scope of this work and will not be discussed.

A manifold of NLO chromophores has been tested for application in PR polymer composites and even more have been suggested based on arguments referring to eq. (2.5 - 123) and the BLA model. It is beyond the scope of this work to give a comprehensive overview of all these chromophores. Therefore, only the most prominent representatives actually used in PR polymer composites up to now will be discussed in more detail below.

3.2.5.5.1.)Bond-length alternation (BLA) model and related approaches

Typical NLO chromophores for application in PR organic polymers are rod-like donor-acceptor substituted π -conjugated systems as depicted in figure (2.4 - 8). This archetype of a NLO chromophore may approximately be taken as an one-dimensional (1D) push-pull (PP) system. This suggests to consider only the linear and second order polarizabilities (α and β , respectively) along the long molecule axis (z-axis in the molecular frame, PP-axis). In fact this is a good approximation since the off-axis components of both polarizabilities are typically substantially smaller as compared to the in-axis components for 1D chromophores.

BLA has been identified as a useful structural parameter to predict trends for the linear and for the second order polarizability along the PP-axis in the type of molecules considered. The BLA parameter may be defined in several ways, however, always yielding the same general trend of the polarizabilities as a function of the BLA parameter. The most ostensive definition (for chemists) of the BLA parameter has been provided by Barzoukas et. al. [163], who introduced a parameter "MIX" characterizing the mixing between the two limiting mesomeric forms of the PP system. Originally, the BLA parameter was defined as the relative difference between the average lengths of carbon-carbon single and double bonds involved in the π -electron resonance. It is clear, that this is in fact very similar to MIX. In both cases, the BLA parameter varies between +1 and -1 (sometimes only "+" and "-" are written) being the limiting cases for 100% localized bonds in the limiting mesomeric structures. The sign is actually not significant as long as it is clear how the signs are correlated with the neutral and the zwitterionic limiting mesomeric structures. Wortmann et. al. used a parameter derived from LCAO (linear combination of atomic orbitals) theory, which varies from 0 to 1 describing the position of the electron pair, which is formally displaced by the internal charge transfer leading to the limiting

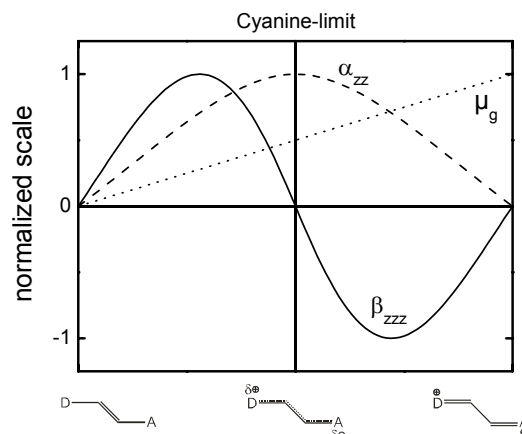


Figure (3 - 2): Normalized variations of the ground state dipole moment μ_g (dotted line), the polarization α_{zz} (dashed line), and the hyperpolarizability β_{zzz} (solid line) along the long molecule axis as a function of the BLA parameter

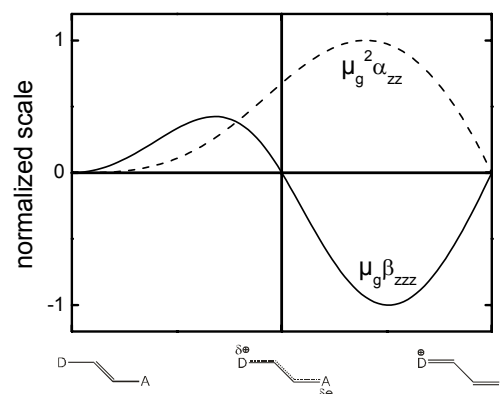


Figure (3 - 3): General trend of the terms of the PR figure of merit for low- T_g PR polymers in the BLA model. Dashed line: birefringence contribution. Solid line: electro-optic contribution. Both curves are normalized to their maximum modulus value.

mesomeric structures. For “0“, the electron pair is completely localized at the donor and for “1“ it is localized at the acceptor [161]. Please note, that the LCAO parameter must be used squared in order to be phenomenologically compatible with the MIX (or the original BLA) parameter. Here, the BLA parameter and the theoretical background of the BLA model will not be elaborated upon. Instead of that the trends to be discussed will be displayed in terms of the chemical valence bond representation of an arbitrary model system. Please note, that the valence bond representations refer to the electronic ground state of the system considered.

The general qualitative trends of the polarizabilities and the ground state dipole moment are depicted in figure (3 - 2). It becomes clear that the optimization of both, the linear and the second order polarizabilities of some 1D NLO chromophore, will not be possible, since the latter is zero when the first has its optimum. This point corresponds to a state of ideal mesomerism, which is equal to the BLA parameter being zero (all involved C-C-bonds exhibit equal length) and the LCAO parameter being $1/\sqrt{2}$ (0.5 in squared form). This state is often referred to as “cyanine limit“, since it is typical for cyanine dyes.

The PR FOM for low- T_g PR polymers according to eq. (2.5 - 123):

$$F_C = \frac{9k_B T \beta_{zzz} \mu + 2\Delta\alpha \mu^2}{k_B T M}$$

depends nonlinearly on the ground-state dipole moment. Assuming in reasonable approximation for 1D systems that the polarization anisotropy $\Delta\alpha$ is basically modelled by α_{zz} , the qualitative trends of the birefringence and the electro-optic terms of the FOM as a function of BLA can be estimated according to figure (3 - 3).

The absolute maximum of the birefringence contributions to the PR FOM in the BLA model is mostly markedly larger than the absolute maximum of the electro-optical contribution [167 - 169]. In these cases, the electro-optic contribution may be neglected and the optimum chromophore will be localized in the right half of the diagram in figure (3 - 3) towards a zwitterionic structure. Accordingly, in this case neutral chromophores existing around the cyanine limit should be most favorable for application in low- T_g PR polymer composites. Merocyanines known to meet this condition have been successfully used in PR polymer composites [165]. However, if the chromophore becomes too polar, one will face compatibility problems with the polymer matrix making this BLA region scarcely accessible for PR polymer composites. This problem has already been reported for the aforementioned merocyanines [165] and may safely be expected to become a major issue for chromophores being even more polar [166].

Focussing on an optimization of the birefringence contribution based on the above considerations successfully led to a variety of novel chromophores for high performance PR composites [161, 91, 170, 171].

Please note eventually, that the theory of the BLA model is based on a two-level-model (TLM) formally mixing the neutral and the zwitterionic state of a 1D NLO PP chromophore. The TLM model is a reasonable approximation for the hyperpolarizability in systems exhibiting an extended π -conjugated system. On the contrary, the approximation is crude for the linear polarizability and tends to underestimate the real value. However, since α is always positive the TLM contribution is always a lower bound [161], and the general trends are depicted correctly. Furthermore, one must keep in mind, that both α and β will be subjected to dispersion. Hence, the absolute values of the molecular polarizabilities will depend on the operating wavelength. The aforementioned TLM model provides analytical expressions approximating the dispersion (see e.g. eq. (32) to (36) in [161]).

3.2.5.5.2.)Characteristic examples

In this section a selection of the most prominent NLO chromophores investigated for application in PR polymer composites up to now will be presented. As far as available, the PR FOM according to eq. (2.5 - 123), F_λ (λ : operating wave length), will be provided. The chromophores to be discussed and their available electro-optical characteristics are listed in table (3 - 1).

Table (3 - 1): Chromophore molecular parameters and PR FOM

	DMNPAA	ATOP-1	PDCST	DPDCP	2BNCM	DHADC -MPN	F- DEANST
λ_{\max} [nm]	391*	536*	422*	352*	378*	n.a.	417*
μ_g [10^{-30}Cm]	21*	47*	29*	27*	31*	40***	21*
$\Delta\alpha_0$ [$10^{-40}\text{Cm}^2/\text{V}$]	22*	55*	25*	16*	19*	n.a.	22*
β_0 [$10^{-50}\text{Cm}^3/\text{V}^2$]	56*	27*	52*	1*	-9*	23***	78*
F_0 [10^{-74} $\text{C}^2\text{m}^4\text{mol}/\text{V}^2\text{kg}$]	0.20*	1.40*	0.48*	0.24*	0.30*	n.a.	0.27*
LCAO- c^2 [scale: 0-1; cyanine limit: 0.5]	0.16*	0.45*	0.22*	0.49*	0.59*	n.a.	0.12*
$\Delta\alpha_x$ (x[nm] [#]) [$10^{-40}\text{Cm}^2/\text{V}$]	n.a.	n.a.	n.a.	n.a.	n.a.	25*** (830)	n.a.
F_x (x[nm] [#]) [10^{-74} $\text{C}^2\text{m}^4\text{mol}/\text{V}^2\text{kg}$]	0.28** (790)	2.63** (790)	n.a.	n.a.	n.a.	n.a.	n.a.

* from [172]; ** from [173]; *** from [170] converted to SI units

[#]wavelength the listed values have been determined for.

DMNPAA and its derivatives have been the most common NLO chromophores used in PR polymer composites up to now. Typical performance data have already been discussed in “3.2.5.1.) Milestones” above. Furthermore, this chromophore has been used in the frame of this work. Since low- T_g PR polymer composites containing DMNPAA have been recognized as being unstable against crystallization soon after the first high-performance PR polymer has been presented, research efforts focussed on solving this problem. As already mentioned before, eutectic mixtures of 2,5-DMNPAA and 3,5-DMNPAA were a first approach. Later on, eutectic mixtures of 2,5 DMNPAA and MNPAA turned out to be more favorable, since this chromophore mixture exhibits less absorption at 633nm operating wavelength, the corresponding composites are even more stable and the PR performance is notably improved as well [136]. The latter system has also been investigated in [92, 141, 151] and in detail in the frame of this work. Derivatives of DMNPAA carrying extended aliphatic side groups, which improve the solubility of the chromophore in the polymer matrix have been presented and tested in PVK based PR composites yielding more or less similar performance as compared to the original system [174, 175].

ATOP-1 is one of the highest performing NLO chromophore for PR polymer composites known to date. Its first test using the well known PVK/ECZ host matrix showed excellent steady-state performance at low chromophore concentrations of only 20%wt and at 790nm operating wavelength [171]. The low chromophore concentration used was a consequence of compatibility problems with the only little polar PVK matrix causing anti-parallel aggregation of ATOP-1 when present in the matrix in substantial concentration. These problems could be solved by increasing the polarity of the matrix surrounding the ATOP-1 moieties, which was achieved by adding the NLO chromophore DMNPAA to the composite in the ratio 1:1 with respect to ATOP-1 [166]. The resulting composite ATOP-1:DMNPAA:PVK:ECZ:TNFM in the ratio of 25:25:34:15:1%wt exhibited a glass transition temperature close to room temperature. DFWM measurements were carried out on 105 μ m thick polymer films with s-polarized recording beams of equal external intensity of 25mW/cm² each, intersecting at an external angle of 20° and p-polarized read-out. The sample was tilted by an external angle of 60°. The 2BC experiments were carried out using the same geometrical configuration but p-polarized recording beams at 25mW/cm² total external intensity and a beam ratio of 1:100 (undepleted pump beam regime). An operating wavelength of 790nm was used. The first maximum ($\eta_{\max} = 85\%$) of the DFWM diffraction efficiency occurred at $E_{\text{ext}} = 33\text{V}/\mu\text{m}$ and a PR gain of $\Gamma = 140\text{cm}^{-1}$ at $E_{\text{ext}} = 60\text{V}/\mu\text{m}$ was obtained [165, 173]. These steady-state PR performance data are among the best reported up to now. Please note, that the PR response behavior of PVK based ATOP-1 containing systems is complicated and not yet understood [176]. A first rough estimate indicated a response time of about 3sec at $E_{\text{ext}} = 68\text{V}/\mu\text{m}$ [171]. This is comparable to the response behavior observed for a similar system containing solely DMNPAA [177].

Grunnet-Jepsen et. al. reported on a high performance PR composite based on a PVK/BBP polymer matrix and using the NLO chromophore PDCST [178], however, the chromophore itself was presented before for PR application [179]. Since then PR polymer composites containing PDCST or derivatives have intensively been studied [142, 156, 180]. The typical steady-state performance of these systems is basically similar to PVK based DMNPAA containing systems. The first composite developed by Grunnet-Jepsen et. al. consisted of PDCST:PVK:BBP:C₆₀ in the ratio of 35:49.5:15:0.5%wt and showed a glass-transition temperature of $T_g = 28^\circ\text{C}$. The first maximum of the DFWM diffraction efficiency ($\eta_{\max} = 82\%$) occurred at $E_{\text{ext}} = 80\text{V}/\mu\text{m}$ and a gain coefficient of $\Gamma = 200\text{cm}^{-1}$ has been achieved at $E_{\text{ext}} = 100\text{V}/\mu\text{m}$ in a 75 μ m thick polymer film. These data have been obtained on a setup showing the fairly uncommon configuration of 30° external intersection angle of the recording beams and 45° external tilt angle. The recording beams were s-polarized for the DFWM experiments and p-polarized for the 2BC experiments exhibiting an absolute external intensity of 1W/cm² at 676nm operating wavelength in both cases. The resulting PR grating spacing of 1.7 μ m favours fast response due to short displacement lengths for the mobile charge carriers on the one hand but the steady-state performance is reduced according to eq. (2.5 - 2), eq. (2.5 - 3), and eq. (2.5 - 1)) on the other as compared to the typically adjusted value of the grating spacing of about 3 μ m. The smaller tilt angle as compared to the typically adjusted value of around 60° results in a reduced projection of the external field onto the grating wave vector, which is unfavorable for fast response as well as the steady-state performance values. Some comparative data obtained on a setup of common configuration, which would enable a trade-off of these counteracting influences was not provided preventing a reasonable comparison of the presented steady-state performance data with corresponding data obtained for other systems on setups showing the aforementioned more common configuration. The fastest response time for this kind of PR polymer composites has been reported for the aforementioned composition however containing the PDCST derivative 7-DCST as NLO chromophore. The response time was determined from fitting the PR gain obtained as a function of time to a stretched exponential

associative growth function (KWW-fit) yielding $\tau_{\Gamma} \approx 5\text{ms}$ for the experimental configuration described above and $E_{\text{ext}} = 100\text{V}/\mu\text{m}$, however, at 645nm operating wavelength [156]. The sample thickness used in this experiment was not reported but only stated as being in-between 60 and 100 μm . Since the PR gain combines the evolution of the PR phase shift and the evolution of the refractive index modulation, which are strongly indicated to show significantly different dynamics, the presented response time cannot be related to the response times obtained from the evolution of the refractive index modulation in DFWM experiments as already mentioned before in “3.1.1.2.) Photorefractive response time” on page 152. However, for comparison the authors estimated the response time of the PR gain for the first presented high performance PR polymer composite from [13] to be roughly $\tau_{\Gamma} \approx 100\text{ms}$. Please note that this comparison is unreasonable, since neither the applied external field nor the experimental configuration nor the recording intensity are similar enough to even give a crude estimate of the relation to be expected if the compared systems would be tested under identical conditions. Nevertheless, PVK based systems containing PDCST or derivatives appear to be somewhat faster than the aforementioned DMNPAA containing pendants.

The first NLO chromophores explicitly developed in terms of optimizing the PR FOM for low- T_g systems have been DPDCP and 2BNCM [91, 161]. The latter is a PR low molecular mass glass and its PR properties have already been discussed in “3.2.3.) Low molecular mass glasses” on page 157. DPDCP has only been tested for its potential application in PR polymer composites in a proof of principle. DFWM and 2BC experiments on a model system consisting of 55%wt of the inert matrix PMMA doped with 15%wt TPD as CTA, 0.5%wt C_{60} as sensitizer, and 30%wt of DPDCP were carried out using an operating wavelength of 676nm. The recording beams were s-polarized for the DFWM experiments and p-polarized for the 2BC experiments and intersected at an external angle of 30° yielding a grating spacing of 1.66 μm . The sample was tilted by 45°. The read-out of the hologram in the DFWM experiment was performed p-polarized at 760nm wavelength. The recording intensities were not provided but rather only beam powers and some not accurately specified beam diameters. However, the intensity ratio of the recording beams was reported as 1:1 in any case. A DFWM diffraction efficiency of $\eta = 25\%$ at $E_{\text{ext}} = 100\text{V}/\mu\text{m}$ not showing overmodulation and a PR gain coefficient of $\Gamma_p = 35\text{cm}^{-1}$ at $E_{\text{ext}} = 80\text{V}/\mu\text{m}$ were reported. A single exponential initial response time constant of $\tau = 850\text{ms}$ was determined. Due to the uncommon setup configuration these performance data cannot be compared with data obtained on a setup showing the typical configuration as discussed above. The comparatively low performance in general may be attributed to the unfavorable host matrix containing a substantial amount of inert matter and only 15%wt CTA. Furthermore the small absorption reported to be only $\alpha = 2\text{cm}^{-1}$ at operating wavelength should be expected to condition small charge generation efficiency as compared to the other composites discussed in this section. Thus a better performing composite may be expected by choosing a more favorable host system.

Kippelen et. al. presented the NLO chromophore DHADC-MPN, which was developed based on BLA considerations as well [170]. The chromophore was tested in two PR composites targeted at the two different operating wavelengths of 633nm and 830nm and consisting of DHADC-MPN:PVK:ECZ:TNF in the ratio of 40:39:19:2%wt and of DHADC-MPN:PVK:ECZ:TNFM in the ratio of 25:49:25:1%wt, respectively. The typical holographic setup configuration was applied with the recording beams intersecting at an external angle of 20° and an external tilt angle of the sample of 60°. The recording intensity was 800mW/cm² for 633nm operating wavelength and 560mW/cm² for 830nm with a beam ratio of 1:1 in both cases. DFWM experiments were carried out with s-polarized recording beams and s- as well as p-polarized read-out. For the latter the first (external) diffraction maximum was obtained at $E_{\text{ext}} = 30\text{V}/\mu\text{m}$ for 633nm operating wavelength ($\eta_{\text{max}, 633\text{nm}} = 10\%$) and at $E_{\text{ext}} = 59\text{V}/\mu\text{m}$ for 830nm operating wavelength ($\eta_{\text{max}, 830\text{nm}} = 74\%$). The small absolute maximum diffraction

efficiency $\eta_{\max, 633\text{nm}}$ was attributed to absorption and reflection losses. For comparison DMNPAA containing composites have been tested under identical conditions as well. The first diffraction maximum of $\eta_{\max, 633\text{nm}} = 54\%$ has been obtained at $E_{\text{ext}} = 65\text{V}/\mu\text{m}$ for a sample DMNPAA:PVK:ECZ:TNF = 40:39:19:2%wt and of $\eta_{\max, 830\text{nm}} = 88\%$ at $E_{\text{ext}} = 60\text{V}/\mu\text{m}$ for a sample DMNPAA:PVK:ECZ:TNF = 50:33:16:1%wt. The sample thickness of all samples was reported as $105\mu\text{m}$. Response times were not reported but rather a sample dynamic DFWM curve for the DHADC-MPN containing sample for 830nm operating wavelength. From this curve response time constants in the range of several seconds must be expected. 2BC experiments are not reported. The authors pointed out, that the systems containing DHADC-MPN showed high stability against crystallization and phase separation. Formal derivatives of DHADC-MPN were reported by Van Steenwinckel et. al. [181]. The performance data presented for PVK based composites containing these chromophores are almost identical to typical PVK based systems containing DMNPAA. Based on the presented performance data DHADC-MPN competes with ATOP-1 in chromophore quality for PR application.

Please note, that F-DEANST has been listed for comparison since this chromophore and its derivatives were widely used in PR polymer composites of the early stage. These chromophores show reasonable performance in today's low- T_g high performance PR polymer hosts, which, however, cannot compete with nowadays established reference systems. Therefore DEANST derivatives are now at discount. The most current work referring to this chromophore type focussed on general temperature dependent studies of PR polymers using a PVK based model-system containing DEANST [157]. No work (except review articles) referring to this chromophore type has been published more recently.

In conclusion, a representative selection of the best NLO chromophores for PR application presently known are listed in this section and literature reporting derivatives is mentioned. Among the listed chromophores ATOP-1 and DHADC-MPN are highest performing. However, both are not favorable for use at an operating wavelength of 633nm (He-Ne Laser) due to fairly high absorption but rather for application in the near infrared. For operating wavelengths in the visible range DMNPAA (and its derivatives) as well as PDCST (and its derivatives) are more suitable.

3.2.5.6.)The sensitizer

The task of the sensitizer is to provide the minimum degree of absorption necessary to generate free charge carriers for the PR grating build-up. Up to now, only two types of sensitizers have been widely used in amorphous organic PR materials, which are the TNF, TNFM, and the Buckminster Fullerene C_{60} , or its derivative PCBM, which exhibits significantly improved solubility in the polymer host matrix as compared to C_{60} .

TNF and TNFM form charge transfer (CT) complexes with the CTA's, which exhibit a certain degree of optical absorption at the operating wavelength of the PR system. Upon optical excitation, an electron is transferred from the CTA moiety to the sensitizer molecule within the CT complex. Thus the sensitizer becomes negatively and the CTA positively charged and the CT complex dissociates subsequently. The hole left behind on the CTA then is ready to be displaced by hopping transport under the influence of the externally applied field. The theory behind the underlying processes has been elaborated upon in "2.4.3.) Electrical conduction in organic polymers" on page 95 and in "2.4.4.) Charge generation and recombination in organic polymers" on page 109.

In contrast, C_{60} and its derivatives do not form CT complexes with the CTA's but already absorb at the operating wavelength. Upon optical irradiation, an electron of the sensitizer is

excited from the HOMO to the LUMO. The resulting hole in the HOMO of the sensitizer is thereafter filled up with an electron stemming from a neighboring CTA thus yielding a hole in the CTA manifold.

The aforementioned sensitizers differ in their spectral range of optical excitation. TNF and the Fullerene derivatives may be applied as sensitizers for the visible spectrum. Due to its higher electronegative character, the absorption maximum of the TNFM-CTA CT complex is red shifted as compared to the corresponding TNF-CTA CT complex, which makes TNFM an appropriate sensitizer for operating wavelengths in the near infrared optical spectrum. In order to illustrate the described spectral relations, the differential absorption spectra of TNF/ECZ, TNFM/ECZ and PCBM/ECZ in chloroform with respect to pristine ECZ in the same solvent are depicted in figure (3 - 4).

The applicability of a sensitizer depends strongly on the ability of the sensitizer to form a CT complex with the CTA of the conducting polymer matrix, or on the ability to transfer a hole to the CTA manifold. It is well-known for TNF, that it forms a strong CT complex with the carbazole moiety in a PVK matrix [47, 182, 184]. Thus, TNF and TNFM will be the sensitizer of choice for systems using carbazole as CTA, whereas they are less preferable for other known CTA's or conducting polymers like TPD, TPA, or PPV, respectively. The particular behavior of C_{60} and its derivatives as sensitizers in certain conducting polymer matrices is less well known. Fullerene derivatives have been applied in almost all types of polymer hosts for PR composites including PVK with varying success. A clear trend has not been worked out up to now. The most comprehensive study of C_{60} as sensitizer in PR polymers is provided in [86], however, the model systems are PR polymer composites of the early stage and no more up to date. In last consequence, the choice of the most suitable sensitizer for a particular amorphous organic PR material as well as its most appropriate concentration in the system finally resulting in best performance desired for a particular application is a matter of trial and error.

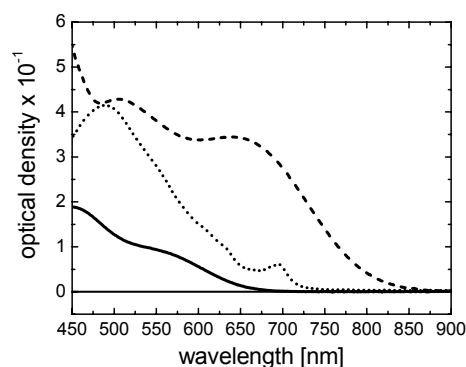


Figure (3 - 4): Differential absorption spectra for 50mg ECZ and 2mg TNF (solid line), 2.3mg TNFM (dashed line) and 2mg PCBM (dotted line) with respect to pristine 50 mg ECZ, each dissolved in 10ml $CHCl_3$. This correlates to a particle ratio of roughly ECZ:TNF:TNFM:PCBM \approx 110:3:3:1. Spectra measured with a Varian CARY 50 UV/VIS spectrometer.

4.) Experimental techniques and general evaluation

PVK-based photorefractive polymer composites have been investigated in the frame of this work by means of holographic determination of the PR grating strength and PR phase shift where appropriate. These characteristics have been derived from degenerate four-wave-mixing (DFWM) and degenerate two-wave-mixing experiments, commonly referred to as two-beam-coupling (2BC). Furthermore simple transmission ellipsometric (ELP) experiments were carried out in order to determine the parallel plate poling behavior of the systems. The capabilities of the investigated composites for potential application as mass data storage systems have been examined by means of peristrophic multiplexing experiments.

Subsequently, the procedure of material preparation will be described, and the typical structure of the samples will be sketched. The holographic setups built up for the DFWM and the 2BC experiments will be described focussing on the substantial components without elaborating upon trivial aspects. Special features will be pointed out and particular problems recognized will be discussed where advisable. Please note, that the DFWM and the 2BC setup will be described separately for the sake of clarity, however, they were actually merged in a single setup. The peristrophic multiplexing experiments were carried out on a different setup, which will also be described separately. The setup for the ELP experiments, which was incorporated in the setup used for the DFWM and 2BC experiments will not be described due to its simplicity but only depicted in principle. The evaluation procedure for all experiments carried out will be discussed and a consideration of systematic errors accepted will be included.

All experiments subsequently described were carried out in air conditioned laboratories exhibiting a constant room temperature, which will be noted in the section devoted to the experimental results in the subsections concerning aspects of the particular experiments performed.

4.1.) Preparation of materials and sample structure

All materials investigated consisted of a PVK polymer matrix plasticized by various amounts of ECZ and sensitized with TNF. At first, DMNPAA was used as NLO chromophore and later on an eutectic mixture of DMNPAA and MNPAA (eutectic ratio 1:1 [136]). For introducing extrinsic traps in the system small amounts of TPD were added for certain experiments. PVK was purchased from Sigma/Aldrich in highest degree of purity available and used as is. The specifications state an average molar mass of 1,100,000 g/mol equivalent to an average chain length of approximately 5,500 repeating units, and a glass-transition temperature of $T_g \approx 200^\circ\text{C}$. ECZ was also purchased from Sigma/Aldrich but in technical degree of purity and recrystallized from chloroform three times for purification. The NLO chromophores were synthesized by standard azo-coupling between purchased anisole (methoxy-benzene) derivatives corresponding to the substitution pattern desired and nitro aniline by means of borontetrafluoride-acid and sodium-nitride for generating the precursor diazonium ion. The reaction solution in DMF (dimethyl-formamide) was separated by mixing with chloroform and the resulting azo-dye solution was purified by column chromatography over silica gel. TNF was ordered from Sigma/Aldrich and TPD was ordered from Syntec as technical mixture of mono- and dimethylated isomers. Both these chemicals were purchased in the highest degree of purity available and used as is.

The components required for the PR polymer composites were dissolved in methylen-chloride to the amount desired and the solution was filtrated thereafter through a ceramic filter in order to minimize the number and size of solid state particles, which cause undesired scattering of light. Then the solvent was allowed to evaporate. The solution should not be evaporated by cooking, since this may aggravate the further processing. The resulting polymer composite was put between clean glass plates and subsequently homogenized mechanically at elevated temperatures (about 150°C to 200°C depending on the particular material). The polymer block thus obtained was finally cut into small pieces.

The glass-transition temperatures of the particular polymer composites was determined by differential scanning calorimetry (DSC) using a Mettler Toledo DSC 821^e calorimeter. Absorption spectra were measured in solid phase using a Varian CARY 50 or a Kontron UViCON 860 UV/Vis spectrometer.

Indium-tin-oxide (ITO) coated glass sheets were purchased from various suppliers. However, within experimental series to be compared only one type of ITO coated glass was used. This turned out to be advisable since the ITO coated glasses purchased from different suppliers turned out to exhibit notable differences in properties like refractive index, absorption spectrum, thickness and electrical conductivity. The purchased ITO coated glass sheets were cut into suitable pieces and the ITO coating was partially removed by etching with an aqueous solution of 1mol/l FeCl_3 in 5n HCl at elevated temperature of 60°C for about 1 minute. ITO coating to remain was protected before by adhesive tape. The resulting ITO glass slides are sketched in figure (4 - 1).

The polymer pieces prepared as described above were melt-pressed between two of these ITO coated glass slides under elevated temperatures using glass spacer beads to adjust the film thickness. The polymer film thickness and sample parallelism was regularly

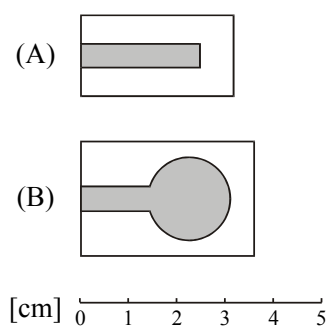


Figure (4 - 1): ITO glass slides used for sample preparation. Grey areas are ITO coated. (A) and (B) are typical slides for standard and peristrophic multiplexing experiments, respectively.

counterchecked by a micrometer screw and occasionally by a Dektak-3 profilometer. The structure of the samples finally obtained is depicted in figure (4 - 2). Please note, that special care must be taken to avoid bubbles in the overlapping area of the opposing ITO traces since these will dramatically decrease the dielectric strength of the sample.

After having the material melt-pressed between the ITO glass slides, the samples to be characterized within a certain series of measurements must be cooled down to room temperature applying a consistent and constant cooling procedure. Among others, the cooling procedure determines the amount of free volume enclosed in the system as discussed in “2.4.1.) Relaxation and thermodynamics in polymers” on page 70. Thus, geometrically identical samples made from the same material will behave slightly different, if inconsistent cooling procedures have been performed. When advisable, particular cooling procedures applied will be mentioned in correlation with the corresponding experiments to be discussed in the section devoted to the experimental results.

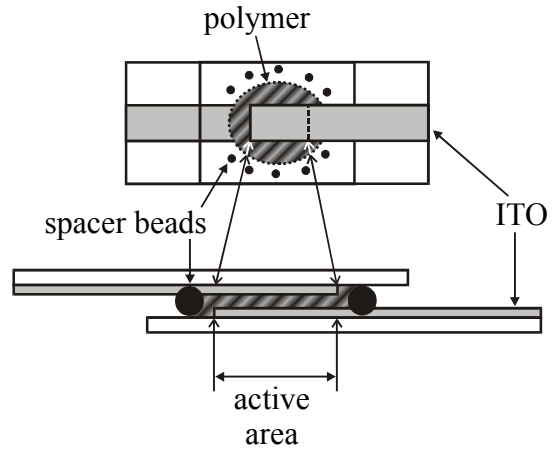


Figure (4 - 2): Typical sample structure. Above: top view; below: side view.

Sample holders according to figure (4 - 3) were made from PVC (polyvinyl-chloride) and Pertinax (phenol resin plastics of excellent electrical resilience). The structure depicted allows for external angles of incidence for the recording beams of up to $\alpha_2 = 85^\circ$ (see next section) and provides sufficient mechanical stability to ensure a stable sample position even with fairly heavy wires (strongly insulated due to high voltage) attached to the sample for applying a strong electrical field. The sample holder can be opened by opening the 4 screws in the edges enabling easy and quick access to the samples.

The sample holder for the peristrophic multiplexing experiments is described in “4.2.1.5.) Holographic multiplexing experiments” on page 201.

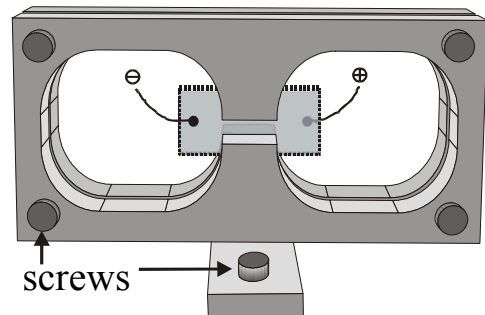


Figure (4 - 3): Standard sample holder. The semitransparent object in the center indicates the position of the sample. The indicated field direction is not stringent.

4.2.) Wave mixing experiments

In this section the general setup configuration and parameters, which apply to all the diffraction experiments will be discussed first. Furthermore, the equipment used will be described. Thereafter, the 2BC, DFWM and peristrophic multiplexing experiments will be considered in detail. General problems impacting all diffraction experiments using the configurations to be described will be discussed. The section will close with a short discussion of how absolute beam intensities were determined.

4.2.1.) General wave mixing setup configuration and parameters

All diffraction experiments in the frame of this work were carried out using an operating wavelength of $\lambda_0 = 632.8\text{nm}$ originating from commercial HeNe lasers (Melles Griot) having an output power of 10, 20 or 30mW. Prior to particular experiments, the laser system was allowed to warm up for at least one hour in order to ensure stable steady-state working conditions. The laser setups were mounted on laser tables decoupled from ground by air-cushions and were covered by closed nontransparent plastic boxes in order to exclude influence of airflow on the laser beams in critical areas and to minimize background light in the setup.

The general setup configuration applied for the holographic diffraction experiments is depicted in figure (4 - 4). I_{01} and I_{02} are the incident recording beams 1 and 2, respectively, and I_1 and I_2 are the corresponding beams after having traversed the sample. The incident angles of I_{01} and I_{02} are α_1 and α_2 , respectively. For all diffraction experiments $\alpha_1 = 50^\circ$ and $\alpha_2 = 70^\circ$ (external) applies resulting in an external tilt angle of $\Psi_t = 60^\circ$. According to eq. (2.1 - 45) and taking into account the refractive index of $n = 1.7 \pm 0.05$, valid for all the PR polymer composites investigated, an interference grating fringe spacing of $\Lambda = 3.15 \pm 0.1 \mu\text{m}$ is obtained for this configuration.

I_{03} is the incident probe beam for the performed DFWM experiments. The configuration according to figure (4 - 4) is referred to as phase-conjugate read-out configuration. I_{3t} is the transmitted portion of the probe beam after having traversed the sample and I_{3d} is the portion diffracted by the holographic grating.

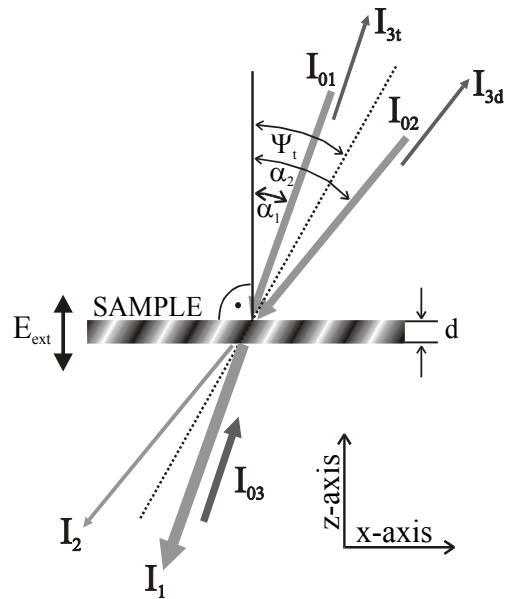


Figure (4 - 4): Illustration of the general setup configuration for holographic wave-mixing in PR polymer samples. d is the thickness of the polymer layer and E_{ext} depicts the external field applied. The indicated 2BC energy transfer direction ($I_2 \rightarrow I_1$) is illustrative.

4.2.1.1.) Experimental wave mixing setup and equipment

The following basic equipment was used for all except the peristrophic multiplexing experiments: The laser beam powers were measured with non calibrated standard photodiodes purchased from Silicon Sensor AG, Germany. Amplifiers for the photodiodes were homemade by the electronic workshop of the department for Physical Chemistry of the University of

Munich. Absolute laser beam powers were determined with a power meter from Newport, type 835. For applying an electrical field to the polymer samples a remotely controllable high voltage power supply from Heinzinger Elektronik, Germany, type PNC 40000-1pos was used, providing high voltage of up to 40kV at maximum output of 1mA. Small laser beam intensities were determined by chopping the beams with a HMS-Elektronik light beam chopper, type 221 and using the single channel lock-in amplifiers ITHACO-NF 3921 (two amplifiers), ITHACO Dynatrac 393 and EG&G Brookdeal 393, each triggered by the chopper controller. In some cases homemade constructions were used showing similar working principle (i.e. homemade chopper and retrieving the trigger signal by a separate laser diode and detector). The laser beams were controlled using fast bistable magnetic shutters (Newport) operating with 5ms switching time. Digital remotely controllable shutter controllers were homemade by the aforementioned electronic workshop.

The setup was controlled by a Pentium 133MHz Intel computer system (OS: Windows 95, 32MB RAM) using either an ISA multifunction PC card from Meilhaus Elektronik, Germany, type ME300LG or GPIB bus. Kinematic components of the setup were controlled by a PI-Instruments (Germany) motion controller card type C8242. Measurement programs were developed with National Instruments LabVIEW 16bit version 3.11, which turned out to operate more reliably and to process considerably faster on the employed computer system than newer software versions (up to version 5.1/32bit). Data were sampled using the aforementioned multifunction card exhibiting a maximum sampling rate of 200kHz and 12bit resolution of the A/D converter.

A manifold of additional homemade devices was temporarily incorporated into the setup in order to provide special functionalities. Wherever of essential importance, these will be discussed in the section devoted to the experimental results in context with the experiments making use of these functionalities.

The peristrophic multiplexing experiments were carried out in the working group of Prof. Dr. Demitri Psaltis, CalTech, Pasadena, California, USA, using the measurement equipment provided there.

4.2.1.1.1.) 2BC setup

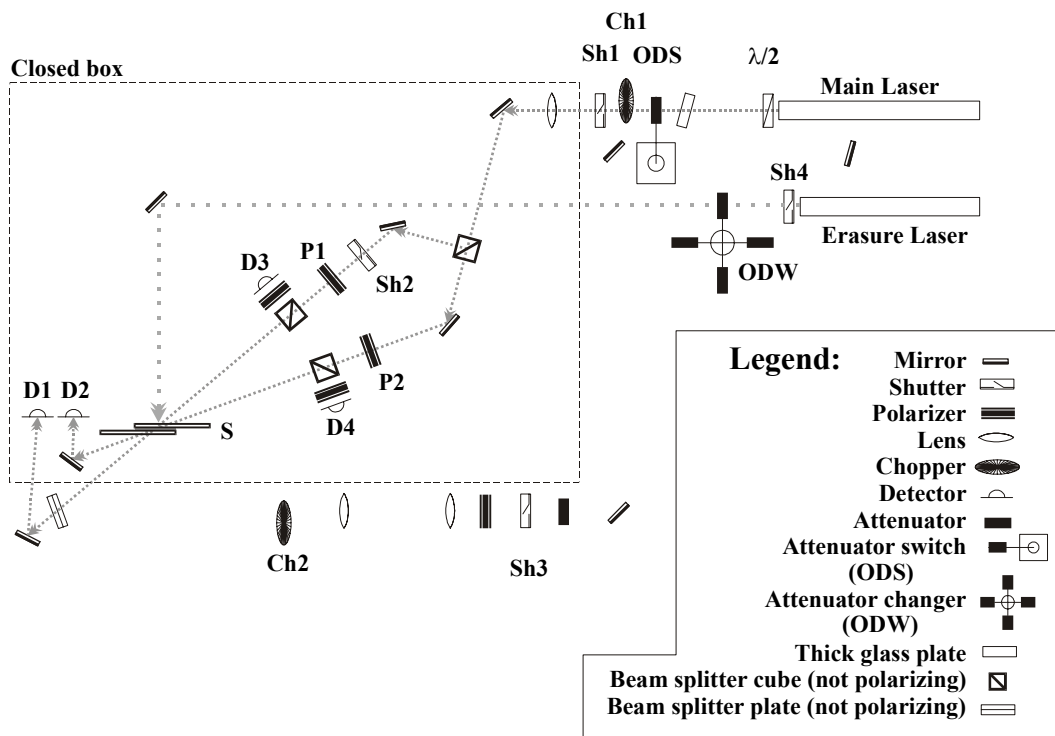


Figure (4 - 5): 2BC experimental setup including recording beams (short dotted lines) and erasure beam (widely dotted line). Arrows indicate propagation directions. Components of the setup referred to in the text while describing the measurement sequences are explicitly marked in the sketch. For the other components see legend. A manifold of pinholes (and/or irises) was incorporated as well in order to block undesired beam reflections and to facilitate the adjustment of the setup. Furthermore a Mach-Zehnder interferometer was included in order to back-check the setup stability using appropriate reflected beam portions, which was not used otherwise. The latter and the pinholes are not relevant for holographic wave-mixing and, thus, not shown. Please note that the attenuator switch moves an attenuator quickly into or out of the beam path and operates out of the propagation plane of the beams. In contrast, the attenuator changer changes attenuators by rotation in the propagation plane of the beams, which is a slow process taking several seconds. The beam path of the DFWM probe beam is shown in figure (4 - 6).

Steady-state and dynamic 2BC measurements were performed using the setup depicted above, which represents the latest configuration used. The setup was rebuilt and modified several times in the frame of this work, however, the basic configuration was not altered notably. Thus, the measurement procedures as described later apply in general.

4.2.1.1.2.)DFWM setup

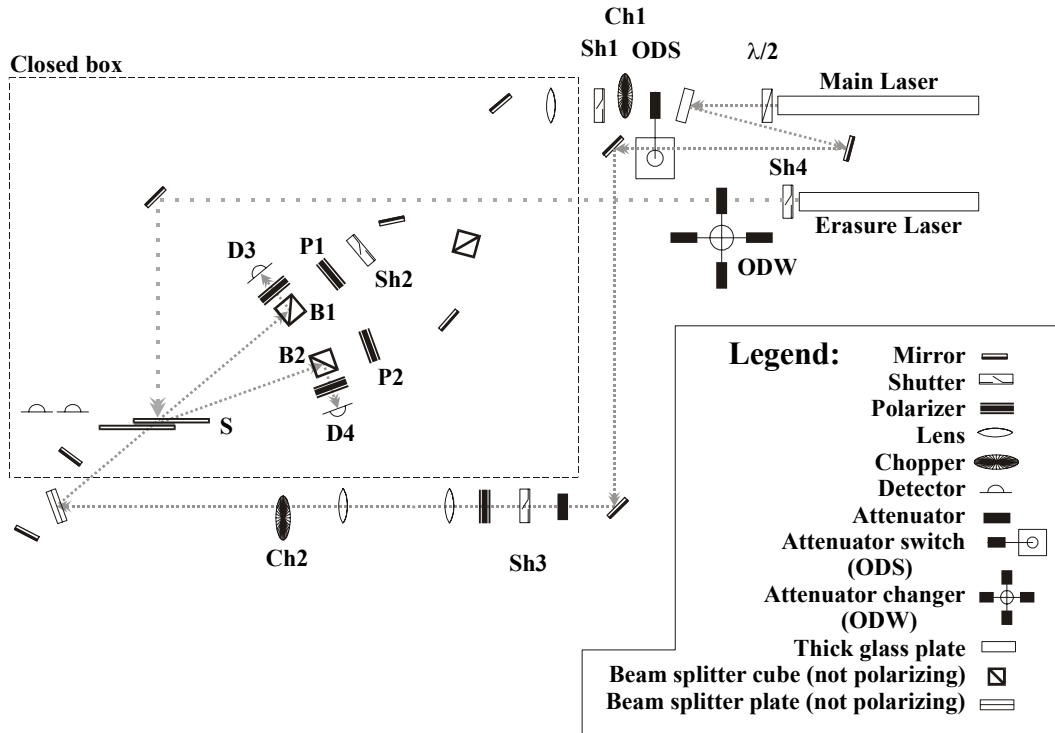


Figure (4 - 6): DFWM experimental setup including transmitted and diffracted probe beams (short dotted lines) and erasure beam (widely dotted line). Arrows indicate propagation directions. Please note the remarks made in the legend of figure (4 - 5) on the setup components.

Steady-state and dynamic DFWM measurements were performed using the setup depicted above, which represents the most current configuration. The setup was rebuilt and modified several times in the frame of this work, however, the basic configuration has not been altered. Thus, the measurement procedures as described later will apply in general.

4.2.1.1.3.) Wave mixing measurement circuitry

For the functional configuration and related equipment used for wave mixing measurements reference is made to figure (4 - 7).

Prior to all measurements, possible constant offset values of the output of the measurement circuitry were determined by blocking the beams in question with shutter Sh1, while other beams present were allowed to enter the setup. The offset values were subtracted from the output values obtained for channel 1 (detector D1) to channel 4 (detector D4). The output characteristics of the measurement circuitry as a function of the incident light power was determined whenever the circuitry had been modified and was counterchecked randomly during the operating periods at constant configuration. If necessary, data obtained were numerically matched to the characteristics of the circuitry. Special care was taken of this issue if rectifiers were used to obtain dc-output values from chopped beams. The threshold voltage and transfer characteristics of the rectifiers were carefully determined as a function of the input ac voltage and accounted for as numerical offset in the data obtained by appropriately folding the transfer function with the experimental data. Attention was paid to the fact, that ac-signals are not reliably detectable if below or only slightly above the onset voltage of the rectifiers. If necessary, appropriate dc voltage offset was provided to the signal lines in order to avoid this regime of non-linear operation.

The time resolution of the setup measurement circuitry was limited by the adjustable time constant of the lock-in amplifiers on the one hand and by the cut-off frequency of the rectifiers' smoothing circuitry (20Hz) on the other. With disconnected lock-in amplifiers and rectifiers, the time resolution was limited by the sampling rate of the A/D converter (in total 200kHz, i.e. to be divided by the number of channels if more than one channel was used).

The signal resolution limit cannot be discussed in general terms, since it depends on the particular setup configuration. If relevant, the signal resolution limit will be discussed in the corresponding sections devoted to the experimental results.

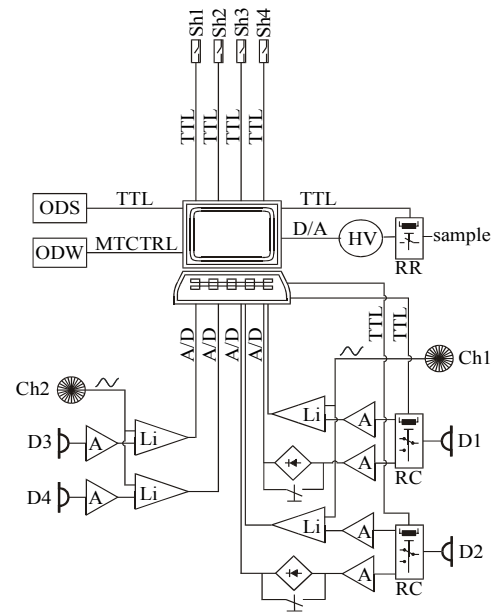


Figure (4 - 7): Measurement circuitry for diffraction experiments. TTL: TTL signal line; A/D: analog signal line to A/D converter; D/A: analog signal line from D/A converter; RR: reed relay (on/off); RC: reed relay (line changer); A: simple amplifier (provided amplification factors: 10/100/1000); Li: lock-in amplifier (reference line indicated by a tilde); HV: high voltage source (remote controllable by analog dc-signal); MTCTRL: signal from motion controller card. Residual abbreviations are explained in the context with figure (4 - 5).

4.2.1.2.) Two-beam-coupling (2BC)

2BC experiments were carried out during recording as well as erasure of a PR grating in the materials investigated. Please note, that the latter represents some sort of contradiction in terms since erasure of the PR grating requires the absence of the recording beams and thus no beam coupling can be observed. The problem was solved by shutting down the recording beams to an extremely low level as compared to the light intensity used for erasing the grating. Please note furthermore, that grating erasure must be determined using an erasure beam, which is not Bragg-matched to the PR grating in order to avoid grating refreshment by a Bragg-matched erasure beam and its diffracted portion, which will distort the actual grating decay process.

4.2.1.2.1.) 2BC measurement procedures

The quantities to be directly measured in the 2BC experiments carried out are recording beam powers as a function of the applied field or of the time and the reference beam powers at zero field or prior to the onset of the 2BC effect, respectively. The data obtained were evaluated as described in “4.2.1.2.2.) Evaluation of the 2BC experiments” on page 188.

For the steady-state 2BC experiments the sample was first illuminated with both the recording beams without an external field applied in order to obtain the reference values for the powers of the recording beams. Then the external field was increased stepwise by an appropriate increment, which was chosen based on a trade-off between a suitable number of data points and the resulting required total measurement time. After increasing the field by one step the material was given sufficient time to relax to quasi steady-state. The relaxation time required was estimated by previous determination of the dynamic behavior of the refractive index modulation in a DFWM experiment at some low external field value necessary to obtain a reasonable signal strength and subsequent evaluation as described in “4.2.1.3.2.) Evaluation of the DFWM experiments” on page 195. At least 5 times the thus obtained logarithmically averaged response time was provided as relaxation time. Subsequently, 500 single measurements were performed at a sampling rate of 100sec^{-1} , hence, covering a time span of 5 seconds, and the data obtained were arithmetically averaged to get the corresponding data point.

For determination of the build-up dynamics of the 2BC effect at constant externally applied field, the field was always applied for half an hour in advance to the start of the measurement in order to provide quasi steady-state poling conditions for the material under investigation and held constant throughout the complete measurement sequence. If desired, the sample was pre-illuminated during this period as well using either one of the recording beams (typically beam 2 (I_{02})) or the erasure beam. This time period is referred to hereafter as “initial relaxation“ (time). Data sampling was initialized about 500ms in advance to the beginning of the measurement in order to monitor the onset of the actual measurement procedure, which defines $t = 0$. Then the recording process was started by switching on recording beam 1 (or both of the recording beams if the initial relaxation was performed with the erasure beam) using fast magnetic shutters exhibiting a mechanical switching time of about 5ms and, if necessary, simultaneously switching off the erasure beam. The total switching time of the complete process from initial relaxation to holographic grating recording was less than 10ms in any case. The recording beams' powers were monitored as a function of time typically applying an initial sampling rate of 10sec^{-1} , which was decreased down to 1sec^{-1} at minimum in several steps as the sampling process proceeded in order to reduce the total amount of data sampled in experiments extending over several tens of minutes up to hours. The sampling schedule of a dynamic experiment as described here was pre-programmed defining steps of sampling rates

and the number of data to be sampled per rate step, the total sum of all of which eventually defined the total length of holographic grating recording. The first values obtained immediately after both the recording beams had been switched on were numerically averaged in order to get the reference beam powers with the 2BC effect having not yet set on. Depending on the response speed of the systems investigated, typically 5 to 10 data points were used therefor.

Furthermore a technique was developed in order to monitor the coherent energy transfer due to 2BC while erasing the grating. For this purpose, the writing beams were shut down by more than three orders of magnitude in intensity after the holographic grating recording process as described above had been completed. Then the erasure beam was switched on. The recording beams reduced in intensity will be referred to hereafter as „gain probe beams“. For shutting down the recording beams an appropriate attenuator was switched into the main laser beam path by a home made device consisting of a magnetic relay, which carried the attenuator attached to its movable part (“ODS“ in figure (4 - 5)). The relay was triggered by a TTL line and an electronic power relay. Due to the relatively high mass of the parts to be moved, this switching process was fairly slow. Using the same detectors now the gain probe beams showing very small intensity (and power, of course) had to be detected besides the original recording beams. It is clear, that this required a second signal line of much higher sensitivity than for the original recording beams. Therefore, a TTL controlled signal line changer was built and inserted into the measurement circuitry. The sensitivity required could only be achieved using lock-in amplifiers, which demanded the recording beams to be chopped. As a consequence, the original recording beams also could no more be detected directly but the signal had to be rectified before. Please note, that rectifiers introduce an additive offset due to the diodes' onset voltage, which has to be corrected for calculating the gain values. This correction was performed by measuring the electrical characteristic of the rectifiers with respect to the input AC voltage, fitting this curve with polynomial regression and convolving the resulting function with the experimental curves. The process of changing the signal lines from low sensitivity to high sensitivity required a considerable relaxation time due to a signal overshoot occurring in the lock-in amplifiers. Thus, in conclusion, the sequence applied for switching from recording the grating to erasing it again while further monitoring the coherent energy transfer proceeded as follows. First data sampling was stopped. The original writing beams were shut down in intensity. Then the signal lines were changed to high sensitivity and an idle period of two seconds was provided for the lock-in amplifiers to relax from the occurring signal overshoot. Finally data sampling was restarted and the erasure beam was switched on simultaneously.

The powers of the gain probe beams were then monitored as a function of time basically as described above. However, a sampling rate of 16.67sec^{-1} was applied for the first 5000 data points, which was then decreased to 2.083sec^{-1} sampling another 5000 points. This sampling schedule was applied to all experiments in question here resulting in a total erasure time of the grating of 45min. The last values obtained were averaged to get the reference beam powers with the grating already erased. Typically 500 data points were used for averaging in this case. The evaluation process is described in more detail below including a discussion of the problem of getting meaningful reference values for the gain probe beams.

Please note, that the circuitry intended to carry out the experiments described above was disabled for experiments, which focussed only on the build-up dynamics of the 2BC effect or its steady-state values. Then, the chopper Ch1 (see figure (4 - 5)) was removed and the recording beam powers were monitored as dc-signals. The rectifiers were then bridged or absent. Furthermore, the waiting loops in the switching process from recording to erasing were disabled and the time resolution of the switching process was then accordingly determined by the maximum time resolution of the MS Windows based setup control software ($\leq 50\text{ms}$).

It is to be pointed out that the measurement technique as described above introduces a

phase reference “from outside” the PR grating. This does only make sense, if there are components of the PR grating, the spatial position of which can be considered as unchanged at least during the initial erasure process.

4.2.1.2.2.) Evaluation of the 2BC experiments

Subsequently, the basic equations for evaluation of the PR gain in the 2BC experiments carried out in the frame of this work will be discussed. Systematic errors accepted will be discussed. Finally, the evaluation procedure for the experiments will be outlined.

4.2.1.2.2.1.) Basic equations for evaluation of the 2BC experiments

The PR gain coefficient Γ is calculated from the PR “gain factor“ γ , which is derived from eq. (2.5 - 108) and eq. (2.5 - 109) and, hence, experimentally accessible. However, these equations must be adapted to the tilted geometry applied for PR polymers and depicted in figure (4 - 4). Subsequently, this will be performed ostensibly by modifying the coupling constant of the symmetric coupled wave problem discussed in “2.5.4.) Photorefractive two-wave mixing” on page 138. First, eq. (2.5 - 108) and eq. (2.5 - 109) will be applied directly to the tilted geometry. The fact that the optical paths of the writing beams are differently long in this geometry will at first be ignored. Then the absorption terms will be eliminated by making use of both the equations eq. (2.5 - 108) and eq. (2.5 - 109) to calculate the gain coefficient and by introducing the demand for energy conservation. Finally a modified coupling constant will be introduced and, thus, the different optical path lengths will be accounted for in context with the gain coefficient. The following discussion assumes s-polarization of the involved beams which allows to set the consideration of the polarization vectors aside.

The net gain factors for the particular recording beams are given by:

$$\gamma_1(l) = \frac{I_1(l)}{I_{01}} = \frac{1+b}{1+be^{-\Gamma l}} e^{-\alpha l_1} \quad \text{eq. (4 - 1)}$$

and:

$$\gamma_2(l) = \frac{I_2(l)}{I_{02}} = \frac{1+\frac{1}{b}}{1+\frac{1}{b}e^{\Gamma l}} e^{-\alpha l_2} \quad \text{eq. (4 - 2)}$$

where α is the absorption coefficient, b the initial intensity ratio of the recording beams given by eq. (2.5 - 110), l the average interaction length with the PR grating and $l_{1,2}$ are the actual lengths of the path of the light beams through the material. The intensity quantities have been defined before in context with eq. (2.5 - 108) and eq. (2.5 - 109). Please note, that the interaction length with the PR grating is connected with the z -coordinate used for the derivation of eq. (2.5 - 110) in “2.5.4.) Photorefractive two-wave mixing” on page 138 via the internal tilt angle θ_t , i.e. l is the actual length of the bisector between the recording beams inside the PR material given by:

$$l = \frac{d}{\cos \Psi_t}, \quad \text{eq. (4 - 3)}$$

where d is the sample thickness. The actual length $l_{1(2)}$ of the path of beam 1(2) through the material is given by:

$$l_{1(2)} = \frac{d}{\cos \alpha_{1(2)}}. \quad \text{eq. (4 - 4)}$$

The subsequent consideration will focus on beam 1 but apply similarly to beam 2 as well.

Solving eq. (4 - 1) for the net gain coefficient Γ_1 yields:

$$\Gamma(l) = \frac{1}{l} [\ln b \gamma_1(l) - \ln((1 + b) e^{-\alpha l_1} - \gamma_1(l))], \quad \text{eq. (4 - 5)}$$

where γ_1 , b and α are experimentally accessible. In order to derive an expression for the actual gain coefficient, the PR gain factor γ_{01} for the case of zero absorption shall be introduced with:

$$\gamma_1 = \gamma_{01} e^{-\alpha l_1}, \quad \text{eq. (4 - 6)}$$

which eliminates the absorption term at the right hand side of eq. (4 - 5) resulting in:

$$\Gamma(l) = \frac{1}{l} [\ln b \gamma_{01} - \ln(1 + b - \gamma_{01})]. \quad \text{eq. (4 - 7)}$$

With eq. (4 - 6) one obtains from eq. (4 - 1):

$$\gamma_{01}(l) = \frac{I_1(l)}{I_{01} e^{-\alpha l_1}} = \frac{1 + b}{1 + b e^{-\Gamma l}} = \frac{I_1}{I_{10}}, \quad \text{eq. (4 - 8)}$$

where I_{10} represents the intensity of the beam after having traversed through the sample without PR grating. This allows to obtain the PR gain factor γ_{01} from the ratio of the intensities of the recording beam behind the sample for the case of the 2BC effect being absent on the one hand (I_{10}) and being present on the other (I_1). I_1 and I_{10} are directly accessible by the experiment. Furthermore, b may be expressed as:

$$b = \frac{I_{20} e^{-\alpha l_1}}{I_{10} e^{-\alpha l_2}}. \quad \text{eq. (4 - 9)}$$

and energy preservation must be accounted for, which writes:

$$\frac{I_1}{e^{-\alpha l_1}} + \frac{I_2}{e^{-\alpha l_2}} = \frac{I_{10}}{e^{-\alpha l_1}} + \frac{I_{20}}{e^{-\alpha l_2}}. \quad \text{eq. (4 - 10)}$$

Inserting eq. (2.5 - 110) for b and eq. (4 - 8) for γ_{01} into eq. (4 - 7) and using eq. (4 - 10) yields:

$$\Gamma(l) = \frac{1}{l} [\ln \gamma_{01} - \ln \gamma_{02}], \quad \text{eq. (4 - 11)}$$

where γ_{02} is the corresponding absorption-free PR gain factor for beam 2 given by:

$$\gamma_{02} = \frac{I_2}{I_{20}} \quad \text{eq. (4 - 12)}$$

in analogy to eq. (4 - 8), however, referring to eq. (4 - 2). Please note, that the absorption terms have cancelled in eq. (4 - 11) as notified above.

The oblique incidence of the recording beams leading to different actual length of the optical paths results in different losses, which are not accounted for in eq. (4 - 5) and eq. (4 - 7) but have already been eliminated in eq. (4 - 11). For the gain coefficient, however, still symmetric incidence of the recording beams is presumed and thus equal interaction length for both the recording beams with the PR grating. In order to correct for this inconsistency, the expression for the gain coefficient according to eq. (2.5 - 102) must be modified, which is the real part of the coupling constant in the underlying coupled wave problem:

$$\Gamma = \frac{2\pi \Delta n}{\lambda_0 \cos \theta} \sin \phi. \quad \text{eq. (4 - 13)}$$

Here 2θ is the intersection angle of the recording beams at symmetric incidence. The factor $\cos \theta$ was introduced in order to express the components of the wave propagation vectors of the recording beams along the z -direction according to eq. (2.5 - 93) for the geometry depicted in figure (2.5 - 8) on page 141. Accordingly, this form of the 2BC coupling constant will not hold any more if oblique incidence as depicted in figure (4 - 4) shall be accounted for. In this case the

projection of the beam propagation vectors onto the z -direction must be considered independently for each of the beams and, hence, must not be merged into the coupling constant. It follows the correct expression for calculating the gain coefficient at oblique incidence of the recording beams:

$$\Gamma(d) = \frac{1}{d}[(\cos \alpha_1) \ln \gamma_{01} - (\cos \alpha_2) \ln \gamma_{02}], \quad \text{eq. (4 - 14)}$$

where d is the sample thickness and the coupling constants reads now:

$$\Gamma = \frac{2\pi\Delta n}{\lambda_0} \sin \phi. \quad \text{eq. (4 - 15)}$$

Using the gain coefficient according to eq. (4 - 15), the original form of eq. (2.5 - 108) and eq. (2.5 - 109) expressing the beam intensities as a function of the sample thickness (i.e. the z -coordinate) is basically restored. Eq. (4 - 1), eq. (4 - 2), and eq. (4 - 8) with “ Γ ” in the exponential argument can be dropped again, since they have only been intermediate steps introduced in order to illustrate the problem discussed and to derive the correct expressions ostensibly without carrying out a coupled wave analysis once more for the case of oblique incidence. Eq. (4 - 14) may as well be derived starting with eq. (2.5 - 108) and eq. (2.5 - 109) with the actual optical paths already inserted. Two expressions of the form of eq. (4 - 5) will then be obtained, which must be merged in order to get eq. (4 - 14).

Please note that there is a mistake in the interpretation of the gain equations often observable in the literature about PR polymers. The gain coefficients calculated by eq. (4 - 14) are often used together with eq. (4 - 13) instead of eq. (4 - 15). However, the error made is usually small due to the geometry typically used for these experiments, which results in $3^\circ < \theta < 4^\circ$ and, thus, $\cos \theta \approx 1$ anyway.

4.2.1.2.2.2.) Consideration of systematic errors in the 2BC experiments

The theoretical solution of the coupled wave problem underlying 2BC (page 141) assumes a slowly varying amplitude of the involved waves as a function of the interaction length, an approximation which allows to neglect the second order derivative of the wave amplitude with respect to the interaction length in the wave equation. In high performance PR polymers showing strong 2BC, however, this approximation may become poor. Figure (4 - 8) shows that the approximation is still reasonably valid for the 2BC experiments carried out in the frame of this work, where usually gain coefficients of $\Gamma \leq 50\text{cm}^{-1}$ in samples with $d \leq 125\mu\text{m}$ were obtained. In the worst case (i.e. $\Gamma = 50\text{cm}^{-1}$ and $d = 125\mu\text{m}$), the grating contrast is reduced by less than 2% in average and less than 5% at maximum due to 2BC.

Systematic errors in obtaining the gain coefficient from the experimental data on the absolute or relative recording beam intensities behind the sample may be made by not accounting correctly for effects other than the coherent energy transfer due to 2BC, which alter the intensities of the beams while traversing the sample. For symmetric incidence of the recording beams, these errors cancel by principle. However, for oblique incidence this is not the case. The effects, which must be accounted for are absorption effects as well as the transmission coefficients of the various interfaces in the sample structure depicted in figure (4 - 2). Since there is still a considerable amount of publications coming up, which report on PR gain coefficients obtained for oblique incidence of the recording beams by means of eq. (4 - 7) it seems advisable to estimate the order of magnitude of these effects.

Subsequently the orders of magnitude of these effects shall exemplarily be considered for a model system of the composition DMNPAA:PVK:ECZ:TNF = 50:33:16:1%wt operated at an operating wavelength of $\lambda_0 = 633\text{nm}$ and showing a basic absorption coefficient of $\alpha_{633} = 22\text{cm}^{-1}$ [140]. The sample thickness shall be $125\mu\text{m}$ and the refractive indices n of the layers of different materials present in a sample according to figure (4 - 2) are about $n_{\text{glass}} = 1.5$, $n_{\text{ITO}} = 2$ and $n_{\text{polymer}} = 1.7$. The geometrical configuration of the setup is described in “4.2.1.) General wave mixing setup configuration and parameters” on page 181.

For equal initial intensities in front of the sample, the initial intensity ratio will be $b = 1$. For the aforementioned parameters, one obtains actual optical path lengths of $140\mu\text{m}$ for beam 1 and $150\mu\text{m}$ for beam 2. Thus, according to the Lambert Beer law:

$$I = I_0 e^{-\alpha l}, \quad \text{eq. (4 - 16)}$$

an intensity ratio of $b = 0.98$ behind the sample is obtained. Please note, that the absorption will be increased notably but not dramatically by applying an external electrical field to the system, which will increase the error slightly. However, a much larger error is made by disregarding the transmission of the light through the optical interfaces inside the sample. Calculating the amplitude transmission coefficients by means of Fresnel's equations eq. (2.1 - 116) and eq. (2.1 - 123) and applying eq. (2.1 - 125) one obtains for the relative transmissions T of the beams 1 and 2 throughout the whole sample (6 interfaces) for s(p)-polarized light $T_1 = 0.724(0.960)$ and $T_2 = 0.438(0.884)$, respectively. Thus follows for s-polarized light $b = 0.60$ and for p-polarized light $b = 0.92$

However, in most cases Γ is calculated by means of eq. (4 - 7), b is obtained according to eq. (4 - 9), and the error made is thus smaller than described above, since then only the interfaces behind the PR optical nonlinear layer (3 interfaces) will cause systematic deviations in b as present inside the active polymer layer. The energy transmission coefficients to be taken into account in this case are $T_1 = 0.850(0.978)$ and $T_2 = 0.662(0.947)$ for s(p)-polarized light, respectively. Nevertheless, eq. (4 - 7) will yield erroneous values for Γ , since b contains T_1 as well as T_2 , whereas the gain factor for a single beam only accounts for the transmission coefficients of the beam in question.

Please note finally that the application of eq. (4 - 7) will, depending on the applied field, yield different results if applied to recording beam 1 or recording beam 2 due to the different path lengths in connection with electro-absorption effects, which will additionally lead to a field dependence of b .

Most of the aforementioned errors arising from disregarding the oblique incidence of the recording beams can be avoided if eq. (4 - 14) is used for calculating the gain coefficient, since they are multiplicative and thus cancel, as already shown above for the basic absorption: Replacing $I_{x(0)} \rightarrow I_{x(0)}/T_x$ with $x = 1,2$ additionally accounts for the different energy transmission. As for the absorption, also T_x will cancel during the derivation of eq. (4 - 14). It is to be pointed out that eq. (4 - 14) in fact represents the combination of eq. (4 - 7) and its

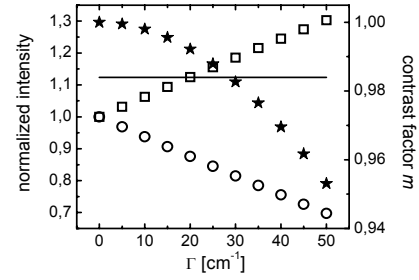


Figure (4 - 8): Grating contrast factor at the rear interface of a PR device of thickness $d = 125\mu\text{m}$ as a function of the gain coefficient calculated using eq. (2.5 - 108) and eq. (2.5 - 109) for $b = 1$ (solid stars). Furthermore, the corresponding normalized intensities of the writing beams are shown. The plot implicitly contains the grating contrast and the normalized beam intensities as a function of z (see figure (4 - 4)) if the Γ -axis up to a given value of Γ is divided into 125 steps and read as the z -axis of the system in units of $[\mu\text{m}]$. The solid line represents the average grating contrast throughout a sample with $d = 125\mu\text{m}$ for $\Gamma = 50\text{cm}^{-1}$. The reduction of the average grating contrast as compared to unity contrast (i.e. without beam coupling) in this case is still well below 2%.

pendant for beam 2, as already mentioned before.

However, a small systematic error will remain if the gain coefficient is monitored as a function of the external field. In this case, the initial intensities I_{10} and I_{20} will only account for the basic absorption (no external field applied) whereas the intensities obtained for the external field applied will be afflicted additionally with the absorption induced by the applied field [184]. This electro-absorption effect, however, is comparatively small in the systems investigated [13] and can be neglected with good approximation. This error may be avoided by monitoring the initial intensities without PR grating as a function of the external field as well and use these for calculating Γ . However, this is an extensive procedure which is not reasonably counterweighted by the small gain in accuracy.

4.2.1.2.2.3.) 2BC evaluation procedure

The PR gain coefficient as a function of the external field was evaluated by monitoring the beam powers behind the sample as a function of the applied field and dividing them by their initial values obtained for zero external field. As described above, electro-absorption of the materials cause a small systematic error in this case, which increases with the external field applied.

The PR gain coefficient as a function of time was evaluated by monitoring the beam powers behind the sample as a function of time and dividing them by their initial values obtained when the PR grating had not yet been developed. Since the external field applied in this case was constant for all experimental data monitored, no systematic error was made.

For determining the PR gain as a function of time during grating erasure, no initial values for the 2BC probe beams (i.e. the strongly attenuated recording beams) for a PR grating not being present are available. Monitoring the initial values for the 2BC probe beams prior to the recording process yielded values, which were obviously wrong. This might be attributed to the fact, that the system should be expected to experience changes in transmission also upon illumination due to the ionization of sensitizer molecules and CTA's changing their absorption spectrum. Therefore, the erasure process was maintained considerably longer than necessary for the 2BC and the DFWM signals to drop to zero, and a large number of data from the far edge of the curves where no signal is observed any more were averaged for obtaining reference 2BC probe beam powers without PR grating. However, this procedure bears the inherent problem, that a very weak PR grating may persist due to the existence of the 2BC probe beams required for monitoring the energy exchange. Thus, this evaluation procedure may suffer from some systematic error due to this problem. On the other hand, this procedure ensures, that changes of the sample's transmission upon illumination are accounted for, since the erasure beam is present during determination of the reference values of the 2BC probe beams.

The error possibly made by the above described procedure will occur as some offset being constant in time throughout all experiments. However, a countercheck was performed by applying the procedure described above, then switching off the 2BC probe beams and erasing further on to definitely ensure that no PR grating will be present. Finally the 2BC probe beam powers were detected once more. The data thus obtained were identical with the reference values determined as described above with the 2BC probe beams present throughout the complete erasure process within experimental accuracy. This indicates, that the error discussed is below the resolution limit of the employed setup.

Gain coefficients were calculated from experimental data according to eq. (4 - 14) and PR phase shift angles ϕ from eq. (4 - 15) according to:

$$\phi = \text{asin}\left(\frac{\lambda_0 \Gamma}{2\pi \Delta n}\right). \quad \text{eq. (4 - 17)}$$

Please note, that the application of eq. (4 - 15) requires insertion of a refractive index modulation Δn obtained for the same polarization as applied in the 2BC experiment due to the polarization anisotropy of poled polymers according to “2.4.2.) Electrical poling of organic polymers - the oriented gas model” on page 83. The refractive index modulations were determined by DFWM experiments, which will be considered subsequently. If the refractive index modulation is determined with orthogonal polarization as compared to the 2BC experiment, the polarization anisotropy must be accounted for by correcting the index modulation with some anisotropy factor derived from the theory as discussed below in “4.2.1.4.) Polarization anisotropy for PR wave mixing experiments” on page 199.

4.2.1.3.) Degenerate four-wave-mixing (DFWM)

DFWM experiments were carried out during recording of PR gratings in the materials investigated. Furthermore, the erasure as well as the quasi dark decay of previously recorded PR gratings were probed by the formal analogy to DFWM experiments with the recording beams being absent. Please note, that grating erasure must be determined using an erasure beam which is not Bragg-matched to the PR grating as already discussed before in “4.2.1.2.1.) 2BC measurement procedures” on page 186. Furthermore, it must be clear, that the dark decay of some photosensitive holographic grating cannot be determined without causing a minimum extent of grating erasure. Therefore, any diffraction experiments on the dark decay of PR grating will only determine a quasi dark decay, which depends on the photon flux the sample has been exposed to while reading out the grating.

4.2.1.3.1.) DFWM measurement procedures

The quantities in question to be directly measured in the DFWM experiments carried out in the frame of this work are the transmitted and the diffracted probe beam powers as a function of the applied field or of the time. The data obtained were evaluated as described below in “4.2.1.3.2.) Evaluation of the DFWM experiments”.

For all DFWM experiments, the probe beam intensity was at least two orders of magnitude smaller than the sum of the intensities of the recording beams in order to minimize partial erasure of the recorded grating by the probe beam. In order to achieve high resolution while using small absolute beam powers, the probe beam was usually chopped (with chopper Ch2 in figure (4 - 6)) and lock-in amplifiers were used for detection. This furthermore minimized the possible impact of some background light, which might have been caught by the photodetectors used for detecting the transmitted and the diffracted DFWM probe beam (detectors D3 and D4 in figure (4 - 6)). Please note that this was not an issue for detecting the relatively strong recording beams, but the low power of the DFWM probe beams made their reliable detection much more sensitive against undesired light sources.

Furthermore, in most cases, the probe beam was polarized perpendicularly to the recording beams, since using s-polarized recording beams and a p-polarized probe beam are the preferred working conditions for DFWM due to minimized 2BC in this configuration while the p-polarized probe beam senses maximum Δn as discussed in “2.5.3.3.) Orientational enhancement effect” on page 131. Furthermore, by using orthogonal polarizations for recording the grating and read-out, the possible formation of additional weak PR gratings due to

interference of the probe beam with the recording beams is avoided. However, for experiments, which focused in particular on the photorefractive phase shift the DFWM probe beam and the recording beams were polarized parallelly in order to probe directly the refractive index modulation relevant for the 2BC effect. The polarization states actually applied will explicitly be noted in the respective sections devoted to the experimental results.

Steady-state DFWM experiments as well as experiments on the PR grating build-up dynamics were typically carried out together with the corresponding 2BC experiments and, thus, the general procedures discussed in this context will apply here as well.

However, as opposed to the 2BC experiments, the transmitted and the diffracted DFWM probe beams were monitored. Furthermore the DFWM probe beam could be controlled separately by a fast magnetic shutter (shutter Sh3 in figure (4 - 6)) and was typically switched on only for grating read-out in the steady-state experiments (i.e. at the end of the relaxation of the system to quasi steady-state).

In by far most experiments on the build-up dynamics of the PR grating, the DFWM signal has even been the main object of interest, since it probes solely the dynamics of the refractive index build-up, which is directly indicative for the build-up of the PR space-charge field. In contrast, the dynamics of the 2BC signal represents a mix of the dynamics of the PR space-charge field build-up and the dynamic evolution of the PR phase shift. In the experiments on the grating build-up dynamics, the DFWM probe beam was switched on in advance of the instant when both the recording beams were provided.

For determining the PR grating erasure or dark decay, the grating was first recorded using the procedure described for the experiments on the PR grating build-up. As soon as the grating build-up was performed for the time span pre-programmed in the data sampling schedule for the recording process the data sampling process was stopped and the setup was switched to erasure or dark decay mode.

For the erasure mode the recording beams were both switched off (shutter Sh2) and the erasure beam was switched on (Sh4) simultaneously, and data sampling was restarted. The complete switching process was faster than 100ms. Grating erasure was typically performed for 45min corresponding to a sampling schedule covering 5000 data points at 16.67sec^{-1} sampling rate and subsequently 5000 data points at 2.083sec^{-1} . The erasure intensity could be adjusted in 4 steps by inserting different attenuators in the erasure beam path by means of the attenuator changer ODW (see figure (4 - 6)), which enabled extensive automation of the experiments on the PR grating erasure.

For measuring the PR grating dark decay, all beams were at first switched off. Special care was taken to provide the least photon flux achievable through the sample during the read-out process in order to approximate real "dark" decay as best as possible. Therefore, the lowest DFWM probe beam intensity, which could still be resolved reliably by the used setup has been adjusted for these experiments. In this context a lower resolution limit of up to 0.01 (1%) internal diffraction efficiency was accepted for the sake of low reading power but at the cost of the absolute accuracy of the data obtained. Furthermore, the read-out process was modified such that the sample was kept completely in the dark most of the time and the reading beam was only switched on for short times required for the lock-in amplifiers to relax to steady-state and subsequent data sampling. For the latter, 10 single measurements at a rate of 5sec^{-1} were performed and arithmetically averaged to form one data point. By all of these measures, a ratio of up to almost 10^6 was achieved between the total of the recording beam intensities and the DFWM probe beam intensity for recording at high intensity. For recording at the lowest intensities applied, a ratio of better than 10^3 could still be achieved. The recording intensities applied will be noted in the corresponding section devoted to the experimental results.

4.2.1.3.2.) Evaluation of the DFWM experiments

Subsequently, the basic equations for evaluating the DFWM experiments will be discussed. Simplifications of Kogelnik's equation eq. (2.3 - 45) will be introduced and the errors thus made will be considered. Finally, the evaluation procedure for the experiments will be described.

4.2.1.3.2.1.) Basic equations for evaluation of the DFWM experiments

The following considerations are based on the geometrical configuration depicted in figure (4 - 4). Intensity and angle parameters used in this section and not explicitly explained in the text are defined therein.

The evaluation of the DFWM experiments is based on Kogelnik's coupled wave theory discussed in "2.3.2.) Coupled wave theory for thick hologram gratings" on page 53. In order to apply this theory, first the holographic gratings to be evaluated must be identified as volume holograms. According to eq. (2.3 - 2), some hologram may safely be considered as a volume hologram if:

$$l \geq 1.6 \frac{\Lambda^2 n}{\lambda_0}, \quad \text{eq. (4 - 18)}$$

where l is the actual grating thickness given by the length of the bisector between the recording beams and is connected with the sample thickness via eq. (4 - 3). With $n = 1.7$, $\Lambda = 3\mu\text{m}$, and $\lambda_0 = 633\text{nm}$ and using eq. (4 - 3), eq. (4 - 18) will be fulfilled for samples thicker than $20\mu\text{m}$. The least sample thickness used in the frame of this work was $37\mu\text{m}$. Please note, that notable diffraction into higher orders could already be observed for this thickness. Data presented in the section devoted to the experimental results refer to sample thicknesses of $63\mu\text{m}$ to $125\mu\text{m}$. Higher order diffraction for $63\mu\text{m}$ thick samples was found to be negligibly small and no more detectable for $125\mu\text{m}$ thick samples.

The theoretical expressions for the diffraction efficiency in question here are eq. (2.3 - 44) to eq. (2.3 - 46), since the grating was read out with p-polarized light in all DFWM experiments performed. The diffraction efficiency thus defined is the ratio between the diffracted beam power behind the grating (not behind the sample) $I_{\text{diffracted}}$ and the incident beam power in front of the grating (not in front of the sample) I_{incident} . This is referred to as „external diffraction efficiency“:

$$\eta_{\text{ext}} = \frac{I_{\text{diffracted}}}{I_{\text{incident}}}. \quad \text{eq. (4 - 19)}$$

However, in the frame of this work η_{ext} according to eq. (4 - 19) is not appropriate for two reasons. Firstly, the experimentally monitored diffracted beam power will be afflicted with losses due to restricted transmittance of all the 6 optical interfaces of the sample as discussed before in "4.2.1.2.2.) Evaluation of the 2BC experiments" on page 188, which must be corrected for if Kogelnik's equations shall be applied. Secondly, the quantity in question is not the diffraction efficiency but the refractive index modulation. Thus, the absorption (including electro-absorption) of the system (which is accounted for by the theory) must be eliminated, which requires the absorption coefficient to be determined as well, extending the experimental efforts markedly. Thus it would be more appropriate to find a way to determine the diffraction efficiency more conveniently.

This can be achieved by defining an „internal diffraction efficiency“ η_{int} according to:

$$\eta_{\text{int}} = \frac{I_{3d}}{I_{3t} + I_{3d}}, \quad \text{eq. (4 - 20)}$$

where I_{3d} (diffracted portion) and I_{3t} (transmitted portion) are the (DFWM) probe beam powers

both monitored simultaneously after the beams have traversed the sample. Using eq. (4 - 20) to calculate the diffraction efficiency from experimental data, the only error made will arise from the difference in energy loss due to different optical path lengths and different transmittances of the interfaces of the samples, whereas the basic quantities of these losses due to the general tilt of the sample will cancel.

External and internal diffraction efficiency are connected by the following relations:

$$I_{incident} = \frac{I_{3t} e^{\frac{\alpha d}{\cos \alpha_1}}}{T_1^{(4)} T_1^{(5)} T_1^{(6)}} + \frac{I_{3d} e^{\frac{\alpha d}{\cos \alpha_2}}}{T_2^{(4)} T_2^{(5)} T_2^{(6)}} \quad \text{eq. (4 - 21)}$$

and:

$$I_{diffracted} = \frac{I_{3d}}{T_2^{(4)} T_2^{(5)} T_2^{(6)}} \quad \text{eq. (4 - 22)}$$

where $T_a^{(b)}$ is the energy transmittance for p-polarized light according to eq. (2.1 - 123) and eq. (2.1 - 125) for beam path number a and interface number b counted in propagation direction of the beam (i.e. here interface 4 is the polymer/ITO-interface, interface 5 is the ITO/glass interface etc.). Please note for the sake of completeness, that the beam incident on the sample is connected with $I_{incident}$ by:

$$I_{incident} = I_{03} T_1^{(1)} T_1^{(2)} T_1^{(3)}. \quad \text{eq. (4 - 23)}$$

4.2.1.3.2.2.) Simplification of Kogelnik's equation and error discussion

The error made by working with the internal diffraction efficiency instead of the external diffraction efficiency can be estimated from eq. (4 - 21) and eq. (4 - 22). At first, the absorption term from Kogelnik's equation is transferred to eq. (4 - 20). According to eq. (2.3 - 45) the complete relation may thus be written:

$$\eta_{ext} e^{\frac{\alpha d}{2} \left(\frac{1}{c_T} + \frac{1}{c_D} \right)} = \frac{\frac{I_{3d} e^{\frac{\alpha d}{2} \left(\frac{1}{c_T} + \frac{1}{c_D} \right)}}{T_2^{(4)} T_2^{(5)} T_2^{(6)}}}{\frac{I_{3t} e^{\frac{\alpha d}{\cos \alpha_1}}}{T_1^{(4)} T_1^{(5)} T_1^{(6)}} + \frac{I_{3d} e^{\frac{\alpha d}{\cos \alpha_2}}}{T_2^{(4)} T_2^{(5)} T_2^{(6)}}} = \frac{(\sin \sqrt{v^2 - \xi^2})^2}{1 - \frac{\xi^2}{v^2}}. \quad \text{eq. (4 - 24)}$$

The parameters not explained in this section are defined in "2.3.2.) Coupled wave theory for thick hologram gratings" on page 53. For calculating the correction terms, the representative model system as described in "4.2.1.2.2.2.) Consideration of systematic errors in the 2BC experiments" on page 190 is used and the geometrical configuration according to figure (4 - 4) is assumed. Using eq. (2.3 - 21) one obtains for the obliquity factors $c_D = 0.829$ and $c_T = 0.893$. The transmittances for p-polarized light are calculated according to Fresnel's equation eq. (2.1 - 123) and eq. (2.1 - 125). For a sample of 125 μ m thickness one finally obtains:

$$\frac{I_{3d}}{0.96 I_{3t} + 1.01 I_{3d}} = \frac{(\sin \sqrt{v^2 - \xi^2})^2}{1 - \frac{\xi^2}{v^2}}. \quad \text{eq. (4 - 25)}$$

Thus, by working with η_{int} , the maximum relative error for $\eta_{int} \rightarrow 0$ will be -4% and $+1\%$ for $\eta_{int} \rightarrow 1$, respectively.

Now the error will be discussed, which is made by reasonably simplifying the right hand side of eq. (4 - 25). The key problem is to get rid of the obliquity factors c_D and c_T . The values of these have already been calculated above. Setting:

$$\bar{c} = c_T = c_D = (c_D + c_T)/2 \quad \text{eq. (4 - 26)}$$

will yield a relative error for \bar{c} relative to $\sqrt{c_T c_D}$ of less than 0.07% , which is excellent an approximation. By that a dramatic simplification of eq. (4 - 25) is achieved, since ξ vanishes according to eq. (2.3 - 44) yielding:

$$\eta_{int} = (\sin v)^2. \quad \text{eq. (4 - 27)}$$

The coupling constant v of the coupled wave is given by eq. (2.3 - 44), however, for s-polarized light. In order to account for p-polarization one may write according to eq. (2.3 - 27), eq. (2.3 - 38), eq. (2.3 - 44) and eq. (4 - 26):

$$v = \frac{\pi \Delta n d}{\lambda_0 \bar{c}} (\hat{e}_T \bullet \hat{e}_D) \quad \text{eq. (4 - 28)}$$

where \hat{e}_T and \hat{e}_D are the polarization unit vectors of I_{3t} and I_{3d} . The scalar product of the polarization unit vectors, however, for the geometric configuration according to figure (4 - 4) yields: $\hat{e}_T \bullet \hat{e}_D = 0.993$, and, hence, can be ignored (i.e. set to unity).

Finally the geometrical meaning of \bar{c} must be clarified. From eq. (2.3 - 12), eq. (2.3 - 13), eq. (2.3 - 21) and eq. (2.1 - 45) one obtains for the geometrical configuration according to figure (4 - 4):

$$\bar{c} = \frac{2 \cos \alpha_1 - 2 \sin\left(\frac{\alpha_1 - \alpha_2}{2}\right) \sin\left(\frac{\alpha_1 + \alpha_2}{2}\right)}{2} = \frac{\cos \alpha_1 + \cos \alpha_2}{2}. \quad \text{eq. (4 - 29)}$$

In conclusion one ends up with the following expression for the internal diffraction efficiency:

$$\eta_{int} = \left[\sin\left(\frac{2\pi d \Delta n}{\lambda_0 (\cos \alpha_1 + \cos \alpha_2)}\right) \right]^2. \quad \text{eq. (4 - 30)}$$

Please note, that electro-absorption effects as discussed for the 2BC experiments have not been regarded here, but nevertheless will show an impact as well. Furthermore, the bulk refractive index of the materials investigated will depend on the external field applied leading to a slight field dependence of the transmittance and the reflectance of the ITO/polymer and the polymer/ITO interfaces, which is omitted as well. However, both these effects are secondary as compared to errors discussed above for the materials investigated.

4.2.1.3.2.3.) DFWM evaluation procedure

The internal diffraction efficiency according to eq. (4 - 20) was determined experimentally by simultaneously monitoring the transmitted and the diffracted probe beam.

The maximum internal diffraction efficiency achieved always falls short of its theoretical value of unity, which is generally observed in diffraction experiments on PR polymers. This has been commented by nearly all authors having published some work on PR polymers and was attributed to various effects including restricted grating dimensions, absorption effects, bending of the PR grating due to the imaginary part of the complex PR gain coefficient and others. However, the actual reason for this effect is still not understood. It will be shown in the section devoted to the results of this work, that at least hologram bending cannot be made responsible

for this observation. Typically internal diffraction efficiencies in the range of $\eta_{int} \approx 0.85$ to $\eta_{int} \approx 0.9$ are achievable in the first diffraction maximum for the experimental configuration according to figure (4 - 4) and sample thicknesses of around $100\mu\text{m}$. The first diffraction maximum on the other hand clearly corresponds to:

$$\frac{2\pi\Delta nd}{\lambda_0(\cos\alpha_1 + \cos\alpha_2)} = \frac{\pi}{2}. \quad \text{eq. (4 - 31)}$$

Thus, if the refractive index modulation was calculated according to eq. (4 - 30) the absolute internal diffraction efficiency obtained experimentally was normalized beforehand by its maximum value. In experiments where the grating was recorded to some point before a diffraction maximum occurred (e.g. in experiments on the grating dynamics), the latter was determined with the same sample in a standard DFWM experiment using measurement parameters (i.e., recording intensity and external field), which have proven by practice to yield reliable values for the maximum diffraction efficiency.

Accordingly, the refractive index modulation was always calculated according to:

$$\Delta n = \frac{\lambda_0(\cos\alpha_1 + \cos\alpha_2) \text{asin} \sqrt{\frac{\eta_{int}}{\eta_{int,max}}}}{2\pi d}. \quad \text{eq. (4 - 32)}$$

For evaluation of experiments on the PR grating build-up or decay (i.e. erasure by uniform illumination as well as dark decay) dynamics, data on the refractive index modulation obtained from monitoring η_{int} as a function of time and calculating Δn according to eq. (4 - 32) were fitted to the following exponential expressions.

The grating build-up dynamics was fitted to exponential associative growth functions of the form:

$$\Delta n(t) = \sum_i A_i \left(1 - e^{-\frac{t}{\tau_i}} \right), \quad \text{eq. (4 - 33)}$$

where A_i is the absolute weighting factor of the corresponding exponential associative growth term and τ_i is the corresponding time constant. Relative weighting factors used for comparing the fractions the particular exponential terms contributing to the overall process were obtained from normalizing the particular absolute weighting factors by the sum of all absolute weighting factors, i.e.:

$$A_{i,rel} = \frac{A_{i,abs}}{\sum_i A_{i,abs}}. \quad \text{eq. (4 - 34)}$$

Typically, two exponential terms (i.e. $i = 1, 2$) were sufficient to obtain good agreement with the experimental curves, which is in agreement with the theory according to eq. (2.5 - 24). In most cases more than two exponential terms even led to apparent over-parameterization, resulting in a diverging fitting algorithm. In few cases tri-exponential fits yielded obviously better fits, but these cases were restricted to certain materials and/or certain experimental conditions. Mono-exponential behavior was never observed for the grating build-up dynamics. Details will be discussed in the associated sections devoted to the experimental results.

The grating decay dynamics was fitted to exponential decay functions of the form:

$$\Delta n(t) = \sum_i A_i e^{-\frac{t}{\tau_i}}, \quad \text{eq. (4 - 35)}$$

where A_i is the absolute weighting factor of the corresponding exponential term and τ_i is the

corresponding time constant. Relative weighting factors were obtained using eq. (4 - 34). As for the build-up dynamics, typically two exponential terms (i.e. $i = 1, 2$) were sufficient in agreement with the theory according to eq. (2.5 - 28) and the discussion on page 130. However, in very few cases tri-exponential behavior occurred which, however, does not agree with the general behavior proposed by eq. (2.5 - 29). Furthermore, mono-exponential behavior could be observed as well, however, only under certain experimental conditions. Details will be discussed in the sections devoted to the experimental results.

In order to enable unifying considerations of the dynamic behavior of the systems investigated, the obtained particular time constants were merged into an average response time constant $\langle \tau \rangle$ by means of logarithmic averaging using the expression:

$$\langle \tau \rangle = e^{\sum_i A_{i,rel} \ln \tau_i} \quad \text{eq. (4 - 36)}$$

This technique has been proposed in the frame of this work and will be discussed in more detail in “5.2.3.) The relation between the glass-transition temperature and the dynamic performance in PVK based PR polymers” on page 243.

In some cases the dynamic behavior of the systems investigated was considered within a series of measurements, where basically bi-exponential but to a minor fraction also tri-exponential behavior was observed. In these cases, the two slower exponential terms were merged appropriately according to:

$$\langle \tau \rangle = e^{\sum_j A_{j,rel} \ln \tau_j} \quad \text{eq. (4 - 37)}$$

in order to enable reasonable comparability within the series of experiments concerned. The index j indicates a subset of the index i , which corresponds to the slow exponential terms. It will explicitly be noted in the discussion of the experimental results, if this approach has been applied in the evaluation procedure.

Please note, that correct application of eq. (4 - 36) and eq. (4 - 37) demands, that

$$\sum_{i(j)} A_{i(j),rel} = 1, \quad \text{eq. (4 - 38)}$$

i.e. the weighting factors must be normalized by the sum of the weighting factors of the exponential terms to be logarithmically averaged.

4.2.1.4.) Polarization anisotropy for PR wave mixing experiments

The refractive index modulation probed by diffraction experiments in PR polymers will be different for different polarizations of the light diffracted as already discussed theoretically in “2.4.2.) Electrical poling of organic polymers - the oriented gas model” on page 83, in “2.5.3.3.) Orientational enhancement effect” on page 131 and repeatedly mentioned before in “4.2.1.2.2.) Evaluation of the 2BC experiments” on page 188. In order to allow for an approximate conversion between the refractive index modulations probed by diffraction experiments using both the polarization states applied in the frame of this work, a reasonable value for the polarization anisotropy must be determined. According eq. (2.5 - 83) the total refractive index modulation in low- T_g PR polymers consists of a birefringence (BR) and an electro-optic (EO) contribution, the polarization anisotropies of which are summarized in eq. (2.5 - 52) and eq. (2.5 - 53) and may be rewritten in short terms as:

$$\frac{\Delta n_z^{(BR)}}{\Delta n_x^{(BR)}} = -2 \quad \text{eq. (4 - 39)}$$

and:

$$\frac{\Delta n_z^{(EO)}}{\Delta n_x^{(EO)}} = 3. \quad \text{eq. (4 - 40)}$$

The total polarization anisotropy may be expressed by the ratio of the molar PR Kerr susceptibilities parallel and perpendicular to the direction of the applied external field, $\zeta_{ZZZZ}^{(3)}$ and $\zeta_{ZZXX}^{(3)}$, respectively. According to [161] these can be written as:

$$\zeta_{ZZZZ}^{(3)} = \frac{N_A}{90} \left[\frac{6}{kT} F_0^2 F_\infty^2 \mu_0 \beta_0 + \frac{4}{3k^2 T^2} F_0^2 F_\infty^2 \mu_0^2 \Delta\alpha \right] \quad \text{eq. (4 - 41)}$$

$$\zeta_{ZZXX}^{(3)} = \frac{N_A}{90} \left[\frac{2}{kT} F_0^2 F_\infty^2 \mu_0 \beta_0 - \frac{2}{3k^2 T^2} F_0^2 F_\infty^2 \mu_0^2 \Delta\alpha \right], \quad \text{eq. (4 - 42)}$$

where the first term in the brackets represents the electro-optic contribution and the second term the birefringence contribution. N_A is the Loschmidt number, μ_0 is the permanent dipole moment of the NLO chromophore, $\Delta\alpha$ and β_0 are its first order polarizability anisotropy and its second order polarizability, respectively, and F_0 and F_∞ are the local field correction factors according to eq. (2.4 - 89) and eq. (2.4 - 90). The index “zero“ denotes the dc value and the index “infinite“ its value at fields oscillating with optical frequencies.

Kippelen et. al. [185] determined the molecular constants to be inserted in eq. (4 - 41) and eq. (4 - 42) for a PR polymer system, which is almost identical to the type of systems investigated in the frame of this work by means of ellipsometry using an angle of light incidence of 45°. Their results are listed in table (4 - 1):

Table (4 - 1)

unit system	μ_0	β_0	$\Delta\alpha$
CGS	$5.5 \times 10^{-18} \text{esu}$	$60 \times 10^{-30} \text{esu}$	$5.5 \times 10^{-23} \text{cm}^3$
MKS	$18.41 \times 10^{-30} \text{Cm}$	$22.27 \times 10^{-50} \text{Cm}^3 \text{V}^{-2}$	$61.19 \times 10^{-40} \text{Cm}^2 \text{V}^{-1}$

The authors furthermore provided data on the bulk refractive index and the dc dielectric permittivity. They quoted values of $n = 1.75$ and $\epsilon_0 = 6.4$, respectively, which allows for the calculation of the local field factors to:

$$F_0 = \frac{\epsilon(n^2 + 2)}{2\epsilon + n^2} = 2.0425 \quad \text{eq. (4 - 43)}$$

$$F_\infty = \frac{n^2 + 2}{3} = 1.6875. \quad \text{eq. (4 - 44)}$$

Applying the above numerical values to eq. (4 - 41) and eq. (4 - 42), one obtains for the molar Kerr susceptibilities:

$$\zeta_{ZZZZ}^{(3)} = 80.71 \frac{10^{-34} \text{Cm}^4}{V^3 \text{mol}} \quad \text{and} \quad \zeta_{ZZXX}^{(3)} = -36.42 \frac{10^{-34} \text{Cm}^4}{V^3 \text{mol}}. \quad \text{eq. (4 - 45)}$$

It follows for the polarization anisotropy occurring in wave-mixing experiments performed at

s- and p-polarization:

$$\frac{\Delta n_p}{\Delta n_s} = \frac{\zeta_{ZZZZ}^{(3)}}{\zeta_{ZZXX}^{(3)}} = -2.22. \quad \text{eq. (4 - 46)}$$

This value correlates with a typical PR polymer composite as investigated in the frame of this work with 50%wt DMNPAA in a PVK/ECZ matrix. It may safely be assumed that the polarization anisotropy according to eq. (4 - 46) also applies to composites containing 25% DMNPAA and 25% MNPAA instead of 50% DMNPAA in reasonable approximation. Hence $\Delta n_p/\Delta n_s = -2.22$ will be used as anisotropy factor if polarization conversions of the refractive index modulation are necessary. As already pointed out above, this will be the case, if the PR phase shift according to eq. (4 - 17) is to be estimated from experimental data on the PR gain coefficient and the DFWM diffraction efficiency, whereby these parameters have been determined with perpendicular polarization states. However, since eq. (4 - 46) only represents a rather crude approximation (among others, it is the theoretical dc-field value), absolute values of the PR phase shift calculated by means of eq. (4 - 46) show limited comparability to the shift values obtained by direct methods, making a correction for the polarization anisotropy dispensable. However, general trends found considering data, which are consistently corrected for polarization anisotropy using one and the same procedure will be reliable. Furthermore, thus obtained phase shift values were very similar to values (if available) presented for comparable systems operated under comparable conditions in the literature, which were obtained applying independent methods (e.g., the moving grating technique).

4.2.1.5.)Holographic multiplexing experiments

The peristrophic multiplexing experiments were intended as proof of principle, for showing the orders of magnitude to be expected and to reveal unexpected problems. Please note here, that the sequential order of the experimental results as shown later in this work does not represent the actual chronological order the results were obtained. In fact, the experiments on the erasure and decay behavior of the systems investigated were motivated by the problems encountered in context with the peristrophic multiplexing experiments, which were performed prior to these investigations.

4.2.1.5.1.)Experimental holographic multiplexing setup, sample holder and measurement procedure

Referring to figure (4 - 10) and figure (4 - 9), prior to a peristrophic multiplexing experiment, all beams were switched off by means of the shutters Sh1 and Sh2 (figure (4 - 9)) and the electric field was switched on. Then, the sample was rotated to an appropriate zero position. The sample holder, which was mounted on a rotation stage, enabled rotation by about 175° in one direction without causing some parts of the sample holder to pass through the beam paths while rotating the sample. In order to make this possible, the sample holder was fixed on the rotation stage using only three mounts as indicated in figure (4 - 10). Then the sample was pre-illuminated for 15 minutes by opening shutter Sh2 while shutter Sh3 was kept closed. For recording the first hologram to be multiplexed, the recording beams were switched on by opening Sh3. Then the first hologram was written for a given time, calculated in principle according to the recording schedule as described in principle in “2.3.3.3.) System metrics for holographic multiplexing in erasable media” on page 65. The particular exposure schedule applied here will be described in the section devoted to the experimental results. Once the first

hologram had been recorded, both writing beams were switched off by Sh2 and the sample was rotated by a fraction of the total range of 175° , the upper limit of which results from the total range divided by the number of holograms intended to be multiplexed in the experiment. Then the next hologram was recorded by opening Sh2. After all holograms had been recorded, the recording beams were switched off and the sample was rotated back to the initial position used for recording the first hologram. Then the reading beam was switched on by means of shutter Sh1 for two seconds and the diffracted reading beam power was measured at the end of this time period. This minimum reading interval was demanded by the relaxation time required by the powermeter used for detecting the reading beam power to auto-adjust its metering range. After that, the reading beam was blocked again and the sample was rotated to the position of the second hologram recorded, which then was read out as described before and so on. Please note, that the sample was held under field throughout the whole experiment.

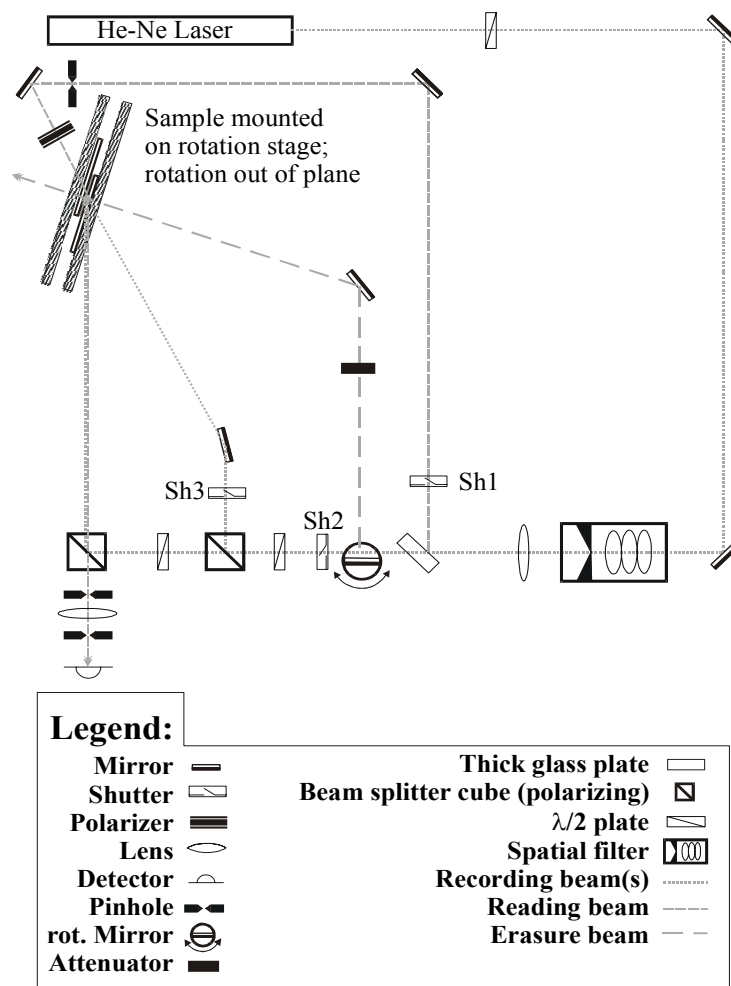


Figure (4 - 9): Scheme of the setup applied in peristrophic multiplexing experiments. The transmitted reading beam is not indicated.

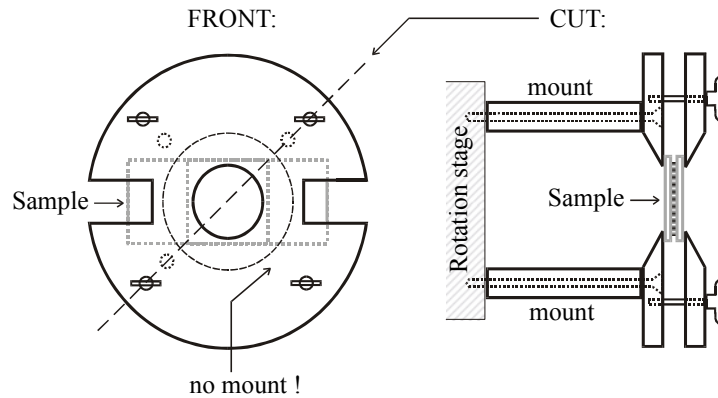


Figure (4 - 10): Sample holder developed for peristrophic multiplexing experiments. The sample structure is indicated in figure (4 - 1) - (B) and figure (4 - 2). The sample holder was made from Pertinax.

4.2.1.5.2.) Evaluation of the peristrophic multiplexing experiments

The peristrophic multiplexing experiments carried out in the frame of this work are DFWM experiments. Accordingly, points discussed for the DFWM experiments principally apply here as well. However, the peristrophic multiplexing experiments were not carried out in order to determine general physical properties of the materials investigated but rather in order to test the potential technical application of these as storage media. Therefore, the point of view, which the evaluation is considered from is different. This is manifested mainly in the treatment of the diffraction efficiency. As for the DFWM experiments the internal diffraction efficiency has been considered, however, a normalization of the maximum diffraction efficiency to unity has not been performed. This must be seen in the context, that the physical value of the refractive index modulation was not the point of interest but the actually diffracted light power available. In technical applications of multiplexing techniques for mass data storage purposes datasheets will be stored as holograms, retrieved if addressed and converted into electrical signals by a light detector array (CCD). The basic process is illustrated in figure (2.3 - 6), figure (2.3 - 8), figure (2.3 - 9) and figure (2.3 - 11). The actually available diffracted light power obtained from the hologram retrieved thus must exceed a lower threshold, which is determined by the sensitivity of the detector array. Hence, the physics determining the diffraction efficiency is secondary as long as enough light is diffracted, which can be reliably detected.

Since the detection limit of today's CCD cameras is very low, very small diffraction efficiencies may be allowed for, which are in the order of magnitude of $\eta \ll 10^{-3}$. For such small diffraction efficiencies, the power of the transmitted probe beam may in good approximation be considered as unchanged. Therefore, the diffraction efficiency was determined by means of the ratio of the absolute beam power diffracted and the absolute beam power transmitted, which was taken prior to the holograms being recorded, however, with the electric field applied to the sample in order to account for field-induced absorption changes. For both cases background light was measured and subtracted from the obtained data. From the diffraction efficiencies obtained and the number of holograms multiplexed the M-number $M/\#$ was calculated according to eq. (2.3 - 66). A detailed consideration of experimental errors has not been performed.

4.2.1.6.) Intensity determination

The intensity relation between the recording beams is of essential significance for the PR effect. The same applies for the erasure beam in relation to the sum of the recording beams. The tilted geometrical configuration according to figure (4 - 4) and the sample structure according to figure (4 - 2) requires a careful determination of the intensity relations inside the material, which will be discussed now. The subsequent considerations apply for all intensity quantities quoted for recording and erasure beams in the 2BC and DFWM experiments carried out except the peristrophic multiplexing experiments, which will be discussed in the corresponding section devoted to the experimental results.

The intensity of the probe beam in DFWM experiments was typically adjusted to be at least three orders of magnitude smaller than the intensity of the recording beams

In general, the intensities of the recording beams were determined by measuring the beam power and determining the beam profiles. The latter then were evaluated for the particular geometrical configuration on hand yielding the area A illuminated with power P . The intensities were then calculated by:

$$I = \frac{P}{A}. \quad \text{eq. (4 - 47)}$$

The beam powers were determined inside the employed optical setup in front of the sample using a calibrated power meter and ensuring normal incidence onto the detector of the power meter. The portion of the transmitted energy entering the polymer layer in the sample was calculated according to Fresnel's equations eq. (2.1 - 116) and eq. (2.1 - 123) and using eq. (2.1 - 125) and using the model system described in "4.2.1.2.2.2.) Consideration of systematic errors in the 2BC experiments" on page 190. This yields for the recording beams 1 and 2 for s(p)-polarization $T_1 = 0.85(0.98)$ and $T_2 = 0.66(0.94)$, respectively, and for the erasure beam, which entered the sample perpendicularly to the sample surface $T_e = 0.93$ (with eq. (2.1 - 113) or eq. (2.1 - 121) and eq. (2.1 - 125)).

In order to obtain the illuminated area A , the profile of a beam was measured monitoring the beam power while blocking the beam stepwise perpendicularly to its propagation direction by a razor knife edge. The resulting curve was differentiated numerically and then fitted by a Gaussian profile to obtain the beam profile functions. These were then normalized to unity and adapted to oblique incidence by stretching the variance for the axis, which is parallel to the propagation plane of the beams according to the transfer projections of the beam diameters through the involved interfaces until the beams entered the polymer layer. Please note, that the transfer projections are obtained by simply taking the cosine ratio between the incident angles of the beams onto the sample surface and the propagation angles of the beams in the polymer layer. Thus, two beam profile functions are obtained representing the sections through the beam profile in plane and perpendicular to the propagation plane of the beams. Typical results are depicted in figure (4 - 11) and figure (4 - 12). The beams originated from HeNe-lasers and thus should be radially symmetric outside the sample, which was presumed here without explicit countercheck. In this work, the full width of half maximum (FWHM) of the obtained beam profiles was used to calculate the illuminated area A according to eq. (4 - 47).

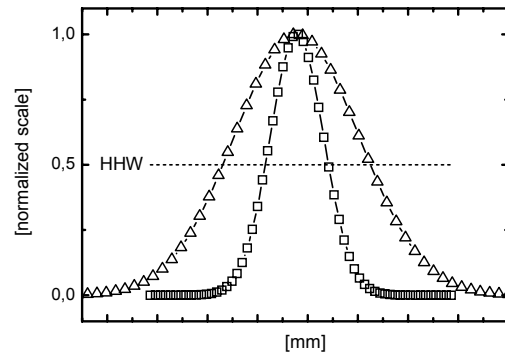


Figure (4 - 11): Normalized beam profiles out of the propagation plane. Squares: Recording beams; triangles: erasure beam.

Please note that there are other conventions using the $1/e$ -height-width or the $1/e^2$ -height-width for calculating the illuminated area. The FWHM convention was chosen for this work, since it slightly overweighs the center with respect to the edges of the beam profile, which are not of interest in the frame of this work.

Based on the above considerations, multiplication factors for the experimentally obtained beam powers of the recording beams and the erasure beam can be derived, which yield the corresponding intensities. Table (4 - 1) shows typical examples. The particular intensities applied in the experiments performed will be noted in the corresponding sections.

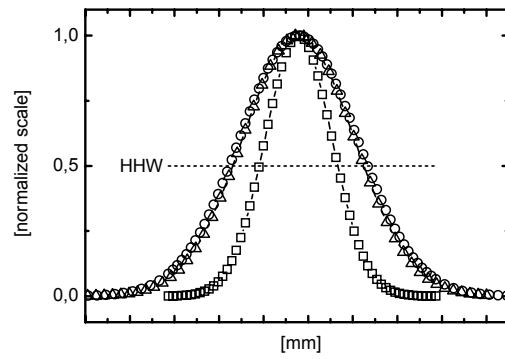


Figure (4 - 12): Normalized beam profiles in the propagation plane. Squares: recording beam I_{01} ; circles: recording beam I_{02} ; triangles: I_{erase}

Table (4 - 1) : Typical data used for intensity determination

beam	s-polarization			p-polarization		
	transmittance	area [cm ²]	multiplication factor [1/cm ²]	transmittance	area [cm ²]	multiplication factor [1/cm ²]
I_{01}	0.85	0.02	42.5	0.98	0.02	49
I_{02}	0.66	0.03	22	0.94	0.03	31
$I_{e(erase)}$	0.93	0.06	15.5	0.93	0.06	15.5

4.2.1.7.) Isomerization gratings

The wave-mixing experiments carried out in the frame of this work bear the inherent problem of the occurrence of isomerization gratings in the materials investigated at the operating wavelengths applied. This problem has already been mentioned before in “3.2.5.2.2.) Absorption and the problem of isomerization gratings” on page 167. The isomerization gratings are due to the circumstance, that the NLO chromophores used in the PR polymers investigated were azo dyes showing non-vanishing absorption at the operating wavelength of 633nm. Upon appropriate optical excitation, the bond order of the azo group of the chromophores is reduced from two to one resulting in the possibility of free intramolecular rotation of the chromophores. Thus a photoinduced isomerization equilibrium arises the general scheme of which process is depicted in figure (4 - 13). The chromophores may be optically excited as long as the polarization vector of the incident light has a notable projection onto the long molecule axis. This process is completely random, however, it stops as soon as the molecule is oriented perpendicular to the polarization direction of the incident light. After some time, this yields an accumulation of chromophores oriented perpendicularly to the polarization vector in the regions illuminated. Hence, if the illumination is non-uniform, a refractive index grating is built up, which is shifted by 180° with respect to the illumination pattern (i.e. the refractive index is reduced in the illuminated areas with respect to the isotropic case), if probed with light of

identical polarization as the light causing the isomerization process. On the other hand, light with a polarization state perpendicular to the polarization state of the light building up the isomerization grating will sense a grating which is much weaker. This is, because chromophores oriented perpendicular to the “recording polarization” will be randomly distributed for the perpendicular polarization state, however, only in two rather than three dimensions like in the isotropic case. This yields a refractive index change as well, however with smaller amplitude. Furthermore, the grating sensed by perpendicularly polarized light will formally be shifted by 0° (i.e. the refractive index increases in the areas illuminated by “the other” light generating the grating).

Isomerization gratings may have a significant impact especially on 2BC experiments, since some local grating component is implied, the actual contribution of which to the PR effect cannot be probed independently from the purely PR grating at the same operating wavelength. However, it is possible to determine the isomerization grating in absence of the PR effect (by simply applying no field to the sample while recording a grating), which has been conducted sometimes in the frame of this work to check for the possible existence of a detectable isomerization grating at particular experimental conditions. Nevertheless, it is not possible to anyhow quantify this problem reliably, since the strength of the refractive index grating due to isomerization will be different if occurring

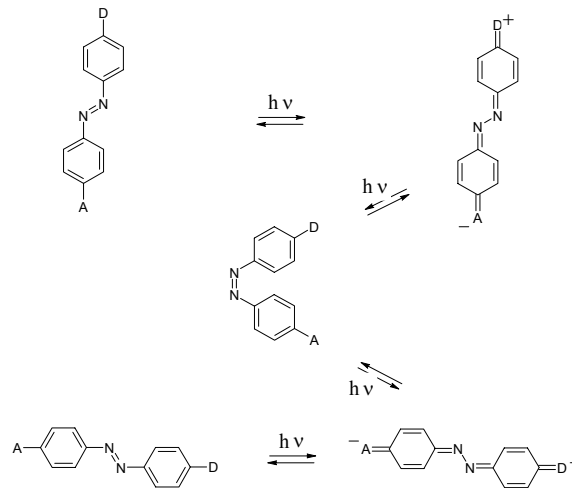


Figure (4 - 13): Photoinduced isomerization equilibrium. D: donor; A: acceptor

together with a PR grating, i.e. if an electrical field is applied. In this case, the applied field as well as the internal space-charge field will affect the isomerization equilibrium thus connecting the isomerization grating with the PR grating and making their independent determination impossible. Therefore, especially any kind of PR phase shift obtained from 2BC experiments performed here must be considered very carefully if the absolute values are compared with the PR phase shift obtained for similar materials using some independent method not afflicted with such problems. However, as already discussed before in context with the polarization anisotropy, general trends found within a consistent series of experiments under identical experimental conditions relevant for the problem discussed here (i.e. especially the polarization states of the recording and the reading beams and the contrast of the interference pattern) will hold. If necessary, the possible impact of isomerization gratings on the experimental data will explicitly be discussed in the corresponding sections presenting experimental results.

The problem of the isomerization gratings is much less pronounced when considering the DFWM experiments, which are inherently not phase sensitive. Actually, the influence of isomerization gratings will only be notable in DFWM experiments, if the materials investigated are operated at conditions yielding very small PR grating strength at simultaneously relatively high light intensity or considerable recording times. Typical DFWM experiments carried out in the frame of this work do not meet these conditions and, thus, the problem of isomerization gratings can be ignored in good approximation for the DFWM experiments to be discussed in the section devoted to the experimental results.

Please note finally that isomerization gratings generated by the mechanism as described above are undesired in PR materials but are utilized in another class of reversible holographic organic recording materials, the so called “photo-addressable polymers” (PAP’s) [186 - 190]

4.3.)Transmission ellipsometric experiments

Transmission ellipsometric (ELP) experiments were carried out in order to obtain the electrical poling properties of the materials investigated in an independent manner. Subsequently the experimental principle will be outlined. Thereafter, the transmission equation will ostensibly be derived and discussed. A detailed error consideration is not included since no physical conclusions will be drawn from absolute transmission values and the general trends in the ELP experiments discussed in the frame of this work are not subjected to any kind of experimental error requiring a closer consideration.

4.3.1.)Experimental transmission ellipsometry setup and procedure

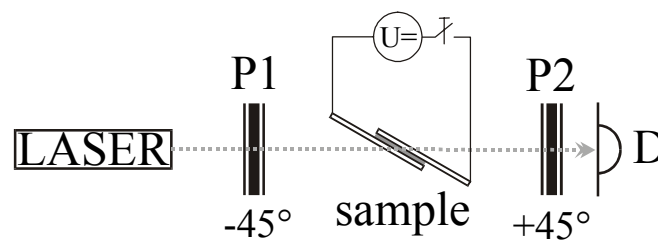


Figure (4 - 14): Principle of ELP experiments. P1, P2: polarizers; D: detector; U: high voltage power supply

For the transmission ellipsometric experiments carried out a setup as depicted in figure (4 - 14) was applied. A He-Ne laser was used for determining the steady-state poling behavior, since the wavelength of the light source impacts the ellipsometric transmission as a function of the applied field. According to eq. (4 - 52), the field induced birefringence necessary to achieve a transmission maximum increases with the wavelength of the applied light source. Hence, in order to obtain a transmission maximum as a function of the applied field at lower risk of possible dielectric breakdown of the sample, it is advisable to use a smaller wavelength. However, for determining the dynamic poling behavior of the materials investigated this was not an issue, and therefore, then mostly an infrared laser diode was used, the operating wavelength of which was far beyond the operating wavelength of the PR effect of the materials. By that, dynamic ellipsometric and holographic PR measurements could be performed simultaneously without notably influencing the PR response. For all ellipsometric experiments completely relaxed samples were used, which was ensured either by heating the samples to the temperature region of viscoelastic flux or by waiting sufficiently long to ensure complete thermodynamic relaxation of some orientational order at room temperature in advance of the experiment.

The steady-state poling behavior of the materials investigated was determined by increasing the applied electrical field stepwise by an appropriate increment, which was chosen on the basis of a trade off between a desired number of data points and the total measurement time required. After increasing the field by one step the material was given sufficient time to relax to quasi steady-state. The relaxation time required was estimated by previous determination of the build-up dynamics of the ellipsometric transmission. At least 5 times the logarithmically averaged response time was provided as relaxation time. As in the DFWM experiments 500 single measurements were performed for a certain value of the applied field at

a sampling rate of 100sec^{-1} , hence, covering a time span of 5 seconds, and the data obtained were arithmetically averaged to get the corresponding data point.

For determining the build-up dynamics of the ellipsometric transmission at constant externally applied field, the field was switched on by a TTL signal controlling a high-voltage Reed relay. The high voltage power supplied by the power supply used was up to 40W enabling very fast charging of the capacitor formed by the sample structure. Together with the fast Reed relay used, the switching-on of the external field can thus be regarded as a δ -function in very good approximation. Data sampling was initialized about 500ms ahead of the begin of the measurement (i.e. switching on the electrical field) in order to monitor the onset of the actual measurement procedure, which defines $t = 0$. The power of the transmitted light beam was monitored as a function of time at a typical initial sampling rate of 10sec^{-1} , which was decreased down to 1sec^{-1} at minimum in several steps as the sampling process proceeded in order to reduce the total amount of data sampled in experiments extending over several tens of minutes up to hours. The sampling schedule of a dynamic experiment as described here was pre-programmed defining steps of sampling rates and the number of data to be sampled per rate step, the total sum of all of which eventually defined the overall length of the parallel plate poling experiment.

For determining the dynamics of the relaxation of the orientational order, the material was first parallel plate poled using the procedure described above. As soon as the build-up of the field induced birefringence had been conducted for the time span pre-programmed in the data sampling schedule for the build-up process, data sampling was stopped and the external field was switched off by the Reed relay. Almost simultaneously the sample was short circuited by another Reed relay in order to quickly discharge the capacitor formed by the sample structure. Please note that the sample structure forms a very slowly responding RC-circuit due to the very high electrical resistance of the polymer layer. If the sample would not be short circuited the response behavior of the RC-circuit would be determined by the experiment instead of the relaxation of the orientational order as intended. After the sample was short circuited data sampling was restarted and the decay of the ellipsometric transmission was monitored by a recording schedule covering 5000 data points at 33.3sec^{-1} sampling rate and subsequently 5000 data points at 2.5sec^{-1} for the low- T_g materials ($T_g < \text{RT}$) For materials exhibiting a glass-transition temperature above the ambient temperature three decay loops of 5000 data points each were applied at sampling rates of 33.3sec^{-1} , 2.5sec^{-1} , and 1sec^{-1} .

4.3.1.1.)Evaluation of the transmission ellipsometric experiments

The transmission of light as a function of the birefringence of the sample in a setup according to figure (4 - 14) may easily be derived based on ostensive considerations. The polarization of the light incident on the sample is adjusted to be polarized by 45° with respect to the optical axis of the birefringent sample by means of the polarizer P1. The optical axis of the sample is oriented perpendicular to the sample surface (the sample structure is depicted in more detail in figure (4 - 2)), since it is determined by the direction of the applied field. Thus, the incident light is split into two orthogonally polarized contributions of equal amplitude, the one of which is the ordinary beam and the other is the extraordinary beam. As long as the sample is not birefringent, both the ordinary and the extraordinary beam propagate with identical velocity through the sample and superimpose behind the sample to a single beam of unaltered polarization. In this case, the light is blocked by polarizer P2, which is adjusted in crossed configuration with respect to P1. If an electrical field is applied to the sample it becomes birefringent and the ordinary and the extraordinary beam propagate with different velocity

inside the sample. This can be expressed by different lengths of the optical paths in the birefringent material, resulting in a phase difference between the ordinary and the extraordinary beam. This phase difference $\Delta\varphi$ may be easily expressed as a function of the real geometrical distance l , which the beams cover in the sample:

$$\Delta\varphi = \vec{k}_e \vec{l}_e - \vec{k}_o \vec{l}_o, \quad \text{eq. (4 - 48)}$$

where k is the modulus of the wave propagation vector and the indices e and o indicate the extraordinary and the ordinary beam, respectively. Assuming in good approximation that the change of the refractive indices for the ordinary and the extraordinary beam is small as compared to the average bulk refractive index of the material, the real geometrical distances may be expressed as:

$$l_e = l_o = \frac{d}{\cos\Psi_t}, \quad \text{eq. (4 - 49)}$$

where d is the sample thickness and Ψ_t is the internal angle of incidence of the light beam, i.e. the internal tilt angle of the sample. Accordingly, the vectorial description may be set aside, since both the o -beam and the e -beam propagate in approximately identical directions. Thus, with eq. (2.1 - 85) one obtains:

$$\Delta\varphi = \frac{2\pi d(n_e - n_o)}{\lambda_0 \cos\Psi_t} \quad \text{eq. (4 - 50)}$$

where n stands for the refractive index and λ_0 is the optical wavelength in free space. After the extraordinary and the ordinary beam have merged again behind the sample, the phase difference $\Delta\varphi$ will correspond to the angular displacement of the polarization of the beam with respect to the original state.

A polarizer will only transmit the amplitude component of the incident beam, which is oriented parallelly to its polarization director. The latter of P2 has been adjusted to be perpendicular to the one of P1 and thus all light of the original polarization state will be blocked. However, if the polarization has been rotated according to eq. (4 - 50), P2 will transmit some amplitude component of the beam according to:

$$T_A^{ELP} = \sin\Delta\varphi \quad \text{eq. (4 - 51)}$$

where T_A^{ELP} is the amplitude transmission. In order to get the transmitted light power (or intensity), according to eq. (2.1 - 33) one has to square eq. (4 - 51), which finally yields for the transmission in an ELP experiment:

$$T^{ELP} = \left[\sin\left(\frac{2\pi d\Delta n_{ELP}}{\lambda_0 \cos\Psi_t}\right) \right]^2 \quad \text{eq. (4 - 52)}$$

with:

$$\Delta n_{ELP} = n_e - n_o. \quad \text{eq. (4 - 53)}$$

Please note, that T^{ELP} has only been explicitly denoted here as ellipsometric transmission in order to avoid confusion with the transmittances discussed in the section dealing with the diffraction experiments. Throughout the rest of this work this notation will no more be used and the ellipsometric transmission according to eq. (4 - 52) will simply be referred to as „ T^e “.

The apparent similarity in the general form of eq. (4 - 52) and eq. (4 - 30) suggests the application of eq. (4 - 52) in order to determine the parallel plate poling behavior of the systems investigated in comparison with the DFWM diffraction properties. The comparability, however, is restricted to general trends rather than numerical values, since the refractive index difference according to eq. (4 - 53) is not directly comparable with the PR refractive index modulation. Furthermore, the optical effects described by eq. (4 - 52) and eq. (4 - 30) are fundamentally

different in their underlying physics. Nevertheless, eq. (4 - 52) provides a very precious insight into the poling behavior of the materials investigated, which in turn is essential for the PR effect in these systems.

For evaluation of the transmission ellipsometric experiments the transmitted light was monitored as a function of the externally applied field applying constant (and sufficiently long for achieving quasi steady-state poling conditions) relaxation times or as a function of time at constant field applied. The ellipsometric transmission shows oscillatory behavior as a function of the externally applied field due to the $(\sin)^2$ -dependency like the diffraction efficiency in DFWM experiments. Thus a first transmission maximum as a function of the applied field can be obtained, which was normalized to unity in order to obtain functional dependencies for Δn_{ELP} . Then, a measure for Δn_{ELP} reproducing general trends correctly was calculated according to:

$$\Delta n_{ELP} \propto a \sin \sqrt{T^{ELP}}. \quad \text{eq. (4 - 54)}$$

Physically exact numerical values of Δn_{ELP} were not considered in the frame of this work but only general relations and trends.

The dynamics of the evolution or the decay of Δn_{ELP} was evaluated in a way identical to the DFWM experiments and has already been discussed in detail in the corresponding section. Please note, that the number of exponential terms necessary to describe the dynamic behavior to a sufficient degree of accuracy need not be identical for DFWM and ELP curves. In these cases, exponential terms were merged appropriately by means of logarithmic averaging as also already described in “4.2.1.3.2.3.) DFWM evaluation procedure” on page 197 in order to compare DFWM and ELP experiments.

Please note eventually that eq. (4 - 52) only represents an approximation, the quality of which becomes worse with increasing Δn_{ELP} and Ψ_t as depicted by figure (4 - 15), since eq. (4 - 52) was derived neglecting the distance “B-D“ in the optical paths. Within the frame of this work, this approximation is sufficient since absolute values of the ellipsometric transmission are not considered, but rather only the position of the transmission maximum as a function of the applied field, or the dynamic evolution of the ellipsometric transmission, both of which are not effected by the applied approximation. The correct solution of the problem yielding accurate values for the absolute ELP transmission is obtained replacing eq. (4 - 50) by the expression:

$$\Delta\phi = \frac{2\pi d}{\lambda_0} (n_e \cos \Psi_{t1} - n_o \cos \Psi_{t2}), \quad \text{eq. (4 - 55)}$$

where the parameters used are obvious from figure (4 - 15). Eq. (4 - 55) can easily be derived from figure (4 - 15) the same way as already described above, however, the derivation is more extensive containing vast trigonometric manipulations. Since eq. (4 - 55) was not used in the frame of this work, its derivation will not be demonstrated here.

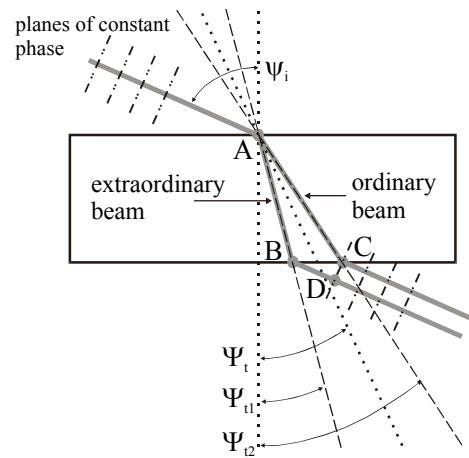


Figure (4 - 15): Geometry of transmission ellipsometry. The considered beam is incident on the birefringent medium at point “A“, splits into two, which exit the medium at the points “B“ and “C“. At point “C“ and “D“, respectively, the beams superimpose. Hence, the actual optical paths of the two single beams between splitting point and subsequent reunion are “A-B-D“ and “A-C“, respectively.

5.)Results

This work focuses on identifying, systematizing and interpreting general trends in PVK based PR polymers when the composition and/or experimental parameters of the material are methodically altered. Accordingly, this work is primarily dealing with a single type of PR polymer composite, which is based on the first high performance PR polymer developed in 1994 by K. Meerholz et.al. [13], the composition of which was already explained in “3.2.5.1.) Milestones” on page 165. In 1998, a novel type of PR polymer was invented, which is closely related with the aforementioned first high performance material, but shows significantly improved thermodynamic stability at even slightly improved steady state PR performance [136]. For this material, an eutectic mixture of the NLO chromophores DMNPAA and MNPAA at otherwise unaltered composition was used instead of solely DMNPAA as in the material according to [13]. Due to the clearly superior properties of the novel PR polymer, investigations on the general material properties were thereafter performed using this material. Please note, that the aforementioned difference in the basic composition may limit the comparability of results obtained with these two types of materials. However, one can safely presume that both types of materials behave similarly as far as the general trends are concerned, since neither the type of the polymer matrix (i.e. the basic electrical properties) nor the sensitizer nor the general type of NLO chromophores has been altered. All materials investigated in the frame of this work, their compositions as well as glass-transition temperatures are listed in table (5-1). The glass-transition temperatures were determined by differential scanning calorimetry (DSC) using a heating rate of 20K/min.

Table (5-1): Chemical composition and glass transition temperature of the investigated materials

Material	DMNPAA (NLO chromophore 1)	MNPAA (NLO chromophore 2)	PVK (Polymer matrix)	ECZ (Plasticizer)	TNF (Sensitizer)	TPD (Extrinsic trap dopant [*])	T _g
units	[%wt]	[%wt]	[%wt]	[%wt]	[%wt]	[%wt]	[°C]
20a	20		59	20	1	-	60
20b	20	-	54	25	1	-	30
20c	20	-	49	30	1	-	14
20d	20	-	44	35	1	-	-2
30a	30	-	59	10	1	-	62
30b	30	-	54	15	1	-	37
30c	30	-	49	20	1	-	12
30d	30	-	44	25	1	-	6
30e	30	-	39	30	1	-	1
40a	40	-	59	0	1	-	72
40b	40	-	54	5	1	-	48
40c	40	-	49	10	1	-	25

Table (5-1): Chemical composition and glass transition temperature of the investigated materials

Material	DMNPAA (NLO chromophore 1)	MNPAA (NLO chromophore 2)	PVK (Polymer matrix)	ECZ (Plasticizer)	TNF (Sensitizer)	TPD (Extrinsic trap dopant ^{*)})	T _g
40d	40	-	44	15	1	-	17
40e	40	-	39	20	1	-	10
40f	40	-	34	25	1	-	2
50a	50	-	49	0	1	-	35
50b	50	-	44	5	1	-	24
50c	50	-	39	10	1	-	14
50d	50	-	34	15	1	-	7
50e	50	-	29	20	1	-	1
TNF01	25	25	35	14.9	0.1	-	3
TNF02	25	25	35	14.8	0.2	-	3
TNF04	25	25	35	14.6	0.4	-	3
TNF08	25	25	35	14.2	0.8	-	3
TNF2	25	25	35	13	2	-	4
TNF5	25	25	35	10	5	-	9
A	25	25	47	2	1	-	27
B	25	25	43	6	1	-	17.5
C	25	25	39	10	1	-	14
D (TNF1)	25	25	37	12	1	-	11.5
AT	25	25	42	6.18	1	0.82	18.5
BT	25	25	40	8.18	1	0.82	17
CT	25	25	38	10.18	1	0.82	14
CT1	25	25	36	11.36	1	1.64	10
CT2	25	25	34	10.1	1	4.9	12
CT3	25	25	30	9	1	10	12.5
DT	25	25	36	12.18	1	0.82	13

^{*)} Please note that the HOMO levels of the commonly used hole conductor TPD (N,N'-bis(3-tolyl)-N,N'-diphenyl-benzidine) are situated about 0.5eV below those of PVK. Thus, TPD moieties in low concentration constitute deep traps within the carbazole charge transport manifold.

This section will be organized as follows: First, by means of a simple numerical simulation based on Kogelnik's formalism it will be shown that hologram bending due to 2BC does not notably affect the DFWM (DFWM: degenerate four-wave-mixing) diffraction properties of organic PR thin film devices. Thereafter, the influence of the glass-transition temperature on the steady-state diffraction properties as well as on the PR grating build-up dynamics in PVK based PR polymers will be investigated in detail. These investigations have been performed on materials based on the first high-performance PR polymer according to [13]. Subsequently, the role of the sensitizer will be elaborated upon with respect to the same properties, however, using the improved material according to [136]. Then the dynamic erasure and dark-decay behavior of holographic PR gratings in PVK based PR polymers will be looked into extensively. For the latter investigations, materials with and without extrinsic deep traps (introduced by doping the material with TPD) were considered. Within the frame of those latter investigations the application of PVK based PR polymers in holographic multiplexing will also be discussed. Finally, in the last section the application of PVK based PR polymers in holographic multiplexing will be demonstrated experimentally. Please note that the sequence of investigations as described above does not reflect the actual chronology in which the investigations have been carried out. In fact, the multiplexing experiments discussed last were performed in advance of the investigations on the erasure and dark-decay dynamics, which in turn were motivated in view of the problems revealed by the multiplexing experiments.

5.1.) Influence of hologram bending on the diffraction efficiency in PR thin film devices: A simple model calculation

In photorefractive materials, strong 2BC leads to bending of the recorded hologram, which, in turn, may affect the diffraction properties of the latter as already mentioned in “2.5.4.2.) Theoretical formulation of two-beam coupling” on page 141. Among others this effect has been made responsible for the fact that even under ideal conditions complete diffraction has not yet been achieved in organic photorefractive thin film devices, even with the best PR materials presently known [155]. However, this assumption has not been confirmed up to now. In order to get a first insight into the effect of hologram bending on the diffraction properties of organic thin-film devices operated in tilted configuration according to figure (4 - 4), the diffraction efficiency of a typical PR organic thin film device was numerically simulated using Kogelnik’s coupled wave theory. The Bragg-mismatch was taken into account, which is introduced by the imaginary part of the complex PR gain according to eq. (2.5 - 101) to eq. (2.5 - 112). This numerical simulation was carried out using typical operating parameters of the material type 50b according to table 5-1 on page 211. Furthermore, physically unrealistic values of the PR gain at otherwise typical operating parameters for the same type of material have been used in the simulation in order to demonstrate general trends in the influence of hologram bending on the diffraction properties.

5.1.1.) The simulation model

The external diffraction efficiency η_{ext} given by eq. (4 - 19) is limited by the absorption of the material, which is not constant due to absorption induced by the applied electrical field [13]. In order to exclude absorption effects in typical organic PR thin film devices (i.e. showing small absorption coefficients of $\alpha < 30\text{cm}^{-1}$ even with a strong external electrical field applied), commonly the internal diffraction efficiency η_{int} according to eq. (4 - 20) is considered. The small difference in the optical paths of the diffracted and the transmitted probe beam in the tilted configuration according to figure (4 - 4) causes only a small error as already discussed in “4.2.1.3.2.) Evaluation of the DFWM experiments” on page 195. Thus, by using the internal diffraction efficiency η_{int} , the holographic grating in the simulation can be considered as loss-free in good approximation.

According to the theory of 2BC, the coherent energy exchange between the interfering laser beams is accompanied by a relative phase shift of the recording beams as expressed by eq. (2.5 - 111) and eq. (2.5 - 112). Consequently, when 2BC occurs, the interference pattern is continuously slanted as a function of the propagation of the recording beams through the PR material, leading to hologram bending [71]. It is clear, that this will affect the diffraction properties of the hologram in four-wave-mixing experiments since the Bragg condition cannot be met throughout the entire grating even for ideal adjustment of the experimental setup. Please note, that this problem has been made responsible for the experimental observation that a slight misalignment of the probe beam relative to the pure geometrical Bragg-condition is necessary in order to achieve maximum diffraction efficiency [154, 155]. The geometrical Bragg-condition is met in a phase conjugate DFWM experiment if the probe beam exactly counterpropagates one of the recording beams. However, in a typical DFWM experiment using crossed polarization for the recording beams and the probe beam, the actual optical Bragg-condition cannot coincide with the geometrical Bragg-condition due to the birefringence

induced by the applied electrical field, which will be discussed later in more detail. On the other hand, at this point it cannot be safely excluded that hologram bending may contribute to the above mentioned experimental observation.

In order to estimate the order of magnitude the diffraction process in a DFWM experiment is affected by hologram bending, the diffraction efficiency was numerically simulated using Kogelnik's coupled wave theory according to "2.3.2.) Coupled wave theory for thick hologram gratings" on page 53 and a simplified theoretical model of a high performance PR polymer according to "2.5.3.3.) Orientational enhancement effect" on page 131.

According to the coupled wave theory the complex amplitude D of a p-polarized probe beam diffracted at a "thick" transmission grating can be described by the general formula eq. (2.3 - 40), which simplifies in the case of a loss-free grating to:

$$D(d) = -i\sqrt{c_{TD}} e^{\xi} \frac{\sin \sqrt{v^2 - \xi^2}}{\sqrt{1 - \frac{\xi^2}{v^2}}} \quad \text{eq. (5.1 - 1)}$$

The particular parameters are explained in "2.3.2.) Coupled wave theory for thick hologram gratings" on page 53. The parameter ξ must be understood with the absorption set to zero for the case considered here. Additionally, a variance of the slant angle of the holographic grating must be allow for, which is not accounted for in the basic coupled wave theory discussed on page 53. The variance of the slant angle is a result of a changing diffraction angle of the signal beam with respect to the reference beam as a function of hologram bending. Therefore, the slant factor c_D according to eq. (2.3 - 13) and eq. (2.3 - 21) is rewritten as:

$$c_D = c_T - \frac{K}{\beta} \cos(\psi - \Delta\psi), \quad \text{eq. (5.1 - 2)}$$

where $\Delta\psi$ describes the deviation of the slant angle due to hologram bending with respect to the slant angle of the undistorted grating. Furthermore, the dephasing measure \mathfrak{S} according to eq. (2.3 - 18) can be simplified omitting dephasing due to a wavelength mismatch, which does not occur in the considered case of DFWM. Thus, one obtains for the dephasing measure \mathfrak{S} :

$$\mathfrak{S} = \Delta\theta_B K \sin((\psi - \Delta\psi) - \theta_{0B}), \quad \text{eq. (5.1 - 3)}$$

where θ_{0B} and $\Delta\theta_B$ are the Bragg-angle and the „Bragg - error“, respectively. Both $\Delta\psi$ and $\Delta\theta_B$ will be derived from the degree of hologram bending due to 2BC, as described below. Eq. (5.1 - 1) refers to the external (laboratory) reference frame (x,y,z) as depicted in figure (5.1 - 1).

The external diffraction efficiency for an incident wave of unit amplitude is defined by eq. (2.3 - 36):

$$\eta = \frac{DD^*}{|c_{TD}|}$$

where the slant factor c_{TD} is defined by eq. (2.3 - 37).

According to the orientational enhancement model (page 131), Δn depends quadratically

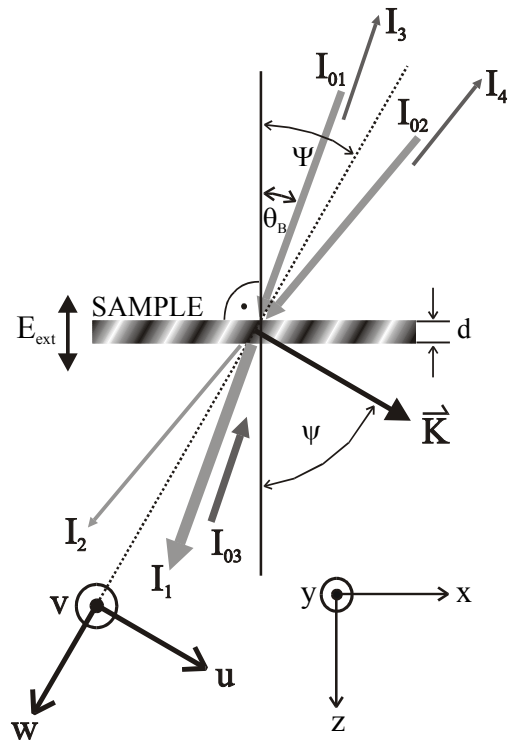


Figure (5.1 - 1): Geometrical configuration considered.

on the local total poling field E_{pol} . For the sake of simplicity, this basic relation is approximated by:

$$\Delta n \approx C_{mol} E_{ext}^2 \quad \text{eq. (5.1 - 4)}$$

where E_{ext} is the externally applied electrical field and C_{mol} is a constant, containing, among others, the local field corrected molecular constants of the NLO chromophore, its density in the matrix, geometrical factors (for example a projection factor for the PR space-charge field onto the external field direction), and direction cosines of the involved laser beams. Please note, that this approximation will not affect the aspects under investigation (maximum diffraction with and without hologram bending), but rather only introduce some error in the field dependence of the diffraction efficiency with respect to the experimental curve used for comparison. Accordingly, the quality of this approximation is of minor importance as long as it reproduces the general trend with reasonable accuracy, which applies here. The constant C_{mol} can be estimated from the experiment using the strongly simplified form of Kogelnik's equation for slanted transmission holograms according to eq. (2.3 - 43):

$$\eta = \left[\sin \left(\frac{\pi d C_{mol} E_{ext}^2}{\lambda_0 \sqrt{c_D c_T}} \right) \right]^2 \quad \text{eq. (5.1 - 5)}$$

The argument of eq. (5.1 - 5) must equal $\pi/2$ for the external electrical field required for maximum internal diffraction efficiency $E_{ext}(\eta_{max})$.

According to "2.5.4.) Photorefractive two-wave mixing" the complex gain coefficient (Γ , eq. (2.5 - 101) to eq. (2.5 - 103)) can be expressed as:

$$\Gamma = i \frac{2\pi \Delta n}{\lambda_0 \cos \theta} e^{-i\phi}, \quad \text{eq. (5.1 - 6)}$$

where ϕ is the phase shift between the interference pattern and the resulting hologram, and 2θ is the internal angle between the recording beams. By introducing eq. (5.1 - 6) one obtains two sets of differential equations from the coupled wave theory of PR two-wave mixing, the one of which applies to the energy transfer (eq. (2.5 - 104) and eq. (2.5 - 105)) and the other to the dephasing of the two waves with respect to their initial phase (eq. (2.5 - 106) and eq. (2.5 - 107)). For the sake of simplicity, the slightly different optical paths of the recording beams are neglected. The imaginary component of Γ is the coupling constant for the phasing of the two waves and, thus, results in hologram bending as discussed on page 144. In order to account for the hologram bending, a second internal reference frame (u, v, w) is introduced as shown in figure (5.1 - 1), which is described by the transformation:

$$\begin{bmatrix} u \\ v \\ w \end{bmatrix} = \begin{bmatrix} \cos \Psi & 0 & \sin \Psi \\ 0 & 1 & 0 \\ -\sin \Psi & 0 & \cos \Psi \end{bmatrix} \begin{bmatrix} x \\ y \\ z \end{bmatrix}. \quad \text{eq. (5.1 - 7)}$$

Here, Ψ is the tilt angle of the undistorted hologram (not the slant angle according to Kogelnik's coupled wave theory, which is denoted by " ψ " in figure (5.1 - 1)). In the (u, v, w) frame the interference pattern formed by the recording beams is described by the expression:

$$I(u, w) = I_0 (1 + m(w) \cos[Ku + \Delta\phi_0 - \Delta\phi(w)]). \quad \text{eq. (5.1 - 8)}$$

K is the modulus of the grating vector, the direction of which is oriented parallelly to the u -axis. For the sake of simplicity only two dimensions of the volume hologram will be considered without loss of generality. The dimension along the grating planes and perpendicular to the propagation direction of the beams is not relevant in a simple sinusoidal hologram, which, according to the coupled wave theory, may even be read out in out of plane direction at arbitrary angles, however, yielding a different diffraction efficiency corresponding to the actual

interaction length. $\Delta\varphi_0$ is the initial phase difference of the recording beams, which is arbitrary and, therefore, is set to zero. $\Delta\varphi(w)$ is the induced dephasing at penetration depth w due to 2BC, $I_0 = I_{01} + I_{02}$ is the total incident intensity, and $m(w)$ is the grating contrast at penetration depth w , which is assumed constant in this simple simulation. It must be emphasized, that $m(w)$ is in fact not a constant due to energy transfer between the beams. The grating contrast recursively influences the space-charge field, limiting the actual physical relevance of the simulation to fields where the gain is relatively small. From eq. (2.5 - 111) and eq. (2.5 - 112) one obtains the following expression for the depth-dependent relative dephasing $\Delta\varphi(w)$:

$$\Delta\varphi(w) = \frac{1}{2 \tan \phi} \ln \left[\frac{(1+b)^2}{e^{\operatorname{Re}\{\tilde{\Gamma}\}w} \left(1 + b e^{-\operatorname{Re}\{\tilde{\Gamma}\}w}\right)^2} \right], \quad \text{eq. (5.1 - 9)}$$

where b is the initial intensity ratio of the writing beams. Please note, that $\Delta\varphi(w)$ changes sign when changing the direction of the externally applied field, since ϕ changes sign. Thus, the hologram bending direction depends on the sign of the applied field. In order to calculate the hologram bending, lines of equal light intensity in the interference pattern (e.g. $I(u, w) = 2I_0$) are selected, eq. (5.1 - 9) is inserted into eq. (5.1 - 8) and the resulting equation is rewritten to the form $u(w)$, which now expresses the position of the grating planes in the (u, v, w) frame as a function of the penetration depth w :

$$u(w) = -\frac{1}{2K \tan \phi} \ln \left[\frac{(1+b)^2}{e^{\operatorname{Re}\{\tilde{\Gamma}\}w} \left(1 + b e^{-\operatorname{Re}\{\tilde{\Gamma}\}w}\right)^2} \right]. \quad \text{eq. (5.1 - 10)}$$

By differentiating eq. (5.1 - 10) one finally obtains the following expression for the slope of the grating planes relative to the unaffected grating:

$$\dot{u}(w) = \frac{\operatorname{Re}\tilde{\Gamma}}{2K \tan \phi} \left\{ \frac{2b e^{-\operatorname{Re}\{\tilde{\Gamma}\}w}}{1 + e^{-\operatorname{Re}\{\tilde{\Gamma}\}w}} - 1 \right\}. \quad \text{eq. (5.1 - 11)}$$

Hologram bending leads to a deviation $\Delta\theta_B$ from the ‘‘Bragg-angle’’ θ_{B0} accompanied by a variation $\Delta\psi$ of the slant angle ψ of the hologram, both as a function of w and E_{ext} . $\Delta\theta_B$ and $\Delta\psi$ are identical and equal to $\operatorname{atan}(\dot{u})$ in the (u, v, w) frame, since the slope of the grating is zero in this frame if no bending occurs. According to the relation between Ψ and ψ this applies to $\Delta\psi$ as well (see figure (5.1 - 1)). Since the penetration depth can be handled one-dimensional the transformation back to the laboratory frame is straight forward and equivalent to a simple rotation, which does not affect the angle deviations:

$$w = z / \cos \Psi. \quad \text{eq. (5.1 - 12)}$$

Thus, by substituting eq. (5.1 - 12) into eq. (5.1 - 11) one finally obtains:

$$\Delta\theta_B(z, E_{ext}) = \Delta\psi(z, E_{ext}) = \operatorname{atan}(\dot{u}(z / \cos \Psi)). \quad \text{eq. (5.1 - 13)}$$

Therewith one can calculate the theoretical complex signal amplitude for a DFWM experiment from eq. (5.1 - 1) and the expected diffraction efficiency using eq. (2.3 - 36). Please note, that eq. (5.1 - 1) cannot be solved analytically, since the parameter ξ is complex. As described above, the results obtained from eq. (2.3 - 36) can be directly compared with experimental results on the internal diffraction efficiency giving rise to only a small error due to the assumption of equal interaction length of the beams involved. However, one must keep in mind that the simulation model used is in general only valid for small PR gains due to the neglect of the influence of the PR gain on the grating contrast.

5.1.2.)Simulation parameters

In order to carry out the simulation and to compare the results with the experiment, material 50b (see table 5-1 on page 211 for details) was chosen as model system and parameters specific for this system were derived from the experiment. Details about the setup geometry are given in table 5-2 on page 219 and the setup configuration is depicted in figure (5.1 - 1).

As mentioned before, the argument of the sine function in eq. (5.1 - 5) equals $\pi/2$ in the first maximum of the internal diffraction efficiency η_{max} , which allows to estimate the value of the constant C_{mol} . According to eq. (5.1 - 5) and for the configuration under discussion, the refractive index modulation at η_{max} is $\Delta n_p = 2.6 \times 10^{-3}$, which applies for the p-polarized light used for grating read out. Δn_p has positive sign, due to the fact that the refractive index increases with the applied field as compared to the bulk index of the isotropic material (see “2.4.2.) Electrical poling of organic polymers - the oriented gas model” on page 83). Accordingly, from the experimental value for the external field $E(\eta_{max}) = 59 \text{ V}/\mu\text{m}$ one obtains $C_{mol} = 7.4 \times 10^{-7}$. Running the simulation without accounting for hologram bending but modeling the field dependent refractive index modulation $\Delta n_p(E)$ according to eq. (5.1 - 5) shows general agreement between the simulated diffraction curve and the experimentally determined internal diffraction efficiency for externally applied fields of up to about $75 \text{ V}/\mu\text{m}$ as indicated by the arrow in figure (5.1 - 2). This experimentally validates the application of eq. (5.1 - 5). The problem, which is focussed upon is also clearly visible: the diffraction efficiency in its first maximum is significantly smaller than expected from the simple model. The strong deviations between the simulated curve and the experimental curve for external fields exceeding $75 \text{ V}/\mu\text{m}$ are due to the neglect of the contrast loss of the grating, caused by the coherent energy exchange in 2BC.

In order to introduce hologram bending now the experimentally obtained PR gain is considered (the real part of the gain coefficient), which was calculated from the experiment by means of eq. (4 - 14). The writing beams were s-polarized. Thus, in order to apply eq. (5.1 - 5) to the refractive index modulation $\Delta n_s(E)$ sensed by the s-polarized writing beams using the constant C_{mol} as determined above, the polarization anisotropy according to “4.2.1.4.) Polarization anisotropy for PR wave mixing experiments” on page 199 must be taken into account. As theoretically derived in the aforementioned paragraph, $\Delta n_p / \Delta n_s = -2.22$ may be considered as a reasonable value for PR polymer composites containing DMNPAA and closely related derivatives as NLO chromophores. Please note, that Δn_s has negative sign in this case, since the refractive index decreases with respect to the isotropic bulk refractive index when the field is increased due to the dominant BR contribution as discussed in “2.5.3.3.) Orientational enhancement effect” in context with “2.4.2.) Electrical poling of organic polymers - the oriented gas model”. It must be pointed out that the sign of the refractive index modulation does not result from the pure mathematical formalism applied here, since Δn can only be derived with unclear sign from DFWM experiments as can be seen from eq. (5.1 - 5). Thus, additional and more detailed considerations of the material in question are required in order to determine the sign of the refractive index modulation for a certain experimental configuration as demonstrated above.

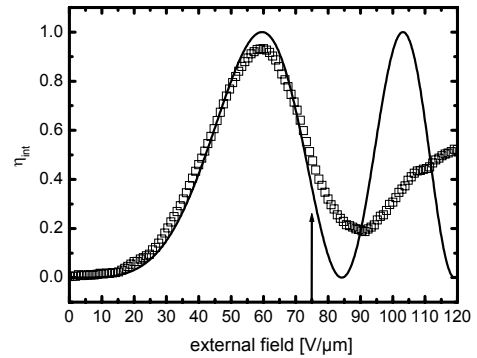


Figure (5.1 - 2): Simulated diffraction efficiency without hologram bending (solid line) and experimental internal diffraction efficiency calculated according to eq. (4 - 20) (open squares).

In order to derive the PR phase shift ϕ , the refractive index modulation modeled according to eq. (5.1 - 5) (corrected for the polarization anisotropy) is used together with the experimentally obtained PR gain and eq. (4 - 15) is applied. It turns out, that the PR phase shift takes a constant value of about 20° for external fields exceeding $40\text{V}/\mu\text{m}$, which is in reasonable agreement with experimental results obtained with a similar material using the moving grating technique [207]. Thus, a constant $\phi = 20^\circ$ will be used for the simulation. Recalculating the PR gain according to eq. (4 - 15) with $\phi = 20^\circ$ for the entire range of external fields applied (0 to $120\text{V}/\mu\text{m}$) shows very good agreement with the experiment (see figure (5.1 - 3)), which validates the described procedure. Please note, that a constant phase shift as a function of the applied field cannot be implied in general but will suffice for the present purpose. As can be seen from the inset of figure (5.1 - 3), the phase shift tends to increase for small fields applied, which is in agreement with experimental results obtained using the moving grating technique [207]. This was attributed to the influence of an isomerization grating component as discussed in “4.2.1.7.) Isomerization gratings” on page 205.

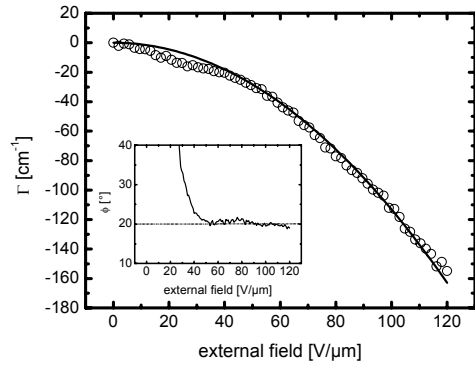


Figure (5.1 - 3): Calculated gain as described in the text (solid line) and experimentally determined gain (open circles). Inset: PR phase shift derived from 2BC experiments using the theoretically modeled refractive index modulation as described in the text

Please note furthermore that Γ appears to be negative in the considered experiment and, hence, ϕ is positive, resulting in $\Delta\phi(w) \leq 0$. Thus, the grating is bent towards the x -axis, resulting in a decreasing ψ (increasing Ψ) as a function of z in the present case. It is important to point out, that the bending direction depends both on the direction of the applied field as mentioned before, as well as on the polarization of the writing beams.

The intensity ratio of the recording beam was set constant to $b = 1$ (i. e., $m = 1$), which correlates with the initial condition of zero externally applied field in the experiment. It must be pointed out that setting the beam intensity ratio and the grating contrast to unity and assuming these parameters to remain constant for the complete simulation is a dramatic simplification, which strongly restricts the range of validity of the calculations.

The total set of parameters used in the simulation is subsumed in table (5-2):

Table (5-2): Simulation parameters

Parameter	External value	Internal value	Parameter meaning
Ψ	60°	29.2°	Tilt angle of the hologram
ψ	-	60.8°	Slant angle of the hologram
α_1	50°	26°	Incident angle of recording beam 1
α_2	70°	32.5°	Incident angle of recording beam 2
θ_B	50°	26°	Bragg angle
ϕ	-	20°	PR phase shift

Table (5-2): Simulation parameters

Parameter	External value	Internal value	Parameter meaning
2θ	20°	6.5°	Angle between the writing beams
E_{ext}	variable	not determined	Externally applied electrical field
n_0	-	1.75	Materials' bulk refractive index
λ_0	633nm	633nm	Operating vacuum wavelength
C_{mol}	-	$7.4 \times 10^{-7} \mu\text{m}^2/\text{V}^2$	Constant for eq. (5.1 - 5)
$\Delta n_P / \Delta n_S$	-	-2.22	Anisotropy factor
b	-	1	Recording beam ratio
m	-	1	Grating contrast (assumed constant)
d	$105 \mu\text{m}$	n.a.	sample thickness

The simulations were carried out using MATLAB for Windows (16bit). The program code for the simulations is given in Appendix A.

5.1.3.)Results and discussion of the diffraction efficiency simulations

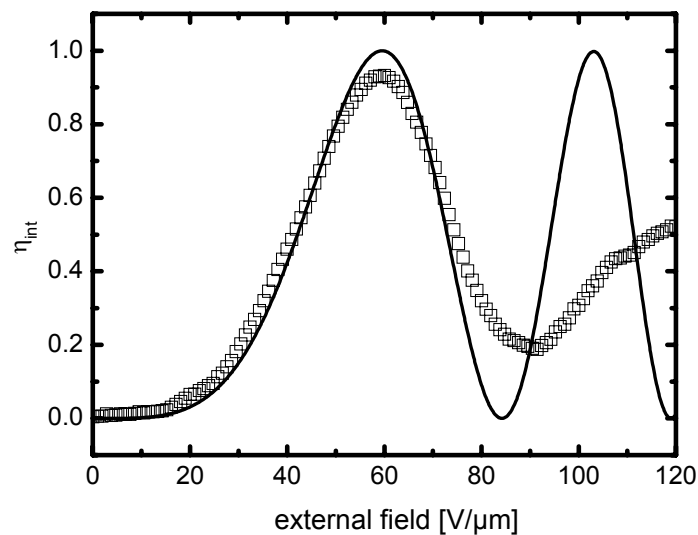


Figure (5.1 - 4): Simulated diffraction curve with hologram bending (solid line) and experimental internal diffraction efficiency (open squares).

Now the diffraction efficiency can be modelled for the geometry and conditions used in the experiment by applying eq. (5.1 - 1) and eq. (2.3 - 37). By means of eq. (5.1 - 13) and eq. (5.1 - 12) hologram bending will be taken into account. The individual parameters for the simulation are listed in table (5-2). For comparison the corresponding diffraction curves not taking into account hologram bending were also calculated.

Figure (5.1 - 4) compares the calculated diffraction curve including hologram bending with the corresponding experimental data. The result is virtually (but not actually) identical to figure (5.1 - 2), where the theoretical curve has been calculated without hologram bending and applying the strongly simplified model according to eq. (5.1 - 5). Indeed, the theoretical curves calculated with and without hologram bending using the complete simulation model are very similar within the field range, which can be experimentally studied. However, slight differences exist, which are due to hologram bending as shown in figure (5.1 - 5). Since the graphs are too similar to be distinguished in a plot covering the total range of external fields used for the simulation, the sections of interest have been enlarged in figure (5.1 - 5).

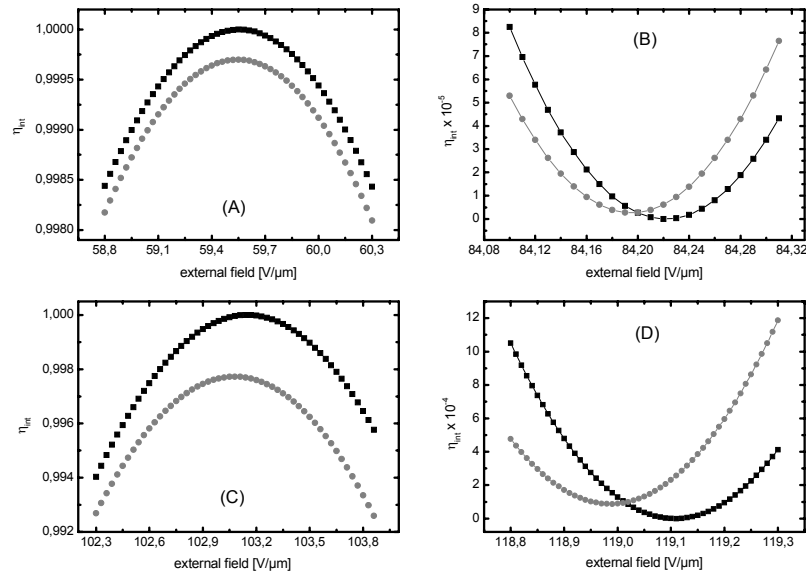


Figure (5.1 - 5): Zooms to the areas of interest of the calculated diffraction curves taking and taking not into account hologram bending (solid circles and solid squares, respectively): First (A) and second (C) diffraction maxima and first (B) and second (D) diffraction minima are depicted.

In figure (5.1 - 5) the theoretical influence of hologram bending is clearly visible, but, within the range of external fields experimentally accessible, of very small magnitude. The revealed deviations are far below the typical experimental error made in DFWM experiments with organic thin film devices operated in tilted configuration as described in “4.2.1.3.2.) Evaluation of the DFWM experiments” on page 195. The diffraction efficiency is lowered by about 3×10^{-4} (0.03%) in the first diffraction maximum and 3×10^{-3} (0.3%) in the second diffraction maximum due to hologram bending. Furthermore, an offset diffraction can be observed in the first and second minimum (remaining diffraction efficiency about 3×10^{-6} and about 9×10^{-5} , respectively), whereas the diffraction efficiency drops to zero, if simulated without hologram bending. The deviation of the diffraction magnitude from the values without hologram bending increases monotonously with the order number of the maxima or minima, but shows a larger absolute magnitude for the maxima as compared to the minima. As could be expected from eq. (5.1 - 1) ($\xi^2 > 0$ in the sine argument), hologram bending shifts the diffraction curves slightly towards smaller external fields. Taking into account hologram bending, the first diffraction maximum occurs about $9 \text{ mV}/\mu\text{m}$ earlier on the external field axis than without bending. As opposed to the diffraction efficiency the reduction of the external field increases monotonously throughout the straight sequence of both the diffraction extrema (i.e. maxima and minima) in the direction of increasing field. These results prove unambiguously, that the experimental observation of incomplete diffraction even for ‘perfect’ alignment of all beams

[154, 155] can not be attributed to this effect. It should be noted, that this validates the common practice to compare the performance of different materials considering the external fields necessary to achieve the first diffraction maximum as already mentioned in “3.1.1.1.) Dynamic range” on page 151.

In general, the experimental and the calculated diffraction curves are quite similar for external fields below $70 \text{ V}/\mu\text{m}$, whereas they start to deviate strongly from each other for higher fields. This should be attributed to the increasing influence of the contrast factor m , which, according to eq. (2.5 - 1), determines E_{SC} [71, 140]. The contrast factor at the rear exit plane can be calculated from the measured intensities of the writing beams after passing through the device. For $E_{ext} \leq 70 \text{ V}/\mu\text{m}$ m varies very little (> 0.95), but it strongly decreases to 0.57 at $E_{ext} = 120 \text{ V}/\mu\text{m}$. However, a detailed study of the influence of the contrast factor on the DFWM diffraction properties would require a very complex simulation model taking into account the recursive influence of the contrast factor on the PR space-charge field and the PR phase shift. Furthermore, while the impact of m on the refractive index modulation may be approximated by calculating the relative recording beam intensities as a function of increasing penetration depth according to eq. (2.5 - 108) to eq. (2.5 - 110), deriving the contrast factor according to eq. (2.1 - 47) and correcting the refractive index modulation according to eq. (5.1 - 4) by multiplication with the contrast factor, there is currently no theoretical model for the influence of the grating contrast on the PR phase shift for PR polymers. Erwin Mecher experimentally investigated the correlation between the grating contrast and the PR phase shift in detail and found a very complicated behavior [T1]. Hence, a consistent solution of the overall problem cannot be provided at this point.

Only under extreme conditions, which cannot be reached experimentally, hologram bending affects the diffraction properties of a PR grating notably. In order to show the general relations, which result from the simulation parameters according to table 5-2 on page 219, the simulation was formally extend to external fields of $1000 \text{ V}/\mu\text{m}$ (figure (5.1 - 6) keeping in mind that these results do not represent a real physical state of the materials investigated. Figure (5.1 - 6) clearly demonstrates, that even under extreme conditions hologram bending is not supposed to show a significant impact on the diffraction efficiency in PR polymers. The functional dependence of the diffraction efficiency on the external field (i.e. the refractive modulation) is determined by the mathematical behavior of eq. (5.1 - 1) and will not be considered here in detail. However, obviously the effect of hologram bending on the diffraction efficiency as a function of increasing refractive index modulation shows a maximum and decreases again for even higher index modulations. In contrast, the shift of the position of the diffraction extrema on the field axis towards lower fields, as compared to the undisturbed grating, increases monotonously within the simulation interval (figure (5.1 - 7)). This proves, that the dephasing parameter does not show oscillatory behavior as might be expected from eq. (5.1 - 3). However, oscillatory behavior would imply a “rolling“ grating (i.e. a change from a transmission type to a reflection type grating as a function of the penetration depth), which is not allowed for by the applied model. That fact, that oscillatory behavior actually does not occur even for the highest fields applied in the current consideration may be taken as indication that the simulation model is not only mathematically but also physically correct in principle. However, it must be pointed out that the simulation model does not provide results of actual physical relevance for the high field values formally used here, since the approximations applied will by no means represent the physical truth any more. For example, the PR gain simply extrapolated to an external field of $1000 \text{ V}/\mu\text{m}$ would exceed $\Gamma = 10^4 \text{ cm}^{-1}$, which implies that the intensity of the depleted beam normalized by its initial (i.e. undepleted) value will drop to about $I/I_0 \approx 10^{-55}$. Accordingly, the grating contrast will almost immediately virtually drop to zero as the recording beams pass through the active PR layer, which would even violate the basic assumption of a thick holographic grating underlying Kogelnik’s coupled wave theory.

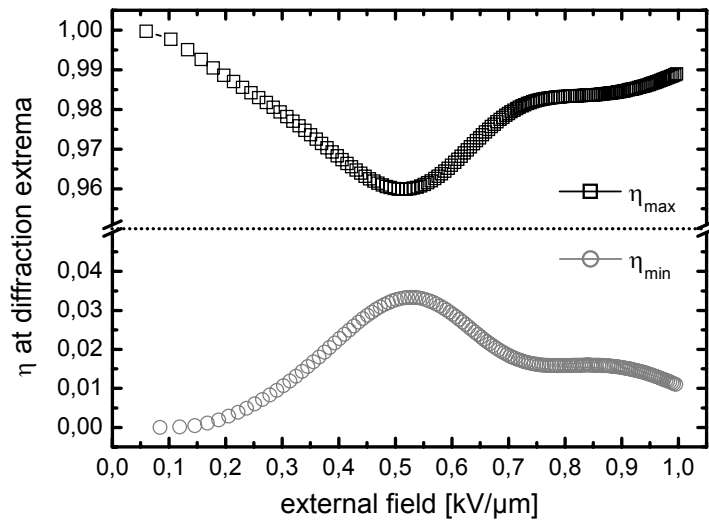


Figure (5.1 - 6): Formal diffraction maxima and minima as a function of the external field for field values beyond experimental accessibility.

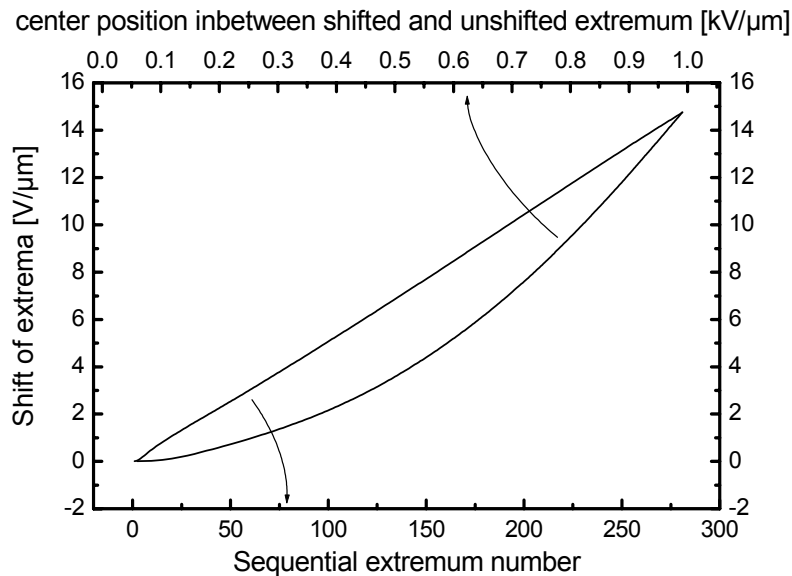


Figure (5.1 - 7): Shift of diffraction extrema towards lower external fields for the case when bending occurs with respect to the undisturbed grating. Field values beyond experimental accessibility are included.

Furthermore, the results of the simulation model will be considered for the case of higher PR phase shifts than experimentally determined from the employed model system of a PR polymer. This point of view is justified by the fact, that the model system utilizes the azo dye DMNPAA as NLO chromophore, which is known to be capable of forming a local isomerization grating at the operating wavelength applied here (for more details see “4.2.1.7.)

Isomerization gratings” on page 205). Thus, one may assume, that the apparent PR phase shift calculated from the experimental data on the PR gain and the DFWM diffraction efficiency may consist of a local contribution with zero phase shift corresponding to an isomerization grating and PR contribution of higher phase shift than calculated. In fact, a considerably higher PR phase shift approaching almost 90° has been determined for a PR polymer using an AC modulation technique, which is a method enabling the determination of the purely photorefractive phase shift independently from a possible local contribution to the overall refractive index grating [192]. Although the system investigated in the related work is significantly different from the systems investigated here, the results presented indicate that one may have to account for a higher PR phase shift than has actually been done in the simulations discussed above. Moreover, in order to obtain the PR phase shift, a theoretical anisotropy factor has been applied for adapting the refractive index modulation calculated from DFWM experiments (carried out using a p-polarized reading beam) to the 2BC experiments, which have been carried out with s-polarized recording beams. As already discussed in “4.2.1.4.) Polarization anisotropy for PR wave mixing experiments” on page 199, this theoretical anisotropy correction factor is only a rather crude approximation afflicted with an error of unclear magnitude. Accordingly, besides the possible occurrence of a local grating as discussed above, the crude approximation of the anisotropy factor may as well result in an erroneous estimate of the absolute phase shift from the experiment. The simulated diffraction efficiencies as a function of the phase shift are shown in figure (5.1 - 8).

Please note, that simply the PR phase shift was varied keeping the refractive index modulation constant. However, in both cases discussed above, which possibly give rise to misestimates of the PR phase shift, the refractive index modulation sensed by the recording beams for the 2BC process must in fact be understood as a function of the PR phase shift or vice versa.

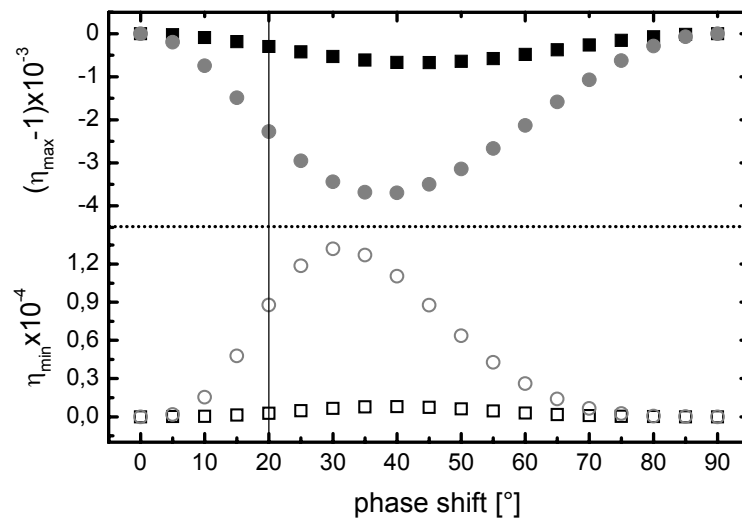


Figure (5.1 - 8): Diffraction efficiencies in the first (squares) and second (circles) diffraction maximum (solid symbols) and minimum (open symbols) simulated for different PR phase shifts. Data for 20° represent simulation results for the real model system.

Figure (5.1 - 8) reveals, that there is a maximum deviation from the undisturbed grating for about 35° PR phase shift. The phase shift history of the simulation curves can easily be understood when considering eq. (5.1 - 11). For a given refractive index modulation, the (real part of the) PR gain coefficient increases with increasing phase shift ($\Gamma \propto \sin \phi$) as does the

denominator (due to $\tan \phi$) of eq. (5.1 - 11). However, for high phase shifts $\tan \phi$ grows faster and, hence, the slope of the grating planes decreases again, approaching zero for ϕ approaching 90° . For $\phi = 90^\circ$ the grating is undisturbed again, which corresponds to a relative dephasing of the recording beams of 180° , yielding a grating, which is shifted by half a period with respect to the undisturbed grating (i.e. for $\phi = 0^\circ$), but which is not subjected to bending. Figure (5.1 - 8) shows that the impact of hologram bending on the diffraction efficiencies remains negligibly small for all values of the PR phase shift. Please note that for $\phi \geq 20^\circ$, the deviations of the diffraction efficiencies from the case of an undisturbed grating as depicted in figure (5.1 - 8) will be upper bounds for the real situation, if there is a local grating as discussed above, or if the anisotropy factor is erroneous, since in both cases the refractive index modulation of the purely photorefractive grating will be smaller than determined from DFWM experiments. On the contrary, for $\phi \leq 20^\circ$ the situation is reversed, i.e. the purely PR refractive index modulation is larger than determined from DFWM experiments. Nevertheless, in all cases the general trend can safely be assumed to be similar to the situation as depicted in figure (5.1 - 8): The deviations in the diffraction efficiency between the disturbed grating and the undisturbed grating vanish for $\phi = 0^\circ$ and $\phi = 90^\circ$ and show a maximum in-between.

5.1.4.) Quintessence of the diffraction efficiency simulations

Although the presented simulation model contains strong simplifications, it could unambiguously be shown that hologram bending due to strong 2BC does not notably affect the diffraction properties of a grating in organic PR devices within the range of the externally applied fields experimentally possible. This contradicts earlier statements in the literature, where hologram bending was made responsible for the observed misalignment of the probe beam required in order to achieve maximum diffraction efficiency [154, 155] and, among others, incomplete diffraction at the maximum [155]. The misalignment of the probe beam, thus, must be attributed to the common setup geometry (s-polarized writing, p-polarized reading, tilted geometry), which leads to different refraction properties for the writing beams and for the reading beam due to the field-induced birefringence of the material, rather than to hologram bending. The real physical background for incomplete diffraction at the diffraction maximum in PR polymers remains unclear.

5.2.)The PR performance of PVK based polymer composites at varying glass-transition temperatures

The glass-transition temperature T_g is of outstanding importance for today's high-performance PR polymers. According to "2.5.3.3.) Orientational enhancement effect" on page 131, their excellent performance is basically due to the possibility of in-situ orienting the NLO chromophores by means of the total electrical field, which emerges in the systems through superposition of the externally applied field E_{ext} with the internal space-charge field E_{SC} , the latter being effected by the PR response of the material. As a result, the PR refractive index modulation Δn originates mostly from an orientational birefringence [13, 88, 91, 161, 165, 168, 170, 178]. Therefore, the orientational mobility of the NLO chromophores in the polymer matrix is a vital parameter for the performance of PR polymers, which determines on the one hand whether the orientational enhancement effect may take place and to which extent it affects the PR response behavior on the other. As already discussed in "2.4.1.) Relaxation and thermodynamics in polymers" on page 70, at a given ambient temperature the orientational mobility of molecular entities in an amorphous polymer matrix is mainly determined by its T_g .

The mechanical force required in order to orient the NLO chromophores to a certain degree along the total internal field direction is (besides the thermal energy) determined by their orientational mobility in the polymer matrix. Furthermore, it turned out that the electrical properties of the photo conducting polymer matrix [196, T2] are affected by T_g as well. While the first aspect leads to an improved steady-state PR performance as a function of decreasing T_g , the latter takes influence on the internal PR space-charge field, resulting in a reduction of the PR performance as T_g decreases for T_g below the ambient temperature (referred to as RT , „room temperature“, hereafter). These two counteracting effects result in a complicated dependence of the steady-state PR properties of PR polymers on T_g .

If orientational enhancement takes place, it is clear that the dynamic response behavior of PR polymers will also depend on the molecular mobility of the NLO chromophores embedded in the photo-conducting polymer matrix and, consequently, for a given RT depend on T_g .

5.2.1.)Experimental aspects

Subsequently, the T_g dependence of the steady-state and the dynamic properties of PVK based PR polymer systems will be elaborated upon in detail. The materials investigated are derived from the first high-performance PR polymer presented in [13] and already described in detail in "3.2.5.1.) Milestones" on page 165. Investigations on systems exhibiting different T_g as well as containing different concentrations of NLO chromophores (2,5 DMNPAA) were carried out. The particular composition of the materials investigated in this section and their corresponding glass-transition temperatures in the range of $-1^\circ\text{C} < T_g < 70^\circ\text{C}$ are listed in table 5-1 on page 211 as well as at the end of this section. For a general overview of the mentioned components see "3.2.5.4.) The plasticizer" on page 169, "3.2.5.3.) The polymer matrix" on page 168, and "3.2.5.5.) The chromophore" on page 170, respectively. The glass-transition temperature of such composites can be adjusted by varying the ratio of PVK to ECZ, whereas the basic electronic properties are expected to remain approximately constant. Depending on the chromophore content, the range of accessible T_g 's is delimited by the case, that no ECZ is added on the one hand yielding materials of relatively high T_g , and material instability due to phase separation and/or dielectric breakdown for very low T_g materials on the other. Phase separation occurs, because the materials are thermodynamically metastable, i.e. they represent oversaturated solid solutions of the highly polar NLO chromophore in the only

slightly polar polymer matrix. Furthermore, the components of low molecular mass show high diffusion mobility in the polymer matrix. Thus, phase separation eventually results in partial crystallization at room temperature and the material becomes opaque. However, it must be emphasized that all materials investigated in this section showed unchanged performance long enough to allow for their careful experimental examination. Devices were prepared according to “4.1.) Preparation of materials and sample structure” on page 179. The film thickness of the PR polymer was adjusted to $d = 105\mu\text{m}$. In order to prevent possible crystallization effects, which may occur in those materials exhibiting very low T_g as described above, all devices were consistently cooled down to room temperature at a cooling rate of approximately $30^\circ\text{C}/\text{sec}$. The devices thus obtained were stable against phase separation from few hours for the composites of very low T_g and high chromophore concentration (e.g. 50e, 40f), up to several months and longer for materials of high T_g and low chromophore concentration ($\leq 30\%wt$). All samples were characterized immediately after preparation which resulted in excellent reproducibility of all experimental results for all systems investigated here. The temperature in the air-conditioned laboratory, inside of which the experiments were performed was $RT = 18\pm 0.5^\circ\text{C}$ for all measurements.

DFWM and 2BC experiments were carried out using s-polarized recording beams, the internal intensities of which were determined as described in “4.2.1.6.) Intensity determination” on page 204, yielding $I_{01} = 20\text{mW}/\text{cm}^2$ and $I_{02} = 25\text{mW}/\text{cm}^2$. The reading beam was p-polarized and its intensity was $I_R = 90\mu\text{W}/\text{cm}^2$. The internal diffraction efficiencies η_{int} and the PR gain coefficients Γ were determined as a function of the external field E_{ext} and/or as a function of time, applying the setup and procedures according to “4.2.) Wave mixing experiments” on page 181. Recording beam I_2 was used for the initial relaxation in the dynamic experiments. The initial relaxation time was 30 minutes in all cases. Lock-in amplifiers were not used here.

In order to study the poling process separately from the formation of the PR space-charge field, the field-dependent and/or time dependent changes of the bulk refractive index was furthermore determined for the same devices as investigated holographically. Therefore, ellipsometric transmission experiments according to “4.3.) Transmission ellipsometric experiments” on page 207 were carried out using the same operating wavelength as applied in the holographic wave mixing experiments. The devices, were tilted by the internal angle $\Psi_t = 26^\circ$ and the ellipsometric transmission was determined as a function of the externally applied electrical field as well as as a function of time.

Table (5-3): Chemical composition and glass transition temperature of the materials investigated in “5.2.) The PR performance of PVK based polymer composites at varying glass-transition temperatures”

Material	DMNPAA	MNPAA	PVK	ECZ	TNF	TPD	T_g
units	[%wt]	[%wt]	[%wt]	[%wt]	[%wt]	[%wt]	[$^\circ\text{C}$]
20a	20		59	20	1	-	60
20b	20	-	54	25	1	-	30
20c	20	-	49	30	1	-	14
20d	20	-	44	35	1	-	-2
30a	30	-	59	10	1	-	62

Table (5-3): Chemical composition and glass transition temperature of the materials investigated in “5.2.) The PR performance of PVK based polymer composites at varying glass-transition temperatures”

Material	DMNPAA	MNPAA	PVK	ECZ	TNF	TPD	T _g
30b	30	-	54	15	1	-	37
30c	30	-	49	20	1	-	12
30d	30	-	44	25	1	-	6
30e	30	-	39	30	1	-	1
40a	40	-	59	0	1	-	72
40b	40	-	54	5	1	-	48
40c	40	-	49	10	1	-	25
40d	40	-	44	15	1	-	17
40e	40	-	39	20	1	-	10
40f	40	-	34	25	1	-	2
50a	50	-	49	0	1	-	35
50b	50	-	44	5	1	-	24
50c	50	-	39	10	1	-	14
50d	50	-	34	15	1	-	7
50e	50	-	29	20	1	-	1

5.2.2.)The relation between the glass-transition temperature and the steady-state performance in PVK based PR polymers

The in-situ poling of the materials by the local total internal electrical field $E_{T,loc}$, which is the vector sum of the externally applied field E_{ext} and the internal space-charge field E_{SC} , results in an enhancement of the electro-optic effect as well as in a birefringence contribution to the index modulation Δn , unlike in PR crystals. This mechanism is known as the orientational enhancement effect (for details see page 131). The quality of the grating formation process (besides its kinetics, which will be discussed later) is strongly influenced by the orientational mobility of the dipoles. According to “2.4.1.) Relaxation and thermodynamics in polymers” on page 70, the latter may be considered as being delimited by the internal free volume of the polymer matrix, for which the relative temperature T_r may be regarded a measure. The relative temperature is defined as:

$$T_r = T_g - RT \quad \text{eq. (5.2 - 1)}$$

In earlier investigations, T_g was adjusted by varying the concentration of a plasticizer, while the measurement temperature (i.e. RT) was kept constant [191]. In analogy, the measurement temperature was varied for one given material by selectively heating the sample,

the glass-transition temperature of which was constant [157]. Qualitatively, the PR performance was found to improve in both cases as a function of decreasing T_g . Unfortunately, the T_g 's of the composites were not explicitly given, which prevents a detailed comparison of the reported results with the results presented here. As a result of the aforementioned earlier investigations, for a long time, simply lowering T_g was considered as an easy way to consistently improve the performance of PR polymers. Furthermore, both the aforementioned studies were restricted to composites with rather low chromophore concentrations and the chromophore content was held constant throughout the investigations carried out. However, typical high-performance organic PR materials known to date contain much more NLO chromophore [13, 178, 171, 165, 170] or even consist of chromophores only [161, 91].

Therefore, the influence of T_g on the steady-state performance of the PVK based PR polymer composites being subject of this work was investigated at room temperature with the chromophore content varying between 20 and 50%wt. According to the orientational enhancement effect, an improvement of the PR performance is expected for increasing chromophore concentration as well as decreasing T_g . Both trends are confirmed for $T_g > RT$. Materials fulfilling this relation between T_g and the ambient temperature will be referred to as „high- T_g “ systems hereafter. However, a performance optimum was found for the highly-doped materials at $T_g < RT$. Materials with $T_g < RT$ will be referred to as „low- T_g “ materials hereafter. Subsequently, it will be demonstrated that this is a result of two counteracting effects, both of which scale with T_g : On the one hand, the degree of the orientation of the chromophores along the local direction of \vec{E}_{tot} for a given \vec{E}_{ext} improves as a function of decreasing T_g , yielding higher PR performance. On the other hand, the relative strength of E_{SC} decreases as a function of decreasing T_g for $T_g < RT$, which leads to a reduction of the spatial average of $|\vec{E}_{tot}|$ as well as to a reduction of the modulation of the direction of \vec{E}_{tot} with respect to the direction of the externally applied field, both of which lowering the PR performance.

5.2.2.1.) Experimental results on the T_g dependence of the steady-state PR performance

In order to gain a more detailed insight into the influence of T_g on the steady-state performance of organic PR materials, four series of PVK-based PR polymer composites with different chromophore content were studied. In almost all cases (see caption of figure (5.2 - 1) for details), a maximum of the diffraction efficiency was observed at specific field values $E_{ext}(\eta_{max})$. The normalized experimental diffraction curves are shown in figure (5.2 - 1). The actual maximum of the internal diffraction efficiency was $\eta_{int} = 80 \pm 5\%$ in all cases.

According to “2.3.2.) Coupled wave theory for thick hologram gratings” on page 53, η_{int} reaches its first maximum for the sine argument equaling $\pi/2$, which corresponds to $\Delta n(\eta_{int,max}) = 2.6 \times 10^{-3}$ for all materials and for the experimental geometry applied here. Hence, $E_{ext}(\eta_{int,max})$ can be used to compare the steady-state performance of PR polymers. Lower $E_{ext}(\eta_{int,max})$ corresponds to better PR performance.

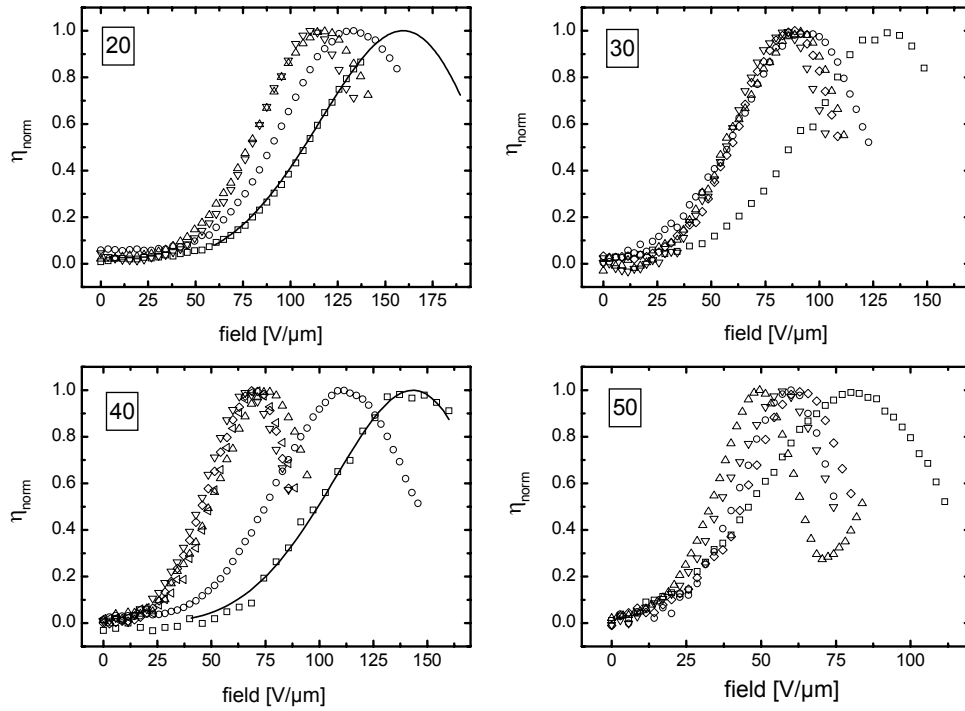


Figure (5.2 - 1): Normalized experimental diffraction curves for 20, 30, 40, and 50%wt content of chromophore. The glass-transition temperature decreases in the sequence of the type of open symbols as follows: squares, circles, up triangles, down triangles, diamonds, left triangles. The diffraction curve for the material containing 20%wt chromophore and exhibiting highest T_g was completed by fitting the experimental curve fragment to an expression according to eq. (2.3 - 43) and eq. (5.1 - 4), however, setting the field-exponent as a fitting variable as well. This procedure was tested before with complete diffraction curves and verified as yielding excellent agreement with the experiment. Finally the high- T_g curve in “20“ was extrapolated numerically to higher external field values (solid line in “20“). The same fitting procedure was applied to the high- T_g diffraction curve of the material containing 40%wt chromophore in order to smooth the experimental curve (solid line in “40“). Please note, that only one of three experimental data points is shown in the graphs and that the graphs are manually cut at about $\eta_{\text{int}} = 0.5$ after the first diffraction maximum. The complete graph as experimentally determined is only shown for material 50C in order to illustrate the occurrence of the first diffraction minimum (up triangles in “50“).

Figure (5.2 - 2) shows $E_{\text{ext}}(\eta_{\text{int,max}})$ for all materials as a function of the reduced temperature T_r , calculated according to eq. (5.2 - 1) with $RT = 18^\circ\text{C}$. Data are additionally included, which were obtained on similar [13] or even identical [140] materials under similar experimental conditions. They are in perfect agreement when taking into account the slightly longer wavelength $\lambda_0 = 675$ nm used in reference [13], which leads to a slight performance reduction as compared to $\lambda_0 = 633$ nm.

Starting from the high- T_g materials the PR performance for a particular chromophore concentration was initially found to consistently improve with decreasing T_r , as commonly assumed and already shown [157, 191]. However, unexpectedly it was found, that the highly-doped materials (containing 40 wt% or 50 wt% chromophore, respectively) show an optimum of the PR performance for reduced temperatures slightly below $T_r = 0$ and then decrease again in performance for even lower T_r . Furthermore, for a given T_r and otherwise constant experimental conditions the PR performance improves with increasing chromophore content. This is generally predicted by eq. (2.5 - 44) to eq. (2.5 - 46), eq. (2.5 - 48), and eq. (2.5 - 49), provided that $E_{T,\text{loc}}$ does not notably depend on the chromophore concentration. Hence, this result was to be expected.

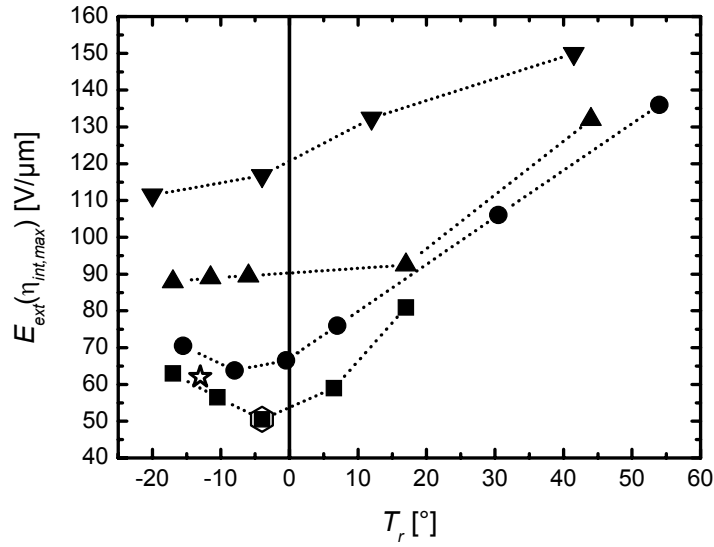


Figure (5.2 - 2): Dependence of the externally applied field to achieve maximum DFWM diffraction efficiency $E_{ext}(\eta_{int,max})$ for $\lambda_0 = 633\text{nm}$ on the reduced temperature T_r , according to eq. (5.2 - 1) for different chromophore contents: 20%wt (down triangles), 30%wt (up triangles), 40%wt (circles), and 50%wt (squares). The open symbols represent data on very similar or even identical materials with 50%wt chromophore concentration taken from the literature and obtained for $\lambda_0 = 633\text{nm}$ (open hexagon, [140]) and $\lambda_0 = 675\text{nm}$ (open star, [13]). The dotted lines are guide to the eye.

In order to study the poling process separately from the space-charge-field formation, the ellipsometric transmission was determined as a function of the externally applied electrical field. For all materials except those containing only 20%wt chromophore, a maximum in the transmission was observed at specific field values $E_{ext}(T_{max})$. For the series with 20%wt chromophore content T_{max} only occurred far beyond the dielectric breakdown limit. The curve fragments were even too short to reasonably estimate $E_{ext}(T_{max})$ by fitting and extrapolation as described in the caption of figure (5.2 - 1). The normalized experimental ellipsometric transmission curves are shown in figure (5.2 - 3). The transmission reaches its first maximum for the sine argument of eq. (4 - 52) equaling $\pi/2$, which corresponds to $\Delta n_{ELP}(T_{max}) = 1.35 \times 10^{-3}$ for all materials and for the experimental geometry applied here. Therefore, $E_{ext}(T_{max})$ can be regarded as a measure for the poling properties of the materials for a given chromophore concentration in analogy to $E_{ext}(\eta_{int,max})$ obtained from the DFWM experiments. A lower $E_{ext}(T_{max})$ indicates more efficient poling. The similarity of eq. (4 - 52) and eq. (2.3 - 43) shows that trends in the two experiments can be directly compared.

Figure (5.2 - 4) shows $E_{ext}(T_{max})$ for the materials containing 30%wt, 40%wt, and 50%wt chromophore as a function of the reduced temperature T_r calculated according to eq. (5.2 - 1) with $RT = 18^\circ\text{C}$.

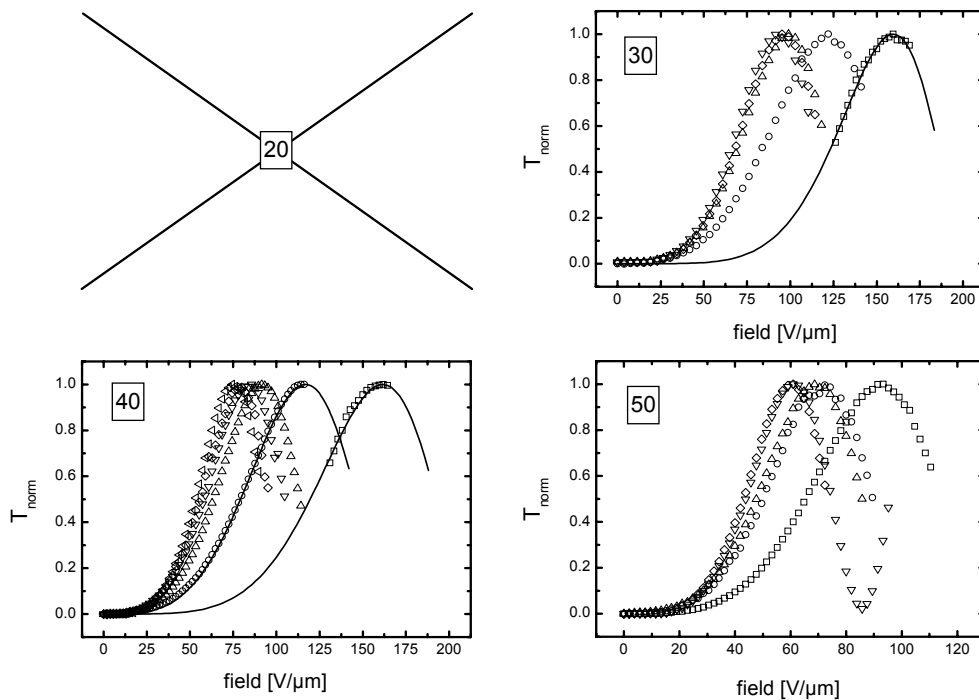


Figure (5.2 - 3):Experimental ellipsometric transmission curves for 30, 40, and 50%wt chromophore content. The glass-transition temperature decreases in the sequence of open symbols as follows: squares, circles, up triangles, down triangles, diamonds, left triangles. For the materials containing 20%wt chromophore the first transmission maximum turned out to be experimentally inaccessible due to dielectric breakdown of the samples. Solid lines depict numerically extrapolated graphs from fitting the experimental graph fragments as described in the caption of figure (5.2 - 1). Please note, that only each second experimental data points is shown and that the graphs are manually cut in length. The complete graph as experimentally determined is only shown for material 50D in order to illustrate the occurrence of the first transmission minimum (down triangles in „50“).

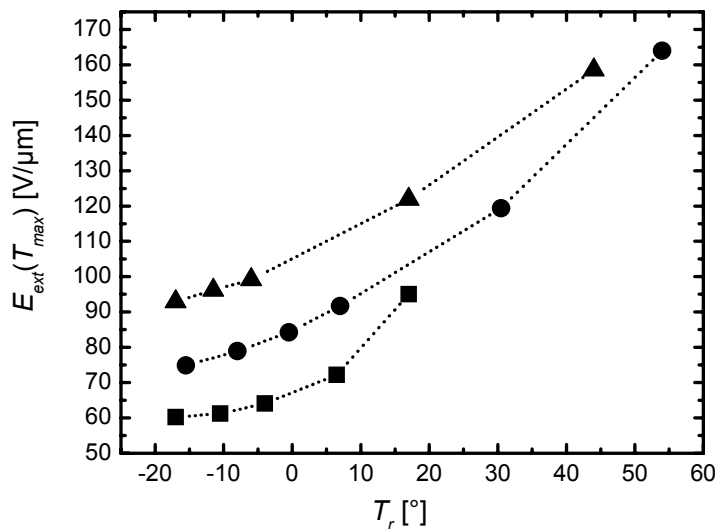


Figure (5.2 - 4):Dependence of the externally applied field to achieve maximum transmission $E_{ext}(T_{max})$ for $\lambda_0 = 633\text{nm}$ in the ELP measurements on the reduced temperature T_r , according to eq. (5.2 - 1) for different chromophore contents: 30%wt (up triangles), 40%wt (circles), and 50%wt (squares). The dotted lines are guide to the eye.

As shown in figure (5.2 - 4), $E_{ext}(T_{max})$ decreases monotonously with decreasing T_r for all materials with constant chromophore content due to the improved orientational mobility of the chromophores in the matrix and apparently eventually levels off. For a given T_r and otherwise constant experimental conditions, $E_{ext}(T_{max})$ decreases with increasing chromophore concentration as is to be expected from the oriented gas model (eq. (2.4 - 69) and eq. (2.4 - 72)). The influence of T_r on the degree of orientation increases with the chromophore concentration. Similar observations have been made for the grating build-up dynamics, which will be elaborated upon later. This effect might be attributed to the brick-like shape of the chromophores, leading to self-hindrance at high loading. This would explain the relative performance reduction observed in figure (5.2 - 2) and figure (5.2 - 4) for the high- T_g materials with large chromophore content as compared to those containing markedly smaller amounts of chromophore but exhibiting similar T_g .

5.2.2.2.) Discussion of the T_g dependence of the steady-state PR performance

The optimum in PR performance observed in figure (5.2 - 2) at high doping levels might be due to the T_g -dependence of (i) the poling efficiency, or (ii) the internal space-charge field E_{SC} . Piezoelectric and electrostriction effects are small and can safely be neglected. However, the absence of a minimum of $E_{ext}(T_{max})$ as a function of T_r in the ELP experiments (figure (5.2 - 4)) for all chromophore concentrations proves that the PR performance optimum observed for the highly-doped materials for T_r slightly below $T_r = 0$ cannot be attributed to the poling properties.

Since the main difference between the ELP and DFWM experiments is the influence of the PR space-charge field, the latter remains as possible T_g -dependent parameter, which may explain the observed DFWM behavior. At $E_{ext}(\eta_{int,max})$ charge-carrier migration is the transport process dominating the formation of the space-charge field, and diffusion can safely be neglected (i.e. diffusion field $E_d = 0$). Thus, following Kukhtarev's model developed for inorganic PR crystals (see page 119), the amplitude of the PR space-charge field is the modulus of the complex PR space-charge field E_1 according to eq. (G - 24), which, under these conditions, can be expressed as:

$$E_{sc} = |E_1| = m \cdot m^* \cdot \sqrt{\frac{E_0^2}{1 + (E_0/E_q)^2}} \quad \text{eq. (5.2 - 2)}$$

Here, m is the contrast factor of the illuminating interference pattern for s-polarized beams according to eq. (2.1 - 47) and the parameter m^* is the conductivity contrast according to eq. (2.5 - 4), which reads:

$$m^* = \frac{\sigma_{ph}}{\sigma_d + \sigma_{ph}},$$

where σ_d and σ_{ph} are the dark and the photo conductivity, respectively. E_0 is the projection of the external electrical field onto the grating wave vector and E_q is the saturation field according to eq. (2.5 - 3).

Thus, for a given m the space-charge field amplitude is delimited by (i) the field term, containing E_0 and E_q , and by (ii) the conductivity contrast m^* . In the original theory of Kukhtarev the dark conductivity is caused by thermal generation of charge carriers in the bulk, which competes with the space and time dependent photo-generation of charge carriers as expressed by eq. (G - 2). In organic thin film samples as used in this work (see "4.1.) Preparation of materials and sample structure" on page 179), however, the dark conductivity should include

a major contribution due to the injection of holes from the ITO contacts, which are directly attached to the polymer layer. Since the polymer matrix is a hole conductor an unipolar current, thus, flows through the polymer layer, which may either be injection-limited or space-charge-limited. In the latter case and according to the theory of space-charge-limited currents (see “2.4.3.1.) Space-charge-limited currents” on page 96) one would expect an approximately quadratic increase of the dark current as a function of the externally applied field for sufficiently high fields. Figure (5.2 - 5) shows the dark current density measured as a function of the external field applied to a 0.9 μm thick layer of the polymer blend type 30a ($T_g = 62^\circ\text{C}$) between ITO bottom and Aluminium top electrode at different ambient temperatures [196, T2].

In order to obtain the power law dependence between the current and the applied field the experimental curves in figure (5.2 - 5) were fitted to the simple expression:

$$y = A + B \cdot E_{ext}^C, \quad \text{eq. (5.2 - 3)}$$

where E_{ext} is the externally applied field. This procedure yielded $C = 2.26 \pm 0.26$ with correlation factors of better than 0.997 for all ambient temperatures considered indicating that the dark current in the investigated polymer blends is indeed space-charge limited.

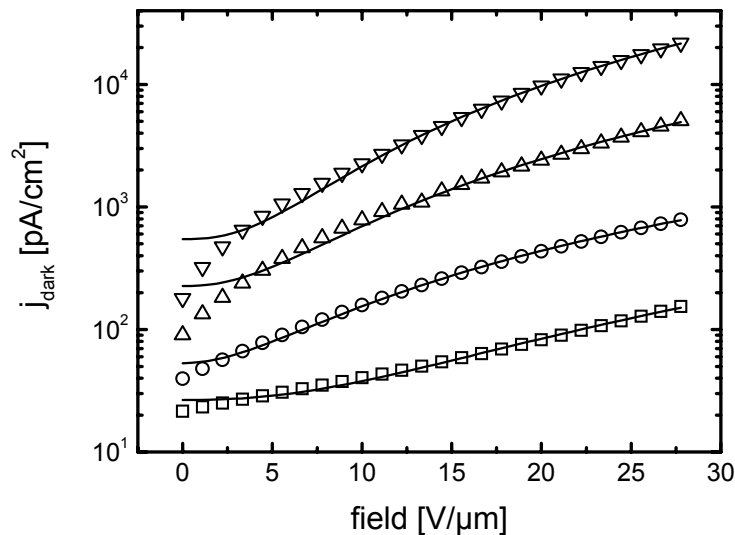


Figure (5.2 - 5) Dark I-V-characteristics of a 0.9 μm thick layer of material 30a between Al top and ITO bottom electrode. The dark current density j_{dark} was measured at reduced temperatures of $T_r = 19^\circ\text{C}$ (squares), 9°C (circles), -3°C (up triangles), and -13°C (down triangles). The measurements were performed in dry nitrogen ($p = 1\text{bar}$) starting with negative polarity at the bottom electrode from zero bias. The bias was varied cyclically and the back cycle from positive bias to zero bias is shown, which thus includes capacitive discharge of the sample structure. For more details on the measurement technique see [T2]. The solid lines represent fits to eq. (5.2 - 3).

Unfortunately Kukhtarev’s model does not include a contribution due to injected charge carriers. However, one can presume that the phenomenological influence of this process on the PR space-charge field should equal the influence of thermal charge generation, since both are insensitive against non-uniform illumination (provided there is no material heating by the incident light). Hence, in both cases solely the zero order charge carrier density is affected.

In order to obtain a lower limit of the conductivity contrast factor m^* for a particular material, the dark- and the photo current passing through 37 μm thick PR devices of standard structure according to figure (4 - 2) were measured for an externally applied field of $E_{ext} = 54\text{V}/\mu\text{m}$, thus providing reasonably similar conditions as applied in the holographic wave mixing

experiments. This is an important premise, since either using lower field at the same thickness of $37\mu\text{m}$ or markedly thinner films of below $1\mu\text{m}$ at similar fields of about $50\text{-}60\text{V}/\mu\text{m}$ will yield results, which may not be representative for the problem under consideration (see below for an example). Due to the strong field dependence of the charge carrier photo-generation efficiency, the photo current would be underestimated in the first case, while the dark current would be overestimated in the latter, where the thickness is already of similar order of magnitude of (or even smaller than) the average drift length of the holes in the systems concerned [202, 203]. Hence, in both cases the absolute magnitude of m^* will be underestimated. The aforementioned currents were both determined in air (atmospheric humidity $\approx 50\%$) using a commercial electrometer (Keithley 6512) and the photo current was measured at $\lambda_0 = 633\text{nm}$ while applying a light intensity of $I = 45\text{mW}/\text{cm}^2$. The conductivity contrast m^* as calculated from the current measurements decreased as T_r was reduced, but for larger chromophore concentration the decrease in m^* was steeper than for smaller chromophore content (figure (5.2 - 6)). However, the overall reduction in m^* was found to be very small, i.e. $m^* > 0.98$ in all cases investigated. Thus, even though the T_g -dependence of m^* and the poling efficiency were found to counteract for $T_r \leq 0^\circ\text{C}$, this can not explain the observed optimum in the DFWM experiments.

Please note, that violating the aforementioned premise of comparable conditions between the current measurements and the holographic experiments may lead to wrong implications. For example, one obtains $m^* = 0.85$ for material 50e and $m^* = 0.99$ for material 50a, if determined at an external field of $5.4\text{V}/\mu\text{m}$ applied to a $37\mu\text{m}$ thick sample, which, in a misleading way, seemingly explains the observed PR performance optimum.

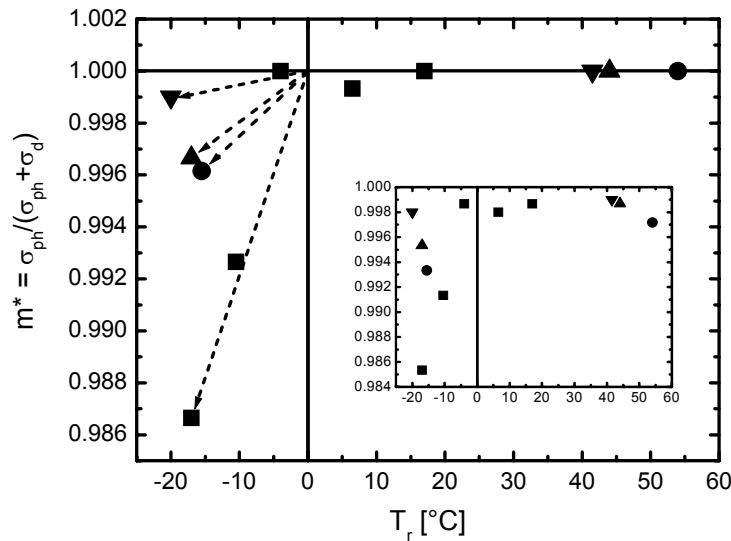


Figure (5.2 - 6): Conductivity contrast factor m^* , normalized to m^* obtained for the material of the highest T_g of each series. Squares: 50%wt content of chromophore, circles 40%, up triangle 30%wt, down triangles 20%wt. The inset shows the same data but not normalized

Having excluded that the PR performance optimum as a function of T_r , as observed for the highly doped materials may be due to a T_g dependence of the conductivity contrast, the field term in eq. (5.2 - 2), in particular the saturation field E_q must be implied to be responsible for this effect. According to eq. (2.5 - 3), E_q reads:

$$E_q = q \frac{N_A}{\langle \varepsilon \rangle K},$$

where q is the elementary charge, N_A is the number of traps, $\langle \varepsilon \rangle$ is the average bulk permittivity,

and K is the modulus of the grating vector. An apparent reduction of E_q when T_r is decreased is not supposed to be effected by an increase of $\langle \varepsilon \rangle$, because this would affect the DFWM as well as the ELP experiments, the latter of which then must be expected to reveal a similar optimum in the poling performance as observed for the PR performance. Therefore, an apparent reduction of E_q as a function of T_r must be attributed to a reduction in the effective number of PR traps N_A . However, at the current state of research on organic PR materials the exact nature of the PR traps is still unclear. Thus, discussing the trap situation in PR polymers is problematic and can only be performed phenomenologically on the basis of plausible assumptions.

The PR traps in polymers could be, for example, due to chemical impurities in the polymer matrix. However, this kind of trap should not be affected very much by T_g , since their electronic levels are constant and their number density does not depend on the physical state of the polymer matrix. Furthermore, traps in disordered organic materials can also result from a variation in the orientation and distance between the charge-transporting molecular sites and the surrounding polar and non-polar molecules. This model of positional and conformational disorder has been developed and successfully applied to the transport of electrical charges in organic photoconductors by Baessler et al. As already discussed in “2.4.3.2.3.) The Baessler formalism (disorder model)” on page 104, in a first approximation the energy landscape may be modeled by a Gaussian-type density of states distribution (DOS), characterized by the width σ . In [B27] σ has been described by two contributions, a dipolar component σ_{dipole}^2 and a van-der-Waals component σ_{vdW}^2 :

$$\sigma^2 = \sigma_{dipole}^2 + \sigma_{vdW}^2. \quad \text{eq. (5.2 - 4)}$$

The dipolar component is proportional to the concentration of dipoles and the van-der-Waals component is in the order of 0.1eV. In the case under consideration, the dominant contribution to the concentration of dipoles stems from the highly polar NLO chromophores, whereas the contribution by the only little polar carbazole moieties is secondary. Sites located close to the center of the DOS will contribute most to the charge transport as outlined in Appendix E on page E4, which elaborates upon the disorder model. In contrast, states located energetically deep in the DOS are supposed to act as persistent traps for the charge carriers.

For high- T_g systems (i.e. $RT < T_g$), the DOS must be considered as frozen in space and time and, according to eq. (2.4 - 146) and accounting for the experimental conditions applied here (i.e. $C\sqrt{E} \ll 2/3$), the charge carrier mobility will decrease with increasing width σ of the distribution, i.e., basically with increasing concentration of NLO chromophores. With increasing σ , also the number density (and average depth) of deep traps, which should contribute most to the space-charge field will increase. According to [195], for decreasing T_r slow collective motions of the glass-forming elements in a random potential occur as soon as T_r drops below zero (i.e. T_g drops below RT), leading to a slight broadening of the preexisting DOS. Within the small temperature range with $T_r < 0^\circ\text{C}$ studied here, a change of the positional disorder can be neglected in good approximation. However, conformational changes may occur: A site located deep in the DOS as defined above can change its site energy within the distribution due to the thermally induced changes of its conformation and orientation relative to the neighboring molecules. Thus, charge carriers trapped in such a conformational trap should be released more easily due

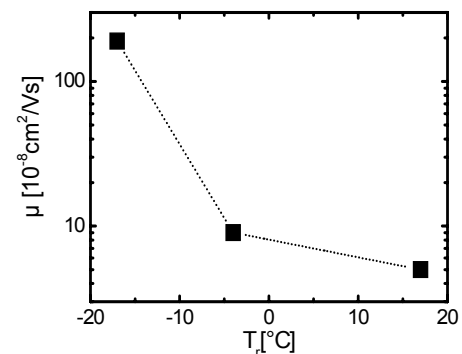


Figure (5.2 - 7): Hole mobilities for selected systems containing 50%wt chromophore as estimated from the dark current density ($U = 2\text{kV}$, $d = 37\mu\text{m}$) using Child’s law. The lines are guide to the eye.

to the thermally induced conformation changes. This interpretation is supported by a strong increase of the hole drift mobility μ with decreasing $T_r < 0^\circ\text{C}$, found for the materials containing 50%wt chromophore (figure (5.2 - 7)). Assuming that the dark current in the investigated systems is space-charge limited as already discussed above, the hole drift mobilities can be estimated from the dark current measurements discussed before using Child's law (eq. (2.4 - 123)) and the dielectric constant of $\epsilon = 6.5$ as previously determined for this type of material [185]. The absolute values for μ are in a similar range as determined by the holographic time-of-flight technique on a similar PVK-based PR composite [138, 139].

Following this argumentation one might speculate that the apparent number of conformational traps (N_A) and, thus, the saturation field E_q according to eq. (2.5 - 3) might decrease for decreasing $T_r < 0^\circ\text{C}$. This in turn should affect the gain coefficient Γ . The gain coefficients as experimentally determined for the materials containing 50%wt chromophore are shown in figure (5.2 - 8).

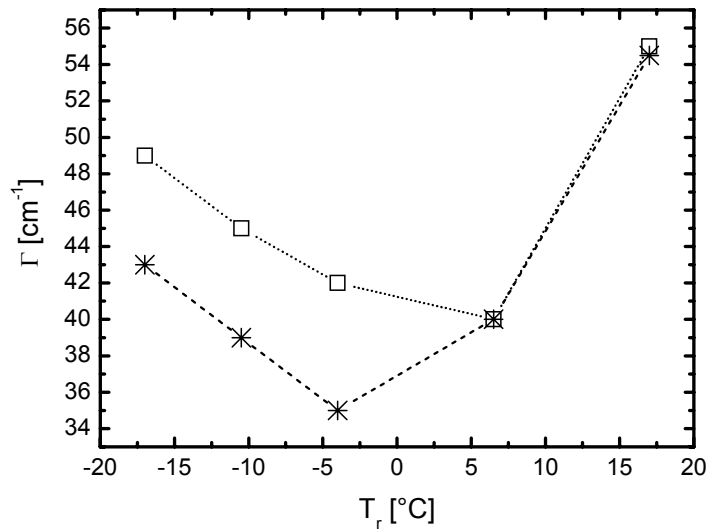


Figure (5.2 - 8): Dependence of the absolute gain coefficient $|\Gamma|$ as determined for s-polarized writing beams at $E(\eta_{max})$ on the reduced temperature $T_r = T_g - RT$ for the series containing 50%wt chromophore (open squares). The stars represent the corresponding gain values expected assuming a constant saturation field of $E_q = 80 \text{ V}/\mu\text{m}$. The lines are guides to the eye.

The values experimentally obtained for Γ (open squares) at $E_{ext}(\eta_{max})$ first decrease as T_g decreases and approaches RT , and then slightly increase again. According to eq. (2.5 - 102), Γ depends on $\sin\phi$, where ϕ is the (PR) phase shift between the light interference pattern and the refractive index grating. According to eq. (2.5 - 5) and neglecting E_d as discussed before, the PR phase shift is given by:

$$\phi = \text{atan} \frac{E_0}{E_q}. \quad \text{eq. (5.2 - 5)}$$

E_0 is the projection of E_{ext} onto the grating vector K . Since Δn at $E_{ext}(\eta_{max})$ is identical in all cases, a smaller Γ reflects a smaller ϕ . For the materials 50a and 50b, it is reasonable to assume that $E_q = \text{constant}$, since $RT < T_g$. The reduced gain in 50b is a result of the significantly smaller $E_{ext}(\eta_{max})$ (see figure (5.2 - 2)). From eq. (2.3 - 34), eq. (2.5 - 102) and eq. (5.2 - 5) and with the polarization anisotropy according to eq. (4 - 46) a value of $E_q \approx 80 \text{ V}/\mu\text{m}$ can be estimated for the materials 50a and 50b. Assuming, therefore, a constant $E_q = 80 \text{ V}/\mu\text{m}$ for all materials, one can calculate the theoretically expected values of Γ for the materials 50a - 50e by means of eq. (5.2 - 5) and eq. (2.5 - 102). For the materials 50c - 50e this yields smaller gain values (figure

(5.2 - 8), stars) than found experimentally, which can only be interpreted as a relative decrease of E_q with respect to E_0 for $T_r < 0^\circ\text{C}$ meeting the expectations.

In order to get a more detailed picture a measure for the absolute value of the PR space-charge field E_{SC} was derived from the field dependence of the PR refractive index modulation Δn_{DFWM} according to eq. (2.5 - 69) (and according to [161]) and the field dependence of the field induced birefringence Δn_{ELP} according to eq. (2.4 - 75). Assuming, that there is no persistent poling, these quantities may be expressed by:

$$\Delta n_{DFWM} = C_{DFWM} E_{DFWM} E_{SC} \text{ and} \quad \text{eq. (5.2 - 6)}$$

$$\Delta n_{ELP} = C_{ELP} E_{ELP}^2, \quad \text{eq. (5.2 - 7)}$$

where E_{DFWM} and E_{ELP} are the externally applied fields in the DFWM and the ELP experiments, respectively. For a material of constant chromophore content and assuming that the oriented gas model is reasonably valid for all considered materials, C_{DFWM} and C_{ELP} are constants for a certain and constant experimental configuration. Among others they contain the particular effective Kerr susceptibilities as well as geometrical factors. Please note, that the birefringence contribution included in the effective PR Kerr susceptibility as well as the effective ELP Kerr susceptibility are due to the reorientation of the NLO chromophores in the polymer matrix by the (local total) poling field and, thus, may depend on the time dependent progression of the externally applied electrical field, if the latter changes too fast for the chromophores to follow. However, this does not apply here. Furthermore, all the susceptibility contributions in question are expected to show the same dependence on the chromophore concentration, which becomes clear considering eq. (2.4 - 75) and eq. (2.5 - 44) to eq. (2.5 - 51). In the first DFWM diffraction maximum Δn_{DFWM} is constant for all experiments, which also applies to Δn_{ELP} in the first ELP transmission maximum. Thus, the ratio

$$\frac{\Delta n_{DFWM}}{\Delta n_{ELP}} = \frac{C_{DFWM} E_{DFWM} E_{SC}}{C_{ELP} E_{ELP}^2} \quad \text{eq. (5.2 - 8)}$$

is constant for all experiments carried out. Rewriting eq. (5.2 - 8) to the form:

$$\frac{E_{SC}}{E_{DFWM}} = C' \frac{E_{ELP}^2}{E_{DFWM}^2} \quad \text{eq. (5.2 - 9)}$$

one obtains a measure for the PR space-charge field normalized by the externally applied field, which is related to the real normalized space-charge field by the unknown, but constant parameter C' . Figure (5.2 - 9) shows the ratio E_{ELP}^2/E_{DFWM}^2 for all investigated materials as a function of the reduced temperature.

For $T_r > 0^\circ\text{C}$, the ratio E_{ELP}^2/E_{DFWM}^2 is approximately constant, whereas it decreases significantly for decreasing T_r , below $T_r \cong -5^\circ\text{C}$. This general trend is excellently reproduced by theoretical considerations based on photophysical measurements and applying the more sophisticated Schildkraut model according to "2.5.3.2.) Schildkraut's model" on page 124 to calculate the PR space-charge field [196] (figure (5.2 - 9)). A decrease of the normalized space-charge field of up to almost 40% for material 50e is observed as compared to the average normalized space-charge field for all materials with $T_r > 0^\circ\text{C}$. This perfectly explains the relative performance reduction observed for the highly doped materials at low T_r . As already discussed above, the decrease of the normalized space-charge field must be attributed to a decrease of the effective PR trap density N_A , resulting in a decrease of the PR saturation field E_q . The decrease of the effective PR trap density can be explained by enhanced detrapping of charge carriers captured in conformational traps due faster conformational dynamics of the conducting polymer matrix for $RT > T_g$ (i.e. $T_r < 0$). This, in turn, indicates that conformational traps are an important trap species in the type of PR polymers investigated here.

Please note, that the term “conformational traps“ in this case may include PR traps, which have been postulated to arise from the complex formation between two carbazole moieties [193, 194]. Conformational changes in the polymer matrix may crack such a sandwich complex, thus releasing the captured charge carrier. However, it is to be pointed out that carbazole sandwich complexes are supposed to be deep traps in contrast to classical conformational traps, which are commonly considered as shallow traps. As will be discussed in “5.4.1.3.6.) Conclusions on the nature of the PR traps” on page 296 and in “5.5.3.) Discussion of the dark decay behavior” on page 322, there is indeed indication for the occurrence of carbazole sandwich complexes acting as deep PR trapping sites in the materials under consideration.

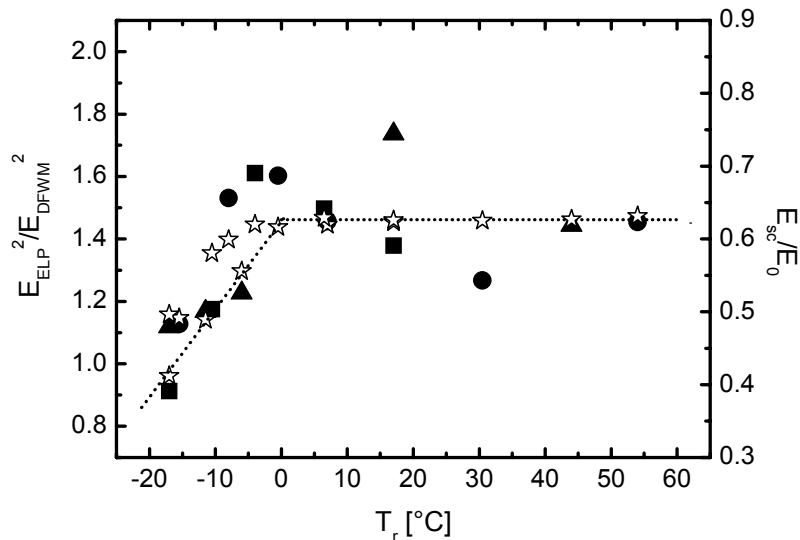


Figure (5.2 - 9): Ratio E_{ELP}^2/E_{DFWM}^2 as a function of the reduced temperature $T_r = T_g - RT$ for the materials containing 50%wt (solid squares), 40%wt (solid circles) and 30%wt (solid triangles) chromophore. The open stars depict the theoretical dependence of the normalized space-charge field on T_r , as calculated from photo-physical measurements for the same set of materials using Schildkraut’s model [196]. The dotted lines are guide to the eye.

Finally, the experimental observation will be discussed that seemingly no performance optimum occurs for the lowly doped materials containing only 20%wt and 30%wt chromophore within the range of reduced temperatures investigated (figure (5.2 - 2)). This might be due to two reasons.

At first, it might be due to the poling properties of the materials considered. As just discussed above, the PR space-charge field decreases for decreasing T_r below $T_r \cong -5^\circ\text{C}$. Considering figure (5.2 - 4), the external fields required in order to achieve the first transmission maximum apparently tend to level off for the lowest values of T_r for the material containing 50%wt chromophore. In contrast, for the materials containing less chromophore, this tendency is less pronounced within the range of reduced temperatures tested experimentally. As discussed before, the occurrence of a performance optimum as a function of T_r observed for the highly doped materials must be attributed to two counteracting processes, namely an increasing orientational mobility of the NLO chromophores improving the steady-state PR performance as a function of decreasing T_r , on the one hand, and a decreasing PR space-charge field lowering the steady-state PR performance as a function of decreasing T_r on other. While the latter has been found to be very similar for all materials investigated, the first process seemingly loses in importance as the chromophore content increases. Thus, one may conclude that the “crossing point” of these processes leading to a change of the general trend of the PR performance as a

function of decreasing T_r shifts to lower values of T_r as the chromophore content is reduced. This would agree with the experimental results, since the performance optimum occurs a higher T_r for the materials containing 50%wt chromophore as compared to those containing 40%wt chromophore. Following this argumentation, one should expect performance optima also for the materials containing even less chromophore, however, for even lower T_r .

Secondly, the fact that seemingly no performance optimum occurs for the lowly doped materials may be explained considering again the PR space-charge field. The decrease of the normalized space-charge field as depicted in figure (5.2 - 9) is very similar for the materials containing 50%wt down to 30%wt chromophore. Hence, one can safely assume that the materials with 20%wt chromophore content will follow the same trend. The absence of a performance optimum for lower chromophore doping levels, therefore, cannot be understood by means of a less pronounced decrease of the effective PR trap density N_A . However, the observed performance optimum as a function of the relative temperature seemingly shifts to lower T_r , when the doping level is reduced, as is indicated by comparing the experimental data on the materials containing 50%wt and 40%wt chromophore. Consequently, one may assume a performance optimum for the even lower doped materials occurring at further reduced relative temperatures, which are already beyond the range investigated. Since the decrease of the effective PR trap density as a function of the reduced temperature was found to be similar for all four material series investigated, this implies an increase of the PR saturation field as a function of a decreasing doping level, i.e. as a function of an increasing density of charge transporting moieties. According to eq. (2.5 - 3) an increase of E_q may be due to a decreasing permittivity $\langle \epsilon \rangle$ and/or an increasing trap density N_A . An increase of the trap density as a function of an increasing density of charge transporting moieties must be expected for the case of conformational traps, which is supposed to be an important trap species in the investigated materials, as already proposed before. Furthermore, $\langle \epsilon \rangle$ must be expected to decrease as a function of decreasing doping level, since the number density of a strongly polar material component (the NLO chromophores) is reduced. Since both these effects cooperate, one need not judge their relative strength but only prove their cooperative result. For this purpose, the absolute PR saturation field E_q was estimated from the experimentally determined PR gain for a set of materials with different chromophore content but reasonably similar relative temperature by applying eq. (2.3 - 34), eq. (2.5 - 102) and eq. (5.2 - 5) and with the polarization anisotropy according to eq. (4 - 46). The results are depicted in figure (5.2 - 10). As expected E_q increases significantly when the chromophore doping level decreases, which strongly supports the interpretation given above.

Please note that E_q increases markedly stronger as a function of decreasing chromophore doping level as one might expect considering only the proposed increase of the trap density as a result of the increasing number density of charge transporting sites. This might be attributed to the cooperative influence of the bulk permittivity. This point of view may be tested assuming that $\langle \epsilon \rangle$ is directly proportional to the number density of chromophores and that N_A is directly proportional to the number density of carbazole moieties in the considered materials. Therewith one can calculate the relative increase of E_q as a function of the chromophore content with respect to its value for 50%wt chromophore as it might be expected from eq. (2.5 - 3). The inset of figure (5.2 - 10) shows the thus obtained results together with the corresponding relative increase of the PR saturation field experimentally estimated as described above. Accounting for the strong simplifications applied, the agreement is very reasonable, which gives further support for the interpretation discussed above.

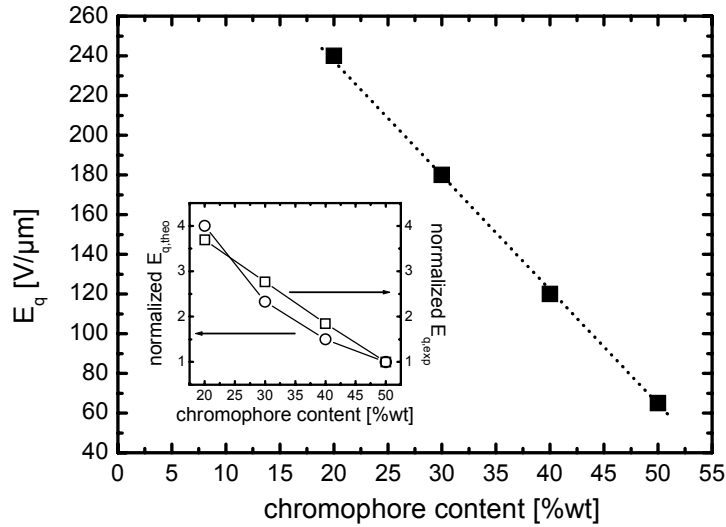


Figure (5.2 - 10): Estimated absolute E_q for the materials 50c at $T_r = -4^\circ\text{C}$, 40d at $T_r = -1^\circ\text{C}$, 30c at $T_r = -6^\circ\text{C}$, and 20c at $T_r = -4^\circ\text{C}$. The dotted line is a linear fit.

Inset: Relative change of E_q as a function of the chromophore doping level with respect to E_q for material 50c. Open squares: Experimental data corresponding to the main plot. Open circles: Theoretical values as calculated from eq. (2.5 - 3). For details see text. The lines are guide to the eye.

Presuming free orientational mobility of the chromophores it is clear from eq. (2.5 - 69) that, for a decreasing chromophore content (i.e. A and C in eq. (2.5 - 69) will be smaller), a larger value of the product $E_{ext}E_{SC}$ will be necessary in order to achieve a certain PR refractive index modulation. However, according to eq. (5.2 - 2) for small values of E_0 (which is the projection of E_{ext} onto the grating wave vector) as compared to E_q , E_{SC} first increases linearly as a function of E_0 , whereas it is limited by E_q if E_0 becomes much larger than E_q . Thus, according to eq. (2.5 - 69), the PR refractive index modulation first increases as a function of E_{ext}^2 for small values of E_0 as compared to E_q and finally becomes a linear function of E_{ext} for values of E_0 much larger than E_q , i.e.:

$$\Delta n_{DFWM} \propto N E_{ext}^a \quad \text{eq. (5.2 - 10)}$$

where N is the number density of chromophores and with $a \rightarrow 2$ for $E_0 \ll E_q$ and $a \rightarrow 1$ for $E_0 \gg E_q$. Hence, the larger is the ratio E_0/E_q the more E_{ext} must be increased in order to compensate for a decreasing effective PR trap density (and, thus, a decreasing E_q) if a given PR refractive index modulation is to be achieved. It is clear from the discussion before that an increase of the ratio E_0/E_q is the basic reason for the occurrence of an PR performance optimum in T_r for $T_r < 0^\circ\text{C}$. As discussed before, E_q (at a fixed T_r) is the larger the smaller the chromophore content, however, the same applies to E_0 according to eq. (2.5 - 69). On the other hand, according to figure (5.2 - 10) E_q increases by almost a factor of 4 from material 50c to material 20c, whereas E_0 only increases by about a factor of 2. This relationship can be taken as representative for the entire set of materials investigated, i.e., for a given T_r both $E_{ext}(\eta_{max})$ (i.e. E_0 required in order to reach the first diffraction maximum) as well as E_q increase as a function of a decreasing chromophore content, but the latter increases markedly stronger than the first. Hence, for a given T_r the ratio E_0/E_q decreases as a function of a decreasing chromophore content. In quantitative terms, $E_0/E_q \approx 0.38, 0.28, 0.25,$ and 0.24 for the materials 50c, 40d, 30c, and 20c, respectively. This results in an increase of the power exponent a in eq. (5.2 - 10) as a function of decreasing chromophore content. Figure (5.2 - 9) indicates that the relative decrease of the effective PR trap density as discussed above is similar for all materials investigated. Thus, the

relative decrease of E_q is similar as well, but its effect on eq. (5.2 - 10) decreases with decreasing chromophore content. In turn, if the effect on eq. (5.2 - 10) shall be similar for all chromophore doping levels, one must imply that the effective PR trap density would have to decrease the stronger the smaller the doping level, i.e. T_r would have to be the lower the smaller the doping level. Accordingly, the position of the performance optimum in T_r , which can be observed for the series of materials containing 50%wt should shift to smaller values of T_r if the chromophore content is decreased, as proposed before, which was indeed observed for the material series containing 40%wt chromophore. Based on the current discussion, the occurrence of a performance optimum in T_r furthermore may also be expected for the materials containing 30%wt chromophore and 20%wt chromophore, however, at even smaller reduced temperatures below the range covered by the presented experiments, as assumed before.

Please note that a threshold condition for the expected occurrence of the performance optimum in terms of the ratio E_0/E_q cannot be provided on basis of the above theoretical considerations due to the nonlinear character of the problem. This becomes clear when inserting eq. (5.2 - 2) into eq. (2.5 - 69) which yields the following simplified relationship for the PR refractive index modulation underlying the even more simplified expression eq. (5.2 - 10):

$$\Delta n_{DFWM} \propto NE_0^2 \sqrt{\frac{1}{1 + (E_0/E_q)^2}}, \quad \text{eq. (5.2 - 11)}$$

where the trigonometric term relating E_0 to E_{ext} is omitted. According to figure (5.2 - 10), E_q scales almost linearly with the chromophore content. In contrast, the required E_0 in order to compensate for a decrease of E_q due to a decreasing apparent trap density as discussed before enters into eq. (5.2 - 11) to the power of a with $2 < a < 1$ (here a is even close to 2). Accordingly, a smaller relative increase in E_0 will be required for the aforementioned compensation if N is smaller. Hence, the threshold condition for the ratio E_0/E_q must be expected to decrease as a function of decreasing chromophore content. Indeed, the performance optimum for the material series containing 40%wt chromophore is correlated with a ratio $E_0/E_q \approx 0.33$ (material 40e).

Both explanations for the experimental fact that seemingly no performance optimum occurs for the lowly doped materials predict the same trend and, thus, cooperate. Accordingly, one should expect a steady-state PR performance optimum as a function of T_r in any case, however, the performance optimum should occur at lower T_r as the chromophore content is reduced. In the case of the lowly doped materials this point is already beyond the lowest T_r experimentally applied and, thus, not observed here.

5.2.2.3.) Quintessence of the investigations on the steady-state performance at varying glass-transition temperatures

In conclusion, the glass-transition temperature T_g was found to be a factor of outstanding importance for optimizing the steady-state performance of organic PR materials containing large amounts of molecular dipoles. It was demonstrated that there is a performance optimum in highly-doped materials, which is a result of two counteracting effects: On the one hand, the orientational mobility of the chromophores becomes better with decreasing T_g at constant ambient temperature leading to a reduction of the external field required to achieve a certain degree of poling. This was confirmed by transmission ellipsometric experiments. On the other hand, the conductivity contrast m^* and, most importantly, the PR saturation field E_q decrease, both lowering the PR space-charge field E_{SC} . The decrease of E_q as a function of the reduced temperature $T_r = T_g - RT$ for $T_r < 0^\circ\text{C}$ can be attributed to a decrease of the effective PR trap

density due to slow collective motion of the photoconducting polymer matrix, which leads to a relieved release of charge carriers trapped in conformational traps. Observations similar to the ones reported here have been made with various other chromophores in the PVK matrix [165, 171]. However, it remains unclear whether this can be generalized also to PR materials based on different photoconductors.

5.2.3.)The relation between the glass-transition temperature and the dynamic performance in PVK based PR polymers

The possibility of in-situ poling, i.e. the orientation of electrical dipoles in an electrical field, is essential for the “orientational enhancement mechanism“ to take place and, thus, for the excellent performance of the material class of PR polymer composites. It is clear, that the quality and the dynamics of the poling process strongly depend on the orientational mobility of the dipoles in the surrounding polymer matrix, which may be considered as delimited by the internal free volume of an amorphous polymer. According to “2.4.1.3.1.) Free-volume theory” on page 74, the glass-transition temperature T_g can be regarded as a measure for this and is, therefore, of outstanding importance for the steady-state and the dynamic performance of PR polymers. After having investigated the influence of T_g and the chromophore content on the steady-state performance of PVK based PR polymer composites in the preceding section, now the influence of these parameters on the dynamic properties of the investigated materials will be studied by means of DFWM and ELP experiments. The influence of T_g on the dynamic properties of PVK based PR polymer composites was investigated first by Bolink et. al. [191]. Surprisingly the authors found only little dependence of the PR grating dynamics on T_g . Since the response time is one of the technically most important properties of holographic storage media such as PR polymers, this feature will be elaborated upon in much more detail here, covering the influence of the glass-transition temperature as well as the chromophore content. For now the build-up dynamics of the holographic grating will be focussed upon, whereas its decay dynamics will be elaborated upon later.

In order to determine the build-up dynamics of PR gratings in the concerned materials, DFWM experiments were carried out and evaluated according to “4.2.) Wave mixing experiments” on page 181 and as described on page 226 ff. The experiments were initialized by switching the first laser beam (I_{01}) on, while the sample was already illuminated by the second beam (I_{02}). The externally applied field required for maximum diffraction efficiency $E_{ext} = E_{ext}(\eta_{int,max})$ was chosen for the experiments. Under identical experimental conditions all samples then reach the same the total index modulation, independently from T_g . Accordingly, different field values were applied for the different materials investigated (figure (5.2 - 2)), depending on the chromophore content and on T_g . One might expect, that the electrical field has noteworthy influence on the response times. However, only a slight decrease of the response times was found for a particular material with increasing external field up to $E_{ext} = E_{ext}(\eta_{int,max})$. In contrast, for constant chromophore content, it was found that the change of the response times as a function of T_g is up to three orders of magnitude as will be shown later. Furthermore, $E_{ext}(\eta_{int,max})$ increases with T_g , as do the response times (figure (5.2 - 12)), while the latter slightly decrease when increasing the field for a particular material (i.e. at constant T_g). Also, the change of the response times for constant T_g above the ambient temperature, but varying chromophore content, is at least one order of magnitude larger than a change which may be attributed to the different fields applied to the samples. Accordingly, the influence of the different external fields on the response times is of minor importance and can be safely neglected as compared to the influence of T_g and the chromophore content. Finally in the low-

T_g regime the response times are quite similar and there is no consistent trend which allows some correlation of the response times with different field values or varying orientational diffusion dynamics.

In order to study the poling process separately from the formation of the PR space-charge field, time-resolved ELP measurements were furthermore carried out. These experiments were initialized by switching on the external field using a fast Reed relays, and the ellipsometric transmission due to the changing birefringence was followed as a function of time. For the sake of consistency, $E_{ext} = E_{ext}(\eta_{int,max})$ as determined by the steady-state DFWM experiments was applied.

Depending on the investigated material, the time resolution of the measurements varied between about 1ms for the materials with the fastest response time and 3s for the slowest material in both the DFWM and ELP experiments. The maximum time resolution of the employed experimental setup could be reasonably estimated to be approximately 100 μ s. In all cases, the total measurement time exceeded three times the response time constant of the slow process in the bi-exponential fit procedure, which was used to determine the DFWM and ELP response behavior (see below).

5.2.3.1.) Theoretical consideration of the relaxation dynamics in poled polymers

In today's high performance PR polymers the build-up dynamics of the PR grating is basically determined by the build-up dynamics of the PR space-charge field and the reorientational dynamics of the chromophores. The first has been theoretically elaborated upon in "2.5.2.1.2.1.) Build-up dynamics" on page 121 and in "2.5.3.2.2.) Build-up dynamics for the space-charge field in polymers" on page 126. The latter may be described by the transient solutions of the oriented gas model as discussed in "2.4.2.2.) Transient solutions of the oriented gas model" on page 92, as long as the oriented gas model is a valid approximation. Although these two processes actually cannot be clearly separated from each other, the dynamic response of PR polymers will be dominated by only one of them if their kinetics are sufficiently different.

The theory for the build-up dynamics of the PR space-charge field in polymers yields a bi-exponential growth law (eq. (2.5 - 24) to eq. (2.5 - 26)), the particular parameters of which are very complicated expressions containing a very large number of unknown parameters, some of which are experimentally barely accessible. Therefore, eq. (2.5 - 24) may serve as a general model for the PR space-charge field build-up dynamics, but the magnitude of some involved parameters presently cannot be reasonably estimated, which prevents direct comparison between theory and experiment. According to eq. (2.5 - 68) and eq. (2.5 - 69), the PR refractive index modulation depends linearly on the PR space-charge field. Hence, if the build-up dynamics of the PR grating is dominated by the formation of the PR space-charge field according to eq. (2.5 - 24), one would expect a bi-exponential growth law of the PR refractive index modulation Δn having the general form:

$$\Delta n_0 - \Delta n(t) \propto A_1 \cos(a_1 + \omega_1 t) e^{-t/\tau_1} + A_2 \cos(a_2 + \omega_2 t) e^{-t/\tau_2}, \quad \text{eq. (5.2 - 12)}$$

where Δn_0 is the steady-state value. Eq. (5.2 - 12) implies an oscillation during recording a PR grating, which has never been observed in PR polymers so far, which questions the applicability of this growth law to PR polymers on the one hand, or implies that the PR response in polymers is not limited by the build-up dynamics of the space-charge field on the other. Please note, that the theory for the build-up dynamics of the PR space-charge field in crystals yields a mono-exponential growth law (eq. (2.5 - 6) to eq. (2.5 - 9)), which also implies an oscillation, as

already discussed in the corresponding section elaborating upon the photorefractive theory (page 121). As opposed to PR polymers, this oscillation has indeed been observed experimentally during the PR grating build-up, which verifies the theory in this case. The theoretical model for PR crystals, however, does not describe the behavior of the PR space-charge field in polymers correctly, as already discussed in “2.5.3.1.) Limitations of Kukharev’s model” on page 123.

In contrast, if the build-up of the PR space-charge field is much faster than the reorientational dynamics of the NLO chromophores in the polymer matrix, the latter would determine the build-up of the PR grating. According to the preceding discussion, preliminarily this shall be assumed for the PR polymer composites under investigation. Subsequently a general growth law for the PR refractive index modulation will be derived for this limiting case. Please note already here that the assumption of reorientation limited response behavior is only valid for the materials with $T_g > RT$ (i.e. $T_r > 0^\circ\text{C}$). In contrast, the space-charge field formation becomes the limiting factor for the low- T_g materials as will be shown below.

According to “2.5.3.3.) Orientational enhancement effect”, the total refractive index modulation in the investigated materials consists of two contributions, the electro-optic (EO) and the birefringence (BR) contribution. If the polymer is pre-poled as in the present case (i.e. the external field was applied in advance of recording the PR grating), a part of the EO contribution occurs simultaneously to the build-up of the PR space-charge field. After some delay, the chromophores reorient in the total local poling field $E_{T,loc}$, which is the superposition of the PR space-charge field and the externally applied field. As a result, according to eq. (2.5 - 44), eq. (2.5 - 45), eq. (2.5 - 50), and eq. (2.5 - 51) the total refractive index modulation Δn_{tot} becomes the sum of two contributions, an orientationally enhanced electro-optic (EO) contribution and a birefringence (BR) contribution, both of which show the same dependence on the total local poling field $E_{T,loc}$. The particular contributions are:

$$\Delta n_{z, EO, loc} = \frac{1}{2n} C_{EO} E_{T, loc}^2 \quad \text{and} \quad \text{eq. (5.2 - 13)}$$

$$\Delta n_{x, EO, loc} = \frac{1}{6n} C_{EO} E_{T, loc}^2, \quad \text{eq. (5.2 - 14)}$$

and

$$\Delta n_{z, BR, loc} = \frac{1}{2n} C_{BR} E_{T, loc}^2 \quad \text{and} \quad \text{eq. (5.2 - 15)}$$

$$\Delta n_{x, BR, loc} = -\frac{1}{4n} C_{BR} E_{T, loc}^2, \quad \text{eq. (5.2 - 16)}$$

respectively. The constants C_{BR} and C_{EO} are defined in eq. (2.5 - 46) and in eq. (2.5 - 48) and contain, among others, the microscopic optical constants of the NLO chromophores.

From the microscopic constants determined for the DMNPAA chromophore by means of electro-absorption measurements [171] one can estimate the ratio between the orientationally enhanced EO and BR contribution for the experimental geometry on hand, which yields $(\Delta n_{EO} / \Delta n_{BR}) \approx 0.25$ (i.e. $\Delta n_{EO} \approx 0.2 * \Delta n_{tot}$, $\Delta n_{tot} = \Delta n_{EO} + \Delta n_{BR}$). According to “2.5.3.3.3.) The enhancement - a comparison” on page 136, the not-enhanced EO contribution, i.e. when the polymer is purely parallel-plate poled, is 50% of the orientationally enhanced contribution. Thus, assuming instantaneous development of the PR space-charge field, one can estimate the index modulation at the time $t = 0$ as $\Delta n_{EO(not\ enhanced)} \approx 0.1 * \Delta n_{tot}(\eta_{max})$. The assumption of an instantaneously developing E_{SC} , will naturally never be fulfilled in reality. However, this quick calculation can be used to define a cut-off diffraction efficiency, after achievement of which the further grating dynamics can be assumed to be mainly due to orientation. An index modulation of $0.1 * \Delta n_{tot}$ is correlated with a DFWM diffraction efficiency of approximately 3% of the maximum diffraction efficiency. Preliminarily the limiting case of dominantly

reorientation limited response behavior shall be assumed for the investigated systems as noted above and in order to make sure that any change of Δn is then actually due to reorientation, only the data for diffraction efficiencies of more than 10% have been fitted. The good agreement between the observed ellipsometric and DFWM-dynamics for the high- T_g materials validates this procedure.

In order to find an appropriate growth law for the reorientation limited build-up dynamics of the photorefractive grating, the oriented gas model according to “2.4.2.) Electrical poling of organic polymers - the oriented gas model” on page 83 is applied, which is also the basis of the orientational enhancement mechanism. According to this model and for the case of turning on the poling field, the dynamics of the electrical field induced poling process is described by equation eq. (2.4 - 113), which reads:

$$\Delta n_z^{(\omega)}(t) = \frac{N\Delta\alpha^{(\omega)}i_2(a)}{3n^{(\omega)}i_0(a)} \left\{ 1 - e^{-D_2t} - \frac{3ai_1(a)}{10i_2(a)} \left[e^{-D_1t} - e^{-D_2t} \right] + \frac{ai_3(a)}{5i_2(a)} \left[e^{-D_2t} - e^{-D_3t} \right] \right\}.$$

The inverse time constants (i.e. the rate constants) D_n are given by eq. (2.4 - 111):

$$D_n = n(n+1)D$$

where n is a natural number, i_n are the spherically modified Bessel functions of the order n , and a is the energy of interaction between the poling field and the molecular dipoles of the chromophores normalized by the thermal energy, as defined by eq. (2.4 - 57). Further parameters occurring in eq. (2.4 - 113) are not of interest here and are explained in the corresponding section dedicated to the oriented gas model. The build-up rates relevant for the PR grating are D_1 and D_2 , whereas the contribution of D_3 is negligibly small due to the small amplitude of the third-order spherically modified Bessel function $i_3(a)$, i.e. $2ai_3(a)/15i_0(a) \ll 2i_2(a)/3i_0(a)$ and $ai_1(a)/5i_0(a)$. Thus, in first approximation eq. (2.4 - 113) simplifies to:

$$\Delta n_z^{(\omega)}(t) \propto \frac{2i_2(a)}{3i_0(a)} - \left(\frac{2i_2(a)}{3i_0(a)} - \frac{ai_1(a)}{5i_0(a)} \right) e^{-D_2t} - \frac{ai_1(a)}{5i_0(a)} e^{-D_1t} \quad \text{eq. (5.2 - 17)}$$

which can be rewritten to the general form:

$$\Delta n_z^{(\omega)}(t) \propto A_1(1 - e^{-D_1t}) + A_2(1 - e^{-D_2t}) \quad \text{eq. (5.2 - 18)}$$

with:

$$A_1 = \frac{ai_1(a)}{5i_0(a)} \quad \text{eq. (5.2 - 19)}$$

$$A_2 = \frac{2i_2(a)}{3i_0(a)} - \frac{ai_1(a)}{5i_0(a)}$$

Eq. (5.2 - 18) and eq. (5.2 - 19) apply to the DFWM experiments in the limiting case of reorientation limited PR response behavior as well as to the ELP experiments, which are reorientation limited by nature. It must be pointed out, that the reorientation dynamics in the latter experiment may possibly compete with the response characteristics of the electrical RC circuit formed by the capacitance of the PR device and the combined external and internal electrical resistances of the PR device and the high voltage power supply applied, respectively. Since the internal resistance of the power supply is definitely smaller than 40M Ω (maximum output: 1mA at 40kV), whereas the external resistance of a typical PR sample is in the order of G Ω , the load of the latter can be neglected. The zero frequency electrical capacitance of a typical PR sample according to figure (4 - 2) is safely smaller than 100pF, as extrapolated from oscillator detuning at low frequency. Hence, the purely electrical response time of the circuitry

of the applied experimental setup is safely smaller than 0.4ms. From eq. (5.2 - 18) one obtains a bi-exponential growth law similar to eq. (5.2 - 12), but without oscillating prefactors to the exponential terms:

$$\Delta n_0 - \Delta n(t) \propto A_1 e^{-t/\tau_1} + A_2 e^{-t/\tau_2} \quad \text{eq. (5.2 - 20)}$$

Here $\Delta n_0 = A_1 + A_2$ is the steady-state value of the refractive index modulation or the steady-state field-induced birefringence for a given externally applied field in the DFWM experiments or in the ELP experiments, respectively. The time constants τ_1 and τ_2 refer to the rotational diffusion coefficients as $1/\tau_n = D_n$. Please note that the rotational diffusion coefficients do not refer to molecular axis of the chromophores (there is only one molecular rotation axis). According to eq. (2.4 - 111), the oriented-gas model predicts a constant ratio of $\tau_1/\tau_2 = 3$. Furthermore, in the weak poling limit ($0 < a \leq 0.1$) the ratio of the pre-exponential factors according to eq. (5.2 - 19) is predicted as $A_1(a)/A_2(a) \approx -6 \approx \text{constant}$. The experimental data (see next paragraph for details), however, do not agree with the above predictions, which strongly indicates that the oriented-gas model cannot be applied to this problem as assumed before. The basic flaws of this model are (i) that interactions between the chromophores are neglected, and (ii) that it does not take into account interactions of the chromophores with the surrounding polymer matrix.

Therefore, in analogy to poled EO polymers, it seems most reasonable to describe the grating build-up dynamics in PR polymers phenomenologically, using either a stretched exponential fit (often referred to as Kohlrausch-Williams-Watts (KWW) fit) according to the general growth law:

$$y(t) \propto e^{-\left(\frac{t}{\tau_{KWW}}\right)^\beta}, \quad \text{eq. (5.2 - 21)}$$

where $\beta > 1$ is the stretching factor and τ_{KWW} is the time constant, or a bi-exponential fit function [199]. A KWW fitting function with $\beta = 2$ was already successfully applied to describe the initial onset of the holographic grating build-up in a PR polymer composite, assuming that the PR space-charge field build-up dynamics determines the dynamic behavior in the interval considered [225, 226]. However, changes at longer times were not taken into account. Bi-exponential fits (i.e. formally like in eq. (5.2 - 20)) turned out to result in the best possible agreement with the experimental data on a linear and on a logarithmic scale even for changes at longer times. For completeness, as an experiment the data were also fitted to a tri-exponential growth law, but the fit algorithm (Levenberg-Marquardt) did not reliably converge. It is clear that it is a priori not appropriate to attribute the two exponential terms to distinct physical processes, since there is no clear physical model justifying this evaluation method.

Relaxation times obtained using a KWW fitting formalism cannot be directly compared to relaxation times determined by means of bi- or, more generally, multi-exponential fitting. Thus, a unified measure is required, which enables a reasonable judgement of the dynamic behavior of the relaxation dynamics in PR polymers independent from the particular fitting formalism applied. According to [199] the exponential terms of a bi-exponential fit may represent a distribution of relaxation times for the chromophores due to differences in the local environment. Hence, an average logarithmic relaxation time may be defined by the first logarithmic moment m_1 according to:

$$\langle \ln \tau \rangle = m_1 = \int_{-\infty}^{\infty} \ln(\tau) \rho(\ln(\tau)) d(\ln(\tau)) \quad \text{eq. (5.2 - 22)}$$

where ρ is the distribution function of the relaxation times τ . This definition can be understood considering a strongly simplified dependency of the relaxation times on T_g which may be written as:

$$\tau = \tau_0 e^{\left[\frac{E_A(T-T_g)}{k_b T} \right]}, \quad \text{eq. (5.2 - 23)}$$

It is physically more reasonable to assume a distribution of activation energies $E_A(T-T_g)$ in eq. (5.2 - 23), rather than of pre-exponential factors τ_0 . An average activation energy $\langle E_A(T-T_g) \rangle$ then corresponds directly to $\langle \ln(\tau) \rangle$ [199]. As shown in [200], $\langle \ln(\tau) \rangle$ for a bi-exponential description of time-dependent changes in the polar order can be expressed by:

$$\langle \ln \tau \rangle = A_1 \ln \tau_1 + (1 - A_1) \ln \tau_2. \quad \text{eq. (5.2 - 24)}$$

The $\langle \ln(\tau) \rangle$ values can be compared with the corresponding values obtained by a KWW-fit, using the expression [199]:

$$\langle \ln \tau \rangle_{KWW} = \left(\frac{1}{\beta} - 1 \right) \Pi(1) + \ln \tau_{KWW}, \quad \text{eq. (5.2 - 25)}$$

where Π are the digamma functions. This formalism must be applied with care, since the comparison of mean relaxation times according to eq. (5.2 - 24) and eq. (5.2 - 25) is only meaningful, if the distribution is reasonably symmetric, i.e. for $\beta > 1$ and $A_1 \approx 0.5$ [199].

Eq. (5.2 - 24), furthermore, provides the opportunity to combine the time constants obtained from multi-exponential fitting to an average relaxation time parameter, taking into account the weighting of the particular relaxation times. This average relaxation time, of course, does not correctly describe the dynamic behavior of the considered system in detail, but rather may serve as a generalized measure for its relaxation behavior. Hereafter, a generalized form of eq. (5.2 - 24) reading:

$$\langle \tau \rangle = \exp \left[\frac{1}{\sum_i A_i} \left(\sum_i \{ A_i \cdot \ln \tau_i \} \right) \right] \quad \text{eq. (5.2 - 26)}$$

will be utilized in order to obtain a mean relaxation time, if it appears appropriate and reasonable for considering general trends of the dynamic behavior of PR polymer systems investigated within a consistent series of measurements. In particular, in the frame of this thesis this procedure will be applied, (i) in order to combine the two slow relaxation components (times) of a tri-exponential fit, if bi-exponential as well as tri-exponential fitting must be applied to achieve sufficient agreement between fit and experiments carried out on different materials and/or experimental conditions, and (ii) in order to obtain a mean relaxation time from bi- and/or tri-exponential fitting, if only general trends in the relaxation behavior are considered. Please note, that this formalism is not restricted by the symmetry of the distributions of the relaxation times as long as no comparison with KWW fits is attempted.

It must be emphasized that average relaxation times obtained when applying eq. (5.2 - 26) may only represent a rather crude approximation for the “real” relaxation behavior. Hence, eq. (5.2 - 26) must be applied with care, since on the one hand important details may get lost. On the other hand it is an inherent feature of multi-exponential fits that slight variations of the parameters may give similarly good agreement with the experimental data. Therefore, one should in general pay attention to the trends rather than the absolute values. A careful consideration may be necessary in order to draw meaningful conclusions. In the frame of this thesis, this problem will be addressed explicitly whenever advisable.

5.2.3.2.) Experimental results on the T_g dependence of the build-up dynamics of PR gratings in polymers

Figure (5.2 - 11) shows typical examples for the kinetics of the time-dependent build-up of the refractive index modulation in the DFWM experiments carried out, as well as the corresponding fitting curves obtained when using the bi-exponential growth law eq. (5.2 - 18). As already discussed above, only data corresponding to an internal diffraction efficiency larger than $\eta_{int} = 10\%$ were considered.

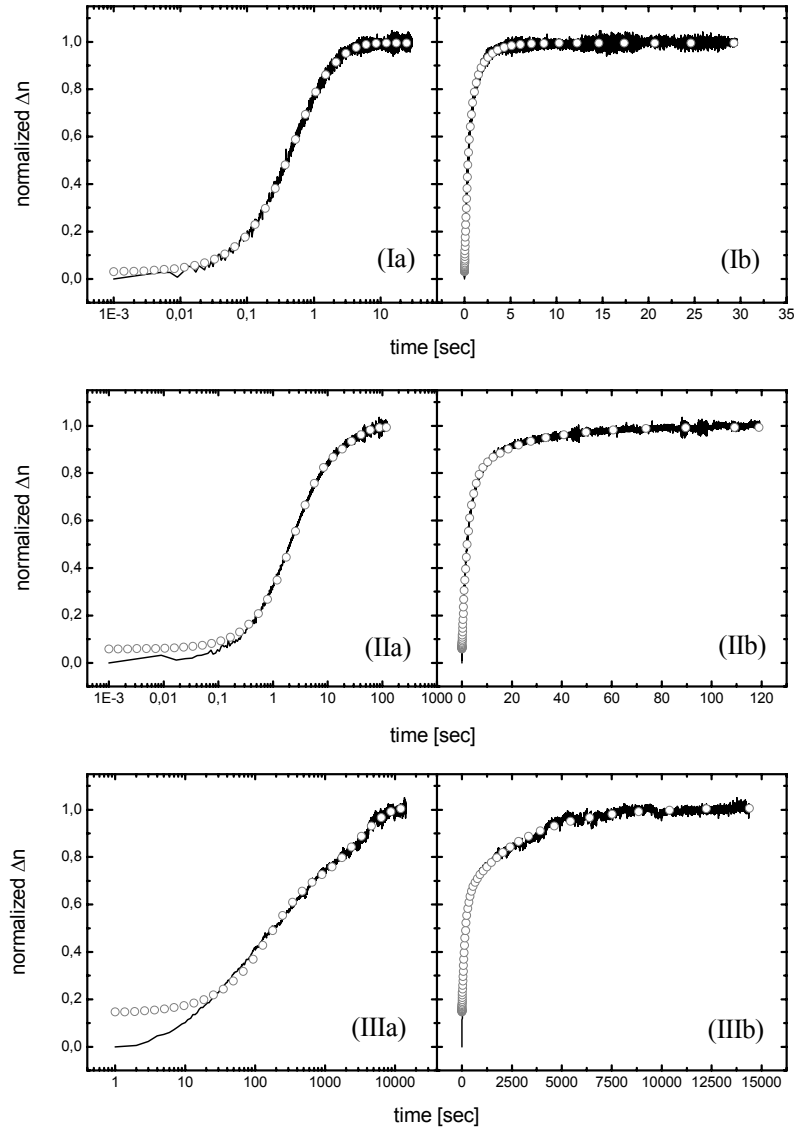


Figure (5.2 - 11): Typical examples of normalized dynamic DFWM growth curves (solid lines) and corresponding fits (open circles) using eq. (5.2 - 20), depicted on logarithmic (Ia - IIIa) and on linear scale (Ib - IIIb). (I) corresponds to material 50e ($T_g = 1^\circ\text{C}$), (II) to 50c ($T_g = 14^\circ\text{C}$), and (III) to 50a ($T_g = 35^\circ\text{C}$). The reduced temperature according to eq. (5.2 - 1) increases from (I) over (II) to (III) from $T_r = -17^\circ\text{C}$ over -4°C to $+17^\circ\text{C}$.

The quality of the bi-exponential fits for reduced temperatures according to eq. (5.2 - 1) of $T_r > 0^\circ\text{C}$, i.e. in the high- T_g regime (figure (5.2 - 11) (III)), is worse than for $T_r < 0^\circ\text{C}$, i.e. in the low- T_g regime (figure (5.2 - 11) (I)). However, the agreement between experiment and fit is

still reasonable even for the worst case of disagreement (figure (5.2 - 11) (III)) and will suffice to consider general trends in the dynamic behavior of the systems investigated. Please note, that case (III) could actually be better approximated using a tri-exponential fit. However, in order to keep a consistent evaluation procedure, in this section all experimental DFWM growth curves were fitted to eq. (5.2 - 20).

The build-up times in four-wave mixing experiments decreased monotonously for decreasing T_g and constant chromophore content, as expected, because the orientational mobility of the chromophores in a viscoelastic matrix increases for decreasing T_g (figure (5.2 - 12)). These results are in contradiction to earlier results reported by Bolink et. al., who found that the decay times were independent from T_g (i.e. independent from T_r) within experimental error [191]. The slow response time τ_2 is roughly one order of magnitude larger than the fast response time τ_1 .

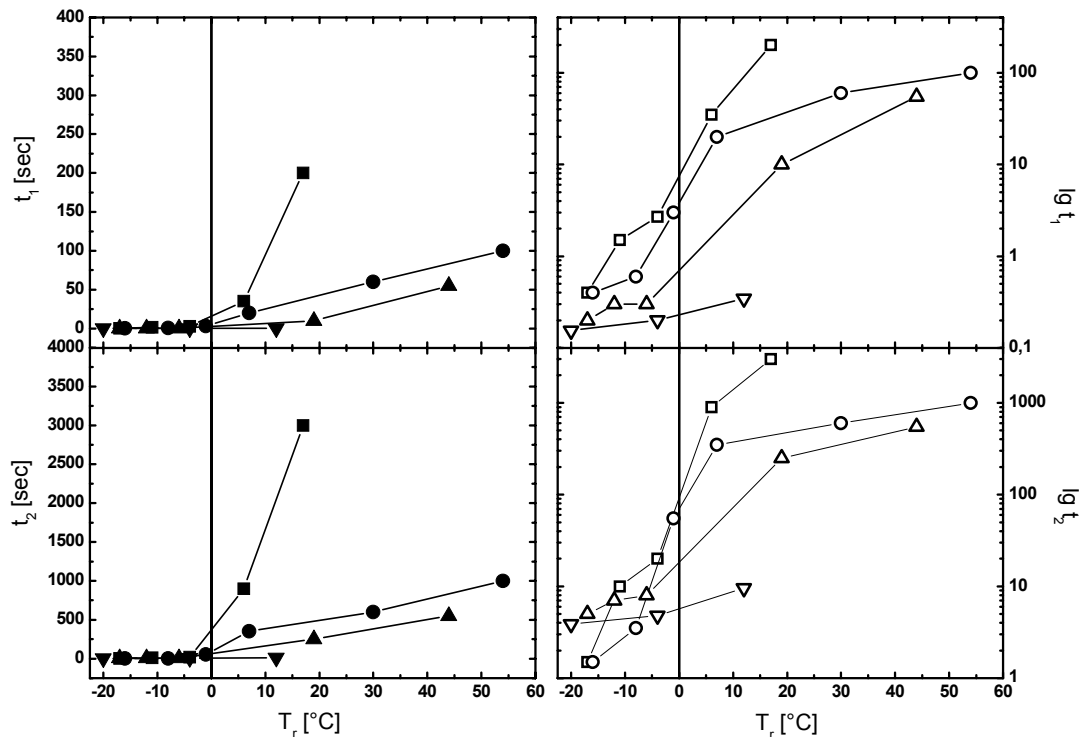


Figure (5.2 - 12): Dependence of the time constants τ_1 (solid symbols) and τ_2 (open symbols) on the glass-transition temperature T_g for different chromophore concentrations: 20%wt (down triangles), 30%wt (up triangles), 40%wt (circles), and 50%wt (squares). Plots to the left: linear time scaling; plots to the right: logarithmic time scaling. The lines are guide to the eye.

The weight factors A_1 and A_2 of the exponential terms in the fit function eq. (5.2 - 20) are shown in figure (5.2 - 13). For the sake of a unified scaling, the sum of A_1 and A_2 was normalized to unity. For $T_r \geq 0^\circ\text{C}$ the factor A_1 increases approximately linearly as a function of decreasing T_r , whereas A_2 decreases, i.e. the faster component becomes more pronounced at lower T_g . For $T_r \leq 0^\circ\text{C}$, there is no consistent trend.

Finally, figure (5.2 - 14) shows the average response times $\langle\tau\rangle$ calculated according to eq. (5.2 - 24) as a function of T_g . The general tendency is naturally similar to the tendencies of the particular response times τ_1 and τ_2 as depicted in figure (5.2 - 12).

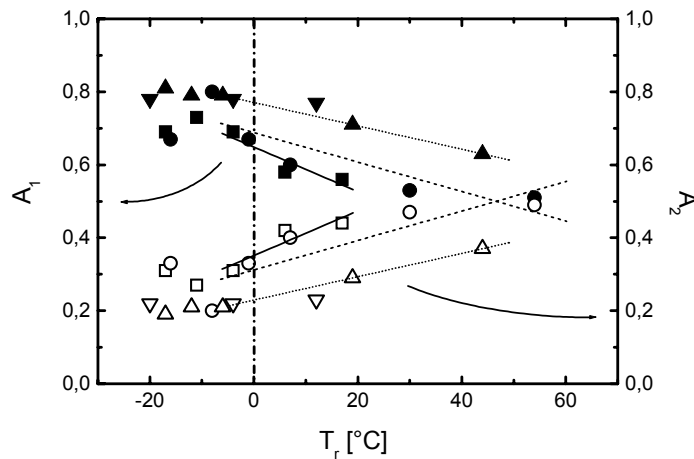


Figure (5.2 - 13): Dependence of the pre-exponential factors A_1 (solid symbols) and A_2 (open symbols) on the glass-transition temperature for different chromophore concentrations: 20%wt (down triangles, dash-dotted line), 30%wt (up triangles, dotted line), 40%wt (circles, dashed line), and 50%wt (squares, solid line). The near-horizontal lines are linear fits to the data for $T_r > 0^\circ\text{C}$ down to the first data point for $T_r < 0^\circ\text{C}$. The vertical line depicts the change from reorientation limited response (to the right) to space-charge field limited response (to the left).

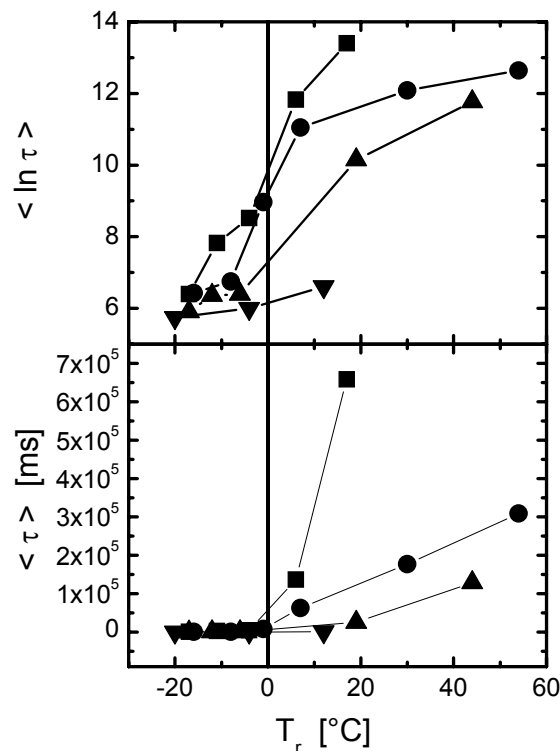


Figure (5.2 - 14): Dependence of the average response times $\langle \tau \rangle$ calculated according to eq. (5.2 - 24) on the glass-transition temperature for different chromophore concentrations: 20%wt (down triangles) 30%wt (up triangles), 40%wt (circles), and 50%wt (squares); (A) logarithmic plot, (B) linear plot. The lines are guides to the eye.

5.2.3.3.) Discussion of the T_g dependence of the dynamic PR performance

According to figure (5.2 - 12), the response times decrease as a function of decreasing T_r . For $T_r < 0^\circ\text{C}$ (i.e. $T_g < RT$, room temperature) they seem to approach limiting values of $\tau_1 \approx 200\text{-}500\text{ms}$ and $\tau_2 \approx 2\text{-}5\text{s}$. This indicates either that the ideal case of gas-like orientational mobility is approached, or that the orientation of the chromophores is no more the delimiting factor for the dynamic behavior of the investigated systems for $T_r < 0^\circ\text{C}$. The former explanation seems rather unlikely, since chromophores embedded in a polymer matrix actually never will act like “free molecules“ in a strict sense. In order to prove the latter assumption, for two samples the pure poling dynamics was determined in a simple transmission ellipsometric experiment. The one of these samples represents the low- T_g regime (composite 50e, $T_r = -17^\circ\text{C}$), whereas the other sample showed a glass-transition temperature little above RT (composite 50b, $T_r = +6^\circ\text{C}$), thus representing the high- T_g regime. The externally applied field was the same as in the holographic experiments. The resulting ellipsometric transmission curves were normalized to the same signal scale as the DFWM-curves and plotted together for each sample (figure (5.2 - 15)).

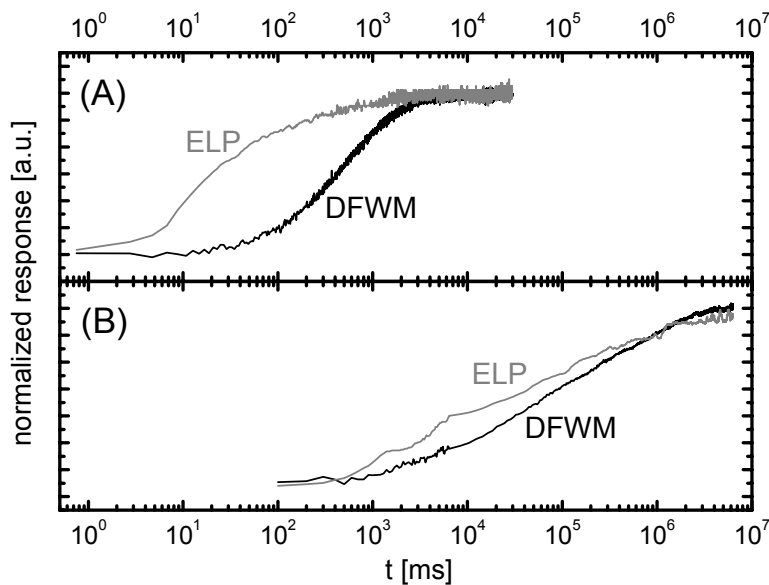


Figure (5.2 - 15): Time dependence of the diffraction efficiency in a DFWM-experiment and the transmission in an ellipsometric (ELP) experiment for two materials with identical chromophore content and different glass-transition temperatures at constant ambient temperature ($RT = 18^\circ\text{C}$): (A) 50e ($T_r = -17^\circ\text{C}$), (B) 50b ($T_r = 6^\circ\text{C}$).

Figure (5.2 - 15) proves that the PR grating in the low- T_g material builds up significantly slower than the ellipsometric transmission, whereas the sample with T_g little above RT shows very similar dynamics in holography and ellipsometry. This strongly indicates, that the response behavior of the materials with $T_g \geq RT$ (i.e. $T_r \geq 0^\circ\text{C}$) is determined by the dynamics of the chromophore orientation in the polymer matrix, as was assumed before. In contrast, in the low- T_g regime, the PR response is apparently delimited by the build-up of the PR space-charge field rather than by the electrical poling process.

At first the high- T_g regime will be considered. According to figure (5.2 - 11), the agreement between the bi-exponential fitting curves and the experimental curves for the high- T_g samples is only moderate (see (figure (5.2 - 11) (IIIa))). This might be attributed to the fact that the orientational dynamics of the NLO chromophores in the polymer matrix is actually not

correctly described by a bi-exponential growth law but rather by two stretched exponential growth terms [204, 205]. Only in the limiting case of vanishing disorder the growth dynamics of the orientational order of the chromophores under the influence of an electrical field in systems like the ones investigated here becomes bi-exponential. In any other case bi-exponential fitting can only be an approximation. However, for the present purpose, i.e. to investigate general trends in the grating build-up dynamics disregarding the different limiting processes, bi-exponential fitting appears sufficiently accurate. Please recall, that multi-exponentially fitting the results of dynamic DFWM PR experiments eventually must be considered as a phenomenological formalism, as discussed above. Thus, it is not necessarily restricted to a certain number of exponential terms.

At constant T_g and for $T_r > 0^\circ\text{C}$ the response times increased consistently for increasing chromophore content, whereas very similar response times were obtained for all materials in the low- T_g regime (figure (5.2 - 12)). This observation leads to the conclusion, that the formation of the PR space-charge field is only slightly affected by the chromophore content, whereas the dynamics of the poling process shows a very strong dependence. This might be attributed to an increasing package density of the chromophores for increasing chromophore content. The chromophore moieties in a guest-host composite like the investigated materials are embedded in random coils of polymer chains. In materials containing a relatively small amount of chromophores, the particular chromophore moieties are mainly surrounded by the viscous polymer matrix (including the plasticizer) and do not notably interact with each other. When the chromophore content is increased at the cost of the matrix, the average distance between the brick-like dye molecules decreases, which may lead to the formation of micro-domains with colligative poling properties and, thus, to the occurrence of self hindrance effects. It seems plausible that it is much more difficult to orient a brick surrounded by other bricks as compared to a single brick surrounded by polymer chains in a composite of the same glass-transition temperature. Further indication for this interpretation comes from the very strong T_g -dependence of the response times for the materials with 50%wt chromophore content as compared to the materials containing less chromophore. Furthermore, the response times for the high- T_g materials with similar T_g increase dramatically when increasing the chromophore content from 40%wt to 50%wt, whereas the corresponding increase of the response times is much less pronounced when going from 30%wt to 40%wt chromophore content.

In contrast to the high- T_g regime, the bi-exponential fit curves correlate very well with the experimental curves for the low- T_g samples figure (5.2 - 11). This supports the basic validity of eq. (5.2 - 12) describing the dynamics of the space-charge field formation in PR polymers. However, oscillatory behavior is implied by this theory, which is not observed unlike in PR crystals, i.e. the prediction of oscillatory behavior cannot be attributed to a general shortcoming of the basic PR theory, which is not that much different for PR crystals and PR polymers. Thus, eq. (5.2 - 12) fails at least partially for describing the build-up dynamics of the PR space-charge field in polymers.

Therefore, the question, which parameter involved in the build-up of the PR space-charge field might determine its dynamic behavior, shall be entered into from another point of view. According to the general PR theory (page 118 ff), the generation of mobile charge carriers and their mobility should be considered the most important parameters in this context. Several investigations of the charge carrier mobility in carbazole based PR polymers have been performed applying time of flight as well as holographic time of flight techniques. On the one hand, results were presented indicating that the charge carriers are able to pass distances in the range of the grating spacing applied here within several milliseconds [138, 201]. This suggests that the charge generation limits the PR response speed in the low- T_g regime. On the other hand, a comparison of holographic time of flight with standard time of flight experiments strongly indicated that the effective drift lengths of the mobile charge carriers is significantly smaller

than the grating spacing applied here [202, 203]. This, in turn, suggests that the charge-carrier mobility is the speed-limiting factor in the low- T_g materials. Further support for the latter assumption comes from investigations on the influence of the sensitizer concentration on the PR performance of PVK based PR polymers, which will be elaborated upon in the next section.

The response times of the low- T_g materials with different chromophore content are quite similar and do not show clear trends (figure (5.2 - 12)). This supports the interpretation given above that the chromophore content affects the poling properties of the materials rather than their electrical properties. In the low- T_g regime the influence of the orientation on the response times becomes secondary as compared to the kinetics of the PR space-charge field formation and, hence, the chromophore content then becomes irrelevant for the PR response behavior.

The normalized weight factors A_1 and A_2 of the exponential terms in eq. (5.2 - 20) are shown in figure (5.2 - 13). For $T_r \geq 0^\circ\text{C}$ the factor A_1 increases approximately linearly with decreasing T_r , whereas A_2 decreases. For $T_r \leq 0^\circ\text{C}$ no consistent trend is observed, but the general impression suggests that A_1 and A_2 may level off for $T_r \leq 0^\circ\text{C}$. These results can be rationalized when taking into account that the limiting process for the grating build-up speed changes at about $T_r \approx 0^\circ\text{C}$ from orientation limited to space-charge field limited, as discussed before.

At first again the high- T_g regime will be discussed. Assuming that the two exponential terms in eq. (5.2 - 20) represent a distribution of relaxation times for chromophores with slightly different local environments as discussed in “5.2.3.1.) Theoretical consideration of the relaxation dynamics in poled polymers” on page 244, the systematic variation of A_1 and A_2 with T_r might indicate that the overall distribution varies as a function of the glass-transition temperature and is narrower for lower T_r , as was found for EO polymers in general [199]. This seems plausible, because the polymer matrix becomes softer as a function of decreasing T_r , which effectively leads to an equalization of the individual molecular environments inside the matrix due to the increased mobility of the moieties of low molecular mass. Accordingly, the contribution of the faster component should increase at the expense of the contribution of the slower component, provided that the latter can be attributed to those local environments of the chromophores, which aggravate their reorientation (i.e., according to eq. (5.2 - 23) require a large activation energy $E_A(T-T_g)$). The strong dependence of the pre-exponential factors on T_g for the materials with 50%wt chromophore content may be attributed to a formation of microdomains, as discussed before. The latter, due to their bigger size, should be more sensitive to a changing elasticity of the matrix than one particular chromophore moiety. Therefore, a stronger dependence of $\langle E_A(T-T_g) \rangle$ in eq. (5.2 - 23) on T_g should be expected. Support for this interpretation comes from the fact that the dependence of the pre-exponential factors on T_g decreases monotonously with decreasing chromophore doping level. However, this interpretation implies that the particular exponential terms are correlated with dedicated physical processes, which is rather speculative as already discussed.

In contrast, in the low- T_g regime the dynamics of the PR space-charge field takes over ruling the grating build-up kinetics, and the distribution of orientational relaxation times for the chromophores due to slightly different local environments becomes unimportant (however, it still may exist). Accordingly, one may expect that the trend described above is not continued for $T_r < 0^\circ\text{C}$, which agrees with the experimental results. The weighting factors seemingly tend to level off, however, there are not enough data points to clearly identify a new trend for $T_r < 0^\circ\text{C}$.

Figure (5.2 - 14) depicts the logarithmically averaged response times obtained according to eq. (5.2 - 24). For $T_r < 0^\circ\text{C}$, i.e. when the space-charge field formation becomes dominant for the dynamic behavior of the investigated materials, one must use an appropriate scaling, which accounts for the mathematical formalism of eq. (5.2 - 24). If the scaling in units of seconds, as

in figure (5.2 - 12), would have been maintained, time constants $\tau_1 < 1$ would have been used in eq. (5.2 - 24) and $\langle \ln(\tau) \rangle$ resulting from this procedure would have become negative. Therefore, in order to interpret $\langle \ln(\tau) \rangle$ as an average logarithmic relaxation time with physical meaning, an appropriate scaling must be applied, for which units of milliseconds were chosen here. As already pointed out in “5.2.3.1.) Theoretical consideration of the relaxation dynamics in poled polymers” on page 244, the logarithmically averaged response times for materials in the low- T_g regime cannot be interpreted as average response times correlated with a distribution of activation energies. They are rather simply weight-averaged response times, since the underlying physical mechanism is not orientational relaxation. Comparing figure (5.2 - 14) with figure (5.2 - 12) proves, that the general trends in the dynamic behavior of the investigated materials are correctly reproduced.

It seems even technically more useful to refer to the average response time than to the individual response times, since the first already contains the appropriate individual weight factors. For optical signal processing and real-time holography only materials with fast response times are useful, i.e. in the present case the materials with low glass transition temperature. The fastest response was obtained with the material 20c, yielding $\langle \tau \rangle = 300$ ms. In contrast, the slow materials of high T_g may be potentially interesting for long-time storage, because they should be expected to show relatively long decay times for a stored hologram as well. However, the time necessary to record the hologram can be problematic, since the advantage of long storage times in the high- T_g materials might be voided by the disadvantage of tremendously long recording times. The decay dynamics of PR gratings, as well as their relation to the recording dynamics will be discussed in detail in later sections.

Last but not least it is important to point out that not only T_g and the chromophore content determine the response times of PVK-based PR polymer composites of the guest-host type. The dynamic behavior is affected by a lot of other factors influencing the orientational dynamics of the chromophores and/or the build-up dynamics of the PR space-charge field. For instance, geometrical factors like the grating spacing are also important [206]. An overview of various PR polymers including their most important benchmarks is given in “3.) Photorefractive polymers” on page 150.

5.2.3.4.) Summary of the investigations on the build-up dynamics of PR gratings at varying glass-transition temperatures

In conclusion, it could be demonstrate that the holographic build-up times in organic PR composites for $T_r > 0^\circ\text{C}$ (i.e. $T_g > RT$) are limited by the (re)orientation of the EO chromophores under the influence of the local total poling field. The response times decrease monotonously with decreasing T_g , mainly due to an improved orientational mobility of the chromophore moieties in the viscoelastic polymer matrix. The dynamic data could be fitted to a bi-exponential decay function with reasonable accuracy in all cases. The fast component strongly dominates at low T_g , whereas the slow and the fast component become almost equally important for high- T_g materials. This observation might be interpreted in terms of a changing distribution of the orientational diffusion time constants for the chromophores in the different materials. The rise time of the PR grating also depends strongly on the chromophore density for constant $T_r > 0^\circ\text{C}$, which might be attributed to a self-hindrance of the chromophores in the highly-doped materials, which reduces the apparent orientational mobility.

In the low- T_g regime the response times of the materials with different chromophore content become rather similar. In this regime, the formation of the space-charge field is the rate-

limiting step in the onset dynamics of the refractive index modulation. In the next section, it will be demonstrated that the charge-carrier mobility must be considered as rate limiting parameter in the build-up dynamics of the PR space-charge field in systems like those investigated in the present paragraph.

Finally, an averaging formalism for the PR response times is introduced, which will be used throughout this work, if appropriate, for reducing the amount of experimental data and to work out general trends.

5.3.)The influence of the sensitizer concentration on the PR performance of PVK based polymer composites

In this section, the influence of the sensitizer concentration on the performance of PVK based PR polymers is investigated. The sensitizer concentration determines the bulk cross section for photoinduced charge generation, which, in turn, determines the photoinduced charge generation rate according to eq. (G - 2) and eq. (H - 7). Since the PR effect is an integral effect, i.e. a large number of charge carriers must be generated in order to obtain a notable PR response, the sensitizer content is thus expected to have a major impact on the PR grating build-up dynamics. One may furthermore expect that the sensitizer concentration might influence the steady-state PR properties, since charged sensitizer molecules may act as coulombic traps within the PVK charge transport manifold, as will be discussed in more detail later in this paragraph.

5.3.1.)Experimental aspects

In contrast to the above investigations on the T_g -dependence of the PR performance, a slightly different type of material was used here, which proved to be more stable against phase separation than the materials investigated in the preceding sections [136]. The improvement in thermodynamical stability was achieved by the utilization of an eutectic mixture of two similar NLO chromophores, i.e. 2,5 DMNPAA and MNPAA (see Appendix D for the chemical structures), instead of solely 2,5 DMNPAA [13]. The materials thus obtained were stable against phase separation up to several months and longer, even for the low glass-transition temperatures T_g adjusted here.

The concentration of the sensitizer (TNF) was varied at the cost of the plasticizer (ECZ) while the content of the component of high molecular mass (the polymer PVK) was kept constant in order to achieve an approximately constant T_g . The particular composition of the investigated materials and their corresponding glass-transition temperatures of $3^\circ\text{C} < T_g < 9^\circ\text{C}$ are listed in table 5-1 on page 211 as well as at the end of this section. The ambient temperature was $20 \pm 0.5^\circ\text{C}$ for all measurements. A general overview of the components, which the investigated materials were composed of, is given in “3.2.5.) Polymer composites” on page 164. PR devices were prepared according to “4.1.) Preparation of materials and sample structure” on page 179. The PR polymer film thickness was adjusted to $d = 63\mu\text{m}$ and the devices were consistently cooled down to room temperature at a cooling rate of approximately $20^\circ\text{C}/\text{sec}$. All samples were characterized immediately after preparation, which resulted in excellent reproducibility for all systems investigated.

DFWM and 2BC experiments were carried out with s-polarized recording beams, the internal intensities of which were determined as described in “4.2.1.6.) Intensity determination” on page 204 yielding $I_{01} = 20\text{mW}/\text{cm}^2$ and $I_{02} = 20\text{mW}/\text{cm}^2$. The reading beam was p-polarized and its intensity was $I_R = 100 \mu\text{W}/\text{cm}^2$. The internal diffraction efficiencies η_{int} , the PR refractive index modulation Δn , and the PR gain coefficients Γ were determined as a function of time applying the setup and evaluation procedures according to “4.2.) Wave mixing experiments” on page 181. An initial relaxation period was applied to the samples in all cases. For this purpose the samples were illuminated uniformly for 30 minutes using recording beam 2. The maximum time resolution of the applied experimental setup could be reasonably estimated to be approximately $100\mu\text{s}$. Lock-in amplifiers were not used for the experiments discussed in this section.

In order to correlate Δn as determined from the DFWM experiments performed with a p-

polarized reading beam with the PR gain coefficient obtained for s-polarized recording beams, the optical polarization anisotropy of the investigated systems as described in “4.2.1.4.) Polarization anisotropy for PR wave mixing experiments” on page 199 was accounted for by the correction factor according to eq. (4 - 46):

$$\frac{\Delta n_p}{\Delta n_s} = - 2.22 .$$

Since many material properties relevant for the PR effect (among others the charge carrier mobility, the charge generation efficiency, and the linear and second order optical properties) depend on the externally applied electrical field E_{ext} , the latter was held constant at $E_{ext} = 39.7V/\mu m$ for all holographic experiments in this section.

In order to ensure that the dynamic behavior of the investigated materials is mainly determined by the build-up kinetics of the PR space-charge field, the poling process was considered separately from the space-charge-field formation by ellipsometric transmission experiments according to “4.3.) Transmission ellipsometric experiments” on page 207. The ellipsometric transmission was determined as a function of time applying the same external electrical field as in the holographic experiments. In analogy to the evaluation procedure described in the preceding section, the resulting curves of the dynamic evolution of the ellipsometric birefringence were normalized and compared with the corresponding normalized curves of the dynamic evolution of the DFWM refractive index modulation. As expected for a relative temperature T_r of $T_r \leq -11^\circ C$ (T_r according to eq. (5.2 - 1)) in all cases, for all investigated materials a relation according to figure (5.2 - 15) (A) rather than to figure (5.2 - 15) (B) was obtained. Thus, one can safely presume that the dynamic evolution of the DFWM refractive index modulation is dominantly determined by the build-up dynamics of the PR space-charge field rather than by the orientational dynamics of the NLO chromophores in the polymer matrix.

The absorption coefficients of the investigated materials were determined as a function the sensitizer content in solid phase by means of UV-VIS spectroscopy using a UViCON 860 spectrometer. A sample containing no sensitizer was used as reference.

Table (5-4): Chemical composition and glass transition temperature of the materials investigated in “5.3.) The influence of the sensitizer concentration on the PR performance of PVK based polymer composites”

Material	DMNPAA	MNPAA	PVK	ECZ	TNF	TPD	T_g
units	[%wt]	[%wt]	[%wt]	[%wt]	[%wt]	[%wt]	[$^\circ C$]
TNF01	25	25	35	14.9	0.1	-	3
TNF02	25	25	35	14.8	0.2	-	3
TNF04	25	25	35	14.6	0.4	-	3
TNF08	25	25	35	14.2	0.8	-	3
(TNF1)	25	25	37	12	1	-	11.5
TNF2	25	25	35	13	2	-	4
TNF5	25	25	35	10	5	-	9

5.3.2.)Experimental results on the sensitizer concentration dependence of the PR performance

As already discussed above, one may safely presume that the build-up dynamics of the PR grating in the materials examined in this section is mainly determined by the dynamic behavior of the PR space-charge field. Hence, there is no reason to fit only internal diffraction efficiencies of more than 10% as done in the section before and as discussed in “5.2.3.1.) Theoretical consideration of the relaxation dynamics in poled polymers” on page 244. Instead, here in all cases the complete diffraction curves were fitted. In contrast to the results presented in “5.2.3.) The relation between the glass-transition temperature and the dynamic performance in PVK based PR polymers” on page 243, the time dependent build-up of the PR refractive index grating for the materials containing 0.1%wt up to 0.4%wt TNF could only be fitted mono-exponentially. For the materials containing 0.8%wt or more TNF, bi-exponential fitting according to eq. (5.2 - 18) was required for a good approximation of the experimental data, in agreement with the results presented in the preceding section.

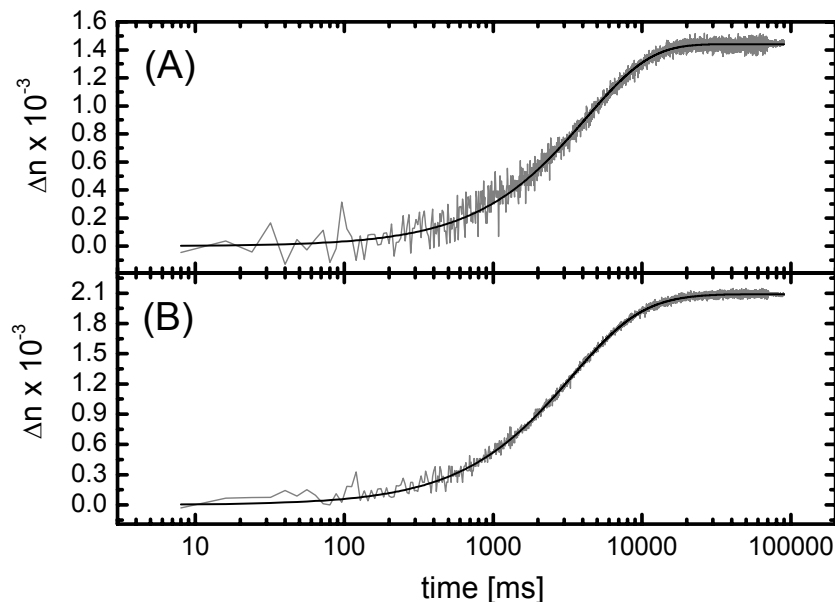


Figure (5.3 - 1): Characteristic examples of the experimental curves for the evolution of the PR refractive index modulation as a function of time (grey lines) and related fitting curves (black lines): (A) Material TNF04 (containing 0.4%wt TNF) and mono-exponential fit; (B) Material TNF08 (containing 0.8%wt TNF) and bi-exponential fit.

Figure (5.3 - 1) shows characteristic examples of the experimentally observed PR grating build-up and the corresponding fitting curves for both cases, mono- and bi-exponential dynamics. The response times for the PR grating build-up in the investigated materials are depicted in figure (5.3 - 2) as a function of the sensitizer content. In order to get a unified measure for the PR grating build-up dynamics for all investigated materials, the time constants obtained from bi-exponential fitting by means of eq. (5.2 - 26) were logarithmically averaged.

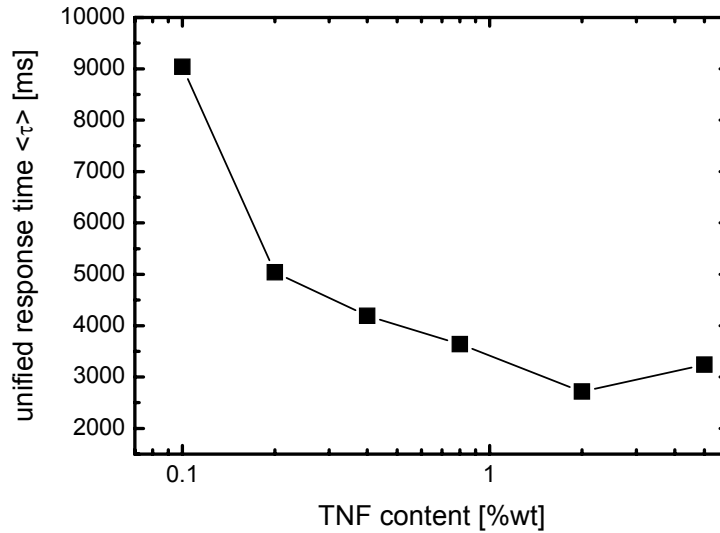


Figure (5.3 - 2): Average response time constants $\langle \tau \rangle$ as a function of the sensitizer content. The response time constants of the materials containing 0.1%wt, 0.2%wt, and 0.4%wt TNF were obtained by mono-exponential fitting, whereas the time constants for the materials containing 0.8%wt or more TNF are logarithmically averaged response times calculated from the results of bi-exponential fitting by means of eq. (5.2 - 26). The solid line is a guide to the eye.

From dynamic measurements of the intensities of the transmitted s-polarized recording beams, the PR gain coefficients Γ were calculated according to eq. (4 - 13) as function of time. The corresponding PR phase shifts ϕ as a function of time were then estimated from $\Delta n(t)$ (for p-polarization) and $\Gamma(t)$ by means of eq. (4 - 17). The polarization anisotropy was accounted for applying eq. (4 - 46). Please note, that the values obtained for ϕ can only be approximations of the actual absolute values, since there may be an unshifted contribution to the overall refractive index modulation determined by DFWM, which is due to an isomerization grating as discussed in “4.2.1.7.) Isomerization gratings” on page 205 and, thus, not of PR origin. Furthermore, the correction factor for the polarization anisotropy is only an approximation as well, as discussed in “4.2.1.4.) Polarization anisotropy for PR wave mixing experiments” on page 199. However, the absolute values for ϕ thus obtained are in reasonable agreement with PR phase shift data determined applying an independent method (moving grating technique) to a PR polymer system similar to the materials investigated here [207]. This proves, that the error made by the aforementioned approximations is small. Moreover, the chromophore content was constant for all investigated materials (i.e. a possible contribution of an isomerization grating was constant) and consistently the same correction factor for the polarization anisotropy was used. Therefore, general trends of the PR phase shift within this series of measurements will be reproduced correctly anyway. Characteristic examples for the PR gain coefficient and the corresponding phase shift calculated as described above are shown in figure (5.3 - 3).

The quasi steady-state PR parameters of the investigated systems were obtained from the experimental values of the time dependent measurements after 90 seconds of recording of the PR grating, i.e. when the experimentally determined holographic parameters (the internal DFWM diffraction efficiency and the PR gain coefficient) do not notably change any more as a function of time for all materials investigated (see figure (5.3 - 1) and figure (5.3 - 3)(A)). The values obtained therewith for the PR refractive index modulation Δn , the modulus of the PR gain coefficient Γ , and the corresponding PR phase shift ϕ as a function of the sensitizer concentration are depicted in figure (5.3 - 4). Both the refractive index modulation and the PR phase shift show a clear trend as a function of the sensitizer concentration.

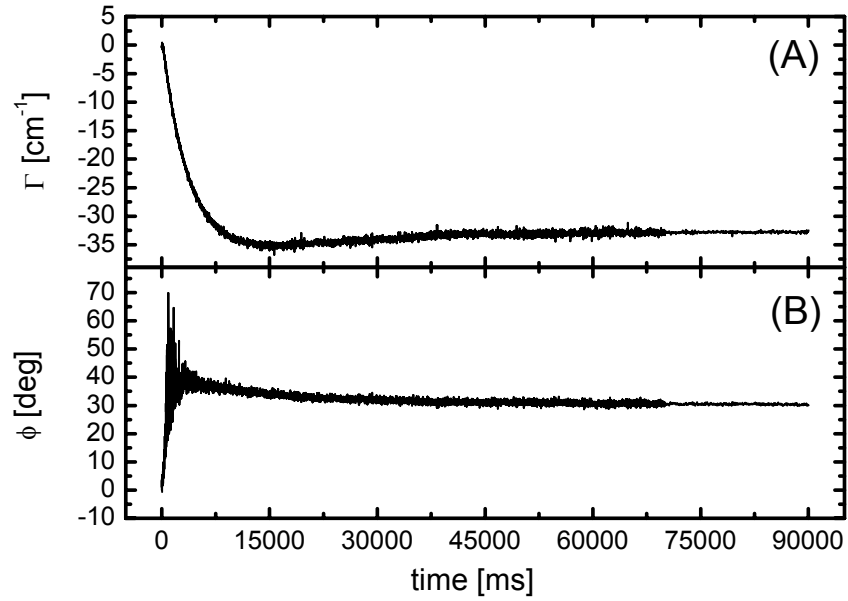


Figure (5.3 - 3): Characteristic examples for the PR gain Γ (A) and the PR phase shift ϕ (B) as a function of time for material TNF04 (containing 0.4%wt TNF).

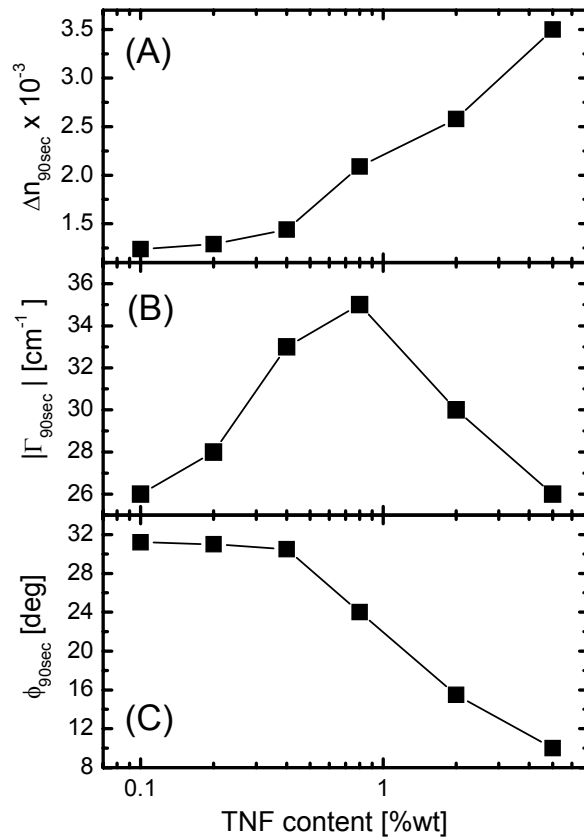


Figure (5.3 - 4): PR refractive index modulation Δn (A), modulus of the PR gain coefficient $|\Gamma|$ (B), and PR phase shift ϕ (C) achieved after 90sec of recording (i.e. quasi steady-state values) as a function of the TNF content for $E_{ext} = 39.7V/\mu m$. Please note, that Γ is in fact negative for the present experimental configuration in the sign systematics used in the frame of this work. The solid lines are guides to the eye.

5.3.3.)Discussion of the influence of the sensitizer concentration on the PR performance in polymers

In the following, at first the absorption of the investigated materials as a function of the sensitizer content will be considered and the expected influence on the charge generation rate according to eq. (G - 2) will be discussed. Then, the results of the holographic experiments will be elaborated upon in the context of the theoretical model of the PR effect according to “2.5.2.1.) The band-transport model of the photorefractive effect (Kukhtarev-model)” on page 119. Although this theoretical model can only be applied to PR polymers with strong restrictions, it will suffice for the purpose of the current discussion. Finally, the influence of the sensitizer concentration on the dynamic DFWM behavior of the investigated materials will be discussed.

The sensitizer molecule TNF forms a charge-transfer complex with the charge transporting moieties (carbazole), which represents the active charge generation site, as already discussed in “2.4.4.) Charge generation and recombination in organic polymers” on page 109 and in “3.2.5.6.) The sensitizer” on page 176. For a low concentration of TNF with respect to the concentration of carbazole moieties, it can be presumed that the number density of charge-transfer complexes increases linearly with the concentration of TNF [182]. Since neither carbazole/PVK ($\lambda_{max} \approx 370\text{nm}$) nor TNF ($\lambda_{max} \approx 450\text{nm}$) for themselves absorb at the operating wavelength of $\lambda_0 = 633\text{nm}$, one should therefore expect a linear increase of the absorption coefficient α_{633} as a function of the TNF concentration, which indeed is found experimentally (figure (5.3 - 5)).

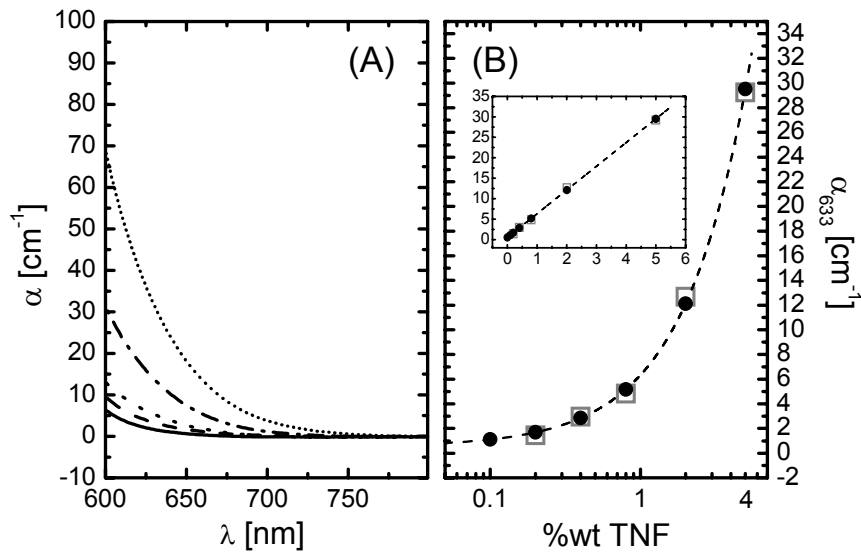


Figure (5.3 - 5): Absorption of the investigated materials. (A) UV-Vis absorption spectra of materials containing 0.2%wt (solid line), 0.4%wt (dashed line), 0.8%wt (dotted line), 2%wt (dash-dotted line), and 5%wt TNF (short dotted line). (B) Absorption coefficients at $\lambda_0 = 633\text{nm}$ as a function of the TNF content. The grey open squares represent experimental data obtained from plot (A), whereas the dashed line is a linear fit and the solid circles are the absorption values for all materials as derived from the linear fit. The inset of (B) is a plot of (B) on linear scale.

Thus, one can conclude that the number density of active charge generation sites increases linearly as a function of the sensitizer content within the range investigated here. For a sample of $63\mu\text{m}$ thickness containing 0.1%wt TNF, the total intensity loss due to absorption after passing the sample is 0.7% with respect to the incident light intensity. The loss in intensity

increases as a function of the sensitizer concentration up to 17% for 5%wt TNF content. Accordingly, it may be presumed that the overall charge generation rate according to eq. (G - 2) (which is the relevant parameter for the PR effect) in a PR device also increases approximately linearly as a function of the sensitizer concentration, since the average illuminating light intensity throughout the device (i.e. averaged from the incident side to the back side approximating the dependence of the intensity on the propagation length as linear) decreases only by about 8% (i.e. from 0.7/2% to 17/2%) as the TNF concentration increases by a factor of 50 (from 0.1%wt to 5%wt).

At first, the relation between the steady-state PR parameters (figure (5.3 - 4)) and the sensitizer concentration in the investigated systems will be discussed and subsequently their dynamic behavior as a function of the TNF content.

As mentioned before (page 233), for the high external fields applied here ($E_{ext} = 39.7V/\mu m$), charge-carrier migration is the dominating transport process for the formation of the PR space-charge field and diffusion can safely be neglected (i.e. diffusion field $E_d \approx 0$). Thus, following Kuktharev's model for the PR effect in crystals, according to eq. (2.5 - 5) and neglecting E_d , the PR phase shift is given by eq. (5.2 - 5):

$$\phi = \text{atan} \frac{E_0}{E_q}$$

Eq. (5.2 - 5) allows for an estimation of the PR saturation field E_q achieved after 90sec of recording as a function of the sensitizer content from the PR phase shifts according to figure (5.3 - 4)(C). E_0 is the projection of the externally applied field onto the grating wave vector K . According to eq. (2.5 - 3) E_q depends on the number density of active PR traps N_A :

$$E_q = q \frac{N_A}{\langle \varepsilon \rangle K},$$

where q is the elementary charge and $\langle \varepsilon \rangle$ is the average bulk permittivity. The small total amount of TNF molecules at otherwise unchanged composition of the investigated materials safely excludes a notable change of $\langle \varepsilon \rangle$ as a function of the sensitizer content. Therefore, any dependence of E_q on the TNF concentration must be due to a varying number density of the PR traps N_A . The history of E_q as a function of the TNF content, c_{TNF} , in the investigated materials as calculated from eq. (5.2 - 5) is depicted in figure (5.3 - 6). Additionally, the value of E_q as estimated for material 50d ($T_g = 7^\circ C$, $T_r = -11^\circ C$) in "5.2.) The PR performance of PVK based polymer composites at varying glass-transition temperatures" on page 226 is shown. The good agreement between the values obtained for the different series of measurements proves the inherent consistency of the evaluation procedure applied.

Apparently, for small amounts of TNF the saturation field does not notably depend on the sensitizer concentration, whereas E_q increases markedly as a function of TNF concentrations exceeding $c_{TNF} = 0.4\%wt$. This indicates that the trap situation in the materials changes significantly between 0.4%wt and 0.8%wt TNF content.

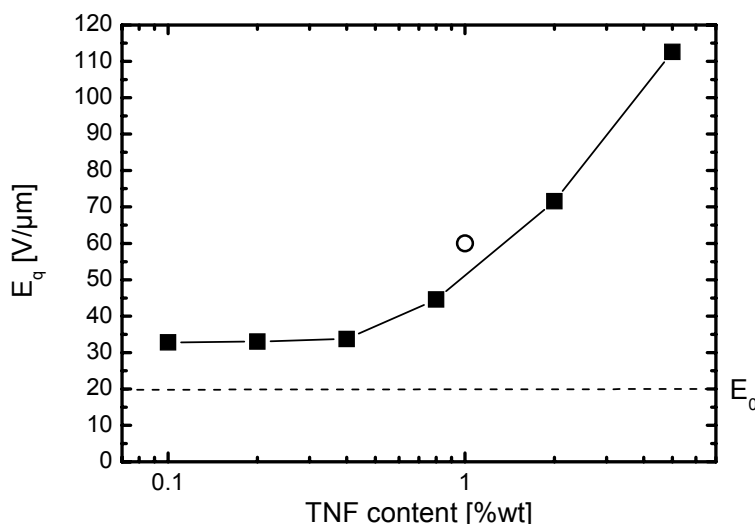


Figure (5.3 - 6): Estimated PR saturation field E_q as a function of the sensitizer content (solid squares). The solid circle represents E_q for material 50d calculated on the basis of the experimental data presented before in “5.2.) The PR performance of PVK based polymer composites at varying glass-transition temperatures” on page 226. The line is a guide to the eye.

Although the exact nature of the charge-carrier traps in PR polymers is still unclear, conformational traps may be considered as an important trap species as already discussed above in “5.2.2.) The relation between the glass-transition temperature and the steady-state performance in PVK based PR polymers” on page 228. Having this in mind, one may assume that the density of states (DOS) of the charge transport manifold should be slightly broadened as a function of an increasing TNF concentration, since the concentration of strongly polar molecular moieties in the investigated systems increases. However, the number density of TNF moieties in the polymer blends is very small as compared to the high concentration of the strongly polar NLO chromophore molecules. Thus, the influence of a changing TNF content on the width of the DOS can safely be neglected. Therefore, neither the depth nor the number density of conformational traps should be notably affected by the sensitizer concentration within the range investigated here.

However, the experimental results may be rationalized assuming that TNF moieties themselves may act as charge carrier traps. It is known from the mechanism of the photoinduced charge carrier generation in a PVK matrix doped with TNF, that a negatively charged, immobile TNF molecule is left behind when a mobile hole is generated (see “3.2.5.6.) The sensitizer” on page 176 and “2.4.4.) Charge generation and recombination in organic polymers” on page 109). Such an immobile, negatively charged TNF moiety represents a localized coulombic pot within the transport manifold of the conducting polymer matrix and, accordingly, may act as a coulombic trap for mobile holes. Coulombic charge carrier traps are often referred to as Poole-Frenkel (-type) traps or Langevin (-type) traps. The Poole-Frenkel effect describes the field assisted thermal emptying of this kind of traps [B5, B20] and the Langevin theory of geminate recombination (see page 115) the recombination coefficient as well as the trapping coefficient for a coulombic trap interacting with a free charge carrier. In the frame of this work coulombic traps will be referred to as „Poole-Frenkel traps“. Poole-Frenkel traps in PR organic amorphous materials have also been proposed by other authors [208]. Assuming the existence of Poole-Frenkel traps as well as conformational traps in the investigated systems the experimental observations according to figure (5.3 - 6) may be explained as follows: For very small sensitizer concentrations (i.e. up to about $c_{TNF} = 0.4\%$ wt) conformational traps dominate the PR behavior

of the materials, since the number density of ionized sensitizer moieties is significantly smaller than the number density of conformational traps. The latter does not depend on the TNF concentration, neither does, therefore, the PR saturation field E_q for $c_{TNF} \leq 0.4\%wt$ (figure (5.3 - 6)). For $c_{TNF} > 0.4\%wt$ the number density of Poole-Frenkel traps stemming from ionized TNF moieties approaches and finally even exceeds the number density of conformational traps leading to a corresponding increase of E_q (figure (5.3 - 6)). Please note, that the number density of Poole-Frenkel traps may be assumed to increase linearly as a function of increasing c_{TNF} in all cases as does the total trap density. This assumption is based on the discussion at the beginning of this section.

The interpretation given above can be verified estimating the involved total trap densities from earlier investigations on the same type of PR polymers focussing on charge-carrier photo-generation, trapping and space-charge field formation in materials of varying chromophore content and glass-transition temperature [196]. In this work, the charge generation efficiency Φ was determined to roughly $\Phi \approx 2 \times 10^{-3}$ at an external field of $E_{ext} = 40V/\mu m$ for material 20c (see table 5-1 on page 211 and [196], figure 5). Furthermore, Φ was found to be almost independent of the chromophore content. Thus, assuming in first approximation that Φ represents the fraction of TNF/ECZ complexes, which have already generated a hole and accounting for the mass density of the investigated materials of approximately $\rho = 1g/cm^3$, one can estimate the number densities of ionized TNF moieties N_{negTNF} as a function of the TNF concentration c_{TNF} , which yields $N_{negTNF}(c_{TNF} = 0.1\%wt) = 3.8 \times 10^{15}cm^{-3}$ up to $N_{negTNF}(c_{TNF} = 5\%wt) = 9.6 \times 10^{16}cm^{-3}$. In [196] a total PR trap density of $N_A \approx 5 \times 10^{16}cm^{-3}$ was estimated from independent measurements (xerographic discharge experiments) for a sample of the type 50c containing 50%wt chromophore and 1%wt TNF (for details see table 5-1 on page 211), whereas $N_{negTNF}(c_{TNF} = 1\%wt) = 1.9 \times 10^{16}cm^{-3}$ is obtained according to the above considerations. Thus, one may conclude that a trap density of $N_A = 3.1 \times 10^{16}cm^{-3}$ should be attributed to conformational traps, the number density of which should not notably depend on the TNF content as discussed above. For the average bulk permittivity $\epsilon = 6.5$ was assumed [185]. By means of eq. (2.5 - 3), one can now estimate the theoretical values for E_q , which might be expected for $N_{A,conformational} = 3.1 \times 10^{16}cm^{-3} = \text{constant}$ and for $N_{A,coulombic}$ according to N_{negTNF} .

Figure (5.3 - 7) shows the resulting theoretical values of E_q . They differ by a factor of about 2.7 from the experimental values but excellently reproduce the experimentally obtained general trend in E_q as a function of c_{TNF} . It is important to point out, that $E_{q,theoretical}$ was calculated from the sum of a constant term (related to $N_{A,conformational}$) and a variable term (related to $N_{A,coulombic}$) changing as a function of c_{TNF} . Thus, a constant offset factor for all c_{TNF} can only occur for a particular relation between the constant term and the variable term, whereas the aforementioned offset factor becomes a function of c_{TNF} for other relations. (For instance, if the constant term is set to zero (doubled), i.e. $N_{A,conformational} = 0$ ($N_{A,conformational} = 6.2 \times 10^{16}cm^{-3}$) is assumed, the offset factor would be 0.14 (4.8) for $c_{TNF} = 0.1$ and increase (decrease) as a function of c_{TNF} to 2.1 (3.5) for $c_{TNF} = 5$). Furthermore, calculating $E_{q,theoretical}$ from eq. (2.5 - 3) for a trap density of $N_A \approx 5 \times 10^{16}cm^{-3}$ [196] naturally yields the same offset factor as compared to the experimental results. This suggests that the general framework of the presented calculations is physically meaningful, but afflicted with systematic errors due to the application of the Kukhtarev model for the current discussion. Therefore, although the absolute values of $E_{q,theoretical}$ and $E_{q,experimental}$ are significantly different, the excellent agreement in the general trends strongly supports the assumption of a coexistence of conformational and Poole-Frenkel traps in the investigated materials and an increasing contribution of the latter as a function of increasing TNF content.

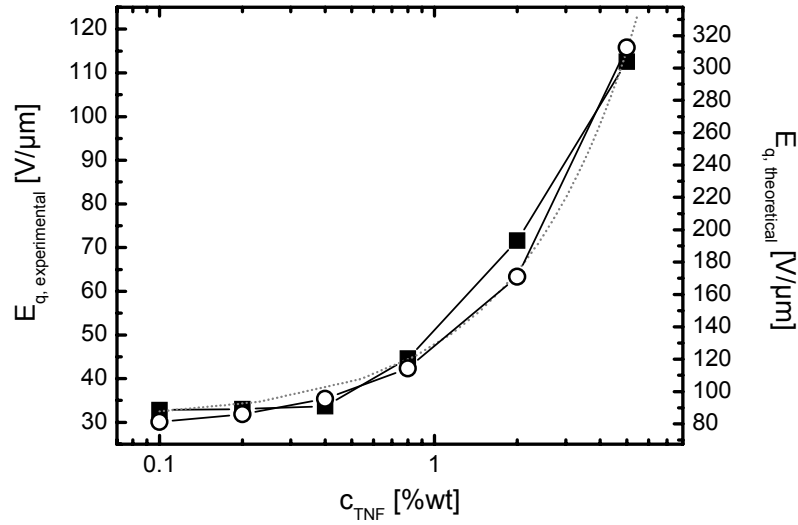


Figure (5.3 - 7): Theoretical (solid squares) and experimental values (open circles) for the PR saturation field E_q . The first were estimated assuming a constant number density of conformational traps and an increasing number of coulombic traps related to the sensitizer concentration as explained in the text. The lines are guide to the eye. The grey dotted line is a linear fit to $E_{q, experimental}$ on linear scale.

As already mentioned before, the number density of Poole-Frenkel traps as well as $E_{q, theoretical}$ increase linearly as a function of increasing c_{TNF} in all cases. This suggests to fit $E_{q, experimental}$ linearly, which yields a function of slightly smaller slope than found for $E_{q, theoretical}$. Hence, besides the aforementioned offset factor of about 2.7 the trap density seemingly increases slightly sublinearly as a function of increasing c_{TNF} . However, the deviation is very small, which also supports the general validity of the interpretations given above.

Subsequently, the dynamic DFWM behavior of the investigated materials as a function of the TNF content as depicted in figure (5.3 - 2) will be discussed.

The PR effect is an integral effect, i.e. a large number of charge carriers must be generated and redistributed in order to achieve a notable PR response, as already discussed in “2.5.1.) Phenomenology of the photorefractive effect” on page 118. Thus, the build-up dynamics of the PR space-charge field may be determined either by the charge carrier generation process or by the charge carrier redistribution process (i.e. by the charge carrier mobility).

In the case of a charge carrier generation limited PR response dynamics the charge carriers are faster redistributed than generated, and the more charge carriers per unit time are generated, the faster becomes the PR response. Considering the time constant for the build-up of the space-charge field τ_g according to eq. (2.5 - 8) one may estimate the relation, which might be expected between an increasing number of charge carrier donors (i.e. TNF/ECZ complexes) and the corresponding increase of the PR response speed:

$$\tau_g = t_0 \frac{(E_\mu + E_d)^2 + E_0^2}{E_d^2 + E_d E_\mu + E_q E_\mu + E_d E_q + E_0^2}.$$

Here, t_0 is the characteristic time constant according to eq. (2.5 - 11):

$$t_0 = \frac{N_A}{f_0 N_D},$$

where f_0 is the microscopic (i.e. in polymers the molecular) charge carrier generation rate, N_D

is the number density of charge carrier donors, and N_A is the number density of charge carrier acceptors (traps). In the Kukhtarev model the characteristic time constant t_0 connects τ_g according to eq. (2.5 - 8) to the charge carrier generation rate.

Charge carrier diffusion is negligibly small in PR polymers, as is accordingly the diffusion field E_d according to eq. (2.5 - 2). Thus, eq. (2.5 - 8) simplifies to:

$$\tau_g = t_0 \frac{E_\mu^2 + E_0^2}{E_q E_\mu + E_0^2}, \quad \text{eq. (5.3 - 1)}$$

where E_q is the well known PR saturation field according to eq. (2.5 - 3):

$$E_q = \frac{q N_A}{\langle \varepsilon \rangle K}$$

and E_μ is the drift field according to eq. (2.5 - 11):

$$E_\mu = \frac{\gamma_R N_A}{\langle \mu \rangle K}.$$

Here $\langle \mu \rangle$ and $\langle \varepsilon \rangle$ are the average bulk charge carrier mobility according to eq. (G - 14) and the average bulk permittivity, respectively, q is the (modulus of the) elementary charge, K is the grating wave vector, and γ_R is the charge carrier recombination rate. For a given γ_R and N_A , E_μ grows large for a small charge carrier mobility and eq. (5.3 - 1) may be approximated by:

$$\tau_g \approx t_0 \frac{E_\mu}{E_q}, \quad \text{eq. (5.3 - 2)}$$

which may be rewritten as:

$$\tau_g = \frac{\langle \varepsilon \rangle}{q \mu n_0}, \quad \text{eq. (5.3 - 3)}$$

where n_0 is the density of free charge carriers. Eq. (5.3 - 3) represents the dielectric relaxation time, which is well-known from the band theory of electrical conduction. The dielectric relaxation time may be interpreted as a measure for the time period, for which a free charge carrier may be unhinderedly accelerated by an applied electrical field. Thus, in this case, the PR response time is solely limited by the charge carrier mobility.

In contrast, if the charge carrier mobility is large, E_μ becomes small and eq. (5.3 - 1) may be approximated by:

$$\tau_g \approx t_0 \frac{E_0^2}{E_q E_\mu + E_0^2}. \quad \text{eq. (5.3 - 4)}$$

This represents the case of charge carrier generation limited response of PR polymers in the applied model.

According to “2.4.4.3.) Langevin theory of geminate recombination” on page 115 and accounting for the fact, that the negatively charged recombination centers are considered as immobile in the investigated materials in very good approximation (i.e. molecular diffusion is neglected as well as possibly occurring electron transfer between neighboring TNF sites, which may occur at sufficiently high TNF concentration), γ_R (according to eq. (2.4 - 188)) may be expressed as:

$$\gamma_R = \frac{\langle \mu \rangle q}{\langle \varepsilon \rangle}. \quad \text{eq. (5.3 - 5)}$$

Inserting eq. (5.3 - 5) into eq. (2.5 - 11) reveals that then E_μ becomes identical to E_q . Furthermore, according to eq. (G - 2) and the discussion in Appendix G on page G4, here the molecular charge carrier generation rate f_0 must be understood as the product of the zero order Fourier component of the illuminating light intensity and the molecular cross section for photo-

excitation of the TNF/ECZ complexes, both of which do not change as a function of c_{TNF} . Therewith, from eq. (5.3 - 2),

$$\tau_g \approx t_0 \quad \text{eq. (5.3 - 6)}$$

should be expected for the case of charge carrier mobility limited PR response and accordingly:

$$\tau_g \propto \frac{N_A}{N_D}. \quad \text{eq. (5.3 - 7)}$$

In contrast, for the case of charge carrier generation limited PR response, eq. (5.3 - 4) must be considered, yielding:

$$\tau_g = t_0 \frac{1}{\frac{E_q^2}{E_0^2} + 1} \quad \text{eq. (5.3 - 8)}$$

and consequently:

$$\tau_g \propto \frac{N_A}{N_D} \cdot \frac{1}{\frac{E_q^2}{E_0^2} + 1}. \quad \text{eq. (5.3 - 9)}$$

For sufficiently small c_{TNF} the number density of potential donors N_D corresponds directly to c_{TNF} , which applies here as discussed before. The number density of acceptors N_A corresponds to the trap density, which is the sum of conformational and Poole-Frenkel traps, as calculated before for figure (5.3 - 7). Therewith one can estimate the history of a normalized measure τ_{gn} for τ_g as a function of c_{TNF} starting with $\tau_{gn}(c_{TNF} = 0.1\%wt) = 1$ and compare it with the corresponding history of the unified PR response times normalized to the response time constant $\langle \tau \rangle_n$ for the material TNF01 ($c_{TNF} = 0.1\%wt$). For eq. (5.3 - 9), the theoretical as well as the experimental values for E_q as depicted in figure (5.3 - 7) were used. The results are shown in figure (5.3 - 8).

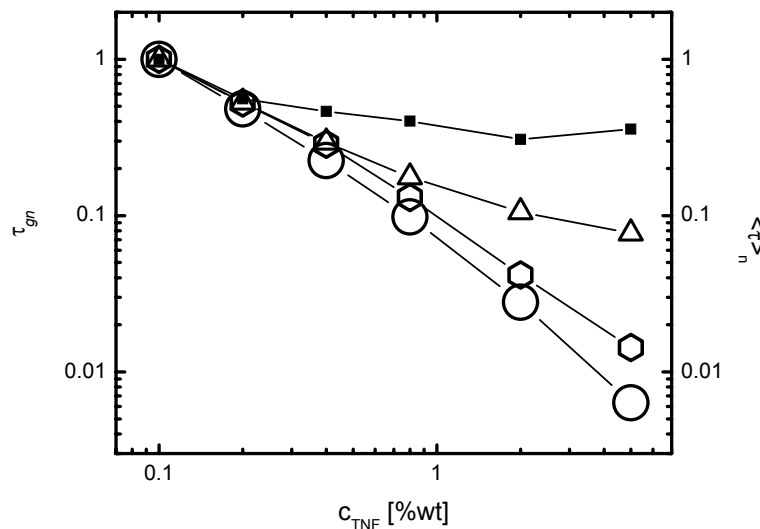


Figure (5.3 - 8): General history of the normalized theoretical time constant τ_{gn} for the case of charge carrier mobility limited PR response (open triangles) and for the case of charge generation limited PR response (calculated with $E_{q,experimental}$ (open diamonds) and with $E_{q,theoretical}$ (open circles)). The solid squares are the unified response time constants normalized to their values for material TNF01 ($c_{TNF} = 0.1\%wt$). The lines are guide to the eye.

For the materials containing more than 0.2%wt TNF apparently none of the theoretically estimated dependencies for τ_{gn} on c_{TNF} actually matches the experimental curve (i.e. $\langle \tau \rangle_n$). However, the general trend for the case of charge carrier mobility limited PR response shows a reduction for the relative acceleration of the PR response as a function of increasing c_{TNF} , i.e. the curvature on double logarithmic scale is positive. The same global trend is found for the experimental curve. In contrast, the theoretical curves for the case of charge carrier generation limited PR response show the opposite trend, i.e. the curvature on double logarithmic scale is slightly negative. Furthermore, also the relatively most reasonable match between the experimental curve and one of the theoretical curves is found for the case of charge carrier mobility limited PR response. These results may be taken as a strong indication for the PR response being limited by the charge carrier mobility in the investigated materials containing more than 0.2%wt TNF. For the materials with $c_{TNF} \leq 0.2\%$ wt the above argumentation does not allow a clear statement.

Please note, that the charge carrier mobility limiting the dynamic PR response does not necessarily correspond to the charge carrier mobility, which is determined by time-of-flight experiments. It has been shown by means of comparison of holographic time-of-flight experiments and “standard” time-of-flight experiments, that the mean free path length of a free charge carrier in a PVK matrix is probably smaller than the grating spacing of $3.1 \mu\text{m}$ resulting from the experimental configuration used here [202, 203]. Therefore, a charge carrier once generated becomes trapped before it reaches its “final destination” and requires detrapping before it can continue migrating. This process must be expected to reduce the apparent charge-carrier mobility. Furthermore, there is indication that detrapping of trapped charge carriers may be induced thermally as well as optically [83]. This questions a clear distinction between charge-generation limited and charge-carrier mobility limited PR response behavior in polymers, since the charge-carrier migration may involve several “charge-generation-steps” for a single carrier.

Finally, the change will be discussed, which is observed for fitting algorithm, which must be applied in order to approximate the dynamic build-up behavior of the PR space-charge field. The build-up dynamics for small $c_{TNF} \leq 0.4\%$ wt could be approximated by a mono-exponential fit, whereas bi-exponential fitting is required when the sensitizer concentration equals or even exceeds 0.8%wt. This threshold coincides with the occurrence of a significant contribution of a second trap species (Poole-Frenkel traps) to the overall PR trap manifold, as discussed before. According to the theory of the PR effect in inorganic crystals, the dynamic response of a material having a single type of PR traps, the number density of which is constant in time, should be mono-exponential. If the trap situation in the PR system is more complicated (e.g. different trap species and/or a time dependent number density), the response behavior is supposed to become more complicated as well. In the investigated PR polymers, when the TNF content exceeds 0.4%wt, two very different trap species must be accounted for, the number density of the one of which (i.e. the Poole-Frenkel traps) is even additionally a function of time, since the number density of negatively charged TNF moieties increases as a function of time. Therefore, a more complicated PR grating build-up dynamics should be expected for the materials doped with more than 0.4%wt TNF as compared to the materials with $c_{TNF} \leq 0.4\%$ wt, which indeed is found experimentally.

Please note that this interpretation does not inherently assume that the particular exponential terms of the applied fitting algorithm might be correlated with distinct physical processes. It has only been stated that the dynamic behavior of a PR material is supposed to become more complicated, if the trap situation becomes more complicated, which agrees with the experimental observations.

5.3.4.) Conclusions from the influence of the sensitizer concentration on the PR performance

In conclusion, there is strong indication that the active PR trap manifold in the common type of PVK-based PR polymers utilizing TNF as sensitizer with a typical concentration of about 1%wt consists of two different types of traps. On the one hand there are conformational traps, which exist ab initio and the number density of which does not depend on the sensitizer content of the particular materials. The conformational traps are the predominant species in materials doped with very small amounts of sensitizer up to 0.4%wt. On the other hand, there are Poole-Frenkel traps (Coulombic traps) stemming from ionized sensitizer moieties. This kind of traps adds to the conformational traps and becomes important for higher sensitizer concentrations of at least 0.8%wt, leading to higher PR saturation fields. For even markedly higher TNF concentrations Poole-Frenkel traps are supposed to become the predominant species in the systems concerned. It is an inherent property of this kind of PR traps that they are generated during the PR recording process and, thus, that their number density is a function of time. The more complicated trap situation for TNF contents exceeding 0.4%wt apparently complicates the PR response behavior.

A comparison of the build-up behavior of the PR grating for increasing TNF content with theoretical considerations on the basis of the Kukhtarev model strongly indicates that the PR build-up dynamics in the investigated type of materials is limited by the charge carrier mobility for TNF concentrations exceeding 0.2%wt.

Please note, that the discussion of the nature of the PR traps and their behavior as a function of time will be picked up again in a forthcoming section when considering the erasure behavior of PR gratings. In this context, the question for the physical process limiting the PR build-up dynamics will also be entered into once more. Another indication for the charge carrier mobility to be the crucial parameter will be found, which additionally supports the interpretations given in this section.

5.4.)The erasure behavior of PR gratings in PVK based polymer composites

Due to the reversible character of the PR effect and the achievable high refractive index modulation, PR polymers are preferable candidates for holographic data storage in re-writable optical memories utilizing multiplexing techniques, i.e., many holograms are written into the same volume element using slightly different Bragg-conditions for each hologram. The theory of holographic multiplexing is elaborated upon in detail in “2.3.3.) Holographic data storage” on page 60. Such memories, among others, are also very useful for associative retrieval of data and promise very high storage density [B8, 210]. As discussed in the section referred to, an appropriate exposure schedule with varying recording times must be applied in order to achieve approximately equal strength of all holograms in the volume, since by writing a particular hologram, all holograms written before are partially erased. Hence, the relation between the dynamics of recording and subsequent erasure of a particular hologram is crucial in order to obtain a large “M-number” $M/\#$, which is defined as the sum of the grating strength of all multiplexed holograms. $M/\#$ is the commonly accepted holographic figure-of-merit describing the multiplexing capabilities of a holographic recording medium. The definition of $M/\#$ requires that all multiplexed holograms are of approximately equal strength. Otherwise the parameter $M/\#$ loses its physical relevance [21].

Up to now, most research efforts in the field of organic PR materials have focussed upon seeking for better steady-state performance (i.e., larger dynamic range), faster response times, and understanding of the basic physics of the PR effect in amorphous polymeric systems. However, only small attention has been paid to the details of the erasure behavior of PR gratings in high performance PR polymers, although fitting erasure curves was performed by few working groups in order to get a general measure for the dynamics of PR polymers. However, this has not become common practice. The results presented in this section unambiguously prove this approach to be unreasonable. The details of the erasure behavior of a PR grating are crucial for almost every potential application proposed for PR polymers. Theoretical works on the PR grating erasure have been published by Liphardt et. al. [211] and Cui et. al. [83], the latter reference of which is also elaborated upon in the theoretical section in this work (“2.5.3.2.3.2.) Cui’s approach to the erasure dynamics” on page 128). Khand et. al. recently presented a comprehensive study of the correlation of the fast growth and erasure rates of a PVK based PR polymer [209]. They found a nearly constant growth/erasure time ratio of approximately 1.5 for a wide variety of applied electric fields and sensitizer concentrations. From the strong correlation between the mentioned rates the authors conclude that a single trap model of the PR effect suffices to describe the dynamics in PR polymers as known from the standard model of the PR effect in crystals (Kukhtarev model). The authors, furthermore, attribute the dominant trap species to Poole-Frenkel type traps formed by ionized sensitizers as already proposed by Grunnet-Jepsen et. al. [208] and as also proposed with restrictions in the preceding chapter “5.3.) The influence of the sensitizer concentration on the PR performance of PVK based polymer composites” on page 257. However, simply using the fast rates for evaluating a practical schedule for multiplexing will fail as shown in [212]. It is necessary to consider the complete erasure behavior of PR polymers in order to obtain a comprehensive picture of the kinetics of the PR effect in polymers and to judge of potential applications.

Subsequently, at first the PR grating erasure in PVK based PR polymer composites derived from the first high performance PR polymer [13] will be investigated in detail taking into account different glass transition temperatures. It will be shown that the grating erasure dynamics depends on the duration, the hologram has been recorded. For the case of polymer

systems having a glass-transition temperature above the ambient temperature (high- T_g systems), evidence will be given that this is attributed to the orientational relaxation of the NLO chromophores embedded in the conducting polymer matrix. On the other hand, it will be shown that a similar experimental phenomenology arises from a changing PR trap situation in the systems with T_g below the ambient temperature (low- T_g systems). Optical activation of deep trapping sites was found to occur in the investigated systems and the impact of this effect on the PR grating erasure will be discussed by means of a theoretical model for the space-charge field erasure in PR polymers. Thereafter the possible nature of the traps occurring in the investigated materials will be discussed. Finally, the influence of the recording time dependence of the hologram erasure dynamics on the potential applicability of the investigated type of holographic storage media in holographic multiplexing will be considered.

In the second part, low- T_g PVK based PR polymer composites will be considered, which are similar to the ones investigated in the first part, but additionally extrinsically doped with relatively high amounts of deep trapping sites. For these systems was observed that the hologram erasure dynamics also depends on the recording time, but is fundamentally different as compared to the case if no extrinsic traps are present. In particular, it was found that the hologram further builds up even after the recording beams have been switched off and the grating is going to be erased by a non Bragg-matched erasure beam. This phenomenon also depends on the duration the hologram has been recorded before. A first experimental indication for a possible explanation of this effect will be given and the influence of typical experimental parameters as well as different material compositions will be considered. The observed behavior will be interpreted in terms of the given phenomenological explanation. A systematic map of the data obtained for systems of different composition applying different experimental conditions will be provided. However, a detailed investigation of the mechanisms underlying the observed erasure behavior as performed for the systems without extrinsic traps was no more conducted in the frame of this work.

5.4.1.)PR grating erasure in systems without extrinsic deep traps

A systematic investigation of the complete erasure behavior of highly modulated PR gratings in today's high-performance PR polymers is presented, where different glass-transition temperatures were taken into account. The rather unfavorable ratio between recording and erasure kinetics basically limits the M/# in PR polymers as shown in [212] and as will be elaborated upon in a later section in the frame of this theses. This finding has been reproduced in [209]. Furthermore, it was found that recording and erasure of a PR grating in polymers are not independent from each other, which significantly complicates the derivation of a recording schedule for multiplexing experiments, as already mentioned above and as also discussed in [212]. The goal of the present work was to get an insight into the mechanism connecting recording and erasure dynamics in PR polymers, which may serve as a basis to solve the aforementioned scheduling problems e.g. by designing materials showing independent recording and erasure dynamics. Furthermore, since kinetics and steady-state performance are affected by even small changes of the glass-transition temperature, a second objective of this study was to find out whether there is an optimum T_g for the application of PVK-based PR composites for multiplexing purposes, as was found for the steady-state performance of the systems investigated ("5.2.) The PR performance of PVK based polymer composites at varying glass-transition temperatures" on page 226).

5.4.1.1.)Experimental aspects

The investigated materials are derived from the first high performance PR polymer [13], but with strongly improved long-term stability [136]. The compositions and the glass-transition temperatures as determined by DSC are listed in table 5-1 on page 211 as well as at the end of the current section. PR devices were prepared according to “4.1.) Preparation of materials and sample structure” on page 179. The active layer thickness was $d = 125\mu\text{m}$. The ambient temperature was $20\pm 0.5^\circ\text{C}$ for all measurements.

For all experiments carried out, the following conditions apply: An electrical field of $E_0 = 32\text{V}/\mu\text{m}$ was applied to the samples. DFWM experiments were carried out using the standard DFWM setup as described in “4.2.) Wave mixing experiments” on page 181 and evaluated by the procedures described in the same section. Lock-in amplifiers were used, which limited the reliable time resolution of the applied setup to about 10ms (10 times the integration time constant of the lock-in amplifiers). The recording beams 1 and 2 were s-polarized exhibiting internal intensities of $I_{01} = 23\text{mW}/\text{cm}^2$ and $I_{02} = 19\text{mW}/\text{cm}^2$, which yields a grating contrast of the interference pattern of $m = 0.995$. A weak (appr. $3\mu\text{W}/\text{cm}^2$) p-polarized beam counterpropagating to recording beam 1 was used for readout. The beam intensities were determined according to “4.2.1.6.) Intensity determination” on page 204. For a typical grating erasure experiment the material was held in the dark for one hour prior to each writing process. For initial relaxation, the devices were then pre-illuminated for $t_p = 30\text{min}$ by beam 2. Hereafter, beam 1 was switched on and after writing the grating for a certain time t_{rec} , both writing beams were switched off simultaneously. The recorded grating was then erased again by a uniform Laser beam having an internal intensity of $17\text{mW}/\text{cm}^2$. Throughout the complete sequence, the external field was applied to the sample. For some particular experiments carried out conditions and procedures slightly deviating from the aforementioned ones were applied in this phase of the work, which will be described together with the correlated particular experiments.

Please note, that the grating must not be erased with a Bragg-matched erasure beam, e.g. by simply switching off one of the writing beams. This would lead to grating refreshment by the interference pattern, which then is formed by the transmitted beam and its portion, which is diffracted by the grating to be erased. Depending on the strength of the existing refractive index grating, significant retardation of the grating erasure process would occur and the erasure dynamics thus obtained would not represent the actual erasure behavior of the PR material. In order to absolutely exclude any kind of grating refreshment during erasure, in the experiments underlying the results presented here the erasure beam originated from an independent Laser and was perpendicularly incident onto the sample.

Since the samples were usually permanently operated for several days, all devices were checked after preparation for their dielectric stability by applying for three hours an external field of $E_{ext} = 40\text{V}/\mu\text{m}$ under uniform illumination by a HeNe Laser beam of similar intensity like the sum of both recording beams. Subsequently, the samples were stored in the dark for three days. As a result, no systematic long-term changes were observed if an identical measurement sequence was repeated several times without manipulating the samples in-between.

In order to investigate the orientational relaxation dynamics of the chromophores in the materials independently from the dynamics of the PR space-charge field, transmission ellipsometric (ELP) experiments according to “4.3.) Transmission ellipsometric experiments” on page 207 were carried out at 690nm operating wavelength using a semiconductor laser diode. The devices were tilted by an internal angle of $\Psi_t = 29^\circ$ and the ellipsometric transmission was determined as a function of time at the same external electrical field as applied in the holographic experiments. The transmission T according to eq. (4 - 52) as a result of the field-induced birefringence Δn_{ELP} according to eq. (4 - 53) was measured for both the growth

(poling) as well as the decay (relaxation) of the orientational order. In the latter case, the sample was short circuited after the sample was poled for a certain time in order to avoid any influence of the slowly responding RC-circuit, which is formed by the samples capacitance and its high electrical resistance.

Table (5-5): Chemical composition and glass transition temperature of the materials investigated in “5.4.1.) PR grating erasure in systems without extrinsic deep traps”

Material	DMNPAA	MNPAA	PVK	ECZ	TNF	TPD	T_g
units	[%wt]	[%wt]	[%wt]	[%wt]	[%wt]	[%wt]	[°C]
A	25	25	47	2	1	-	27
B	25	25	43	6	1	-	17.5
C	25	25	39	10	1	-	14
D	25	25	37	12	1	-	11.5
CT	25	25	38	10.18	1	0.82	14

5.4.1.2.)Results of the PR grating erasure experiments in systems without extrinsic deep traps

Hereafter, materials with T_g above the ambient temperature (i.e. the reduced temperature according to eq. (5.2 - 1) $T_r > 0^\circ\text{C}$) will be referred to as “high- T_g materials”, while materials with T_g below room temperature (i.e. $T_r < 0^\circ\text{C}$) will be referred to as “low- T_g materials”. The reduced temperatures of the investigated materials are listed in table (5-6).

Table (5-6): Reduced temperatures, maximum PR index modulation amplitude and logarithmically averaged recording time constants of the investigated materials.

Material	A	B	C	D
T_r [°C]	7	-2.5	-6	-8.5
$\Delta n_{max}@32\text{V}/\mu\text{m}$	-*)	$1.57*10^{-3}$	$1.47*10^{-3}$	$1.41*10^{-3}$
$\langle\tau_{rec}\rangle^{**})$ [sec]	142 ^{***)}	40	22	27

*) Material A did not saturate within the longest recording time applied here. After 83.3 minutes recording $\Delta n = 1.11*10^{-3}$ was achieved.

**) For the definition of $\langle\tau\rangle$ see equation eq. (5.2 - 26)

***) Please note, that fitting a non-saturating multi-exponential curve may yield time constants different from those obtained by fitting a curve, which at least closely approaches saturation, since in the first case the fitting algorithm underestimates the saturation value. Thus, the actual dynamics is underestimated as well and the material is even slower than indicated by the given $\langle\tau_{rec}\rangle$.

In general agreement with the results presented in “5.2.3.) The relation between the glass-transition temperature and the dynamic performance in PVK based PR polymers” on page 243, the recording speed is quite similar for the low- T_g materials B through D ($\langle\tau\rangle \approx 31 \pm 9$ sec, see table (5-6)), while the high- T_g material A has a much slower response (figure (5.4 - 1)). This is generally attributed to the fact that the recording dynamics in the “hard” high- T_g material is dominantly determined by the orientational dynamics of the EO chromophores (reorientation under the influence of the local total electrical field, i.e., the sum of the external dc and the internal space-charge field), while in the “soft” low- T_g materials the build-up of the PR space-charge field determines the dynamics of the DFWM response. This becomes obvious when comparing the DFWM recording dynamics (figure (5.4 - 1) (A)) and the ELP poling dynamics (figure (5.4 - 2) (A)). The maximum achievable diffraction efficiency at the given external field varies slightly for the investigated materials (table (5-6)) in agreement with the results discussed in “5.2.2.) The relation between the glass-transition temperature and the steady-state performance in PVK based PR polymers” on page 228.

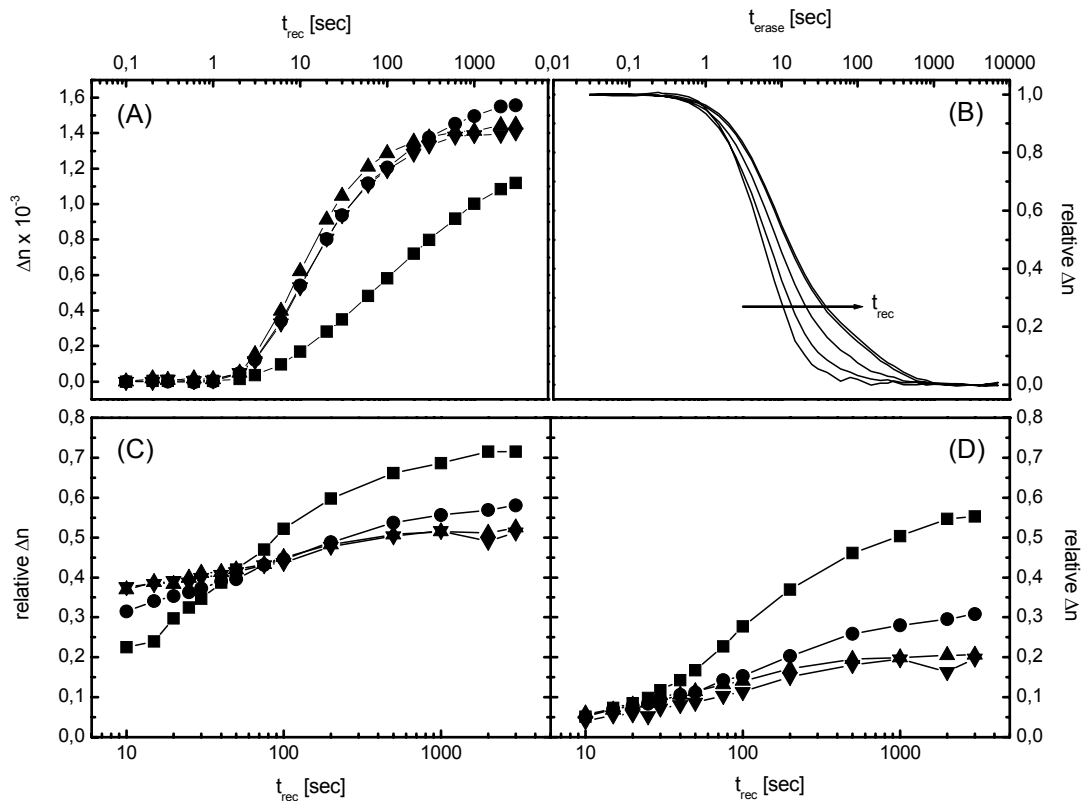


Figure (5.4 - 1): Holographic recording and erasure behavior of the materials A (squares), B (circles), C (up triangles), and D (down triangles). (A) shows the recording curves. (B) shows a selected set of normalized erasure curves for material B. The arrow indicates increasing recording time for the depicted five curves, the last two of which (i.e. for long recording times) are no more clearly distinguishable. (C) and (D) depicts the portion of the initial refractive index modulation remaining after 10sec and 30sec erasure, respectively, as a function of the recording time. The pre-illumination fluency for the initial relaxation was $36\text{J}/\text{cm}^2$ (recording beam 2, $I_{02} = 20\text{mW}$, $t_p = 30\text{min}$). The solid lines in plot (A), (C), and (D) are guide to the eye.

Considering the erasure process, a strong dependence of the erasure kinetics on the recording time of the PR grating is revealed for all materials under investigation (a characteristic example is shown in figure (5.4 - 1) (B)). Similarly, the relaxation dynamics in ELP depended on the poling time (figure (5.4 - 2) (B)). This is further illustrated in figure (5.4 - 1) (C) and (D)

and in figure (5.4 - 2) (C) and (D), which summarize the refractive index modulation amplitude Δn in DFWM and the amplitude of the field-induced birefringence Δn_{ELP} in ELP remaining after 10sec and 30sec, respectively. Obviously, the erasure (relaxation) process slows down with increasing recording (poling) time. The strength of this dependence (represented by the slope of the plots) decreases from material A to material C; material D behaves very similar to material C. For the longest recording times applied here, the DFWM-erasure behavior of each particular material finally levels off and becomes independent from the recording time. In contrast, such a saturation effect is not observed in the ELP experiments (figure (5.4 - 2) (C) and (D)). Surprisingly, for short recording times ($t_{rec} < 60\text{sec}$) in DFWM the short-term erasure dynamics (i.e. after 10sec, figure (5.4 - 1) (C)) is fastest for the high- T_g material A and slows down as T_g decreases, while the opposite trend holds for long t_{rec} . The observed “crossing point” (identical relative Δn for all materials) shifts to shorter recording times for longer erasure times and is no longer detected after 30sec of erasure (figure (5.4 - 1) (D)).

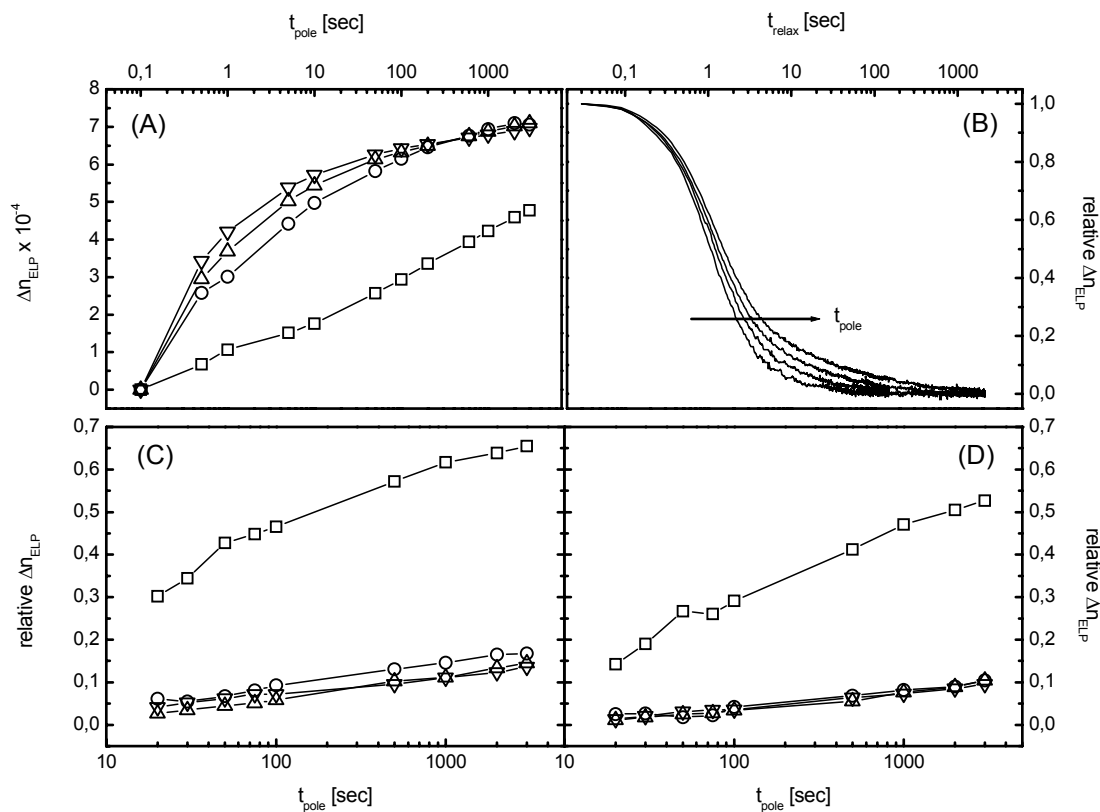


Figure (5.4 - 2): Growth and decay behavior of the field induced birefringence in the materials A (squares), B (circles), C (up triangles), and D (down triangles). (A) shows the growth curves. (B) shows a selected set of normalized decay curves for material B. The arrow indicates increasing recording time underlying the particular erasure curves. (C) and (D) depict the portion of the birefringence remaining after 10s and 30s decay as a function of the growth time, respectively. The solid lines in plot (A), (C), and (D) are guide to the eye.

The DFWM build-up and erasure dynamics as well as the ELP growth and relaxation dynamics (examples of which are shown in figure (5.4 - 1) and figure (5.4 - 2), (A) and (B), respectively) were fitted by the following multi-exponential functions:

$$\frac{\Delta n_r}{\Delta n_{0,r}} = 1 - \sum A_{i,r} \exp(-t/\tau_{i,r})$$

$$\frac{\Delta n_e}{\Delta n_{0,e}} = \sum A_{i,e} \exp(-t/\tau_{i,e}) \quad , \quad \text{eq. (5.4 - 1)}$$

$$\sum A_i = 1$$

where the indices ‘*r*’ and ‘*e*’ denote recording in DFWM (poling in ELP) and erasure in DFWM (relaxation in ELP) and *i* is the number index for the exponential terms. $\Delta n_{0,r}$ is the quasi steady-state value of refractive index modulation amplitude for the recording process in DFWM (induced birefringence in ELP), as resulting from the fitting process, and $\Delta n_{0,e}$ is the refractive index modulation in DFWM (induced birefringence in ELP) before the erasure (relaxation) process is going to start.

For the DFWM data, bi-exponential fitting appeared to be sufficient for the low- T_g materials B, C, and D. For some of the shortest writing times only mono-exponential fits could be applied to the erasure curves, since fits by more than one exponential term did not converge due to over-parametrization of the fitting algorithm. In order to stay consistent, this will be interpreted as an identity of the fast and the slow erasure rates (i.e. only one rate). However, for the high- T_g material A, bi-exponential fitting did not yield reasonable agreement with the experimental curve. Instead, three exponential terms were necessary to fit the dynamic behavior of material A. Please note, that tri-exponential fitting even yielded better results than bi-exponential fitting for the shortest writing times applied.

In contrast to the DFWM data, the ELP erasure data could only be approximated using three exponentials for all materials investigated. Following a similar trend as found for the DFWM erasure data, the agreement between the experimental and the fitting curves was notably worse for material A as compared to material B, C, and D, which particularly applies to longer growth times. This indicates that the dipolar relaxation behavior in the high- T_g case is in fact only roughly approximated by three exponential decay terms. It is to be pointed out, that the described fitting procedure is a strictly phenomenological formalism, i.e. the time constants do not necessarily reflect distinct physical processes, as discussed several times before in the fame of this thesis.

Except for material A, the pre-exponential factors of the fastest component in the DFWM as well as in the ELP experiments were always of similar magnitude (between 0.8 and 1.0), i.e. dominated the dynamic response. For better comparison of the DFWM and ELP data, all fitting data were reduced to two exponential decay terms by calculating the combined logarithmic averages of the two slow response times, $\langle \tau_{slow} \rangle$, in the cases where tri-exponential fitting has been applied. Furthermore, the combined logarithmic average of all response times in DFWM and ELP were calculated in order to obtain an overview of the general decay dynamics in the two experiments in question. The logarithmic averaging was performed according to eq. (5.2 - 26). Please note, that the forthcoming discussion of the ELP relaxation behavior will not be altered, if all three exponential terms are considered instead of the fast component and the logarithmically averaged slow components as conducted here. However, the discussion will become much more extensive and cumbersome. The general trends revealed are identical for both points of view even though some details may be dropped due to the averaging formalism applied. Hereafter, the slow relaxation time (as obtained by bi-exponential fitting or by tri-exponential fitting with subsequent logarithmic averaging of the two slow relaxation times) will be referred to as “ τ_{slow} ” and the fast relaxation time as “ τ_{fast} ”.

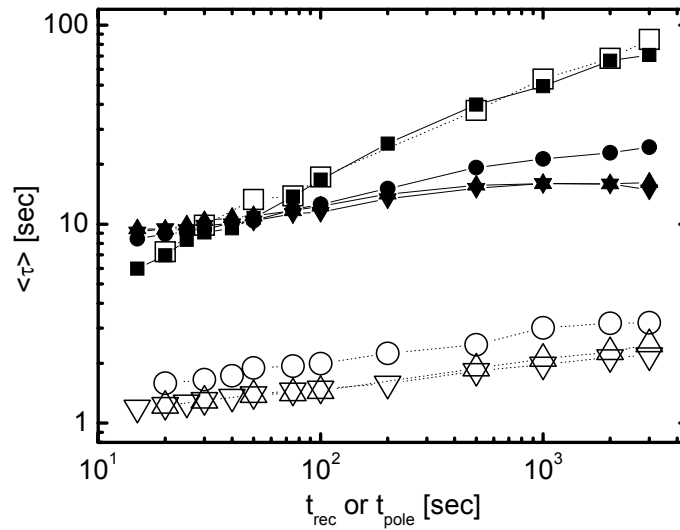


Figure (5.4 - 3): Logarithmically averaged holographic (solid symbols) and ellipsometric (open symbols) response times $\langle \tau \rangle$ of materials A (squares), B (circles), C (up triangles) and D (down triangles) as a function of the recording and the poling times, respectively. The solid and dotted lines are guide to the eye.

Figure (5.4 - 3) summarizes the logarithmically averaged total response times for the DFWM erasure and the ELP relaxation. The general dynamic response dynamics of the high- T_g material A is almost identical for both experiments, which leads to the conclusion that this material is dominantly ruled by the orientational relaxation of the NLO chromophores in the polymer matrix. In contrast, the orientational relaxation is about one order of magnitude faster than the erasure of the holographic grating in the low- T_g materials B, C, and D. Therefore, one can safely presume that the DFWM erasure behavior of these materials is dominantly determined by the decay of the PR space-charge field. However, the picture is not that simple, as becomes obvious when considering the particular time constants and their relative weighting in more detail. Figure (5.4 - 4) and figure (5.4 - 5) show the fast and slow time constants τ_{fast} and τ_{slow} and the corresponding weighting factors for the ELP relaxation and the DFWM erasure, respectively.

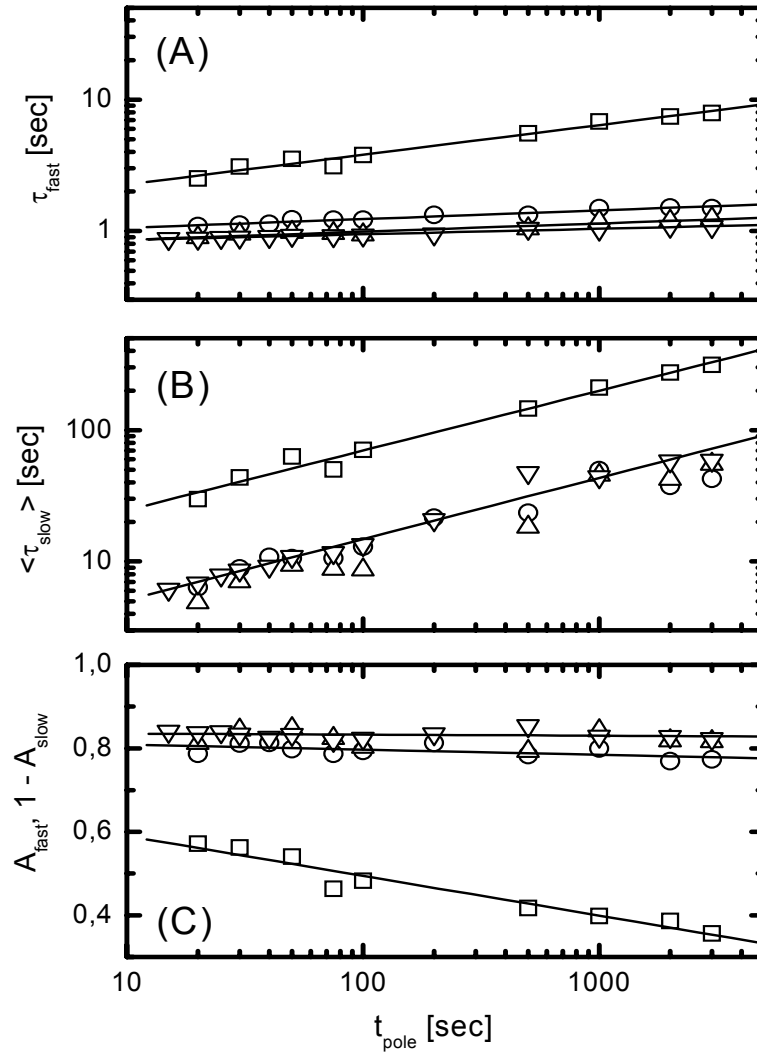


Figure (5.4 - 4): Fit results of the ELP relaxation curves for the materials A (squares), B (circles), C (up triangles), and D (down triangles): (A) fast time constant. (B) logarithmically averaged "slow" time constants. (C) relative weight factor of the fast relaxation term. The solid lines are linear fits to the data.

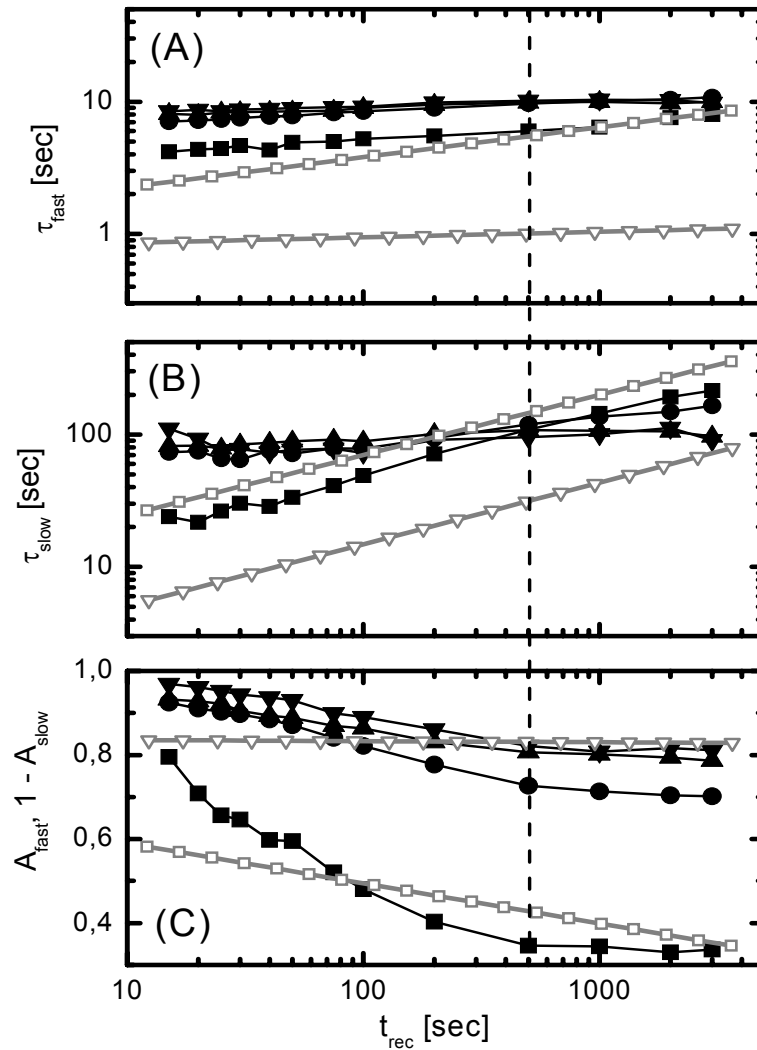


Figure (5.4 - 5): Fit results of the DFWM erasure curves for the materials A (squares), B (circles), C (up triangles), and D (down triangles): (A) fast time constant. (B) slow time constant. (C) relative weight factor of the fast erasure term. The lines are guide to the eye. The solid lines with small open symbols are the linear fits to the ELP data taken from figure (5.4 - 4) for material A (squares) and D (down triangles). The perpendicular dashed line marks the recording time for which the DFWM pre-exponential factors level off and for which $\tau_{fast,ELP}$ becomes equal to $\tau_{fast,DFWM}$ for material A. The pre-illumination fluency for the initial relaxation was $36\text{J}/\text{cm}^2$.

5.4.1.3.)Discussion of the erasure behavior of PR polymers without extrinsic deep traps

5.4.1.3.1.)Discussion of the ellipsometric experiments

Figure (5.4 - 4) and figure (5.4 - 5) summarize the particular fit data for the ELP experiments and DFWM experiments, respectively. First the ELP data will be considered in more detail. The orientational dynamics in the high- T_g material A is much slower than in the low- T_g materials B - D, whereas the latter behave very similarly. In all materials studied here, both time constants increase with the poling time t_{pole} (figure (5.4 - 4), (A) and (B)), seemingly following a power law of the general form:

$$\tau_{i, decay} = t_{build-up}^x, \quad \text{eq. (5.4 - 2)}$$

which reads here: $\tau_{i,ELP} = t_{pole}^x$. For the fast component $\tau_{fast,ELP}$ and the high- T_g material A the exponent $x = 0.23$ is relatively large, indicating a rather strong dependence. For the low- T_g materials x is about a factor of 4 smaller ($x = 0.06$), i.e., $\tau_{fast,ELP}$ can be considered as constant in good approximation. In contrast, for the slow component (i.e. $\langle \tau_{slow,ELP} \rangle$) all materials exhibit an identical, rather strong dependence on the recording time with $x = 0.46$ (material A being about a factor of 6 slower).

Regarding the pre-exponential fit factors $A_{i,ELP}$ (figure (5.4 - 4), (C)) there is very little change for the low- T_g materials when the recording time increases. The fast component dominates over the slow component by a factor of about 4. In contrast, in material A the factor $A_{fast,ELP}$ is significantly smaller than in the low- T_g materials and decreases exponentially when t_{pole} increases (the opposite holds for $A_{slow,ELP}$). For $t_{pole} > 70$ sec the slow process becomes dominant (i.e. $A_{slow,ELP} > A_{fast,ELP}$). Thus, the relaxation dynamics in the high- T_g material A is not only slower but differs substantially from the one in the low- T_g materials B, C, and D.

The observations regarding the poling-time dependence of the relaxation dynamics in the low- T_g materials may be rationalized assuming that the exponential terms used for fitting the experimental data may represent different physical processes, although the multi-exponential fitting procedure was introduced as a phenomenological formalism. The fast process in the low- T_g materials might represent a quick relaxation of the chromophore dipoles according to the oriented gas model, the transient solution of which yields a single exponential decay for the orientational relaxation after turning off the poling field according to eq. (2.4 - 117) in “2.4.2.2.2.) Turning off the poling field” on page 95. Furthermore and in agreement with the experimental results, the oriented gas model does not imply a poling-time-dependence of the relaxation dynamics, since the relaxation of the orientational order is due to free rotational diffusion as discussed in “2.4.2.2.) Transient solutions of the oriented gas model” on page 92. However, even for the low- T_g materials the oriented gas model only represents a zero-order approximation of the actual relaxation process, since it presumes a highly diluted conglomerate of free molecules, which does not strictly apply to all the systems under investigation here.

Therefore, the situation shall be considered, which is found in a typical viscoelastic system being subjected to mechanical stress. According to the standard theory of viscoelasticity, a viscoelastic system subjected to mechanical stress for a sufficiently long time (represented here by the electric-field-induced reorientation of dipoles embedded in a glassy polymer matrix) will attempt to reduce the stress. Hence, the material slowly flows towards a new equilibrium state. In a glassy polymer this process includes long range conformational changes of the polymer chains. The longer the stress is applied, the closer this new equilibrium is approached. In the case of relaxation as discussed here, the reverse situation is observed, i.e., after the mechanical stress is withdrawn (i.e. the electric field is switched off) the material relaxes back

into its initial thermodynamical equilibrium state, provided the thermodynamical equilibrium state under stress represents a non-equilibrium state without external stress. In the case under consideration, when there is some degree of orientational order of the molecular dipoles and the external field is switched off, the system exists in a thermodynamical non-equilibrium state, since random distribution of the dipoles would represent the equilibrium state. Accordingly, the closer the thermodynamical equilibrium under applied field had been approached during the poling period (i.e., with increasing poling time), the longer it will take to return to the initial state without field. The general trend thus described agrees with the experimental observation of a poling-time-dependence of the slow component of the orientational relaxation dynamics. The fact that the slow component itself is actually bi-exponential may be indicative for the existence of a distribution of viscoelastic relaxation times, which is due to different local environments for the particular NLO chromophores [199]. However, even though there is clear indication for the presence of a notable viscoelastic contribution to the overall orientational relaxation process as described above, the “free“ relaxation according to the oriented gas model is the by far dominant contribution in the low- T_g materials, as can be seen from the relatively small weighting of the slow component (figure (5.4 - 4)).

The viscoelastic interpretation of the poling process given above is additionally supported by the observation that the poling process itself (i.e. the build-up of the orientational order when turning on the poling field, figure (5.4 - 2) (A)) seemingly does not saturate in any case even for the longest poling times applied, in contrast to the DFWM diffraction efficiency (which clearly saturates for materials C and D, figure (5.4 - 1) (A)). In the context of the model described above, the mechanical stress applied to the system is not constant but decreases when the system approaches the new equilibrium, since the interaction force between the molecular dipoles and the applied field according to eq. (2.4 - 45) decreases with increasing orientational order. Thus, the flow process is supposed to become slower with increasing poling time resulting in an asymptotic behavior for the build-up of the orientational order, which is supposed to show dynamics different from that predicted by the oriented gas model yielding bi-exponential build-up dynamics with fixed relations between the parameters of the particular exponential terms (see “2.4.2.2.1.) Turning on the poling field” on page 94).

In contrast, the situation is significantly different for the high- T_g material A. In this case, there is no reason to assume a notable contribution to the relaxation process, which refers to the oriented-gas model. Instead, the relaxation process should be viscoelastic in general. This view is supported by three experimental observations. At first, not only the slow but also the fast relaxation time increases significantly with increasing poling time, as mentioned before and opposed to the low- T_g systems. In terms of the model discussed above, this strongly indicates viscoelastic behavior underlying both the fast and the slow component. Secondly, the weightings of the relaxation terms are fairly similar on the one hand but change notably as a function of the poling time on the other, both of these observations in contrast to the low- T_g systems. This may indicate that not different physical processes as proposed for the low- T_g systems are observed, but rather a change in the distribution of viscoelastic relaxation times. Finally, the approximation of the relaxation behavior by three exponential terms is notably poorer as compared to the low- T_g systems. This might indicate a more pronounced influence of the local environment on the relaxation behavior of the chromophores, i.e. a broader distribution of relaxation times. A broader distribution is supposed to require more exponential terms for good approximation than a more narrow one. Hence, one can conclude that the relaxation behavior of the high- T_g material A is dominated by the viscoelastic properties of the polymer matrix.

On the basis of the above viscoelastic interpretation of the poling behavior of the high- T_g system one also may speculate about the reason why the weighting of the exponential decay terms changes strongly as a function of increasing poling time (figure (5.4 - 4) (C), $A_{slow,ELP}$

increases significantly and finally becomes even larger than $A_{fast,ELP}$ for poling times exceeding 100sec), whereas such a trend is not observed in the low- T_g materials. This behavior may be indicative for an increasing spatial range of the conformational changes in the rigid polymer matrix with increasing degree of poling. In a rigid polymer matrix, long-range conformational changes are significantly aggravated as compared to short-range conformational changes and should gain in importance with increasing degree of poling. By that, an existing distribution of viscoelastic relaxation times due to different local environments of the molecular dipoles to be oriented may change as a function of the degree of poling as proposed before. In contrast, in a soft polymer matrix, the influence of the areal range of the conformational changes involved in the poling process should be much less important. In fact, a good long-range conformational mobility is characteristic for the low- T_g state of polymers as discussed in “2.4.1.1.) Phenomenology of viscoelastic transitions” on page 71.

It is to be pointed out that a theoretical model has recently been developed in order to describe the poling behavior of system like those investigated here more accurately [204]. Therefor disorder in analogy to the disorder model for the charge transport in polymers was introduced in order to solve the rotational diffusion equation eq. (2.4 - 94). However, this approach is not very useful here, since an accurate solution of the relaxation problem under consideration is not the focus of interest, but rather the correlation between the time span the electrical poling has been performed and the corresponding decay dynamics of the orientational order.

5.4.1.3.2.)Discussion of the DFWM experiments

Now the fitting results for the DFWM experiments will be considered in more detail (figure (5.4 - 5)). The time scale of the DFWM erasure dynamics in material A is similar to the relaxation in the ELP experiments as shown by figure (5.4 - 3), figure (5.4 - 4) and figure (5.4 - 5). In contrast, in the low- T_g materials B, C, and D the orientational relaxation is basically more than one order of magnitude faster than the PR grating erasure. However, in more detail, this statement does only apply in general for the fast components, whereas the slow components of the PR grating erasure are only more than one order of magnitude faster than the slow components of the orientational relaxation for short recording times of the holograms. For longer recording times, the slow component of the orientational relaxation approaches more and more the slow component of the PR grating erasure kinetics. This is an important aspect, which will be discussed later in more detail.

Counterintuitively, both erasure time constants for material A are smaller (i.e. the erasure is faster) than for the low- T_g materials except for $t_{rec} > 500$ sec, where at least the slow component becomes larger than in the low- T_g materials. Since the relaxation of the orientational order in material A is faster than the DFWM erasure in the low- T_g systems, this does not contradict the above conclusion that the PR grating erasure kinetics of material A is limited by the orientational relaxation of the NLO chromophores, but indicates that the decay of the PR space-charge field is faster as compared to the low- T_g systems. However, surprisingly $\tau_{fast,DFWM} > \tau_{fast,ELP}$ for $t_{rec} < 500$ sec for material A (figure (5.4 - 5)(A)). This unexpected relation might be attributed to an overlap of the PR grating erasure kinetics with the “fast portion“ of the distribution of viscoelastic relaxation times. In this range the high- T_g material A may be limited by the decay of the PR space-charge field, even though the orientational relaxation process is still viscoelastic and does not follow the oriented gas model. This indicates in general that the PR response is not mandatorily hindered by a rigid matrix, which opens new ways of thinking about thermodynamically stable high-performance PR polymers utilizing in-situ orientation of the NLO chromophores (and, thus, showing orientational enhancement of the PR effect) with fast response behavior for applications not requiring very high index

modulations. Indeed, it has been shown recently, that even high- T_g PR polymers showing orientationally enhanced PR response may show fast PR response [137, 153, 217]. However, the reported materials are based on organic photoconductors showing significantly better charge carrier mobilities than the PVK matrix.

Following the same trend as found in the ELP experiments, the fast time constants $\tau_{fast,DFWM}$ (figure (5.4 - 5)(A)) are almost independent from the recording time for all three low- T_g materials B, C and D.

Considering the slow time constants $\tau_{slow,DFWM}$ (figure (5.4 - 5)(B)), the trend found for the fast time constants in all investigated low- T_g materials is continued, however, only for the low- T_g materials C and D and unlike the relaxational behavior in the ELP experiments (figure (5.4 - 4)(B)). Material B behaves similarly to the materials C and D only for $t_{rec} < 500\text{sec}$, whereas there is a notably stronger dependence on the recording time for $t_{rec} > 500\text{sec}$, seemingly following then a similar trend as in ELP. In contrast, for the high- T_g material A, $\tau_{slow,DFWM}$ and $\tau_{slow,ELP}$ show identical qualitative dependence on the recording/poling time, however, $\tau_{slow,DFWM}$ being consistently smaller than $\tau_{slow,ELP}$. On first sight, this contradicts the general rule that a process involving dipolar relaxation cannot be faster than the relaxation itself. On the other hand, the fact that identical power-law exponents according to eq. (5.4 - 2) are obtained for $\tau_{slow,DFWM}$ as well as for $\tau_{slow,ELP}$ (see figure (5.4 - 5)) proves that the slow component in DFWM is attributed to the relaxation of the chromophore dipoles. The discrepancy in the absolute speed, hence, must be attributed to the fact that in ELP only the external field was switched off, i.e. the polar orientation of the chromophores relaxes back to the isotropic state driven by the accompanied gain in entropy. In contrast, in DFWM the external field remains, and only the internal PR space-charge field is erased. Hence, in the latter case the chromophores are reoriented by the externally applied dc electrical field in order to adjust to the new situation. This is expected to be faster than the purely thermodynamical relaxation in ELP, re-establishing the relations according to the aforementioned general rule for processes involving dipolar relaxation. It is to be pointed out, that for very long recording times ($t_{rec} \gg 3000\text{sec}$) $\tau_{slow,DFWM}$ and $\tau_{slow,ELP}$ seemingly become similar, even for the low- T_g materials, the slow DFWM erasure component of which then may be expected to become orientation limited as well. However, this regime was not yet approached in the experiments carried out.

Nevertheless, the situation remains ambiguous, which requires a more detailed consideration. As mentioned before, $\tau_{slow,DFWM}$ for material B shows a stronger dependence on the recording time for $t_{rec} > 500\text{sec}$ as compared to the materials of lower T_g (figure (5.4 - 5)(B)). On the one hand, this might indicate some influence of orientational effects at longer recording times. On the other hand, if there are two dynamic processes in a system, both of which showing the same functional dependence on the time, the slower process will rule the overall kinetics. A comparison of the ELP relaxation time constants (figure (5.4 - 4) (A) and (B)) and the DFWM erasure time constants (figure (5.4 - 5) (A) and (B)) for material B undoubtedly reveals that the DFWM erasure is the slower process. Consequently, the DFWM erasure in material B cannot be determined by orientational relaxation. However, as mentioned before in “5.4.1.3.1.) Discussion of the ellipsometric experiments” on page 281, the ELP relaxation dynamics could not be approximated by bi-exponential but rather tri-exponential fitting, and figure (5.4 - 4) (B) shows the logarithmic average of the slow time constants. In fact, the slowest (i.e. the third) ELP relaxation time constant is larger than the slow DFWM erasure time constant even for all the low- T_g materials, however contributes only very little (less than 5%). In more detail, a small birefringence (i.e. a non-zero signal in the ELP experiments) could still be observed in the low- T_g materials, even when the DFWM signal has already vanished. This, in turn, again contradicts the general rule that a process involving dipolar relaxation cannot be faster than the relaxation itself. As discussed before for material A, this observation can be attributed to the fact, that the orientational relaxation dynamics as determined by the ELP

experiment actually cannot be compared directly with the dipolar relaxation occurring during DFWM erasure but yields too large time constants. The degree of this “mismatch“ can be estimated considering the build-up dynamics of the ELP signal as depicted in figure (5.4 - 2)(A). Obviously, the electrical poling of the low- T_g systems is significantly faster for the materials C and D as compared to material B. It is consequent to take this trend as representative for the influence of an external electrical field on changes of the orientational order and to assume that the relative acceleration of the field driven decay of the orientational order occurring during DFWM erasure will follow the same trend. Furthermore $\tau_{slow,DFWM}$ does not notably depend on the recording time for the materials C and D for all recording times in contrast to the slow time constants in ELP. On the other hand, for material B this is only valid for $t_{rec} < 500s$, whereas $\tau_{slow,DFWM}$ increases with the recording time for $t_{rec} > 500s$ like found in the ELP experiments.

Summing up all the arguments given above, one can draw the following conclusion: In material B there might be a small contribution of dipolar relaxation to the slow component of the DFWM erasure behavior for recording times of $t_{rec} > 500s$ (“small contribution“ must be understood as a lowly weighted additional exponential decay term included in the slow time constant). This contribution does not dominate the slow component of the DFWM erasure since it represents only about 30% of the logarithmically averaged slow component of the dipolar relaxation dynamics (and about 5% of the overall relaxation dynamics), the dominant portion of which decays much faster than the PR grating is erased. Furthermore, the contribution of the slow component to the overall DFWM erasure in material B is about 30% for $t_{rec} > 500s$ (figure (5.4 - 5)(C)), whereas the contribution of the logarithmically averaged slow component to the overall ELP relaxation dynamics is only about 20% for $t_{rec} > 500s$ (figure (5.4 - 4)(C)). In contrast to material B, in the materials C and D no contribution of dipolar relaxation is implied for all recording times applied, since the general trend of $\tau_{slow,DFWM}$ as a function of the recording time does not agree with the trend found for the slow time constants in the ELP experiments. Accordingly, in these materials one can safely presume that the “field driven dipolar relaxation”, as discussed above, is in general faster than the DFWM erasure within the range of recording times investigated here. Therefore, accounting for the ambiguous situation in material B as just discussed, hereafter mainly the materials C and D will be focussed upon, where orientational effects can safely be neglected within the range of experimental parameters applied in this work.

Finally, the pre-exponential factors in DFWM (figure (5.4 - 5)(C)) change significantly as a function of increasing recording time, but level off for $t_{rec} > 500 s$ for all materials. The slow component starts at lower level and gains in influence, while the fast component shows the opposite trend. For material A this is the same basic trend as found for the ELP experiment. In contrast, in the case of the low- T_g systems, the general trend is fundamentally different from the one found for the orientational relaxation (constant weighting for all recording times, figure (5.4 - 4)(C)). This strongly indicates that there must be a process in DFWM, the importance of which depends on the recording time and which is not correlated with dipolar relaxation.

5.4.1.3.3.) Experimental verification of optical trap activation

The crucial question now is, which mechanism might cause the slowing of the PR space-charge field erasure as a function of the recording time in low- T_g materials, where orientational effects are of minor importance. It seems reasonable, that this might somehow be correlated with the trapping sites for the mobile charge-carriers in the materials. Silence et al. reported earlier about the so-called “optical trap activation” (OTA) in a PR polymer [74]. Following their formalism, the relationship of the trap density before $N_{PR}^{(b)}$ and after (or during) optical irradiation $N_{PR}^{(a)}$ may be expressed as:

$$N_{PR}^{(a)} = N_{PR}^{(b)} + CJ^x \quad \text{eq. (5.4 - 3)}$$

where J is the actual fluence, C is a constant, and x is a power-law exponent.

Assuming that the PR grating build-up dynamics of the low- T_g systems is mainly determined by the charge-carrier mobility as already proposed before in “5.3.) The influence of the sensitizer concentration on the PR performance of PVK based polymer composites” on page 257 and that the latter is inversely proportional to the trap density (which is typically valid for photoconductive polymers and low trap densities [83, 74]), Silence et al. obtained the following relationship between the PR grating build-up time constants before irradiation $\tau^{(b)}$ and after irradiation $\tau^{(a)}$ [74]:

$$[\tau^{(a)}/\tau^{(b)}] - 1 = C'J^y \quad \text{eq. (5.4 - 4)}$$

Here, C' is another constant different from the one in equation eq. (5.4 - 3) and y is another power-law exponent.

In accordance with this formalism, the build-up dynamics for the systems under investigation were determined for different pre-illumination intensities $I_p = 49.2\text{mW/cm}^2$, 17mW/cm^2 , 6.9mW/cm^2 , and 2.8mW/cm^2 , applied for 30 minutes each, and the resulting rates were set in relation to a reference rate obtained without pre-illumination. In order to exclude the influence of a changing trap situation during the grating recording process [74, section 5.3.) herein], which is inherently included when fitting an entire data set (i.e. up to steady-state), the time to achieve 5% diffraction efficiency, τ_5 , was chosen as a measure of the undisturbed initial grating build-up rate. The left-hand side of equation eq. (5.4 - 4) is plotted on double-logarithmic scale in figure (5.4 - 6). In all cases, the response time of the materials was increased by pre-illumination similar to [74], but unlike reported recently for TPD-PPV [4]. In agreement with equation eq. (5.4 - 4), a linear dependence is observed, the slope of which yields the power law exponent y . For the high- T_g material A this procedure yielded $y = 0$ (figure (5.4 - 6), inset), which was expected, since in this case the response is determined by the orientational dynamics of the chromophores and the trap situation is, thus, irrelevant. This finding underlines the validity of the proposed procedure in obtaining information on changes in the trap situation upon optical irradiation. Furthermore, the fact that $[\tau^{(a)}/\tau^{(b)}] - 1 \geq 0$ proves that the dynamics of the PR space-charge field in the investigated materials is indeed mobility limited. In contrast, $[\tau^{(a)}/\tau^{(b)}] - 1 \leq 0$ would be observed for the case of the charge carrier generation limiting the grating build-up kinetics, a phenomenon referred to as “gating“, since a higher pre-illumination fluency will provide a higher density of “free“ holes prior to the writing process and, thus, accelerated PR response [4].

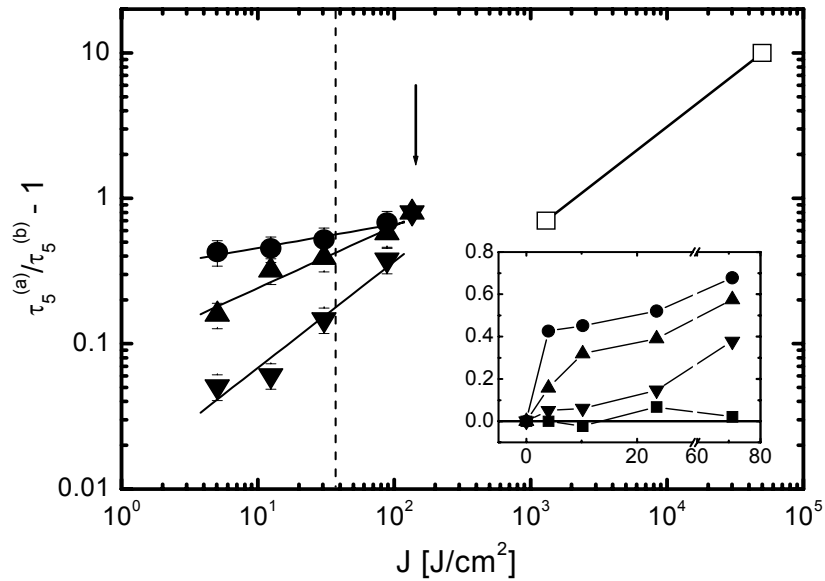


Figure (5.4 - 6): Dependence of the recording dynamics on the pre-illumination fluency J for the materials B (circles), C (up triangles), and D (down triangles). For comparison, the data from Silence et al. are included (open squares [74]). The solid lines are linear fits. The dashed line indicates the pre-illumination in the DFWM experiments underlying figure (5.4 - 5). The arrow indicates the conditions used for the relaxation experiments (figure (5.4 - 7)), corresponding data of which are also included (the “star“ results from the superposition of an up triangle and a down triangle). The inset shows the data for all materials A - D (material A: solid squares) on linear scale.

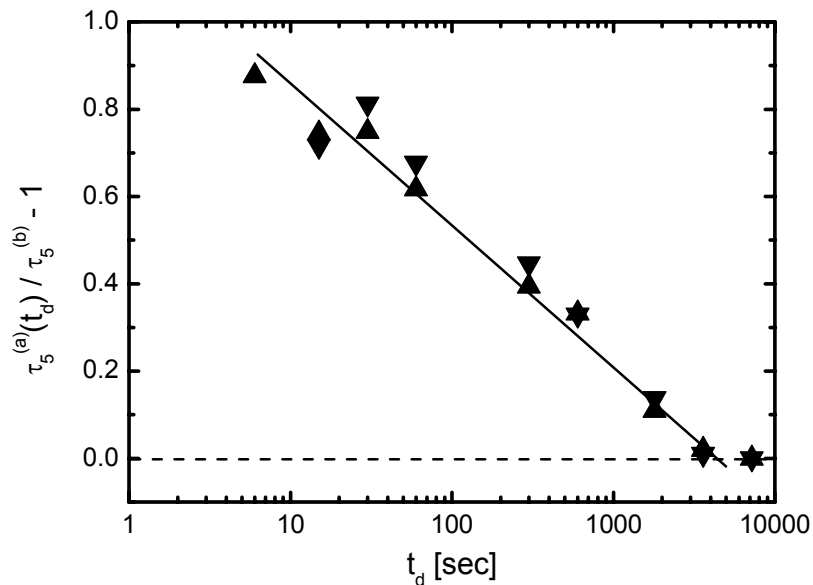


Figure (5.4 - 7): Dependence of the recording dynamics on the delay time between pre-illumination and recording for the materials C (up triangles) and D (down triangles). The dashed line indicates the initial response without pre-illumination. The solid line is a linear fit to the data. The pre-illumination fluency was $J = 135 \text{ J/cm}^{-2}$

From figure (5.4 - 6), one can conclude that OTA indeed occurs in the investigated low- T_g materials, as discussed above. Please note, that the result of $y = 0$ for the high- T_g material A does not imply a constant trap situation, but rather that the described experiment is not indicative for a change of the trap situation, if the dynamic behavior does not depend on this parameter. Hence, OTA may be implied for material A as well since it is electrically similar to the low- T_g systems. The optically activated traps emerge faster with increasing glass-transition temperature (figure (5.4 - 6)): The recording of holograms is strongly slowed down in material B even for very small pre-illumination fluency, while the low-exposure retardation is significantly smaller in material C and eventually barely detectable in material D. This indicates that it is obviously more difficult to change the trap situation in a soft material. On the other hand, the decrease of the recording speed as a function of the pre-illumination fluency is significantly stronger in material D ($y = 0.73$) than in material B ($y = 0.16$). For $J > 100 \text{ J/cm}^2$ the effects become fairly similar in all materials. This proves a strong impact of T_g on the OTA effect, which will be discussed later in more detail. The results presented here are within the same order of magnitude as those reported in [74]. Please note, that the OTA formalism does not provide information about the depth of the activated traps, but rather implies a change of their number density.

In [74] the optically activated traps persisted for a very long time, up to several months. There was no indication that their formation might be reversible. In contrast, in the materials considered here, the OTA effects were reversible. In order to quantify the relaxational dynamics of the traps, experiments with an equal pre-illumination fluency were carried out, however, the dark periods t_d under field between pre-illumination and the recording process were varied. For evaluation of the data the same procedure was applied as for the OTA-measurements discussed above. The results are shown in figure (5.4 - 7). Obviously, the OTA effect decays mono-exponentially and vanishes after about one hour.

OTA not only takes place during pre-illumination, but also occurs while holograms are recorded. However, the reversibility of the OTA effect complicates the situation, if the system has been illuminated uniformly in advance of the recording process, since during holographic recording trap relaxation must be expected to take place in the dark fringes, while further trap activation will take place in the bright fringes. In any case, if the writing process is interrupted after a given recording time t_{rec} and, if then the grating is erased, OTA should manifest itself in different erasure kinetics depending on t_{rec} . A leveling of the erasure rates in dependence of t_{rec} might, therefore, indicate that the trap situation during recording has come to some quasi-steady-state equilibrium.

Interestingly, this equilibration time appears to be identical (about 500sec) in all materials studied here, i.e. to be independently of T_g (figure (5.4 - 5)). This, in turn, might indicate that the nature of the optically activated traps is identical in all cases. Note, that this reaching of an equilibrium does not necessarily coincide with the finishing time of the recording of the PR grating (as indicated by the fact that the modulation amplitude still increases, figure (5.4 - 1)). It is noteworthy, that the influence of OTA on the grating decay dynamics was already investigated in [74]. However, the grating decay dynamics was determined with only the very weak reading beam being present during the decay process, i.e. under almost dark decay conditions. As will be discussed in a later section of this work, a pronounced retardation of the dark decay dynamics with increasing PR phase shift occurs. The latter, on the other hand, was found to increase as well due to OTA [74]. Thus, it remains unclear from the results presented in [74], whether the PR grating erasure dynamics is directly affected by OTA.

5.4.1.3.4.)A theoretical approach to PR space-charge field erasure

After having established that OTA may be responsible for the retardation of the erasure process as a function of the recording time in the low- T_g systems B - D, the dependence of the erasure rates on the recording time was studied in these materials for four different erasure intensities I_e . All three materials behaved very similarly, and as a typical example the data for material C are shown in figure (5.4 - 8). Please note, that material B did not show any indication of a deviating behavior, which might be implied by the uncertainty about a possible contribution of orientational relaxation to the PR grating erasure process in this material as discussed before. Both erasure rates (inverse time constants) increase with increasing erasure intensity. However, the dependency is clearly different for the fast and the slow component. When normalized to the value at $t_{rec} = 500\text{sec}$, i.e., after the trap situation has reached a quasi steady-state equilibrium as proposed before, it becomes obvious, that $1/\tau_{1,norm}$ is identical for all erasure intensities, decreasing by about 30% from its initial value at short exposure times and remaining constant for $t_{rec} \geq 500\text{sec}$. In contrast, $1/\tau_{2,norm}$ is almost independent from the recording time for low erasure intensities, while it decreases by a factor of approximately 2 as a function of the recording time for high erasure intensities. Thus, there is a relative acceleration of the slow erasure component at short recording times. Systematic trends in T_g for the investigated “soft” materials were not observed.

For a given recording time t_{rec} , the PR grating erasure rates were found to follow a power-law dependence on the erasing light intensity I_e of the form:

$$\frac{1}{\tau_{e,i}(t_{rec})} \propto I_e^{\sigma_i(t_{rec})}, \quad \text{eq. (5.4 - 5)}$$

where $\tau_{e,i}$ is the erasure time constant, and the index $i = \text{fast (slow)}$ denotes the fast (slow) erasure time constant. While the exponent of the fast erasure component, σ_{fast} , depends only slightly on the recording time (figure (5.4 - 8)(C)), the exponent for the slow component, σ_{slow} , decreases strongly with increasing writing time.

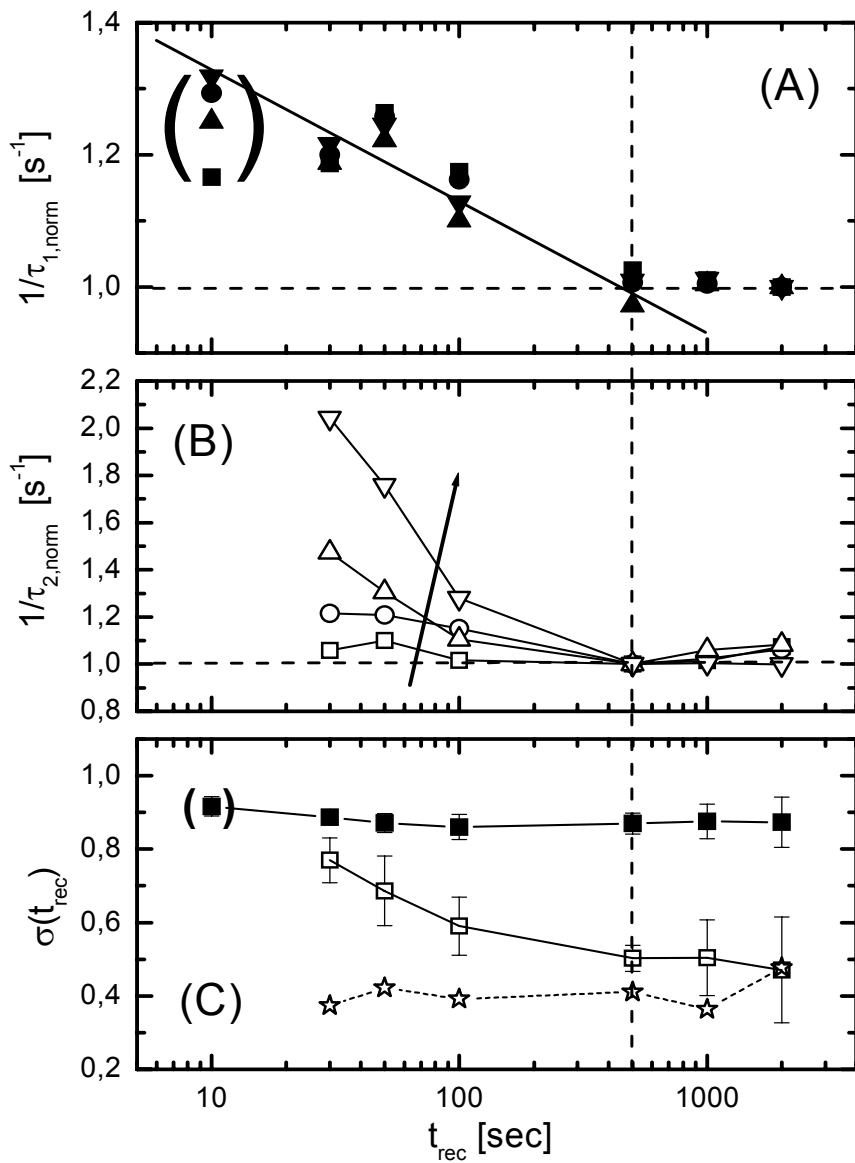


Figure (5.4 - 8): Dependence of the normalized erasure dynamics of material C on the erasure intensity I_e . (A) and (B) are the normalized inverse fast (solid symbols) and slow (open symbols) erasure time constants $1/\tau$, respectively, for the erasure intensities: $I_e = 2.8 \text{ mW/cm}^2$ (squares), 6.9 mW/cm^2 (circles), 17 mW/cm^2 (up triangles), and 49.2 mW/cm^2 (down triangles). The arrow indicates increasing erasure intensity. (C) depicts the erasure rate slopes of material C vs. the recording time. The solid (open) squares represent the rate slopes for the fast (slow) erasure rates. The open stars refer to the slow rates obtained for another material of the same type, however, extrinsically doped with a high amount of deep traps (see text for details). The pre-illumination fluency was 36 J/cm^2 in all cases. All lines are guide to the eye.

Cui et al. proposed a theoretical framework for the PR grating erasure process [83], which has been elaborated upon in detail in “2.5.3.2.3.2.) Cui’s approach to the erasure dynamics” on page 128. Neglecting charge-carrier diffusion, which is a valid assumption for the materials considered here and under the experimental conditions applied, they described the PR grating erasure in organic polymers by three contributions with individual rate constants (see eq. (2.5 - 30) to eq. (2.5 - 32)):

$$\begin{aligned} 1/\tau_1 &= (q\mu n_0)/\varepsilon + iK\mu E_0 \\ 1/\tau_2 &= \alpha_G + \gamma_R n_0 \\ 1/\tau_3 &= \delta + \gamma_T n_0 \end{aligned} \quad \text{eq. (5.4 - 6)}$$

Here, q is the elementary charge, μ is the charge-carrier mobility, n_0 is the steady-state zero-order component of the hole density, ε is the (bulk) dielectric constant, γ_R is the coefficient for geminate recombination, γ_T is the hole-trapping coefficient, α_G is the photo-generation rate, δ is the detrapping rate, and E_0 is the projection of the externally applied electric field onto the grating wave vector K . The detrapping rate is given by:

$$\delta = sI + \beta, \quad \text{eq. (5.4 - 7)}$$

where s is the cross-section for light induced detrapping, I is the light intensity, and β is the thermal detrapping rate. The first part of eq. (5.4 - 6) is complex and implies an oscillation, which, however, was not observed within the series of experiments discussed here. Please note, that some oscillation-like behavior can be observed under certain experimental condition as shown in “5.4.2.) PR grating erasure in systems doped with extrinsic traps” on page 300. These, however, are significantly different as compared to the conditions applied here. Therefore, it seems reasonable to assume that the imaginary part of the complex component is of minor importance in the cases discussed here and that this term can be omitted. If furthermore predominant Langevin-type recombination is presumed (i.e. $\gamma_R = q\mu/\varepsilon$, see eq. (2.4 - 188)) and low light intensity approximation is applied (i.e. small photo-generation rate α_G as compared to the geminate recombination rate $\gamma_R n_0$), $1/\tau_1 \approx 1/\tau_2$ and a single fast rate is obtained from eq. (5.4 - 6). This point of view is in general agreement with [83], stating that the first two rate constants in eq. (5.4 - 6) are both fast and experimentally barely distinguishable. The third rate, on the other hand, represents a relatively slow erasure process. Thus, eq. (5.4 - 6) simplifies to:

$$\begin{aligned} 1/\tau_{fast} &= 1/\tau_1 = 1/\tau_2 = \gamma_R n_0 \\ 1/\tau_{slow} &= 1/\tau_3 = \delta + \gamma_T n_0 \end{aligned} \quad \text{eq. (5.4 - 8)}$$

and one gets a new set of equations, proposing two experimentally distinguishable exponential terms for fitting the experimental erasure curves.

5.4.1.3.5.)Discussion of the relation between the PR trap situation and PR grating erasure

First, the experimental results will be discussed in the context of [209], which has already been mentioned in the general introduction to this section on page 271. In [209] the authors found a nearly constant growth/erasure time ratio of approximately 1.5 for a wide variety of applied electrical fields and sensitizer concentrations in a PVK based PR polymer similar to the systems under consideration here. From the strong correlation between the mentioned rates, the authors conclude that a single trap model of the PR effect suffices to describe the dynamics in PR polymers like that known from the standard model of the PR effect in crystals. They attribute the dominant trap species to Poole-Frenkel type traps formed by ionized sensitizers as already proposed by Grunnet-Jepsen et. al. [208]. On the one hand, the occurrence of OTA in the materials investigated here in general agrees with this conclusion, since ionized sensitizer

moieties are generated by optical irradiation and, thus, represent optically activated trapping sites. Even further support for this interpretation comes from the reversibility as observed for the OTA effect as demonstrated above, since the optically activated traps of this kind will vanish again after some time due to recombination with “free“ holes. On the other hand, the T_g -dependence as observed for the OTA effect contradicts this interpretation. It is known that TNF and PVK form charge-transfer complexes (CTC), which represent the active charge-generation sites. After a CTC has been optically excited a bound electron hole pair is formed, which then separates under the influence of the externally applied field yielding mobile holes. Thus, the CTC dissociates leaving a negatively charged immobile TNF molecule behind. According to [196] the generation efficiency of “free“ holes does not depend on T_g , which consequently applies to the generation efficiency of negatively charged sensitizer moieties as well. Hence, if these shall represent the dominant PR trap species, one must conclude, that the OTA effect should also not depend on T_g . However, the opposite case was observed experimentally (figure (5.4 - 6)). Accordingly, the attribution of the OTA effect solely to the generation of ionized sensitizers appears over-simplified, and a more complex situation is implied involving more than only one trap species. This, furthermore, agrees with the results presented in “5.3.) The influence of the sensitizer concentration on the PR performance of PVK based polymer composites” on page 257, where it was shown, that Poole-Frenkel traps are an important but not the only kind of PR traps in polymers.

Now the results can be discussed, which were obtained from the experiments studying the PR erasure kinetics as a function of the erasure intensity as well as of the recording time (figure (5.4 - 8)).

Taking into account the OTA effect and assuming Langevin-type recombination, eq. (5.4 - 8) implies a decrease of $1/\tau_{fast}$ (and, thus, an increase of τ_{fast}) as a function of increasing recording time at constant erasure intensity, since the charge carrier mobility decreases with increasing trap density and/or depth, thus, lowering the recombination coefficient. The experimental results seemingly follow this prediction consistently for recording times of $t_{rec} \leq 500\text{sec}$ as is shown in figure (5.4 - 8)(A). For longer recording times the fast rates level off, indicating that the trap situation does no longer change, as already mentioned before.

In contrast, equation eq. (5.4 - 8) does not necessarily imply a recording time dependence for $1/\tau_{slow}$. However, before this point can be discussed, the detrapping rate δ in equation eq. (5.4 - 8) must be accounted for. For very small erasure intensities, the zero-order hole density will be very small as well, which allows to neglect the term $\gamma_T n_0$. The slow rates then should dominantly be determined by the detrapping rate, which will not be altered by the trap density, but rather by the trap depth. Accordingly, it follows from figure (5.4 - 8)(B), that the depth of the optically activated traps seems to be constant, since there is no more a notable recording time dependence of the slow erasure rates for the smallest erasure intensity applied. Accordingly, the retardation of the slow erasure component as a function of increasing recording time at high erasure intensity (where the term $\gamma_T n_0$ cannot be neglected) should be attributed to an increasing trap density due to OTA. It shall now be assumed that Langevin-behavior applies not only for the charge carrier recombination process, but also for the trapping process (i.e. $\gamma_T = (q\mu)/\varepsilon$, see eq. (2.4 - 188)) as is implied by the assumption that negatively charged sensitizers may be the dominant trap species [208, 209]. In this case, also the slow erasure rates will depend on the recording time and an increase of the trap density due to OTA will lead to a decreasing slow erasure rate as a function of increasing recording time like for the fast rates. However, there are strong arguments against the assumption that Langevin-behavior applies also for the trapping process:

At first, a Langevin-type hole trapping coefficient γ_T (i.e. γ_T equals γ_R) would imply that δ equals the photo-generation rate α_G and, hence, becomes negligible in low light intensity

approximation. As a result, the slow erasure component would vanish, i.e., equal the fast erasure rate (see eq. (5.4 - 6)). This also contradicts the aforementioned assumption that there is only a single trap species following Langevin-behavior as proposed by [209], the number density of which increases with increasing recording time. Please note that the described situation is indeed observed for the shortest recording times applied (i.e. when OTA has not yet notably taken place) when the erasure behavior becomes mono-exponential as already pointed out before.

Secondly, for higher erasure intensities, an increasing dependence of the slow rates on the recording time can be observed, which is even stronger than observed for the fast rates at the highest erasure intensity applied (figure (5.4 - 8)(B)). If Langevin-behavior would be implied for the trapping process, the recording time dependence of the slow erasure rates would be determined by the decrease of the charge carrier mobility for increasing trap density, as discussed above for the fast rates. Moreover, the detrapping rate δ is not affected by a changing trap density as discussed before, i.e. is not affected by OTA and, thus, independent from the recording time. Therefore the recording time dependence of the slow erasure rates at high erasure intensity may at maximum be as strong as found for the fast rates (for $\delta \approx 0$), but never be stronger, which contradicts the experimental observations (figure (5.4 - 8)(B)).

It follows that the recording time dependence of $1/\tau_{slow}$ at high erasure intensity cannot be explained assuming a single trap species following Langevin-behavior. This, in turn, indicates another, second trap species, which rules the slow erasure process. These „new“ traps must be optically activated deep traps and of fundamentally different physical nature as compared to Poole-Frenkel traps showing Langevin behavior.

The basic properties of these traps can be better understood, if the ratio between the slow and the fast rates is considered at the different erasure intensities and for different recording durations. The ratios for two very different recording times are depicted in figure (5.4 - 9).

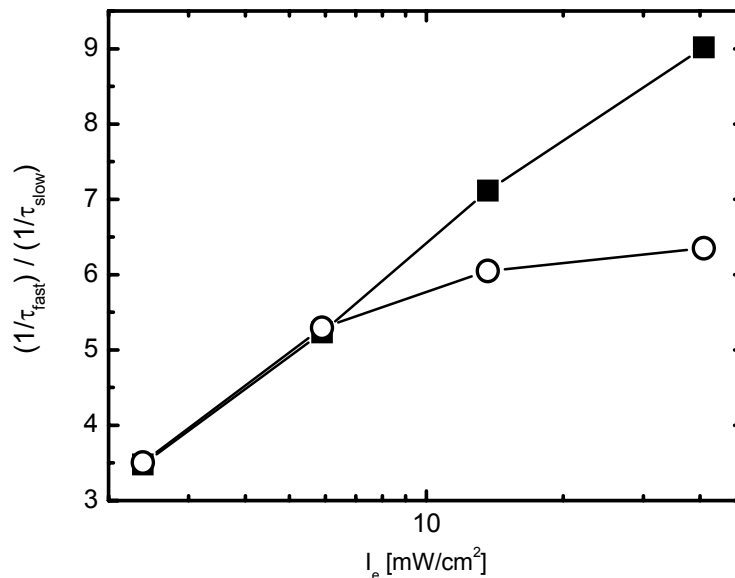


Figure (5.4 - 9): Dependence of the erasure ratios for material C on the erasure intensity I_e for long (1000sec; solid symbols) and short (30sec; open symbols) recording time.

As already discussed above, for the long recording time there is strong indication, that the trap situation has already come to an equilibrium state. In contrast, for the short recording time the OTA effect is not yet pronounced, if observable at all. Figure (5.4 - 9) demonstrates that the rate ratios increase with increasing erasure intensity, however, the dependence is

remarkably different for the different recording times. This result may be understood when considering the rate ratio according to eq. (5.4 - 8), which reads:

$$\frac{1/\tau_{fast}}{1/\tau_{slow}} = \frac{\gamma_R n_0}{\delta + \gamma_T n_0} \quad \text{eq. (5.4 - 9)}$$

The zero-order hole density n_0 may be assumed to increase approximately linearly with the intensity of the uniform illumination applied during erasure of the grating, since one may safely assume, that the investigated systems are operated in the range of non-saturation. In contrast, γ_T and γ_R do not depend on the erasure intensity. The detrapping rate δ according to eq. (5.4 - 7), on the other hand, cannot a priori be presumed to be independent from the erasure intensity. However, for now it shall be assumed that the optically activated traps are optically inactive, i.e. can only be emptied thermally. In this case, δ will not depend on the erasure intensity as well. It will be shown below that this is indeed a reasonable assumption.

Figure (5.4 - 9) shows that the rate ratios according to eq. (5.4 - 9) increase almost linearly as a function of the erasure intensity on logarithmic scale for the long recording time, which demands that the terms of the sum in the denominator of eq. (5.4 - 9) are of similar order of magnitude (neither term must clearly dominate) for all erasure intensities. In contrast, the $(1/\tau_{fast})/(1/\tau_{slow})$ seemingly saturates for higher erasure intensities, which requires that a change of n_0 does no longer effect the ratio $(1/\tau_{fast})/(1/\tau_{slow})$. Hence, $\gamma_T n_0$ must be significantly larger than δ for short recording times and higher erasure intensities. As a third case, one may assume that δ may be much larger than $\gamma_T n_0$, which would lead to a positive curvature of the corresponding function in the diagram of figure (5.4 - 9). This case, however, is not observed. Furthermore, the denominator in eq. (5.4 - 9) must be smaller than the numerator, which again excludes that the hole trapping coefficient follows Langevin behavior, since otherwise $\gamma_T n_0$ would equal $\gamma_R n_0$ and, thus, $(1/\tau_{fast})/(1/\tau_{slow}) \leq 1$ would apply for all recording times. On the other hand, if the mono-exponential erasure behavior observed for the shortest recording times is interpreted as a coincidence of the fast and the slow erasure rates as proposed above, the rate ratio for this case may be considered as unity and independent from the erasure intensity. Hence, for very short recording times, Langevin behavior is indeed implied for the hole trapping coefficient, i.e. the numerator and the denominator are identical, as already discussed above.

Combining the results presented above leads to the conclusion, that the slow erasure rate as a function of the recording time (and, hence, as a function of increasing optical activation of traps) must be described by a more complex formalism, which might read as follows:

$$\begin{aligned} 1/\tau_{slow}(t_{rec}) &= W_1(t_{rec}) \cdot (\delta + \gamma_T n_0) + W_2(t_{rec}) \cdot \gamma_{LT} n_0 \\ &= W_1(t_{rec}) \cdot \delta + [W_2(t_{rec}) \cdot \gamma_{LT} + W_1(t_{rec}) \cdot \gamma_T] n_0 \end{aligned} \quad \text{eq. (5.4 - 10)}$$

Here, $W_1(t_{rec})$ and $W_2(t_{rec})$ are weight factors ($W_1 + W_2 = 1$) taking into account optical activation of traps and γ_{LT} is a Langevin-type hole trapping coefficient (one may as well just write γ_R). γ_T is significantly smaller than γ_{LT} and, hence, for typical erasure intensities $\delta + \gamma_T n_0$ is also markedly smaller than $\gamma_{LT} n_0$ (only for very small erasure intensities $W_1 \delta$ becomes the dominant term for $1/\tau_{slow}$). For very short recording OTA has not yet evolved and $W_1(t_{rec}) = 0$ ($W_2(t_{rec}) = 1$). As the recording time increases, OTA takes place, $W_1(t_{rec})$ increases, whereas $W_2(t_{rec})$ decreases. As a result, $1/\tau_{slow}$ decreases, and the rate ratio according to equation eq. (5.4 - 9) increases. On the other hand, the intensity dependence of the rate ratio increases as well, since the prefactor of the zero-order hole density (the term in squared brackets) decreases and the denominator in eq. (5.4 - 9), thus, shows a reduced intensity dependence as compared to the numerator.

Now the validity of this model will be tested for the exponents $\sigma_i(t_{rec})$ according to eq. (5.4 - 5) (figure (5.4 - 8)(C)). Both the fast and the slow rates exhibit a sublinear dependence on

the erasure intensity, which has been observed several times before in PR polymers [83, 213]. In the model applied here, the dependence of the erasure rates on the erasure intensity is due to the intensity dependence of the zero-order hole density n_0 . The exponent σ_{fast} is found to be approximately independent from the recording time, which is in agreement with equation eq. (5.4 - 5) in combination with equation eq. (5.4 - 8), and yields $\sigma_{fast} \approx 0.9$ (figure (5.4 - 8)(C)). The exponent σ_{slow} , on the other hand, decreases strongly with increasing recording time, finally levelling off at $\sigma_{slow} \approx 0.45$ (figure (5.4 - 8)(C)). This can be explained qualitatively by the model proposed above, if one assumes that the optically activated traps are optically inactive (i.e. cannot be emptied optically; consequently, δ does not change as a function of the erasure intensity) as already assumed before and combines eq. (5.4 - 5) with eq. (5.4 - 10). For increasing recording time $W_1(t_{rec})$ increases and $W_2(t_{rec})$ decreases, as discussed before. Accounting for the relations between δ , γ_T and γ_{LT} , as also discussed before, this requires that the intensity dependence of the slow rates decreases as well, which agrees with the experimental results.

Furthermore, the presented model can explain why the decrease of the slow erasure rates $1/\tau_{slow}$ as a function of the recording time for the highest erasure intensities applied in figure (5.4 - 8)(B) is more pronounced as compared to the corresponding decrease of the fast erasure rates (figure (5.4 - 8)(A)). Since for increasing recording time $W_1(t_{rec})$ increases and $W_2(t_{rec})$ decreases, as discussed before, the weighting of the Langevin-type hole trapping coefficient γ_{LT} in the prefactor of n_0 in eq. (5.4 - 10) decreases, whereas the weighting of γ_T increases. As also mentioned before, γ_T must be assumed to be significantly smaller than γ_{LT} . Additionally, γ_{LT} will decrease as a function of increasing recording time as discussed before for γ_R . Therefore, one can safely assume that the prefactor of n_0 in eq. (5.4 - 10) decreases much more pronounced as a function of increasing recording time as compared to γ_R , which determines the decrease of the fast erasure rates as a function of increasing recording time, as discussed above. On the other hand, an increase of $W_1(t_{rec})$ as a function of increasing recording time leads to an increasing contribution of δ to the slow erasure rates counteracting the described relationship, since δ is independent from the recording time as mentioned before. Therefore, the decrease of $1/\tau_{slow}$ as a function of the recording time will become the more pronounced the higher the erasure intensity and, for sufficiently high erasure intensities, may well be more pronounced than observed for $1/\tau_{fast}$, which is indeed observed experimentally.

In order to further verify the model proposed above and in order to prove the assumption of optical inactivity of the optically activated traps, the complete measurement and evaluation procedure as described in the preceding section was also applied to a material of the type C, however, doped with 0.82%wt of TPD (N, N, N', N' - tetraphenyl - p - diaminobiphenyl, "triphenyldiamine"). This material is denoted "CT" in table 5-1 on page 211 as well as hereafter. The HOMO of TPD constitutes deep traps within the charge transport manifold, if doped in small molar ratio into a PVK polymer matrix. TPD is located about 0.5eV below the PVK charge transport manifold. Since the photon energy at operating wavelength is about 2eV, TPD sites here act as optically inactive deep hole traps. Material CT showed a T_g of 14°C and its erasure kinetics proved to be limited by the decay of the PR space-charge field as well. A slope of about $\sigma_{slow} \approx 0.4$ as a function of the erasure intensity was found, which did not depend on the recording time (figure (5.4 - 8)(C)). This meets the expectations according to the model described above. Furthermore, the magnitude of σ_{slow} for material CT strongly indicates that the optically activated traps in the not doped material C are indeed optically inactive. In contrast, if these traps would be optically active, δ in the not doped material would be a function of the erasure intensity as well, which would imply a notably stronger intensity dependence of the slow erasure rates as compared to the TPD doped material, i.e. σ_{slow} for material C should then be significantly larger than 0.4.

5.4.1.3.6.)Conclusions on the nature of the PR traps

In conclusion, the presented results indicate (at least) two important and fundamentally different species of hole traps occurring in the investigated PR polymer blends, both of which are optically activated. At first, there are Poole-Frenkel traps showing Langevin behavior, as already proposed before several times [208, 209] and as was found in “5.3.) The influence of the sensitizer concentration on the PR performance of PVK based polymer composites” on page 257. Since these traps require negatively charged trapping centers, they are directly correlated with the negatively charged sensitizer moieties (TNF), the number density of which increases as a function of the recording time. Poole-Frenkel traps seem to govern the fast component(s) of the PR erasure process, as already proposed by Khand et. al. [209]. Secondly, there is another trap species, which does not follow Langevin behavior. These traps seem to govern the slow erasure component and should be considered as optically inactive as discussed above. One may speculate, that this second kind of traps should be conformational, since conformational traps are neutral when empty and, thus, do not show Langevin behavior. However, conformational traps are believed to be shallow traps, which does not agree with the experimental results presented here, indicating deep traps as discussed above. Furthermore, there is no reason to assume that conformational traps are optically activated. Conformational traps in PVK are due to unfavorable orientation (i.e. poor overlap of the π -electron systems) of neighboring carbazole moieties in migration direction, thus, forming a “dead end“ for a migrating charge carrier [87]. However, a hole trapped in such a dead end will stay relatively long on the “last“ carbazole moiety of the dead ended migration path. In order to stabilize the unfavorable carbazole radical cation at such a position a sandwich complex with a neighboring carbazole moiety located “behind“ (i.e. against the migration direction) the cation in question may be formed. Such dimer radical cations have been proposed several times as deep traps in the transport manifold of amorphous organic conductors like PVK [214 - 216]. Excimer-forming sites of this kind would meet the requirements demanded for the second trap species under discussion: (i) They are neutral when empty and, therefore, do not show Langevin behavior. (ii) The dimer radical cation is initiated by a hole already generated and captured in a conformational trap, i.e. the dimer formation can be considered as optically activated. Please note, that a neutral excimer formed by two uncharged carbazole moieties would of course be an optically activated trap as well. However, the formation of a neutral excimer would require optical excitation of one of the involved carbazole moieties, which can safely be excluded here, since the applied wavelength is far beyond the absorption band of PVK. (iii) The formation of dimer radical cations is reversible, which agrees with the experimental results on OTA (figure (5.4 - 7)). (iv) The carbazole dimer radical cations represent optically inactive traps at the applied wavelength.

The assumption of carbazole dimers acting as optically activated deep traps may also qualitatively explain the T_g -dependence observed for the OTA effect (figure (5.4 - 6)). It has been discussed earlier, that slow collective motion of the conducting polymer matrix occurring in the investigated low- T_g PVK-based PR polymer composites leads to partial cancellation of conformational traps. This effect was made responsible for a reduction of the apparent PR trap density leading to a reduced steady-state PR performance for $T_g < RT$ (see “5.2.2.) The relation between the glass-transition temperature and the steady-state performance in PVK based PR polymers” on page 228 and [196]). Such an effect will counteract the formation of the carbazole dimers proposed above. Hence, for decreasing T_g , the formation of carbazole dimers is increasingly aggravated, since the apparent density of conformational traps is reduced, which were assumed above to be the precursor for the formation of the carbazole dimers. Therewith, for small pre-irradiation fluency (i.e. small density of free charge carriers during the pre-illumination period) and low T_g , the formation of the dimer trapping sites may be assumed as still insignificant as found for material D. In contrast, in material B with T_g close to RT , the

apparent density of conformational traps is markedly higher, leading to a more pronounced formation of dimers as compared to the materials of lower T_g . As the pre-irradiation fluency increases and therewith the density of free charge carriers, the cancellation effect for the conformational traps in the materials of lower T_g becomes less significant as compared to the number density of charge carriers actually trapped in conformational traps. As a result, the formation of carbazole dimers is strongly accelerated, finally reaching the same level as for the materials of higher T_g .

However, it must be pointed out that the experiments presented do not provide any direct evidence for the occurrence of carbazole dimer radical cations acting as optically activated deep traps. This renders the above implications speculative.

5.4.1.3.7.)The impact on holographic multiplexing in PR polymers

The first time within the frame of this work, now the potential application of the investigated materials in holographic multiplexing may be considered. According to the theory of holographic multiplexing, which has been elaborated upon in “2.3.3.3.) System metrics for holographic multiplexing in erasable media” on page 65, for erasable holographic media showing mono-exponential dynamic behavior, an analytical expression can be derived for the writing schedule as well as for the M-number $M/\#$, the latter of which then writes:

$$M/\# = A_0 \cdot \frac{\tau_e}{\tau_r} . \quad \text{eq. (5.4 - 11)}$$

A_0 characterizes the total dynamic range of the holographic medium, and τ_e and τ_w are the erasure and recording time constants of the holographic grating, respectively. For all materials under investigation, the available dynamic range is similar and, hence, the quantity τ_e/τ_r will be the crucial parameter for achieving high $M/\#$ s. In this case, a larger ratio τ_e/τ_r generally implies better multiplexing capability. Figure (5.4 - 10)(A) shows the ratio of the logarithmically averaged erasure and recording time constants versus the recording time. A clear trend of τ_e/τ_r as a function of the recording time was found. The ratio of the time constants becomes relatively more favorable with increasing recording time due to the retardation of the PR grating erasure with increasing recording time, as demonstrated and discussed above. The slow down of the fast erasure component was attributed to a reduction of the charge carrier mobility as a result of OTA. This trend is markedly enhanced for the logarithmically averaged total response times of the systems investigated due to the weighted inclusion of the slow erasure component.

For comparison with Khand's data [209], figure (5.4 - 10) (B) depicts the ratios of only the fast erasure and recording time constants as a function of the recording time. These ratios have been stated to be constant within a range of 0.68 ± 0.08 for a wide variety of applied fields, operating wavelengths, and various concentrations of different sensitizers for PVK based low- T_g systems similar to the materials under investigation [209]. This general relation could basically be confirmed. However, it must be pointed out that different experimental techniques were applied. Khand et. al. used the reading beam of their DFWM setup for erasure, which had the same intensity as the sum of the recording beams. Since the reading beam must be Bragg-matched to the holographic grating, it must be expected that grating refreshment effects are induced by the transmitted reading beam and its diffracted portion. This leads to a significant reduction of the observed erasure speed, as discussed several times before. In contrast, a non Bragg-matched erasure beam was used here, which, however, had only about half the intensity of the sum of the recording beams. Therefore, also here a reduced erasure speed must be anticipated as compared to a real multiplexing experiment, where the grating erasure is performed at the same intensity as the grating recording. Hence, the agreement between data

presented here and the data published in [209] may be taken as coincidental. Khand et. al. did not consider the recording time dependence of τ_e/τ_r .

Please note, that a saturation effect for long recording times, especially for material C and D, is indicated in both the cases, when considering the ratio of the fast time constant as well as the ratio of the logarithmically averaged time constants. This might be attributed to a saturation effect in the trap situation, which applies to the fast as well as to the slow erasure time constants, as discussed above, and, accordingly, also to the logarithmically averaged time constants. The ratio of the logarithmically averaged time constants is basically smaller as compared to the ratio of the fast components and the difference between the particular materials is more pronounced.

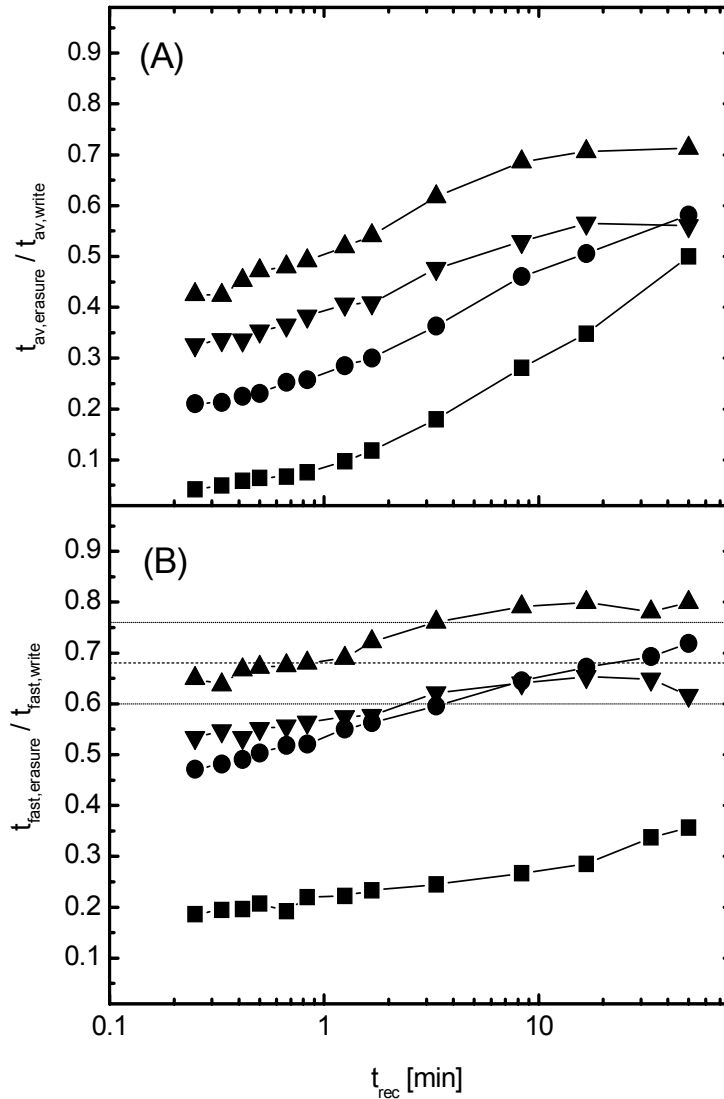


Figure (5.4 - 10): Ratio of the erasure and recording time constants for material A (squares), B (circles), C (up triangles) and D (down triangles) vs. the recording time of a particular hologram. (A) logarithmically averaged response times, (B) only fast response times. The dashed and dotted lines mark the range proposed in [209].

Obviously, among the investigated materials, type C is most preferable for multiplexing purposes, which clearly implies an optimum T_g for multiplexing in this type of materials. However, it must be pointed out that the actual inapplicability of equation eq. (5.4 - 11) to the investigated class of materials due to their multi-exponential recording/erasure behavior renders

this statement academical. This is additionally underlined by the fact, that τ_e/τ_r , always shows a strong systematic dependence on the recording time, even if only the fast time constants are considered.

Please note finally that logarithmically averaging the time constants is actually unacceptable in order to obtain a suitable exposure schedule. However, simply using the fast time constants will fail as well, since it is clear that an exposure schedule derived from only a part of the overall dynamic behavior of the systems will not work either.

5.4.1.4.) Quintessence of the investigations on the PR grating erasure in systems without extrinsic deep traps

It was found that the PR grating erasure dynamics in the investigated high- T_g PVK based PR polymers is governed by the orientational relaxation of the NLO chromophores in the polymer matrix, whereas it is determined by the decay of the PR space-charge field in the low- T_g systems. This agrees with the expectations from “5.2.3.) The relation between the glass-transition temperature and the dynamic performance in PVK based PR polymers” on page 243, In all cases, the erasure dynamics of the PR grating depended on the recording time of the grating. This was attributed to a viscous flow of the polymer matrix in the high- T_g regime. In contrast, in the low- T_g regime, the retardation of the grating erasure as a function of the recording time was found to be due to optical activation of trapping sites. Based on a theoretical model for the PR grating erasure in polymers proposed by Cui et. al. [83], two fundamentally different types of optically activated traps could be identified. On the one hand, Poole-Frenkel traps showing Langevin behavior are generated, which is in agreement with earlier findings [208, 209]. These traps seem to determine the initial grating erasure. On the other hand, deep traps not showing Langevin behavior are optically activated, which might be carbazole dimer radical cations and which seem to govern the erasure behavior on longer time scale. Thus, single trap theoretical models for the PR effect in PR polymers as proposed in [208] appear inadequate in order to describe these systems with sufficient accuracy. The formation of the carbazole dimers apparently strongly depends on T_g , which may be attributed to slow collective motion of the conducting polymer matrix occurring in materials with $T_g \ll RT$. This leads to a smaller apparent density of conformational traps (see “5.2.2.) The relation between the glass-transition temperature and the steady-state performance in PVK based PR polymers” on page 228 and [196]), which were proposed as precursor for the dimer formation. It is to be pointed out, that the fact that the trap situation in PR polymers obviously changes significantly during recording of a grating renders any fitting of PR recording data purely phenomenological, since the fitting parameters are time dependent. Finally, the potential applicability of the systems investigated for holographic multiplexing was considered. A relative optimum of the theoretical multiplexing capabilities as a function of the reduced temperature $T_r = T_g - RT$ for $T_r = -6^\circ\text{C}$ was found on the one hand. However, due to the recording time dependence of the erasure dynamics PR polymers of the investigated type appear unfavorable for holographic multiplexing in general on the other.

5.4.2.)PR grating erasure in systems doped with extrinsic traps

It has been shown in the preceding section, that the ratio between the recording and the erasure dynamics is rather unfavorable, which must be expected to limit the multiplexing capabilities of the PVK based PR polymers under investigation. However, an even bigger problem for a potential application of PR polymers in holographic mass data storage devices arises from the recording time dependence of the erasure dynamics, since this property makes the selective erasure and re-recording of particular holograms within a manifold of existing multiplexed holograms very difficult. By that, a major advantage of PR holographic media for data storage applications, namely their rewritability, is nearly counted out. In the preceding section was furthermore shown that the recording time dependence of the hologram erasure dynamics in low- T_g systems is due to the optical activation of deep trapping sites. Thus, in order to stabilize the erasure dynamics, as a first approach, a novel material was designed by adding extrinsic deep traps to the systems in question. As will be shown in a later section (“5.6.) Holographic multiplexing in PVK based PR polymers” on page 329), this action led to a significant improvement in the number of holograms, which could be multiplexed, as compared to similar systems without extrinsic traps, while the M-number $M/\#$ remains similar. However, the initial goal, i.e. stabilization of the hologram erasure behavior, was not achieved but rather an even more complex erasure behavior was found as compared to materials without extrinsic traps, which still strongly depends on the recording time.

It was found that holograms recorded into the newly designed materials applying short recording times and low recording intensity increase considerably in strength during a subsequent erasure process if performed at low erasure intensity as well. This feature (which, on the other hand, caused the aforementioned improvement of the general multiplexing capabilities), despite showing some similarity to holographic time of flight (HTOF), has not been observed so far under the standard holographic recording conditions, i.e. by recording a hologram over several seconds up to minutes with low intensity as opposed to high-intensity sub-millisecond pulse recording of a hologram usually performed for HTOF experiments [138, 148, 218, 219].

Subsequently, a phenomenological investigation of this new feature is presented focussing on a general qualitative explanation for the observed behavior. Therefore, the build-up dynamics of PR gratings was investigated with respect to the important relation between the phase shift of the index grating and its actual modulation depth. Furthermore, the first investigation on the erasure dynamics concerning the same parameters will be presented.

Many PR polymers exhibit a fairly small phase shift ϕ between the refractive index grating and the optical interference pattern of about $\phi \approx 20^\circ$ or even less in the steady state regime [220]. Furthermore, there are indications, that the phase shift of a PR grating changes during recording. These circumstances open the way to speculations about what may happen during grating erasure. It is particularly interesting, whether the grating starts shifting again to higher values of ϕ while simultaneously decaying in amplitude. Since the initial phase shift at the beginning of erasure is typically close to the steady state value and, thus, considerably smaller than 90° representing the ideal case of the PR space charge distribution in PR materials, such a behavior may significantly contribute to the observed erasure dynamics. As the charge separation increases, the modulation depth of the space-charge distribution improves (and, accordingly, the space charge field increases), while the total space-charge density decreases, which reduces the space-charge field. Thus, one may assume that the erasure dynamics of the PR space-charge field should be determined by two counteracting processes of unknown magnitude.

5.4.2.1.)Experimental aspects

The investigated materials are derived from the first high performance PR polymer [13], but with significantly improved long-term stability [136] and doped with different amounts of TPD (N, N, N', N' - tetraphenyl - p - diaminobiphenyl, "triphenyldiamine"). TPD constitutes deep hole traps of approximately 0.5eV depth if doped in small molar ratio into a PVK polymer matrix. The compositions and the glass-transition temperatures, as determined by DSC, of the investigated materials AT, BT, CT, CT1 - 3 and DT are listed in table 5-1 on page 211 as well as at the end of the current section. PR devices were prepared according to "4.1.) Preparation of materials and sample structure" on page 179. The active layer thickness was $d = 125\mu\text{m}$. The ambient temperature was $20\pm 0.5^\circ\text{C}$ for all measurements.

A new measurement technique was devised, which allows to obtain a measure of the PR phase shift during erasure together with a measure of the time history of the magnitude of the PR space-charge field. The general experimental setup and the evaluation procedure for this experiment are described in detail in "4.2.) Wave mixing experiments" on page 181. Please note that this measurement technique introduces a phase reference "from outside" the PR grating. This does only make sense, if there are components of the PR grating, the spatial position of which can be considered as unchanged at least during the initial erasure process. In the case under consideration here, this is the distribution of the immobile negative charge carriers, which may additionally be assumed to be in phase with the phase reference introduced by the measurement technique at least during the initial erasure process.

Using the setup described in the aforementioned section, dynamic phase-conjugate degenerate four-wave-mixing (DFWM) experiments as well as two-beam-coupling (2BC) experiments were carried out using a HeNe laser. Therewith, the dynamic response behavior of the investigated materials was determined. Unless otherwise noted, the following experimental configurations were applied: For determining solely the recording/erasure behavior of the refractive index modulation, a configuration with s-polarized recording beams (not chopped) at intensities of $I_{01} = 2.8\text{mW}/\text{cm}^2$ (recording beam 1) and $I_{02} = 2.3\text{mW}/\text{cm}^2$ (recording beam 2) was used, and the grating was erased without probing the dynamics of the phase shift, i.e. with the recording beams switched off. In this configuration, a resolution of better than $\eta = 5 \cdot 10^{-3}$ was achieved. Hereafter this configuration will be referred to as configuration (1). For determining the recording/erasure behavior of the refractive index modulation as well as the dynamics of the PR phase shift, the recording beams were p-polarized and chopped and had time averaged intensities of $I_{01} = 4.7\text{mW}/\text{cm}^2$ and $I_{02} = 3.8\text{mW}/\text{cm}^2$ when recording the PR grating. For the erasure process the recording beams were attenuated to time averaged intensities of $I_{01} = 3.7\mu\text{W}/\text{cm}^2$ and $I_{02} = 3\mu\text{W}/\text{cm}^2$. This configuration yielded a resolution of better than $\eta = 5 \cdot 10^{-3}$ and $\Gamma = 0.25\text{cm}^{-1}$ and will be referred to as configuration (2) hereafter. The modulation depth of the interference pattern was $m = 0.994\pm 0.001$ for recording at both polarizations. The reading beam intensity was appr. $I_r = 5\mu\text{W}/\text{cm}^2$ in all cases. The erasure beam originated from a second HeNe laser and had perpendicular incidence onto the sample surface in all cases. The erasure intensities were $I_{e1} = 3.2\text{mW}/\text{cm}^2$ in configuration (1) and $I_{e2} = 5.1\text{mW}/\text{cm}^2$ in configuration (2). Unless otherwise noted, prior to recording a PR grating, a dark period under field of 90min as well as a pre-illumination period of 30min performed by recording beam 2 was applied for each measurement. For all measurements an electrical field was continuously applied to the samples with a polarity causing minimized beam-fanning effects [221], i.e. the field directions for recording with s-polarized and with p-polarized beams, respectively, were reversed. Please note that configuration (2) allows for direct calculation of the PR phase shift from the experimental data since both the refractive index modulation in DFWM as well as the PR gain are determined for p-polarized light.

Considering the continuity of the PR phase shift curves over the switching process from

recording to erasure, an offset in the data occurs (see corresponding figures). This can be attributed to the problem to find appropriate reference values for the intensity of the beams involved in the 2BC effect, as discussed in “4.2.) Wave mixing experiments” on page 181. In the case of recording it is clear, that these reference values are the initial values of the recording beams obtained in advance of the development of a PR grating. In the case of erasure, however, when the intensity of the recording beams was dramatically reduced as described before, average value of the beam intensities were used, which were obtained after the grating had been completely erased. This method suffers from the problem that the two methods to obtain the reference values represent different working conditions of the material. The observed offset is only clearly visible when the total signal strength is small, whereas it is almost absent when the total signal strength is large. This indicates, that there is a small constant offset occurring in a parameter used for calculating the PR phase shift ϕ , which does not effect the general dynamic trends revealed by the experimental results.

Please note, that the phase shift can no more be stated reasonably for very small experimental values of Γ and Δn in view of too bad a signal to noise ratio, which causes an unreasonably large error for ϕ . The experimental curves shown hereafter are either cut shortly before this point, or are covered by hatchings beyond this point, respectively.

Table (5-7): Chemical composition and glass transition temperature of the materials investigated in “5.4.2.) PR grating erasure in systems doped with extrinsic traps”

Material	DMNPAA	MNPAA	PVK	ECZ	TNF	TPD	T_g
units	[%wt]	[%wt]	[%wt]	[%wt]	[%wt]	[%wt]	[°C]
AT	25	25	42	6.18	1	0.82	18.5
BT	25	25	40	8.18	1	0.82	17
CT	25	25	38	10.18	1	0.82	14
CT1	25	25	36	11.36	1	1.64	10
CT2	25	25	34	10.1	1	4.9	12
CT3	25	25	30	9	1	10	12.5
DT	25	25	36	12.18	1	0.82	13

5.4.2.2.) Experimental results on PR grating erasure in trap-doped systems

Figure (5.4 - 11) shows a characteristic example for the short term recording behavior of the materials C (without extrinsic deep traps) and CT (with extrinsic deep traps), both of which having almost identical T_g . As expected, a significant slow down of the grating build-up dynamics for the trap doped material CT as opposed to the trap free material C is observed, which is due to the reduced charge-carrier mobility due to the trap doping [46]. Taking the time to achieve 5% diffraction efficiency as a measure for the speed of the grating build-up, the recording speed of a PR grating is reduced by approximately a factor of five under identical experimental conditions (set-up configuration (1)). Furthermore, figure (5.4 - 11) shows a characteristic example for the short term recording behavior of material CT3. This material was doped with an amount of extrinsic deep traps, high enough to enable partial charge transport by

hopping between the trapping sites. T_g of material CT3 was slightly lower than that of material C or material CT and the recording curve was obtained using set-up configuration (2). Thus, the recording curve of material CT3 cannot be compared directly with the curves for the materials C and CT. However, it is clear that material CT3 exhibits significantly faster build-up dynamics as compared to the other two materials. This is due to an increased charge carrier mobility in material CT3 as compared to material C, which is in general found in PVK when the TPD concentration is high enough to form a new charge transport manifold, i.e. TPD contributes significantly as charge transporting site to the overall charge carrier transport process [46].

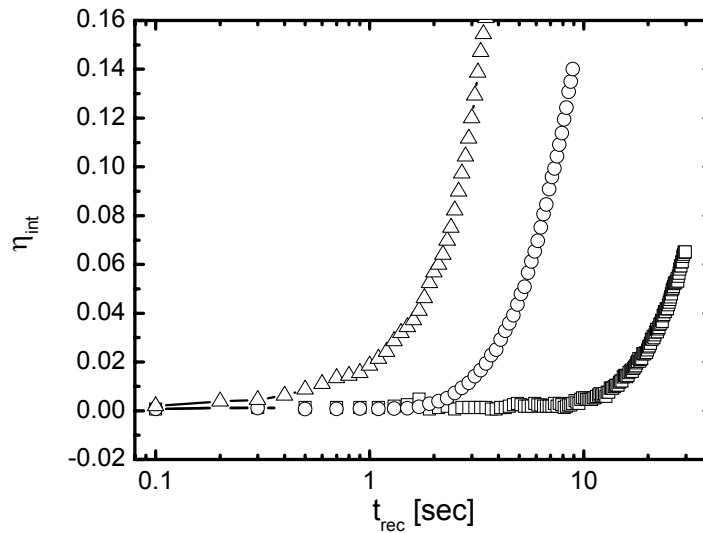


Figure (5.4 - 11): Grating buildup in the trap free material C (open circles), and in the trap doped materials CT (open squares) and CT3 (open triangles).

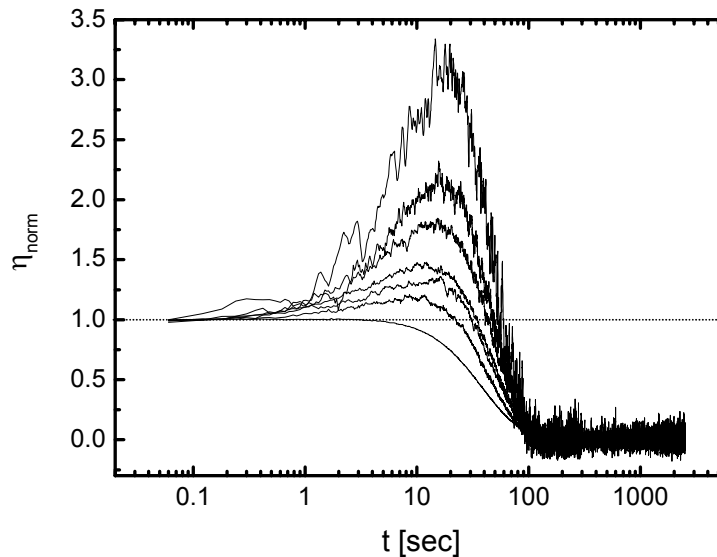


Figure (5.4 - 12) Time dependent evolution of the normalized diffraction efficiency during erasure of PR gratings in material CT recorded applying different recording times of $t_{rec} = 9, 12, 15, 20, 25, 30,$ and 75 seconds. For longer recording times, further increase of the diffraction efficiency in the erasure process was not observed. The arrow points into the direction of increasing recording times. The erasure curves are normalized to their initial value at the beginning of the erasure process.

Figure (5.4 - 12) depicts characteristic sets of normalized erasure curves of the PR grating in material CT (figure (5.4 - 12)(B)) for short recording times, as obtained using set-up configuration (1). A further increase of the diffraction efficiency during the initial erasure process is observed. The occurrence of the relative diffraction maximum seems to shift towards the starting point of the erasure process, if the recording time is increased.

In order to get an overview over the quality of the effect of further increasing diffraction efficiency during the initial erasure process, the observed behavior was empirically systematized for different materials and experimental conditions. Therefore standard recording/erasure experiments were carried out applying different recording times to a series of materials containing different amounts of TPD at similar T_g (CT and CT1 - 2) and using configuration (1). For this series of measurements an external field of $E_{ext} = 48\text{V}/\mu\text{m}$ was applied in all cases. Figure (5.4 - 13) shows the relative increase of the diffraction efficiency and the delay of the occurrence of the relative diffraction maximum for the aforementioned materials as a function of the applied recording time span. For this purpose, the beginning of recording was chosen as time origin $t = 0$.

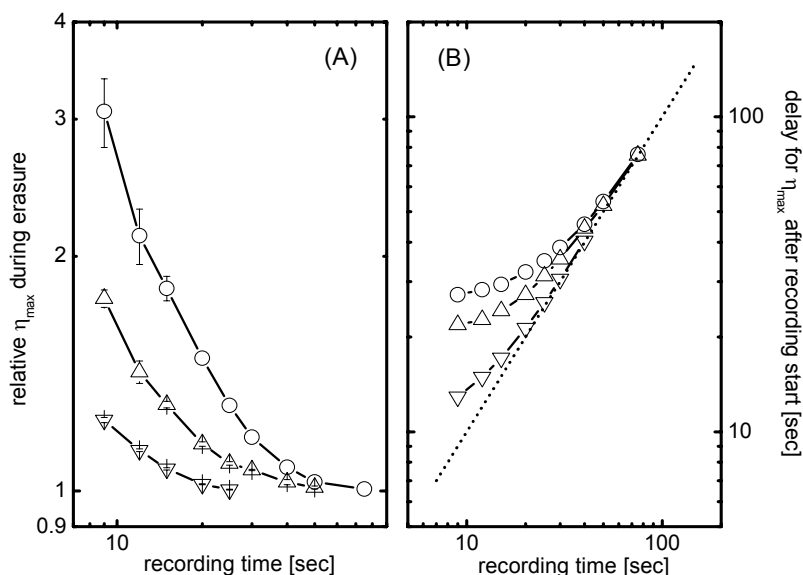


Figure (5.4 - 13): (A) Relative increase of the diffraction efficiency and (B) delay of the occurrence of the relative diffraction maximum $\tau_{\eta_{\text{max}}}$ after start of the recording process as a function of the recording time for materials containing different amounts of deep traps: CT (circles), CT1 (up triangles) and CT2 (down triangles). An external field of $E_{ext} = 48\text{V}/\mu\text{m}$ was applied in all cases. The dotted line in (B) depicts the end of recording.

Obviously, the effect is most pronounced for material CT containing a moderate amount of deep traps and decreases for even higher concentrations of TPD. The decreasing quality of the investigated effect with increasing TPD concentration exceeding 0.82%wt might be attributed to an increasing contribution of TPD to the charge transport as a hopping site within the polymer matrix. This interpretation is supported by the observation that material CT3 (containing 10%wt TPD) did not show a further increase in the diffraction efficiency within the interval of experimental parameters applied here, but only for recording times considerably shorter than 5 seconds (not shown). It was already proposed above that the charge transporting properties of the PVK polymer matrix in material CT3 is significantly determined by hopping between TPD sites, which are already dense enough to form a new charge transport manifold

[46]. Accordingly, the decreasing quality of the investigated effect with increasing TPD concentration exceeding 0.82%wt indicates that the materials CT1 to CT3 cannot safely be considered as typical “PVK-based” materials but may show a contribution of the TPD sites to the charge transporting process. Thus, the materials CT1 to CT3 fall beyond those, this work is focussed upon. Therefore, the further investigations will focus on material CT.

Please note, that materials containing a non-zero amount of TPD below 0.82%wt were not taken into account. Therefore, one cannot be sure that material CT exhibits the most pronounced effect. However, one can safely assume that material CT out of the considered series of trap doped systems is closest to the case of trap controlled charge transport in PVK. Please note furthermore, that, according to [46], even material CT3 should still exhibit dominantly trap controlled charge transport and a significantly smaller charge carrier mobility than material C. If this would be true, a retarded PR grating build-up dynamics as compared to material C should be expected for material CT3, since the PR grating build-up dynamics of the investigated systems is limited by the charge carrier mobility as several times discussed before. However, according to figure (5.4 - 11) this is clearly not the case, which indicates that the results presented in [46] cannot directly be applied here. A possible reason for that might be that the samples investigated in [46] did not contain further components as, for instance, ECZ as plasticizer, and exhibited a significantly different (i.e. higher) T_g . Especially the latter strongly affects the charge transporting properties of PVK based PR polymers as discussed in “5.2.) The PR performance of PVK based polymer composites at varying glass-transition temperatures” on page 226. However, a detailed consideration of this aspect is beyond the scope of this investigation.

Accounting for the experimental results indicating a strong dependence of the charge transporting properties on T_g as already noted above, a series of materials, AT, BT, CT and DT, was designed, which contained identical amounts of TPD, but exhibited different glass-transition temperatures. Details about the materials composition and their corresponding T_g 's are listed in table 5-7 on page 302. Recording/erasure experiments were carried out for the T_g -series applying different recording times and additionally three different external fields of $E_{ext} = 40, 48, \text{ and } 56 \text{ V}/\mu\text{m}$. For evaluation, in all cases the erasure curves were normalized to the value at the beginning of the erasure process and the relative increase in diffraction efficiency was plotted as a function of the recording time. Moreover, the time span, which has been elapsed when the diffraction maximum occurred, was plotted as a function of the recording time. For this purpose, again the beginning of recording was chosen as time origin $t = 0$. The results are shown in figure (5.4 - 14) and figure (5.4 - 15).

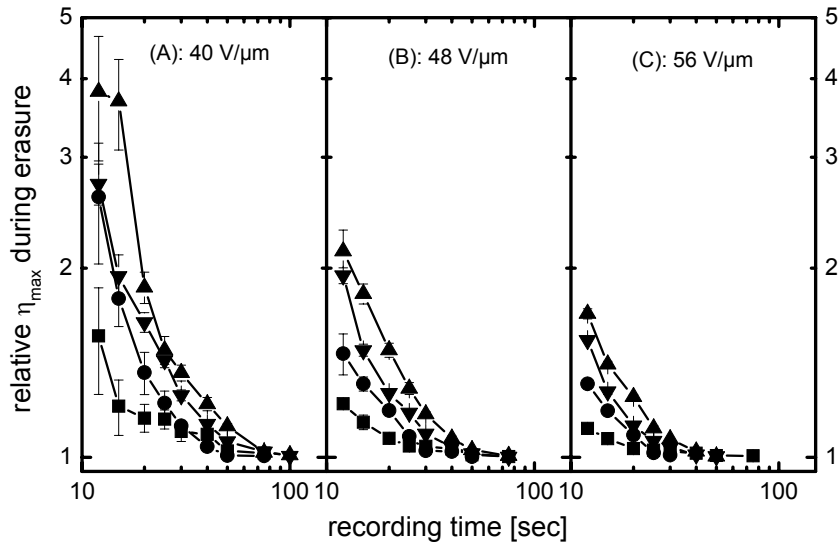


Figure (5.4 - 14): Relative increase in diffraction efficiency as a function of the recording time for the material series doped with 0.82%wt TPD but having different T_g : AT (squares), BT (circles), CT (up triangles), and DT (down triangles). Three different external fields of $E_{ext} = 40, 48,$ and $56\text{V}/\mu\text{m}$ were applied. The lines are guide to the eye.

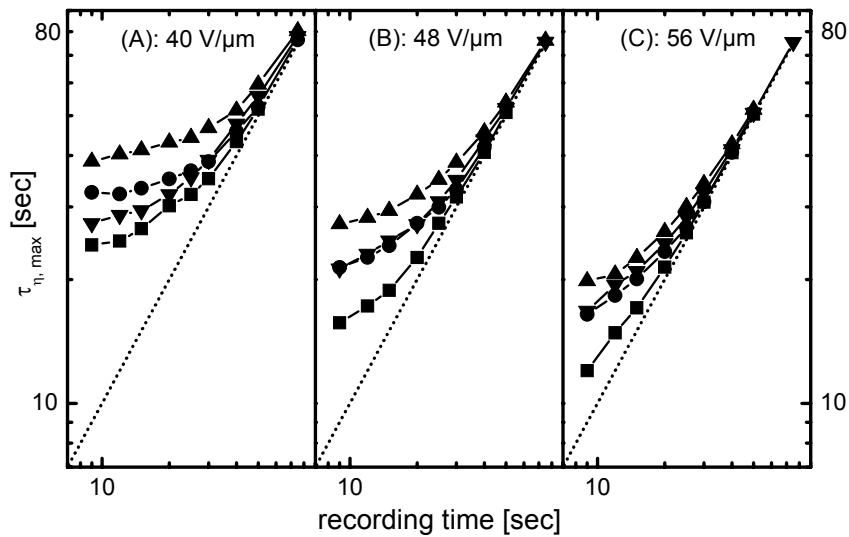


Figure (5.4 - 15): Delay of the occurrence of the diffraction maximum $\tau_{\eta, \max}$ after start of recording as a function of the recording time span for the material series doped with 0.82% TPD but having different T_g : AT (squares), BT (circles), CT (up triangles), and DT (down triangles). Three different external fields of $E_{ext} = 40, 48,$ and $56\text{V}/\mu\text{m}$ were applied. The dotted lines depict the end of recording, the solid lines are guide to the eye.

As expected from several results presented earlier in this work, an optimum in T_g could be identified for the effect in question. The observed T_g dependence will not be discussed in detail, but rather serves to identify the material showing the most pronounced effect, which is again material CT. Furthermore, it was found that the investigated effect relatively increases when the externally applied field is decreased. This result will be discussed in more detail later on. Subsequently, a first, basic, explanation of the mechanisms underlying the investigated effect will be focussed upon.

In order to gain a more detailed insight into the mechanism, which might cause the further increase of the refractive index modulation even when the PR grating is already in process to be erased, a measure of the PR phase shift during erasure (referred to as “apparent phase shift”, hereafter) in material CT was determined as a function of time for various experimental conditions. In all these experiments the PR phase shift during recording of the PR grating was determined as well.

Figure (5.4 - 16) shows the evolution of the PR phase shift for material CT (figure (5.4 - 16)(A)) during recording and the apparent PR phase shift during erasure (figure (5.4 - 16) (B)) for different recording times at otherwise identical experimental conditions applying an external field of $E_{ext} = 48V/\mu m$.

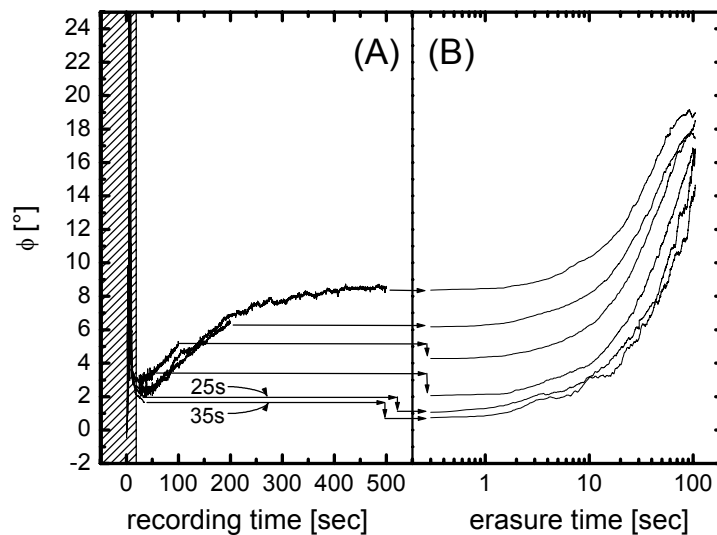


Figure (5.4 - 16): Phase shift of the PR grating material CT during recording (A) and erasure (B) for 25, 35, 50, 100, 200 and 500 seconds recording. The hatchings over areas, which cannot be interpreted reliably as described in “5.4.1.1.) Experimental aspects” on page 273.

The time history of the apparent phase shift during erasure applying three different erasure intensities is depicted in figure (5.4 - 17). The externally applied field was again $E_{ext} = 48V/\mu m$. The recording data (not shown) are identical within experimental error and similar to the corresponding curve in figure (5.4 - 16).

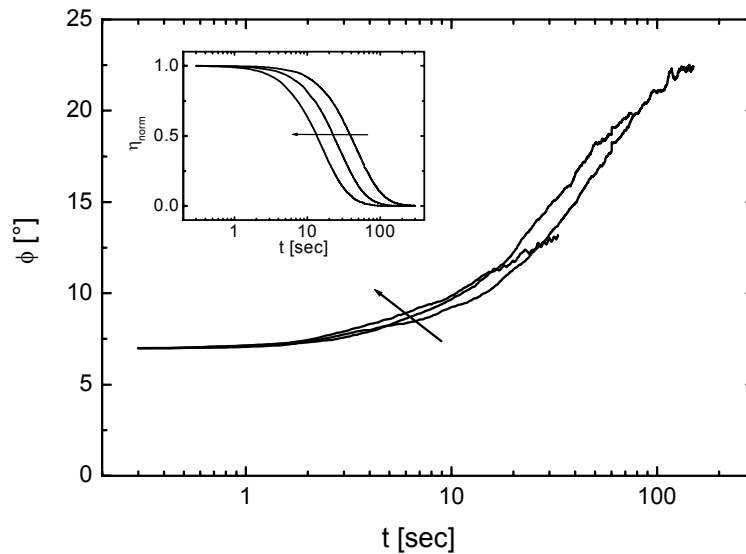


Figure (5.4 - 17): Apparent phase shift during erasure in material CT applying the erasure intensities I_{e0} , $2.5 \cdot I_{e0}$ and $5 \cdot I_{e0}$ (I_{e0} = standard erasure intensity as described in “5.4.2.1.) Experimental aspects” on page 301). The inset shows the corresponding normalized diffraction efficiencies. The recording time was 100sec and an external field of $E_{ext} = 48V/\mu m$ was applied. The arrows point in the direction of increasing erasure intensity.

Figure (5.4 - 18) shows the time histories of the PR phase shift and the apparent PR phase shift during recording and erasure, respectively, in material CT for different externally applied electrical fields of $E_{ext} = 40, 48,$ and $56V/\mu m$.

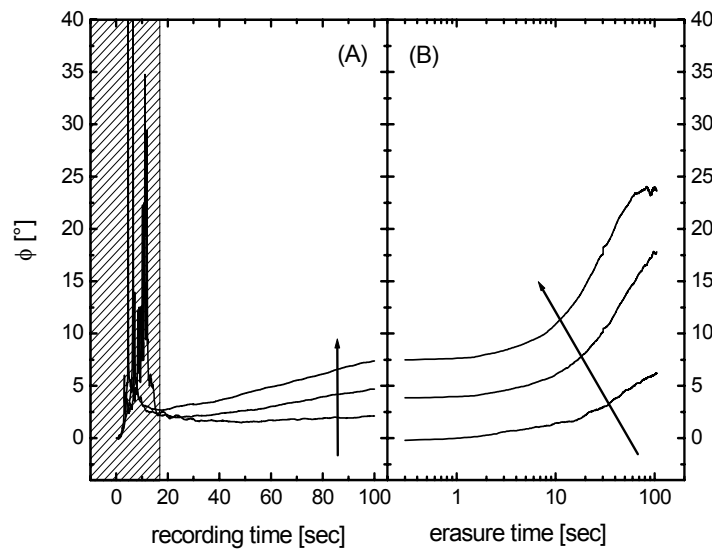


Figure (5.4 - 18): Phase shift during recording (A) and apparent phase shift during erasure (B) in material CT for 100sec recording and applying different external fields of $E_{ext} = 40, 48$ and $56V/\mu m$. The arrows point into the direction of increasing field. The hatched areas cannot be interpreted reliably, as described in the experimental section (the width of the hatched areas increases with decreasing E_{ext} and the depicted hatching covers the worst case.)

5.4.2.3.) Discussion of the PR grating erasure in the trap-doped polymer composites

At first, the possible occurrence of isomerization gratings in the investigated materials has to be discussed, since they contain azo-dyes and are operated at wavelength, where these dyes still show slight absorption. This applies especially to the setup configuration working with p-polarized beams used for recording as well as for read-out of the holograms. There may be a local phase grating arising besides the PR grating during the recording process as described in “4.2.1.7.) Isomerization gratings” on page 205. If there is an isomerization grating of notable strength, it cannot be probed independently from a simultaneously present PR grating and will most probably exhibit a different dynamic behavior as compared to the PR grating. Hence, the dynamic evolution of the PR phase shift measured includes a significant contribution resulting from the superposition of the different dynamic evolution of the amplitude of these two gratings. However, charge carrier diffusion in the investigated materials is negligibly small, i.e., no notable PR grating will be formed without an externally applied field. Thus, the refractive index modulation due to an isomerization grating in absence of a PR grating can be probed independently by a DFWM experiment, if no external field is applied, but under otherwise identical experimental conditions as applied in the PR wave mixing experiments. Figure (5.4 - 19) shows the build-up and the subsequent erasure of the isomerization grating in material CT.

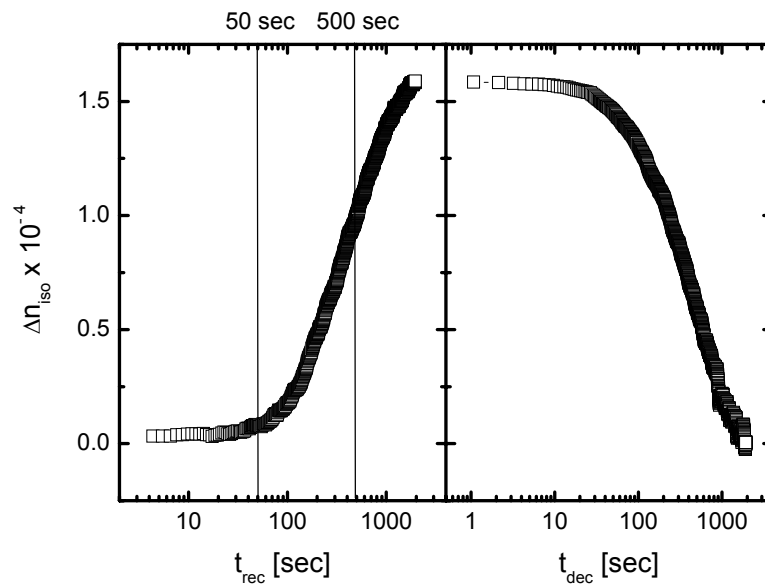


Figure (5.4 - 19): Build-up and erasure of the photo-induced isomerization grating in material CT, recorded under identical experimental conditions as in the PR experiments, but without external electrical field.

Within experimental accuracy, no notable holographic grating is observed within the first 50sec of the recording process. The longest recording time applied in the experiments on the evolution of the PR phase shift during erasure was 500sec, which is correlated with a refractive index modulation due to an isomerization grating of $\Delta n_{ISO} = 1.0 \cdot 10^{-4}$. This is a factor of about 14 smaller than in the corresponding PR experiments. The isomerization grating is erased considerably slower than a corresponding PR grating. After 100sec erasure of an isomerization grating recorded for 2000sec before (finally yielding $\Delta n_{ISO} = 1.6 \cdot 10^{-4}$), Δn_{ISO} has dropped to $\Delta n_{ISO} = 1.3 \cdot 10^{-4}$ (i.e. approximately 80% of its initial value), which is still about 3 times less

than a corresponding PR grating in material CT, recorded for 500sec. Assuming that an isomerization grating recorded for 500sec and subsequently erased for 100sec should as well exhibit about 80% of its initial value (i.e. $\Delta n_{ISO} = 0.8 \cdot 10^{-4}$), a corresponding PR grating then is still more than 5 times stronger. After 50sec of erasure, the corresponding factors are almost 6 and almost 9, respectively. These results demonstrate that the possible occurrence of isomerization gratings must be taken into account for recording times exceeding 50sec. Although their contribution to the overall holographic grating even then may be considered as small enough to be neglected in reasonable approximation for considering general trends, subsequently the possible influence of an isomerization grating on the PR data will be discussed when advisable.

There are theoretical models developed for the PR effect in polymers (see “2.5.3.2.3.1.) Erasure dynamics in Schildkraut’s model” on page 127 and “2.5.3.2.3.2.) Cui’s approach to the erasure dynamics” on page 128), the solution for the decay of the PR space-charge field of which implies some oscillatory behavior. This seemingly agrees with the experimental results presented before. However, the resulting expressions for the decay of the PR space charge field as a function of time (eq. (2.5 - 28) and the real part of eq. (2.5 - 29)) contain several unknown parameters and, thus, are not useful for the current discussion. Hence a brief ostensive phenomenological explanation for the experimental observations will be given.

In order to find such a phenomenological explanation for the time history of the diffraction efficiency in the PR grating erasure experiments (see figure (5.4 - 12)), at first the mechanism underlying the holographic time of flight (HTOF) technique shall be considered. In HTOF experiments, the hologram is recorded applying a short but intense light pulse of a few nanoseconds. Charge carriers are thereby generated in the bright regions of the spatially non-uniform light pulse, however, due to the flash-character of the illumination, the positive and negative charge distributions are still in phase just after the recording process. The mobile charge carrier distribution then starts to displace relative to the distribution of the immobile charge carriers, giving rise to the PR space-charge field E_{SC} . The latter increases as the displacement Δ increases and reaches its maximum amplitude for the case of anticoincidence of the oppositely charged charge carrier distributions (i.e., $\Delta = 180^\circ$), since the mutual screening of the particular charge distributions is then at its minimum. For a further increase of Δ with $180^\circ < \Delta < 360^\circ$, E_{SC} will decrease again. If Δ becomes larger than the holographic grating period, oscillatory behavior of E_{SC} as a function of Δ is observed. The modulation depth of the particular space-charge distributions thereby decreases (e.g. due to recombination effects) and finally vanishes. The time necessary to reach (the first) anticoincidence is called „transit time“. The evolution of the space-charge field is probed continuously by cw-DFWM. This technique has been applied to PR polymers several times, in order to determine the bulk (i.e. average) charge carrier mobility [138, 148, 218, 219]. At first sight, the observation of increasing diffraction efficiency during erasure might be attributed to a similar mechanism as underlying HTOF, i.e. that Δ increases during the erasure of a PR grating by uniform illumination. In fact, there is strong experimental indication for this interpretation, as will be discussed below. However, HTOF experiments represent a highly dynamic situation due to the almost instantaneous generation of a large amount of charge carriers, which are then statistically distributed within the density of states (DOS) of the charge transport manifold, most of them ready to drift under the influence of the externally applied field. This is usually reflected in correspondingly short transit times of several hundreds of microseconds up to a few milliseconds. In contrast, here the holographic grating was recorded for up to several tens of seconds at low intensity and the time necessary to achieve maximum diffraction after the erasure process had begun (“transit time”) was also in the order of seconds up to several tens of seconds (depending on the investigated material). Therefore, one may assume that the basic

mechanism underlying the experimental observations presented above may somehow be similar to HTOF, however, the details should be significantly different.

Please note, that a change in Δ affects the magnitude of the PR space-charge field distribution as discussed above as well as its spatial position, i.e. the PR phase shift. Hence, as Δ changes as a function of time, the entire PR grating shifts. This already implied by the aforementioned dynamic theories of the PR effect in polymers. Both theories imply two PR space-charge field components spatially moving with different velocity, which may yield an experimental phenomenology as observed here.

Since an increase of Δ as a function of time during erasure yields the entire PR grating shifting, the phasing between the PR grating and the original interference pattern during recording (i.e. the PR phase shift ϕ) changes as well. This opens the way to experimentally test the assumption of a basically HTOF-like mechanism underlying the experimental observation of further increasing DFWM diffraction efficiency during initial erasure of a PR grating. Therefore, a new measurement technique was devised, which allows to determine the apparent PR phase shift during the erasure process, as already described in the experimental section. This technique was applied to different materials for a variety of experimental conditions. The results are depicted in figure (5.4 - 16) to figure (5.4 - 18)).

Subsequently, at first the recording process of a PR grating in material CT will be discussed focussing on the time history of the PR phase shift. Thereby, the basic ideas of the phenomenological picture of the dynamic processes taking place during recording as well as erasure will be explained. Thereafter, these ideas will be applied to the PR grating erasure process in material CT.

5.4.2.3.1.)The PR recording process in the trap-doped systems

The forthcoming discussion refers to figure (5.4 - 20), where the interaction between E_{ext} and E_{SC} as described in this section is illustrated for the ideal case of anticoincidence between the negative (immobile) charge carrier distribution and the positive (mobile) charge carrier distribution. The upper vector diagram illustrates the direction and the amplitude of the PR space-charge field, as it will emerge during the recording process. The second to upper vector diagram illustrates the initial external electrical field in area (I) and area (II) when the PR space-charge field has not yet emerged. At first area (I) will be considered, i.e. the left hand side diagrams. Initially, when there is not yet a PR space-charge field, holes generated in the bright area will drift alongside the external field vector towards the dark areas. The thus resulting E_{SC} adds to $E_{ext \parallel}$ reducing this component of the external field in the considered area. This yields a local total field $E_{T,loc}$, which is reduced in strength and is altered in direction as compared to the initial E_{ext} as depicted in the lower vector diagram. In comparison with E_{ext} , $E_{T,loc}$ shows a less favorable orientation for promoting the hole drift from the bright regions towards the dark areas, i.e. the effective drift distance for a hole to reach the dark area has become longer.

It may safely be assumed that the trap doping is the determining factor for the charge carrier redistribution process in material CT. The PR phase shift ϕ obviously starts at small values close to 0° and then increases when recording proceeds, finally levelling off at $\phi \approx 9^\circ$ (figure (5.4 - 16)(A)). Material CT is doped with deep traps in approximately the same number density as the sensitizer moieties (TNF). Accordingly, on the average there exists a deep trap in the system for each charge carrier generated. Therefore, it is reasonable to assume that, when recording starts, the holes generated firstly are trapped at once by a deep trap in the close neighborhood of their generation centers in the direction of the current local field (i.e. here E_{ext}). When recording proceeds and more holes are generated, a part of the trapping sites near to the generation centers in the bright areas are already occupied and, hence, some holes are able to displace further in the drift direction now defined by the current direction of $E_{T,loc}$, until they

meet a deep trap still unoccupied. Thus, during recording ϕ initially starts at small values and increases when the recording process proceeds until it reaches the steady-state condition. The steady-state condition is reached when E_{SC} and $E_{ext \parallel}$ just cancel, since then there is no longer a component of the driving field for the charge carrier drift oriented parallelly to the grating wave vector, i.e. no more holes will be redistributed in order to contribute to E_{SC} .

Please note that this phenomenological model implies some correlation between the recording time of the holograms and the recording intensity. One must expect that the phase shift changes faster as a function of time when recording a hologram at higher intensity. On the other hand, as discussed several times in preceding sections, the PR grating build-up speed in the low- T_g regime is limited by the mobility of the charge carriers inside the polymer matrix, which applies particularly for the case of trap controlled transport like in material CT. However, if more charge carriers are generated and redistributed per unit time, the recording process as described above will become faster although the redistribution process and not charge generation is the limiting factor. This is an important implication on this type of PR material since holograms carrying some picture information (i.e. they do not represent a uniform interference pattern like a simple sinusoidal pattern) might be recorded to varying states inside a single hologram, which formally would correspond to spatially varying recording times for a single hologram. Probably the frame of this argumentation may be expanded to other PR polymer materials.

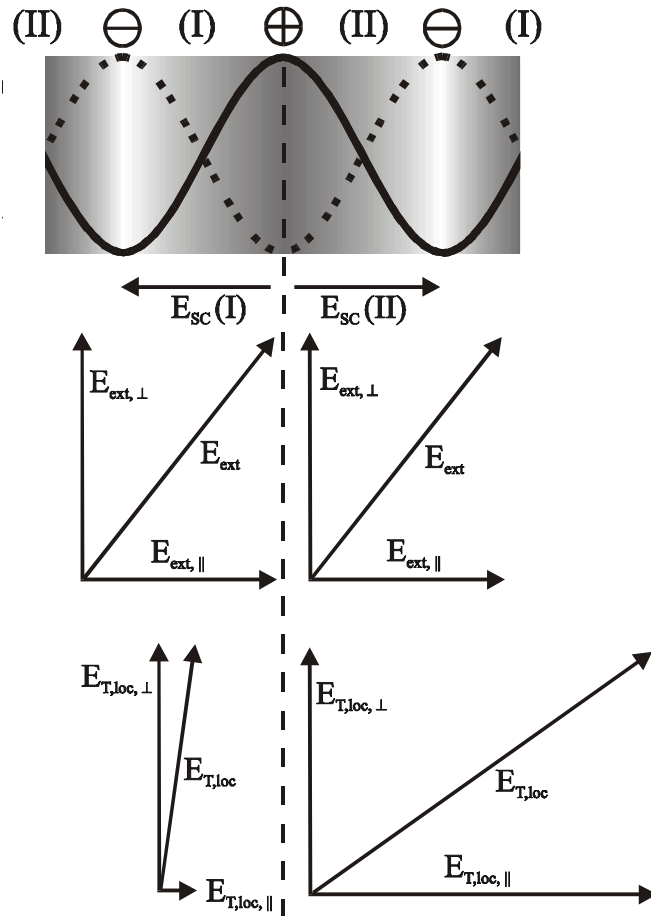


Figure (5.4 - 20): Illustration of the electrical fields inside a PR grating in a polymer for the ideal case of anticoincidence between the oppositely charged charge-carrier distributions.

The solid sinusoidal curve represents the positive charge carrier distribution and the dotted sinusoidal curve represents the negative charge carrier distribution. The shading behind the sinus curves depicts the illumination pattern (bright and dark areas). $E_{T,loc}$ is the sum of the externally applied field E_{ext} and the PR space-charge field E_{SC} . The spatial areas referred to in the text are denoted (I) and (II). For a similar but more detailed illustration see figure (2.5 - 5) on page 132.

5.4.2.3.2.)The PR erasure process in the trap-doped systems

Referring to figure (5.4 - 20), the terms “left” and “right” will be used hereafter (for example: area (I) is located left from a neighboring formerly dark area; the term “formerly dark/bright area” refers to the intensity distribution during recording).

The effect of a further increase of η during erasure in material CT (figure (5.4 - 12)) could be determined experimentally up to recording times of about $t_{rec} \approx 75\text{sec}$. For longer recording times a net increase of η during erasure was no longer observed. However, the approach to fit

the erasure curves by a series of exponential terms yielded very good agreement with the experimental curves, when using one growing exponential term and two decaying exponential terms. This procedure turned out to be valid for all recording times, which have ever been applied within this series of measurements (i.e. up to 2000sec recording; fit curves and results are not shown). This indicates that the erasure process in material CT always includes some mechanism, which leads to an increase of η during initial erasure, even if a net increase of η is not observed.

In analogy to the recording process, the trap doping and the thus required filling of the traps in advance of a further proceeding charge transport should also determine its dynamic erasure behavior. Due to the high amount of deep extrinsic traps in material CT providing a deep trap for each possibly generated charge carrier, one can safely assume that the charge carriers firstly generated in an illuminated area are captured immediately by a deep trap in the close proximity of the generation center, as already discussed for the recording process. Only if a substantial amount of the deep traps in the considered illuminated area is already occupied, charge carriers will have the chance to migrate for a longer distance until they get trapped. For applying this concept to the erasure process, first the situation at the end of the recording process must be considered. When recording ends, the hole distribution has displaced to some degree with respect to the distribution of the negatively charged charge generation centers. When the material now is uniformly illuminated for erasure, in the area where the center of the hole distribution is located a substantial amount of the deep traps is already occupied. Thus, charge carriers generated now within this area may migrate relatively free to the right until they reach the right edge of the currently existing hole distribution where they get trapped by an unoccupied deep trap. Hence, the hole distribution should shift to the right from the beginning of erasure, which may be observed experimentally as an increasing PR phase shift.

On the other hand, charge carriers generated within area (II) migrate towards the neighboring formerly bright area, where they compensate (i.e. cancel by recombination or compensate by being trapped nearby) negatively charged charge generation centers formed during recording. These charge carriers have left a negatively charged generation center behind, which is located left from the formerly bright area. Accordingly, this process is supposed to cause a left shift of the negative charge distribution. However, most charge carriers generated within area (II) should instantaneously be trapped by a deep trap in the close neighborhood of their generation center as discussed before. Hence, during the initial erasure only very few charge carriers generated at the very right edge of area (II) are able to reach the formerly bright area. This is not yet supposed to cause some notable left shift of the distribution of negative charges since the number of charge carriers contributing to this process is still just too small. When the erasure process now proceeds further, more and more deep traps become occupied in area (II) and, thus, an increasing number of newly generated charge carriers are able to reach the formerly bright area. Accordingly, although the negative charge distribution should remain more or less spatially localized for some time after beginning of erasure, it is supposed to start to shift to the left for longer erasure times. For the PR phase shift, this left shift of the negative charge distribution counteracts the right shift of the hole distribution. Accordingly, for longer erasure times one may expect the right shift of the entire PR grating (i.e. the increase of ϕ) to slow down, level and finally possibly even change its direction for sufficiently long erasure times. This situation is in fact observed in figure (5.4 - 16)(B) for the two longest recording times applied. The PR phase shift lows down and seemingly levels. A change of the shift direction (i.e. a decreasing ϕ), however, is not observed. Furthermore, the above described situation is indicated in figure (5.4 - 18)(B) for the highest external field applied. The fact, that the situation described above can only be observed applying longer recording times or higher external field may be rationalized considering $E_{T,loc}$ according to figure (5.4 - 20). If the PR

grating is strong (i.e. E_{SC} is large), $E_{T,loc}$ in area (II) has a large amplitude and favorable direction for promoting charge carrier migration towards the formerly bright area. Hence one may even speculate that a decreasing ϕ as mentioned before might be observable for sufficiently long recording times.

In conclusion, the effect of further increasing η during the initial erasure process may be attributed to the pronounced right shift of the hole distribution while the negative charge distribution remains more or less localized. As assumed before, this mechanism is similar to the HTOF mechanism, however, with the significant difference that it operates on a much longer time scale. Furthermore, there is indication for a left shift of the negative charge distribution, which has no phenomenological counterpart in the HTOF mechanism.

Please note, that a mechanism as suggested here renders the application of HTOF in order to determine charge carrier mobilities in materials with high amounts of deep traps impossible. The problem about the applicability of HTOF to PR polymers has already been discussed in [202, 203] for materials without extrinsic deep traps leading to a similar conclusion.

5.4.2.3.3.)The dependence on the erasure intensity

In order to test the presented phenomenological model for different experimental conditions, the apparent PR phase shift during erasure at varying erasure intensities and otherwise constant experimental conditions was determined. The results are shown in figure (5.4 - 17). By increasing the erasure intensity, more charge carriers per unit time are generated during erasure while the experimental situation otherwise remains unaltered as compared to the experiments described in the preceding section. Hence, increasing the erasure intensity will have the same effect like (formally) increasing the charge carrier generation efficiency throughout the entire PR grating at otherwise unchanged experimental parameters. This should have the following effects: The overall modulation depth of the space-charge distributions should decrease faster. As a result, the erasure process in general is accelerated as a function of increasing erasure intensity (figure (5.4 - 17), insets). It furthermore shows up in the apparent PR phase shift during erasure, since the corresponding curves break off after shorter erasure time (figure (5.4 - 17)) because the signal levels become too small for a reasonable evaluation of the experimental data as mentioned in the experimental section. Furthermore, increasing the charge carrier generation efficiency should accelerate the increase of ϕ during erasure for material CT, since the deep traps along the general migration direction of the holes should be filled faster. This is indeed indicated by the experimental data (figure (5.4 - 17)(B)), however, the effect is too small to unambiguously confirm the aforementioned expectation.

5.4.2.3.4.)The dependence on the applied electrical field

Further support for the empirical model may be found, when considering the dependence of the evolution of the apparent PR phase shift ϕ during recording and erasure of a PR grating in the investigated materials on the externally applied field. Increasing the external field will improve the charge carrier generation efficiency as well as the charge carrier mobility during recording as well as erasure. Hence, in general more charge carriers will be generated per unit time and the redistribution will be faster for higher externally applied fields. Accordingly, while recording a PR grating at higher externally applied fields, E_{SC} will emerge faster and, constant recording time provided, will be higher at the end of recording. Moreover, the maximum achievable E_{SC} will be higher for higher externally applied fields since $E_{ext \parallel}$ is larger, which, according to figure (5.4 - 20) and as described above, limits E_{SC} in steady-state. Consequently, the start conditions for the subsequently performed grating erasure will depend on the externally applied field. The erasure process itself must be expected to depend on the externally applied

field according to its dependence on the bulk charge carrier generation efficiency and the bulk charge carrier mobility, both of which depend on E_{ext} as well E_{SC} . The experimental results on the time history of the apparent PR phase shift during recording and erasure are shown in figure (5.4 - 18).

First the recording process will be discussed (figure (5.4 - 18)(A)). For increasing externally applied field the deep traps located along the main drift direction of the holes should be filled up faster due to the larger amount of holes generated per unit time in the bright areas of the nonuniform illumination pattern. Furthermore, the charge carrier mobility will in general be higher. Accordingly, while ϕ should still start at small absolute values close to $\phi = 0$ (ideally exactly at $\phi = 0$) as discussed before, the subsequent increase of the PR phase shift should be faster for higher fields externally applied. The experimental results clearly agree with this expectation.

The time history of ϕ during erasure as a function of the externally applied field is shown in figure (5.4 - 18)(B). As discussed before, the hole distribution during erasure in material CT may be assumed to shift to the right from the beginning of erasure, whereas the distribution of negative charges at first remains spatially fixed. Thus, ϕ increases. When increasing the externally applied field, charge carrier generation efficiency as well as charge carrier mobility are increased throughout the entire PR grating. On the one hand, this should accelerate the right shift of the hole distribution due to a faster filling of the extrinsic deep traps as discussed before. As a result a more pronounced increase of ϕ as a function of an increasing externally applied field should be expected, which is indeed observed experimentally (figure (5.4 - 18)(B)). Please note, that the aforementioned different start conditions for the erasure process due to different externally applied fields but constant recording durations only cause different start offsets in ϕ , which increase with increasing applied field. On the other hand, according to the model presented here, after some erasure time the negative charge distribution should start shifting to the left as already discussed before. This effect should be expected to be observed earlier during the erasure process when the external field is increased, again due to a faster filling of the extrinsic deep traps located along the mean hole migration path, now referring to area (II). Indeed, such a saturation effect for ϕ is observed for the highest external field applied (figure (5.4 - 18)(B)). For smaller external fields, the described saturation effect should occur later during the erasure process but can no more be observed experimentally.

In conclusion, the experimental results obtained for variations of the externally applied field at otherwise unchanged experimental conditions can easily be interpreted on the basis of the phenomenological model proposed here. This further supports the given interpretations.

5.4.2.4.)Summary of the investigations on the PR erasure behavior of trap-doped polymers

A phenomenological mechanistic picture of the recording and the erasure process of a hologram in a PVK based PR polymer (material CT) showing trap controlled charge transport is presented taking into account the spatial distribution of electrical fields within the PR grating and the particular charge transporting mechanism.

During recording the negative space-charge distribution remains located at the bright fringes. The hole distribution starts with a small displacement close to 0° with respect to the negative space-charge distribution and subsequently displaces to about 9° when recording proceeds, which can be explained by means of a charge transporting mechanism requiring the filling of the deep traps before a notable drift of charge carriers over longer distances may take place.

Within the frame of the proposed model, the negative and the positive space-charge distributions spatially displace again when the PR grating is erased. However, the negative space-charge distribution stays more or less localized for a relatively long time span, while the hole distribution displaces markedly. Only for rather long erasure times there is indication that the negative space-charge distribution starts shifting as well, however, in opposite direction as compared to the hole distribution. This behavior can also be explained by the proposed model accounting for a charge transport mechanism as described above. The electrical fields inside the material and their influence on the charge carrier generation efficiency and charge carrier mobility determine the details of the time history of the PR phase shift.

The presented model can explain the experimental observation of further increasing DFWM diffraction efficiency during erasure of a PR grating applying low recording and erasure intensity. The quality of this effect depends on the applied electrical field and, in particular, on the applied recording time, both of which are inherent features of the proposed model.

The model furthermore infers that holograms in the investigated type of material are inherently non-stable neither during recording nor during erasure. Please note that this is also implied by the theoretical models of the transient behavior of PR gratings in polymers discussed in “2.5.3.2.) Schildkraut’s model” on page 124. This inherent feature of the PR effect in polymers could be proven by experimental results on the PR phase shift, which turned out to be a function of time during recording as well as erasure. Moreover, the time history of the PR phase shift as well as of the DFWM diffraction efficiency during erasure is a function of the time the PR grating was recorded before, which is also an inherent feature of the proposed model.

The instability of holograms in the investigated type of PR polymer during erasure as well as the dependence of the general form of their erasure kinetics on the recording time implies image distortions during the processing of the holograms. Moreover, a hologram carrying some picture information might formally be recorded differently long inside the hologram depending on the local recording intensities, which also might result in image distortions during processing. Finally, the complicated correlation between recording time and erasure dynamics of the holograms must be expected to pose severe problems when trying to apply this class of materials in holographic multiplexing. Please note, that the latter was also proven experimentally in the frame of this thesis, which is elaborated upon in a later section (“5.6.) Holographic multiplexing in PVK based PR polymers” on page 329).

5.5.) Dark decay of PR gratings in PVK-based polymer composites

One of the most important aspects for the potential application of PR polymers for holographic data storage is the stability of the stored data against degradation when the storage system is idle, i.e. stored holograms are neither newly written nor refreshed. In this context, two different kinds of idle situations for a photorefractive medium must be distinguished. Firstly, the material may be disconnected from the externally applied dc electrical field and additionally held in the dark. Secondly the material may be held in the dark with the external field still applied. In this section the latter situation will be focussed upon.

PR polymers require the application of a strong external electrical field and exhibit a non-zero electrical conductivity even in the dark leading to a dark current permanently flowing through the system. This feature has already been shown and discussed in section 5.2.2.). Furthermore, due to the typically rather low dielectric constant in polymers ($\epsilon < 10$), oppositely charged charge carriers show a rather strong tendency to recombine. As a result of both of these features, the PR space-charge distribution is slowly wiped out even when no light is applied to the material and, hence, only rather short storage times are anticipated as well as found experimentally. Thus, PR polymers are supposed to be not very promising candidates for application as long term holographic data storage media in general. However, the dark decay of holograms has always significant implications for a potential data storage system utilizing PR polymers, since also a short term data storage device like e.g. a buffer system may be held in the dark for some time with the external field still applied. So far, the dark decay of holograms has mostly been neglected in the literature on organic PR materials.

In this section, a detailed investigation of the dark decay behavior of PVK based PR polymers is presented. Different experimental conditions were applied and different glass-transition temperatures T_g were taken into account. Furthermore, materials with and without extrinsic deep traps were investigated. In order to obtain a unified measure of the dark decay behavior, the combined logarithmic averages of the relaxation times were considered rather than the particular decay time constants. Evidence will be given that the phase shift between the illuminating interference pattern and the recorded index grating, the commonly accepted fingerprint of photorefractivity, is one of the key parameters, yielding slower dark decay for larger PR phase shift.

5.5.1.) Experimental aspects

The investigated materials are derived from the first high performance PR polymer [13], but with strongly improved long-term stability [136]. The compositions and the glass-transition temperatures of the investigated materials A, B, C and D (not containing extrinsic deep traps) and CT (doped with extrinsic deep traps) are listed in table 5-1 on page 211 as well as at the end of the current section. PR devices were prepared according to “4.1.) Preparation of materials and sample structure” on page 179. The active layer thickness was $d = 125\mu\text{m}$. The ambient temperature was $20 \pm 0.5^\circ\text{C}$ for all measurements.

In order to determine and explain the dark decay behavior of the investigated materials DFWM and 2BC experiments were carried out using a HeNe Laser ($\lambda_0 = 633\text{ nm}$) and the standard DFWM and 2BC setups as described in “4.2.) Wave mixing experiments” on page 181. The experimental data were evaluated by the procedures described in the same section. If required, the polarization anisotropy of the NLO chromophores was taken into account as discussed in section 4.2.1.4.) on page 199. The decay dynamics of the PR gratings

were fitted by bi- or tri-exponential decay functions. The combined logarithmic averages of the particular relaxation times $\langle \tau \rangle$ were calculated according to eq. (5.2 - 26). In this section $\langle \tau \rangle$ will be used as the only relaxation time measure. This point of view is based on theoretical considerations to be discussed later in the text. The recording beams 1 and 2 were s-polarized and exhibited varying internal intensities, which will be noted in the text below in close correlation with the corresponding experiments. In all cases, a grating contrast of the interference pattern close to unity was adjusted ($m = 0,997 \pm 0,003$).

During recording and dark decay the recorded hologram was probed by a p-polarized beam counterpropagating to beam I_{01} . Due to erasure of the PR grating upon uniform illumination, the following precautions were taken in order to reasonably approximate “real“ dark decay: Firstly, the reading beam had more than 3 (for the lowest recording intensity) up to almost 6 (for the highest recording intensity) orders of magnitude lower time-averaged intensity (appr. 250 nW/cm^2) than the recording beams. Secondly, the reading beam was only applied from time to time using a fast magnetic shutter. Between the read-outs, the sample was held completely in the dark. The applied reading beam intensity was a result of a trade-off between the requirement of lowest light exposure possible during the dark decay of the probed holograms and reasonable resolution for the diffraction signal to be obtained. A more detailed discussion of the experimental procedure is given in “4.2.1.3.1.) DFWM measurement procedures” on page 193. For all experiments the samples were pre-illuminated for 30min by beam 2 in advance of recording a hologram. Unless otherwise noted, an external electrical field of $E_{ext} = 32 \text{ V}/\mu\text{m}$ was applied to the samples. It is to be pointed out, that the maximum achievable refractive index modulation at a given external field is different for the materials investigated here. This has been discussed several times before in the frame of this work and will not be elaborated upon again. It must be emphasized, that the applied measurement technique can only approximate the actual dark decay of a holographic grating, since by probing the grating light induced erasure occurs in any case. This is an inherent feature of DFWM experiments and cannot be avoided. However, the quality of the approximation achieved with the procedure as described above safely suffices in order to consider general trends.

Furthermore, results on the relaxation dynamics of the orientational birefringence in the investigated materials as determined by transmission ellipsometric experiments will be included, which have already been presented and elaborated upon in detail in “5.4.1.3.1.) Discussion of the ellipsometric experiments” on page 281. The setup used for these experiments and the applied evaluation techniques are described in detail in “4.3.1.) Experimental transmission ellipsometry setup and procedure” on page 207.

Table (5-8): Chemical composition and glass transition temperature of the materials investigated in “5.5.) Dark decay of PR gratings in PVK-based polymer composites”

Material	DMNPAA	MNPAA	PVK	ECZ	TNF	TPD	T_g
units	[%wt]	[%wt]	[%wt]	[%wt]	[%wt]	[%wt]	[°C]
A	25	25	47	2	1	-	27
B	25	25	43	6	1	-	17.5
C	25	25	39	10	1	-	14
D	25	25	37	12	1	-	11.5
CT	25	25	38	10.18	1	0.82	14

5.5.2.) Results of the dark decay experiments

Firstly, the relation between the relaxation dynamics of the orientational order of the NLO chromophore dipoles in the investigated materials as determined by transmission ellipsometric experiments and the dark decay kinetics of a PR grating in these materials (figure (5.5 - 1)) was considered. For all materials, it was found that the PR dark decay kinetics is at least 30 times (material A) and typically more than two orders of magnitude slower than the relaxation of the orientational order of the chromophore dipoles in the materials. This proves that the PR grating dark decay in all investigated materials is governed exclusively by the decay of the PR space-charge field, i.e. in the dark essentially by the recombination of oppositely charged charge carriers. The obtained dark decay curves exhibit multi-exponential behavior in contrast to earlier results on a low-molecular-weight glass, where a simple mono-exponential behavior was observed [90]. Please note, that the latter results were obtained using a rather strong reading beam which, moreover, was applied at all times. Hence, the approximation of the real dark decay behavior in the system investigated in [90] was significantly worse as compared to here.

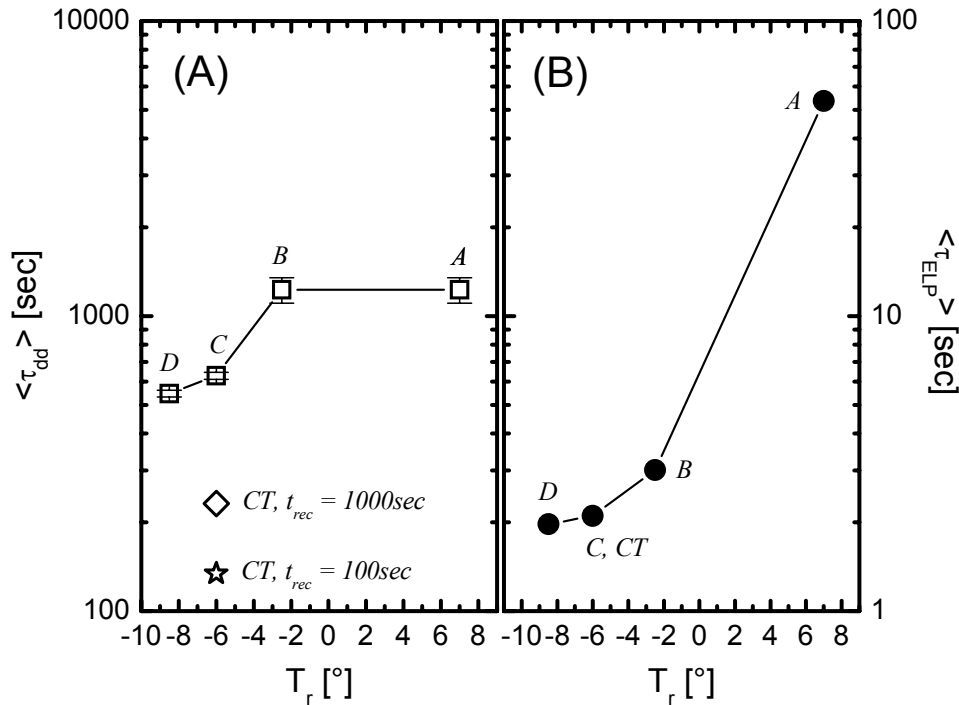


Figure (5.5 - 1): (A) Dependence of the PR dark decay kinetics in the materials A, B, C and D on the reduced temperature T_r , according to eq. (5.2 - 1) (open squares). The dark decay behavior was almost independent from the recording time of the PR grating and, thus, the data obtained for different recording times have been averaged here. The error bars indicate the variance of the logarithmically averaged PR dark decay response times for the applied interval of recording times. Furthermore, the fastest logarithmically averaged dark decay time constant obtained within the frame of this work is shown (material CT, 100sec high-intensity recording, open star) as well as the corresponding dark decay time constant of the same material but determined for 1000sec recording (open diamond). The PR dark decay behavior of material CT will be discussed in more detail later on. Figure (B) shows the decay of the orientational birefringence for material A, B, C (which is identical to material CT within experimental accuracy), and D as determined after 1000sec poling (solid circles). All data were obtained at $E_{ext} = 32\text{V}/\mu\text{m}$. The lines are guide to the eye. Please note the different y -scaling in plot (A) and plot (B).

In order to get a more detailed insight into the PR dark decay behavior of the investigated materials under varying experimental conditions, the dark decay was determined for the different experimental conditions denoted below. As will be discussed later, it was found

necessary to also consider the initial PR phase shift ϕ at hand when the dark decay is about to start, i.e. at the end of the recording process.

The dark decay including the initial PR phase shift in material C (not doped with extrinsic deep traps) was determined as a function of the externally applied field as well as of the recording time of the PR grating. One should expect that these parameters show a similar influence as found before for the erasure behavior of a PR grating in the investigated type of materials (“5.4.) The erasure behavior of PR gratings in PVK based polymer composites” on page 271). The same experiments were carried out on a material containing extrinsic deep traps (material CT). The recording process in material CT is much slower (about a factor of 5) as compared to material C, which is in general agreement with earlier results reported by Malliaras et. al. [16]. This is basically due to the reduced charge carrier mobility found in an electrically conducting polymer matrix in the presence of deep traps [46] and has already been illustrated before (figure (5.4 - 11)). Therefore, an improved dark stability of a hologram in material CT as compared to material C should be anticipated. The results of the aforementioned experiments are depicted in figure (5.5 - 2) and figure (5.5 - 3).

Furthermore, the PR dark decay behavior and the initial PR phase shift for material C and material CT were investigated for different recording intensities. For material C the dark decay was determined for 6 different recording times and the decay curves were averaged in order to obtain a master curve which then was fitted to yield the relaxation times. This procedure is justified by the fact, that no recording time dependence of the dark decay behavior was found for material C within experimental error (figure (5.5 - 3)), which was reproduced for each recording intensity applied here (not shown). For material CT this procedure could not be applied and in order to obtain the intensity dependence of the PR dark decay, a moderate recording time of $t_{rec} = 500\text{sec}$ was chosen, which already assured quasi steady-state conditions for the recorded holograms. A higher external field of $E_{ext} = 48\text{V}/\mu\text{m}$ was required in order to get a satisfactory diffraction signal at the very low recording intensity. The results of the described experiments are depicted in figure (5.5 - 4).

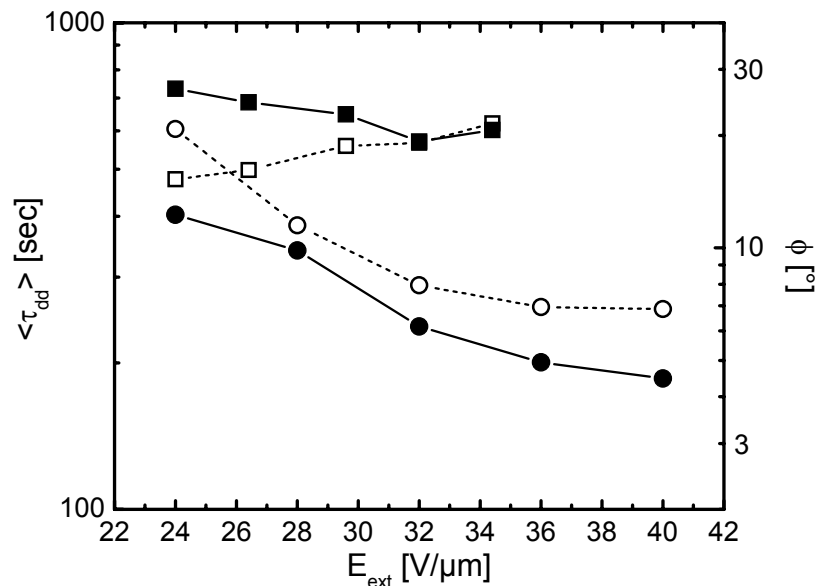


Figure (5.5 - 2): Dependence of the PR dark decay kinetics (solid symbols) and the PR phase shift (open symbols) for the materials C (squares) and CT (circles) on the externally applied electrical field E_{ext} for $t_{rec} = 500\text{sec}$ (material C) and $t_{rec} = 1500\text{sec}$ (material CT) at $I_{rec} = 42 \text{mW}/\text{cm}^2$. The lines are guide to the eye.

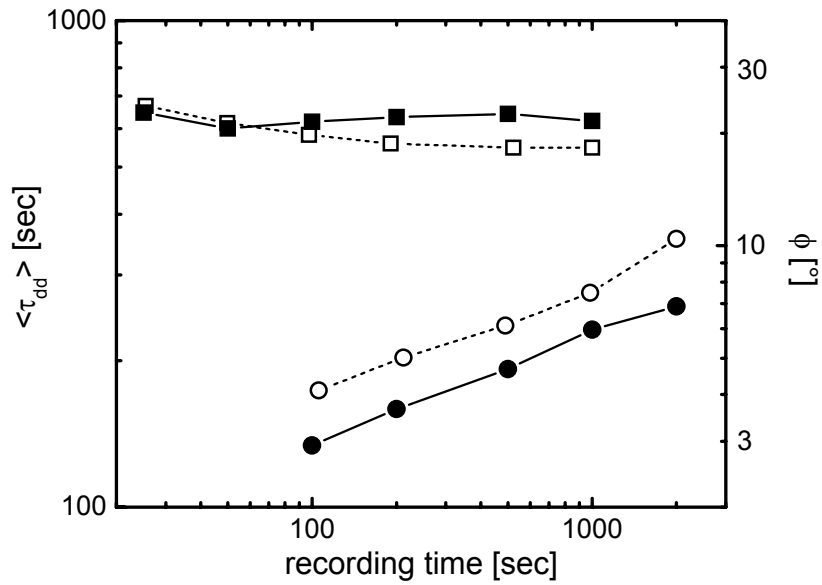


Figure (5.5 - 3): Dependence of the dark decay kinetics (solid symbols) and the PR phase shift (open symbols) for material C (squares) and material CT (circles) on the recording time t_{rec} of the PR grating at $E_{ext} = 32V/\mu m$ and $I_0 = 42 mW/cm^2$. The lines are guide to the eye.

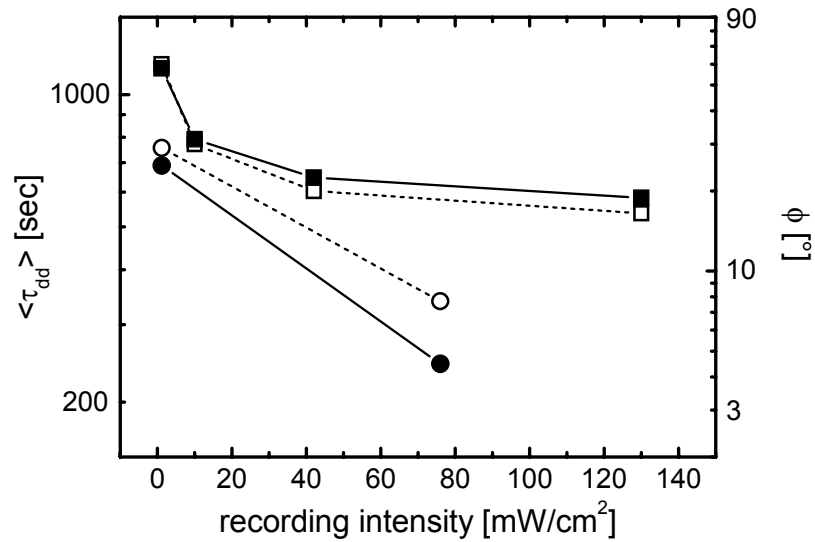


Figure (5.5 - 4): Dependence of the PR dark decay kinetics (solid symbols) and the PR phase shift (open symbols) for material C (squares) and material CT (circles) on the recording intensity I_{rec} at $E_{ext} = 32V/\mu m$ and for arbitrary recording times t_{rec} for material C (for details see text) and at $E_{ext} = 48V/\mu m$ and $t_{rec} = 500sec$ for material CT. The lines are guide to the eye.

5.5.3.) Discussion of the dark decay behavior

Cui et al. proposed a theoretical framework for the PR grating erasure process [83] in polymers, which has been elaborated upon in detail in “2.5.3.2.3.2.) Cui’s approach to the erasure dynamics” on page 128 and which was also successfully applied to the PR grating erasure in “5.4.1.) PR grating erasure in systems without extrinsic deep traps” on page 272. Neglecting charge-carrier diffusion, which is a valid assumption for the experimental conditions applied here, they described the PR grating erasure by three contributions with the individual rate constants according to eq. (5.4 - 6):

$$1/\tau_1 = (e\mu n_0)/\varepsilon + iK\mu E_0$$

$$1/\tau_2 = \alpha_G + \gamma_R n_0$$

$$1/\tau_3 = \delta + \gamma_T n_0$$

Here, e is the elementary charge, μ is the charge-carrier mobility, n_0 is the steady-state zero-order component of the hole density, ε is the (bulk) dielectric constant, γ_G is the coefficient for geminate recombination, γ_T is the hole-trapping coefficient, α_G is the photo-generation rate, δ is the characteristic value of the detrapping rate as discussed on page 129, and E_0 is the projection of the externally applied electrical field vector onto the grating wave vector K . The detrapping rate is given by eq. (5.4 - 7):

$$\delta = sI + \beta,$$

where s is the cross-section for light induced detrapping, I is the light intensity, and β is the thermal detrapping rate. In the dark, the photo-generation rate is zero and, furthermore, the steady-state zero-order hole density may be expected to become negligibly small in first approximation. Therefore, the dark decay of a PR grating in polymers should eventually be determined by the detrapping coefficient δ , which equals the thermal detrapping rate for $I = 0$. Accordingly, the model predicts a mono-exponential dark decay behavior. However, mono-exponential behavior in fact cannot be expected to be found experimentally, since the steady-state zero-order hole density cannot be assumed to vanish completely for two reasons: At first, the investigated type of PR polymers shows a notable dark conductivity resulting in a dark current flowing permanently through the system as long as the external field is applied (see figure (5.2 - 5) and [196]). The dark current in this case results from injection of charge carriers from the ITO-polymer interfaces. Thus, even for the case when no light is applied, some zero-order hole density must be implied. Secondly, a very weak uniform reading beam was applied from time to time to the systems in order to probe the holographic grating, as described in the experimental section. This also yields a non vanishing zero-order hole density, which is refreshed or at least re-established periodically as long as the grating is probed. Accordingly, multi-exponential behavior should be expected for the „real experiment“, although one may safely assume that the detrapping coefficient δ dominates the overall dark decay behavior. This point of view is supported by the experimental fact, that the slowest component of the multi-exponential dark decay was by far the dominant component in all cases. In contrast, for light induced PR grating erasure (i.e. $n_0 > 0$) the slowest component has always been found to be the least weighted component except for material A when the relaxation of the orientational order dominated the PR grating decay. However, this can safely be excluded for the dark decay in all materials investigated here, as illustrated by figure (5.5 - 1).

The fact that a single parameter (the detrapping coefficient δ) should theoretically dominate the overall PR dark decay behavior in the considered materials in the ideal case (i.e. without any exposure during the grating decay and neglecting charge carrier injection from the ITO-polymer interfaces) suggests to reduce the experimentally obtained bi- or tri-exponential

dark decay behavior to a single relaxation time serving as a unified measure for the dark decay of the PR grating. Accordingly, the combined logarithmic averages of the relaxation times $\langle \tau \rangle$ according to eq. (5.2 - 26) was calculated.

Figure (5.5 - 1)(A) shows, that the materials A and B exhibit very similar dark decay kinetics, although they were operated at significantly different reduced temperatures T_r according to (eq. (5.2 - 1):

$$T_r = T_g - RT,$$

where T_g is the glass transition temperature of the material in question and RT is the ambient temperature. $T_r \gg 0$ for material A ($T_r(\text{A}) \approx +7$), which, thus, is clearly a high- T_g material. In contrast, $T_r < 0$ for material B ($T_r(\text{B}) \approx -2.5$), which, accordingly, should already be considered as a low- T_g system. However, in its dark decay behavior material B apparently is very similar to material A, which will be discussed below in detail. At reduced temperatures even lower than for material B, the PR dark decay becomes significantly faster in material C ($T_r(\text{C}) \approx -6$) and then further accelerates for material D, i.e., as a function of further decreased T_r ($\langle \tau_{\text{dd}} \rangle_{\text{C}} > \langle \tau_{\text{dd}} \rangle_{\text{D}}$, $T_r(\text{D}) \approx -8.5$, figure (5.5 - 1)(A)). These results can be rationalized accounting for the findings presented in “5.2.3.) The relation between the glass-transition temperature and the dynamic performance in PVK based PR polymers” on page 243.

Low- T_g systems exhibit slow collective motions inside the polymer matrix due to an increasing long range coordinated molecular mobility of the polymer chain atoms as a function of decreasing $T_r < 0$, as discussed in “2.4.1.1.) Phenomenology of viscoelastic transitions” on page 71. Therewith, the local environment of the carbazole moieties acting as charge transporting sites as well as trapping sites in the PR process changes as a function of time and carbazole moieties currently acting as PR trapping sites may release their charge carriers. The corresponding PR traps are thus cancelled. As also discussed in the above quoted paragraph, the range of the coordinated motions of the polymer chain atoms in a glassy polymer matrix increases significantly, when the reduced temperature T_r is decreased passing through zero from $T_r > 0$. Accordingly, the degree of PR trap cancellation as a result of the slow collective motion of the polymer matrix of a PR polymer is more pronounced for lower $T_r < 0$ and the effective trap density is accordingly smaller. However, for the dark decay behavior, the effective PR trap density is not the major concern but, as discussed before, the detrapping coefficient δ . The detrapping coefficient, on the other hand, is not related to the trap density but to the dwell time of a trapped charge carrier in a PR trap and, consequently, also the persistence of a PR trap carrying a trapped charge carrier. The latter is also affected by the ability to collective motions of the photoconducting polymer matrix since it is reasonable to assume that therewith also the average life time of the PR traps is reduced, which is phenomenologically identical to a reduced average dwell time of a trapped charge carrier in a PR trap. Accordingly, the detrapping coefficient δ is decreased and an accelerated dark decay kinetics should be expected for increasing ability to long range coordinated molecular motions of the polymer chain atoms. In contrast, for $T_r > 0^\circ$ the polymer matrix becomes “frozen” and the effective PR trap density as well as the average life time of PR traps is relatively large (i.e. the detrapping coefficient is small) and independent from T_r .

The above described status of a “frozen” polymer matrix clearly applies to material A, the dark decay of which is slow due to the aforementioned small detrapping coefficient. In contrast, material B behaves ambiguously in that it mechanically acts already approximately like a low- T_g system, whereas its dark decay behavior clearly corresponds to a high- T_g system as already mentioned (figure (5.5 - 1)(B)). This ambiguity of material B concerning its dark decay behavior may be explained as follows: The aforementioned range of the coordinated molecular mobility of the chain atoms in a polymer is a function of T_r and increases as T_r decreases for T_r ,

$\leq 0^\circ$ as discussed in “2.4.1.1.) Phenomenology of viscoelastic transitions” on page 71 (for $T_r > 0^\circ\text{C}$, there is only a short range coordinated molecular mobility of the chain atoms). Furthermore, the molecular orientational mobility of the chromophores can safely be assumed to require a significantly shorter range of the coordinated molecular mobility of the polymer chain atoms than a change of the energy landscape of the photoconducting polymer matrix, as it is required for the cancellation of PR traps. Accordingly, material B, which has only a slightly negative $T_r(\text{B}) \approx -2.5$ may mechanically (i.e. in its poling properties) behave like a low- T_g system rather than like a high- T_g system, whereas its inherent effective PR trap density as well as its inherent detrapping coefficient may correspond to the situation found in a high- T_g system. For the materials C and D the situation is clear again; they behave like low- T_g systems whereby the detrapping coefficient in material D is smaller than in material C due to the smaller $T_r \leq 0^\circ$, which results in a longer range coordinated molecular mobility of the chain atoms.

Please note that the above implications on the T_g -dependence of the dark decay behavior are derived from the model developed in “5.2.3.) The relation between the glass-transition temperature and the dynamic performance in PVK based PR polymers” on page 243 in order to explain the appearance of a steady-state PR performance optimum as a function of T_r . The applicability of this model to the current problem, in turn, strongly supports its general validity.

Now the dependence of the dark decay on the externally applied field (figure (5.5 - 2)) will be considered. According to “2.5.3.2.3.2.) Cui’s approach to the erasure dynamics” on page 128, the detrapping coefficient δ in the present case is to be considered as an average detrapping coefficient covering different kinds of traps.

Besides conformational traps and related species (e.g. carbazole dimers), which have been referred to in order to explain the T_g dependence of the dark decay behavior in the systems without extrinsic deep traps, charged sensitizers may be presumed as another important PR trap species in material C as several times proposed in the frame of this work (e.g. in “5.3.) The influence of the sensitizer concentration on the PR performance of PVK based polymer composites” on page 257). Charged sensitizers are Poole-Frenkel traps, the detrapping behavior of which is field dependent. Thus, a field dependence of the detrapping coefficient δ is implied leading to accelerated PR dark decay as a function of an increasing external field E_{ext} in agreement with [90]. It was found that the dark decay basically becomes faster as a function of the externally applied field in material C, which in general agrees with these considerations.

However, it is not reasonable to assume that charged sensitizers are also a major PR trap species in material CT, which is doped with an amount of extrinsic deep traps as large as the concentration of sensitizer moieties. Since one can safely presume that the concentration of charged sensitizers is always much smaller than the total concentration of sensitizer moieties as discussed in “5.3.) The influence of the sensitizer concentration on the PR performance of PVK based polymer composites” on page 257, the extrinsic deep traps should rather determine the behavior of material CT as discussed in “5.4.2.) PR grating erasure in systems doped with extrinsic traps” on page 300. The extrinsic deep traps are uncharged when empty why Poole-Frenkel behavior cannot be implied. Accordingly, the detrapping coefficient δ in material CT should exhibit a much less pronounced field dependence than in material C, if at all. Therefore, the field dependence of the dark decay behavior of material CT, which is even more pronounced than in material C, cannot solely be attributed to a field dependence of the detrapping coefficient. This indicates that there must be another important factor besides δ , which determines the dark decay behavior in the materials considered.

Another important result is that the dark decay is generally faster in material CT than in material C. This is a surprising result, since one should expect to observe a slower dark decay in material CT as compared to material C due to the following reasoning: Comparing the

magnitude of the T_g -dependence of the dark decay dynamics of the systems without extrinsic deep traps according to figure (5.5 - 1)(A) with the magnitude of the field dependence of the dark decay dynamics of material C according to figure (5.5 - 2), Poole-Frenkel traps appear to be of minor importance as compared to conformational traps and closely related trap species. As discussed above, in low- T_g systems like material C or CT, these are subjected to a trap cancellation process due to slow collective motions of the photoconducting polymer matrix. However, the energetic depth of the extrinsic deep traps is constant and, thus, they cannot be subjected to this trap cancellation process. This suggests that the dark decay of material CT should be slower as compared to material C as mentioned before.

It was even more striking that in both materials the dark decay depended strongly on the intensity of the recording (!) beams $I_0 = I_{01} + I_{02}$ (figure (5.5 - 4)). Since the detrapping coefficient δ at a given E_{ext} and in the dark (i.e. $I = 0$) is a characteristic material constant, there is no reason to anticipate a dependence of the PR dark decay on the intensity, which the hologram was recorded with. One may now argue that δ is not constant and that optical activation of deep trapping sites as discussed in “5.4.1.3.3.) Experimental verification of optical trap activation” on page 285 may play a role, however, this would even imply the opposite trend as found experimentally, i.e. the dark decay then should be accelerated for decreasing recording intensity. In conclusion, it is once more strongly indicates that there must be a factor not taken into account up to now, which significantly or even dominantly influences the dark decay behavior of the investigated systems.

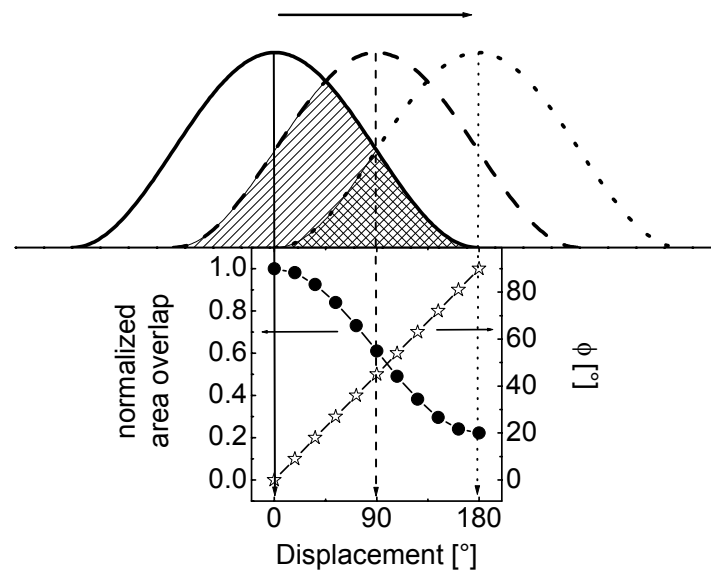


Figure (5.5 - 5): Illustration of the correlation between the displacement Δ of the space-charge clouds and their mutual overlap for sinusoidal distributions. Solid line: one fringe of the intensity pattern corresponding to one fringe of the negative space charge distribution as well as one fringe of the positive space-charge distribution at 0° displacement. Dashed and dotted lines: one fringe of the positive space-charge distribution at 90° and 180° displacement, respectively. Hatched areas: overlap area at 90° displacement (single line hatching + crossed line hatching) and 180° displacement (solely crossed line hatching).

Diagram below: relative overlap (solid circles) normalized to 1 at 0° displacement and correlated PR phase shift ϕ (open stars), both as a function of the displacement Δ . The relative overlap is calculated for the actually implied periodicity of the space-charge clouds, whereas the upper illustration does not account for neighboring fringes involved.

In order to find an explanation, the PR phase shift ϕ at the end of recording (which corresponds to the beginning of the dark decay) as estimated from concomitant PR gain measurements during recording was taken into account, which revealed a strong correlation between the trends for ϕ as a function of the experimental variable and the corresponding trends for the PR dark decay. This suggests that the recombination of charge carriers eventually leading to the decay of the PR space-charge field depends on the displacement Δ between the positive and negative charge carrier distributions. Assuming that the negative carriers are immobile and remain on the TNF sites, where they were initially generated, in zero-order approximation (i.e. neglecting geminate recombination effects and, thus, allowing for mutually unaffected coexistence of the oppositely charged space-charge clouds) the PR phase shift ϕ would correspond to half the displacement Δ and could, therefore, serve as a qualitative measure for Δ . Accordingly, a larger ϕ would correspond to a larger Δ with reduced mutual overlap between the positive and negative charge carrier distributions. The described situation is illustrated in figure (5.5 - 5). As the overlap is reduced, on the average an increasing number of detrapped charge carriers may not find a suitable recombination site available, get trapped again and, thus, contribute further to the overall PR space-charge field. Ostensively, the number of detrapping and retrapping steps until a carrier will recombine and, thus, vanish for the PR space-charge field should be expected to increase with decreasing overlap, since then less recombination centers are available near a just detrapped and then mobile charge carrier. As a result, the average number of recombination events per detrapping event should be reduced as the displacement Δ is increased and the dark decay, hence, would take longer. As depicted in figure (5.5 - 4), ϕ indeed increases strongly with decreasing I_{rec} yielding slower dark decay, in agreement with the provided explanation.

Now this interpretation will be checked for the field dependence of the dark decay in material C as well as in material CT: With increasing externally applied field ϕ decreases strongly in material CT (figure (5.5 - 2)) and, since simultaneously the dark decay becomes faster, this is in agreement with the interpretation given above. In contrast, in material C ϕ increases slightly when the externally applied field increases, which should lead to a deceleration of the dark decay, but instead the decay is basically even slightly accelerated as a function of increasing field. Obviously, in this case the phase-shift effect is compensated by the field-induced decrease of δ due to the Poole-Frenkel effect, as discussed above. One may speculate whether the phase shift effect eventually takes over determining the trend in the PR dark decay as a function of E_{ext} for the last field step, however, a single data point does not suffice to make this a clear statement.

As elaborated upon in “5.4.1.) PR grating erasure in systems without extrinsic deep traps” on page 272, a strong dependence of the erasure kinetics on the recording time was found in non-doped PVK-based materials. Therefore, one should expect a similar influence on the dark decay kinetics, which, surprisingly, was not the case for material C (figure (5.5 - 3)). This finding shows that the dark decay kinetics is independent of the actual strength of the hologram (i.e., the number of charges involved in the formation of the space-charge field), which varies by a factor of almost 5 from the shortest to the longest recording time applied to material C. In contrast, in material CT doped with extrinsic deep traps, the dark decay strongly depends on the recording time. Both these findings can also be explained by the phase-shift effect, since ϕ increases strongly as a function of increasing recording time in material CT, while it varies little in material C (figure (5.5 - 3)). The occurrence of optically activated deep traps as already mentioned before may be responsible for a slight retardation of the dark decay at longer recording times, whereas the phase shift seemingly slightly decreases. Although this is indicated in figure (5.5 - 3), the effect is very small rendering this statement speculative.

On the other hand, the apparent fact that optical activation of deep trapping sites in material C, the occurrence of which has been proven in “5.4.1.3.3.) Experimental verification

of optical trap activation” on page 285, is of minor importance for the dark decay may indicate that the detrapping process of these trapping sites is similar as for “normal” conformational traps. One may assume that a mechanism similar to the trap cancellation process determines the thermal detrapping of conformational traps. This would give further indication for the attribution of the optically activated deep traps in PVK based polymers to carbazole dimers as discussed in “5.4.1.3.6.) Conclusions on the nature of the PR traps” on page 296, since slow collective motion of the conducting polymer matrix may not only release a carrier trapped in a “normal” conformational trap, but may also crack such a carbazole dimer sandwich complex.

Finally, figure (5.5 - 6) depicts the logarithmically averaged dark decay times plotted versus the estimated PR phase shifts for all experiments performed. This diagram reveals a clear correlation between these quantities. The fact, that the observed trend is consistent even for both the investigated materials indicates, that the PR phase shift represents a dominant factor for the dark decay behavior, the general influence of which should not depend significantly on the particular type of PR polymer.

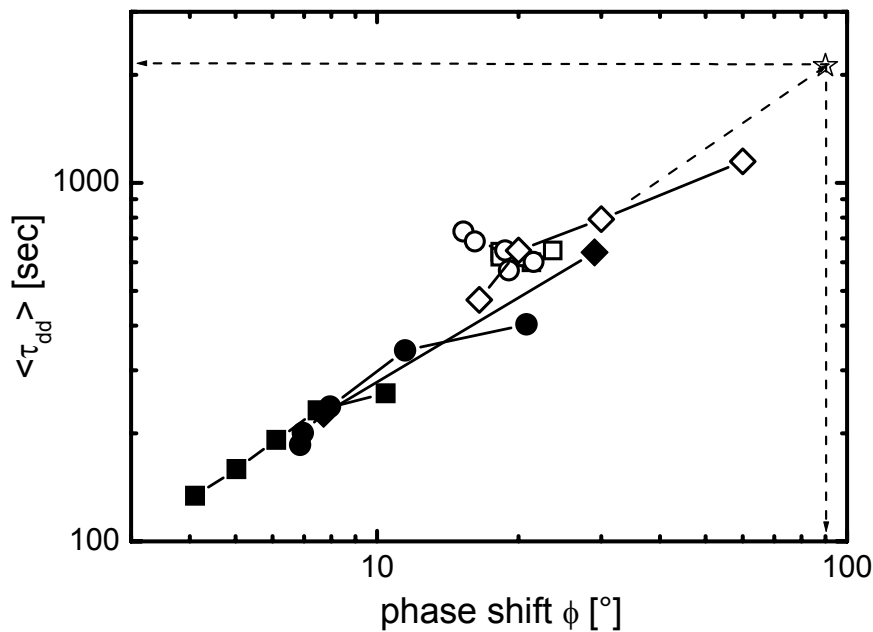


Figure (5.5 - 6): Dark decay time constants for all experiments (squares: recording time dependence; circles: field dependence; diamonds: recording intensity dependence) carried out on the dark decay of material C (open symbols) and material CT (solid symbols) depicted as a function of the corresponding PR phase shifts ϕ at the end of recording the holograms. Details of the particular experimental parameters are explained in the figure captions of figure (5.5 - 2) to figure (5.5 - 4). The lines are guide to the eye. The star indicates a manual extrapolation to $\phi = 90^\circ$, yielding $\langle \tau_{dd} \rangle \approx 2100$ sec.

5.5.4.) Quintessence of the investigations on the PR dark decay behavior

In conclusion, a systematic investigation of the dark decay of holograms in PR polymers was performed. The dark decay was found to be governed by the decay of the PR space-charge field and - most remarkably - depended on the phase shift of the PR grating. This is particularly important for the application of PR polymers. In order to store distortion-free images, the energy transfer between the recording beams (2BC “gain”) is undesired, because it leads to fringe

bending and to contrast loss of the hologram [B8, B16]. In order to avoid this, small gain coefficients Γ are required, which (simultaneously assuming large index modulation amplitudes) are correlated with small PR phase shifts. The latter, however, yield a fast dark decay of the recorded information as is clearly demonstrated by the results presented here. Thus, a trade-off between these counteracting trends will be necessary. The phase-shift effects may even vary in different areas of an image (e.g. due to different intensities and/or different fringe visibility m according to eq. (2.1 - 47)), leading to time-dependent contrast and distortion of images subjected to idle periods during processing, where dark decay can take place.

5.6.)Holographic multiplexing in PVK based PR polymers

In this section, the actual experimental application of the PVK based photorefractive polymers investigated in the frame of this work for holographic data storage will be elaborated upon. Holographic data storage is a promising technology for the storage of large amounts of data. The basic theory underlying this storage technology has already been outlined in “2.3.3.) Holographic data storage” on page 60. As discussed therein, in order to be useful for holographic data storage applications, a material must be capable of achieving a high M-number $M/\#$, a property dependent on both the recording and erasure dynamics of the stored holograms. In the preceding sections, the recording, erasure, and dark decay behavior of holograms in PVK based photorefractive polymers was elaborated upon. In this section, the actual recording of multiple holograms in the concerned materials by peristrophic multiplexing shall be considered. The technique of peristrophic multiplexing has been explained in “2.3.3.2.2.) Holographic multiplexing methods” on page 63. It will be demonstrated, that the simple multiplexing schedule as derived in “2.3.3.3.) System metrics for holographic multiplexing in erasable media” on page 65 fails for the investigated class of materials. Therefore, a new recording schedule is devised in order to account for the variation of the erasure time constants as a function of the recording time. Applying the new exposure schedule, the $M/\#$ measured from the recording of 20 equalized holograms was 0.3.

5.6.1.)Experimental aspects

The compositions and the glass-transition temperatures of the used materials B (not containing extrinsic deep traps) and BT (doped with extrinsic deep traps) are listed in table 5-1 on page 211 as well as at the end of the current section. PR devices for the peristrophic multiplexing experiments were prepared according to “4.1.) Preparation of materials and sample structure” on page 179. The active layer thickness was $d = 125\mu\text{m}$. The temperature in the air-conditioned laboratory was $24\pm 0.5^\circ\text{C}$ for all measurements.

The recording and erasure dynamics of the used materials was determined by DFWM experiments using a HeNe Laser ($\lambda_0 = 633\text{ nm}$) and the peristrophic multiplexing setup as described in “4.2.1.5.) Holographic multiplexing experiments” on page 201, however, without operating the rotation stage. The experimental data were evaluated as described in “4.2.1.3.2.3.) DFWM evaluation procedure” on page 197.

The peristrophic multiplexing experiments were carried out using a HeNe Laser ($\lambda_0 = 633\text{ nm}$) and using the setup and experimental procedures as described “4.2.1.5.) Holographic multiplexing experiments” on page 201. The experimental data were evaluated as described in the same section.

For all experiments the recording beams were both s-polarized and had internal intensities of $I_{01} \approx 400\mu\text{W}/\text{cm}^2$ and $I_{02} \approx 250\mu\text{W}/\text{cm}^2$ yielding a grating contrast of $m \approx 0.95$. The readout beam was p-polarized with an internal intensity of approximately $3\mu\text{W}/\text{cm}^2$. For erasure, a fourth non-Bragg matched beam with normal incidence was used having an internal intensity of approximately $650\mu\text{W}/\text{cm}^2$. An external dc electrical field of $E_{ext} = 62\text{ V}/\mu\text{m}$ was applied to the samples in all cases.

Prior to each experiment on the recording/erasure dynamics as well as prior to each sequence of peristrophic multiplexing experiments (i.e. a complete recording sequence of multiple holograms and their subsequent readout) the samples were pre-illuminated by recording beam I_{02} for 15min with the external field already applied.

Table (5-9): Chemical composition and glass transition temperature of the materials investigated in “5.6.) Holographic multiplexing in PVK based PR polymers”

Material	DMNPAA	MNPAA	PVK	ECZ	TNF	TPD	T _g
units	[%wt]	[%wt]	[%wt]	[%wt]	[%wt]	[%wt]	[°C]
B	25	25	43	6	1	-	17.5
BT	25	25	40	8.18	1	0.82	17

5.6.2.)Theoretical considerations - derivation of a suitable multiplexing schedule

Today, the M-number $M/\#$ is widely accepted as a general measure for the data-storage capacity of an arbitrary holographic storage system. According to “2.3.3.3.2.) The M-number ($M/\#$)” on page 68, $M/\#$ is calculated by eq. (2.3 - 65):

$$M/\# = \left(\frac{A_0}{\tau_r}\right)\tau_e,$$

where A_0 is the maximum single-hologram grating strength, τ_r is the recording time constant, and τ_e is the erasure time constant. As already discussed in “2.3.3.3.) System metrics for holographic multiplexing in erasable media” on page 65, this formalism presumes mono-exponential recording and erasure dynamics for a single hologram and implies fairly small refractive index modulations for the individual holograms (i.e. $\eta < 0.1$, which allows for the approximation: $\Delta n \propto \sqrt{\eta}$). The first assumption, however, is not fulfilled in organic PR materials since the recording as well as the erasure behavior of this class of materials is multi-exponential, as demonstrated several times in the frame of this work. Moreover, the formalism leading to eq. (2.3 - 65) presumes that the recording and the erasure dynamics are independent from each other, which is also not the case in the materials under investigation, as elaborated upon in “5.4.) The erasure behavior of PR gratings in PVK based polymer composites” on page 271. Thus, eq. (2.3 - 65) cannot be applied here in order to obtain a reasonable value of $M/\#$.

However, $M/\#$ can alternatively be determined experimentally on the basis of eq. (2.3 - 64):

$$\eta = \left[\frac{M/\#}{M}\right]^2,$$

which, therefore, is rewritten as:

$$M/\# = M\sqrt{\eta}, \quad \text{eq. (5.6 - 1)}$$

where M is the number of recorded holograms and $\sqrt{\eta} \propto \Delta n$ is the grating strength of a single hologram. It is clear that $M/\#$ calculated by means of eq. (5.6 - 1) only has physical significance, if the recorded holograms exhibit equal or at least very similar grating strengths. Then, eq. (5.6 - 1) may be formulated in terms of a sum over the grating strengths of the particular holograms recorded:

$$M/\# = \sum_{i=1}^M \sqrt{\eta_i}. \quad \text{eq. (5.6 - 2)}$$

The most important issue for the above approach is to have a suitable exposure schedule, which allows to record multiple holograms of approximately equal strength. Figure (5.6 - 1) shows a characteristic example, which indicates that a standard exposure schedule calculated according to eq. (2.3 - 51) and eq. (2.3 - 61) and using a logarithmically averaged erasure time constant calculated according to eq. (5.2 - 26) does not meet this requirement. As already mentioned above, this is due to the complex recording/erasure behavior of the investigated materials. In order to solve for this problem, single-hologram erasure curves were measured for different recording times between 2 seconds and 50 minutes. They were each fitted by a series of decaying exponentials for material B or a series of decaying and growing exponentials for material BT, which exhibits the effect of further increasing PR grating strength during the initial erasure process, as discussed in “5.4.2.) PR grating erasure in systems doped with extrinsic traps” on page 300. Accounting for the complex recording/erasure behavior of the materials considered, the strength w_m of the hologram m , after being erased for the time t_e calculates according to:

$$w_m = w(t_m, t_e) = A_{e1}(t_m)e^{-t_e/\tau_{e1}(t_m)} + A_{e2}(t_m)e^{-t_e/\tau_{e2}(t_m)} + \dots, \quad \text{eq. (5.6 - 3)}$$

where t_m is the time the hologram m was recorded for. The coefficients $A_{ei}(t_m)$ as well as the time constants $\tau_{ei}(t_m)$ were determined experimentally by fitting the erasure curves. The formalism allows for taking into account a recording time dependence of the erasure dynamics. Therefore, the pre-exponential factors as well as the time constants of the exponentials describing the grating decay are taken as a function of the recording time of the particular holograms. The strength w_M of the last hologram M is:

$$w_M = w(t_M, 0), \quad \text{eq. (5.6 - 4)}$$

i.e., $t_e = 0$ is presumed. The second to last hologram $M-1$ must be recorded for the time t_{M-1} , which can then be computed by numerically solving the relation:

$$w(t_{M-1}, t_M) = w_M, \quad \text{eq. (5.6 - 5)}$$

since the second to last hologram will be partially erased while the last hologram is recorded. Therewith, the times necessary for recording all holograms can numerically be obtained recursively using the relation:

$$w\left(t_m, \sum_{m'=m+1}^M t_{m'}\right) = w_M. \quad \text{eq. (5.6 - 6)}$$

When using this method for computing the recording schedule, the recording time for the last hologram must be chosen with special care depending on the dynamics of the material and the total number of holograms to be recorded. If, for instance, the recording time for the last hologram is chosen too long, the holograms to be recorded earlier can physically not be recorded to sufficient strength in order to finally yield equal strength for all holograms. Thus, a solution for the recording schedule cannot be found. In contrast, if the recording time for the last hologram is chosen too short, a solution will be found, however, the strength of all the holograms will not be optimal, i.e. the dynamic range of the material is not entirely used. In order to find the recording schedule that would give best performance, a numerical routine for the optimization of t_M was used. As upper limit for the recording time the maximum recording time was taken for which experimental values stemming from the single-hologram recording/

erasure experiments were on hand. In order to numerically solve eq. (5.6 - 6) it is necessary to evaluate eq. (5.6 - 3) for arbitrary values of t_m . Since the coefficients $A_{ei}(t_m)$ and erasure time constants $\tau_{ei}(t_m)$ were only obtained experimentally for discrete values of t_m , the measured data were interpolated for values of t_m not corresponding to a direct measurement.

5.6.3.)Results and discussion of the holographic multiplexing experiments

Please note at first, that the investigated materials B and BT were operated at an ambient temperature of $RT = 24 \pm 0.5^\circ\text{C}$. Therefore, a reduced temperature of $T_r \approx -6^\circ\text{C}$ according to eq. (5.2 - 1) applies for the investigated materials whose PR behavior as a function of the reduced temperature corresponds to the materials C and CT in the preceding sections, respectively.

Figure (5.6 - 1) shows a typical example of an attempt to record a number of holograms into material B using peristrophic multiplexing and the standard exposure schedule calculated according to eq. (2.3 - 51) and eq. (2.3 - 61) and using the logarithmically averaged erasure time constant. The latter was calculated according to eq. (5.2 - 26) from the particular time constants obtained in one single-hologram recording/erasure experiment carried out applying an arbitrary recording time. Obviously, the requirement of similar strength of the recorded holograms is not met and, thus, no $M/\#$ with physical meaning can be calculated. This proves that the standard exposure scheduling is inadequate for the materials concerned.

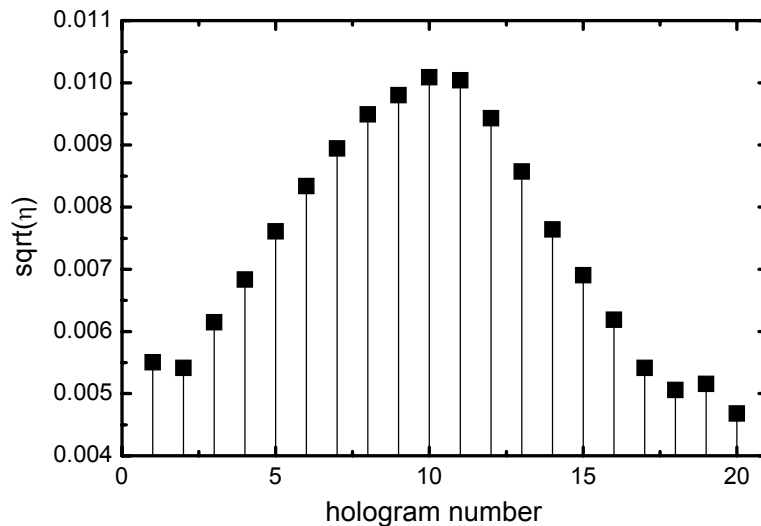


Figure (5.6 - 1): Peristrophic multiplexing of 20 holograms in material B using the standard exposure schedule, i.e. presuming mono-exponential recording/erasure dynamics.

Therefore, a novel exposure schedule was devised, which accounts for the complex recording/erasure behavior of the investigated materials as described in the preceding section. By means of this method, a schedule for the recording of 11 holograms using peristrophic multiplexing was calculated, but only the last 10 recording times were used to multiplex 10 holograms, since the first of the computed recording times was unreasonably long ($\gg 1\text{h}$). The grating strengths obtained are shown in figure (5.6 - 2) (solid symbols).

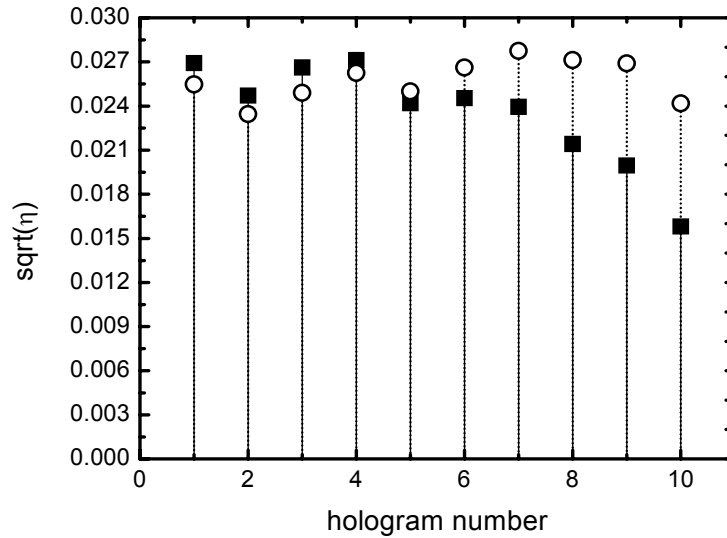


Figure (5.6 - 2): Strength of 10 multiplexed holograms recorded in material B using the novel expanded exposure schedule for multi-exponential dynamics (solid circles) and with the empirically altered schedule (open circles)

Figure (5.6 - 2) proves that the novel schedule works in principle, however, the last few holograms are decreasing in strength. One suspected reason for this might be the grating erasure, which was performed by the weak reading beam during readout of the holograms. Since the erasure behavior of a particular hologram depends on the time the hologram was recorded, each multiplexed hologram experiences another degree of erasure during the readout sequence, which was not taken into account when deriving the recording schedule. On the other hand, it seems questionable whether it would make sense to take this effect into account for the exposure schedule, since the exposure schedule then would be a function of the succeeding readout sequence(s). Another reason for the decreasing strength of the last few holograms may be found in an experimental mistake, which was not recognized until this project was closed. The single-hologram recording/erasure experiments underlying the numerical calculation of the exposure schedule were performed using a non Bragg-matched erasure beam, whereas the erasure of the earlier holograms during peristrophic multiplexing was conducted Bragg-matched by the reference beam as well as non Bragg-matched by the signal beam. The Bragg-matched erasure by the reference beam must be expected to cause some degree of grating refreshment as several times pointed out in preceding sections. Thus, earlier holograms are supposed to be a little less erased during recording of the later holograms than assumed for the exposure schedule.

Please note, that dark decay effects as stated in the original publication ([212]) cannot be made responsible for the decreasing strength of the last few holograms, since the dark decay of the holograms in material B does not depend on their recording time as shown in “5.5.) Dark decay of PR gratings in PVK-based polymer composites” on page 317.

In order to compensate for the deviations in the hologram strength, the recording schedule was empirically modified by adding 1 second to each recording time, resulting in more even holograms with an average strength of 0.0235 to 0.0277 (figure (5.6 - 2), open symbols). The $M/\#$'s obtained from the two schedules according to eq. (5.6 - 2) were $M/\# = 0.24$ original schedule and $M/\# = 0.26$ for the empirically modified schedule.

Under the experimental conditions applied here a diffraction efficiency of $\eta \approx 0.1$ was achieved for a single hologram, which corresponds to a grating strength of 0.32. It must be pointed out, that the obvious similarity of this value with the $M/\#$'s given above is accidental and that

the single hologram diffraction efficiency must not be considered as an indicator of the possible $M/\#$ for a material. The measurement of $M/\#$ takes into account dynamic effects, which are completely ignored in a steady-state single-hologram experiment. Thus, a material capable of a large single hologram index modulation is not necessarily capable of a correspondingly large $M/\#$.

In an attempt to modify the dynamics of the material allowing to record more than 10 holograms, material BT was created, which contained a small fraction of the hole conductor TPD acting as a deep hole trap in the photoconducting PVK matrix. As repeatedly discussed before, this results in a reduced charge-carrier mobility in the PR composite in question and, hence, slower response in both build-up and erasure of a hologram was anticipated as well as found experimentally. On the other hand, the steady-state diffraction efficiency for a single hologram was found almost unchanged as compared to the material without TPD (material B). The first experimental results, furthermore, showed that for short recording times subsequent “erasure” actually yields further development of the hologram. The diffraction efficiency reaches a maximum during initial erasure and then begins to decay. A detailed investigation on this effect is presented in “5.4.2.) PR grating erasure in systems doped with extrinsic traps” on page 300. This was taken into account for the exposure schedule by including a growing exponential term into the fits. Figure (5.6 - 3) illustrates the time history of the hologram strength during recording with an exposure schedule for recording 10 holograms in material BT.

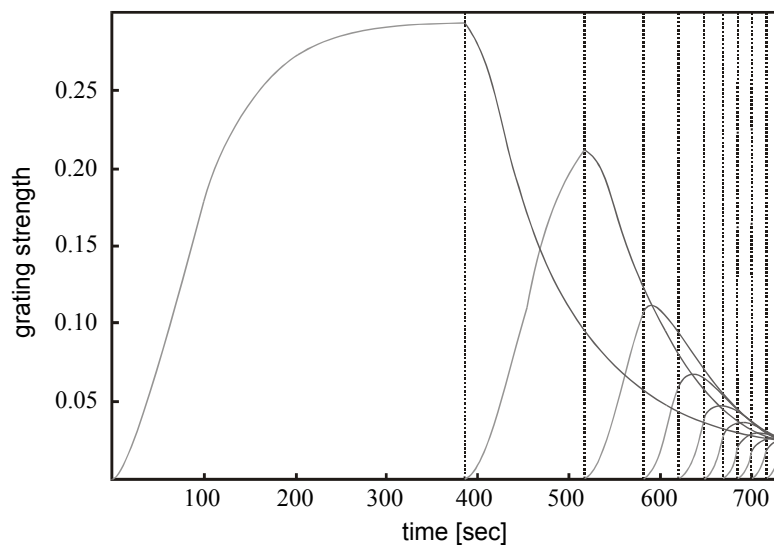


Figure (5.6 - 3): Illustration of the time history of the hologram strengths during multiplexing 10 holograms in material BT. The vertical dashed lines mark the end of recording for one hologram and the start of recording for the next hologram. The build-up of holograms is indicated by light grey lines, whereas dark grey lines indicate the subsequent erasure period during which succeeding holograms are processed.

Using the same procedure as described above, peristrophic multiplexing experiments were carried out on material BT in order to record 20 and 30 holograms. The results are depicted in figure (5.6 - 4).

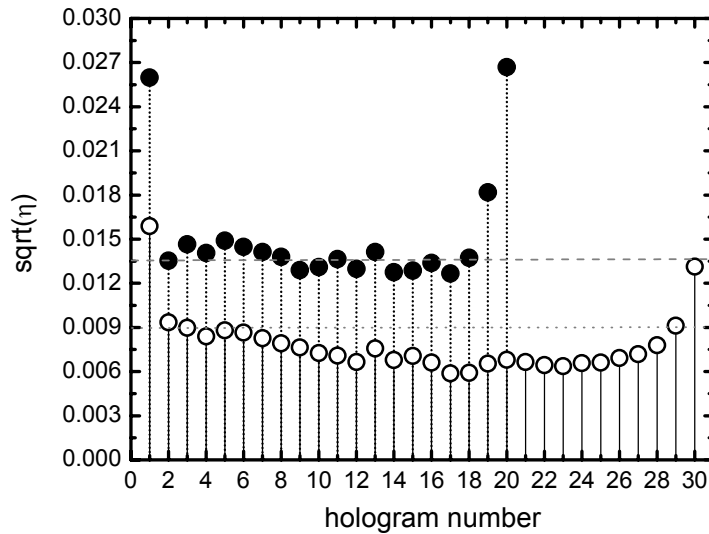


Figure (5.6 - 4): Strength of multiplexed holograms recorded in material BT using the empirically altered, expanded exposure schedule for multi-exponential dynamic behavior of the recording medium. 20 holograms (solid circles) and 30 holograms (open circles) were recorded. The grey horizontal dashed (for 20 holograms) and dotted lines (for 30 holograms) indicate the average hologram grating strength yielding $M/\# = 0.27$ in both cases.

Overall, the uniformity of the recorded holograms was very good with the major deviations occurring only at the boundaries. Using eq. (5.6 - 2), $M/\# = 0.30$ was obtained for the case of 20 holograms and $M/\# = 0.23$ for the case of 30 holograms. The smaller $M/\#$ for the case of 30 holograms as compared to the case of 20 holograms may be attributed to the correspondingly longer erasure period by the weak readout beam for the readout sequence as already discussed above. This point of view is supported when considering the average hologram strength, which would yield $M/\# = 0.27$ for both cases (figure (5.6 - 4), grey horizontal lines). Obviously, the notably higher $M/\#$ achieved for 20 holograms must be attributed on the one hand to the deviations in the hologram strengths at the boundaries, whereas the notably smaller $M/\#$ achieved for 30 holograms seems to be due to a loss in hologram strength occurring for larger hologram numbers on the other. The hologram strength increasing again for the last few holograms in the latter case may be attributed to the complex erasure behavior of material BT as mentioned before.

In the case of material BT, one may have to account for a dark decay behavior of the particular holograms depending on the recording time as shown in “5.5.) Dark decay of PR gratings in PVK-based polymer composites” on page 317. This is an important issue, since the recorded manifold of holograms may lose its equality in strength, if there is a notable delay between recording and read-out where dark decay can take place. Therefore, in order to get a more detailed insight into the influence of dark decay on the relative strength of the multiplexed holograms in material BT, 20 holograms were recorded with the schedule discussed above and then read out after varying delay times t_d . Prior to each cycle, gratings remaining from previous recording were completely erased. Figure (5.6 - 5) depicts the resulting $M/\#$'s as a function of the delay time t_d .

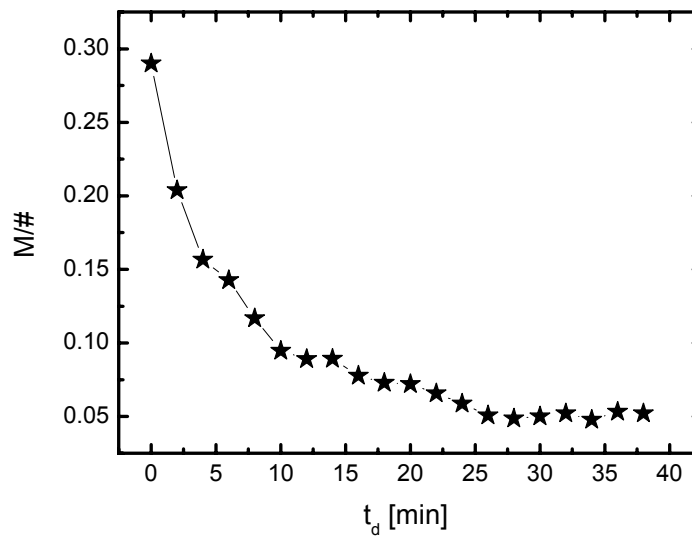


Figure (5.6 - 5): Dependence of M/# on the delay time t_d between recording and the beginning of readout in material BT. The line is guide to the eye.

As expected, the apparent M-number decreases with increasing delay time t_d , because all holograms decay with time. A similar dependence should be expected for material B, however, according to the results presented in “5.5.) Dark decay of PR gratings in PVK-based polymer composites” on page 317 less pronounced than for material BT.

However, since the dark decay is different for each individual hologram in material BT due to the recording time dependence of the dark decay in this material, the inequality between the holograms increases as a function of t_d (figure (5.6 - 6)), and the calculated M/# therewith loses its physical significance.

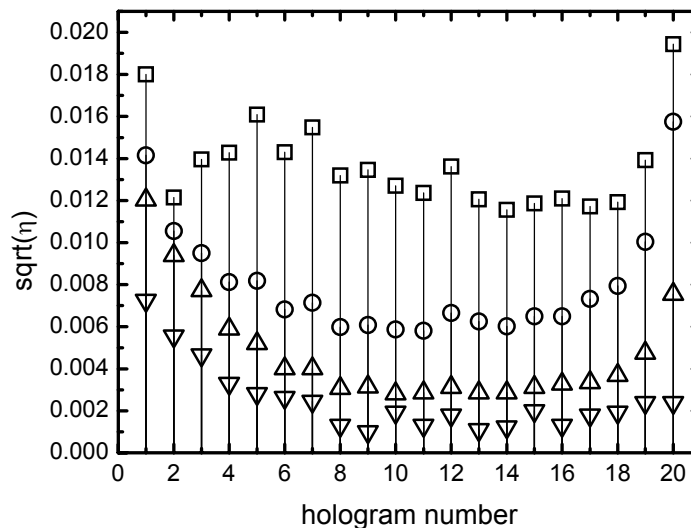


Figure (5.6 - 6): Strength of 20 multiplexed holograms in material BT after delays of $t_d = 0$ min (squares), $t_d = 4$ min (circles), $t_d = 10$ min (up triangles), and $t_d = 30$ min (down triangles)

5.6.4.)Conclusions from the holographic multiplexing experiments in PR polymers

An expanded numerical formalism for a multiplexing exposure schedule derived from the standard model as outlined in “2.3.3.3.1.) The exposure schedule” on page 66 and based on multiple exponential build-up and erasure dynamics of the holograms was developed. This novel formalism in general allows to determine a suitable recording schedule for an arbitrary storage medium not exhibiting mono-exponential dynamic behavior.

Peristrophic multiplexing experiments using this novel formalism were carried out in order to experimentally test the storage capabilities of PVK based PR polymers. An M-number $M/\# \approx 0.25$ was obtained and proved to be very similar in both types of materials investigated. The material doped with extrinsic deep traps allowed for multiplexing of more holograms, which can be attributed to the fact that for short recording times the holograms still increase in strength while being erased.

While PR polymers are capable of achieving very large single-hologram diffraction efficiencies, several problems have been revealed, which remain to be solved before this novel class of materials may be applied in holographic data storage. The dependence of the erasure time constants and, in the case of the trap-doped material, also the dark decay time constants on the recording time causes the holograms to lose their equality shortly after recording has been completed. Furthermore, in general relatively fast dark decay times pose serious problems for persistent data storage. However, in its current state the material might be useful in associative memories, where one image is simultaneously compared with all images of a data base, but long-term storage is not intended.

6.) Summary and Conclusion

In the frame of this work PVK-based PR polymer composites closely related to the first high performance PR polymer [13] were investigated. Therefore, the composition of the investigated type of material was systematically altered, and various experimental conditions were applied. The main objective of this work was to get a more detailed insight and a better understanding of the dynamic recording, erasure and dark decay behavior of holograms in this type of PR polymer. Steady-state performance issues were also addressed as they yield important information on the general properties of the PR space-charge field for the varying material compositions and experimental conditions applied. All investigations eventually focussed on the question, whether PR polymers may be suitable candidates as recording media in holographic mass data storage devices. This point was finally addressed experimentally, when the general holographic multiplexing capabilities of the investigated type of material were examined.

In chapter 5.1.), a simplified model calculation based on Kogelnik's coupled equations was carried out in order to obtain an overview of the general diffraction properties of a hologram in PR polymers in presence of strong beam coupling. The latter was suspected to be responsible for the incomplete diffraction at the diffraction maximum in PR polymers, which is commonly observed experimentally. Although the applied simulation model contains strong simplifications, it could be proven that hologram bending due to strong 2BC does not notably affect the diffraction properties of a grating in organic PR devices within the range of the externally applied field experimentally possible. The degree of incomplete diffraction commonly observed experimentally could not be reproduced by the simulation. Hence, the physical reason for this observation remains unclear.

In chapter 5.2.) the dependence of the steady-state and the dynamic PR performance of the considered materials on the glass-transition temperature T_g was focussed upon. Material compositions containing various amounts of molecular dipoles were investigated. T_g was varied by adding different amounts of plasticizer. The reduced temperature $T_r = T_g - RT$ (ambient temperature) was identified as a factor of outstanding importance.

A steady-state performance optimum in the highly-doped materials as a function of the reduced temperature was observed for the first time. The performance optimum is a result of two counteracting effects: On the one hand, the orientational mobility of the chromophores becomes better with decreasing T_r , leading to a reduction of the external field required to achieve a certain degree of poling. On the other hand, for decreasing $T_r < 0^\circ\text{C}$ the PR space-charge field E_{sc} is more and more reduced as a result of a decrease of the effective PR trap density due to slow collective motion of the photoconducting polymer matrix, which facilitates the release of charge carriers trapped in conformational traps.

Investigating the holographic recording dynamics in the high- T_g (i.e. $T_r > 0^\circ\text{C}$) organic PR composites it was found that the grating build up speed is limited by the (re)orientation of the EO chromophores under the influence of the local total poling field leading to faster response at lower T_r . The grating build-up time also depends strongly on the chromophore density. This may be attributed to the self-hindrance of the chromophores molecules in the highly-doped materials, which reduces the apparent orientational mobility of the chromophore dipoles in the polymer matrix. In the low- T_g regime (i.e. $T_r < 0^\circ\text{C}$) the response times of the materials with different chromophore content become rather similar and do no longer depend systematically on T_r . In this regime, the formation of the space-charge field is the rate-limiting step in the onset dynamics of the refractive index modulation.

In chapter 5.3.) the influence of the sensitizer concentration on the steady-state and the dynamic PR behavior of the investigated type of PR polymers was considered. Strong indication was found that the active PR trap manifold in the common type of PVK-based PR polymers utilizing TNF as sensitizer consists of two different types of traps. On the one hand there are conformational traps, which exist ab initio and the number density of which does not depend on the sensitizer content. The conformational traps are the dominant species in materials doped with very small amounts of sensitizer up to 0.4%wt. On the other hand, there are Poole-Frenkel traps (Coulombic traps) stemming from ionized sensitizer moieties. These add to the conformational traps and become important for higher sensitizer concentrations of about 0.8%wt, leading to improved steady-state PR performance. For even markedly higher TNF concentrations, the Poole-Frenkel traps finally dominate the PR behavior. It is an inherent property of Poole-Frenkel traps that they are generated during the PR recording process and, thus, that their number density is a function of time. The more complicated trap situation for higher TNF concentrations apparently complicates the PR recording behavior, which is mono-exponential for very low TNF concentration and then becomes multi-exponential as the TNF content increases and exceeds 0.4%wt. The build-up behavior of the PR grating for increasing TNF content was compared with theoretical considerations based on Kukhtarev's model. Strong indication was found that the PR build-up dynamics of the investigated type of PR polymers is limited by the charge carrier mobility for TNF concentrations exceeding 0.2%wt.

In order to serve as a suitable storage medium in holographic mass data storage devices, a holographic recording medium must be capable of achieving good performance in holographic multiplexing. The crucial parameters defining the performance of a holographic recording medium in holographic multiplexing, however, are the dynamic range, i.e. the steady-state performance, and the relation between the build-up dynamics and the erasure dynamics of the holograms. Therefore, in chapter 5.4.) the general erasure behavior of PR gratings in the considered type of materials was investigated in detail applying various experimental conditions and taking into account different glass-transition temperatures. Furthermore, the influence of extrinsic trap doping was investigated.

The PR grating erasure in materials without extrinsic deep traps was investigated taking into account different glass-transition temperatures. As expected from the investigations on the T_g dependence of the PR performance of the considered materials, the orientational relaxation of the NLO chromophores in the polymer matrix was found to govern the PR grating erasure dynamics in the high- T_g regime (i.e. $T_g > RT$, ambient ("room") temperature), whereas the decay of the PR space-charge field determines the PR grating erasure dynamics the low- T_g regime (i.e. $T_g < RT$). In all cases, the erasure dynamics of the PR grating depended on the recording time of the grating. The grating erasure process was found to slow down as a function of increasing recording time. In the high- T_g regime this can be attributed to a viscous flow of the polymer matrix. In contrast, in the low- T_g regime optical activation of trapping sites turned out to be responsible for the observed retardation of the grating erasure. By means of a theoretical model for the PR grating erasure in polymers, two fundamentally different types of optically activated traps could be identified. On the one hand, Poole-Frenkel traps are generated as already found before. These traps seem to determine the initial grating erasure. On the other hand, deep traps are optically activated, which might be carbazole dimer radical cations and which seem to govern the erasure behavior on longer time scale. These two kinds of PR traps behave fundamentally different: the former show Langevin behavior and the latter do not. Accordingly, multiple trap theoretical models for the PR effect in PR polymers must be applied in order to describe these systems sufficiently accurate.

The formation of carbazole dimers apparently strongly depends on T_g . Since conformational traps may be assumed to be the precursors for the dimer formation, the T_g -

dependence of the dimer formation may be explained by the slow collective motion of the conducting polymer matrix occurring in materials with $T_g < RT$ leading to a smaller apparent density of conformational traps as already proposed before.

The fact that the charge carrier trap situation (i.e. the number density of traps as well as the structure of the trap manifold) in PR polymers obviously changes significantly during recording of a PR grating leads to important implications: At first, it renders any fitting of PR recording data purely phenomenological, since the fitting parameters are time dependent. Secondly, the resulting recording time dependence of the erasure dynamics in the investigated type of PR polymers may be expected to pose problems when trying to apply this class of materials in holographic multiplexing.

Finally, the potential applicability of the investigated systems for holographic multiplexing was estimated by comparing the ratios between averaged measures of the holographic recording and erasure times. A relative optimum of the theoretical multiplexing capabilities as a function of the reduced temperature was identified for $T_r = -6^\circ\text{C}$, however, the presented results already imply very limited multiplexing capabilities in general.

Furthermore, the erasure behavior of PVK-based PR polymers was investigated, which exhibit trap controlled charge transport [46]. It was observed for the first time, that the DFWM diffraction efficiency further increases during erasure of a PR grating applying short recording times and low recording as well as low erasure intensity. In order to understand this phenomenon, the evolution of the PR phase shift during recording as well as erasure of PR gratings was considered. For this purpose, a novel measurement technique was devised, which allows to obtain a measure for the time dependence of the PR phase shift during erasure of the hologram. The PR phase shift was found to be a function of time during recording as well as erasure.

A phenomenological mechanistic picture of the recording and the erasure process of a hologram in a material showing trap controlled charge transport was developed taking into account the spatial distribution of electrical fields within the PR grating. The model presented is based on the assumption that filling of the traps is required before a notable drift of charge carriers over longer distances may take place. The electrical fields inside the material and their influence on the charge carrier generation efficiency and charge carrier mobility are taken into account in order to explain the details of the time history of the PR phase shift. The model can explain the experimental observation of further increasing DFWM diffraction efficiency during erasure of a PR grating. The quality of this effect depends on the applied electrical field and, in particular, on the applied recording time, both of which are inherent features of the proposed model.

The presented phenomenological model infers that holograms in the investigated type of material are inherently not stable neither during recording nor during erasure. The dependence of the general form of their erasure kinetics on the recording time implies image distortions during the processing of the holograms. The complicated correlation between recording time and erasure dynamics of the holograms must again be expected to pose problems for a potential application of this type of material in holographic multiplexing.

Another important issue when considering the potential applicability of the investigated materials for holographic mass data storage is the stability of the recorded holograms in the dark. Therefore, in chapter 5.5.) a systematic investigation of the dark decay of holograms in PVK-based PR polymers was performed taking into account different glass-transition temperatures as well as extrinsic trap doping. In any case, i.e., even in the high- T_g regime, the dark decay was found to be governed by the decay of the PR space-charge field and - most remarkably - was found to depend on the phase shift of the PR grating. Small PR phase shifts

yielded a fast dark decay of the recorded information, whereas the dark decay is increasingly retarded as the phase shift becomes larger.

These results are particularly important for the application of PR polymers. In order to store distortion-free images, energy transfer between the recording beams (PR gain) is undesired, because it leads to fringe bending and to contrast loss of the hologram. In order to avoid this, small gain coefficients Γ are required. In high performance PR polymers, these are typically correlated with small PR phase shifts, yielding fast dark decay of the hologram. The phase-shift effects may even vary in different areas of an image, leading to time-dependent contrast and distortion of images subjected to idle periods during processing, where dark decay can take place.

Eventually, in chapter 5.6.) the general feasibility of holographic multiplexing in the investigated type of materials was investigated. These investigations were carried at CalTech in the group of Prof. Demitri Psaltis, a well known expert in the field of holographic data storage, and in close cooperation with Dr. Gregory Steckman.

An expanded numerical formalism for a multiplexing exposure schedule was devised, which was derived from the standard model and based on multiple exponential build-up and erasure dynamics of the holograms. This novel formalism in general allows to determine a suitable recording schedule for an arbitrary storage medium not exhibiting mono-exponential dynamic behavior. Furthermore, the formalism allows for taking into account a recording time dependence of the erasure dynamics. In this case, the pre-exponential factors as well as the time constants of the exponentials describing the grating decay are taken as a function of the recording time of the particular holograms. The exposure schedule obtained applying this formalism, however, is strictly limited to a particular material and a certain multiplexing experiment.

Two low- T_g materials exhibiting very similar glass-transition temperatures were chosen for the multiplexing experiments. The one of these materials was doped with extrinsic deep traps and the other one was not. Peristrophic multiplexing experiments were carried out using this novel formalism in order to experimentally test the storage capabilities of the investigated types of materials. An M-number $M/\# \approx 0,25$ was obtained and proved to be very similar in both materials. The material doped with extrinsic deep traps allowed for multiplexing of more holograms, which can be attributed to the fact that for short recording times the holograms still increase in strength while being erased. However, the dependence of the erasure time constants and, in the case of the trap-doped material, also the dark decay time constants on the recording time caused the holograms to lose their equality shortly after recording has been completed.

Holographic mass data storage promises very high storage density. The retrieval of holographically stored data is intrinsically of parallel nature, which allows for fast data rates. Holographic storage media may actively participate in data processing since they offer the possibility of associatively comparing data already inside the holographic storage medium. Although these features are most preferable for mass data storage systems, up to now holographic data storage could not be established for commercial use. This was basically due to technical problems during the first decades, many of which have been solved during the last decade. However, the major problem still remaining is the question for an appropriate storage medium, which could not be answered satisfyingly, yet.

At first sight, photorefractive polymers appear to be very promising candidates for rewritable holographic storage media mainly due to the following properties: PR polymers exhibit good optical quality. They are easy to process, and their particular properties can easily

be tuned. PR polymers are capable of achieving very large single-hologram diffraction efficiencies and feature excellent reproducibility. Last but not least, PR polymers are low cost materials.

However, in this thesis, several problems have been revealed, which render this novel class of materials in its current state not suitable for application as rewritable holographic mass data storage media. Although PR polymers are capable of achieving large single hologram diffraction efficiencies, the rather unfavorable ratio between the hologram recording and erasure dynamics allows for only fairly small M-numbers of about $M/\# \approx 0,25$. Even more importantly, the complicated relationship between the recording and erasure dynamics of holograms in PR polymers requires a very sophisticated exposure scheduling in holographic multiplexing. Especially the pronounced dependence of the erasure dynamics on the recording time of the particular holograms would make it very difficult to operate a holographic storage device using PR polymers as storage medium. Furthermore, in general relatively fast dark decay times, which again depend on the recording conditions in some cases including also the recording time, pose serious problems for persistent data storage as well as for the equality of the diffraction properties of the stored manifold of data pages. Finally, there is strong indication that stored images are subjected to distortion during erasure and, in particular, during idle periods of the storage system, where dark decay can take place. This must be expected to have a negative impact on the bit error rate, which is additionally strongly time dependent.

Summing up all the aforementioned shortcomings of PR polymers leads to the conclusion, that a potential application of this novel class of materials in its current state as storage medium in rewritable holographic mass data storage devices cannot reasonably be implied.

Besides the question for a potential applicability of PR polymers as holographic mass data storage media, this thesis has addressed important mechanistic aspects of the PR effect in polymers leading to the observed dynamic behavior. The photorefractive trapping of charge carriers was identified to play a major role in particular for the decay, but also for the build-up of the PR space-charge field. In order to achieve progress in developing PR polymers, which may be more suitable for a potential application as holographic mass data storage media, concepts will have to be found, which reduce the complexity of the PR trap manifold and provide a trap situation, which is constant in time. However, the present state of knowledge about charge carrier traps in amorphous PR organic materials suggests that both a complex structure of the PR trap manifold as well as a time dependent PR trap situation are inherent properties of this class of materials. Thus, it seems currently out of sight, whether PR polymers may ever be considered as promising candidates for storage media in rewritable holographic mass data storage devices.

However, the material investigated in the frame of this thesis might be useful for real-time holographic applications, where long-term storage is not intended. Examples for such applications are associative memories, where one image is simultaneously compared with all images of a data base, or in applications as holographic buffer memories [224, 227], or in optical coherence tomography applying time gated holographic imaging (TGH_i) [4].

References

Books:

Please note, that books listed below are not necessarily referred to explicitly in the text. Nevertheless, they have been used for writing this work.

- [B1] Bergmann, Schäfer “*Lehrbuch der Experimentalphysik, Bd. 3: Optik*“, deGruyter 1993.
- [B2] Bergmann, Schäfer “*Lehrbuch der Experimentalphysik, Bd. 6: Festkörper*“, deGruyter 1993.
- [B3] Bergmann, Schäfer “*Lehrbuch der Experimentalphysik, Bd. 5: Vielteilchensysteme*“ deGruyter 1992.
- [B4] Born M., “*Optik*“, Springer 1985 (2. Nachdruck der 3. Auflage).
- [B5] Borsenberger P. M., Weiß D. S., “*Organic Photoreceptors for Imaging Systems*“, Marcel Dekker (1993).
- [B6] Boyd R.W., “*Nonlinear optics*“, Academic Press 1992.
- [B7] Czicjos H., “*Hütte, Taschenbuch der Ingenieurwissenschaften*“, Springer 1996.
- [B8] Coufal H.J., Psaltis D., Sincerbox G.T., (Eds.), “*Holographic Data Storage*“, Springer 2000.
- [B9] Cowie J. M. G., “*Chemie und Physik der synthetischen Polymeren*“, Vieweg 1997.
- [B10] Donth E.-J. “*Relaxation and Thermodynamics in Polymers*“, Akademie Verlag 1992.
- [B11] Elias H.-G. “*Polymere*“, Hüthig & Wepf Verlag 1996.
- [B12] Emin D., “*Electronic and structural properties of amorphous semiconductors*“ (Eds: LeComber P. G. and Mort J.), Academic Press, NY (1973).
- [B13] Guenther P. (Eds.) “*Nonlinear Optical Effects and Materials*“, Springer Series in Optical Sciences Vol. 72, Springer 2000.
- [B14] Fouckhardt H. “*Photonik*“, Teubner 1994.
- [B15] Ghatak A.K., Thyagarajan K., “*Optical Electronics*“ Cambridge University Press 1989.
- [B16] Guenther P., Huingard J.-P., (Eds.), “*Photorefractive Materials and their Applications*“, I + II, Springer 1989.
- [B17] Hecht E. “*Optik*“, Addison Wesley 1987.
- [B18] Latimer I., Hawkes J., “*Lasers*“, Prentice Hall 1995.
- [B19] Nolting W., “*Theoretische Physik Bd. 3 - Elektrodynamik*“, Zimmermann-Neufang 1993.
- [B20] Pope M., Swenberg C.E., “*Electronic Processes in Organic Crystals and Polymers*“, Oxford University Press 1999.
- [B21] Sperling L. H., „*Introduction to Physical Polymer Science*“, 2nd edition, Wiley 1992.

- [B22] Yeh P. "Introduction to photorefractive nonlinear Optics" Wiley 1993.
- [B23] Young M., "Optic, Laser, Wellenleiter", Springer 1993.
- [B24] Eason R.W., Miller A., (Eds.) "Nonlinear optics in signal processing", Chapman & Hall 1993.
- [B25] Kippelen B., Meerholz K., Peyghambarian N., „An Introduction to Photorefractive Polymers“ in: Nalwa H. S., Miyata S., (eds.) „Nonlinear Optics of Organic Molecules and Polymers“, CRC press (1997).
- [B26] Meerholz K., Kippelen B., Peyghambarian N., „Noncrystalline Organic Photorefractive Materials: Chemistry, Physics, and Applications“ in: Wise D. I., Wnek G. E., Trantolo D. J., Cooper T. M., Gresser J. D., (eds.) „Photonic Polymer Systems“ Marcel Dekker (1998).
- [B27] Borsenberger P.M. in "Hole transport in triphenylmethane doped polymers" in R.W. Munn, A. Miniewicz, B. Kucta (Eds.) "Electrical and related properties of organic solids", NATO ASI Series 3 Vol. 24, Kluwer Academic Publishers (1997).

Thesis:

- [T1] Mecher E., „Erhöhung der Sensitivität photorefraktiver holographischer Speichermedien auf Basis von amorphen organischen Materialien“ (2001).
- [T2] T. K. Daeubler, *Photophysical characterization of photorefractive polymers (PhD thesis)* (GCA-Verlag, Herdecke, 1999).

Articles:

- [1] Lerner E., *Laser Focus World* (August, 1999).
- [2] Wu W., Campbell S., Yeh P., *J. Opt. Soc. Am. B* **13**(11), 2549 (1996).
- [3] Benaron D., Stevenson D. K., *Science* **259**, 1443 (1993).
- [4] Mecher E., Gallego F., Meerholz K., *Nature* **418**(6901), 959 (2002).
- [5] Hyde S.C.W., Barry N.P., Jones R., Dainty J.C., French P.M.W., Klein M.B., Wechsler B.A., *Opt. Lett.* **20**, 1331 (1995).
- [6] Jones R., Hyde S.C.W., Lynn M.J., Barry N.P., Dainty J.C., P. French M.W., Kwolek K.M., Nolte D.D., Melloch M.R., *Appl. Phys. Lett.* **69**(13), 1837 (1996).
- [7] Steele D.D., Volodin B.L., Savina O., Kippelen B., Peyghambarian N., Rockel H., Marder S.R., *Opt. Lett.* **23**(3), 153 (1998).
- [8] Ashkin A., Boyd G. D., Dziedzic J. M., Smith R. G., Ballmann A. A., Nassau K., *Appl. Phys. Lett.* **9**, 72 (1966).
- [9] Chen F. S., *J. Appl. Phys.* **38**, 3418 (1967).

-
- [10] Sutter K., Hulliger J., Günter P., *Solid State Commun.* **74**, 867 (1990).
- [11] Sutter K., Günter P., *J. Opt. Soc. Am.* **12**, 2274 (1990).
- [12] Ducharme S., Scott J. C., Twieg R. J., Moerner W. E., *Phys. Rev. Lett.* **66**, 1846 (1991).
- [13] Meerholz K., Volodin B., Sandalphon, Kippelen B., Peyghambarian N., *Nature* **371**, 497 (1994).
- [14] Gabor D., *Nature* **161**, 777 (1948).
- [15] Mainman T.H., *Nature* **187**, 493 (1960).
- [16] Leith E.N., Upatnieks J., *J. Opt. Soc. Am.* **52**, 1123 (1962).
- [17] Leith E.N., Upatnieks J., *J. Opt. Soc. Am.* **53**, 1377 (1963).
- [18] Kogelnik H., *Bell Syst. Tech. J.*, **48**(9) 2909 (1969).
- [19] van Heerden P.J., *Appl. Opt.* **2**(4), 393 (1963).
- [20] Barbasthatis G., Levene M., Psaltis D., *Appl. Opt.* **35**(14) 2403 (1996).
- [21] Barbasthatis G., Psaltis D., *Opt. Lett.* **21**(6) 432 (1996).
- [22] Curtis K., Pu A., Psaltis D., *Opt. Lett.* **19**(13) 993 (1994).
- [23] Denz C., Dellwig T., Lembcke J., Tschudi T., *Opt. Lett.* **21**(4) 278 (1996).
- [24] Logere I., Grelet F., Ratsep M., Tian M., Le Gouet J. L., Sidel C., Roblin M. L., *JOSA B*, **13**(10), 2229 (1996).
- [25] Psaltis D., Brady D., Wagner K., *Appl. Opt.* **27**(9), 1752 (1988).
- [26] Mok F. H., Burr G. W., Psaltis D., *Opt. Lett.* **21**(12), 896 (1996).
- [27] Wu J. W., *J. Opt. Soc. Am. B* **8**, 142 (1991).
- [28] Kuzyk M. G., Sohn J. E., and Dirk C. W., *J. Opt. Soc. Am. B* **7**, 842, (1990).
- [29] Holstein et. al., *Ann. Phys.*, **8**, 325 (1959).
- [30] Baessler H., *Phys. stat sol. (b)* **175**, 15 (1993).
- [31] Baessler H., *Philos. Mag. B* **50**, 347 (1984).
- [32] Baessler H., *Phys. stat sol. (b)* **107**, 9 (1981).
- [33] Borsenberger P. M., Pautmeier L., Baessler H., *J. Chem. Phys.* **94**(8), 5447 (1991).
- [34] Schein L. B., *Chem. Phys. Lett.* **149**(1) 109 (1988).
- [35] Schein L. B., *Philos. Mag. B*, 65(4), 795 (1992).
- [36] Mack J. X., Schein L. B., Peled A., *Phys. Rev. B*, **39**(11) 7500 (1989).
- [37] Marcus R. A., *Ann. Rev. Phys. Chem.*, **15**, 155 (1964).
- [38] van der Auweraer M., Verbeek G., de Schryver F. C., Borsenberger P. M., *Chem. Phys.*, **190**, 31 (1995).
- [39] Kenkre V. M., Andersen J. D., Dunlap D. H., Duke C. B., *Phys. Rev. Lett.*, **62**, 1165 (1989).
-

-
- [40] Miller A., Abrahams E., *Phys. Rev.*, **120**(3), 745 (1960) Slowik J., Chen I., *J. Appl. Phys.*, **54**, 4467 (1983).
- [41] Gartstein, Yu. N., Conwell E., *J. Chem. Phys.*, **100**, 9175 (1994).
- [42] Movaghar B., Gruenewald M., Ries B., Baessler H., Würtz D., *Phys. Rev. B*, **33**, 5445 (1986).
- [43] Blumen A., Klafter J., White B. S., Zumofen G., *Phys. Rev. Lett.*, **53**, 1301 (1989).
- [44] Köhler G., Blumen A., *J. Phys. A*, **20**, 5627 (1987).
- [45] Ries B., Baessler H., Gruenewald M., Movaghar B., *Phys. Rev. B*, **37**, 5508 (1988).
- [46] Pai D. M., Janus J. F., Stolka M., *J. Phys. Chem.*, **88**, 4714 (1984).
- [47] Gill W. D., *J. Appl. Phys.* **43**, 5033 (1972).
- [48] Kirkpatrick S., *Rev. Mod. Phys.*, **45**(4), 574 (1973).
- [49] Silver M., Risko K., Baessler H., *Philos. Mag. B*, **40**, 247 (1979).
- [50] Pautmeier L., Richert R., Baessler H., *Philos. Mag. B*, **63**(3), 587 (1991).
- [51] Scher H., Montroll E. W., *Phys. Rev. B*, **12**(6), 2455 (1975).
- [52] Richert R., Pautmeier L., Baessler H., *Phys. Rev. Lett.* **63**(5), 547 (1989).
- [53] Pfister G., *Philos. Mag. B*, **36**, 1147 (1977).
- [54] Grasruck, M., Schreiber, A., Hofmann, U., Zilker, S. J., Leopold, A., Schloter, S., Hohle, C., Strohmriegl, P., Haarer, D., *Phys. Rev. B: Condens. Matter Mater. Phys.* **24**, 60 (1999).
- [55] Pfister G., *Phys. Rev. B*, **16**(8), 3676 (1977).
- [56] Hofmann U., Grasruck M., Leopold A., Schreiber A., Schloter S., Hohle C., Strohmriegl P., Haarer D., Zilker S. J., *J. Phys. Chem. B*, **104**(16), 3887 (2000).
- [57] Zilker S. J., Hofmann U., Leopold A., Grasruck M., Hohle C., Strohmriegl P., *Mol. Cryst. Liq. Cryst. Sci. Technol., Sect. A*, **358** 15 (2001).
- [58] Borsenberger P. M., Pautmeier L. T., Baessler H., *Phys. Rev. B*, **46**(19), 12145 (1992).
- [59] Onsager L., *Phys. Rev.*, **54**, 554 (1938).
- [60] v. Smoluchowski M., *Phys. Zeits.*, **15**, 593 (1914).
- [61] Mozumder A., *J. Chem. Phys.*, **60**(11), 4300 (1974).
- [62] Goliber T. E., Perstein H. J., *J. Chem. Phys.*, **80**(9), 4162 (1984).
- [63] Cimrová V., Kmínek, I., Nešpurek S., Schnabel W., *Synth. Met.*, **64**, 271 (1994).
- [64] Cimrová V., Nešpurek S., *Chem. Phys.*, **184**, 283 (1994).
- [65] Barth S., Baessler H., *Phys. Rev. Lett.*, **79**(22), 4445 (1997).
- [66] Noolandi J., Hong K. M., *J. Chem. Phys.*, **70**(1), 3230 (1979).
- [67] Braun L. B., *J. Chem. Phys.*, **80**(9), 4157 (1984).
-

-
- [68]Nozue Y., Hisamune T., Goto T., Tsuruta H., *J. Phys. Soc. Japan*, **55**, 4053 (1986).
- [69]Langevin P., *Ann. Chim. Phys.* VII, **28**, 433 (1906).
- [70]Amodei J. J., *Appl. Phys. Lett.* **18**, 22 (1971).
- [71]Kuktharev N. V., Markov V. B., Odulov S. G., Soskin M. S., Vinetskii V. L., *Ferroelectrics* **22**, 949 (1979).
- [72]Twarowski, *J. Appl. Phys.*, **65**, 2833 (1989).
- [73]Stepanov S. I., Garcia R. R., Pernas V. C., Mansurova S., Bittner R. Meerholz K., *Proc. SPIE* **4462**, 178 (2002).
- [74]Silence S. M., Bjorklund G. C., Moerner W. E., *Opt. Lett.* **19**(22), 1822 (1994).
- [75]Grunnet-Jepsen A., Wright D., Smith B., Bratcher M. S., DeClue M. S., Siegel J. S., Moerner W. E., *Chem. Phys. Lett.* **291**, 553 (1998).
- [76]Bäumel, G., Schloter, S., Hofmann, U., Haarer, D., *Synth. Met.* **97**, 165 (1998)
- [77]Schildkraut J. S., Cui Y., *J. Appl. Phys.* **72**(11), 5055 (1992).
- [78]Schildkraut J. S., Buettner A. V., *J. Appl. Phys.* **72**(5), 1888 (1992).
- [79]Tayebati P., Mahgerefteh D., *JOSA B*, **8**(5), 1053 (1991).
- [80]Batt R.H., Braun C.L., Hornig J.F., *J. Chem. Phys.* **49**, 1967 (1968).
- [81]Pautmeier L., Richert R., Bäessler H., *Synth. Met.* **37**, 271 (1990).
- [82]Yuan B., Sun X., Hou C., Zhou Z., Jiang Y., Li C., *J. Appl. Phys.* **88**(10), 5562 (2000).
- [83]Cui Y., Swedek B., Cheng N., Zieba R., Prasad P. N., *J. Appl. Phys.* **85**(1), 38 (1999).
- [84]Orzyk M. E., Swedek B., Zieba J., Prasad N. P., *J. Appl. Phys.* **76**, 4995 (1994).
- [85] Silence S. M., Walsh C. A., Scott J. C., Martray . J., Twieg R. J., Hache F., Bjorklund G. C., Moerner W. E., *Opt. Lett.* **17**, 1107 (1992).
- [86]Silence S. M., Walsh C. A., Scott J. C., Moerner W. E., *Appl. Phys. Lett.* **61**, 2967 (1992).
- [87]Slowik J. H., Chen I., *J. Appl. Phys.* **54**(8), 4467 (1983).
- [88]Moerner W. E., Silence S. M., Hache F., Bjorklund G. C., *J. Opt. Soc. Am. B*, **11**(2), 320 (1994).
- [89]Bittner R., diploma thesis (1996).
- [90]Zilker S. J., Hofmann U., *Appl. Opt.*, **39**(14), 2287 (2000).
- [91]Lundquist P. M., Wortmann R., Geletneky C., Twieg R. J., Jurich M., Lee V. Y., Moylan C. R., Burland D. M., *Science* **274**, 1182 (1996).
- [92]Mecher E., Bittner R., Bräuchle C., Meerholz K., *Synth. Met.*, **102**, 993 (1999).
- [93]Chaput F., Riehl D., Boilot J. P., Cargnelli K., Canva M., Lévy Y., Brun A., *Chem. Mater.*, **8**, 312 (1995).
-

-
- [94]Darracq B., Canva M., Chaput F., Boilot J. P., Riehl D., Lévy Y., Brun A., *Appl. Phys. Lett.* **70**(3), 292 (1997).
- [95]Burzynski R., Casstevens M. K., Zhang Y., Ghosal S., *Opt. Eng.*, **35**(2) 443 (1996).
- [96]Khoo I. C., Li H., Liang Y., *Opt. Lett.* **19**(24), 1723 (1994).
- [97]Khoo I. C., *Opt. Lett.* **20**(20), 2137 (1995).
- [98]Khoo I. C., Guenther B. D., Wood M. V., Chen P., Shih M.-Y., *Opt. Lett.* **22**(16), 1226 (1997).
- [99]Wiederecht G. P., Yoon B. A., Wasielewski M. R., *Science* **270**, 1794 (1995).
- [100]Wiederecht G. P., Yoon B. A., Wasielewski M. R., *Adv. Mat.* **8**(6), 535 (1996).
- [101]Wiederecht G. P., Wasielewski M. R., *J. Am. Chem. Soc.* **120**, 3231 (1998).
- [102]Khoo, I. C., *IEEE J. Quant. Elec.* **32**(3), 525 (1996).
- [103]Helfrich W., *J. Chem. Phys.* **51**, 4092 (1969).
- [104]Ono H., Saito i., Kawatsuki N., *Appl. Phys. Lett.* **72**(16), 1942 (1998).
- [105]Ono H., Hanazawa A., Kawamura T., Norisada H., Kawatsuki N., *J. Appl. Phys.* **86**(4), 1785 (1999).
- [106]Ono H., Kawatsuki N., *J. Appl. Phys.* **85**(5), 2482 (1999).
- [107]Ono H., Kawamura T., Frias N. M., Kitamura K., Kawatsuki N., Norisada H., Yamamoto T., *J. Appl. Phys.* **88**(7), 3853 (2000).
- [108]Ono H., Kawamura T., Frias N. M., Kitamura K., Kawatsuki N., Norisada H., *Adv. Mat.* **12**(2) 143 (2000).
- [109]Ono H., Kawatsuki N., *Opt. Lett.* **22**(15), 1144 (1997).
- [110]Golemme A., Kippelen B., Peyghambarian N., *Appl. Phys. Lett.* **73**(17), 2408 (1998).
- [111]Van Steenwinckel D., Hendrickx E., Persoons A., *Chem. Mater.* **13**, 1230 (2001).
- [112]Wang L., Zhang Y., Wada T., Sasabe H., *Appl. Phys. Lett.* **69**(6), 728 (1996).
- [113]Li W., Gharavi A., Wang Q., Yu L., *Adv. Mat.* **10**(12), 927 (1998).
- [114]Wang L., Ng M.-K., Yu L., *Phys. Rev. B* **62**(8), 4973 (2000).
- [115]Mager L., Méry S., *MCLC* **322**, 21 (1998).
- [116]Hohle C., Hofmann U., Schloter S., Thelakkat M., Strohriegel P., Haarer D., Zilker S. J., *J. Chem Mater.* **9**, 2205 (1999).
- [117]Hofmann U., Grasruck M., Leopold A., Schreiber A., Schloter S., Hohle C., Strohriegel P., Haarer D., Zilker S. J., *J. Phys. Chem. B* **104**(16), 3887 (2000).
- [118]Grasruck M., Schreiber A., Hofmann U., Zilker S. J., Leopold A., Schloter S., Hohle C., Strohriegel P., Haarer D., *Phys. Rev. B* **60**(24), 16543 (1999).
-

- [119]Ogino K., Park S.-H., Sato H., *Appl. Phys. Lett.* **74**(26), 3936 (1999).
- [120]Wang L., Ng M.-K., Yu L., *Appl. Phys. Lett.* **78**(6) (2001).
- [121]Boyd G. T., Francis C. V., Trend J. E., Ender D. A., *J. Opt. Soc. Am. B* **8**, 887 (1991).
- [122]Moerner W. E., Silence S. M., *Chem. Rev.* **94**, 127 (1994).
- [123]Zhang Y, Burzynski R., Ghosal S., Casstevens M. K., *Adv. Mat.* **8**(2), 111 (1996).
- [124]Bittner R., Bräuchle C., Meerholz K., *Appl. Opt.* **37**, 2843 (1998).
- [125]Herlokker J. A., Ferrio K. B., Hendrickx E., Guenther B. D., Mery S., Kippelen B., Peyghambarian N., *Appl. Phys. Lett.* **74**(16), 2253 (1999).
- [126]Van Steenwinckel D., Engels C., Gubbelmanns E., Hendrickx E., Samyn C., Persoons A., *Macromolecules* **33**, 4074 (2000).
- [127]Van Steenwinckel D., Hendrickx E., Samyn C., Engels C., Persoons A., *J. Mater. Chem.* **10**, 2692 (2000).
- [128]Yu. L., Chan W. K., Peng Z., Gharavi A., *Acc. Chem. Res.* **29**, 13 (1996).
- [129]Peng Z., Gharavi A., Yu L., *Polym. Prepr.*, **37**(2), 380 (1996).
- [130]Wang Q., Wang L., Yu J., Yu L., *Adv. Mat.* **12**(13), 974 (2000).
- [131]Yu L., *J. Polym. Sci. A* **39**, 2557 (2001).
- [132]Hwang J., Sohn J., Lee J.-K., Lee J.-H., Chang J.-S., Lee J. G., Park S. Y., *Macromolecules* **34**, 4656 (2001).
- [133]Hattemer E., Zentel R., Mecher E., Meerholz K., *Macromolecules* **33**, 1972 (2000).
- [134]Park S.-H., Ogino K., Sato H., *Synth. Met.* **113**, 135 (2000).
- [135]Meerholz K., Bittner R., De Nardin Y., Braeuchle C., Hendrickx E., Volodin B. L., Kippelen B., Peyghambarian N., *Adv. Mat.* **9**(13), 1043 (1997).
- [136]Meerholz K., De Nardin Y., Bittner R., *Mol. Cryst. Liq. Cryst.* **315**, 99 (1998).
- [137]Ogino K., Nomura T., Shichi T., Park S.-H., Sato H., Aoyama T., Wada T., *Chem. Mater.* **9**, 2768 (1997).
- [138]Malliaras G. G., Angermann H., Krasnikov V. V., ten Brinke G., Hadziioannou G., *J. Phys. D* **29**, 2045 (1996).
- [139]Malliaras G. G., Krasnikov V. V., Bolink H. J., Hadziioannou G., *Appl. Phys. Lett.* **66**(9) 1038 (1995).
- [140]Volodin B. L., Sandalphon, Meerholz K., Kippelen B., Kukhtarev N. V., Peyghambarian N., *Opt. Eng.* **34**(8), 2213 (1995).
- [141]Mecher E., Gallego F., Meerholz K., *Proc. SPIE-Int. Soc. Opt. Eng.* **3799**, 4 (1999).
- [142]Hendrickx E., Zhang Y., Ferrio K. B., Herlocker J. A., Andersen J., Armstrong N. R.,

- Mash E. A., Persoons A. P., Peyghambarian N., Kippelen B., *J. Mater. Chem.* **9**, 2251 (1999).
- [143] B., Prasad P. N., Cui Y., Cheng N., Zieba J., Winiarz J., Kim K.-S., *Proc. SPIE-Int. Soc. Opt. Eng.* **2850**, 89 (1996).
- [144] Kippelen B., Hendrickx E., Ferrio K. B., Herlocker J., Zhang Y., Peyghambarian N., Marder S. R., Anderson J., Armstrong N. R., Mery S., *J. Imaging Sci. Technol.* **43**(5), 405-412 (1999).
- [145] Zobel O., Eckl M., Strohhriegl P., Haarer D., *Adv. Mater.* **7**(11), 911-14, (1995).
- [146] Domes H., Fischer R., Haarer D., Strohhriegl P., *Makromol. Chem.* **190**, 165 (1989).
- [147] Baeuml G., Schloter S., Hofmann U., Haarer D., *Synth. Met.* **97**, 165 (1998).
- [148] Wolff J., Schloter S., Hofmann U., Haarer D., Zilker S. J., *J. Opt. Soc. Am B* **16**(7), 1080 (1999).
- [149] Baeuml G., Schloter S., Hofmann U., Haarer D., *Opt. Comm.* **154**, 75 (1998).
- [150] Moerner W. E., Grunnet-Jepson A., Thompson C. L., Bratcher M. S., Twieg R. J., *Proc. SPIE-Int. Soc. Opt. Eng.* 3147, 84 (1998).
- [151] Mecher E., Braeuchle C., Hoerhold H. H., Hummelen J. C., Meerholz K., *Phys. Chem. Chem. Phys.* **1**, 1749 (1999).
- [152] Lebedev E., Dittrich T., Petrova-Koch V., Karg S., Brütting W., *Appl. Phys. Lett.* **71**, 2686 (1997).
- [153] Hofmann U., Schreiber A., Haarer D., Zilker S. J., Bacher A., Bradley D. D. C., Redecker M., Inbasekaran M., Wu W. W., Woo E. P., *Chem. Phys. Lett.* **311**, 41 (1999).
- [154] Moerner W.E., Grunnet-Jepsen A., Thompson C.L., *Annu. Rev. Mater. Sci.* **27**, 585 (1997).
- [155] Grunet-Jepsen A., Thompson C. L., Twieg R. J., Moerner W. E., *Appl. Phys. Lett.* **70**(12) 1515 (1997).
- [156] Wright D., Diaz-Garcia M. A., Casperson J. D., DeClue M., Moerner W. E., *Appl. Phys. Lett.* **73**(11), 1490 (1998).
- [157] Swedek B., Cheng N., Cui Y., Zieba J., Winiarz J., Prasad P. N., *J. Appl. Phys.* **82**(12) 5923 (1997).
- [158] Orcyk M. E., Zieba J., Prasad P. N., *Appl. Phys. Lett.* **67**(3), 311 (1995).
- [159] Marder S. R., Beratan D. N., Cheng L. T., *Science* **252**, 103 (1991).
- [160] Meyers F., Marder S. R., Pierce B. M., Bredas J. L., *J. Am. Chem. Soc.* **116**, 10703 (1994).

- [161] Wortmann R., Poga C., Twieg R. J., Geletneky C., Moylan C. R., Lundquist P. M., DeVoe R. G., Cotts P. M., Horn H., Rice J. E., Burland D. M., *J. Chem. Phys.* **102**(23) 10637 (1996).
- [162] Wolff J. J., Wortmann R., in „*Advances in Physical Organic Chemistry*“ Vol. 32, Academic Press, p. 122-217, in press.
- [163] Barzoukas M., Runser C., Fort A., Blanchard-Desce M., *Chem. Phys. Lett.* **257**, 531 (1996).
- [164] Blanchard-Desce M., Barzoukas M., *JOSA B* **15**(1), 302 (1998).
- [165] Meerholz K., De Nardin Y., Bittner R., Wortmann R., Wuerthner F., *Appl. Phys. Lett.* **73**(1), 4 (1998).
- [166] Wuerthner F., Yao S., Schilling J., Wortmann R., Redi-Abshiro M., Mecher E., Gallego-Gomez F., Meerholz K. *J. Am. Chem. Soc.*, **123**(12), 2810 (2001).
- [167] Marder S., Kippelen B., Yen A. K.-Y., Peyghambarian N., *Nature* **388**, 845 (1997).
- [168] Kippelen B., Meyers F., Peyghambarian N., Marder S., *J. Am. Chem. Soc.* **119**, 4559 (1997).
- [169] Barzoukas M., Blanchard-Desce M., *J. Chem. Phys.* **112**(4), 2036 (2000).
- [170] Kippelen B., Marder S., Hendrickx E., Maldonado J. L., Guillemet G., Volodin B. L., Steele D. D., Enami Y., Sandalphon, Yao Y. J., Wang J. F., Röckel H., Erskine L., Peyghambarian N., *Science* **279**, 54 (1998).
- [171] Würthner F., Wortmann R., Matschiner K., Lukaszuk K., Meerholz K., De Nardin Y., Bittner R., Braeuchle C., Sens R., *Angew. Chem Int. ed. Eng.* **36**(24), 2765 (1997).
- [172] Wortmann R., Glania C., Kraemer P., Lukaszuk K., Matschiner R., Twieg R. J., You F., *Chem. Phys.* **245**, 107 (1999).
- [173] Meerholz K., Bittner R., De Nardin Y., Braeuchle C., Wortmann R., Wuerthner F., *Proc. SPIE-Int. Soc. Opt. Eng.* **3471**, 52 (1998).
- [174] Cox A. M., Blackburn R. D., West D. P., King T. A., Wade F. A., Leigh D. A., *Appl. Phys. Lett.* **68**(29), 2801 (1996).
- [175] Simley E. J., McGee D. J., Salter C., Carlen C. R., *J. Appl. Phys.* **88**(8), 4910 (2000).
- [176] Meerholz K., personal communication.
- [177] Mecher E., personal communication.
- [178] Grunnet-Jepsen A., Thompson C. L., Twieg R. J., Moerner W. E., *Appl. Phys. Lett.* **70**(12), 1515 (1997).
- [179] Silence S. M., Donckers M. C. J. M., Walsh C. A., Burland D. M., Twieg R. J., Moerner

-
- W. E., *Appl. Opt.* **33**, 2218 (1994).
- [180]Diaz-Garcia M. A., Wright D., Casperson J. D., Smith B., Glazer E., Moerner W. E., *Chem. Mater.* **11**, 1784 (1999).
- [181]Van Steenwinckel D., Hendrickx E., Persoons A., Van den Broeck K., Samyn C., *J. Chem. Phys.* **112**(24), 11030 (2000).
- [182]Weiser G., *J. Appl. Phys.* **43**(12), 5028 (1972).
- [183]Gill W. D., *J. Appl. Phys.* **43**(12), 5033 (1972).
- [184]Weiser G., *Phys. Stat. Sol. (a)* **18**, 347 (1973).
- [185]Kippelen B., Sandalphon, Meerholz K., Peyghambarian N., *Appl. Phys. Lett.*, **68**(13), 1748 (1996).
- [186]Natasohn A., Meng X., Rochon P., *Polymer* **38**(11), 2677 (1997).
- [187]Bieringer T., Wuttke R., Haarer D., Gessner U., Ruebner J., *Macromol. Chem. Phys.* **196**(5), 1375 (1995).
- [188]Wuttke R., Fischer K., Bieringer T., Haarer D., Eisenbach C. D., *Polym. Mater. Sci. Eng.* **72**, 520 (1995).
- [189]Zilker S. J., Bieringer T., Haarer D., Stein R. S., Van Egmond J. W., Kostromine, S. G., *Adv. Mater.* **10**(11), 855-859 (1998).
- [190]Eickmans J., Bieringer T., Kostromine S., Berneth H., Thoma R., *Jpn. J. Appl. Phys. Part I*, **38**(3B), 1835 (1999).
- [191]Bolink H. J., Krasnikov V.V., Malliaras G. G., Hadziioannou G., *J. Phys. Chem.* **100**, 16356 (1996).
- [192]Liphardt M., Ducharme S., *J. Opt. Soc. Am. B* **15**(7), 2154 (1998).
- [193]Fujino M., Mikawa H., Yokoyama M., *J. Noncryst. Solids* **64**, 163 (1984).
- [194]Ikeda M., *J. Phys. Soc. Jpn.* **60**, 2031 (1991).
- [195]Borsenberger P..M., Pautmeier L., Bässler H., *J. Chem. Phys.* **95**, 1258 (1991).
- [196]Daeubler T. K., Bittner R., Meerholz K., Neher D., *Phys. Rev. B* **61**(20), 13515 (2000).
- [197]Meerholz K., Bittner R., Braeuchle C., Volodin B. L., Sandalphon, Kippelen B., Peyghambarian N., *Proc. SPIE*, **102**, 2850 (1996).
- [198]Sandalphon, Kippelen B., Meerholz K., and Peyghambarian N., *Appl. Opt.* **35**, 14 (1996).
- [199]Winkelhahn H.-J., Servay Th. K., Neher D., *Ber. Bunsenges. Phys. Chem.* **100**, 123 (1996).
- [200]Burger C., „Transformation von Relaxationsfunktionen“, PhD.-Thesis, University of Marburg, Germany (1994).
-

-
- [201]Malliaras G. G., Krasnikov V. V., Bolink H. J., Hadziiaonnou G., “Transient behaviour of photorefractive gratings in a polymer”, *Appl. Phys. Lett.* **67**, 455 (1995).
- [202] Leopold A., Grasruck M., Hofmann U., Kol’chenk M. A., Zilker J., *Appl. Phys. Lett.* **76**(13), 1644 (2000).
- [203]Leopold A., Kol’chenk M. A., Hofmann U., Zilker J., *J. Lumin.* **86**, 371 (2000).
- [204]Binks D. J., West D. P., *J. Chem. Phys.* **115**(2) 1060 (2001).
- [205]Binks D. J., Khand K., West D. P., *JOSA B* **18**(3) 308 (2001).
- [206]Donckers M.C.J.M., Silence S.M., Walsh C.A., Hache F., Burland D.M., Moerner W.E., Twieg R.J., *Opt. Lett.* **18**, 1044-1046 (1993).
- [207]Grunnet-Jepsen A., Thompson C.L., Moerner W.E., *Opt. Lett.* **22**, 874 (1997).
- [208]Grunnet-Jepsen A., Wright D., Smith B., Bratcher M. S., DeClue M. S., Siegel J. S., Meorner W. E., *Chem. Phys. Lett.* **291**, 553 (1998).
- [209]Khand K., Binks D. J., West D. P., Rah n M. S., *J. Mod. Opt.* **48**(1), 93 (2001).
- [210]Neifeld M. A., Psaltis D., *App. Opt.* **32**(23), 4398 (1993).
- [211]Liphardt M., Gooneskera A., Ducharme S., *J.Opt. Soc. Am. B* **13**(10), 2252 (1996).
- [212]Steckman G., Bittner R., Meerholz K., Psaltis D., *Opt. Comm.* **185**, 13 (2000).
- [213]Silence S. M., Twieg R. J., Bjorklund G. C., Moerner W. E., *Phys. Rev. Lett.* **73**(15), 2047 (1994).
- [214]Giro G., Di Marco P. G., *Chem. Phys. Lett.* **162**(3), 221 (1989).
- [215]Fujino M., Kanazawa H., Mikawa S., Kusabayashi S., Yokoyama M., *Solid State Comm.* **49**, 575 (1984).
- [216]Zboinski Z., *Chem. Phys.* **75**, 297 (1983).
- [217]Herlocker J. A., Ferrio K. B., Hendrickx E., Guenther B. D., Mery S., Kippelen B., Peyghambarian N., *Appl. Phys. Lett.* **74**(16), 2253 (1999).
- [218]Malliaras G. G., Krasnikov V. V., Bolink H. J., Hadziianou G., *Phys. Rev. B*, **52**(20), 324 (1995).
- [219]Zilker S. J., Grasruck M., Wolff J., Schloter S., Leopold A., Kol’chenko M. A., Hofmann U., Schreiber A., Strohriegel P., Hohle C., Haarer D., *Chem. Phys. Lett.* **306**, 285 (1999).
- [220]Grunnet-Jepsen, A.; Thompson, C. L.; Moerner, W. E., *JOSA B* **15**(2), 905 (1998).
- [221]Meerholz K., Bittner R., De Nardin Y., *Opt. Commun.* **150**(1-6), 205 (1998).
- [222]Volodin B. L. , Kippelen B., Meerholz K., Javidi B., Peyghambarian N., *Nature* **383**, 58 (1996).
- [223]Klein M., Wright D., Moerner W. E., *Opt. Commun.* **162**, 79 (1999).
-

- [224] Burr G., Mecher E., Juchem T., Coufal H., Jefferson C. M., Jurich M., Gallego F., Hampp N., Meerholz K., Hoffnagle J., MacFarlane R. M., Shelby R. M., *SPIE-Proceedings* (H. Coufal & D. Psaltis, eds.) **4459** (2001).
- [225] Silence S.M., Scott J.C., Ginsburg E.J., Jenkner P.K., Miller R.D., Twieg R.J., Bjorklund G.C., Moerner W.E., *JOSA B* **10**, 2306 (1993).
- [226] Silence S.M., Scott J.C., Stankus J.J., Moerner W.E., Moylan C.R., Bjorklund G.C., Twieg R.J., *J.Phys.Chem.* **99**, 4096 (1995).
- [227] Burr G. W., Leyva I., *Opt. Lett.* **25**, 499 (2000).
- [228] Buse K., Breer S., Peithmann K., Kapphan S., Gao M., Krätzig E., *Phys. Rev. B* **56**(3), 1225 (1997).

Appendix A

Overview of various storage parameters for selected PR materials.

Material	Dark storage time	Response time [sec] @ 1W/cm ²	M/#, storage capacity
Inorganic PR crystals, room temperature values, $\lambda_0 = 514\text{nm}$, data taken from [B8], table 2, page 120 (except dark storage time of).			
LiNbO ₃	>100a ^a	3	30
LiTaO ₃	10a	0,25 ^b	30
BaTiO ₃	1h - 1a	0,5	1,5
Ba _{0,77} Ca _{0,23} TiO ₃ (BCT)	10s	0,4	2,5
KTa _{0,52} Nb _{0,48} O ₃ (KTN)	0,6a	0,2	1,2
KNbO ₃	1h - 30d	0,1	2,4
Sr _{0,61} Ba _{0,39} Nb ₂ O ₆ (SBN)	1h - 30d	0,1	3,0
Bi ₁₂ TiO ₂₀ (BTO)	10s	2*10 ⁻³ ^c	0,5
GaAs	10 ⁻³ s	2*10 ⁻⁴ ^d	0,12
Organic PR polymers, T _r = -7°C ^e , $\lambda_0 = 633\text{nm}$, data from this work.			
Material C ^f	500s - 1500s ^g	20000 ^h	0,23 ⁱ
Material CT ^j	150s - 650s ^k	~ 100000 ^l	0,30 ^m

- a. thermally fixed (Dr. Theo Woike, University of Cologne, personal communication; see also [228]).
- b. @ 351nm.
- c. @ 3W/cm² and 633nm, Bi₁₂SiO₂₀.
- d. @ 130mW/cm² and 1160nm.
- e. reduced temperature according to eq. (5.2 - 1) on page 228.
- f. for material composition see table 5-1 on page 211.
- g. depending on the PR phase shift, mean response time calculated applying eq. (5.2 - 26) on page 248.
- h. @ 42mW/cm², 633nm, and E₀ = 32V/μm, mean response time calculated applying eq. (5.2 - 26) on page 248.
- i. @ 0,65mW/cm² and E₀ = 62V/μm.
- j. for material composition see table 5-1 on page 211.
- k. depending on the PR phase shift, mean response time calculated applying eq. (5.2 - 26) on page 248.
- l. about 5 times slower than material C under similar experimental conditions.
- m. @ 0,65mW/cm² and E₀ = 62V/μm.

Appendix B

Source code for the numerical simulations in “5.1.) Influence of hologram bending on the diffraction efficiency in PR thin film devices: A simple model calculation”

The simulation program assumes that diffracting a laser beam on a hologram having bent grating planes exhibits the same phenomenology as compared to diffracting a manifold of laser beams having correspondingly different propagation directions but identical phasing at an unbent hologram. In the latter case, the overall diffraction efficiency of the complete manifold of laser beams can be considered as the linear superposition of the single beam diffraction efficiencies, since the diffracted single beam intensities simply add up to a cumulated diffracted intensity. Thus, the diffraction efficiencies for a given number of holograms (defined by the length of the z-vector), which are increasingly slanted with respect to the undisturbed grating due to hologram bending are calculated and eventually averaged by the number of holograms.

The source code given below represents the core of the simulation program, which has been applied in this work using different parameter sets for the applied electrical field and the PR phase shift. The values of these parameters shown below are characteristic examples.

In order to calculate the diffraction efficiency for an undisturbed (i.e. unbent) grating, the parameter “steig” must be set to zero.

This code was written for and used with MATLAB for Windows, version 4.2c, 16bit:

```
% Refractive index
n=1.75;

% Z-axis [ $\mu\text{m}$ ] (i.e. film thickness, here 105 $\mu\text{m}$ ), increment 1 $\mu\text{m}$ 
z=1:105;

% Applied electrical dc-field [ $\text{V}/\mu\text{m}$ ] (here 1 $\text{V}/\mu\text{m}$  - 120 $\text{V}/\mu\text{m}$ ), start:increment:end, E must
% not be zero
E=1:0.01:120;

% Approximation of PR refractive index modulation  $\Delta n(E_0)$  according to eq. (5.1 - 4)
dn=7.4e-7*E.^2;

% Unity vector correlated to z-axis vector, required for matrix operations
a=1:105;
a=a./a;

% Half intersection angle of the recording beams
hisw=3.25/180*pi;

% Slant and tilt angle of the hologram
slant=60.8/180*pi;
tilt=29.2/180*pi;

% Grating wave vector
K=2*pi/(0.633/(2*n*sin(hisw)));
```

```

% Incident angle of recording beam 1
theta=26/180*pi;

% Average propagation constant according to eq. (2.3 - 6)
beta=2*pi*n/0.633;

% Obliquity factor  $c_T$  in eq. (5.1 - 2), according to eq. (2.3 - 13) and eq. (2.3 - 21)
cr=cos(theta);

% PR phase shift
phi=20/180*pi;

% Real part of the complex PR gain coefficient according to eq. (5.1 - 6)
GE=2*pi*sin(phi)*(-1/2.22)*dn/(0.633*cos(hisw));

% Slope of the grating planes relative to the unaffected grating according to eq. (5.1 - 11)
steig=((GE/(2*K*tan(phi)))^a)*((exp(-GE*(z/cos(tilt)))+1).\2*exp(-GE*z/cos(tilt))-1);

% Slant factor  $c_D$  according to eq. (5.1 - 2)
cs=cr-K/beta*cos(slant+atan(steig));

% Parameter  $\nu$  in eq. (5.1 - 1) and according to eq. (2.3 - 38)
nue=((dn*a)*pi*105)/(0.633*(cs*cr)^0.5);

% Dephasing measure according to eq. (5.1 - 3) taking into account hologram bending as
% described in detail in "5.1.1.) The simulation model" on page 214
ktheta=-atan(steig).*sin(slant+atan(steig)-theta)*K;

% Parameter  $\xi$  (loss-free grating) in eq. (5.1 - 1) and according to eq. (2.3 - 39)
xi=105/2*(0-i*ktheta./cs);

% Solving Kogelnik's equation eq. (5.1 - 1) and calculating the diffraction efficiency
% according to eq. (2.3 - 36)
argusin=((nue.^2)-(xi.^2)).^0.5;
nenner=(1-(xi.^2)/(nue.^2)).^0.5;
S=exp(xi).*(sin(argusin)/nenner);
eta=S.*conj(S);
eff=eta*a;
BE=eff/105;

% Writes calculated data to file, fractional format, 8 digit precision (optional)
fwriteid=fopen('absolute path\filename.extension','w');
fprintf(fwriteid,'%1.8f\n',BE);
status=fclose(fwriteid);

% Screen plot of results (optional)
plot(BE);

```

Appendix C

Frequently used abbreviations

Due to the large amount of physical expressions and equations in this work it was not possible to always keep a consistent and stringent naming scheme for all physical variables used throughout the complete text. Thus, this list covers only physical variables and abbreviations, which were used most frequently as well as consistently. Physical variables not listed here are explained in close correlation to their appearance in the text.

2BC	two-beam-coupling
BR	birefringent, birefringence
DFWM	degenerate four-wave-mixing
DMNPAA	“DiMethyl Nitro-Phenole Azo-Anisole”, see also Appendix D
Δn	refractive index modulation (rarely: change)
E_0	projection of the external field onto the hologram grating wave vector
E_q	photorefractive saturation field
E_{ext}	externally applied dc electrical field
ECZ	N-ethylcarbazole, see also Appendix D
ELP	ellipsometric
EO	electro-optic
E_{SC}	photorefractive space-charge field
ϕ	photorefractive phase shift
Γ	photorefractive gain coefficient
η_{int}	internal diffraction efficiency
η_{ext}	external diffraction efficiency
I_{01}	intensity of recording beam 1

I_{02}	intensity of recording beam 2
I_0	total intensity (typically recording intensity)
I_R	reading beam intensity
I_e	erasure (beam) intensity
ITO	Indium-tin-oxide
K	hologram or interference pattern grating wave vector
λ_0	operating wavelength
M/#	M-number
MNPAA	“Methoxy-Methyl Nitro-Phenyle Azo-Anisole”, see also Appendix D
NLO	non-linear optic(al)
PR	photorefractive
PVK	Poly-(N-vinylcarbazole), see also Appendix D
RT	room temperature, ambient temperature
T_g	glass-transition temperature
T_r	reduced temperature
t_{rec}	recording time
TNF	“TriNitro-Fluorenone”, see also Appendix D
TPD	“TriPhenyl-Diamine”, see also Appendix D

Appendix D

Structures

Subsequently, the structures of the chemical compounds referred to by abbreviations in this work will be depicted partitioned in the functionalities:

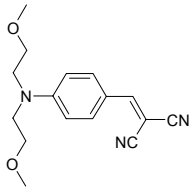
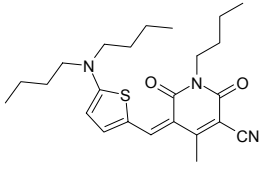
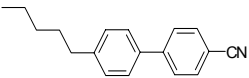
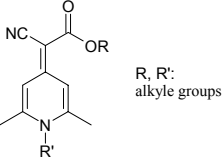
- NLO chromophores
- Sensitizers
- Plasticizers
- Polymers, hole conductors and multifunctional compounds

Within this partitions, the corresponding abbreviations are ordered alphabetically referring only to the characters, i.e. numbers ahead of the names or abbreviations are disregarded.

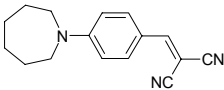
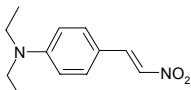
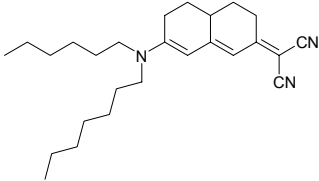
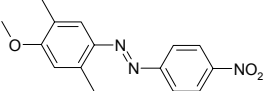
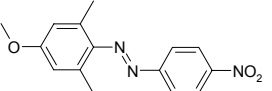
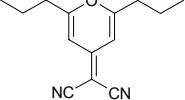
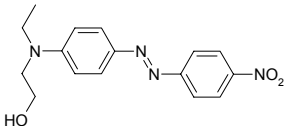
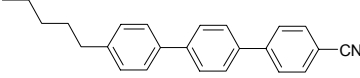
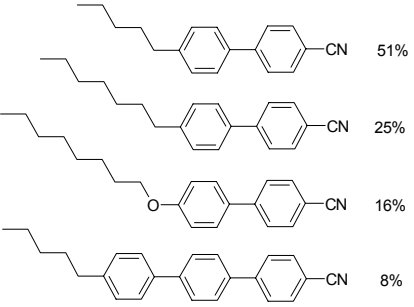
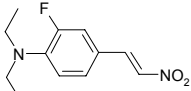
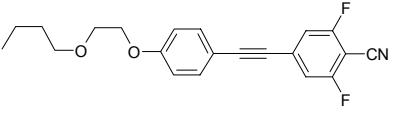
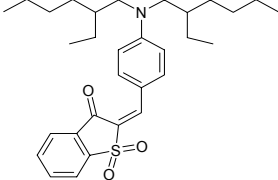
Please note that there are multifunctional compounds, the clear attribution of which to one of the above listed category is not possible although the last category states “multifunctional compounds”. For example 2BNCM forms a PR low molecular glass, but is a NLO chromophore although it may act as a hole conductor without introducing this property explicitly by covalently attaching a hole conducting moiety. In contrast, e.g. DRDCTA, which also forms a PR low molecular glass, consists of a NLO chromophore moiety with a hole conducting moiety (TPA carrying additionally carbazole groups) covalently attached. In the systematics of the tables below, such special cases will be attributed to more obvious category, i.e. 2BNCM will be found in the list of NLO chromophores, whereas DRDCTA will counted as a multifunctional compound.

Please note furthermore that the abbreviation of a compound need not be related to its chemical name, but may as well be related to its trivial name or even may be arbitrary. Abbreviations and trivial names commonly accepted will be marked by a superscript star. Exact chemical names will be marked by a superscript „#“. Eventually, it must be pointed out that „common acceptance“ is not clearly defined, thus, the superscript star reflects the personal opinion of the author.

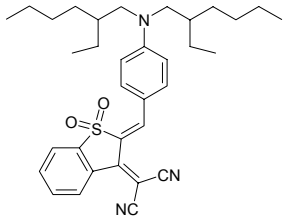
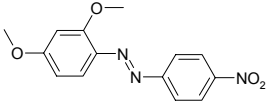
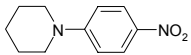
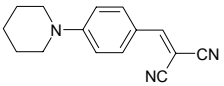
NLO chromophores

	
AODCST	ATOP-1
	 <p style="text-align: right; margin-right: 50px;">R, R': alkyle groups</p>
5CB*	2-BNCM

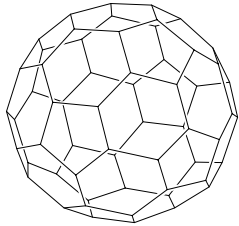
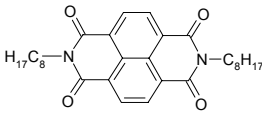
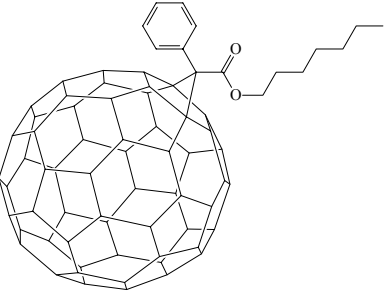
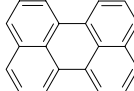
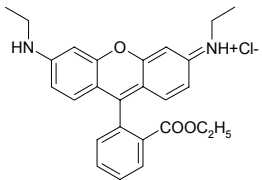
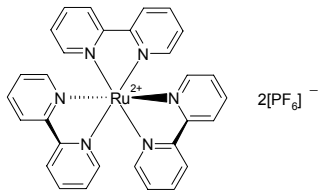
NLO chromophores

	
7-DCST	DEANST*
	
DHADC-MPN	2,5-DMNPAA*
	
3,5-DMNPAA*	DPDCP
	
DR*	E44
	
E7	F-DEANST*
	
FTCN	MG1

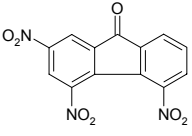
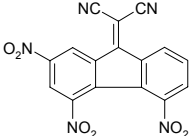
NLO chromophores

	
MG2	MNPAA
	
NPP*	PDCST*

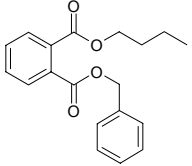
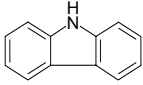
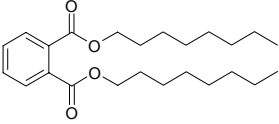
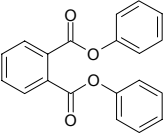
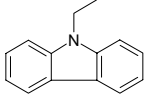
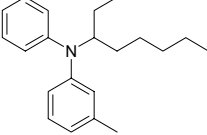
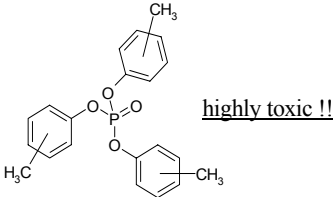
Sensitizers

	
C₆₀[#] (Buckminster Fullerene)	NI
	
[6,6]-PCBM	Perylene
	
Rhodamin6G	[Ru(bpy)₃][PF₆]₂[#]

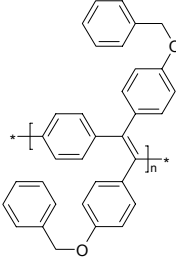
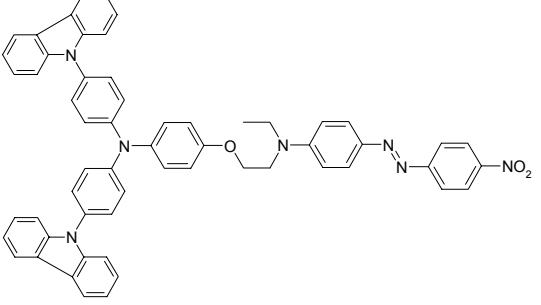
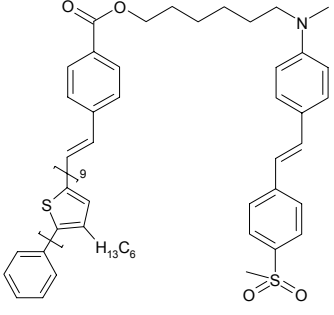
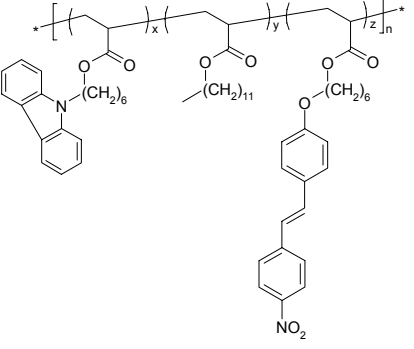
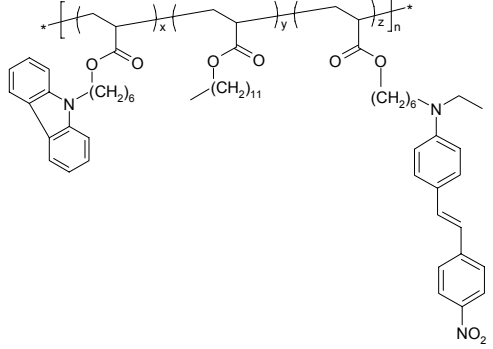
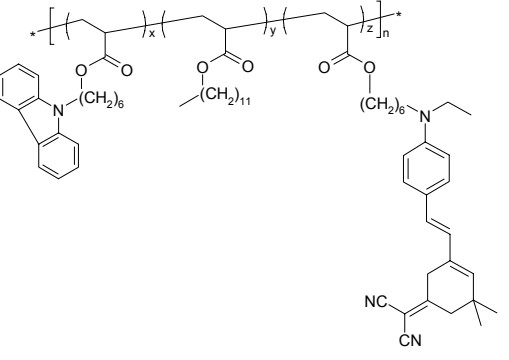
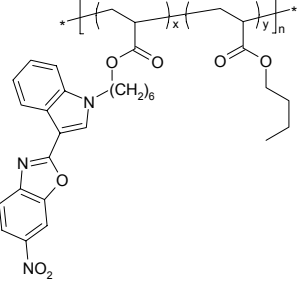
Sensitizers

	
<p>TNF*</p>	<p>TNFM*</p>

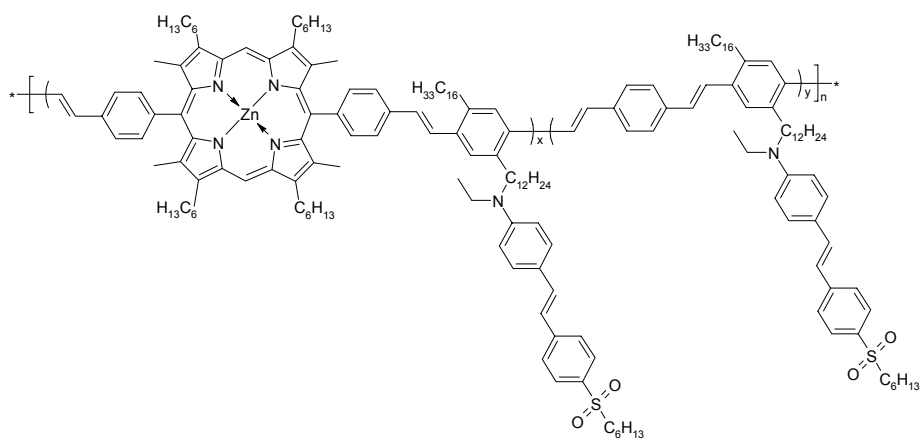
Plasticizers

	
<p>BBP*</p>	<p>Carbazole*</p>
	
<p>DOP*</p>	<p>DPP*</p>
	
<p>ECZ*</p>	<p>EHMPA*</p>
	
<p>TCP*</p>	

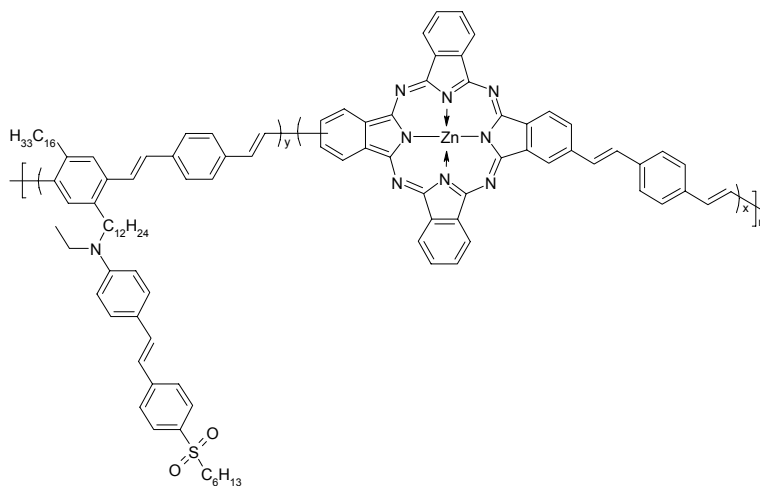
Polymers, hole conductors and multifunctional compounds

	
DPOB-PPV	DRDCTA
	
OT1	P1CHR1a, P1CHR1b
	
P1CHR2	P1CHR3
	
P4	

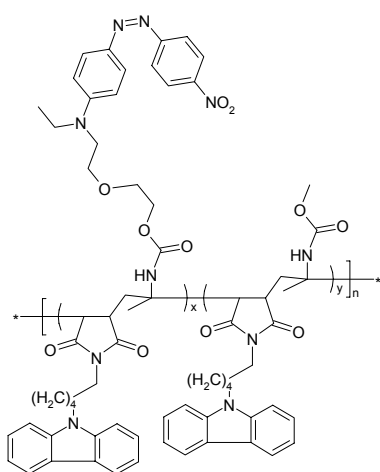
Polymers, hole conductors and multifunctional compounds



P2



P3

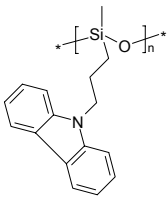
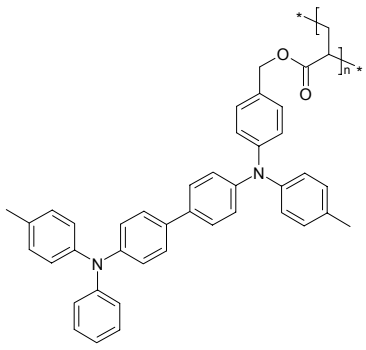
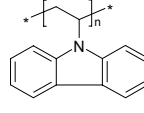
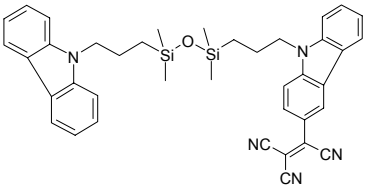
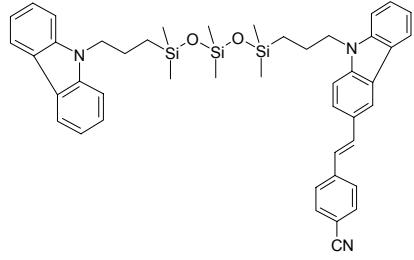
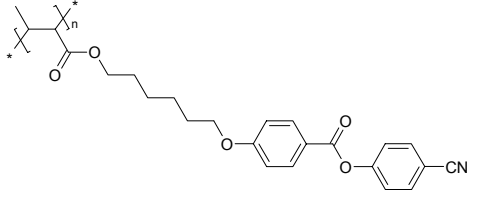
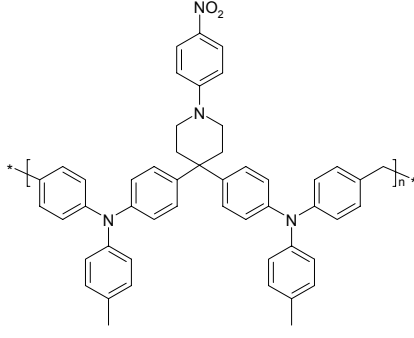
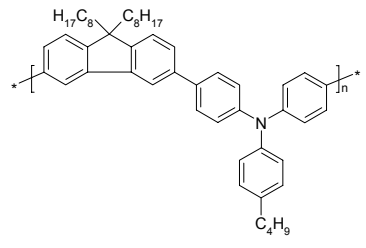


P5

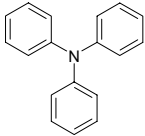
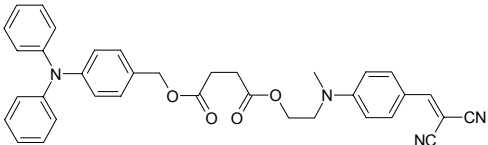
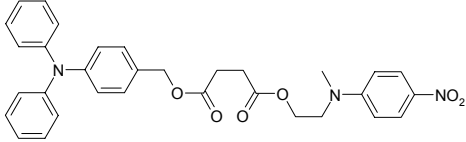
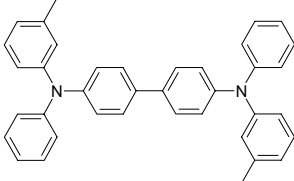
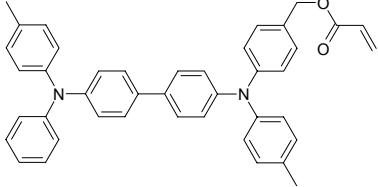
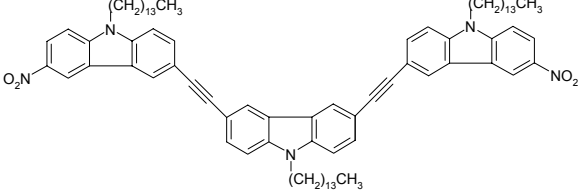


PMMA*

Polymers, hole conductors and multifunctional compounds

	
PSX	PTPD-ac
	
PVK*	Si₂(Cz-Cz/TCNE)
	
Si₃(Cz-Cz/Stilbene)	SLCP
	
TDPANA-FA	TFB

Polymers, hole conductors and multifunctional compounds

	
TPA*	TPA-DCVA
	
TPA-NA	TPD*
	
TPD-ac	TRC1

Appendix E

The Baessler formalism (disorder model)

In the disorder model fluctuations of the molecular energy levels (diagonal disorder) and of the intermolecular distance and mutual orientation (off-diagonal disorder) in amorphous organic solids are considered as determining the charge carrier mobility in disordered organic solids. Polaronic effects are regarded inferior and will be neglected. The formalism has been developed largely by means of Monte Carlo (MC) simulation techniques. Subsequently a few of the most important simulation results will be shown and the resulting expressions for the terms correlating with eq. (2.4 - 133) will briefly be discussed. A discussion of particular results of the MC simulations in context with known experimental results will not be provided. A more comprehensive review is provided in [30].

CONTENT:

E.1.) Basic considerations	E2
E.2.) The disorder model	E2
E.2.1.) Results of the Monte Carlo simulations	E4
E.2.1.1.) Temperature dependence	E4
E.2.1.2.) Field dependence	E5
E.2.1.2.1.) Only diagonal disorder (field dependence)	E6
E.2.1.2.2.) Only off-diagonal disorder (field dependence)	E6
E.2.1.2.3.) Diagonal disorder and off-diagonal disorder (field dependence)	E7
E.2.2.) Conclusions from the monte carlo simulations	E8

E.1.) Basic considerations

A fundamental assumption of the Baessler formalism is that the transport manifold of a disordered organic system abandoning long range order is smeared out into a Gaussian distribution of localized states. The Gaussian shape of the distribution is concluded by analogy from the experimental observation of inhomogeneous broadening of the absorption profiles in disordered organic solids at low temperature. The origin of the distribution is attributed to fluctuations of the entire variety of intermolecular potentials existing in an organic system containing ions, i.e. the interaction of ions, dipoles and induced dipoles with themselves and each other, whereby ion - ion and ion - dipole interactions contribute most. The distribution of localized energetic states is referred to as *diagonal disorder*, since the eigen-energies of the sites thus modified would occur as diagonal elements in the energy matrix. The density of states (DOS) function for the charge transporting sites is neither accessible directly in appropriate experiments (absorption spectroscopy), since excitonic transitions control the optical spectra in these systems, nor theoretically by quantum chemical calculations, since the required resolution of less than 100 meV can not be provided. However, it can be shown by MC simulation, that the width of the DOS for charge carriers originating from a given pattern of positional disorder (referred to as *off-diagonal disorder* and to be discussed below in “E.2.) The disorder model”) may be estimated to be about 1.5 times larger than that for singlet excitation, which is experimentally accessible using absorption spectroscopy. The simulation is based on the principle analogy of the interaction between a charge carrier on the one hand and an exciton on the other hand with the surrounding matrix. Hence, the width σ of the Gaussian DOS for charge carriers may be estimated from the width for a typical absorption band for the systems considered here of typically about 500cm^{-1} (60meV) yielding roughly $\sigma \approx 100\text{meV}$.

Another fundamental assumption is, that charge carrier transfer only occurs between adjacent transporting moieties, henceforth referred to as transport sites. The activation energy for the charge transfer will be the sum of an intermolecular and an intramolecular contribution as discussed before for the polaron model. For $\sigma \approx 100\text{meV}$, the activation energy may be estimated to about 400meV as will be shown later. However, the polaronic binding energy will be much smaller (about one order of magnitude) [39], which is a strong argument for the neglect of polaronic effects as presumed here.

E.2.) The disorder model

The energy of the charge transporting states of the transport sites is assumed to be subject to a Gaussian distribution of energies, which may be expressed as:

$$\rho(\varepsilon) = \frac{1}{\sqrt{2\pi\sigma^2}} e^{-\frac{\varepsilon^2}{2\sigma^2}}, \quad \text{eq. (E - 1)}$$

implying localized states. Here, ε is the energy of some transport site, and σ is the width of the DOS. Equation eq. (E - 1) tacitly assumes, that there is no correlation of the eigen-energies of adjacent transport sites, which may not strictly be true but is a reasonable approximation, since the actual correlation length will not exceed a few sites, and a charge carrier travelling through a real world sample will visit thousands of sites.

The jump rate among two adjacent sites i and j is assumed to be described by an expression proposed by Miller and Abrahams in [40]:

$$v_{ij} = v_0 e^{-2\gamma\bar{\delta}\frac{\Delta R_{ij}}{\bar{\delta}}} \begin{cases} e^{-\frac{\varepsilon_j - \varepsilon_i}{k_B T}} & \forall(\varepsilon_j > \varepsilon_i) \\ 1 & \forall(\varepsilon_j < \varepsilon_i) \end{cases}, \quad \text{eq. (E - 2)}$$

where $\bar{\delta}$ is the average inter-site distance, γ stands for the inverse of the wave function's decay radius, $\Delta R_{ij} = |R_i - R_j|$ is the actual distance between the sites i and j , and ε_i and ε_j are the corresponding site energies, which in the case of an applied field contain the electrostatic potential, i.e.:

$$\varepsilon_j = \varepsilon_i + qE_{ij}\Delta R_{ij}, \quad \text{eq. (E - 3)}$$

where E_{ij} is the external field along ΔR_{ij} . The parameter v_0 is a frequency factor of the order of magnitude of a typical phonon frequency ($v_0 \approx 10^{13}$ Hz). Equation eq. (E - 2) implies weak charge carrier - phonon coupling which allows to ignore polaronic effects but still ensures sufficient coupling to the heat bath (otherwise, the charge carrier could not be activated thermally). Hence, the difference of the site energies (including the electrostatic potential according to eq. (E - 3)) is the only activation energy accounted for and is assumed to be Boltzmannian for uphill jumps in energy. Hops down in energy are assumed not to require some energy matching, since there is always a rich phonon spectrum and the hopping rates are small in the systems considered, which ensures dissipation of the electronic energy differences.

Equation eq. (E - 2) presumes a spherical molecular electronic wave function, which leads to a symmetrical coupling between transport sites. Disordered organic system showing electrical conductivity, however, usually contain aromatic compounds, which are not spherical (with the exception of systems, the conductivity of which bases on fullerene derivatives). Model calculations in [40] showed, that the transfer integrals for charge carrier exchange between two adjacent transport sites may vary by several orders of magnitude as a function of the mutual orientation of the transport sites. Accordingly, the overlap parameter $\Gamma = 2\gamma\bar{\delta}$ in eq. (E - 2) will be subject to a distribution. Furthermore but less important (except for fullerene systems), the inter-site distance will not be constant but subjected to a distribution as well. The subsumption of these distributions is referred to as positional disorder or off-diagonal disorder. The Baessler model operationally accounts for off-diagonal disorder by splitting the inter-site coupling (i.e. overlap) parameter Γ_{ij} into two specific contributions Γ_i and Γ_j fluctuating randomly and independently from each other. Since the actual distribution functions for Γ_i and Γ_j are unknown, a Gaussian probability density with variance σ_Γ is assumed for both of them with:

$$g(\Gamma_{i,j}) = \frac{1}{\Sigma\sqrt{\pi}} e^{-\frac{\Gamma_{i,j} - \gamma\bar{\delta}}{\Sigma^2}}, \quad \text{eq. (E - 4)}$$

where:

$$\Sigma = \sigma_\Gamma\sqrt{2} \quad \text{eq. (E - 5)}$$

is the variance of the convolution of Γ_i and Γ_j , i.e. the variance of the inter-site coupling parameter. However, the parameter Σ cannot be translated directly into a microscopic structural picture like the parameters characterizing diagonal disorder, but should rather be understood as some operationally defined measure for the relative variations of electronic inter-site coupling due to off-diagonal disorder. Please note, that even Baessler grants, that this procedure may be arguable and represents a zero-order approximation. An attempt to describe the off-diagonal disorder more realistically is presented and discussed in [41] but will not be regarded here.

Closed form analytical solutions of the hopping transport problem cannot be obtained due to the Gaussian shape of the DOS and the asymmetry of the jump rates (i.e. $v_{ij} \neq v_{ji}$). The only analytical approach available to date and retaining both the energetic distribution of hopping

sites as well as the distribution of hopping sites themselves is the effective medium approach presented in [42]. The effective medium approach was shown to provide an excellent description of the hopping process in dense systems and for finite temperatures. However, the theory does not provide analytic expressions, which may be used for interpreting experimental data. Another approach is the ultrametric space concept [43, 44], which is mathematically simpler but reduces the problem to iso-energetic sites separated by randomly distributed barriers and is, thus, inferior to the effective medium approach. Baessler et. al. approached the problem applying Monte-Carlo (MC) computer simulation, which may be seen as an idealized experiment carried out on samples of arbitrarily adjustable degree of disorder. The details of the MC simulation technique will not be elaborated upon here. Subsequently, the expressions obtained for the different contributions to the overall charge carrier mobility in the context of eq. (2.4 - 133) will be shown and discussed in short terms ending up with the currently most common equation to describe charge carrier transport through a disordered organic medium.

E.2.1.) Results of the Monte Carlo simulations

The first exponential term in eq. (2.4 - 133) is not subject of the model to be solved for by Monte-Carlo simulation technique and, therefore, will be skipped here and picked up again later in this section. In the framework of the Baessler formalism, the first exponential term is merged into an experimental quantity μ_0 , which is considered as a material constant. Subsequently, the temperature dependence of the charge carrier mobility will be considered first and then the dependence on an external electrical field.

E.2.1.1.) Temperature dependence

If some charge carrier starts within a DOS of Gaussian shape of an undiluted system of hopping sites, it will relax preferably into states of lower energy, since the hopping rate uphill in energy is smaller than the hopping rate downhill (compare eq. (E - 2)). This process will be maintained until thermally activated jumps uphill in energy will occur at similar rates as the downhill jumps. As a specific feature of the Gaussian DOS, the mean energy $\langle \varepsilon \rangle$ of the charge carrier will thus saturate at long times, which indicates the attainment of a dynamic equilibrium. Please note, that Fermi-statistics is irrelevant, as long as the charge carrier density is small enough to exclude some carrier - carrier interaction. The equilibrium mean energy for the relaxation time approaching infinity $\langle \varepsilon_\infty \rangle$ can be calculated analytically (compare eq. (2.4 - 35)) from [45]:

$$\langle \varepsilon_\infty \rangle = \lim_{t \rightarrow \infty} \langle \varepsilon(t) \rangle = \frac{\int_{-\infty}^{\infty} \varepsilon \rho(\varepsilon) e^{-\frac{\varepsilon}{k_B T}} d\varepsilon}{\int_{-\infty}^{\infty} \rho(\varepsilon) e^{-\frac{\varepsilon}{k_B T}} d\varepsilon} = -\frac{\sigma^2}{k_B T}, \quad \text{eq. (E - 6)}$$

where the energies are taken as difference to the center of the DOS of the transport sites. For further proceeding, the result of eq. (E - 6) is expressed as

$$\langle \varepsilon_\infty \rangle = -\sigma \hat{\sigma} \quad \text{eq. (E - 7)}$$

with:

$$\hat{\sigma} = \frac{\sigma}{k_B T} \quad \text{eq. (E - 8)}$$

as normalized width of the DOS. Please note, that the distribution of energies for a package of charge carriers travelling through a disordered organic medium will become Gaussian in the long time limit with the center of the distribution at $\langle \varepsilon_\infty \rangle$, however slightly asymmetric due to different relaxation patterns of mobile and immobilized charge carriers (e.g. trapped at polymer chain ends).

In order to conclude from the energetic relaxation behavior to the temperature dependence of the charge carrier mobility, $\sigma = 100\text{meV}$ at $T = 295\text{K}$ is assumed, which is a very typical case accounting for many experimental systems as already mentioned before. Thus, $\langle \varepsilon_\infty \rangle \approx -4\sigma$. Considering the small fractional DOS of the transport sites for $\varepsilon \leq \langle \varepsilon_\infty \rangle$, i.e., $\int_{-\infty}^{-4\sigma} \rho(\varepsilon) d\varepsilon \approx 3 \times 10^{-5}$, it is proximate to assume, that a charge carrier located at $\varepsilon = \langle \varepsilon_\infty \rangle$ will most probably not jump downwards in energy by its next jump, but uphill after thermal excitation. For the case discussed here, this is simply a question of the number states available for uphill jumps, which is assumed to be considerably larger than the number of states available for further energetic relaxation. Assuming furthermore that by far most of the charge carriers are located at $\varepsilon = \langle \varepsilon_\infty \rangle$ and that the most probable transport level is the center of the DOS of the transport sites at $\varepsilon = 0$, the transport activation energy would be about $\sigma \hat{\sigma}$. Thus, the temperature dependence of the charge carrier mobility will not be of Arrhenius-type according to eq. (2.4 - 135), but rather take the shape of eq. (2.4 - 136). Accounting for the statistics of both the occupational energies of the charge carriers in the DOS of the transport sites as well as the activation barrier heights, MC simulations reveal the charge carrier mobility as a function of the temperature to be expressed by:

$$\mu(T) \propto e^{-\left(\frac{4\hat{\sigma}\sigma}{9k_B T}\right)} = e^{-\left(\frac{2\hat{\sigma}}{3}\right)^2} \quad \text{eq. (E - 9)}$$

The proportionality factor is the experimental quantity μ_0 , which has been mentioned above. Please note, that some off-diagonal disorder as implied by eq. (2.4 - 136) (dependence on $\bar{\delta}$) does not occur in eq. (E - 9).

From eq. (E - 9), an apparent activation energy ΔE_{A0} may be obtained from:

$$\Delta E_{A0} = -k \frac{\partial}{\partial \frac{1}{T}} \ln \mu = \frac{8}{9} \sigma \hat{\sigma}, \quad \text{eq. (E - 10)}$$

which yields about 400meV for $\sigma \approx 100\text{meV}$ at about 300K as mentioned before.

E.2.1.2.) Field dependence

The hopping mobility must depend on an applied electrical field E , since the electrostatic potential will distort the DOS thus reducing the average barrier height for jumps upwards in energy, counted in field direction. Accordingly, the equilibrium energy $\langle \varepsilon_\infty \rangle$ must increase with E . Within the current model and according to eq. (E - 3), this is attributed to a general relative preference of energetic uphill jumps with respect to the equilibrium without field, affecting the ratio of the jump rates according to eq. (E - 2).

The results of the MC simulations of the impact of an electrical field on the considered model reveal complicated behavior, which will not be elaborated upon here in detail. However, it seems advisable to show some basic simulation results in order to clarify the tendencies observed. The basic relations obtained will first be considered for the limiting cases of no off-diagonal disorder and no diagonal disorder and finally allowing for both will be regarded.

E.2.1.2.1.) Only diagonal disorder (field dependence)

MC simulation of the field dependence of μ plotted as $\ln\mu$ versus $E^{1/2}$ as depicted in Figure (E - 1) reveals saturation at low fields (i.e. μ does not depend on the field). For higher fields, behavior in Poole-Frenkel fashion is obtained, which may be expressed as:

$$\ln\mu \propto S\sqrt{E}, \quad \text{eq. (E - 11)}$$

where S is some slope factor, which will be addressed later in more detail. For very high fields the slope S decreases for any width of the DOS and becomes even negative for small diagonal disorder. This may be explained by a saturation of the drift velocity occurring at high fields, when all jumps except in the direction of the applied field are suppressed. Then the Boltzmann term in eq. (E - 2) approaches unity, v_{ij} becomes independent of the applied field and the drift velocity v_D thus constant. In this case, which is also represented by the case of zero diagonal disorder even for low fields, the mobility will obey the relation:

$$\mu = \frac{v_D}{E} \Rightarrow \mu \propto \frac{1}{E} \quad \text{eq. (E - 12)}$$

and thus decrease with the applied field increasing. Please note, that the curves in Figure (E - 1) for $\hat{\sigma} > 0$ reproduce the general shape of the curves for $\langle \varepsilon_\infty \rangle$ as a function of the field. Thus, the increase of $\langle \varepsilon_\infty \rangle$ as a function of E may be interpreted as the phenomenological reason for the increase of $\ln\mu$ with increasing E .

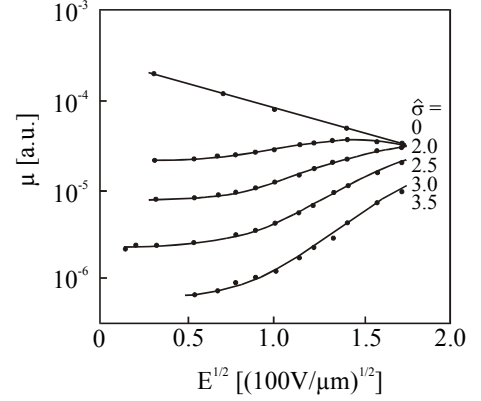


Figure (E - 1): Results of MC simulation of μ for zero off-diagonal disorder. Redrawn after [33].

E.2.1.2.2.) Only off-diagonal disorder (field dependence)

The MC simulation results for $\ln\mu$ as a function of \sqrt{E} are depicted in Figure (E - 2). It turns out, that the introduction of positional disorder results in increased mobility. This may phenomenologically be explained by the occurrence of alternative pathways for charge transport, if the direct path along the direction of the applied field is afflicted with unfavorable inter-site coupling. Although all alternative pathways will be effectively longer than the direct path, more favorable inter-site coupling along the alternative path may overcompensate the loss of the direct path. If the applied field is increased, it will increasingly force the charge carrier to travel along the less favorable and more direct path, leading to a decrease of the mobility, which is then consequently even more pronounced than for zero off-diagonal disorder, which corresponds to the situation for $\sigma = 0$ in Figure (E - 1) and is described by eq. (E - 12). Please note, that off-diagonal disorder does not affect $\langle \varepsilon_\infty \rangle$.

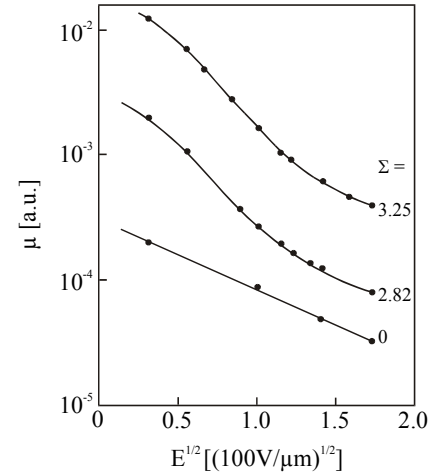


Figure (E - 2): Results of MC simulation of μ for zero diagonal disorder. Redrawn after [33].

E.2.1.2.3.) Diagonal disorder and off-diagonal disorder (field dependence)

Superposition of both types of disorder leads to a complex behavior, which may include some local minimum as depicted in Figure (E - 3). For small applied fields, the off-diagonal disorder appears to be the dominant contribution, whereas diagonal disorder dominates the high field regime. There is a balance between the reduction of the barrier heights for increasing field and the field induced disturbance of the optimal pathway for transport resulting in a drastic reduction of the overall field dependence of the mobility for a certain combination of disorder parameters and eventually even a reversal of the general trend.

In order to quantify the general behavior, the slope S in eq. (E - 11) must be quantified in terms of the disorder parameters $\hat{\sigma}$ and Σ , which is depicted in Figure (E - 4). Please note, that only the regime for E was taken into account, which obeys eq. (E - 11). Apparently, S is proportional to the square of $\hat{\sigma}$ except for $\Sigma = 0$ and additionally $\hat{\sigma} \leq 2$ with the proportionality factor being $C = 2.9 \times 10^{-7} (\mu\text{m}/\text{V})^{1/2}$. Accordingly, $S(\sigma, \Sigma)$ may be expressed as:

$$S(\hat{\sigma}, \Sigma) = C[\hat{\sigma}^2 - B(\Sigma)] \quad \text{eq. (E - 13)}$$

In order to obtain $B(\Sigma)$, the turning points in the plots according to Figure (E - 3) (i.e. where S vanishes) are considered. For these points, the relation:

$$\hat{\sigma}^* = \sqrt{B(\Sigma)} \quad \text{eq. (E - 14)}$$

must be fulfilled. Plotting $\hat{\sigma}^*$ in these points as a function of Σ yields the diagram shown in Figure (E - 5). Obviously there is a linear dependence according to: $\sqrt{B(\Sigma)} = \Sigma$ for $\Sigma > 2$ and for $\Sigma < 2$, the curve flattens saturating at $\hat{\sigma}^* = 1.5$ for $\Sigma = 0$. Approximating the curve by straight lines as illustrated in Figure (E - 5), $B(\Sigma)$ may be expressed as:

$$B(\Sigma) = \Sigma^2 \quad \forall (\Sigma \geq 1.5) \quad \text{eq. (E - 15)}$$

$$B(\Sigma) = 1.5^2 \quad \forall (\Sigma < 1.5)$$

Combining eq. (E - 11) with eq. (E - 13) and eq. (E - 15) eventually results in the field dependence of the charge carrier mobility, which correlates with the third exponential term in eq. (2.4 - 133).

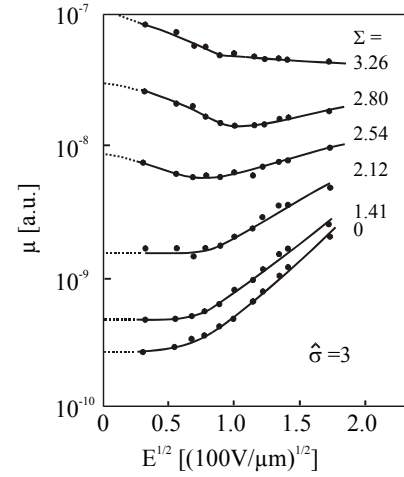


Figure (E - 3): Results of MC simulation of μ accounting for diagonal and off-diagonal disorder (example for $\hat{\sigma} = 3$). Redrawn after [33].

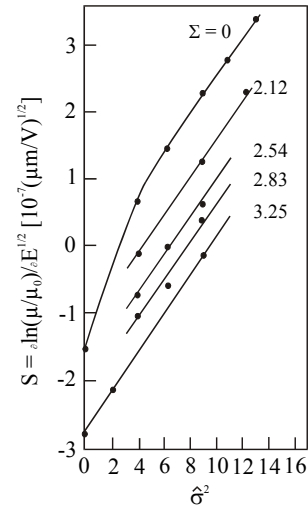


Figure (E - 4): Results of MC simulation of S in terms of Σ and $\hat{\sigma}$. Redrawn after [33].

E.2.2.) Conclusions from the monte carlo simulations

Merging both the temperature dependent and the field dependent contribution as obtained above, the charge carrier mobility in disordered organic solids is described according to the Baessler formalism by:

$$\mu = \mu_0 e^{-\left(\frac{2\hat{\sigma}}{3}\right)^2} e^{C[\hat{\sigma}^2 - \Sigma^2]\sqrt{E}} \quad \forall(\Sigma \geq 1.5) \quad \text{eq. (E - 16)}$$

$$\mu = \mu_0 e^{-\left(\frac{2\hat{\sigma}}{3}\right)^2} e^{C[\hat{\sigma}^2 - 2.25]\sqrt{E}} \quad \forall(\Sigma < 1.5)$$

with:

$$\hat{\sigma} = \frac{\sigma}{k_B T}, \quad \text{eq. (E - 17)}$$

where σ is the (1/e -) width of the DOS of transporting sites, Σ is the positional disorder parameter, $C = 2.9 \times 10^{-7} (\mu\text{m/V})^{1/2}$, and μ_0 is an experimental constant.

The disorder model is able to describe the particular features of charge transport in disordered organic solids consistently and at least qualitatively over a wide range of possible variations of experimental parameters. Unfortunately, also the disorder formalism utilizes parameters, which are not or at least not directly accessible by the experiment. The problem in determining the width of the DOS of transport sites has already been discussed above. The off-diagonal disorder parameter is even more problematic, since up to date there is no really independent method to obtain this parameter. Thus, Σ must be gained by fitting experimental data on conductivity and charge carrier mobility measurements to the equations eq. (E - 16).

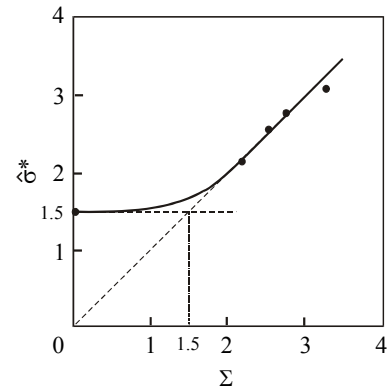


Figure (E - 5): Plot of $\hat{\sigma}^*$ vs. Σ to obtain the form of $B(\Sigma)$. Redrawn after [33].

Appendix F

Dispersive charge transport in disordered organic solids

As described in “2.4.3.3.) Dispersive charge transport” on page 108, conducting polymers are subjected to dispersive charge transport, i.e. a charge carrier packet diverges considerably more than predicted from normal diffusion during its field-driven motion through a disordered organic solid. Subsequently, two formalisms to describe this phenomenon are presented, the Scher-Montroll formalism and the Baessler formalism.

The Scher-Montroll formalism has been widely used for describing dispersive transport phenomena in polymers. However, although the model has been applied successfully to explain TOF experiments, it must not be taken as a general theory for charge transport in dispersive media.

In contrast, the Baessler formalism, which is based on the Baessler model for charge transport in disordered organic solids, may be taken as an approach to some general theory, however, does not provide any analytical expression, which may be applied to experimental results.

CONTENT:

F.1.) The Scher-Montroll formalism	F2
F.2.) The Baessler formalism for dispersive charge transport	F3
F.2.1.) Deviation from Einstein behavior	F4
F.2.2.) Dispersion	F5
F.2.3.) The non-dispersive / dispersive transition	F6
F.2.4.) Phenomenological interpretation	F7

F.1.) The Scher-Montroll formalism

The Scher-Montroll model is based on the traditional perception, that the total displacement of a charge carrier in a bias field is a succession of independent displacements, in which the dwell time a carrier spends on one hopping site as well as the length of the individual displacements are subject to some narrow distribution. Since the time spent for the hopping itself may be considered negligible, the dwell time of a carrier on one hopping site defines the actual „hopping time“, i.e., the time interval between the initiation of successive displacements. According to this traditional model implying only small dispersion of the hopping times, a narrow charge carrier packet will remain (relatively) narrow while traversing through the sample, but the spatial distribution of the packet will become Gaussian with increasing time, and the spreading according to eq. (F - 1) will become negligible as compared to the distance traversed. Furthermore, the time frame of the experiment will be very large as compared to some characteristic time for an individual hop (e.g. the mean hopping time \bar{t}). Thus, the propagation velocity of the packet will become constant and a well defined transit time will be obtained. Please note, that this traditional model only accounts for some small off-diagonal disorder due to a distribution of hopping lengths, but disregards diagonal disorder and the major contribution to off-diagonal disorder according to the Baessler formalism, which is the orientational disorder as discussed in “E.2.1.) Results of the Monte Carlo simulations” on page 4.

Scher and Montroll [51] altered the traditional model by allowing for hopping times similar or even longer than the time frame of the experiment. As opposed to the traditional model assuming a distribution of hopping times $\psi(t)$ expressed by some exponential of the form $\psi(t) \propto \exp(-\lambda t)$, where λ is a constant, they introduced a long tail in the distribution function according to:

$$\psi(t) \propto A t^{-(1+\alpha)}, \quad \text{eq. (F - 1)}$$

where A is a constant and α is a disorder parameter with $0 < \alpha < 1$. The more disordered the material is, the smaller will be the value of α and the more dispersive the transport. Please note, that eq. (F - 1) is only operative for the restricted time frame of the experiment, otherwise $\bar{t} \rightarrow \infty$ is implied for $t_0 < t < \infty$, where t_0 is some arbitrarily chosen time larger than the time frame of the experiment.

A key prediction of the model is a decay of photocurrent transients in TOF experiments according to:

$$\begin{aligned} I(t) &\propto t^{-(1-\alpha)} & \forall (t < t_T) \\ I(t) &\propto t^{-(1+\alpha)} & \forall (t > t_T) \end{aligned}, \quad \text{eq. (F - 2)}$$

where I is the current and t_T is the transit time. The intersection point of these two branches defines a transit time according to:

$$t_T \propto \frac{C}{W_0} \alpha \sqrt{\frac{L}{l(E)}} e^{\frac{\Delta E_{A0}}{k_B T}}, \quad \text{eq. (F - 3)}$$

where C is a constant of the order of unity, W_0 is a scaling parameter, ΔE_{A0} is the zero field activation energy, L is the sample thickness and $l(E)$ is the mean displacement per hop (in field direction). Furthermore, according to [52], eq. (2.4 - 152) will have to be replaced by:

$$\frac{\sqrt{\langle \Delta x^2 \rangle}}{\langle x \rangle} \approx \frac{1}{\sqrt{t}^\alpha}, \quad \text{eq. (F - 4)}$$

which indicates, that the packet spreads faster than described by eq. (2.4 - 152).

At low fields, according to [53] it may be assumed, that:

$$l(E) \propto E. \quad \text{eq. (F - 5)}$$

which implies a variation of the transit time with field and thickness. The theory moreover predicts, that photocurrent transients for a range of fields and thicknesses may be superimposed when normalized to the transit time. This behavior is referred to as ‘‘universality’’ and has been proven experimentally several times (e.g. recently in [54]).

On the basis of eq. (2.4 - 145) (polaron model) the phenomenological relationship:

$$\mu \propto \frac{W_0 L^{(1-\frac{1}{\alpha})}}{E L^{\frac{1}{\alpha}}} \sinh\left(\frac{qE\bar{\delta}}{2k_B T}\right)^{\frac{1}{\alpha}} e^{-\frac{\Delta E_{A0}}{k_B T}} \quad \text{eq. (F - 6)}$$

has been proposed by Pfister et. al. [55], which reduces to:

$$\mu \propto \frac{1}{E} e^{\frac{qE\bar{\delta}}{2\alpha k_B T}} e^{-\frac{\Delta E_{A0}}{k_B T}} \quad \text{eq. (F - 7)}$$

at high fields applied, where the hopping probability in field direction approaches unity. The parameters have been defined in context with the polaron model and will not be listed here once more.

F.2.) The Baessler formalism for dispersive charge transport

Baessler et al. could show by MC simulations, that the features of dispersive charge transport can be explained by means of a Gaussian hopping site manifold, even in the absence of trapping. However, the Baessler formalism does not provide any analytical description but rather an idea of the impact of material and sample parameters on the dispersivity of charge transport in disordered organic solids.

Baessler et. al. conduct their discussion on the basis of two key parameters, the dispersion w , a parameter defined by the extent of the tail of the displacement current in TOF experiments and a function $f(E, \hat{\sigma})$, giving a measure of the deviation of the real system from ideal Einstein behavior, a problem already discussed above.

According to [52] and [50], the current profile $I(t)$ in a TOF experiment may be described by:

$$I(t) \propto \int_{-\infty}^L \frac{1}{\sqrt{4\pi Dt}} e^{-\frac{(x-\mu Et)^2}{4Dt}} dx = 1 - \frac{1}{2} \operatorname{erfc}\left(\frac{L - \mu Et}{\sqrt{4Dt}}\right), \quad \text{eq. (F - 8)}$$

where ‘‘erfc’’ is the inverse error function. Defining the transit time t_0 as the intersection point of the asymptotes of the plateau and the trailing edge of the current transient and a time $t_{1/2}$, which is required for the current to decay to half of its value at t_0 , these times can be expressed based on eq. (F - 8) as:

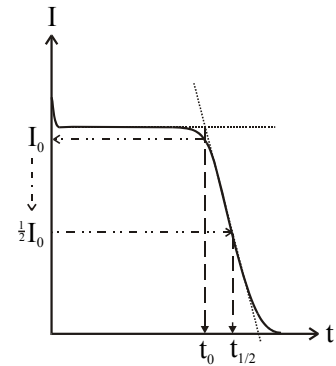


Figure (F - 1): Illustration of the times t_0 and $t_{1/2}$ defining the dispersion w

$$t_0 = \frac{L - \sqrt{\frac{\pi D L}{\mu E}}}{\mu E} \text{ and:} \quad \text{eq. (F - 9)}$$

$$t_{1/2} = \frac{L}{\mu E}. \quad \text{eq. (F - 10)}$$

The times are illustrated in Figure (F - 1). With these times, the dispersion w can be defined as:

$$w = \frac{t_{1/2} - t_0}{t_{1/2}} = \sqrt{\frac{\pi D}{\mu E L}}. \quad \text{eq. (F - 11)}$$

The function $f(E, \hat{\sigma})$ is obtained directly from the Einstein relation by assuming an apparent diffusion constant D_a in disordered systems according to the Einstein-Smoluchowski relation between hop distance and hop time:

$$D_a = \frac{\langle (x - \langle x \rangle)^2 \rangle}{2t} = D_0 + D_f(E, \hat{\sigma}), \quad \text{eq. (F - 12)}$$

where D_0 is the ordinary thermal term and $D_f(E, \hat{\sigma})$ is a contribution depending on the field and the disorder. Since the ratio $qD_0/\mu k_B T$ equals unity according to eq. (2.4 - 141), the deviation from Einstein behavior may be expressed in terms of $f(E, \hat{\sigma})$ as:

$$f(E, \hat{\sigma}) - 1 = \frac{qD_f(E, \hat{\sigma})}{\mu k_B T}. \quad \text{eq. (F - 13)}$$

Subsequently, some major trends for $f(E, \hat{\sigma}) - 1$ and w as revealed by MC simulation will be discussed.

F.2.1.) Deviation from Einstein behavior

For typically applied fields of about 10 - 100 V/ μm , $f(E, \hat{\sigma}) - 1$ increases quadratically in the applied field as long as the diagonal disorder is not large. For $\hat{\sigma}$ considerably exceeding $\hat{\sigma} = 3$, the field dependence approaches linear proportionality. For even higher fields, the parameter levels off and finally decreases again, which may be attributed to the strong tilt of the DOS by the applied field beginning to reduce the dimensionality of the system. For fields lower than 10 V/ μm , the behavior approaches Einstein behavior. Parametric in $\hat{\sigma}$, the deviation from Einstein behavior increases with increasing diagonal disorder, $f(E, \hat{\sigma}) - 1$ finally reaching values of more than 10^3 for $\hat{\sigma}$ approaching $\hat{\sigma} = 4$ (discussed before to be a typical value for polymers) and an applied field of about 100V/ μm as already mentioned before. This proves that the Einstein relation is invalid for a wide range of parameter combinations. Especially photorefractive polymers of the type investigated in the frame of this work must be attributed to this range. It must be pointed out in advance, however, that this is subject to the experimental conditions applied in holographic experiments on photorefractive polymers.

It should be noted, that the linear field dependence of $f(E, \hat{\sigma}) - 1$ (i.e. $D_f \propto E$) for typical photorefractive polymer systems exhibiting $\hat{\sigma} > 3$ will result in ‘‘universality’’ according to the Scher-Montroll model even for apparently non-dispersive transport as can be seen from eq. (F - 11). Thus universality is not necessarily a criterion for dispersive transport as implied by the

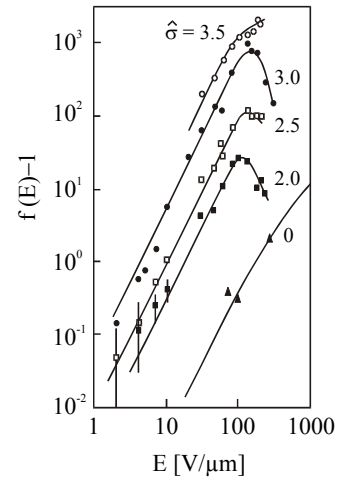


Figure (F - 2): $f(E) - 1$ vs. E parametric in $\hat{\sigma}$. Redrawn after [50].

Scher-Montroll model, but rather an indication for quasi-equilibrium stochastic hopping within a sufficiently wide Gaussian DOS under the action of a drain field.

Please note, that “non-dispersive“ in this context has to be understood in the sense, that the TOF signals show a well-developed plateau region and a thickness independent charge carrier mobility. The correlation of dispersity with a thickness dependence is implied by eq. (F - 5).

F.2.2.) Dispersion

The MC simulation of w as a function of the applied field for some combinations of diagonal and off-diagonal disorder is shown in Figure (F - 3). As can be seen, $w \propto \sqrt{E}$ for a small amount of disorder and for larger degree of disorder, w appears to approach $w \approx \text{const.}$ in the applied field. Constant w implies the observation of universality. For very high fields, the effective diagonal disorder is reduced when $qE\bar{\delta}$ becomes comparable to σ , i.e. when the gain in energy per hop is comparable to the width of the DOS, since then all sites are available disregarding their energy. This results in a decreasing dispersion. The sample length is assumed $4.5\mu\text{m}$ for the MC simulation yielding results according to Figure (F - 3).

Please note, that apparently both the kinds of disorder result in a similar effect as far as the field dependence is concerned.

Considering the dependence of w on the thickness of the sample L , it is found, that w does not depend on L for small values of L , but turns out to depend on L according to:

$$w \propto \frac{1}{\sqrt{L}} \quad \text{eq. (F - 14)}$$

above some critical length, which depends on the diagonal disorder. The corresponding data are shown in Figure (F - 4). As long as w is constant, universality is expected, which correlates with $L \leq 20\mu\text{m}$ for $\hat{\sigma} \geq 4$. On the other hand, the dependence of w on the thickness shows, that the particular shape of TOF signals are not indicative of some absolute degree of dispersity. Depending on the thickness, the TOF signal may appear non-dispersive although the spatial variance of the charge carrier packet is anomalously large or vice versa. The results from Figure (F - 4) may as well be interpreted as indicative for the evolution of the spatial variance of the carrier packet as a function of its position within the sample.

It appears, that charge carrier transport starts with considerable dispersity even for moderate disorder. Considering holographic experiments in disordered photorefractive photoconductors, where the grating spacing of typically $0.5\mu\text{m}$ up to

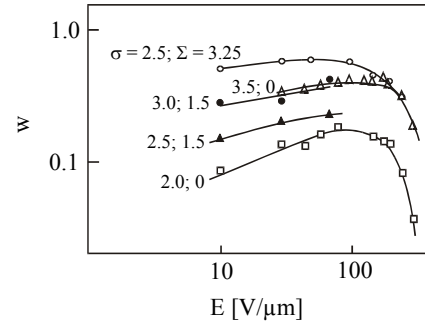


Figure (F - 3): Dispersion vs. field parametric in σ and Σ . Redrawn after [30].

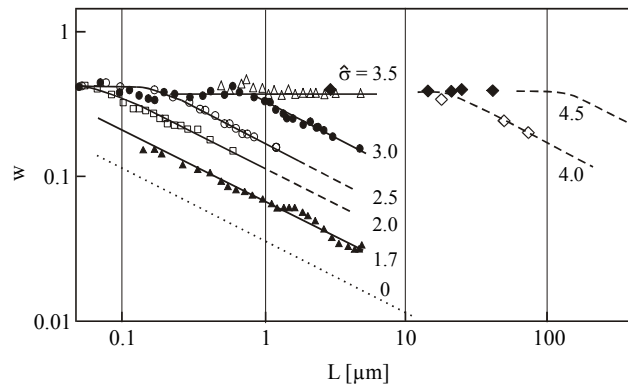
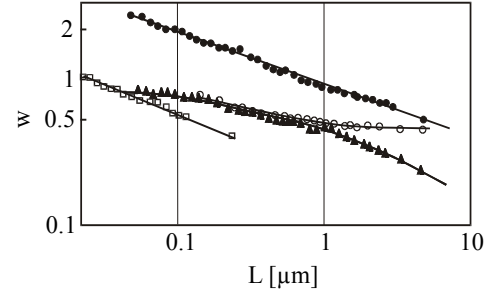


Figure (F - 4): Thickness dependence of w . Dashed lines are extrapolated, the dotted line is calculated according to eq. (F - 11). Diamonds are experimental values, the rest stem from MC simulations with $\Sigma = 0$ and $E = 60\text{V}/\mu\text{m}$. Redrawn after [30].

5 μm will be the relevant length scale, this may be important especially since dispersive charge transport has been made responsible for particular photorefractive behavior [56], [57].

In order to clarify, whether off-diagonal and diagonal disorder have similar effects on the thickness behavior of w , Baessler et. al. carried out a series of MC simulations for various superpositions of energetic and geometric disorder. The results are shown in Figure (F - 5). It is indicated, that off-diagonal disorder does contribute to the spreading of TOF signals (i.e. to dispersive transport behavior). However, apparently off-diagonal disorder does not yield some regime where w is independent from L unless there is not a considerable amount of diagonal disorder as well. Please recall, that both kinds of disorder have been identified to contribute similarly to the field dependence of w .



	□	▲	○	●
$\hat{\sigma}$	0	2,5	3,0	1,5
Σ	2.0	1.5	1.5	2.3
E [V/ μm]	100	70	70	100

Figure (F - 5): Thickness dependence of w for various combinations of disorder parameters and applied fields. Redrawn after [30].

F.2.3.) The non-dispersive / dispersive transition

MC simulations of TOF photocurrent transients show by plotting the mean arrival times $\langle t_T \rangle$ (i.e. the transit times t_T , however, in the dispersive regime the classical “transit time“ is not well defined; therefore the mean arrival time is used, which may be interpreted as the transit time of the center of the anomalously broadened carrier packet) as a function of the sample thickness (Figure (F - 6)), that the $\langle t_T \rangle$ and accordingly the apparent charge carrier mobilities in the dispersive regime vary with the thickness as:

$$t_T \propto L^m, \quad \text{eq. (F - 15)}$$

where $m > 1.0$. In this regime, the apparent charge mobility μ_a derived from TOF according to:

$$\mu_a = \frac{L}{E \langle t_T \rangle} \quad \text{eq. (F - 16)}$$

will exceed the value predicted by the dependence of the mobility on the disorder parameter at moderate fields according to eq. (E - 9). According to [58], $1/\langle t_T \rangle$ in fact will vary approximately as:

$$\frac{1}{\langle t_T \rangle} \propto e^{-\left(\frac{\hat{\sigma}}{2}\right)^2}. \quad \text{eq. (F - 17)}$$

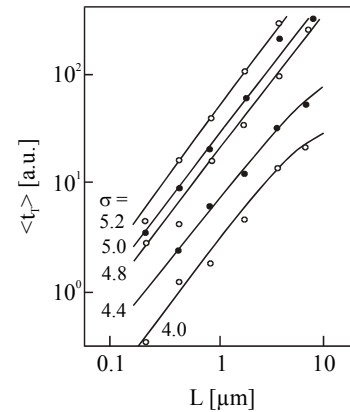


Figure (F - 6): Mean arrival times vs. thickness parametric in $\hat{\sigma}$. Redrawn after [58].

Accordingly the mobility thus derived does not describe the bulk charge transport properties. However, there is a critical value for the disorder parameter $\hat{\sigma}$, below of which the mobilities derived from the mean transit times according to eq. (F - 16) are independent from the thickness, thus yielding the bulk charge carrier mobility. The critical value of the disorder parameter may be illustrated by plotting $\ln(1/\langle t_T \rangle)$ parametric in L as a function of $\hat{\sigma}^2$ simulated for the non-dispersive (according to eq. (E - 9)) and the dispersive regime (according to eq. (F - 17)) as depicted in Figure (F - 7). From the intersection points between the asymptote describing non-dispersive transport and the lines obtained for dispersive transport a relation between the sample thickness and the disorder parameter $\hat{\sigma}$ may be derived as shown in Figure (F - 8). The solid line in Figure (F - 8) obeys the empirical relation:

$$\hat{\sigma}_c^2 = 71.4 + 6.7 \log L, \quad \text{eq. (F - 18)}$$

which eventually relates the width of the DOS to a sample length (i.e. the drift length until discharge or final immobilization) at the transition between non-dispersive and dispersive transport. L is in units of μm . For $\hat{\sigma}^2$ being bigger than given by eq. (F - 18), dispersive transport will be observed in the photocurrent transients.

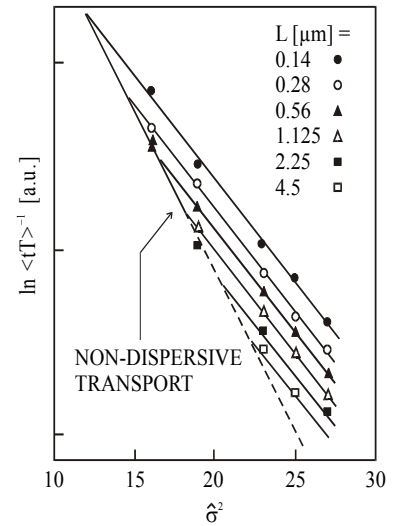


Figure (F - 7): Mean arrival times for non-dispersive and dispersive transport. Redrawn after [58].

F.2.4.) Phenomenological interpretation

The field-induced broadening of a charge carrier packet in disordered organic solids can be illustrated phenomenologically. The ordinary diffusive (i.e. thermal) broadening of a packet of charge carriers drifting under influence of an applied field obeys the Einstein relation only for small fields and in homogenous media as mentioned before in “2.4.3.3.1.) The Einstein relationship” on page 108. The latter condition requires the jump rate being a well-defined quantity in the case of hopping transport, which is violated in a medium afflicted with energetic and/or positional disorder. It has been discussed before, that charge carriers relaxing within a Gaussian DOS tend to settle on the average at a mean energy according to eq. (E - 6) occupying then states of the low energy edge of the DOS. Based on the argumentation succeeding eq. (E - 6) the jump rates of carriers located at bottom states of the low energy edge of the DOS may safely be assumed to exhibit lower jump rates than the average. Thus, the charge carrier packet after having settled at the bottom of the DOS will be subjected to a distribution of jump rates under the influence of an applied field, since the hopping probability will depend on the position of a particular charge carrier within the DOS. It is clear, that this must give rise to non-thermal spreading of the carrier packet.

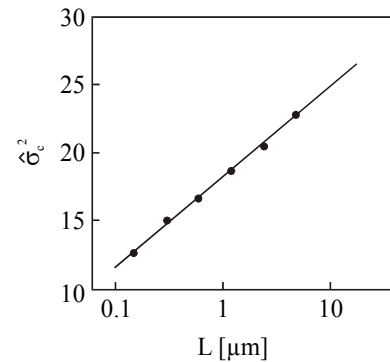


Figure (F - 8): L and $\hat{\sigma}_c^2$ at the transition point for non-dispersive/dispersive transport. Redrawn after [58].

Appendix G

Theoretical treatment of the photorefractive effect in crystals

The band transport model for the photorefractive effect developed by Kukhtarev et.al. [71] will be elaborated upon below. Special aspects, which are absent or at least negligible in PR polymers will be set aside. For example photovoltaic effects, which can be very important in crystals, are negligible in polymers due to the strong external electric field usually applied to these systems. Important extensions of Kukhtarev's model were provided by Twarowski (introduction of an Onsager type field dependent charge carrier generation efficiency [72]) and Tayebati et al. (introduction of a shallow trap level [79]), which are not elaborated upon here.

CONTENT:

G.1.) The band-transport model (Kukhtarev-model)	G2
G.1.1.) Steady-state solution for the space-charge field	G4
G.1.1.1.) Space-charge field without external electrical field	G6
G.1.1.2.) Space charge field with external field applied	G7
G.1.2.) Dynamics of the space-charge field	G7
G.1.2.1.) Build-up dynamics	G7
G.1.2.2.) Erasure dynamics	G10

G.1.) The band-transport model (Kukhtarev-model)

The Kukhtarev-model presumes, that there is a fixed and constant number of impurities and/or defects in the PR medium, which may serve as charge carrier sources or traps depending on their initial ionization state. Such a system will always contain donors as well as traps (i.e. even in the dark when there are no photoinduced traps and charges) as implied by the demand for electro-chemical equilibrium in sufficiently polar solution. Donors and acceptors are presumed to be of identical species, having identical energy levels located somewhere in the band gap of the system. This implies that only ionized donors are considered as traps, which requires the introduction of fictive acceptor sites ensuring a non vanishing trap density in the dark without violating the demand for macroscopic electrical neutrality of the system. These acceptor levels do not take an active part in the photorefractive effect. Figure (G - 1) illustrates the model, upon of which the subsequent mathematical discussion will rely.

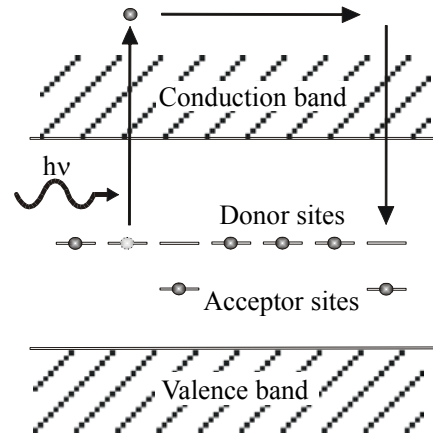


Figure (G - 1): Kukhtarev's band transport model of the photorefractive effect

The change of the density of ionized donors will be determined by the balance between charge generation and trapping:

$$\frac{\partial N_D^i}{\partial t} = f(N_D - N_D^i) - \gamma_R n N_D^i, \quad \text{eq. (G - 1)}$$

where N_D is the total density of donors, N_D^i is the density of ionized donors, n is the density of free (and mobile) charge carriers, I is the intensity, γ_R is the rate constant for (linear) recombination between free charge carriers and ionized traps, and f is the total charge carrier generation rate, which includes both thermal and photoexcitation:

$$f = sI + \beta. \quad \text{eq. (G - 2)}$$

Here, s is the cross section for photoexcitation and β is the thermal charge carrier generation rate. Please note, that γ_R in eq. (G - 1) may as well be considered as trapping rate, which is important, since later on for PR polymers a recombination rate and a trapping rate will explicitly be distinguished, which is dispensable here.

The rates of generation of free charge carriers and of ionized donors are identical, however, the ionized donors are locally fixed. Thence, charge transport will affect the local charge density, which is essential for the PR effect and may be expressed as:

$$\frac{\partial n}{\partial t} = \frac{\partial N_D^i}{\partial t} + \frac{1}{q} \nabla \cdot \vec{j}, \quad \text{eq. (G - 3)}$$

where q is the elementary charge and \vec{j} is the current density. Neglecting photovoltaic effects, the current density will contain a drift term (driven by an electrical field) and a diffusion term (driven by the local charge carrier gradient). Please note, that the occurrence of a drift term does not require an external electrical field, since the displacement of the centers of the mobile and the fixed charge carrier distributions will generate an internal field. Thus, the current density reads:

$$\vec{j} = -qn\mu\vec{E} + k_B T \mu \nabla n, \quad \text{eq. (G - 4)}$$

where μ is the charge carrier mobility tensor, $k_B T$ is the thermal energy, and \vec{E} is the electrical

field which must obey Poisson's equation:

$$\nabla \cdot \varepsilon \vec{E} = \rho(\vec{r}) = q(n + N_A - N_D^i)(\vec{r}). \quad \text{eq. (G - 5)}$$

Here, ε is the permittivity tensor, $\rho(\vec{r})$ is the (space-)charge density, and N_A is the density of acceptors, which is the trap density without illumination. The macroscopic charge neutrality requires:

$$n + N_A - N_D^i = 0. \quad \text{eq. (G - 6)}$$

Upon non-uniform illumination, (a surplus of) free charge carriers will be generated in the bright(er) areas compared to the dark(er) areas. "Brighter" and "darker" will be referred to hereafter simply as bright and dark. The simplest case of a periodic spatially non-uniform optical field is the sinusoidal interference pattern generated by interference of two plane and coherent waves according to "2.1.2.2.) Interference" on page 10 and eq. (2.1 - 46), which may be expressed in complex form as:

$$I = I_0 + I_1 e^{i\vec{K} \cdot \vec{r}}, \quad \text{eq. (G - 7)}$$

where $I_1 = mI_0$ and the parameters are explained in the aforementioned section. The non-uniform illumination determines a non-uniform spatial distribution of the total charge carrier generation rate f , which has the same shape:

$$f = f_0 + f_1 e^{i\vec{K} \cdot \vec{r}}. \quad \text{eq. (G - 8)}$$

Here $f_1 = Mf_0$ and the contrast factor M may be expressed as:

$$M = m \frac{\sigma_{ph}}{\sigma_d + \sigma_{ph}}, \quad \text{eq. (G - 9)}$$

where m is the contrast factor of the light fringe pattern according to eq. (2.1 - 47) and σ_{ph} and σ_d are the photoconductivity and the dark conductivity of the medium, respectively. The latter is due to thermal excitation of charge carriers. The quotient to the right hand side of eq. (G - 9) is commonly referred to as „conductivity contrast“.

Local density gradients of free charge carriers will arise from the spatially different photogeneration rates of free charge carriers as a function of the illumination intensity. In the absence of an external electrical field, these density gradients will be equalized due to diffusion, which results in a local displacement of the centers of the charge distributions. This will give rise to local space-charge fields, which counteract the diffusion by drift until a steady-state situation is reached, where both the contributions to the current density cancel and the current density drops to zero. Eventually, a space-charge distribution $\rho(\vec{r})$ will result, which reproduces the intensity pattern of the nonuniform illumination. According to eq. (G - 5), the space-charge distribution is connected with a space-charge field, the spatial distribution of which is the derivative of the space-charge distribution and, thus, spatially shifted with respect to the latter. Thus, the above set of equations completely covers the basic phenomenology of the PR effect, which has been discussed before.

The space-charge field is the key parameter for the PR effect and can be calculated as a function of the position as well as as a function of time on the basis of eq. (G - 1) to eq. (G - 6). General analytical solutions of the set of equations, however, cannot be obtained. Exact solutions for the space-charge field are only possible for simplified situations, which will be discussed below.

G.1.1.) Steady-state solution for the space-charge field

In the steady-state case, the time derivatives in eq. (G - 1) and eq. (G - 3) vanish and $\nabla \cdot \vec{j} = 0$ (which follows from the continuity condition for a stationary flow-field). Thus, the following set of equations is obtained:

$$\begin{aligned} f(N_D - N_D^i) - \gamma_R n N_D^i &= 0 \\ \nabla \cdot \vec{j} &= 0 \\ \vec{j} &= -qn\mu\vec{E} + k_B T \mu \nabla n \\ \nabla \cdot \epsilon \vec{E} &= \rho(\vec{r}) = q(n + N_A - N_D^i)(\vec{r}) \end{aligned} \quad \text{eq. (G - 10)}$$

Analytical solutions for this set of equations may be obtained in the limit of small modulation depth of the charge generation rate ($M \ll 1$) and small beam coupling, i.e. M is constant throughout the medium. This allows for ignoring second and higher order spatial harmonic terms and the independent variables of the set of coupled nonlinear partial differential equations may be separated (i.e. linearized to ordinary differential equation) by introducing steady-state solutions of the form:

$$\begin{aligned} n(\vec{r}) &= n_0 + n_1 e^{i\vec{K} \cdot \vec{r}} \\ N_D^i(\vec{r}) &= N_{D0}^i + N_{D1}^i e^{i\vec{K} \cdot \vec{r}} \\ \vec{j}(\vec{r}) &= \vec{j}_0 + \vec{j}_1 e^{i\vec{K} \cdot \vec{r}} \\ \vec{E}(\vec{r}) &= \vec{E}_0 + \vec{E}_1 e^{i\vec{K} \cdot \vec{r}} \end{aligned} \quad \text{eq. (G - 11)}$$

where $n_{0,1}, N_{D0,1}^i, \vec{j}_{0,1}$ and $\vec{E}_{0,1}$ are constants. The index “0” denotes the zero order spatial harmonic and the index “1” the amplitude of the first order spatial harmonic. In order to evaluate the space-charge field, the above constants must be solved for. Combining eq. (G - 11) and eq. (G - 7) with eq. (G - 10) and separating into zero order and first order spatial terms results in:

$$\begin{aligned} 0 &= f_0(N_D - N_{D0}^i) - \gamma_R n_0 N_{D0}^i \\ 0 &= q(n_0 + N_A - N_{D0}^i) \end{aligned} \quad \text{eq. (G - 12)}$$

for the zero order terms and in:

$$\begin{aligned} 0 &= f_1(N_D - N_{D0}^i) - f_0 N_{D1}^i - \gamma_R(n_0 N_{D1}^i + n_1 N_{D0}^i) \\ 0 &= -\frac{1}{q} i\vec{K} \vec{j}_1 \Rightarrow \vec{j}_1 = 0 \quad \forall (\vec{K} > 0) \\ 0 &= -q \langle \mu \rangle (n_0 \vec{E}_1 + \vec{E}_0 n_1) - i\vec{K} k_B T \langle \mu \rangle n_1 = \vec{j}_1 \end{aligned} \quad \text{eq. (G - 13)}$$

$$i\vec{K} \langle \epsilon \rangle \vec{E}_1 = q(n_1 - N_{D1}^i)$$

for the first order terms, where $\langle \epsilon \rangle$ is the effective bulk permittivity and $\langle \mu \rangle$ is the effective (bulk) charge carrier mobility defined by:

$$\begin{aligned} \langle \epsilon \rangle &= \frac{\vec{K} \cdot \epsilon \vec{K}}{K^2} \\ \langle \mu \rangle &= \frac{\vec{K} \cdot \mu \vec{K}}{K^2} \end{aligned} \quad \text{eq. (G - 14)}$$

These relations result from $rot \vec{E} + \partial \vec{B} / \partial t = 0$ (see “2.1.1.) The electro-magnetic theory of

light” on page 4), which demands that no rotational electrical field will occur, if there is no magnetic induction changing as a function of time. Accordingly, $\vec{K} \times \vec{E}_1 = 0$ and the space-charge field \vec{E}_1 will be oriented parallelly to the grating vector, which in turn yields $\vec{K} \cdot \vec{E}_1 = KE_1$. Please note, that this need not be valid for some externally applied field, thus, $\vec{K} \times \vec{E}_0 \neq 0$ is possible. Hence, $\langle \varepsilon \rangle$ and $\langle \mu \rangle$ are the effective quantities of the ε and μ tensors along the grating vector.

From eq. (G - 12) and eq. (G - 13) $n_{0,1}, N_{D0,1}^i$ can be obtained and eventually \vec{E}_1 from the last equation in eq. (G - 13) when using the approximations:

$$\begin{aligned} \gamma_R N_A &\gg f_0 \\ \gamma_R N_A^2 &\gg f_0 N_D \cdot \\ f_0 &\gg f_1 \end{aligned} \quad \text{eq. (G - 15)}$$

The first two relations reflect the assumption that the steady-state density of free charge carriers is small (the recombination rate is much higher than the generation rate) and the third expression is another form of $M \ll 1$ as proposed before. After some algebraic manipulations and approximations one obtains the complex amplitude of the space-charge field:

$$E_1 = M \frac{iK \frac{k_B T}{q} - \frac{\vec{K} \cdot \mu \vec{E}_0}{K \langle \mu \rangle}}{1 + \frac{K^2}{k_D^2} + i \frac{q \vec{K} \cdot \mu \vec{E}_0}{k_B T k_D^2 \langle \mu \rangle}}, \quad \text{eq. (G - 16)}$$

where k_D is known as Debye’s wave number given by:

$$k_D^2 = \frac{q^2}{\langle \varepsilon \rangle k_B T} \left(N_A - \frac{N_A^2}{N_D} \right). \quad \text{eq. (G - 17)}$$

Debye’s wave number bases on plasma physics [B3]. The plasma-concept as well as methods of plasma physics may be transferred to certain problems and systems not directly attributed to plasma physics, e.g. electrolytic solutions, metallic conductors, and semiconductors like here. The Debye length λ_D (also referred to as Debye-Hückel-length or Debye screening length or radius), which is correlated with Debye’s wave-number by $k_D = 2\pi/\lambda_D$, may be interpreted as some characteristic length beyond of which the electrical potential of a point charge in a plasma (Debye’s potential) may be considered as negligible for electrostatic interactions. Therefore, this length is determined by the balance between the thermal kinetic energy of and electrostatic interaction energy between two point charges in a plasma-like environment. The Debye length is pretty common in semiconductor physics and known as the characteristic decay length of some surface or interface space-charge layer. Hence, K^2/k_D^2 in eq. (G - 16) may be interpreted as a scaling factor taking into account the mutual interference of neighboring space-charge layers of the PR grating.

In steady-state (i.e. small density of free charge carriers) and provided $N_D \gg N_A$, which is valid for most of the PR inorganic materials, the expression for k_D simplifies to:

$$k_D^2 = \frac{q^2 N_A}{\langle \varepsilon \rangle k_B T} = \frac{q^2 N_{D0}^i}{\langle \varepsilon \rangle k_B T}. \quad \text{eq. (G - 18)}$$

G1.1.1.) Space-charge field without external electrical field

Without an externally applied field, the charge carrier redistribution is exclusively due to diffusion. In steady-state, the diffusion driven current and the drift current cancel as mentioned before. This situation may be interpreted as a situation in which generated charge carriers are no more displaced but recombine again with their generation site yielding a vanishing net current in the system and the density of free charge carriers approaches zero ($n_0 \rightarrow 0$). In this case, eq. (G - 11) becomes $n(\vec{r}) = n_1 \exp(i\vec{K} \bullet \vec{r})$ and eq. (G - 4) may be rewritten as:

$$E = iK \frac{k_B T}{q} \equiv iE_d. \quad \text{eq. (G - 19)}$$

E_d is referred to as diffusion field and does not depend on intrinsic system parameters (in particular, it does not depend on the density of impurities or defects).

A second field quantity may be defined besides the diffusion field for the case that the hypothetical maximum of the charge carrier redistribution is reached, which is formally determined by the intrinsic maximum density of traps given by N_{D0}^i . For $n_0 \rightarrow 0$, this corresponds to the trap density in the dark N_A . Hence, the formally achievable maximum space-charge distribution may be expressed as $\rho(x) = qN_{D0}^i \exp(iKx)$ and the amplitude of the space-charge field thus generated is given by:

$$E_1 = iq \frac{N_{D0}^i}{\langle \epsilon \rangle K} = iq \frac{N_A}{\langle \epsilon \rangle K} \equiv iE_q. \quad \text{eq. (G - 20)}$$

The quantity E_q is referred to as saturation field.

Using the characteristic field quantities according to eq. (G - 19) and eq. (G - 20), the complex amplitude of the PR space-charge field is obtained as

$$E_1 = M \frac{iE_d}{1 + \frac{E_d}{E_q}} \quad \text{eq. (G - 21)}$$

and the real space-charge field as:

$$E_{sc}(\vec{r}) = -M \frac{E_d E_q}{E_d + E_q} \sin(\vec{K} \bullet \vec{r}). \quad \text{eq. (G - 22)}$$

The space-charge field is purely imaginary in this case indicating a phase shift of $\phi = \pm\pi/2$ (ϕ is the phase angle) with respect to the optical interference field as mentioned in "2.5.1.) Phenomenology of the photorefractive effect" on page 118. The sign of the phase angle ϕ is determined by the polarity of the mobile charge carriers. Please note, that E_1 will not exceed the smaller value of the characteristic fields E_d and E_q and reach its maximum for $E_d = E_q$. Apart from the temperature, this is basically a question of the grating spacing, which defines the magnitude of K . Due to the negligibly small diffusion coefficient typically found in polymers, the case of pure diffusion is insignificant for PR polymers.

G1.1.2.) Space charge field with external field applied

Using the characteristic fields according to eq. (G - 19) and eq. (G - 20), the influence of an external electrical field applied to the PR medium becomes illustrative when expressing eq. (G - 16) as follows:

$$E_1 = M \frac{iE_d}{1 + \frac{E_d}{E_q}} \left[\frac{1 + i \frac{E_0}{E_d}}{1 + i \frac{E_0}{E_d + E_q}} \right]. \quad \text{eq. (G - 23)}$$

It becomes clear, that the external field E_0 introduces a complex scaling factor in eq. (G - 21), the term in brackets in eq. (G - 23), which becomes unity for $\vec{E}_0 = 0$. This affects the behavior of the space charge field in two ways.

Firstly, the amplitude of the space-charge field is no more limited by E_d and E_q as discussed above for the case of no external field applied. In contrast, E_1 will now be limited by the strength of E_0 except for $E_q \ll E_d$, when eq. (G - 23) transforms back to eq. (G - 21) disregarding the existence of an external field. However, a corresponding case will not be observed in PR polymers due to the inherently large trap densities.

Secondly, since the scaling factor is complex, the phase angle ϕ will take on values of $0 < \phi < \pm\pi/2$, and the sign of ϕ will depend on the polarity of the mobile charge carriers as well as on the direction of the external field. It is self evident, that ϕ will approach 90° for $E_q \ll E_d$, however, its sign will still depend on the direction of the external field.

Simplifying eq. (G - 23) yields:

$$E_1 = M \frac{iE_d - E_0}{1 + \frac{E_d}{E_q} + i \frac{E_0}{E_q}}, \quad \text{eq. (G - 24)}$$

which correlates directly to eq. (G - 16). Please note, that eq. (G - 24) is the complex amplitude of the complex space-charge field. In order to derive the real space-charge field, the real part of:

$$\underline{E}_{sc}(\vec{r}) = \underline{E}_1 e^{i\vec{k} \cdot \vec{r}} \quad \text{eq. (G - 25)}$$

(the subscript tilde shall point out the complex character) must be extracted as has been done for deriving eq. (G - 22). The resulting expression is presented in “2.5.2.1.1.) Steady-state solution for the space-charge field” on page 120.

G1.2.) Dynamics of the space-charge field

G1.2.1.) Build-up dynamics

The photorefractive effect is a macroscopic phenomenon, which requires the excitation and redistribution of a large number of charge carriers in order to form a notable PR grating. Hence, the build-up velocity of a PR grating will at first predominantly be determined by the photon flux, i.e. by the intensity of the optical interference field. A rough estimate reveals an approximately reciprocal dependency of the build-up time on the intensity ([B22] p. 99ff). Corresponding considerations apply to the erasure dynamics, where the time axis is simply inverted.

Considering not the absolute build-up time of a PR grating but the build-up dynamics, the band transport equations eq. (G - 1) and eq. (G - 5) must be solved as a function of time. For this purpose, the independent variables of the set of nonlinear differential equations eq. (G - 11) will be similarly separated as for the steady-state case by introducing now time dependent solutions:

$$\begin{aligned}
 n(\vec{r}, t) &= n_0(t) + n_1(t)e^{i\vec{k} \cdot \vec{r}} \\
 N_D^i(\vec{r}, t) &= N_{D0}^i(t) + N_{D1}^i(t)e^{i\vec{k} \cdot \vec{r}} \\
 \vec{j}(\vec{r}, t) &= \vec{j}_0(t) + \vec{j}_1(t)e^{i\vec{k} \cdot \vec{r}} \\
 \vec{E}(\vec{r}, t) &= \vec{E}_0(t) + \vec{E}_1(t)e^{i\vec{k} \cdot \vec{r}}
 \end{aligned}
 \tag{G - 26}$$

and the same approximations as above, i.e. $M = \text{const.} \ll 1$.

As discussed in the preceding section, grating vector and space-charge field are parallelly oriented and, accordingly, the current density vector will also be oriented parallelly to these quantities. Therefore and for the sake of simplicity, a vectorial representation shall be set aside hereafter and for this section. It will tacitly be presumed, that all oriented quantities are oriented along the grating vector and, if some external field is applied, only the projection onto the grating wave vector will be accounted for.

By inserting eq. (G - 26) in the band transport equations, separating terms of zero and first order and ignoring terms of higher order, the following sets of equations are obtained for the zero order Fourier component:

$$\begin{aligned}
 \frac{dN_{D0}^i}{dt} &= f_0(N_D - N_{D0}^i) - \gamma_R n_0 N_{D0}^i \\
 \frac{dn_0}{dt} &= \frac{dN_{D0}^i}{dt} \\
 j_0 &= q \langle \mu \rangle n_0 E_0 \\
 0 &= n_0 + N_A - N_{D0}^i
 \end{aligned}
 \tag{G - 27}$$

and the first order Fourier component:

$$\begin{aligned}
 \frac{dN_{D1}^i}{dt} &= f_1(N_D - N_{D0}^i) - f_0 N_{D1}^i - \gamma_R (n_0 N_{D1}^i + n_1 N_{D0}^i) \\
 \frac{dn_1}{dt} &= \frac{dN_{D1}^i}{dt} - i \frac{1}{q} K j_1 \\
 j_1 &= q \langle \mu \rangle (n_0 E_1 + E_0 n_1) - i K k_B T \langle \mu \rangle n_1 \\
 iK \langle \varepsilon \rangle E_1 &= \pm q (n_1 - N_{D1}^i)
 \end{aligned}
 \tag{G - 28}$$

where the effective quantities $\langle \varepsilon \rangle$ and $\langle \mu \rangle$ are defined by eq. (G - 14) and explicit indications of time dependency have been set aside for the sake of clarity.

If there is an external dc electrical field applied to the medium, $E_0(t)$ is constant, and zero otherwise. Therefore only the case of $E_0 \neq 0$ will be considered subsequently, which may easily be rewritten for $E_0 = 0$ if desirable. Applying the approximations eq. (G - 15) also here implies a small the zero order density of free charge carriers, which in turn implies:

$$n_0 \ll N_A \Rightarrow N_{D0}^i(t) = N_A = \text{konst.}
 \tag{G - 29}$$

Please note, that the approximations eq. (G - 15) are not causally determined here but rather presumed, which restricts the validity of the present considerations. Applying the named approximation and assuming linear recombination, one obtains from eq. (G - 27):

$$\begin{aligned}
 n_0(t) &= n_0(1 - e^{-t/\tau_R}) \\
 n_0 &= \frac{(N_D - N_A)f_0}{\gamma_R N_A} \\
 \tau_R &= \frac{1}{\gamma_R N_A}
 \end{aligned}
 \tag{G - 30}$$

The recombination time constant τ_R is usually much smaller than the PR grating build-up time constant in by far most PR media known today. Thus, for calculating $E_1(t)$ by means of eq. (G - 30) only the steady-state solution ($n_0(t) = n_0$) must be accounted for. The approximations of eq. (G - 15) imply furthermore, that the local supply of free charge carriers via the conduction band is much smaller than the recombination rate:

$$q\mu n_0/\varepsilon \ll \gamma_R N_A. \tag{G - 31}$$

Solving now the first order equations for the formation of the space charge field and substituting eq. (G - 29) and eq. (G - 30) yields:

$$\frac{d}{dt}(n_1 - N_{D1}^i) = \frac{q\mu N_0}{\langle \varepsilon \rangle} N_{D1}^i - \left(i\langle \mu \rangle E_0 K + \frac{k_B T \langle \mu \rangle K^2}{q} + \frac{q\mu N_0}{\langle \varepsilon \rangle} \right) n_1. \tag{G - 32}$$

In order to find an analytical expression for $E_1(t)$, the first differential equation of the set eq. (G - 28) must be solved as well as eq. (G - 32) yielding an expression for $(n_1 - N_{D1}^i)(t)$, which then is inserted into the last equation in set eq. (G - 28). Applying then eq. (G - 31) and the first approximation in eq. (G - 15), the final dynamic solution for the complex amplitude of the space-charge field is obtained as:

$$E_1(t) = E_1(1 - e^{-t/\tau}). \tag{G - 33}$$

E_1 is the steady state ($t \rightarrow \infty$) complex amplitude of the space charge field according to eq. (G - 24) and the time constant τ is complex and given by:

$$\tau = t_0 \frac{E_d + E_\mu + iE_0}{E_d + E_q + iE_0}. \tag{G - 34}$$

E_d is the diffusion field according to eq. (G - 19) and E_q is the saturation field according to eq. (G - 20) and E_μ is another characteristic field quantity referred to as drift field:

$$E_\mu = \frac{\gamma_R N_A}{\langle \mu \rangle K}. \tag{G - 35}$$

The parameter t_0 is a characteristic time constant defined by:

$$t_0 = \frac{N_A}{f_0 N_D}. \tag{G - 36}$$

The real part of eq. (G - 33) is the dynamic solution for the physical space-charge field E_{sc} and is shown in “2.5.2.1.2.1.) Build-up dynamics” on page 121.

G1.2.2.) Erasure dynamics

For erasing the space charge field a uniform illumination is applied. Accordingly, there is initially some space-charge field of strength E_1 and the final steady-state will be $E_1(t \rightarrow \infty) = 0$. The resulting dynamic solution for this problem may be formulated in analogy to eq. (G - 33) as:

$$E_1(t) = E_1 e^{-t/\tau}, \quad \text{eq. (G - 37)}$$

where τ is the complex time constant according to eq. (G - 34). The real solution is presented in “2.5.2.1.2.2.) Erasure dynamics” on page 122

Appendix H

Theoretical treatment of the photorefractive effect in polymers

In the following, the theoretical models for the photorefractive effect in polymers as developed by Schildkraut, Cui, et. al. [77, 78] and Cui et. al.[83] will be elaborated upon.

Please note, that photorefractive polymers require an external field not only for breaking the inherent statistical centro-symmetry, but also to support the charge generation and to enable charge carrier redistribution by charge carrier drift. The latter requires that the external field has a non-vanishing projection onto the grating wave vector of the interference pattern. Subsequently, the term “external field” (or similar) or “ E_0 ” always refer to the external field component fulfilling this requirement.

CONTENT:

H.1.) Schildkraut’s model	H2
H.1.1.) Steady state solutions for the space-charge field in polymers	H4
H.1.1.1.) Zero order component	H4
H.1.1.2.) First order component	H5
H.1.2.) Build-up dynamics for the space-charge field in polymers	H7
H.1.3.) Erasure dynamics of the space-charge field in polymers	H9
H.1.3.1.) Erasure dynamics in Schildkraut’s model	H9
H.1.3.2.) Cui’s approach to the erasure dynamics	H10

H.1.) Schildkraut's model

Schildkraut's model [77, 78] is formulated in dimensionless form, which may be appropriate for theoretical considerations but is not very helpful for application to the experiment. Therefore, the model is depicted here in SI units [T2]. The mobile charge carriers are assumed to be holes and to be photogenerated from neutral electron accepting moieties. The negative countercharges are assumed to be fixed at the ionized sensitizer moieties. Both the charge carrier photogeneration efficiency and the hole mobility are allowed to be field dependent. The field dependency of the photogeneration efficiency $\Phi(E)$ is basically described by the Onsager theory (page 110). According to [78], by sense of proportion applied to a plot depicted in [67] within the interval of external fields typically applied to PR polymers (about $10\text{V}/\mu\text{m}$ - $100\text{V}/\mu\text{m}$), the very complicated Onsager field dependence might be approximated with sufficient accuracy by a simple power law:

$$\Phi(E) = \Phi_i E^p, \quad \text{eq. (H - 1)}$$

where Φ_i is a constant and p is a system dependent empirical parameter to be determined experimentally. The field dependency of the hole mobility $\mu(E)$ is described using the hopping transport formalism in disordered organic systems [81]:

$$\mu(E) = \mu_i e^{C(\sqrt{E}-1)}, \quad \text{eq. (H - 2)}$$

where μ_i is a constant and C is an experimentally obtained characteristic parameter. For more details see "2.4.3.) Electrical conduction in organic polymers" on page 95. Please note, that eq. (H - 1) and eq. (H - 2) are of empirical nature and, hence, the fields are considered as dimensionless. A charge carrier once generated may then recombine with one of the fixed countercharges, i.e. an ionized sensitizer N_G^i , or be trapped in a neutral trap N_T . The recombination is assumed to follow the Langevin theory (page 115) and eq. (2.4 - 186) is rewritten as:

$$\gamma_R = \frac{q\mu}{\varepsilon}, \quad \text{eq. (H - 3)}$$

where γ_R is the recombination rate, q the absolute elementary charge (i.e. 1.6×10^{-19} C), $\mu = \mu(E)$ the hole mobility, and ε is the total (effective) permittivity. However, this theory does not account for the trapping rate, since it requires strong Coulomb-interaction between a trapping site and the charge carrier to be trapped and thus is not valid for neutral traps. Eventually, charge carriers trapped in shallow traps may be detrapped again and further participate on the overall process. A schematic of Schildkraut's model is depicted in figure (1).

Without loss of generality, the problem will be considered one-dimensional in x -direction, which also shall be the direction of the externally applied field:

$$\vec{E}_{ext} = E \hat{e}_x, \quad \text{eq. (H - 4)}$$

where \hat{e}_x is the unit vector in x -direction of the system. Accordingly, all occurring oriented quantities can be related to the x -direction and vectorial expressions can be set aside, which makes the discussion more clear.

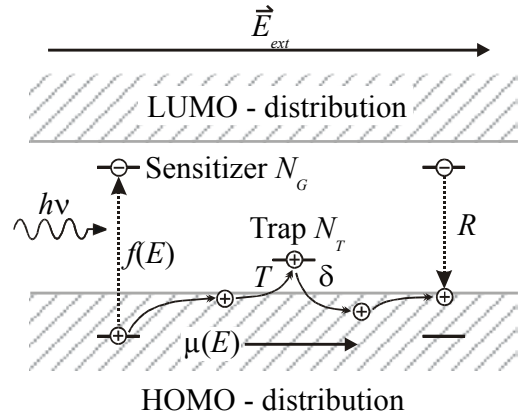


Figure (H - 1): Energy level scheme of Schildkraut's model. $f(E)$ is the generation rate, T represents trapping and R recombination and δ stands for detrapping.

The continuity equation as formulated for the band transport model, i.e., according eq. (G - 1) and eq. (G - 3) for the mobile charge carriers, i.e. the holes, may here be formulated as:

$$\frac{\partial n}{\partial t} = fN_G - \frac{1}{e} \frac{\partial j}{\partial x} - \gamma_R n N_G^i - \gamma_T n N_T + \delta N_T^i, \quad \text{eq. (H - 5)}$$

where n is the hole density, N_G and N_G^i and N_T and N_T^i are the densities of neutral and ionized sensitizers and traps, respectively, γ_T and δ are the trapping and detrapping rates, respectively, and j is the current density as formulated for the band transport mode, i.e., according to eq. (G - 4), here simplified to:

$$j = qn\mu E - k_B T \mu \frac{\partial n}{\partial x}, \quad \text{eq. (H - 6)}$$

where $k_B T$ is the thermal energy. The hole generation rate f is given by:

$$f = f(E) = \Phi(E) \frac{sI}{h\nu}, \quad \text{eq. (H - 7)}$$

where I is the light intensity and s is the light absorption cross section and $h\nu$ is the photon energy. Please note, that eq. (H - 6) premises the validity of the Einstein relation

$$D = \frac{k_B T}{q} \mu, \quad \text{eq. (H - 8)}$$

with D as diffusion coefficient. For polymers, eq. (H - 8) is an approximation of unclear quality in general and may be unacceptable especially for higher fields as discussed in “2.4.3.3.1.) The Einstein relationship” on page 108. However, there is no alternative analytic expression relating diffusion coefficient and mobility. Furthermore, drift will usually dominate for higher fields (i.e. the diffusion term in eq. (H - 6) is of minor influence) and for lower fields, where the diffusion term becomes more important, eq. (H - 8) may be considered as a reasonably valid approximation.

The electrical field must satisfy Poisson’s equation (see Appendix G, eq. (G - 5)), which reads here:

$$\frac{\partial E}{\partial x} = \frac{q}{\epsilon} (n - N_G^i + N_T^i). \quad \text{eq. (H - 9)}$$

Please note, that all variables in eq. (H - 5), eq. (H - 6) and eq. (H - 9) depend on x (position) and t (time) which is self-evident and has neither been explicitly indicated or mentioned above nor will be so hereafter.

The rate equations for the recombination centers (i.e. ionized sensitizers) and for ionized traps are:

$$\frac{\partial N_G^i}{\partial t} = fN_G - \gamma_R n N_G^i \quad \text{eq. (H - 10)}$$

and:

$$\frac{\partial N_T^i}{\partial t} = \gamma_T n N_T - \delta N_T^i, \quad \text{eq. (H - 11)}$$

respectively, and the conservation of sites requires the conditions:

$$N_{G,i} = N_G + N_G^i \quad \text{eq. (H - 12)}$$

and:

$$N_{T,i} = N_T + N_T^i \quad \text{eq. (H - 13)}$$

to be met, where $N_{G,i}$ and $N_{T,i}$ are the initial densities of neutral sensitizers and traps, respectively.

After having formulated the basic equations, eq. (H - 9) is partially differentiated with respect to t using thereby eq. (H - 10) and eq. (H - 11) to substitute the corresponding time derivatives. Then N_G and N_T^i are eliminated by inserting eq. (H - 12) and eq. (H - 13) and finally N_G^i is substituted using eq. (H - 9). This finally yields the following differential equation:

$$\begin{aligned} & \frac{\varepsilon}{q} \frac{\partial^2 E}{\partial x \partial t} - \frac{\partial n}{\partial t} + (\gamma_R n + f) \frac{\varepsilon \partial E}{q \partial x} - (\gamma_R n + \gamma_R N_{T,i} + f) n + f N_{G,i} + (\gamma_R - \gamma_T) n N_T \\ & = (f - \delta)(N_{T,i} - N_T) \end{aligned} \quad \text{eq. (H - 14)}$$

A second fundamental differential equation is obtained by differentiating eq. (H - 6) with respect to x and combining it with eq. (H - 5). Then the local derivative of eq. (H - 2) is inserted and subsequently eq. (H - 9), eq. (H - 12) and eq. (H - 13) are used to eliminate N_G^i , N_G and N_T^i , respectively, eventually resulting in:

$$\begin{aligned} & \frac{\partial n}{\partial t} - \frac{k_B T}{q} \mu \frac{\partial^2 n}{\partial x^2} + \left(\mu E - D \frac{C \mu_i}{2 \sqrt{E}} \frac{\partial E}{\partial x} \right) \frac{\partial n}{\partial x} + \left(n \frac{C \mu_i}{2} \sqrt{E} - f \frac{\varepsilon}{q} \right) \frac{\partial E}{\partial x} + \\ & + (\gamma_R n + \gamma_R N_{T,i} + f) n - f N_{G,i} - (\gamma_R - \gamma_T) n N_T = (f - \delta)(N_{T,i} - N_T) \end{aligned} \quad \text{eq. (H - 15)}$$

If the system is illuminated with a spatially varying intensity distribution according to eq. (G - 7), the variables n , E , μ , Φ , N_T , γ_T , and δ will have the same spatial modulation as the interference pattern and, similar to the procedure as described for the band transport mode (eq. (G - 11)), may be approximated by expressions of the general form:

$$g(x, t) = g_0 + g_1 e^{(iKx + i\zeta v t)}, \quad \text{eq. (H - 16)}$$

where K is the (modulus of the) grating wave vector and ζv represents some characteristic response frequency for the grating build-up. Rewriting eq. (G - 7) in the same form, $g_0 = I_0$ is the zero order constant for the light intensity and $g_1 = m I_0$ is the first order constant.

H.1.1.) Steady state solutions for the space-charge field in polymers

H.1.1.1.) Zero order component

Inserting the approximations according to eq. (H - 16) into eq. (H - 14) (or eq. (H - 15)) yields for the spatially constant zero order Fourier component of the hole density:

$$n_0 = \frac{f_0(N_{G,i} - N_{T,i} + N_{T0}) + \delta_0(N_{T,i} - N_{T0})}{f_0 + \frac{q}{\varepsilon} \mu_0(n_0 + N_{T,i} - N_{T0}) + \gamma_{T0} N_{T0}}, \quad \text{eq. (H - 17)}$$

with:

$$f_0 = \Phi_0 \frac{s I_0}{h \nu} \quad \text{eq. (H - 18)}$$

and μ_0 and Φ_0 given by eq. (H - 2) and eq. (H - 1), respectively, for $E = E_0$.

H.1.1.2.) First order component

In contrast to the zero order Fourier component, insertion of the approximations eq. (H - 16) into eq. (H - 14) and eq. (H - 15) will result in two linear equations for the first order Fourier component.

Expanding eq. (H - 2) in terms of a Taylor series yields:

$$\begin{aligned}\mu(E) &= \mu_0(E_0) + \mu_1(E_0, E_1) + \dots = \\ &= \mu_i e^{C(\sqrt{E_0}-1)} + \frac{C}{2\sqrt{E_0}} \mu_i e^{C(\sqrt{E_0}-1)} E_1 + \dots\end{aligned}\quad \text{eq. (H - 19)}$$

and μ_1 may thus be expressed as:

$$\mu_1 = \frac{C\mu_0}{2\sqrt{E_0}} E_1. \quad \text{eq. (H - 20)}$$

The same procedure yields from eq. (H - 1):

$$\Phi_1 = p \frac{\Phi_0}{E_0} E_1. \quad \text{eq. (H - 21)}$$

With these expressions, the two linear equations for the remaining first order terms are:

$$\begin{aligned}n_1 [i\zeta\nu + \Gamma_I + \Gamma_R - (\gamma_{R0} - \gamma_{T0})N_{T0}] + \\ + E_1 \left[\frac{C}{2\sqrt{E_0}} \Gamma_{die}(n_0 + N_{T,i} - N_{T0}) + f_0 \frac{p}{E_0} (n_0 + N_{T,i} - N_{T0} - N_{G,i}) \right] + \\ + E_1 \left[\frac{\varepsilon}{q} K \zeta \nu - i \frac{\varepsilon}{q} K \Gamma_I \right] + \\ + \gamma_{T1} n_0 N_{T0} - \delta_1 (N_{T,i} - N_{T0}) + N_{T1} (\Gamma_T - \Gamma_I) = \\ = -mf_0 (n_0 + N_{T,i} - N_{T0} - N_{G,i})\end{aligned}\quad \text{eq. (H - 22)}$$

and:

$$\begin{aligned}n_1 [i\zeta\nu + \Gamma_I + \Gamma_R + \Gamma_D + i\Gamma_E - (\gamma_{R0} - \gamma_{T0})N_{T0}] + \\ + E_1 \left[\frac{C}{2\sqrt{E_0}} \Gamma_{die}(n_0 + N_{T,i} - N_{T0}) + f_0 \frac{p}{E_0} (n_0 + N_{T,i} - N_{T0} - N_{G,i}) \right] + \\ + E_1 \left[i \frac{\varepsilon C \sqrt{E_0}}{2q} K \Gamma_{die} + i \frac{\varepsilon}{q} K (\Gamma_{die} - \Gamma_I) \right] + \\ + \gamma_{T1} n_0 N_{T0} - \delta_1 (N_{T,i} - N_{T0}) + N_{T1} (\Gamma_T - \Gamma_I) = \\ = -mf_0 (n_0 + N_{T,i} - N_{T0} - N_{G,i})\end{aligned}, \quad \text{eq. (H - 23)}$$

with:

$$\gamma_{R0} = \frac{q\mu_0}{\varepsilon} \quad \text{eq. (H - 24)}$$

according to eq. (H - 3). The parameters Γ_{die} , Γ_I , Γ_R , Γ_T , Γ_D and Γ_E may be interpreted as the dielectric relaxation rate, the sum of the charge carrier generation and geminate recombination rates, the total hole recombination rate (i.e. geminate and linear recombination), the sum of the hole trapping and detrapping rates, the diffusion rate and the drift rate, respectively. The explicit expressions for these rates are:

$$\Gamma_{die} = \gamma_{R0}n_0, \quad \text{eq. (H - 25)}$$

$$\Gamma_I = f_0 + \gamma_{R0}, \quad \text{eq. (H - 26)}$$

$$\Gamma_R = \gamma_{R0}(n_0 + N_{T,i}), \quad \text{eq. (H - 27)}$$

$$\Gamma_T = \gamma_{T0}n_0 + \delta_0, \quad \text{eq. (H - 28)}$$

$$\Gamma_D = \frac{k_B T}{q} K^2 \mu_0, \text{ and} \quad \text{eq. (H - 29)}$$

$$\Gamma_E = K\mu_0 E_0. \quad \text{eq. (H - 30)}$$

In order to obtain an analytical solution for eq. (H - 22) and eq. (H - 23), three of the five first order quantities must be eliminated, since presently there are only two independent equations. A possible approach would be to seek theoretical or empirical expressions for the hole trapping and detrapping rates, γ_T and δ , in terms of E and deriving the first order expressions by means of a Taylor expansion like conducted before for Φ_I and μ_I . Furthermore, it may be possible to relate N_T to n by means of thermodynamic arguments. However, there are no general expressions of that kind, yet. Therefore, Schildkraut et. al. considered the limiting case of deep traps, i.e. detrapping is considered negligible and $\delta = 0$. All traps can then be considered as filled (i.e. $N_T = N_{T0} = N_{T1} = 0$) if the system has reached its steady-state (i.e. furthermore $\zeta_v = 0$). Since trapping then does not occur any more, γ_{T1} will drop off from the equations as well, however, will not be zero. The remaining system of two linear equations contains the variables E_1 and n_1 and can be solved for the complex space-charge field E_1 by means of Cramers rule, which results in:

$$E_1 = \frac{m\Upsilon E_q(iE_D - E_0)}{\left[E_D + E_q(1 + \Upsilon p) + E_I \left(\frac{E_m}{E_0} + 1 \right) \right] + i \left[E_0 + \frac{E_D E_q}{E_0} \left(\frac{E_m}{E_0} - \Upsilon p \right) \right]}. \quad \text{eq. (H - 31)}$$

The modulus of the complex space charge field is presented in “2.5.3.2.1.) Steady state solutions for the space-charge field in polymers” on page 125.

The parameter Υ given by:

$$\Upsilon = f_0 \frac{(N_{G,i} - N_{T,i} - n_0)}{\gamma_{R0}n_0(n_0 + N_{T,i})}. \quad \text{eq. (H - 32)}$$

The fields are defined as:

$$E_D = \frac{k_B T}{q} K, \quad \text{eq. (H - 33)}$$

$$E_q = \frac{\Gamma_R}{\Gamma_I} E_I = \frac{\gamma_{R0}(n_0 + N_{T,i})qn_0}{(f_0 + \gamma_{R0}n_0)K\varepsilon}, \text{ with} \quad \text{eq. (H - 34)}$$

$$E_I = \frac{qn_0}{\varepsilon K}, \text{ and finally} \quad \text{eq. (H - 35)}$$

$$E_m = \frac{C}{2} \sqrt{E_0} E_0. \quad \text{eq. (H - 36)}$$

Please note, that eq. (H - 36) is partially based on an empirical expression (eq. (H - 2)). Therefore, the “field“ in the square root carries no dimension, but has the value of E_0 . An interpretation of the above field quantities in terms of the field quantities already introduced for the theoretical model of the photorefractive effect in crystals is given in “2.5.3.2.1.) Steady state

solutions for the space-charge field in polymers” on page 125.

From the real part and the imaginary part of eq. (H - 31) one obtains for the phase shift ϕ of the space-charge field with respect to the interference pattern:

$$\tan \phi = \frac{E_0^2 + E_D(E_D + E_I + E_q) + \frac{E_D E_m}{E_0}(E_I + E_q)}{\frac{E_D^2 E_q}{E_0} \left(\frac{E_m}{E_0} - \gamma p \right) - E_0 E_q (1 + \gamma p) - E_0 E_I \left(1 + \frac{E_m}{E_0} \right)}. \quad \text{eq. (H - 37)}$$

H.1.2.) Build-up dynamics for the space-charge field in polymers

Based on Schildkraut’s model, Yuan et. al. derived an analytical expression for the build-up dynamics of the space-charge field in polymers [82]. In analogy to the original Schildkraut model, they formulated their theoretical formalism in dimensionless form as well, which is subsequently rewritten to SI units.

In order to derive an expression for the build-up dynamics of the space-charge field, the expressions eq. (H - 16) for n , E , μ , Φ , N_T , γ_T , I and δ are rewritten into the form:

$$g(x, t) = g_0(t) + g_1(t)e^{iKx}. \quad \text{eq. (H - 38)}$$

It shall be assumed, that the zero order Fourier component evolves much faster than the first order component, as was assumed before for the derivation of the dynamics of the space charge fields in PR crystals. Thus, g_0 may be approximated as having reached its steady state more or less instantaneously compared to g_1 , and will be treated as constant in time.

Eq. (38) is inserted into eq. (H - 14) and eq. (H - 15), which, accounting furthermore for eq. (H - 20) and eq. (H - 21) yields:

$$\text{eq. (H - 39)}$$

$$\begin{aligned} \dot{n}_1 + n_1[\Gamma_I + \Gamma_R - (\gamma_{R0} - \gamma_{T0})N_{T0}] - i\frac{\varepsilon}{q}K\dot{E}_1 + \\ + E_1 \left[\frac{C}{2\sqrt{E_0}}\Gamma_{die}(n_0 + N_{T,i} - N_{T0}) + f_0\frac{p}{E_0}(n_0 + N_{T,i} - N_{T0} - N_{G,i}) - i\frac{\varepsilon}{q}K\Gamma_I \right] + \\ + \gamma_{T1}n_0N_{T0} - \delta_1(N_{T,i} - N_{T0}) + N_{T1}(\Gamma_T - \Gamma_I) = \\ = -mf_0(n_0 + N_{T,i} - N_{T0} - N_{G,i}) \end{aligned}$$

and:

$$\begin{aligned} \dot{n}_1 + n_1[\Gamma_I + \Gamma_R + \Gamma_D + i\Gamma_E - (\gamma_{R0} - \gamma_{T0})N_{T0}] + \\ + E_1 \left[\frac{C}{2\sqrt{E_0}}\Gamma_{die}(n_0 + N_{T,i} - N_{T0}) + f_0\frac{p}{E_0}(n_0 + N_{T,i} - N_{T0} - N_{G,i}) \right] + \\ + E_1 \left[i\frac{\varepsilon C\sqrt{E_0}}{2q}K\Gamma_{die} + i\frac{\varepsilon}{q}K(\Gamma_{die} - \Gamma_I) \right] + \\ + \gamma_{T1}n_0N_{T0} - \delta_1(N_{T,i} - N_{T0}) + N_{T1}(\Gamma_T - \Gamma_I) = \\ = -mf_0(n_0 + N_{T,i} - N_{T0} - N_{G,i}) \end{aligned} \quad \text{eq. (H - 40)}$$

Since it was assumed, that the zero order Fourier component evolves instantaneously, the result for n_0 is the steady-state solution eq. (H - 17). In order to obtain the time dependent first order component of the complex space charge field E_1 , eq. (H - 39) is subtracted from eq. (H - 40)

yielding:

$$n_1 = \left(\frac{-i\frac{\varepsilon}{q}K}{\Gamma_D + i\Gamma_E} \right) \dot{E}_1 - \left(\frac{i\frac{\varepsilon C \sqrt{E_0}}{2q} K \Gamma_{die} + i\frac{\varepsilon}{q} K \Gamma_{die}}{\Gamma_D + i\Gamma_E} \right) E_1 \quad \text{eq. (H - 41)}$$

and the resulting expression is differentiated with respect to t :

$$\dot{n}_1 = \left(\frac{-i\frac{\varepsilon}{q}K}{\Gamma_D + i\Gamma_E} \right) \ddot{E}_1 - \left(\frac{i\frac{\varepsilon C \sqrt{E_0}}{2q} K \Gamma_{die} + i\frac{\varepsilon}{q} K \Gamma_{die}}{\Gamma_D + i\Gamma_E} \right) \dot{E}_1. \quad \text{eq. (H - 42)}$$

Inserting eq. (H - 41) and eq. (H - 42) into eq. (H - 40) results in a second order differential equation for E_1 :

$$a\ddot{E}_1 + b\dot{E}_1 + cE_1 = d \quad \text{eq. (H - 43)}$$

with the coefficients a , b , c , and d given by:

$$a = \frac{-i\frac{\varepsilon}{q}K}{\Gamma_D + i\Gamma_E}, \quad \text{eq. (H - 44)}$$

$$b = \frac{-i\frac{\varepsilon}{q}K(\Gamma_I + \Gamma_R + \Gamma_D + i\Gamma_E - (\gamma_{R0} - \gamma_{T0})N_{T0}) - i\frac{\varepsilon}{q}K\Gamma_{die}\left(\frac{C\sqrt{E_0}}{2} + 1\right)}{\Gamma_D + i\Gamma_E} \quad \text{eq. (H - 45)}$$

$$c = \frac{-\left(i\frac{\varepsilon C \sqrt{E_0}}{2q} K \Gamma_{die} + i\frac{\varepsilon}{q} K \Gamma_{die}\right)(\Gamma_I + \Gamma_R - (\gamma_{R0} - \gamma_{T0})N_{T0})}{\Gamma_D + i\Gamma_E} - i\frac{\varepsilon}{q} K \Gamma_I + \quad \text{eq. (H - 46)}$$

$$+ \frac{C}{2\sqrt{E_0}} \Gamma_{die}(n_0 + N_{T,i} - N_{T0}) + f_0 \frac{p}{E_0}(n_0 + N_{T,i} - N_{T0} - N_{G,i})$$

and:

$$d = -mf_0(n_0 + N_{T,i} - N_{T0} - N_{G,i}) - \gamma_{T1}n_0N_{T0} + \quad \text{eq. (H - 47)}$$

$$+ \delta_1(N_{T,i} - N_{T0}) - N_{T1}(\Gamma_T - \Gamma_I)$$

These expressions may be simplified a bit when inserting the rates given by eq. (H - 25) to eq. (H - 30), however, this will not be formulated here, since calculating some absolute values is not the focus of interest here, but rather obtaining an analytical expression, which gives an idea of the general behavior of the PR space-charge field as a function of time.

In order to solve for eq. (H - 43), boundary conditions must be found. It is ostensibly clear, that $n_1(t=0) = E_1(t=0) = 0$, which requires $\dot{E}_1(t=0) = 0$ as well, according to eq. (H - 41). Furthermore, eq. (H - 39) (or eq. (H - 40)) yields $\dot{n}_1 = -mf_0(n_0 + N_{T,i} - N_{T0} - N_{G,i}) \neq 0$ for $t=0$, which requires $\ddot{E}_1(t=0) \neq 0$ from eq. (H - 42), ensuring, that the solution will not be trivial. The solution of eq. (H - 43) thus writes:

$$E_1(t) = \frac{d}{c} \left[1 - A_1 e^{\frac{1}{\tau_1} t} - A_2 e^{\frac{1}{\tau_2} t} \right], \quad \text{eq. (H - 48)}$$

with:

$$A_1 = \frac{b}{2\sqrt{b^2 - 4ac}} + \frac{1}{2}, \quad \text{eq. (H - 49)}$$

$$\frac{1}{\tau_1} = \frac{-b + \sqrt{b^2 - 4ac}}{2a}, \quad \text{eq. (H - 50)}$$

$$A_2 = \frac{1}{2} - \frac{b}{2\sqrt{b^2 - 4ac}} \quad \text{and} \quad \text{eq. (H - 51)}$$

$$\frac{1}{\tau_2} = \frac{-b - \sqrt{b^2 - 4ac}}{2a}. \quad \text{eq. (H - 52)}$$

The physically relevant real part of the complex space-charge field $E_1(t)$, $E_{sc}(x,t)$, is presented in “2.5.3.2.2.) Build-up dynamics for the space-charge field in polymers” on page 126. The amplitude and phase parameters mentioned therein and referring to the current section are as follows: R_1 and ϕ_1 are the amplitude and the phase of c/d , R_2 and ϕ_2 are the amplitude and the phase of A_1 , and R_3 and ϕ_3 are the amplitude and the phase of A_2 . The real time constants $-\tau_{sc1,2}$ are given by the real parts of the complex time constants $\tau_{1,2}$, respectively, and the phase parameters ω_1 and ω_2 result from the imaginary part of the complex time constants $\tau_{1,2}$.

H.1.3.) Erasure dynamics of the space-charge field in polymers

The erasure dynamics of PR polymers may be considered in two ways. The first and most proximate way is to invert the boundary conditions preceding eq. (H - 48) and solve eq. (H - 43). However, this approach suffers from the basic limitation to a system with solely deep traps, which has been applied in order to obtain an analytical solution for Schildkraut’s model. On the other hand, Cui et. al. recently presented a more detailed analysis of the erasure process in PR polymers [83] taking into account different levels of traps. Both approaches will be outlined below.

H.1.3.1.) Erasure dynamics in Schildkraut’s model

As mentioned before, the erasure dynamics of the space-charge field in PR polymers may be described on the basis of Schildkraut’s model. The path of this analysis has already been outlined above. In order to solve for the erasure of the space-charge field, the boundary conditions for eq. (H - 43) must be altered compared to above. For the erasure process $n_1(t \rightarrow \infty) = E_1(t \rightarrow \infty) = 0$, which requires $\dot{E}_1(t \rightarrow \infty) = 0$ as well, according to eq. (H - 41). Furthermore, eq. (H - 39) (or eq. (H - 40)) yields $\dot{n}_1 = -mf_0(n_0 + N_{T,i} - N_{T0} - N_{G,i}) \neq 0$ for $t \rightarrow \infty$, which requires $\ddot{E}_1(t \rightarrow \infty) \neq 0$ from eq. (H - 42). It is furthermore clear that $n_1(t = 0) = n_1$ and $E_1(t = 0) = E_1$. Thus, the boundary conditions are exactly inverted and the solution of eq. (H - 43) thus writes:

$$E_1(t) = A_1' e^{\frac{1}{\tau_1} t} + A_2' e^{\frac{1}{\tau_2} t}. \quad \text{eq. (H - 53)}$$

In order to obtain an analytical solution for A_1' and A_2' , the boundary condition $E_1(t = 0) = E_1$ must be substantiated. Presuming that the grating has been recorded to steady-state in advance of the considered erasure process, one obtains from eq. (H - 48): $E_1(t = 0) = d/c$. It is furthermore clear that $\dot{E}_1(t = 0) = 0$ will apply for this case. Then one obtains:

$$A_1' = \frac{d}{c} \left(\frac{b}{2\sqrt{b^2 - 4ac}} + \frac{1}{2} \right) \text{ and} \quad \text{eq. (H - 54)}$$

$$A_2' = \frac{d}{c} \left(\frac{1}{2} - \frac{b}{2\sqrt{b^2 - 4ac}} \right) \quad \text{eq. (H - 55)}$$

and the corresponding complex time constants given by eq. (H - 50) and eq. (H - 52).

The physically relevant real part of the complex space-charge field $E_1(t)$, i.e. $E_{sc}(x,t)$, is presented in “2.5.3.2.3.1.) Erasure dynamics in Schildkraut’s model” on page 127. The amplitude and phase parameters mentioned therein are as follows: R_1' and ϕ_1' are the amplitude and the phase of A_1' and R_2' and ϕ_2' are the amplitude and the phase of A_2' . The time constants $-\tau_{sc1,2}$ result from the real parts and the circular frequencies ω_1 and ω_2 result from the imaginary parts of the complex time constants $\tau_{1,2}$, respectively.

H.1.3.2.) Cui’s approach to the erasure dynamics

The main factors affecting the dynamics of the space-charge field in some PR material are the generation, transportation, and trapping of charge carriers. The field dependency of the quantum efficiency of charge generation, the charge trapping rate and the charge carrier mobility result from the positional and energetic disorder of the charge transporting and trapping sites in the polymer matrix. Presumed that holes are the only free charge carriers present in the medium and that their negative countercharges are fixed at the generation sites, the energy levels of the trapping sites should follow some particular distribution, and there will be a certain density of traps for a given energy level E . Trapped holes may be detrapped thermally and/or optically with different detrapping rates depending on the energy levels of the involved trapping sites. Thus, by integration over all energetic levels the following rate equations at constant external field may be formulated:

$$\begin{aligned} \frac{\partial n}{\partial t} &= \int_0^\infty \alpha_G(E) [N_G(E) - N_G^i(E)] dE - \int_0^\infty \gamma_R(E) n N_G^i(E) dE - \frac{\partial N_T}{\partial t} - \frac{1}{q} \frac{\partial \dot{j}}{\partial x} \\ \frac{\partial N_T}{\partial t} &= - \int_0^\infty \delta(E) N_T^i(E) dE + \int_0^\infty \gamma_T(E) n [N_T(E) - N_T^i(E)] dE \end{aligned} \quad \text{eq. (H - 56)}$$

$$\frac{\partial N_D^i}{\partial t} = \frac{\partial n}{\partial t} + \frac{\partial N_T}{\partial t} + \frac{1}{e} \frac{\partial \dot{j}}{\partial x}$$

Here n , N_G , N_G^i , N_T and N_T^i are the absolute densities of free holes, hole generators (i.e. neutral sensitizers), ionized generators (i.e. ionized sensitizers), (neutral) traps and filled (i.e. ionized) traps, respectively, and q is the elementary charge. The quantities $x(E)$ represent the value of x at the energy level E . \dot{j} is the current density according to eq. (H - 6) and $\gamma_R(E)$ and $\gamma_T(E)$ are the geminate recombination rate and the trapping rate, respectively. The photogeneration rate $\alpha_G(E)$ and the detrapping rate $\delta(E)$ may be expressed as:

$$\begin{aligned} \alpha_G(E) &= s_G(E) I \\ \delta(E) &= s_T(E) I + \beta(E) \end{aligned} \quad \text{eq. (H - 57)}$$

where I is the light intensity, $\beta(E)$ is the thermal detrapping rate and $s_G(E)$ and $s_T(E)$ are the light excitation cross sections for generators and filled traps. Please note, that α_G and δ are spatially constant for the erasure process.

By means of the mean value theorem the integrals in eq. (H - 56) can be rewritten into the general form:

$$\int_a^b f(x)g(x)dx = (b-a)f(c)\int_a^b g(x)dx, \quad \text{eq. (H - 58)}$$

where $a < c < b$. A particular consideration of the limiting value of $(b-a)f(c)$, which, strictly speaking, is mathematically required may be replaced by an ostensible physical consideration. The function f in eq. (H - 58) is considered as related to the quantities α_G , γ_R , γ_T and δ . These quantities are always ≥ 0 and $< +\infty$ by definition and, thus, their average value $(b-a)f(c)$ is finite and the characteristic value for the considered system. Accordingly, the integrals in eq. (H - 56) may be rewritten as:

$$\begin{aligned} \int_0^\infty \alpha_G(E)[N_G(E)-N_G^i(E)]dE &= \alpha_G \int_0^\infty [N_G(E)-N_G^i(E)]dE = \alpha_G(N_G-N_G^i) \\ \int_0^\infty \gamma_R(E)nN_G^i(E)dE &= \gamma_R n N_G^i \\ \int_0^\infty \delta(E)N_T^i(E)dE &= \delta N_T^i \end{aligned} \quad \text{eq. (H - 59)}$$

$$\int_0^\infty \gamma_T(E)n[N_T(E)-N_T^i(E)]dE = \gamma_T n(N_T-N_T^i)$$

yielding finally:

$$\begin{aligned} \frac{\partial n}{\partial t} &= \alpha_G(N_G-N_G^i) - \gamma_R n N_G^i - \frac{\partial N_T}{\partial t} - \frac{1}{q} \frac{\partial j}{\partial x} \\ \frac{\partial N_T}{\partial t} &= -\delta N_T^i + \gamma_T n(N_T-N_T^i) \\ \frac{\partial N_G^i}{\partial t} &= \alpha_G(N_G-N_G^i) - \gamma_G n N_G^i \end{aligned} \quad \text{eq. (H - 60)}$$

where α_G , γ_R , γ_T and δ are the characteristic, discrete values of the system and α_G and δ result from eq. (H - 57):

$$\begin{aligned} \alpha_G &= s_G I \\ \delta &= s_T I + \beta \end{aligned} \quad \text{eq. (H - 61)}$$

with the characteristic, discrete values of s_G , s_T and β .

For the analysis of the erasure process it is presumed, that a steady-state PR space charge field has already been recorded. At $t = 0$, the writing beams are switched off, and a uniform erasure beam is turned on instantaneously, which does not match the Bragg condition of the recorded index grating. For $t \geq 0$, the quantities n , N_T , N_G^i and the electrical field may again be expressed in terms of their zero and first order Fourier components according to eq. (H - 38):

$$\begin{aligned} n(t, x) &= n_0 + n_1(t)e^{iKx} \\ N_G^i(t, x) &= N_{G0}^i + N_{G1}^i(t)e^{iKx} \\ N_T^i(t, x) &= N_{T0}^i + N_{T1}^i(t)e^{iKx} \\ E(t, x) &= E_0 + E_1(t)e^{iKx} \end{aligned} \quad \text{eq. (H - 62)}$$

where E_0 is the externally applied field. As above, the zero order components are assumed to reach their steady-state values almost instantaneously and, thus, are treated as constants in time.

The expressions eq. (H - 62) are then inserted into eq. (H - 60), eq. (H - 9), and eq. (H - 6), yielding a set of linear equations, from which all unknown first order components except $E_1(t)$ will be eliminated, yielding finally a differential equation for $E_1(t)$, which then must be solved taking into account appropriate boundary conditions. This procedure in principle has already been outlined above and will not be elaborated upon here once more. The results are presented in “2.5.3.2.3.2.) Cui’s approach to the erasure dynamics” on page 128.

List of publications

Publications:

Meerholz K., Bittner R., Bräuchle C., Volodin B. L., Sandalphon, Kippelen B., Peyghambarian N.

“Improved Long-term Stability of High-Performance Photorefractive Polymer Devices.”
Proc. SPIE - Int. Soc. Opt. Eng. (Organic Photorefractive Materials and Xerographic Photoreceptors) 2850, 100 (1996).

Meerholz K., Bittner R., Bräuchle C., Boldt P., Kirchberger T., Wichern J.

“Use of Highly Non-linear Optical Chromophores in Photorefractive Polymers.”
Proc. SPIE - Int. Soc. Opt. Eng. (Nonlinear Optical Properties of Organic Materials IX) 2852, 74 (1996).

Meerholz K., Bittner R., Bräuchle C.

“Grating Competition in Photorefractive Polymers.”
J. Inf. Rec. 22, 475 (1996).

Meerholz K., Bittner R., De Nardin Y., Bräuchle C., Hendrickx E., Volodin B.L., Kippelen B., Peyghambarian N.

“Stability Improvement of High-Performance Photorefractive Polymers Containing Eutectic Mixtures of Electrooptic Chromophores.”
Adv. Mat. 9, 1043 (1997).

Würthner F., Wortmann R., Matschiner R., Lukaszuk K., Meerholz K., Bittner R., De Nardin Y., Bräuchle C., Sens R.,

“Merocyaninfarbstoffe im Cyaninlimit: Eine neue Chromophorklasse für photorefractive Materialien.”
Angew. Chem. Int. Ed. Engl. 36, 2765 (1997).

Bittner R., Meerholz K., Bräuchle C.

“Influence of the Glass-transition Temperature and the Chromophore Content on the Grating Build-up Dynamics of PVK-based Photorefractive Polymers.”
Appl. Opt., 37, 2843 (1998)

Bittner R., Bräuchle C., Meerholz K.

“Influence of Hologram Bending on the Diffraction Efficiency of Organic Photorefractive Thin Film Devices: A Simple Model Calculation.”
J. Inf. Rec., 24, 469 (1998)

Meerholz K., Mecher E., Bittner R., De Nardin Y.

“Competing Photorefractive Gratings in polymers.”

J. Opt. Soc. Am. B, 15(7), 2114 (1998)

Meerholz K., Bittner R., DeNardin Y.

“Field Asymmetry of the Gain Coefficient in Organic Photorefractive Devices.”

Opt. Comm., 150, 205 (1998)

K. Meerholz, Y. De Nardin, R. Bittner, F. Würthner, R. Wortmann

“Improved Performance of Photorefractive Polymers Based on Merocyanine Dyes in a Polar Matrix.”

Appl. Phys. Lett. 73, 4 (1998).

Meerholz K., Bittner R., De Nardin Y., Bräuchle C.

“Improved Long-term Stability and Performance of Photorefractive Polymer Devices Containing Eutectic Mixtures of Electro-optic Chromophores.”

Mol. Cryst., Liq. Cryst., 315, 99 (1998).

Meerholz K., De Nardin Y., Bittner R., Würthner F., Wortmann R.

" Improved Performance of Photorefractive Polymers Based on Merocyanine Dyes in a Polar Matrix"

Appl. Phys. Lett. 73, 4 (1998).

Bittner R., Däubler T. K., Neher D., Meerholz K.

"Influence of the Glass-transition Temperature and the Chromophore Content on the Steady-state Performance of PVK-based Photorefractive Polymers"

Adv. Mat. 11, 123 (1999).

Bittner R., Stepanov S. I., Meerholz K.

"Non-steady-state Currents and Photo-EMF in Photorefractive Polymers"

Appl. Phys. Lett. 74, 3723 (1999)

Mecher E., Bittner R., Bräuchle C., Meerholz K.

" Optimization of the Recording Scheme for Fast Holographic Response in Photorefractive Polymers "

Synth. Met. 102, 993 (1999)

Bittner R., Stepanov S. I., Meerholz K.

“Non-steady-state Photo-EMF Effect in Photorefractive Polymers.”

Proc. SPIE - Int. Soc. Opt. Eng. (Organic Photorefractives, Photoreceptors, Waveguides, and Fibers) 3799, 67 (1999).

Daubler T. K., Bittner R., Meerholz K., Cimrova V., Neher D.

“Charge Carrier Photogeneration, Trapping, and Space-charge Field Formation in PVK-based Photorefractive Materials.”

Phys. Rev. B 61(20), 13515 (2000)

Steckman G., Bittner R., Meerholz K., Psaltis D.

“Multiplexing in Photorefractive Polymers”

Opt. Comm., 185, 13-17 (2000)

Bittner R., Meerholz K., Steckman G., Psaltis D.

“Dark Decay of Holograms in Photorefractive Polymers.”

Appl. Phys. Lett. 81(2), 211 (2002)

Daubler T. K., Kulikovskiy L., Neher D., Cimrova V., Hummelen J. C., Mecher E., Bittner R., Meerholz K.

“Photoconductivity and Charge Carrier Photogeneration in Photorefractive Polymers.”

Proc. SPIE - Int. Soc. Opt. Eng. (Nonlinear Optical Transmission Processes and Organic Photorefractive Materials) 4462, 206 (2002)

Stepanov S. I., Garcia R. R., Pernas V. C., Mansurova S., Bittner R., Meerholz K.

“Investigation of Reflectance Gratings in PVK-based Photorefractive Polymers by Photo-EMF and Self-diffraction Techniques.”

Proc. SPIE - Int. Soc. Opt. Eng. (Nonlinear Optical Transmission Processes and Organic Photorefractive Materials) 4462, 178 (2002)

Mecher E., Bittner R., Braeuchle C., Meerholz K., Zelichenok A., Wender M., Vaganova E., Yitzchaik S.

“Photorefractive Polymer Composites Based on Poly(4-vinylpyridine).”

Proc. SPIE - Int. Soc. Opt. Eng. (Nonlinear Optical Transmission Processes and Organic Photorefractive Materials) 4462, 159 (2002)

Posters:

Bittner R., Meerholz K., Bräuchle C.

Influence of the Glass-Transition Temperature and the Chromophore Content on the Performance of Photorefractive Polymers
3rd EUROPEAN CONFERENCE ON APPLICATIONS OF POLAR DIELECTRICS
Bled, Slovenia, 26.-29.8.1996

Mecher E., Meerholz K., Bittner R., Bräuchle C.

Competing Photorefractive Gratings in Organic Thin Film Devices
DPG-FRÜHJAHRSTAGUNG, Bayreuth, 9.-13.3.1998

Meerholz K., Bittner R., DeNardin Y., Würthner F., Wortmann R.

Improved Performance of Photorefractive Polymers Based on Merocyanine Dyes in a Polar Matrix
DPG-FRÜHJAHRSTAGUNG, Bayreuth, 9.-13.3.1998

Meerholz K., Bittner R., DeNardin Y., Mecher E., Bräuchle C.

Beam-Fanning-Induced Asymmetric Holographic Performance of Photorefractive Polymer Devices
DPG-FRÜHJAHRSTAGUNG, Bayreuth, 9.-13.3.1998 (u.a.)

Bittner R., Meerholz K., Bräuchle C.

Influence of Hologram Bending on the Diffraction Efficiency of Organic Photorefractive Thin Film Devices: A Simple Model Calculation
DPG-FRÜHJAHRSTAGUNG, Bayreuth, 9.-13.3.1998

Bittner R., Meerholz K., Bräuchle C.

Influence of the Sensitizer Concentration on the Performance of Photorefractive Thin Film Devices
JAHRESTAGUNG DER VW-STIFTUNG, Seeheim-Jugenheim 10.1998

Bittner R., Bräuchle C., Meerholz K.

Einfluß der Sensibilisatorkonzentration auf die Performanz von photorefraktiven (PR) Polymerkompositen
DPG-FRÜHJAHRSTAGUNG, Bayreuth, 22.-26.3.1999

Bittner R., Meerholz K., Steckman G., Psaltis D.

Holographic Multiplexing in Photorefractive Polymers
DPG-FRÜHJAHRSTAGUNG, Berlin, 2.4.2001-6.4.2001

Talks:

Bittner R.

Influence of the Glass-Transition Temperature and the Chromophore Content on the Performance of Photorefractive Polymers

DPG-FRÜHJAHRSTAGUNG, Münster, 17.-21.3.1997

Bittner R.

Investigations on Photorefractive Polymers with Different Glass-Temperatures

SPIE 42nd ANNUAL MEETING, San Diego, 27.7-1.8.1997

Bittner R.

Non-steady-state Currents and Photo-EMF in Photorefractive Polymers

SPIE 44th ANNUAL MEETING, Denver, 18.-23.7.1999

Acknowledgements

First and foremost I would like to thank my advisor Prof. Dr. Klaus Meerholz. The scientific and non-scientific discussions, his suggestions and ideas contributed a great deal to my thesis. The amicable atmosphere and his great support in all issues of scientific work made me enjoy working for this thesis very much.

My special thanks go to Dr. Theo Woike for serving as referee for this thesis.

I would like to acknowledge Prof. Dr. Christoph Braeuchle for the opportunity of working under excellent conditions at the Physical Chemistry Department in Munich. I would also like to thank Dr. Moritz Ehrl for his continuous support in administrative issues and for his funny stories.

I greatly benefited from working together with Dr. Thomas Daeubler and Prof. Dr. Dieter Neher. It was always a pleasure to meet and discuss polymer physics with these experts. The work of Dr. Daeubler contributed substantially to the understanding of the photorefractive properties of the materials investigated in this thesis.

For a very interesting, fruitful, and nice stay at California Institute of Technology in Pasadena my special thanks go to Dr. Gregory Steckman and Prof. Dr. Demetri Psaltis. I enjoyed very much working together with Dr. Steckman and took home a whole bunch of new ideas and problems to solve. A major part of my thesis has been motivated by insights I got during my stay at CalTech.

I would also like to thank the entire working group of Prof. Dr. Demetri Psaltis for their hospitality and nice working atmosphere, which immediately made me feel at home in Pasadena. Special thanks go to the “european fraction” for including me in their spare time activities.

Furthermore, I would like to acknowledge the German Academic Exchange Service (DAAD) for financially supporting my stay at CalTech.

I also enjoyed very much working together with Prof. Dr. Serguei Stepanov from INAOE in Puebla during his stay as guest researcher in the working group of Prof. Meerholz. The atmosphere was very friendly and it was always very fruitful and a pleasure discussing with this expert in photorefractivity in inorganic crystals and non steady-state holographic currents.

My special thanks also go to my colleagues Dr. Erwin Mecher, Francisco (“Paco”) Gallego-Gomez, Dr. Markus (“der Perser”) Groß, Dr. David Mueller, Dr. Elmar Schmaelzlin, and Christian Ritzel for the relaxed working atmosphere and the always funny and mostly fruitful discussions about science and much more.

Last, but not least, I want to thank my family for their constant and unconditional support during my studies. Special thanks belong to my father, who tried hard to smooth my German-English formulations in this thesis without distorting the statements, the scientific background of many of which he has not been familiar with.

I am very grateful to my wife Susi for her understanding and her unconditional love.

Erklärung

Ich versichere, daß ich die von mir vorgelegte Dissertation selbständig angefertigt, die benutzten Quellen und Hilfsmittel vollständig angegeben und die Stellen der Arbeit - einschließlich Tabellen, Karten und Abbildungen -, die anderen Werken im Wortlaut oder dem Sinn nach entnommen sind, in jedem Einzelfall als Entlehnung kenntlich gemacht habe; daß diese Dissertation noch keiner anderen Fakultät oder Universität zur Prüfung vorgelegen hat; daß sie - abgesehen von den im Rahmen der Publikationsliste am Ende dieser Arbeit (siehe: "List of publications") angegebenen und diese Arbeit betreffenden Teilpublikationen - noch nicht veröffentlicht worden ist sowie, daß ich eine solche Veröffentlichung vor Abschluß des Promotionsverfahrens nicht vornehmen werde. Die Bestimmungen der Promotionsordnung der Mathematisch-Naturwissenschaftlichen Fakultät der Universität zu Köln sind mir bekannt. Die von mir vorgelegte Dissertation ist von Prof. Dr. Klaus Meerholz betreut worden.

Gräfelfing, Oktober 2003

Reinhard Bittner
